UNIVERSITAT de
BARCELONA

Modelling of the Chemical and Light Interactions in Individual Metal Oxide Nanowires for Sensing Applications

Juan Daniel Prades García

Modelling of the Chemical and Light Interactions in Individual Metal Oxide Nanowires for Sensing Applications

Juan Daniel Prades García
Director: Dr. Albert Cirera Hernàndez

Departament d'Electrònica
Grup d'Enginyeria i Materials Electrònics (EME)
Institut de Nanociència i Nanotecnologia (IN2UB)
Programa de Doctorat en Nanociències

UNIVERSITAT DE BARCELONA
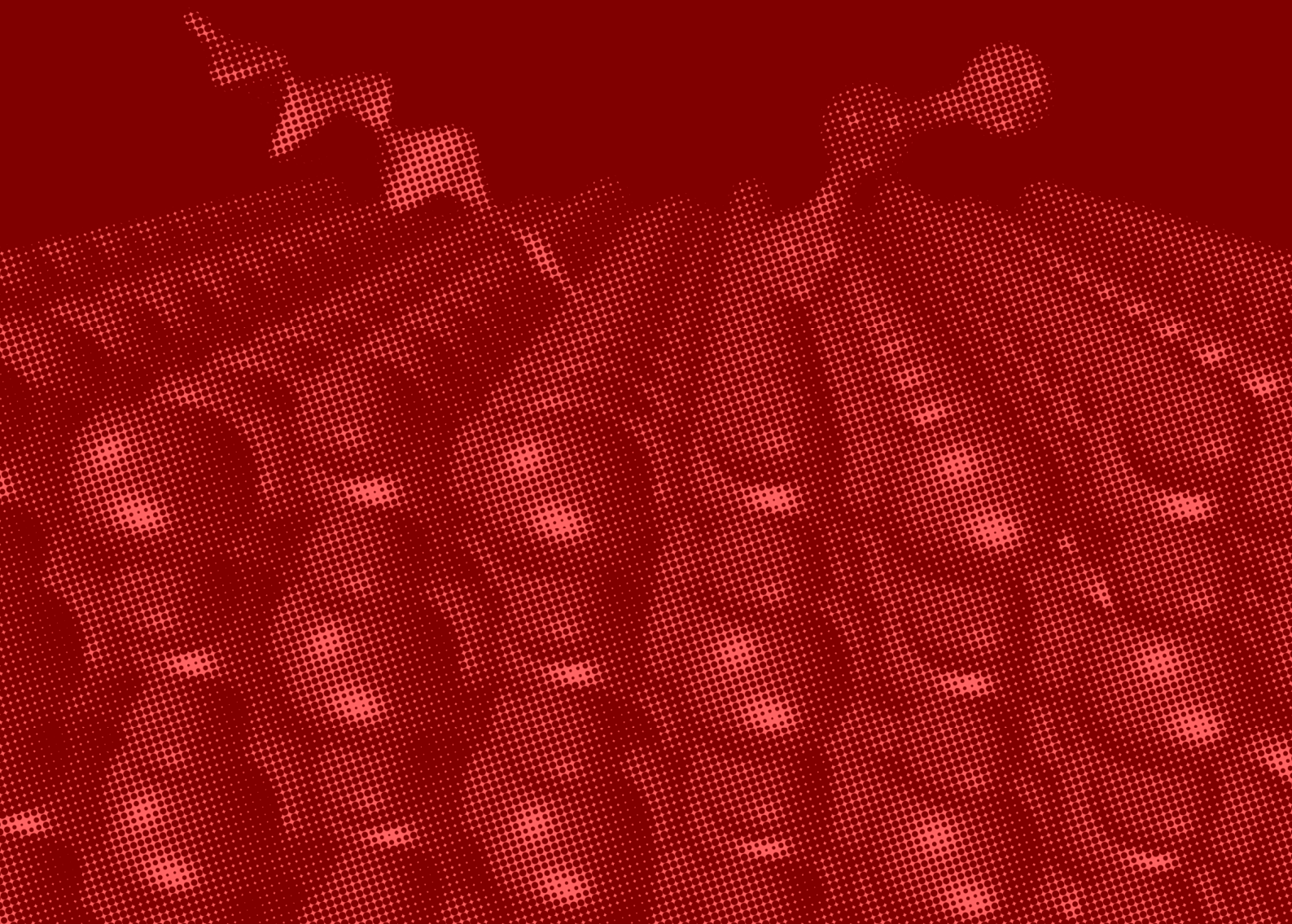
Programa de Doctorat en Nanociències

Modelling of the Chemical and Light Interactions in Individual Metal Oxide Nanowires for Sensing Applications

Tesi que presenta Juan Daniel Prades García

per optar al títol de Doctor per la Universitat de Barcelona

Director de la Tesi:

Dr. Albert Cirera Hernández
Professor Agregat

Departament d'Electrònica
Grup d'Enginyeria i Materials Electrònics (EME)
Institut de Nanociència i Nanotecnologia (IN²UB)

UNIVERSITAT DE BARCELONA

A la Còssima,
el Joan,
la Lola
i l'Albert.

Acknowledgement

First of all, I would like to thank the untiring support of Dr. Albert Cirera during the last four years of work, guiding me through my first steps in research with open-minded and truthful advices. I am also grateful to the rest of Professors of the Department of Electronics for sharing with me their expertise in so many fields. Specially, I appreciate the innumerable enlightening discussions with Prof. Joan Ramon Morante and his contagious energy.

I am thankful to the colleagues of the Department of Electronics: Alberto, Alex, Anna, Cristian, Erik, Eva, Luis, Marta, Olga, Paco, Román, Sònia, Teresa, Xavi, (in alphabetical order!). Without them, any of the here-presented results would have been achieved. Some of them shared with me their friendship, others their know-how and with some others I still share common projects for the future. All these people made me appreciate every single day I spent in the Department.

Moreover, I am indebted to everybody else who has contributed to my work during my Ph.D program in this institution and others, specially (in any specific order now) Dr. J. M. Pruneda and Prof. P. Ordejón (ICMAB–CSIC), Prof. K. Neyman and Prof. F. Illas (IQTCUB, Universitat de Barcelona), Dr. M. Epifani (CNR–IMM), Dr. M. Avella and Prof. J. Jiménez (Universidad de Valladolid), Prof. P. Ugliengo (Università delgi Studi di Torino), Prof. R. Orlando (Università degli studi del Piemonte Orientale), Dr. S. Barth (University College Cork) and Prof. S. Mathur (Universität zu Köln).

Finally, I wanted to express my sincere gratitude to my family and partner, Còssima, for their support and understanding.

0. Index

1. Introduction

Metal oxides (MOXs) are excellent materials for a number of sensing applications [1,2]. Their bulk properties correspond to a wide bandgap semiconductor spontaneously doped in nature by the presence of intrinsic point defects related to oxygen atoms [3]. Their surface properties are determined by the existence of surface trap states, acting as electron acceptor or donor centers [4], which are strongly influenced by chemisorbed molecules, and play a central role in the electron transport properties [5]. These physical and chemical properties (together with their low cost) make MOXs particularly suitable for ultraviolet light detection and chemical gas sensing [2]. Among these materials, zinc oxide (ZnO) [6] and tin dioxide (SnO_2) [7] have attracted great attention in both fields of sensor technology.

Today, the availability of MOX nanowires [8,9] and the possibility to apply them in functional sensing devices [10,11] opens the door to a deeper comprehension of the chemical and light interactions behind their sensing response. This Dissertation is completely devoted to the theoretical modeling and experimental assessment of these processes with individual nanowires. The election of SnO_2 and ZnO nanowires was motivated by their attractive features from the materials science and device development points of view.

Motivations from the materials science point of view.

Materials science is playing a central role in the development of novel and better sensor devices with superior performances. In many cases, these improvements are not based on a trial-and-error approach. Indeed, major advancements are driven by a deeper comprehension of the mechanisms and processes that provide to the materials their functionality [12]. Theoretical modeling of the material's properties is the driving force behind this knowledge-guided approach.

There exists an enormous theoretical background to explain most of the material's properties. From the solid-state and semiconductor physics [13] to the atomistic quantum chemistry [14], every theory makes a number of assumptions regarding the structural and morphological ordering of the materials that must be bear in mind when comparing simulations with experiments. In order words, the experimental validation of the theoretical predictions requires a certain control of the structural properties of the specimens.

The recent progress in the synthesis of a great variety of one-dimensional nanomaterials [15,16] and the development of nanomanipulation and nanocharacterization techniques [16,17] make possible fundamental studies with nanowires not even conceivable few years ago. Besides the new phenomena related to the nanoscale [18], the structural properties of the nanowires are also attractive (*Figure 1.1*). On the one hand, nanowires are single crystalline materials [8,9,15,16]. This essentially is one of the major approximations assumed in solid-state and semiconductor physics (periodic boundary condition or the Block's Theorem [13]). On the other hand, the nanowires are enclosed by well-defined surfaces ordered at atomic level [8,9]. As described in *Chapter 3*, this is the key assumption in the state-of-the-art atomistic models that describe gas-surface interactions.
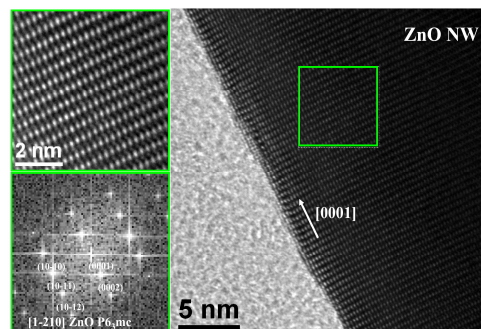
Figure 1.1. High Resolution Transmission Electron Microscopy (HRTEM) analysis of one of the MOX nanowires used in this work. Crystalline and defect-free ZnO grow along the [0001] direction. Surface roughness is less than 2 monolayers. *Images courtesy of Dr. J. Arbiol.*

For all these reasons, the opportunity to study only one of these MOX nanowires opens the door to experimental scenarios which are closer than ever to the theoretical models. To take advantage of this opportunity was one of the most compelling reasons that motivated the present work.

Motivation from the sensor devices point of view.

Current trends in sensors technology are pursuing to integrate both the control electronics and the sensing materials in microelectronic systems [19]. This exciting goal implies reducing the amount of sensing material as much as possible with the only limitation of the electrical access. In the last years, the possibility to control, manipulate and contact individual nanowires of MOXs opened the door to study nanosensors [10,16,17,20] which are close to the ultimate integration limits.

To date, the use of polycrystalline and particulate MOXs has been the best option to implement low-cost sensing devices [2,21]. However, the random nature of the network of crystallites and the key role played by the grain boundary effects [3] obscure the study of the transduction mechanism behind their response to external stimuli. Recent findings demonstrated that, in the appropriate conditions, the conduction along individual nanowires is a relatively straightforward situation that makes possible to gain deeper insight into the connection between transport properties and sensing interactions [10] (see *Figure 1.2*).

In applications where the transduction is a surface mediated process (such as chemical gas sensing), the use of nanomaterials improves the sensor response due to the dramatic increase of the surface-to-volume ratio in these materials [22]. But, what is more important, the well-defined and stable surfaces of the nanowires also improve the stability and reversibility of the sensing processes [11,22]. Moreover, the use of individual nanowires also provides and optimum scenario from the dynamic response point of view: chemicals and other analytes do not need to diffuse across tortuous porous networks and can easily reach the nanowire's surface [23]. In applications where the sensing interactions occur in the bulk (such as light detection), the use of single crystalline nanowires enhances the efficiency of the photon-electron interactions [24].

Despite there are still many technological challenges that hamper their application in real life [20], the study of these devices is contributing to preview and envisage the outstanding properties that can be exploited in the next future. The exploration of these prospects has also encouraged this work.
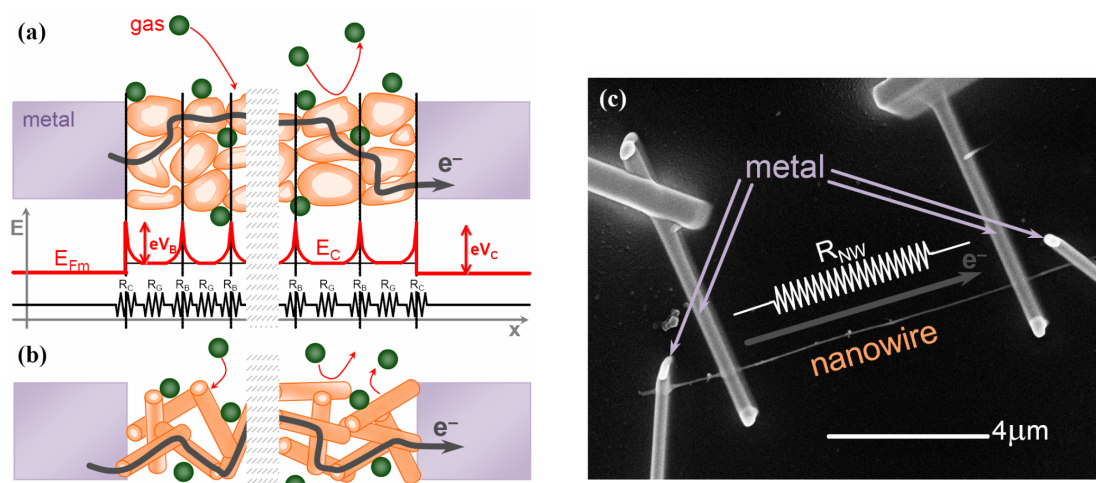
Figure 1.2. Schematic representation of conductometric chemical gas sensors based on MOX nanoparticles and nanowires. **(a)** In the case of a layer of nanoparticles, the electrons must flow across a random network of crystallites of arbitrary sizes and shapes. From the electron energy point of view, the electrons must overcome a number of potential barriers [both metal-semiconductor barriers at the contacts (eV_C) and intergrain boundary barriers (eV_B)]. The influence of the gas on these barriers determines the response of the sensors. From the electrical point of view, this is equivalent to an arbitrary network of resistors corresponding to the metal-semiconductor contacts (R_C), the grain boundary interfaces (R_B) and the MOX grains (R_G). From the dynamic point of view, molecules must diffuse across the inter-grain pores and this process partially determines the response and recovery times. **(b)** In the case of bundles of nanowires, the situation is essentially the same. **(c)** Instead, in the case of individual nanowires in 4-probe configuration, the conductometric response is only determined by the changes in the conduction channel along the nanowire (R_{NW}). In this measurement configuration, the parasitic contributions arising from the metal-semiconductor interface are eliminated. *Micrograph courtesy of R. Jiménez-Díaz.*

To conclude this introduction, I believe that the words of a wiser man may summarize better the spirit of this work. On December 29th of 1959, Richard P. Feynman, later awarded with the Nobel Price in Physics, gave his famous lecture *"There's Plenty of Room at the Bottom"* at an American Physical Society meeting at Caltech. According to his own words, *"The problems of chemistry and biology can be greatly helped if our ability to see what we are doing, and to do things on an atomic level, is ultimately developed – a development which I think can not be avoided"*. I am conscious that we are still far away from this magnificent vision and I only dare to say that this work may humbly contribute to its accomplishment.

1.1 Dissertation Outline

The **objectives** that steered the course of this Ph.D work are summarized in the next chapter (*Chapter 2: Objectives*).

The most relevant aspects of the **methodologies** used by the author during his Ph.D work are presented in the third chapter (*Chapter 3: Methodology*). This includes detailed information about the atomistic calculations performed, about the utilization of MOX nanoparticles and nanowires in sensor devices and about the electronic platform developed to interface with the here–studied devices. All this information is presented as it was published in 2 book chapters and 1 scientific paper.

The **results** of this work and their **discussion** (*Chapter 4: Results and Discussion*) are organized in 3 units, which correspond to the different areas developed by the author during his Ph.D work. Units are organized in a way that they include a short introduction to the particular topic, followed by the main results obtained (presented as they were published in scientific peer-reviewed journals) and finally, the most significant conclusions of every unit are summarized. This third chapter is organized as follows:

Unit 1: Gas Molecules – MOX interaction. This unit is devoted to the study of the chemical processes that take place at the surface of MOX nanowires. Firstly, *ab initio* atomistic calculations were applied to determine which surface terminations are realistic at the typical working temperatures of the sensors. Subsequently, the same theoretical framework was used to analyze their interaction with some relevant target gases (mainly NO and NO_2) yet unexplored from the atomistic point of view. These theoretical conclusions were experimentally validated with individual nanowires. As a result of these findings, other theoretical approaches, which are alternative to the conventional surface-centered description of the gas–MOX interaction, were proposed. Moreover, a novel strategy to operate these sensors that represents an important reduction in the power consumption of these devices was developed. The results of this unit were published in 6 scientific papers.

Unit 2: Light – MOX interaction. In this unit, the photoresponse of MOX nanowires is described and modeled on the basis of the principles ruling the transport properties in semiconductors. The insight obtained in the previous unit into

the surface properties of these materials was used to explain the long-term photoconductive states that limit the performance of MOX nanowires as light detectors. These findings, which are supported experimentally, were reported in 2 scientific papers.

Unit 3: Simultaneous Gas – Light – MOX interaction. The results obtained in the two previous units were used to propose, model, implement and validate an alternative approach to operate these chemical sensors based on the photoactivation of the surface chemical interactions. In addition to this, the influence of the atomic arrangement at the surface of MOXs on their luminescence was shown to be a good experimental method to probe the surface atomistic ordering. The results of this unit were published in 5 scientific papers.

In the last chapter (*Chapter 5: Conclusions*), the most significant **conclusions** of this Ph.D Dissertation are summarized.

At the end of this manuscript two appendices contain the CV of the author (*Appendix A: Scientific Curriculum*) and a mandatory summary in an official language of the Universitat de Barcelona (*Appendix B: Resum en català*).

The author sincerely hopes that this structure, which is relatively new in the Department of Electronics of the Universitat de Barcelona, will facilitate the comprehension of the here–presented results.

1.2 List of Publications

Only the publications contained in this list shall be considered for the evaluation of this Ph.D Dissertation. A copy of all these publications can be found in the **page** indicated. A complete list of publications of the author, updated on December 2008, is included in his the CV (*Appendix A: Scientific Curriculum*).

1. J.D. Prades, A. Cirera, J.R. Morante, *"Applications of DFT Calculations to Chemical Gas Sensors: Desing and Understanding"* in *"Quantum Chemical Calculations of Surfaces and Interfaces of Materials"* (Ed. V. A. Basiuk and P. Ugliengo), chap. 13, pp. 243-288, American Scientific Publishers: Valencia CA (2008). ISBN: 1-58883-138-8. **Page 27**

2. T. Andreu, J. Arbiol, A. Cabot, A. Cirera, J.D. Prades, F. Hernandez-Ramirez, A. Romano-Rodriguez, J.R. Morante, *"Nanosensors: Controlling Transduction Mechanisms an the Nanoscale Using Metal Oxides and Semiconductors"* in *"Sensors Based on Nanostructured Materials"* (Ed. F. Arregui), chap. 5, pp. 79-129, Springer Science + Business Media (2009). ISBN: 978-0-387-77752-8. **Page 73**

3. J.D. Prades, A. Cirera, J.R. Morante, J.M. Pruneda, P. Ordejón, *"Ab initio study of NOx compounds adsorption on SnO$_2$ surface"* Sens. Actuators B-Chem. **126**, 99-110 (2007). **Page 141**

4. J.D. Prades, A. Cirera, J.R. Morante, *"First-Principles Study of NO$_x$ and SO$_2$ Adsorption onto SnO$_2$(110)"* J. Electrochem. Soc. **154**, H675-H680 (2007). **Page 147**

5. J.D. Prades, A. Cirera, J.R. Morante, *"Ab initio calculations of NO$_2$ and SO$_2$ chemisorption onto non-polar ZnO surfaces"* Thin Sol. Films, submitted (2008). **Page 153**

6. J.D. Prades, R. Jimenez-Diaz, F. Hernandez-Ramirez, S. Barth, A. Cirera, A. Romano-Rodriguez, S. Mathur, J.R. Morante, *"Ultralow power consumption gas sensors based on self-heated individual nanowires"* Appl.Phys.Lett. **93**, 123110 (2008). **Page 157**

7. J.D. Prades, R. Jimenez-Diaz, F. Hernandez-Ramirez, A. Cirera, A. Romano-Rodriguez, J.R. Morante, S. Barth, P. Jun, S. Mathur, *"An experimental method to estimate of the temperature of individual nanowires"* Int. J. Nanotechnol., accepted for publication (2008). **Page 161**

8. F. Hernandez-Ramirez, J.D. Prades, A. Tarancon, S. Barth, O. Casals, R. Jimenez-Diaz, E. Pellicer, J. Rodriguez, J.R. Morante, M.A. Juli, S. Mathur, A. Romano-Rodriguez, *"Insight into the role of oxygen diffusion into the sensing mechanisms of SnO₂ nanowires"* Adv. Funct. Mater. **18**, 2990-2994 (2008). **Page 171**

9. J.D. Prades, R. Jimenez-Diaz, F. Hernandez-Ramirez, L. Fernandez-Romero, T. Andreu, A. Cirera, A. Romano-Rodriguez, A. Cornet, J.R. Morante, S. Barth, S. Mathur, *"Toward a systematic understanding of photodetectors based on individual metal oxide nanowires"* J. Phys. Chem. C **112**, 14639-14644 (2008). **Page 181**

10. J.D. Prades, F. Hernandez-Ramirez, R. Jimenez-Diaz, M. Manzanares, T. Andreu, A. Cirera, A. Romano-Rodriguez, J.R. Morante, *"The effects of electron-hole separation on the photoconductivity of individual metal oxide nanowires"* Nanotechnol. **19**, 465501 (2008). **Page 193**

11. J.D. Prades, R. Jimenez-Diaz, F. Hernandez-Ramirez, S. Barth, J. Pan, A. Cirera, A. Romano-Rodriguez, S. Mathur, J.R. Morante, *"High performance UV light-operated gas sensors based on individual SnO₂ nanowires for room temperature applications"* Appl. Phys. Lett., submitted (2008). **Page 207**

12. J.D. Prades, R. Jimenez-Diaz, F. Hernandez-Ramirez, M. Manzanares, T. Fischer, J. Pan, T. Andreu, A. Cirera, A. Romano-Rodriguez, S. Mathur, J.R. Morante, *"On the Role of the Illumination Conditions in the Performance of Room Temperature Gas Sensors Based on Individual SnO₂ Nanowires"* Chem. Mater., submitted (2008). **Page 211**

13. J.D. Prades, J. Arbiol, A. Cirera, J.R. Morante, M. Avella, L. Zanotti, E. Comini, G. Faglia, G. Sberveglieri, *"Defect study of SnO₂ nanostructures by cathodoluminescence analysis: Application to nanowires"* Sens.ActuatorsB-Chem. **126**, 6-12 (2007). **Page 233**

14. J.D. Prades, A. Cirera, J.R. Morante, A. Cornet, *"Ab initio insights into the visible luminescent properties of ZnO"* Thin Sol. Films **515**, 8670-8673 (2007). **Page 241**

15. M. Epifani, J.D. Prades, E. Comini, E. Pellicer, M. Avella, P. Siciliano, G. Faglia, A. Cirera, R. Scotti, F. Morazzoni, J.R. Morante, *"The role of surface oxygen vacancies in the NO₂ sensing properties of SnO₂ nanocrystals"* J. Phys. Chem. C **112**, 19540-19546 (2008). **Page 245**

1.3 References

[1] S. Maekawa, T. Tohyama, S.E. Barnes, S. Ishihara, W. Koshibae, G. Khaliullin, *"Physics of Transition Metal Oxides"*, Springer Series in Solid-State Sciences, vol. 144 (2004).

[2] J.L.G. Fierro, *"Metal Oxides: Chemistry and Applications"*, CRC Press: Boca Raton FL (2006).

[3] D.M. Smyth, *"The Defect Chemistry of Metal Oxides"*, Oxford University Press: Oxford (2000).

[4] V.E. Henrich, P.A. Cox, *"The Surface Science Of Metal Oxides"*, Cambridge University Press: Cambridge (1996).

[5] E.H. Nicollian, J. R. Brews *"MOS (Metal Oxide Semiconductor) Physics and Technology"*, John Wiley & Sons: New Jersey (1982).

[6] Ü. Özgür, Y. I. Alivov, C. Liu, A. Teke, M. A. Reshchikov, S. Dogan, V. Avrutin, S.-J. Cho, H. Morkoç, *"A comprehensive review of ZnO materials and devices"* J. Appl. Phys. **98**, 041301 (2005).

[7] M. Batzill, U. Diebold, *"The surface and materials science of tin oxide"* Prog. Surf. Sci. **79**, 47-154 (2005).

[8] Z.L. Wang, *"Zinc oxide nanostructures: growth, properties and applications"* J. Phys.: Condens. Matter **16**, R829-R858 (2004).

[9] S. Mathur, S. Barth, H. Shen, J.-C. Pyun, U. Werner, *"Size-Dependent Photoconductance in SnO$_2$ Nanowires"* Small **1**, 713-717 (2005). (b) S. Mathur, S. Barth, *"Molecule-Based Chemical Vapor Growth of Aligned SnO$_2$ Nanowires and Branched SnO$_2$/V$_2$O$_5$ Heterostructures"* Small **3**, 2070-2075 (2007).

[10] F. Hernandez-Ramirez, A. Tarancon, O. Casals, E. Pellicer, J. Rodríguez, A. Romano-Rodriguez, J.R. Morante, S. Barth, S. Mathur, *"Electrical properties of individual tin oxide nanowires contacted to platinum electrodes"* Phys. Rev. B. **76**, 085429 (2007).

[11] F. Hernandez-Ramirez, J.D. Prades, A. Tarancon, S. Barth, O. Casals, R. Jimenez-Diaz, E. Pellicer, J. Rodriguez, M.A. Juli, A. Romano-Rodriguez, J.R. Morante, S. Mathur, A. Helwig, J. Spannhake, G. Mueller, *"Portable microsensors based on individual SnO$_2$ nanowires"* Nanotechnol. **18**, 495501 (2007).

[12] See any scientific paper published in the *Journal of Computer-Aided Materials Design* (Springer).

[13] D. Neamen, *"Semiconductor Physics And Devices"*, McGraw-Hill: New York (2003).

[14] N. Levine, *"Quantum Chemistry"*, Prentice Hall, Upper Saddle River NJ (1999).

[15] M. Law, J. Goldberger, P. Yang, *"Semiconductor nanowires and nanotubes"* Annu. Rev. Mater. Res. **34**, 83-122 (2004).

[16] H.J. Fan, P. Werner, M. Zacharias, *"Semiconductor Nanowires: From Self-Organization to Patterned Growth"* Small **2**, 700-717 (2006).

[17] F. Hernandez-Ramirez, A. Tarancon, O. Casals, J. Rodríguez, A. Romano-Rodriguez, J.R. Morante, S. Barth, S. Mathur, T.Y. Choi, D. Poulikakos, V. Callegari, P.M. Nellen, *"Fabrication and electrical characterization of circuits based on individual tin oxide nanowires"* Nanotechnol. **17**, 5577-5583 (2006).

[18] Z. Tang, P. Sheng, *"Nanoscale Phenomena: Basic Science to Device Applications"* Springer Series: Lecture Notes in Nanoscale Science and Technology, vol. **2** (2008).

[19] S. Luryi, J, Xu, A, Zaslavsky, *"Future Trends in Microelectronics: The Nano Millennium"*, John Wiley & Sons: New Jersey (2002).

[20] S. Kumar, S. Rajamaran, R.A. Gerhardt, Z.L. Wang, P.J. Hesketh, *"Tin oxide nanosensor fabrication using AC dielectrophoretic manipulation of nanobelts"* Electrochimica Acta, **51**, 943-951 (2005).

[21] G. Eranna, B.C. Joshi, D.P. Runthala, R.P. Gupta, *"Oxide Materials for Development of Integrated Gas Sensors - A Comprehensive Review"* Critic. Rev. Sol. State Mater. Sci. **29**, 111-188 (2004).

[22] F. Hernández-Ramírez, A. Tarancón, O. Casals, J. Arbiol, A. Romano-Rodríguez, J.R. Morante, *"High response and stability in CO and humidity measures using a single SnO_2 nanowire"* Sens. Actuators B: Chem. **121**, 3-17 (2007).

[23] N. Yamazoe, K. Shimanoe, *"Roles of shape and size of component crystals in semiconductor gas sensors"* J. Electrochem. Soc. **155**, J85-J92 (2008).

[24] C. Soci, A. Zhang, B. Xiang, S. A. Dayeh, D.P.R. Aplin, J. Park, X.Y. Bao, Y.H. Lo, D. Wang, *"ZnO Nanowire UV Photodetectors with High Internal Gain"* Nano Lett. **7**, 1003-1009 (2007).

2. Objectives

The main objectives of this Ph.D Dissertation can be summarized as follows:

1. To understand and model the operation mechanisms of conductometric sensors based on individual metal oxide nanowires. This includes the applications in the field of chemical gas sensors and in the field of light detectors.

2. To take advantage of the well-kown characteristics of the nanowires, such as the large surface-to-volume ratio, the high crystalline quality, or the surface stability, in order to have access to well-defined experimental situations close to the theoretical models.

3. To assess to what extent the above-mentioned characteristics the nanowires are advantageous in gas and light sensing applications. Also, to identify other properties of the nanowires that can be beneficial in the fields treated here.

4. To explore, on the basis of the previous results, alternative approaches to operate the sensors based on individual nanowires and to evaluate their performances for future applications.

3. Methodology

In a Ph.D Dissertation based on a compendium of papers, the inclusion of a chapter devoted to the methodological details of the techniques used during the development of the Ph.D work is not mandatory. For the reasons detailed below, the author has considered convenient to include information concerning selected theoretical and experimental methods. As usual, details of the rest of techniques are given in the experimental section of each paper.

In first place, the fact that this Ph.D work served to start with *ab initio* atomistic calculations in the Department of Electronics motivated the author to describe, in detail, the theoretical and procedural aspects of the formalism used: the Density Functional Theory. These details are presented in the form of a book chapter (*Paper 1*). The author thanks Prof. P. Ugliengo for his exciting invitation to write this chapter and hopes that its contents will be especially useful for the future activities of the group in this field.

In second place, the experimental activities developed in this Ph.D work took advantage of the know-how and the long experience of the group in the synthesis, characterization, manipulation and fabrication of nanomaterials and nanodevices. The

details of this expertise are summarized in a review book chapter of the activities of the group (*Paper 2*). The author of the present Dissertation is thankful to Prof. J.R. Morante, Prof. A. Romano-Rodríguez and the rest of the co-authors for sharing their expertise and encouraging him to contribute to this chapter.

In third place, besides the scientific results presented in this Ph.D Dissertation which are detailed in the *Chapter 4*, the author would like to present his contribution to the technological and methodological background of the group. This is an electronic platform to interface with the nanowires and monitor their conduction properties which has been extensively used during the development of the experimental activities of this work. The details about the platform are presented in a scientific paper (*Paper ♣*) which shall not be considered for the evaluation of the author's work (since it was evaluated in the Ph.D Dissertation of another co-author). The author is thankful to Dr. F. Hernández-Ramírez for his kind invitation to participate in this work.

3.1 Papers

1. J.D. Prades, A. Cirera, J.R. Morante, *"Applications of DFT Calculations to Chemical Gas Sensors: Desing and Understanding"* in *"Quantum Chemical Calculations of Surfaces and Interfaces of Materials"* (Ed. V. A. Basiuk and P. Ugliengo), chap. 13, pp. 243-288, American Scientific Publishers: Valencia CA (2008). ISBN: 1-58883-138-8.

2. T. Andreu, J. Arbiol, A. Cabot, A. Cirera, J.D. Prades, F. Hernandez-Ramirez, A. Romano-Rodriguez, J.R. Morante, *"Nanosensors: Controlling Transduction Mechanisms an the Nanoscale Using Metal Oxides and Semiconductors"* in *"Sensors Based on Nanostructured Materials"* (Ed. F. Arregui), chap. 5, pp. 79-129, Springer Science + Business Media (2009). ISBN: 978-0-387-77752-8.

♣   F. Hernandez-Ramirez, J.D. Prades, A. Tarancon, S. Barth, O. Casals, R. Jimenez-Diaz, E. Pellicer, J. Rodriguez, M.A. Juli, A. Romano-Rodriguez, J.R. Morante, S. Mathur, A. Helwig, J. Spannhake, G. Mueller, *"Portable microsensors based on individual SnO_2 nanowires"* Nanotechnol. **18**, 495501 (2007). Remarks: Cover paper on December 12th of 2007 in Nanotechnology.

J.D. Prades, A. Cirera, J.R. Morante, *"Applications of DFT Calculations to Chemical Gas Sensors: Desing and Understanding"* in *"Quantum Chemical Calculations of Surfaces and Interfaces of Materials"* (Ed. V. A. Basiuk and P. Ugliengo), chap. 13, pp. 243-288, American Scientific Publishers: Valencia CA (2008).

1

CHAPTER 13

Applications of DFT Calculations to Chemical Gas Sensors: Design and Understanding

Joan Daniel Prades

EME/CeRMAE/IN²UB, Departament d'Electrónica, Universitat de Barcelona, C/ Martí i Franqués, 1, E-08028 Barcelona, Spain

Albert Cirera*

EME/CeRMAE/IN²UB, Departament d'Electrónica, Universitat de Barcelona, C/ Martí i Franqués, 1, E-08028 Barcelona, Spain

Joan Ramon Morante

EME/CeRMAE/IN²UB, Departament d'Electrónica, Universitat de Barcelona, C/ Martí i Franqués, 1, E-08028 Barcelona, Spain

CONTENTS

1. INTRODUCTION: HOW SENSING NANOMATERIALS MEET TERAFLOPS

1.1. What is a Chemical Gas Sensor?

During the last 50 years, many laboratories have dedicated great efforts to the development of Chemical Gas Sensors. These devices necessary for safety in home and industrial applications, for combustion control, and for environmental monitoring.

Metal oxide chemical sensors, that exhibit a variation of resistance under gas exposure, seem to fulfill the requirements of the different applications, being low-cost enough to reach mass implementation in domestic, industrial and automotive applications. Because of its lower price in front of the other devices, they are currently the most widely used gas sensors for gas identification.

In the 1950's, Brattain and Barden showed [1] that the gas adsorption at Ge surface lead to a variation of the resistance. Since then, the first structure built to be used as gas sensor is attributed to Seiyama et al. [2] who developed a metal oxide chemical sensor based on ZnO. Few time later, Taguchi patented the first semiconductor gas sensor [3]. The first chemical sensor based on SnO_2 was developed in 1970 by Taguchi [4] and was commercialized by Figaro. Since then SnO_2 has also become the most studied material for chemical gas sensors. During the 80's TiO_2 was investigated as sensing material for exhaust applications and, today, it is widely used as oxygen sensor in vehicles. In fact many metal oxides exhibit a variation of their electrical resistance when exposed to gases [5, 6, 7].

A general sketch of the interaction of the gas with the sensing material from the solid-state point of view is depicted in Figure 1. In fact, chemisorption and reduction with oxygen vacancies mostly dominate the sensing mechanisms in metal oxide chemical sensors. To understand this behavior, answering a variety of related questions is required:

- About the capture of gaseous species at sensing material surface, how are they fixed and which are the involved physic and chemistry.
- Concerning the kinetics of the surface reactions, at which rate the molecules adsorb/desorb onto/from of surface, and which are the rates of the surface reactions.
- Regarding the conductance level, how the presence of gas influences the conduction mechanisms of the electrons through the sensing material.
- At electronic level, which are the consequences of such reactions, and how redistributes the electron bands.

Many authors have partially contributed to answer these questions [6, 8–12] and we summarize an small part of this knowledge in the next section.

1.2. Sensing Phenomena: A Fast Overview

It is accepted [8] that oxidizing molecules (O_2, NO_2 and CO_2) create acceptor levels because they capture electrons at the surface from the bulk, while reducing molecules (H_2, CO, CH_4) introduce donor levels because they give electrons to the metal oxide through the creation of an oxygen vacancy. Consequently the surface charge per area unit Q trapped during the chemisorption can be expressed as

$$Q = e\left[\int_{-\infty}^{\infty} D_D(e)f(E_F - E)dE - \int_{\infty}^{-\infty} D_A(E)f(E - E_F)dE \right] \quad (1)$$
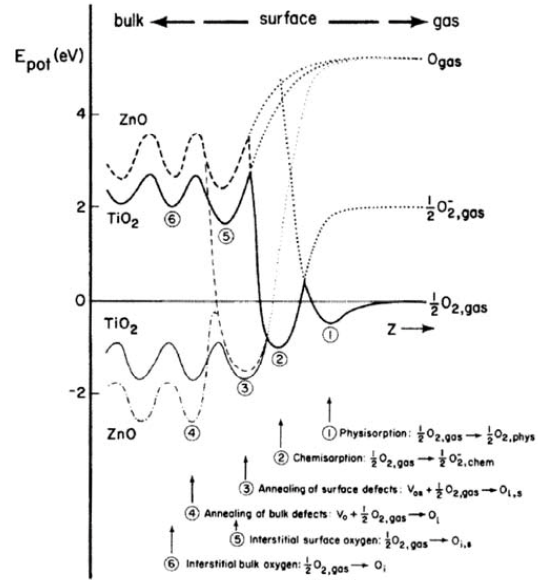
Figure 1. Characteristic solid-gas (O_2) interaction steps by the dependence of the potential energy on distance from the surface with several relative minima. Evaluated surfaces are (110) for TiO_2 and (10–10) for ZnO. Reprinted with permission from [8], W. Göpel et al., *Phys. Rev. B* 28, 3427 (1983). ©1983, American Physical Society.

with $D_D(E)$ and $D_A(E)$ the donor and acceptor surface states densities per area unit. This scheme is shown in Figure 2.

When the molecule is chemisorbed as $(X^{ad})^{\delta-}$ the band bends a value ΔV_s. This bending can be evaluated by using a Kelvin probe that measures the changes in the work function $\Delta\phi$. The variations in the work function can be related with changes in Schottky barrier as,

$$\Delta\phi = -e\Delta V_s + \Delta\chi + \Delta(E_C - E_F)_b \quad (2)$$

although the variations in the bulk Fermi level position can be neglected if bulk diffusion of atoms or ions also can be [9]. In this point, although Romppainen et al. [10] have considered the possibility of mobile oxygen vacancies when the temperature is high enough, in the work [11] it is shown experimentally how the oxygen vacancies distributions seems to be frozen at normal working temperatures (<300°C), at least for SnO_2.

In the case of variations due to changes in the electron affinity, its origin consists in an induced dipole moment attributed to the adsorption complexes:

$$\mu^{ad} = {\varepsilon_s \varepsilon_o \Delta\chi}\Big/{n_s^{ad}} \quad (3)$$

This term was first introduced by Göpel et al. in equation (2) to explain the differences between the changes in the work function and the Schottky barrier.

The bending of the bands evaluated as Schottky barrier can be related with changes in resistivity with

$$\rho^{-1} = \sigma = \sigma_0 \exp\left(\frac{e\Delta V_s}{KT} \right) \quad (4)$$

Applications of DFT Calculations to Chemical Gas Sensors: Design and Understanding   **245**
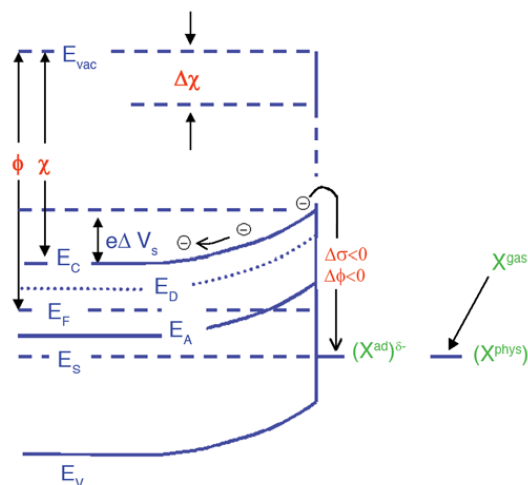
Figure 2. Schematic representation of chemisorption and charge transfer at a semiconductor surface in the surface electron band scheme. The gas phase molecule X^{gas} forms the precursor physisorption state. Similar graph appears in many works such as [13].

Besides, the equation (2) allows relating the chemisorption phenomena (figure 2) with the evolution of the electron bands and gives a useful expression to evaluate this effect both by experimental and theoretical approaches. This effort is absolutely necessary since one of the main drawbacks of this kind of sensors is the selectivity and stability, which make them not usable for many precise or harsh applications. As a part of surface science, this basic knowledge is still under development.

1.3. Present Trends in Sensing Materials and Devices: How Supercomputing Can Assist

Sensing phenomena take place at the surface, as previously shown (*see* Figs. 1 and 2). Actually, as the band bending is a weak phenomenon, much surface is required to transduce the chemical signal into an electrical one. In the recent years, a wide variety of technological routes to produce nanometric sensing materials were exploited and applied to gas sensors. Most of them gave valuable results, and the sensitivity of the devices was dramatically increased [12]. However, basic understanding of gas/surface interaction was still not mature. Despite the use of very sensitive devices, a simple cross exposure with different gases could be difficult to overcome [13]. This problem was mainly associated to the use of spherical nanoparticles.

Since a few years ago, the present trends have significantly changed with the use of new 1D and 2D nanostructures (nanowires, nanobelts, nanoribbons) [14]. Many laboratories can produce nanobelts or nanowires of sensing materials (*see* an example in Fig. 3) and also many of them dispose of facilities for the fabrication of nanodevices such as Focused Ion Beam equipments (an example is shown in Fig. 4 from [15]).

Kolmakov et al. [16] have recently reviewed the use of low dimensional structures for chemical gas sensing and catalysis. Among other outstanding properties suggested by system with low
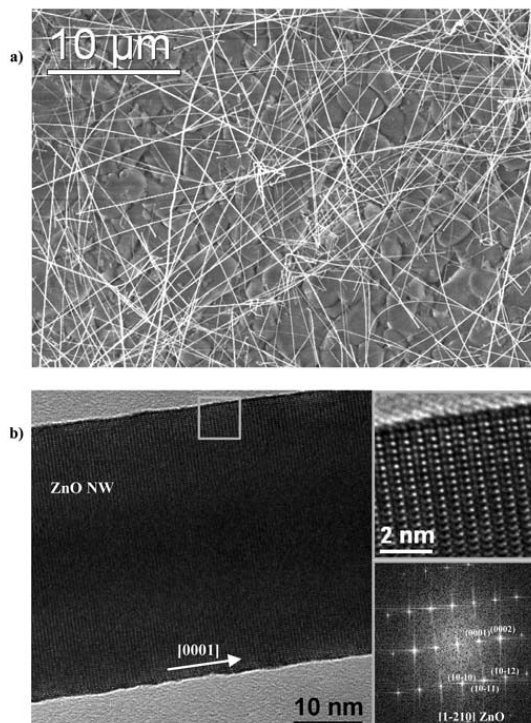
Figure 3. a) SEM micrograph of ZnO nanowires grown in a CVD furnace. With the standard Vapor-Liquid-Solid method using gold as a catalyst, well formed nanowires are obtained: longer than 10 μm and thinner than 100 nm. b) TEM micrographs of the same samples. Notice the crystalline quality of the nanowire and the well terminated surface (High Resolution TEM inset). TEM images courtesy of Dr. J. Arbiol.

dimensionality, these authors indicate that low dimensional sensing materials usually are better defined stoichiometrically and have a higher level of crystallinity than the multigranular (spherical) materials currently used in sensors, potentially reducing the instability associated with percolation or hopping conduction.

This point is crucial for the use of computational techniques. Since today, facilities for the computation of spherical nanocrystals including at least thousands of atoms were not available. However, for the computation of a nanobelt it is possible to simulate a surface, and the straightforward use of symmetries reduces the problem dramatically.

In this context, the use of Density Functional Theory (DFT) becomes a good choice for a plurality of facts:

- It is an Ab Initio technique, and no previous experimental results are required.
- It is a very well established theory (Nobel Prize!) [17, 18].
- DFT allows to take advantage of translational symmetry in crystals (by the applications of the Bloch's Theorem), but it is also possible to describe systems with truncated symmetry (like surfaces) or non-symmetric systems (like molecules).
- Since its development, DFT has been widely used by chemists for the understanding of molecules and some of
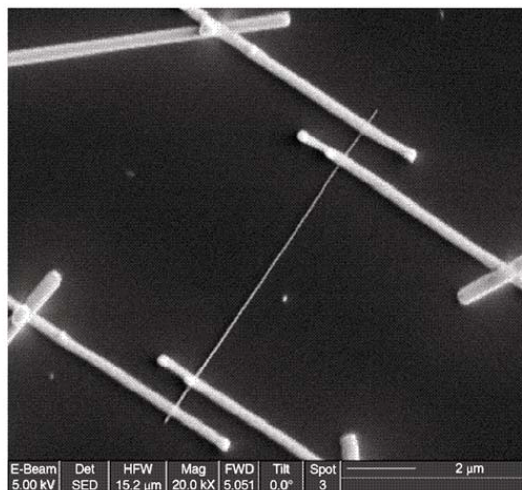
Figure 4. SnO$_2$ nanowire contacted using FIB nanolithography. Dimensions: L = 11 µm (length) and D = 55 ± 5 nm (diameter). Notice the 4 Pt–electron beam contacts fabricated in the proximity of the nanowires for 4-probe measurements. Reprinted with permission from [20], F. Hernández-Ramírez et al., *Nanotechnology* 16, 5577 (2006). © 2006, IOP - Institute of Physics.

them focused on catalysis. Some of the topics and methods of catalysis can be readily interpreted and applied in chemical sensing.

- The obtained results can be linked with experimental results, as we tray to expose in this chapter.

As summary, the opportunity for the application of DFT to chemical gas sensors is recently open and we will try to introduce it. For this, besides this first introductory section, we have structured the present chapter in two more sections. In Section 2, an overview of the DFT procedures applied to chemical sensors is presented, including how to compute surface, bulk and nanoparticles stability (even when reducing/oxidizing atmospheres are present) as well as the basics of chemisorption computation and ab initio thermodynamics. Finally, Section 3 is fully devoted to review the reported work on: SnO$_2$, ZnO and TiO$_2$, three of the most important materials for gas sensing applications.

2. DFT PROCEDURES TO CALCULATE AND MODEL THE PHYSICS AND THE CHEMISTRY OF THE SENSING MATERIALS

2.1. Surface and Bulk Models

As previously remarked, transduction in chemical sensors is essentially a surface phenomena. From the point of view of the sensing materials we could be interested in determining which are the surface orientations that minimize the surface energy to be able to predict the most energetically favorable shape or the most relevant orientation to focus further studies. Latter, we could be interested in understanding the interaction between

surfaces and sensing materials. In all this cases, in order to obtain meaningful (and converged!) results, it is crucial the election of appropriate models to describe the properties in which we are interested. So that, in this section we will center on the different ways a surface can be described. In addition to this, since a bulk analysis is always the preliminary step for a surface study we will give some general ideas on crystal models.

The number of atoms involved in real systems (a solid, a surface or a particle) is virtually "infinite"; so that, the use of models to reproduce the properties of interest with a limited number of atoms is unavoidable. Usually, two approaches are used to idealize the physical reality: the exploit of the periodic symmetry or the use of a finite embedded model. The periodic approach is ideal for bulk solids since not only translational symmetry properties can be used to lighten the calculations but also point symmetry properties can be exploited. Moreover, the properties of interest in solid state science are usually represented taking advantage of the symmetry properties: a good example of this are the band structure plots. Additionally, there exists a number of non-local properties such as the elastic constants, the chemisorption energies, coverage effects, k-space properties,... Under this approach (as explained hereunder) big supercells are needed to represent low density bulk point defects and slab models are necessary to descript surfaces but, in any case, the material must be properly described. Nowadays, there exist a vast variety of efficient and parallel computational codes that use this approach [24–33] but only DFT (and, in some cases HF) Hamiltonians are available. So that, the electronic correlation is roughly described and there are problems with excited states. On the other hand, there are many properties of extended systems that are local in nature as, for example, the geometry of adsorbed species, XPS and IR spectra of adsorbed species, spectroscopic transitions of defects (F centers) and magnetic coupling. For this reason, cluster models are also of great interest since it is possible to use with them the most sophisticate methods of quantum chemistry that provide reference values for other less accurate techniques. Then, in spite of the "infinite" material is roughly represented (cluster always have edges and convergence with respect to cluster size must be carefully checked), an appropriate treatment of the electronic correlation can be achieved and the excited states are not a problem.

From now on, we center on the periodic approach because it is the most usual election in the current literature on chemical sensors. The reader should keep in mind the existence of both approaches that correspond to two extreme points of view and choose one or another depending on the problem: accuracy versus efficiency needs to be carefully considered.

The description of a bulk crystalline solid is usually done in terms of its unit cell: an spatial arrangement of atoms which is tiled in three-dimensional space to describe the crystal. This unit cell is given by its lattice parameters: the length of the cell edges (a,b,c) and the angles between them (α,β,γ). The positions of the atoms inside the unit cell are described by the set of atomic positions (x_i,y_i,z_i) measured from a lattice point. So that the crystal structure consists of the same group of atoms, the basis, positioned around each and every lattice point. This group of atoms therefore repeats indefinitely in three dimensions according to the arrangement of the lattice.

The defining property of a crystal is its inherent symmetry by which we mean that, under certain operations, the crystal remains unchanged. Besides the translational symmetry always present, the crystal may exhibit rotational symmetries, mirror

Applications of DFT Calculations to Chemical Gas Sensors: Design and Understanding   247

Table 1. Lattice parameters and fractional atomic positions of SnO_2-cassiterite tetragonal phase. Data taken from [35].

SnO_2 tetragonal

Space group	a	b	c	α	β	γ
P4$_2$/mnm (136)	4.7374	4.7374	3.1864	90°	90°	90°

Irreducible atomic basis			
Element	x/a	y/b	z/c
Sn	0.0	0.0	0.0
O	0.30562	0.30562	0.0

Translational atomic basis			
Element	x/a	y/b	z/c
Sn	0.0	0.0	0.0
Sn	0.5	0.5	0.5
O	0.30562	0.30562	0.0
O	0.69438	0.69438	0.0
O	0.19438	0.80562	0.5
O	0.80562	0.19438	0.5

symmetries, and the so-called compound symmetries which are a combination of translation and rotation/mirror symmetries. A full classification of a crystal is achieved when all of these inherent symmetries of the crystal, not only the (purely) translational symmetry described by the lattice, are identified.

The characteristic rotation and mirror symmetries of the group of atoms, or unit cell, are described by its crystallographic point group. The space group of the crystal structure is composed of the translational symmetry operations in addition to the operations of the point group. This description in terms of the space group (there are 230 distinct) can reduce the number of atoms in the basis since some of them can be symmetry equivalent.

In practice, the lattice parameters and the atomic positions of the material of interest can be obtained from the literature or from a crystallography database [19]. Let us use the most common phase of tin dioxide (SnO_2) as an example. In Table 1 we present the crystallographic data of tetragonal SnO_2 (so called rutile or cassiterite) produced with data from [20]. The space group, the lattice parameter and the irreducible base (2 atoms) contain all the information needed to generate all the atomic positions within the unit cell (6 atoms) (*see* Fig. 5).

The unit cell for the ideal bulk is the starting point to generate models to study, for example, low density bulk phenomena like defects and impurities or surfaces phenomena. In the first case, a supercell approach is needed and consist on building a bigger periodic cell (so-called supercell) by repeating A×B×C times the unit cell along every crystallographic axis. Following the previous example, a 3×3×3 supercell of SnO_2 cassiterite would contain 162 atoms (54 tin and 108 oxygen). If we are interested in dealing with atomic vacancies a minimum density of 1 vacancy every 162 atoms could be studied with a model of this size. This illustrates clearly that theoretical studies of dopants with concentrations of less than 1 dopant every 10^6 atoms increase the size of the supercell (and thus, the computational cost) dramatically. So that, the study of bulk defects is extremely complex and requires the accurate test of the approximations made in the theoretical models. Some ideas on how to deal with this kind of problems are given in Section 2.2 and further information on this field can be found elsewhere [21].

In the case of surfaces we will focus on the construction of periodic slab models. An ordered surface can be obtained by cutting the three-dimensional bulk structure of a solid along a particular plane to expose the underlying array of atoms. The way in which this plane intersects the three-dimensional structure is very important and is defined by the Miller Indices (this notation is commonly used by both surface scientists and crystallographers since an ideal surface of a particular orientation is nothing more than a lattice plane running through the 3D crystal with all the atoms removed from one side of the plane). The Miller indices can be easily obtained constructing the required atomic plane, taking reciprocals of its intercepts on axis and rationalize to give whole numbers. The example in Figure 6(a) shows the unit cell of SnO_2 cassiterite with a highlighted plane that intercepts the axis at 1, 1, ∞; so that, the Miller indices of this plane are (110).

In fact there are a total of 6 faces related by the symmetry elements and equivalent to the (110) surface: any surface belonging to this set of symmetry related surfaces may be denoted by the more general notation {110} where the Miller indices of one of the surfaces is enclosed in curly-brackets. As a final comment, only in the cubic system the (hkl) plane and the vector [hkl] are normal one to another.

Notice that the selected plane does not define a unique surface termination as shown in Figure 6(b). So that, when modeling surfaces with slabs not only its orientation is important, but also its termination should be specified. The first step is to know what
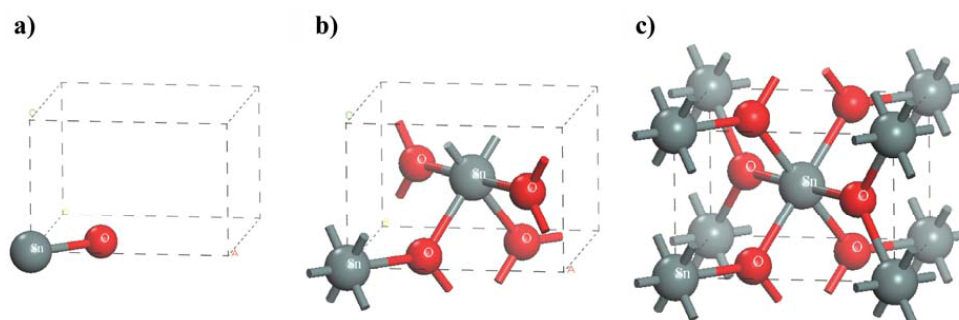

Figure 5. Ball and stick representation of the SnO_2-cassiterite unit cell. a) Irreducible atomic basis (2 atoms), b) atomic basis (6 atoms) obtained applying point symmetries on the previous basis, and c) crystal cell obtained when applying full symmetries on a) or translational symmetries on b).
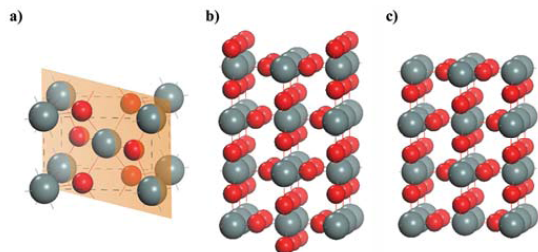
Figure 6. Ball and stick representation of a) the SnO_2-cassiterite unit cell with the 110 plane highlighted, b) a slab obtained when cutting 3 stoichiometric layers of $SnO_2(110)$, and c) another possible 3-layer-thick $SnO_2(110)$ slab: in this case, the outermost layers are substoichiometric.

Figure 7. The low-index surfaces of SnO_2: a) (110); b) (100); c) (101); d) (001), with Sn (light spheres) and O (dark spheres) ions shown in unrelaxed positions. Terminology for referring to surface ions is shown. Reprinted with permission from [37], J. Oviedo and M. J. Gillan, *Surf. Sci.* 463, 93 (2000). ©2000, Elsevier.

is meant by 'layer'. Lets try to shed some light on this point with the description of several low index surfaces of SnO_2-cassiterite (Figure 7 from [22] shows several surfaces orientations of this phase).

In bulk SnO_2, each Sn is coordinated to six oxygens situated at the vertices of a distorted octahedron in which four oxygens (equatorials) lie in the same plane and have shorter Sn-O bonds than the other two oxygens (apicals). On the low-index (110), (100), (101) and (001) surfaces, truncation of the octahedral gives rise to different coordination combinations for the outermost tin cations. On the (110) surface (Fig. 7(a)) we find both five- and six-fold coordinated tin. In the coordination polyhedron of the five-fold coordinated tin, one apical oxygen is missing and the equatorial oxygens lie in the surface plane. For the six-fold coordinated tin cations the equatorial oxygens are located in a plane formed by the [110] and [001] directions, giving rise to rows of two-fold coordinated oxygens in the [001] direction. These oxygens lie above the plane of cations and are called 'bridging oxygens'. The resulting structure is formed by alternating layers O-Sn_2O_2-O with zero charge and the surface has no net dipole. The (100) surface is shown in figure 7.b. In this surface the totality of the tin atoms are five-fold coordinated. One apical oxygen is missing and the equatorial oxygen plane is rotated by 45° with respect to the surface normal, so that bridging oxygens are also found. The resulting surface can be thought of as a layered O-Sn-O structure in which a layer is rotated 90° with respect to the previous one. The (101) surface is shown in Figure 7(c). In this surface all tins are five-fold coordinated, with an equatorial oxygen missing. As we move in the [10–1] direction, the orientation of the truncated octahedra change respect to the surface normal. The octahedra are joined by their vertices through oxygens, and consequently, there is a slight difference between equatorial and apical bond lengths we find two rows of oxygens in the [10–1] direction lying above and below the tin plane. This is because these oxygens are bonded to one tin like an equatorial oxygen and like an apical oxygen to the other structure. The resulting surface is quite corrugated and the layers are, in this case, best formulated as (O_2-Sn_2-O_2). Finally, the (001) surface is shown in Figure 7(d). Here all the tin cations are four-fold coordinated and all the oxygens are two-fold coordinated. The equatorial plane is perpendicular to the surface and the two oxygens above the tin plane are missing. The resulting surface is quite flat and its layer structure is formed by SnO_2 planes. Notice that in all cases, the formulation of the layer preserves the stoichiometric and its repetition normal to the surface arises the same termination.
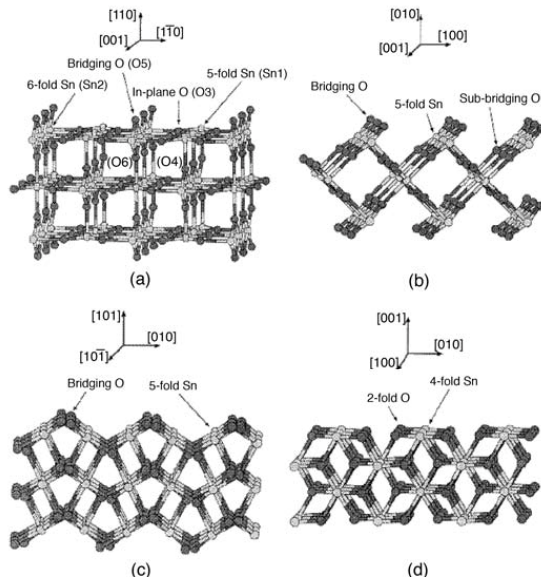
Once understood the surface of the material in terms of stoichiometric layers it is possible to describe its termination in terms of the assumed definition of layer: for example, in the case of $SnO_2(110)$ it is possible to distinguish between the stoichiometric surface (Fig. 6(b)) and the reduced terminated where all the oxygen bridging atoms have been removed.

In the analyzed examples, both sides of the generated slab are equivalent and all the layers are electrically neutral: in these cases, when evaluating surface properties we should keep in mind that we are calculating them twice (more details on this are discussed in Section 2.3). However, there exist systems on which both sides of the slab are intrinsically different and present net dipole moment no matter how thick they are: that is the case of polar surfaces like ZnO(0001) that deserve special treatment.

Once defined the surface model, there exist two different approaches too deal with the new two-dimensional symmetry: while periodic boundary conditions are applied in the plane of the material (Born - Von Karman's boundary conditions) some codes apply them as well in the direction perpendicular to the slab and others force the wavefunctions to zero at infinity. The first approach requires to define a vacuum region between periodic images of the slab (so a supercell must be build) and the second does not. Notice that in the first case we will have to worry about the convergence of the property of interest not only with respect to the thickness of the slab but also with the vacuum gap (apart of the usual convergence issues like basis set, k-point sampling, …).

Before starting to work with ab initio calculated total energies, an important remark must be made to justify why Gibbs free energies are usually approximated by total energies from first

principles calculations [23]. DFT total energies $E_{total}(V,\{N_i\})$ are evaluated for a certain volume V of the unit cell that contains an arrangement of atoms $\{N_i\}$ which is related to a thermodynamic quantity, the Helmholtz free energy F. At zero temperature, neglecting zero-point vibrations:

$$F\left(T,V,\{N_i\}\right) = E_{total}\left(V,\{N_i\}\right) + F_{vib}\left(T,V,\{N_i\}\right) \qquad (5)$$

$$F_{vib}\left(T,V,\{N_i\}\right) = E_{vib}\left(T,V,\{N_i\}\right) - TS_{vib}\left(T,V,\{N_i\}\right), \quad (6)$$

where E_{vib} and S_{vib} are the vibrational energy and entropy. On the other hand, the Gibbs free energy can be written as

$$G\left(T,p,\{N_i\}\right) = F\left(T,p,\{N_i\}\right) + pV\left(T,p,\{N_i\}\right). \qquad (7)$$

For p < 1atm and V ~ 1 Å^3, (pV) $<10^{-3}$ meV which is negligible compared with $F(T,p,\{N_i\})$ (of the order of tenths of meV). Therefore,

$$G\left(T,p,\{N_i\}\right) \approx E_{total}\left(V,\{N_i\}\right) + F_{vib}\left(T,V,\{N_i\}\right). \qquad (8)$$

The E_{vib} and S_{vib} contributions to F_{vib} can be calculated from the corresponding partition function of an N-atomic system [24] and, in general, F_{vib} contribution is of the same order as the numerical accuracy of usual DFT calculations (~20 meV) [23]. Therefore,

$$G\left(T,p,\{N_i\}\right) \approx E_{total}\left(V,\{N_i\}\right). \qquad (9)$$

2.2. Bulk Stability

There exist many properties of the materials that are attributed to its bulk volume; in fact, as previously stated, the first approximation of the study of crystals is assuming an infinite material. In this way, many electron and vibrational properties such as the opto-electronic interaction, transport properties and the vibrational spectra are successfully explained with bulk electron band and bulk phonon diagrams.

The possibility of evaluating these electron and phonon energetic levels is included in the majority of DFT codes so further information on this point can be found elsewhere [24–33]. We will center in how to analyze some bulk properties of interest in gas sensing applications such as the most stable phase of the bulk material (which will determine not only the transport properties but also the surface arrangements) and the stability of (charged) intrinsic point defects (which has dramatic consequences on the electric response of the materials).

A first point of discussion is to determine the most stable atomic arrangement of a material under certain environmental conditions, or, in other words, the most stable phase. In this point, we will center on the bulk phase: surface modifications are discussed in detail in Section 2.3.

The widely accepted argument to determine the way the atoms will arrange is that the most favorable phase is the one that minimizes the energy per formula unit [25]. If small deformations are applied to the unit cell, the total energy per formula unit E_0 as a function of the cell volume (or the volume per formula unit V_0) can be plotted [25]. This total energy will present a minimum corresponding to the equilibrium or relaxed configuration: i.e that lattice parameters that minimize the total energy (or minimize

the forces and the stress over the atoms) for a given phase. The previous plot can be fitted by an equation of state such as the third order Murnaghan equation:

$$E(V) = E_0 - \frac{B_0V_0}{B'-1} + \frac{B_0V}{B'}\left[\frac{(V/V_0)^{B'}}{B'-1}+1\right] \qquad (10)$$

where E_0, V_0, and B_0 are the total energy, volume per formula unit, and bulk modulus at zero pressure (P), respectively, and B′=dB/dP is assumed to be constant. If the zero of energies is set to the sum of total energies of the isolated atoms contained in the unit cell, the absolute value of the energy $|E_0'|$ at the minimum of each curve can be considered as a rough estimate of the equilibrium cohesive energy of the corresponding material phases. So that, the most stable phase will present the maximum cohesive energy $|E_0'|$ at the considered conditions.

A clear example of this can be found in Figure 31, where a phase diagram (data taken from Jaffe and Hess [25]) is presented. The material under consideration was ZnO in three phases: wurtzite, zinc-blende and rocksalt. Their results clearly illustrate that the most stable phase (under ambient conditions) is wurtzite.

The transition pressures (P_T) between one phase an other could be determined by calculating the Gibbs free energy (G) for the two phases that is given by

$$G = E_0 + PV - TS. \qquad (11)$$

Since theoretical calculations are performed at T = 0 K, the Gibbs free energy becomes equal to the enthalpy,

$$H = E_0 + PV. \qquad (12)$$

For a given pressure, the stable structure is the one for which the enthalpy has its lowest value: the common tangent to the curves plotted in figure indicates the phase-transition pressure. This is also illustrated in the example of Figure 31 where a transition pressure of 8.57 GPa is obtained.

When the electron transport properties are important (such as in gas sensing applications), another point of great interest is being able to determine the contribution to the conductivity of the charged intrinsic point defects.

The formation energies of the defects can be calculated using the total energies supercells big enough to reproduce defect concentrations with physical meaning (see Section 2.1). For compound systems, the formation energies depend on the atomic chemical potentials. In addition, those of charged defects also vary with the electronic chemical potential, i.e., Fermi energy. Let us assume a general metal oxide whose formula is M_xO_y. For a defect in a charge state q, the formation energy is given by [41–43]

$$E_{formation}(q) = E_T(q) - n_M\mu_M - n_O\mu_O + qE_F \qquad (13)$$

where E_T is the total energy of the supercell with a defect in a charge state q, n_M and n_O are the number of metal and oxygen atoms in the supercell, μ_M and μ_O are the atomic chemical potentials, and E_F is the Fermi energy*.

For these charged defects, the total charge of supercells has to be neutralized using jellium background. Energy shifts associated

---

*μ_q, the chemical potential of a charge is $\mu_q = EF - TS$. We used $\mu_q \cong E_F$ as usual in solid state physics applications.

with the jellium neutralization can be corrected by the total energy difference between the neutral and charged systems. Further details on this can be found elsewhere [26].

μ_M and μ_O are variables correlated as

$$x\mu_M + y\mu_O = g_{M_xO_y \text{(bulk)}} \qquad (14)$$

where $g_{MxOy\text{(bulk)}}$, the Gibbs free energy the bulk M_xO_y, is a constant value calculated as the total energy per M_xO_y unit formula. The total energies per atom for the bulk metal and the molecular oxygen can be chosen as the upper limits of μ_M and μ_O, respectively. There are two extreme conditions: the oxygen-rich limit ($x\mu_M = g_{MxOy\text{(bulk)}} - y\mu_{O(O2)}$ and $\mu_O = \mu_{O(O2)}$) and the metal-rich limit ($\mu_M = \mu_{M\text{(bulk)}}$ and $y\mu_O = g_{MxOy\text{(bulk)}} - x\mu_{M\text{(bulk)}}$).

While the atomic chemical potentials describe the conditions under which the materials are grown, the Fermi energy depends on the concentrations of native defects and impurities. Therefore, the formation energies of native defects can be discussed as a (linear!) function of the atomic chemical potentials and the Fermi energy on the basis of equation (13). Notice that, when assuming E_F as a variable, the slope correspond to the charge state that gives the lowest formation energy with respect to the Fermi level.

To illustrate this, Figure 8 reprints the Formation energy versus the Fermi level position calculated by Oba et al. [27] for ZnO under oxygen-rich and metal-rich conditions (Fig. 8(a, b), respectively). Different slopes indicate different charge states of each intrinsic defect. For each defect specie, only the state that gives the lowest formation energy with respect to the Fermi energy is shown for clarity. The cross point of two lines of different slope, corresponds to the electron level of the thermal transition between both charge states. Notice that the Fermi energy is measured from the valence band maximum, and the conduction band minimum is shown at 0.95 eV. The calculated value of 0.96 eV is considerably smaller than the experimental band gap of 3.36 eV [28], which is known to be due to the DFT. This may cause some systematic errors in absolute formation energy.

Several methods to correct the formation energies of defects to overcome the underestimation have been suggested. The main ideas are the following: the conduction band can be rigidly shifted upward to match the experimental band gap. Donor-type defect states, which are expected to have characters similar to states in the conduction band, are assumed to follow the upward shift. Acceptor-type defect states are expected to have characters similar to valence states and, thus, left unchanged. According to the upward shift, the formation energies of donor-type defects are assumed to increase by the energy of the conduction band shift multiplied by the occupation number of the defect states. On the other hand, those of acceptor-type defects are assumed to remain unchanged. Since this is still a controverted point, some authors choose to present their results uncorrected.

2.3. Surface Stability

Under ideal crystal conditions, all surfaces are energetically unfavorable since they have a positive free energy of formation. A simple reason for this comes from considering the formation of new surfaces by cleavage of a solid and recognizing that bonds have to be broken between atoms on either side of the cleavage plane in order to split the solid and create the surfaces. Breaking bonds requires work to be done on the system, so the surface free energy contribution to the total free energy of the system must therefore be positive.
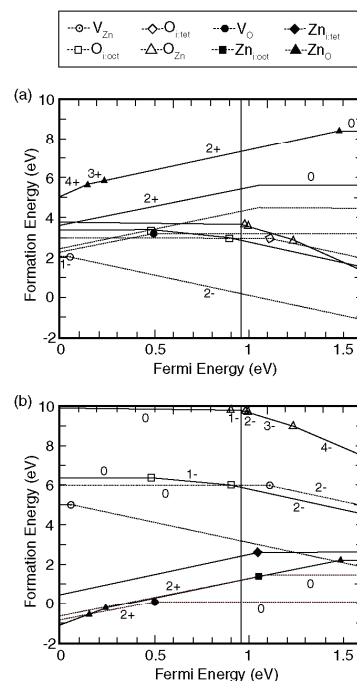
Figure 8. Defect formation energies as a function of the Fermi energy for a) the oxygen-rich limit $\mu_{Zn} = \mu_{ZnO\text{(bulk)}} - \mu_{O(O2)}$ and $\mu_O = \mu_{O(O2)}$ and b) the zinc-rich limit $\mu_{Zn} = \mu_{Zn\text{(bulk)}}$ and $\mu_O = \mu_{ZnO\text{(bulk)}} - \mu_{Zn\text{(bulk)}}$. For each defect species, only the charge state that gives the lowest formation energy with respect to the Fermi energy is shown. Change in the slope indicates transition in the charge state, which is shown with symbols. The valence band maximum is chosen as the zero of the Fermi energy; the vertical line at 0.96 eV corresponds to the conduction band minimum. The subscripts in the notation of defect species indicate defect sites, e.g., "Zn" and "i:oct." denote the zinc lattice and octahedral interstitial sites, respectively. Reprinted with permission from [45], F. Oba et al., *J. Appl. Phys.* 90, 824 (2001). ©2001, American Institute of Physics.

The unfavorable contribution to the total free energy may, however, be minimized in several ways [29]:

(1) By reducing the amount of surface area exposed.
(2) By predominantly exposing surface planes which have a low surface free energy.
(3) By relaxing/reconstructing the local surface atomic geometry in a way which reduces the surface free energy.

The first and second points will be discussed in Section 2.4.

Of course, systems that already have a high surface energy (as a result of the preparation method) will not always readily convert to a lower energy state at low temperatures due to the kinetic barriers associated with the restructuring. Such systems (e.g., highly dispersed materials such as those in colloidal suspensions or supported metal catalysts) are then "metastable".

It should also be noted that there is a direct correspondence between the concepts of "surface stability" and "surface free energy" i.e. surfaces of low surface free energy will be more stable and vice versa. One rule of thumb is that the most stable solid surfaces are those with:

Applications of DFT Calculations to Chemical Gas Sensors: Design and Understanding $\qquad$ **251**

(1) a high surface atom density

(2) surface atoms of high coordination number

For example, if we consider the individual surface planes of an fcc closed packed solid, then we would expect the stability to decrease in the order fcc(111) > fcc(100) > fcc(110). However, note that the two factors are obviously not independent, but are inevitably strongly correlated.

It has to be noticed that the above comments only strictly apply when the surfaces are in vacuum. The presence of a fluid above the surface can drastically affect the surface free energies as a result of the possibility of molecular adsorption onto the surface. Preferential adsorption onto one or more of the surface planes can significantly alter the relative stabilities of different planes. The influence of such effects under reactive conditions (e.g., the high pressure/high temperature conditions pertaining in heterogeneous catalysis) is, yet, poorly understood.

A final comment should be made regarding the equilibrium atomic position on the surface: as a consequence of the removal of part of the neighboring atoms of the outermost layer, their atomic position is expected to change. Their equilibrium position will be the one which minimizes the energy of the system. So that, to obtain meaningful results, energetic calculations on surface always imply the relaxation of the surface (that implies small displacements of the atoms of the most external layers). In other words, the surface atomic positions obtained from the cleavage of a perfect crystal do not appear in the physical reality. Several strategies can be followed for the relaxation process assuming that modern DFT implementations contain routines to fully minimize the total energy with respect to all the geometric degrees of freedom (6 degrees of freedom for the cell an 3 more for the position of every additional atom). If it is not the case, a careful exploration of the space of configurations is necessary and, obviously, this could become virtually impossible for large atomic models [30].

In any case, the optimization of the geometry of the bulk unit cell is necessary before generating the surface slabs. Once the surface models are constructed, different possibilities can be used for further geometry optimizations. In order to simulate the constrains that bulk imposes to surface in physical systems, several constrains can be imposed in the slab relaxation: several authors propose to fix the supercell parameters [22, 31] or to freeze some slab layers such as the inner ones [50–52]. Any the election and as previously stated, slab geometry optimization with respect to the total energy is mandatory when dealing with total energies of surface models.

From the point of view of first principles calculations, the surface energy of stoichiometric surfaces is calculated from the difference in energy of the surface ions to those in the bulk per unit surface area [22]

$$E_{surf} = \frac{E_{slab} - nE_{bulk}}{2A} \qquad (15)$$

where E_{surf} is the surface energy, E_{slab} the total energy per repeated slab supercell, E_{bulk} the energy per unit cell in the bulk, n the ratio between the number of atoms contained in the surface slab and the number of atoms contained in the bulk unit cell (thus, depends on the number of layers used) and A the surface area per repeated unit (both sides are considered). Notice that since all the energies involved in (15) are obtained after geometry optimization, the effective E'_{bulk} energy in the slab may be different than the one obtained in an infinite crystal calculation.
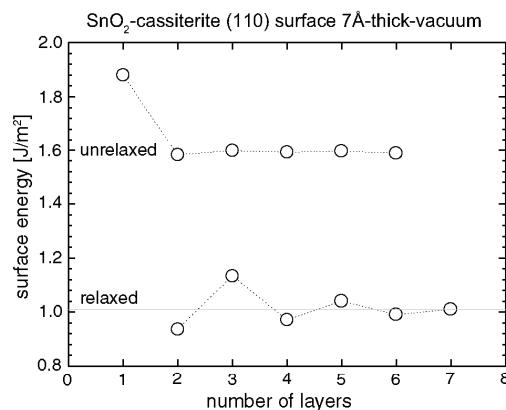
Figure 9. GGA surface free energy for the $SnO_2(110)$ surface as a function of the number of layers in the slab model calculated with equation (2.11). Notice that the surface model relaxation drops the surface free energy value down to 60%.

The most straightforward way to extract the quantity E'_{bulk} is to fit with a straight line the total energy of the slab E_{slab} values versus the slab thickness n (except in the case of the thinnest slab) and to take the slope E'_{bulk} [32]:

$$E_{slab} = 2AE_{surf} + nE'_{bulk}. \qquad (16)$$

Figure 9 shows the surface free energy for the $SnO_2(110)$ surface as a function of the number of layers in the slab model. Notice that the surface model relaxation drops the surface free energy value down to 60%. In this case, the difference between the E_{bulk} corresponding to an infinite crystal and the effective E'_{bulk} value necessary to converge E_{surf} is about 0.15 eV per 6 atoms in the unit cell.

The previous description is valid for non-polar and stoichiometric surfaces. For polar surfaces, the surface free energy value, as described in (15), does not converge when increasing the number of layers since, inevitably, both surface terminations are present in a slab calculation and exhibit a dipole moment perpendicular to the surface that leads to an spontaneous polarization P_s independent of the slab thickness. Consequently, even if no external electric field is applied, an electric field will be present in the inner part of the slab [33]. To make the inner field vanish, appropriate electric charges must be placed in both sides of the slab but, in any self consistent method, this will happen "automatically" producing what is usually referred as the "metallization of polar surfaces". However the amount of charge that can be transferred from one side to the other of the slab is limited by the band gap and the slab thickness. The residual electric field vanishes only with the inverse of the distance between the two surfaces (1/D). Therefore, to get good converged results for the surface geometries and energies, very thick slabs have to be used; this makes the investigation of the polar surfaces computationally very demanding. Ideally, one should calculate all quantities of interest for different slab thickness D and extrapolate the results to $1/D \rightarrow 0$.

For all this, the surface energy is not well defined in polar surfaces and, to be able to compare the relative stability of the nonpolar and polar surfaces, the discussion must be made in

terms of the cleavage energies. In the extreme case of nonpolar surfaces its cleavage energy is twice the surface energy (both sides of the slab are identical). As an example, for the polar surface ZnO(0001) the plot of the cleavage energy versus 1/D presents a simple linear behavior and the converged result is taken as the extrapolation $1/D \to 0$ (or $D \to \infty$) (*see* Fig. 10) [34].

For nonstoichiometric surfaces with different reduction percentages its relative stability not only depends on their relative surface free energy but also on the environment that surround them. In this point we will follow the methodology for the interpretation of ab initio calculations on surface models in terms of oxidation – reduction thermodynamics described by Reuter and Scheffler [23]. We consider the surface of a generic metal oxide M_xO_y in contact with an atmosphere at a given pressure p an temperature T. In the equilibrium,

$$G(T,p,N_M,N_O) - \Sigma(T,p) = N_M\mu_M(T,p) + N_O\mu_O(T,p) \quad (17)$$

where $\Sigma(T,p)$ is the surface free energy, N_M and N_O are the number of metal and oxygen atoms, respectively, and μ_M, μ_O their respective chemical potential. We obtain $\gamma(T,p)$ normalizing $\Gamma(T,p)$ to energy per unit area by dividing through the surface area A and modeling the surface system by a slab with two equivalent surfaces

$$\gamma(T,p) = \frac{1}{2A}\Big[G_{slab}(T,p,N_M,N_O) - N_M\mu_M(T,p) \\ - N_O\mu_O(T,p)\Big]. \quad (18)$$

Now A is the area of the surface unit cell and N_M and N_O are the number of atoms in the 3D supercell. If there is enough M_xO_y bulk to act as a thermodynamic reservoir, then

$$x\mu_M(T,p) + y\mu_O(T,p) = g_{MO}^{bulk}(T,p) \quad (19)$$

where g is the Gibbs free energy per formula unit M_xO_y. Therefore,

$$\gamma(T,p) = \frac{1}{2A}\Big[G_{slab}(T,p,N_M,N_O) - \frac{1}{x}N_Mg_{MO}^{bulk}(T,p) \\ + \Big(\frac{y}{x}N_M - N_O\Big)\mu_O(T,p)\Big] \quad (20)$$

and applying (9)

$$\gamma(T,p) = \frac{1}{2A}\Big[E_{slab}(T,p,N_M,N_O) - \frac{1}{x}N_ME_{MO}^{bulk}(T,p) \\ + \Big(\frac{y}{x}N_M - N_O\Big)\mu_O(T,p)\Big] \quad (21)$$

where E_{slab} is the DFT total energy of the slab and $E_{MO}^{bulk}(T,p)$ the corresponding DFT total energy per M_xO_y unit. Using (15) and assuming that $n = N_M/x$, this formula can be rewritten as:

$$\gamma(T,p) = E_{surf} - \frac{\Gamma_O}{A}\mu_O(T,p) \quad (22)$$

where $\Gamma_O = 1/2 [N_O - (y/x)N_M]$ is the excess of oxygen at the surface. Equation (22) enables to know how γ depends only on μ_O. Notice that $-\Gamma_O/A$ defines the slope of the line representing the surface free energy as a function of μ_O and depends only on the atomic composition of the slab (i.e: surface composition). For stoichiometric surfaces $\Gamma_O = 0$ and (22), is reduced to

$$\gamma(T,p) = E_{surf}. \quad (23)$$
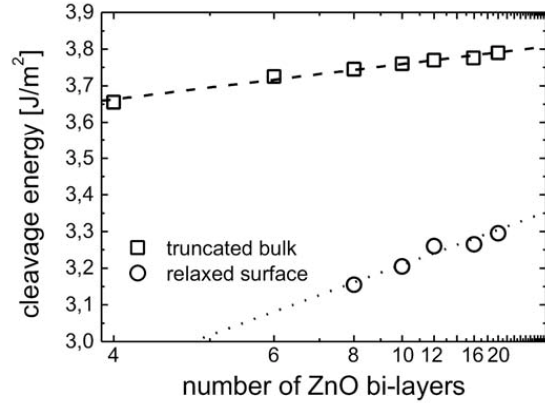
Figure 10. GGA cleavage energy of polar ZnO(0001) versus 1/D (or, equivalently, the number of equally-spaced layers). This presents a simple linear behavior and the converged result is taken as the extrapolation $1/D \to 0$ (or, equivalently, $D \to \infty$). Data taken from [55].

It is important to establish the range of μ_O with physical meaning. For low values of μ_O (oxygen-poor limit) M_xO_y breakdowns into M (solid) and O_2 (gas):

$$\mu_M(T,p) = g_M^{bulk}(T,p), \quad (24)$$

where $g_M^{bulk}(T,p)$ is the Gibbs free energy of the bulk metal. Using (19):

$$\min[\mu_O(T,p)] = \frac{1}{y}\Big[g_{MO}^{bulk}(T,p) - xg_M^{bulk}(T,p)\Big] \quad (25)$$

For high values of μ_O (oxygen-rich limit) O_2 condenses on the metal oxide surface:

$$\mu_O(T,p) = \frac{1}{2}g_{O_2}^{gas}(T,p) \approx \frac{1}{2}E_{O_2}^{gas} \quad (26)$$

where $E_{O_2}^{gas}$ is the total energy of a free O_2 molecule. Introducing the Gibbs free energy of oxide formation:

$$\Delta G(T,p) = g_{MO}^{bulk}(T,p) - xg_M^{bulk}(T,p) - \frac{y}{2}g_{O_2}^{gas}(T,p) \quad (27)$$

and considering again (9)
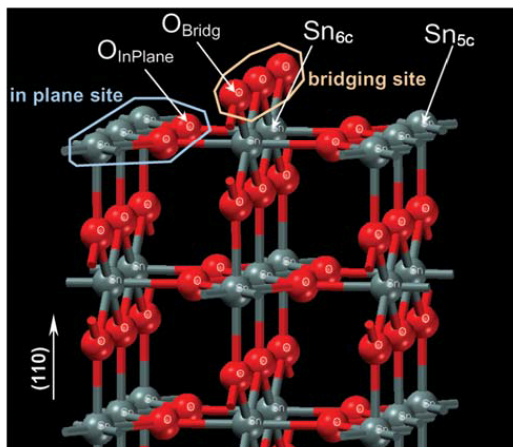
$$\Delta G(T,p) \approx \Delta E(V) = E_{MO}^{bulk}(V) - xE_M^{bulk}(V) - \frac{y}{2}E_{O_2}^{gas}(V). \quad (28)$$

Finally, the range of μ_O is

$$\frac{1}{y}\Delta E(V) < \mu_o - \frac{1}{2}E_{O_2}^{gas} < 0 \quad (29)$$

Equation (22) represents the general recipe of how to retrieve $\gamma(T,p)$ from μ_O, but for chemical and physical purposes it is convenient to relate μ_O to a given T and p. It can be done considering that the surrounding O_2 atmosphere forms and ideal-gas-like reservoir, and then [35]:

$$\mu_O(T,p) = \mu_O(T,p_0) + \frac{1}{2}k_BT\ln\left(\frac{p}{p_0}\right). \quad (30)$$

Applications of DFT Calculations to Chemical Gas Sensors: Design and Understanding 253


Figure 11. Slab model of the SnO_2-cassiterite (110) surface. Relevant surface sites and atoms are identified. Reprinted with permission from [58], J. D. Prades et al., *J. Electrochem. Soc.* 154, H657 (2007). © 2007, The Electrochemical Society.

Figure 12. Surface free energies for different terminations of the SnO_2(110) surface as a function of the oxygen chemical potential. The top axis shows the corresponding O_2 gas temperature for atmospheric air equivalent conditions (i.e., oxygen partial pressure of ∼0.21 bar) [57]. Reprinted with permission from [58], J. D. Prades et al., *J. Electrochem. Soc.* 154, H657 (2007). © 2007, The Electrochemical Society.

For standard pressure, all the terms needed to compute $\mu_O(T,p_0)$ can be found tabulated in thermochemistry charts [36]. Choosing as the zero reference state of $\mu_O(T,p)$ the total energy of oxygen in an isolated molecule, $\mu_O^{O\text{-rich}}(0K,p) = 1/2\ E_{O_2,\text{total}} \equiv 0$, it is possible to calculate $\mu_O(T,p_0)$ as:

$$\mu_O(T,p_0) = \mu_O^{O\text{-rich}}(0K,p_0) + \frac{1}{2}\Delta G(\Delta T,p_0,O_2). \qquad (31)$$

Finally, let us present a brief application of the presented theory to the SnO_2(110) reduced and oxidized surfaces [37]. For SnO_2, the excess of oxygen is defined as $\Gamma_O = 1/2\ (N_O - 2N_{Sn})$. In this case, the oxygen chemical potential $\mu_O(T,p)$ was found tabulated as a function of the temperature and the partial pressure of O_2 in [36]. Following the previous procedure, DFT calculations provided estimations of γ which are to evaluate surface free energy γ of a particular surface termination (Γ_O) for a range of μ_O values that are function of T and p. In order to consider μ_O values with physical meaning, a pair of remarks are necessary: regarding physically reachable temperatures, it is important to keep in mind that SnO_2 dissociates in $SnO + O_2$ at temperatures above 1500°C [38] and, for gas sensing applications under ambient conditions, the oxygen partial pressure can be fixed at atmospheric conditions (i.e.: ∼0.21 bar). With these constrains, μ_O must be restricted to values from −2.7 eV (at 1500°C and 0.21 bar) to 0 eV (at −273°C).

Semancik and co-workers observed that simple heating of a stoichiometric SnO_2-cassiterite(110) surface under UHV to temperatures above 225°C leads to loss of O_{Bridg} and the formation of oxygen bridging vacancies ($O_{BridgVac}$) (*see* Fig. 11) [39, 40]. If the temperature is raised above 525°C, in-plane oxygen vacancies ($O_{InPlaneVac}$) can be produced, but usually forming complex configurations with the presence of $O_{BridgVac}$ and other $O_{InPlaneVac}$. It is worth noting that, as stated in [39], the vacancy generation temperatures may be dependent on the particular samples used and the oxygen pressure. In any case, it is accepted that $O_{BridgVac}$ can be generated at lower temperatures than $O_{InPlaneVac}$ forming these last more complex configurations [41].
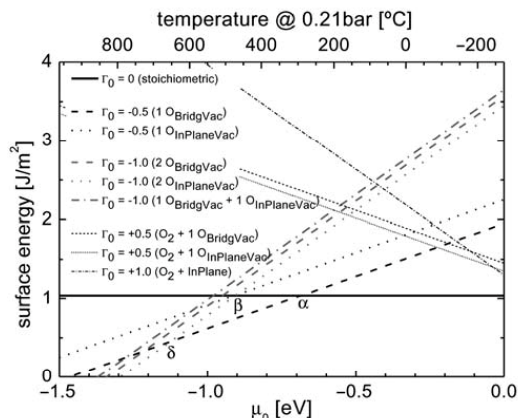
Figure 12 presents $\gamma(\mu_O)$ straight line plots for several surface terminations. Regarding single oxygen vacancies per slab unit ($\Gamma_O = -0.5$) it is remarkable that $O_{BridgVac}$ become more stable than the stoichiometric configuration at 270°C whereas $O_{InPlaneVac}$ do so at 480°C (points α and β). Thus, the thermodynamics of the formation of single $O_{BridgVac}$ results fairly explained with ab initio calculations but, with the model used, it is not possible to determine the threshold temperature above which a single $O_{InPlaneVac}$ will be more stable than an $O_{BridgVac}$. In order to study this point and remembering the complex configurations suggested in [39], double oxygen vacancies per slab termination have been considered ($\Gamma_O = -1$). Notice how all these complex configurations cross the one single $O_{BridgVac}$ line at temperatures between 640 − 780°C (point δ).

In summary, under ambient conditions, the stoichiometric surface configuration is the most stable, as it was expected. When temperature is raised above 270°C the formation of single $O_{BridgVac}$ becomes possible and, even at higher temperatures (above 480°C), the formation of single isolated $O_{InPlaneVac}$ is plausible. Still, at higher temperatures (above 640°C) the multi-vacant configurations are the most probable. This predicted evolution is compatible with the known behavior with slightly higher temperatures than under UHV conditions as expected due to the presence of ambient oxygens that could make harder the vacancy generation.

With the intention of giving a more complete view of the surface stability, several oxidized configurations were considered and, remarkably, these are only metastables in the complete range of temperatures under atmospheric oxygen partial pressure. The difficulty in oxidizing the surface may arise from the fact that the cations in SnO_2 are already in their maximum oxidation states, which prevents the further addition of monatomic O^{-2} species to the surface.

We should stress that here there are compared only certain discrete degrees of oxidation − reduction of the surface because of the size of the slab used in these calculations (2 × 1 unit cells wide). For example, in the case of $O_{BridgVac}$, $\Gamma_O = -0.5$ and $\Gamma_O = -1$ correspond to 50% and 100% reduction of the surfaces,

but, in the real system, intermediate compositions may be stable at different conditions of pressure and temperature. Slightly reduced surfaces can then be stable at temperatures lower than those estimated above.

2.4. Nanoparticles Stability

Many fundamental properties with strong influence in the sensing capabilities of nanomaterials have a strong dependence on particle size [42, 43]. Moreover, to synthesize nanoparticles with uniform and reliable properties many parameters such as size, temperature, chemical environment, electric fields, optical irradiation, choice of substrates, surfactants, and the composition (or choice of dopants) may be used to manipulate shape at the nanoscale [65–73]. Accurate and explicit computational studies of nanoparticles, which account for factors influencing the previous experimental parameters, are very computationally demanding and difficult to extend to sizes above 1–2 nm. This is not only due to the large computational resources required to calculate the optimized shape of nanoparticles with first principles methods, but also because of the large set of structures that must be explicitly examined in order to effectively sample structure space. Even when order-N methods and massively parallel computers become readily accessible. Therefore, it is highly desirable to use a theoretical approach that is predominantly analytical, and is based on a limited set of experimental or theoretical data.

This began with the classical work of Wulff [44] who predicted the shape of macroscopic crystals based on the minimization of the total surface energy. The so-called Wulff construction describes the equilibrium shape of crystals, given by the convex envelope of planes (perpendicular to the surface normals) that minimizes surface energy for a given enclosed volume. The distance of a surface plane from the center of mass of the crystal is proportional to the surface energy of that plane.

Another theory (based on a Gibb's summation) was introduced by Barnard and Zapol for use with isolated (unsupported) nanostructures, which included both surface and edge energies, as well as corner energies, surface tensions and bulk elastic energy. A detailed outline of the range of applicability of the theory can be found elsewhere [45], along with information on how to use the theory to optimize the shape of any nanocrystal as a function of experimentally relevant parameters such as size, temperature, or surface chemistry [46].

Here we will sketch the main ideas of this model. For a given nanoparticle of material in phase x, the free energy may be expressed as a sum of contributions form the particle bulk, surfaces, edges and corners such that,

$$G_0^x = G_x^{bulk} + G_x^{surface} + G_x^{edge} + G_x^{corner} \tag{32}$$

where,

$$
\begin{aligned}
G_x^{bulk} &= \Delta_f G_x^0(T) \\
G_x^{surface} &= \frac{M}{\rho_x} p \sum_j g_j \lambda_{xj}(T) \\
G_x^{edge} &= \frac{M}{\rho_x} q \sum_i f_i \gamma_{xi}(T) \\
G_x^{corner} &= \frac{M}{\rho_x} w \sum_k h_k \epsilon_{xk}(T)
\end{aligned}
\tag{33}
$$

in terms of the molar mass M and density ρ_x of the material on phase x. Here (in terms of the temperature T), $G_x^{surface}$ is expressed in terms of the surface to volume ratio q and $\gamma_{xi}(T)$ the surface free energy of facet i; G_x^{edge} is expressed in terms of the edge to volume ratio p and $\lambda_{xj}(T)$ the edge free energy of edges j; and G_x^{corner} is expressed in terms of the corner to volume ratio w and $\epsilon_{xk}(T)$ the corner free energy of corners k. The weighting factors are defined so that,

$$\sum_i f_i = \sum_j g_j = \sum_k h_k = 1. \tag{34}$$

The values $\gamma_{xi}(T)$, $\lambda_{xj}(T)$ and $\epsilon_{xk}(T)$ must be calculated for all i, j, and k of interest using an appropriate computational method such as Density Functional Theory and the same convergence; and the rations q, p, w weighting factors must be calculated explicitly for each shape and facets therein.

However, this does not account for the effects of surface tension on the particle that are significant at the nanoscale and may not be ignored. The surface tension produces an effective pressure on the particle, which may be addressed by introducing the resulting (usually compressive) volume dilation (or average strain) e. The effect of this dilation is to reduce the molar volume. Therefore, the model including the effective pressure becomes:

$$G_x^0 = \Delta_f G_x^0(T) + \frac{M}{\rho_x}(1-e)$$
$$\left[p \sum_j g_j \lambda_{xj}(T) + q \sum_i f_i \gamma_{xi}(T) + w \sum_k h_k \epsilon_{xk}(T) \right] \tag{35}$$

In general, the volume dilation due to surface tension σ (and the material compressibility β) may be approximated using the Laplace –Young equation, where R is the mean radius of the particle, so that,

$$e = \frac{2\beta\sigma_x(T)}{R} \tag{36}$$

where,

$$\sigma_x(T) = \sum_i f_i \sigma_{xi}(T). \tag{37}$$

This approach assumes that the particles are spherical and that the surface tension is independent of the orientation. The pressure induced at any point of the surface is directed to the center of curvature and proportional to the curvature at that point. The validity of this approximation has been demonstrated for faceted nanoparticles over 500 atoms [45].

Using geometrical arguments it can be shown that the contribution from edges and corners can be neglected for nanocrystals above 5–6 nm. Below this size regime, the explicit morphology could be considered performing calculations of isolated nanoparticles. Similarly, above, 75–100 nm in diameter, the free energy of the surface is negligible compared with the bulk contribution and bulk strain becomes as important as the surface strain. For these reasons, this model is best applied to particles between 3 and 100 nm in the reduced form:

$$G_x^0 = \Delta_f G_x^0(T) + \frac{M}{\rho_x}(1-e)\left[q \sum_i f_i \gamma_{xi}(T) \right] \tag{38}$$
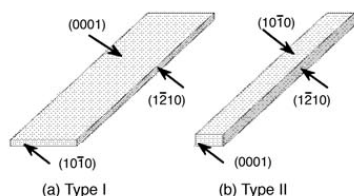
Figure 13. The experimental results show that there are three types of ZnO nanobelts: a) Type I and b) Type II, each with different growing directions and cross-sections. The growing directions are dependent on the size if the nanobelts, and the lengths can be up to few millimeters. Reprinted with permission from [81], A. S. Barnard et al., *Chem. Phys. Lett.* 419, 313 (2006). © 2006, Elsevier.

where only surface and bulk contributions are considered. Notice that while γ_{xi} can be computed as detailed in Section 2.3 surface tension can be approximated by:

$$\sigma = \frac{\partial G}{\partial A} \approx \frac{\Delta G}{\Delta A}.\tag{39}$$

Therefore, applying series of two-dimensional dilations to the slab in the plane of the surface and plotting the computed total energy ($E_T \sim G$) versus the slab area A the surface tension σ can be obtained as the slope.

A successful application of this model to materials used in chemical sensing application is the case of TiO_2, where a broad study has been reported investigating the relative stability of quasi-spherical and faceted anatase nanoparticles [47], and the effect of particle shape on the size-dependent phase transition between anatase and rutile nanoparticles [48]. The study also included an investigation of the effect of water on the shape of TiO_2 nanocrystals, [49] followed by a systematic study on the effects of surface acidity on the shape and phase stability of anatase and rutile nanoparticles less than 100 nm in size [50], with results in good agreement with experiment.

Another example involves the prediction of the grown morphologies of ZnO nanobelts [51]. Two types of nanobelts (experimentally observed) were considered growing along (10–10) [Type I] and growing along (0001) [Type-II] (*see* Fig. 13). When varying the nanobelt length and thickness, Type-II nanobelts were predicted to be consistently lower in free energy than Type-I. In contrast, when varying the nanobelt width (Fig. 14), an orientational transition was observed at a Type-II width of 76 nm (or a Type-I width of 176 nm) in excellent agreement with experimental X-ray nanodiffraction observations.

2.5. Chemisorption

The adsorption of molecules onto a surface is a necessary prerequisite to any chemical process at the surface such as chemical sensing. There are two principal modes of adsorption of molecules on surfaces: the physical adsorption (physisorption) and the chemical adsorption (chemisorption). The basis of distinction is the nature of the bonding between the molecule and the surface. With physisorption: the only bonding is by weak Van der Waals-type forces and there is no significant redistribution of electron density in either the molecule or at the substrate surface. In chemisorption a chemical bond, involving substantial rearrangement of electron
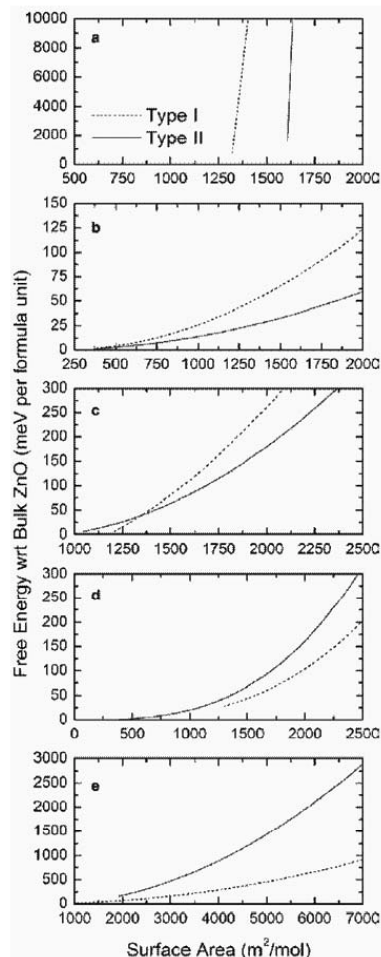
Figure 14. Total Gibbs free energy of Type I and Type II ZnO nanobelts (as defined in Fig. 13). The decreasing surface area corresponds to an increase in: a) length, b) thickness, c) width d) total cross-section area, and e) the width-to-thickness ratio. The cross over in c) at a Type II width of 76 nm indicates the size dependence of the orientational transition. Reprinted with permission from [81], A. S. Barnard et al., *Chem. Phys. Lett.* 419, 313 (2006). © 2006, Elsevier.

density, is formed between the adsorbate and the substrate; the nature of this bond may lie anywhere between the extremes of virtually complete ionic or complete covalent character. Consequently, the second case will deserve the major attention when studying the detection of chemical species by measuring their electric effect on the conductivity of the sensing material.

As previously stated, first principles codes provide the total energies per volume unit of the atomic model contained in the simulation cell. It is possible to evaluate the energetics of the gas-surface interactions building appropriate atomic models of the initial and final configurations of the interaction such as the clean surface slab and the isolated molecule (*see* Fig.15(a, b), and
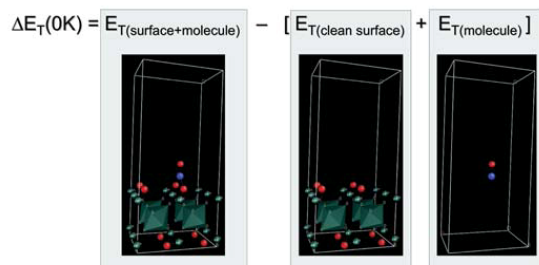
Figure 15. Graphic representation of the atomic models implied in energy valance of equation (40).

Figure 16. Schematic representation of the surface-molecule interaction potential as a function of the distance between them.

the surface plus the molecule system (Fig. 15(c)). With the 3 total energies of these 3 models the interaction energy (now an adsorption) can be obtained as follows:

$$E_{\text{Tinitial}} = E_{\text{T(clean surface)}} + E_{\text{T(molecule)}}$$
$$E_{\text{Tfinal}} = E_{\text{T(clean surface+molecule)}} \qquad (40)$$
$$\Delta E_{\text{ads}} = \Delta E_{\text{T}} = E_{\text{Tfinal}} - E_{\text{Tinitial}}$$

Accordingly, a negative value of ΔE_{ads} means that the adsorption is exothermic, it being possible for this to occur spontaneously without entropic considerations (DFT deals with the ground state at 0K). Obviously, the energetics of the inverse interaction (desorption) exchange the initial and final states.

We will center the discussion on the non-dissociative molecular chemisorption. The depth of the chemisorption well is a measure of the strength of binding to the surface. The location of the global minimum on the horizontal axis corresponds to the equilibrium bond distance (r_e) for the adsorbed molecule on this surface (*see* Fig. 16). In this particular case the energy ΔE_{ads} corresponds to an exothermic adsorption and it is negative (one can also often find the depth of this well associated with the enthalpy of adsorption ΔH_{ads}). Therefore, there is no barrier to be overcome in the adsorption process and there is no activation energy of adsorption (i.e. $E_{\text{act}}^{\text{ads}} = 0$). There is, of course, a significant barrier to the reverse, desorption process. Clearly, in this particular case, the magnitudes of the energy of adsorption and the activation energy for desorption can also be equated:

$$E_{\text{act}}^{\text{des}} = \Delta E_{\text{ads}} \qquad \text{or} \qquad E_{\text{act}}^{\text{des}} \approx -\Delta H_{\text{ads}} \qquad (41)$$

Is important to point out, from the point of view of the computational procedures, that to obtain meaningful total energies an their corresponding interaction energies, it is necessary to ensure the effective cancellation of errors between the large energies that appear in equation (40). From the point of view of the atomic models, supercell dimensions and atomic arrangements must be initially set as similar as possible in initial and final models. Additionally, identical sampling grids for the k (and, in some codes also for r) space must be used. In these conditions, relaxations of the structures must be performed in order to get total energies corresponding to the equilibrium configuration (avoiding as much as possible "user dependant" results due to the initial arbitrariness in the position of the atoms).

Moreover, other sources of error such as the basis set superposition error (BSSE) must be taken into account. BSSE correction
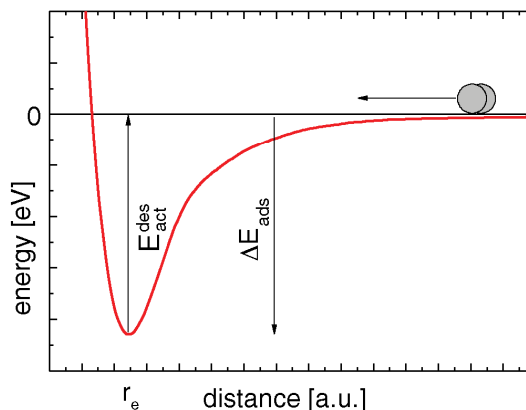
to the binding energy of a system of components A and B (in our case, the surface slab and the molecule) should be estimated as the sum of the energies of component A and component B in the geometries of the combined system AB with the basis sets of A and B, respectively, minus the sum of the energies of component A and component B in the geometries of the combined system AB with the basis set of the combined system AB (i.e. with ghost states). Further details on this can be found elsewhere [52].

As a final remark, the applicability of the approximations made in equation (9) where the vibrational contribution to the Gibbs free energy is assumed to be negligible should also be verified.

From the energetics of the interaction of the gas with the sensor surface, many macroscopic parameters (such as residence times or desorption temperatures) can be estimated providing a deep understanding of the sensing mechanisms.

Let us begin analyzing the adsorption/desorption kinetics. The rate of adsorption of a molecule onto a surface R_{ads} is governed by the rate of arrival of molecules at the surface and the proportion of incident molecules which adsorb effectively. In other words, we can express the rate of adsorption (per unit area of surface) as a product of the incident molecular flux F and the sticking probability S.

$$R_{\text{ads}} = S \cdot F \qquad (42)$$

The flux of incident molecules is given by the Hertz-Knudsen equation

$$F = \frac{P}{\sqrt{2\pi mkT}} \qquad (43)$$

where P is the gas pressure, m the mass of one molecule and T the absolute temperature. The sticking probability is clearly a property of the adsorbate/substrate system under consideration and must lie in the range $0 < S < 1$. It depends on the existing coverage of adsorbed species (θ) and the presence of any activation barrier to adsorption. Therefore,

$$S = f(\theta) \exp\left(\frac{-E_{\text{act}}^{\text{ads}}}{RT}\right) \qquad (44)$$

Applications of DFT Calculations to Chemical Gas Sensors: Design and Understanding 257

where E_{act}^{ads} is the activation energy of the barrier for adsorption and $f(\theta)$ is some, yet undetermined, function of the existing surface coverage of adsorbed species. Combining the equations for S (43) and F (44) we obtain the following expression for the rate of adsorption:

$$R_{ads} = \frac{f(\theta)P}{\sqrt{2\pi mkT}} \exp\left(\frac{-E_{act}^{ads}}{RT}\right) \qquad (45)$$

The above equation indicates that the rate of adsorption is expected to be first order with regard to the partial pressure of the molecule in the gas phase above the surface: this can be generalized introducing the kinetic order of the reaction x as an exponent of P. Additionally, it should be recognized that the activation energy for adsorption may be dependent on the surface coverage (i.e. $E_{act}^{ads} = E(\theta)$). If it is assumed that the sticking probability is directly proportional to the concentration of vacant surface sites (which would be a reasonable first approximation for non-dissociative adsorption) then $f(\theta)$ is proportional to $(1-\theta)$; where θ is the fraction of sites which are occupied (the Langmuir definition of surface coverage).

An adsorbed molecule present on a surface at low temperatures could remain almost indefinitely in that state. As the temperature of the substrate is increased, there will come a point at which the thermal energy of the adsorbed species is enough that one of these possibilities may occur:

- a molecular specie may decompose to yield either gas phase products or other surface species.
- an atomic adsorbate may react with the substrate to yield a specific surface compound, or diffuse into the bulk of the underlying solid.
- the species may desorb from the surface and return into the gas phase.

The last of these options is the non-dissociative desorption process. In the absence of decomposition, the desorbing species will generally be the same as that originally adsorbed but this is not necessarily always true.

The rate of desorption of an adsorbate from a surface R_{des} can be expressed in the general form:

$$R_{des} = kN^x \qquad (46)$$

where N is the surface concentration of adsorbed species, x the kinetic order of the desorption and k the rate constant for the desorption process. The order of desorption can be predicted because we are concerned with an elementary step of a "reaction":

$$x \text{ Atom (ads)} \rightarrow \text{Atom}_x \text{ (gas).} \qquad (47)$$
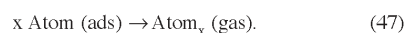
The rate constant for the desorption process can be expressed in an Arrhenius form,

$$k^{des} = A \ \exp\left(\frac{-E_{act}^{des}}{RT}\right) \qquad (48)$$

where E_{act}^{des} is the activation energy for desorption and A is the pre-exponential factor, that can also be considered to be the "attempt frequency" ν at overcoming the barrier to desorption. This then gives the following general expression for the rate of desorption

$$R_{des} = -\frac{dN}{dt} = \upsilon \cdot N^x \exp\left(\frac{-E_{act}^{des}}{RT}\right) \qquad (49)$$

In the particular case of simple molecular adsorption, the pre-exponential/frequency factor (ν) may also be equated with the frequency of vibration of the bond between the molecule and substrate (around 10^{13}Hz). This is because every time this bond is stretched during a vibrational cycle, can be considered an attempt to break the bond and hence an attempt to desorb.

In the following, it is going to be shown how these simple kinetic definitions can be connected with many of parameters relevant in gas sensing.

From the point of view of a gas sensor, a net response to a gas presence will be possible if the average time the target gas molecule remains adsorbed $<t_{resid}>$ bigger than the average time between adsorptions $<t_{ads}>$. These times can be estimated with the previously described R_{ads} and R_{des}:

$$R_{ads} \cdot s = \frac{1}{\langle t_{ads} \rangle}$$

$$R_{des} \cdot s = \frac{1}{\langle t_{resid} \rangle} \qquad (50)$$

where s is the exposed surface of the active material to the gas. So that, sensing will only be possible if $<t_{resid}> >> <t_{ads}>$. In the range of $<t_{resid}> = <t_{ads}>$ the presence of gas will be transduced just like noise.

Once guaranteed the detection with energetic and kinetic arguments, it is possible to determine the effect of the adsorbed gas on the conductivity of the material. As stated previously (Section 1), in the case of independent nanoparticles, the Schottky barrier determines the variation of conductivity after gas exposures. As we will see, this barrier can be calculated from the integration of Poisson equation of the electronic charges at surface. Therefore, the final result depends on the geometry of the sensing material but, for simplicity and in order to illustrate the connection between conductivity and coverage, we will assume spherical geometry as done by some authors [53, 54].

So that, let us assume that we have a set of spherical nanocrystals of diameter L and only one oxidizing specie (such as NO_2 or O atoms) fixed and distributed uniformly on their surface Ox^{-l}. In has been demonstrated that the adsorption sites $O_{SurfVac}$, which are related to oxygen vacancies [55, 37], will fix oxidizing species and will produce a spatial charge region (or depletion region) when ionized. This spatial charge region is depleted of conduction electrons until a certain depth (between ½L and l). Therefore only ionized impurities lay as charged species in the depletion region.

Taking into account the high density of oxygen vacancies present in the material [56, 57] and the fact that this vacancies are the main impurity contribution, we can assume that the conduction electron density will approximately equal to oxygen vacancy density.

The Poisson equation leads to (in 1D for simplicity),

$$\frac{\partial^2}{\partial x^2} V = \frac{-en_b}{\varepsilon \varepsilon_0} \qquad \text{between} 1 < |x| < \tfrac{1}{2}L \qquad (51)$$

where (½L−l) denotes the external depleted shell of the grain. Integrating twice this equation and applying the continuity condition in the potential $(V(0) = V_0)$ and in the field $(\partial V/\partial x|_{x=1} = 0)$ we obtain

$$V(x) = \frac{-en_b}{2\varepsilon \varepsilon_0}(x-1)^2 + V_0 \quad \text{between } 1 < |x| < \tfrac{1}{2}L \qquad (52)$$

and we can obtain the height of the Schottky equation,

$$V_s = V(\tfrac{1}{2}L) - V(l) = \frac{-en_b}{8\varepsilon\varepsilon_0}L^2 \tag{53}$$

in the case of a fully depleted grain, or

$$V_s = V(\tfrac{1}{2}L) - V(l) = \frac{-eI\left[Ox^{-I}\right]^2}{8\varepsilon\varepsilon_0 n_b} \tag{54}$$

in the case of partial depleted grain. But, as pointed out in the work [58], the expression (54) is only valid when the oxygen is fixed with a state below the Fermi level. In general, N_s surface charged states lying in E_s energy bands are distributed by a Fermi-Dirac statistics. This gives the following expression for the Schottky barrier:

$$V_s = \frac{-eN_s^2}{2\varepsilon\varepsilon_0 N_D}\left[1 + \exp\left(\frac{E_s - E_F}{KT}\right)\right]^{-2} \tag{55}$$

In the case of oxidizing molecules, as they fix electrons at the surface, they can be considered as creating acceptor levels and its energy state should be located below the Fermi level. This fact has been experimentally shown for (110) TiO_2 surfaces [59], by LCAO cluster model [60] and DFT calculations [22, 31, 55, 61] in (110) SnO_2 surfaces.

Following the expressions found by Bethe [62], it is possible to calculate the density of current by thermoionic emission between grains as,

$$J_T = -en_b\left(\frac{KT}{2m^*\pi}\right)^{1/2}\exp\left(\frac{eV_s}{KT}\right)\left[\exp\left(\frac{-eV_a}{KT}\right) - 1\right] \tag{56}$$

where V_a is the biasing potential seen by the nanocrystals, therefore if there are G resistors –nanograins– , the actual potential seen by a grain is $V = V_a/G$. Thus, when

$$\frac{eV_a}{G} \ll KT \tag{57}$$

we can approximate,

$$J_T \approx e^2 n_b\left(\frac{1}{2m^*\pi KT}\right)^{1/2}\exp\left(\frac{eV_s}{KT}\right)V_a \tag{58}$$

and deriving we obtain the conductivity as

$$\sigma = e^2 n_b\left(\frac{1}{2m^*\pi KT}\right)^{1/2}\exp\left(\frac{eV_s}{KT}\right) \tag{59}$$

Substituting the expression for the Schottky barrier (54) in this equation and with the definition of coverage

$$\theta = \frac{\left[Ox^{-I}\right]}{\left[O_{SurfVac}\right]} \tag{60}$$

in this case, the conductivity leads to

$$\sigma = e^2 n_b\left(\frac{1}{2m^*\pi KT}\right)^{\tfrac{1}{2}}\exp\left\{\frac{-e^2 I\left[O_{SufVac}\right]^2\theta^2}{8\varepsilon\varepsilon_0 n_b KT}\right\} \tag{61}$$

and this equation gives a useful expression of the conductivity as function of the coverage which can be estimated as a function of the temperature of the sensor-gas system and the pressure of the gas form the DFT energetics.

Note that in the previous derivation, a single electron transfer for every single adsorption is assumed. An approximate value of this charge transfer between surface and adsorbate can be computed with a simple population analysis (such as Mulliken) available in many DFT codes.

The equilibrium that may exist between the molecules adsorbed on a surface and the molecules in the gas phase is a dynamic state. In other words, the equilibrium represents a state in which the rate of adsorption of molecules onto the surface is exactly balanced by the rate of desorption of molecules back into the gas phase. Therefore, it should be possible to simply derive an isotherm for the adsorption process by considering and equating the rates for these two processes. Equaling equations (45) and (49),

$$\frac{P \cdot f(\theta)}{f'(\theta)} = C(T) \tag{62}$$

where the terms $f(\theta)$ and $f'(\theta)$ contain the pre-exponential surface coverage dependence of the rates of adsorption and desorption, respectively, and all other factors have been taken over to the right hand side to give a temperature-dependent "constant" characteristic of this particular adsorption process, $C(T)$.

Certain simplifying assumptions can be made. The first is one of the key assumptions of the Langmuir isotherm that supposes that adsorption takes place only at specific localized sites on the surface and that the saturation coverage corresponds to complete occupancy of these sites. Also, let us further restrict our consideration to a simple case of reversible molecular adsorption. Under these circumstances, it is reasonable to assume coverage dependencies for rates of the two processes of the form:

- *Adsorption:* $f(\theta) = c\,(1-\theta)$ i.e. proportional to the fraction of sites that are unoccupied.
- *Desorption:* $f'(\theta) = c'\,\theta$ i.e. proportional to the fraction of sites which are occupied by adsorbed molecules.

where θ is the fraction of sites occupied at equilibrium. Substitution into equation (62) then arise

$$\frac{P \cdot (1-\theta)}{\theta} = B(T) \tag{63}$$

where $B(T) = (c'/c)\cdot C(T)$ and, after rearrangement this gives the Langmuir Isotherm expression for the surface coverage

$$\theta = \frac{bP}{1 + bP} \tag{64}$$

where b $(= 1/B(T))$ is a function of temperature and contains an exponential term of the form

$$b = ...\exp\left[\frac{\left(E_{act}^{des} - E_{act}^{ads}\right)}{RT}\right] = ...\exp\left[\frac{-\Delta H_{ads}}{RT}\right] \tag{65}$$

Consequently, b can only be regarded as a constant with respect to coverage if the enthalpy of adsorption is independent of coverage (this is the second major assumption of the Langmuir isotherm). Further information on other isotherms or the study of dissociative processes can be found elsewhere [29].

An extremely relevant parameter of a sensor is its working temperature. Heating the active material to the appropriate temperatures can improve dramatically the response to a target gas and even force the desorption of undesired interfering gases. So that, linking the energetics of the surface-gas interaction with temperatures at which the desorption takes place is extremely relevant.

There exist a range of techniques for studying surface reactions and molecular adsorption on surfaces which utilize temperature-programming to discriminate between processes with different activation parameters. Among them, the most useful for single crystal studies is Temperature-Programmed Desorption (TPD).

Conceptually, the experiment is simple, involving the adsorption of one or more molecular species onto the sample surface at low temperature (frequently 300 K, but sometimes sub-ambient) and the subsequent heating of the sample in a controlled manner (preferably so as to give a linear temperature ramp) while monitoring the evolution of species from the surface back into the gas phase.

The data obtained from this experiment consist of the intensity of each recorded mass fragment as a function of time/temperature (*see* Fig. 18). In the case of a simple reversible adsorption process it may only be necessary to record one signal - that attributable to the molecular ion of the adsorbate concerned. The following points are worth noting:

- The area under a peak is proportional to the amount originally adsorbed, so that proportional to the surface coverage.
- The position of the peak (the peak temperature or the maximum desorption rate temperature) is related to the enthalpy of adsorption or, in other words, to the strength of binding to the surface, as shown below.

One implication of the last point is that if there is more than one binding state for a molecule on a surface (and these have significantly different adsorption enthalpies) then this will give rise to multiple peaks in the TPD spectrum.

In a temperature programmed desorption experiment in which the temperature is increased linearly with time from some initial temperature T_0, as:

$$T = T_0 + \beta t \qquad \text{and} \qquad dT = \beta t \qquad (66)$$

The intensity of the desorption signal I(T), is proportional to the rate at which the surface concentration of adsorbed species is decreasing. This is obtained by combining (49) and (66) to give

$$I(T) \propto -\frac{dN}{dT} = \frac{\nu N^x}{\beta} \exp\left(\frac{-E_{act}^{des}}{RT}\right). \qquad (67)$$

This problem may also be considered in a rather simplistic graphical way (*see* Fig. 17): the key is to recognise that the expression for the desorption signal (67) is basically a product of a coverage term (N^x - where N depends on T) and an exponential term (involving both E_{act}^{des} and T). Initially, at low temperatures $E_{act}^{des} \gg RT$ and the exponential term vanishes. However, as the temperature is increased this term begins to augment very rapidly when the value of RT approaches that of the activation energy E_{act}^{des}. By contrast, the pre-exponential term is dependent upon the coverage N(T) at the temperature concerned. This term will remain at the initial value until the desorption rate becomes significant as a result of the increasing exponential term. Then, it
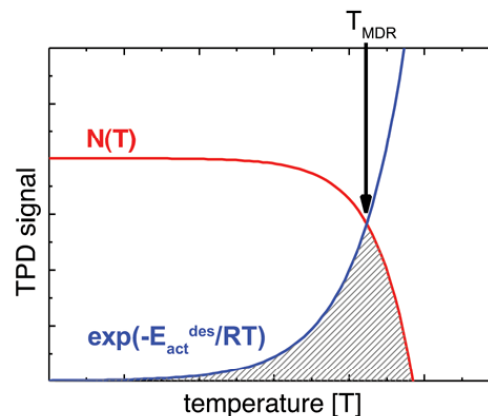
Figure 17. Qualitative representation of the two factors involved in equation (67). While the pre-exponential factor decreases with temperature, the exponential grow: its combination qualitatively leads to the peak shape of the TPD signal with a maximum at T_{MDR}.

will decrease rapidly until the coverage is reduced to zero. The shaded area is an approximate representation of the product of these two functions, and, hence, also an approximate representation for the desorption signal. This illustration may be simplistic but it clearly shows why the desorption process gives rise to a well-defined desorption peak.

In order to relate the activation energy of a desorption process with its associated desorption peak let us assume non-dissociative molecular desorption; in this case the desorption kinetics will usually be first order (i.e. x = 1). The maximum desorption signal in the I(T) trace will occur when dI/dT = 0

$$\frac{d}{dT}\left[\frac{\nu N}{\beta}\exp\left(\frac{-E_{act}^{des}}{RT}\right)\right] = 0 \qquad (68)$$

and, remembering that the surface coverage changes with temperature N = N(T),

$$\frac{\nu N}{\beta}\frac{E_{act}^{des}}{RT^2}\exp\left(\frac{-E_{act}^{des}}{RT}\right) + \frac{\nu}{\beta}\exp\left(\frac{-E_{act}^{des}}{RT}\right)\frac{dN}{dT} = 0 \qquad (69)$$

Substituting dN/dT from equation (67) we obtain

$$\frac{\nu N}{\beta}\left[\frac{E_{act}^{des}}{RT^2} - \frac{\nu}{\beta}\exp\left(\frac{-E_{act}^{des}}{RT}\right)\right]\exp\left(\frac{-E_{act}^{des}}{RT}\right) = 0 \qquad (70)$$

The solution is given by setting the expression in square brackets equal to zero,

$$\frac{E_{act}^{des}}{RT_{MDR}^2} = \frac{\nu}{\beta}\exp\left(\frac{-E_{act}^{des}}{RT_{MDR}}\right) \qquad (71)$$

where we have now defined the temperature at which the desorption maximum occurs to be $T = T_{MDR}$ (the maximum desorption rate temperature). Unfortunately, this equation cannot be re-arranged to make T_{MDR} the subject, but it can be noticed that:
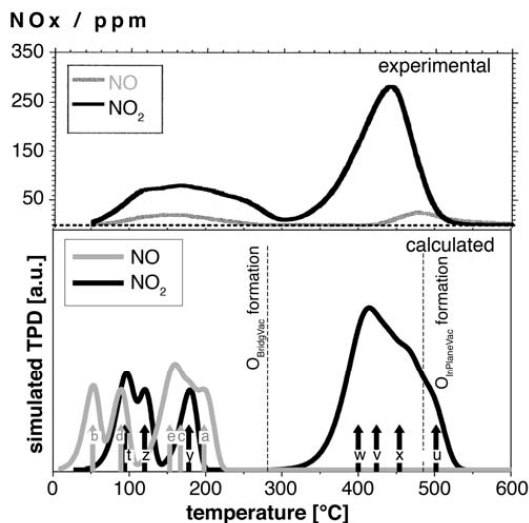
Figure 18. Top: Experimental TPD spectra of NO and NO_2 desorbing form a dehydroxylated $SnO_2(110)$ surface (Reprinted with permission from [93], E. Leblanc et al., *Sens. Actuators B* 62, 67 (2000). © 2000, Elsevier.). Bottom: Calculated TPD spectra for NO and NO_2 considering all the configurations detailed in Table 2 (*see* labels). Reprinted with permission from [58], J. D. Prades et al., *J. Electrochem. Soc.* 154, H657 (2007). © 2007, The Electrochemical Society.

- as E_{act}^{des} increases, then so T_{MDR} (the peak temperature) increases.
- the peak temperature is not dependent on the initial coverage N(t=0); consequently, it does not change with N(t=0).
- the shape of the desorption peak will tend to be asymmetric, with the signal decreasing rapidly after the desorption maximum.

To conclude this section, some results on the interaction of NO_x and SO_2 with the SnO_2-cassiterite (110) surface [37] are presented to illustrate how the theoretical study of surface-adsorbate interactions provides a valuable tool to understand the complex interactions underlying gas detection with metal oxides.

Since the election of realistic adsorption sites at working pressure and temperature is necessary to analyze meaningful adsorptions of target species, the thermodynamic stability results presented in previous sections (Section 2.3) are recovered: in short, surface single oxygen vacancy configurations become stable above 270°C ($O_{Bridging}$, point α) and 480°C ($O_{InPlane}$, point β) while multiple vacancy reductions do so above 650°C (point δ), being all this compatible with previous experimental observations [39, 40]. So that, all these sites are considered in the gas adsorption modeling.

Table 2 summarizes the calculated adsorption energies ΔE_{ads} of NO and NO_2. For NO, oxygen sites are the most energetically favorable. In contrast, the energetically preferred adsorption sites for NO_2 are the oxygen vacancy associated. Additionally, based on Mulliken population analysis results, NO is predicted to release charge to the sensing surface ($\Delta q < 0$) while NO_2 captures charge ($\Delta q > 0$); this is compatible with their reducing and oxidizing character, respectively.

It is important to notice that the difference between the preferred adsorption sites of NO and NO_2 indicates that by generating vacant sites and adjusting their density, the feasibility of adsorption onto SnO_2 of NO versus NO_2 may be changed.

As previously detailed, ΔE_{ads} results can be linked with maximum desorption rate temperatures (T_{MDR}) of temperature-programmed desorption (TPD) experiments. Desorption temperatures are obtained by means of the equation (71). The adjusting parameters were set according to the experimental conditions of [63] where an experimental TPD spectrum can be found for NO and NO_2 desorption from an $SnO_2(110)$. The validity of the calculations is shown in Figure 18 where the simulated TPD spectrum (obtained solving equation (67) for each adsorption configuration) is compared with the experimental TPD result of the desorption of NO and NO_2 from $SnO_2(110)$ [63]. We recall that it is possible to calculate the desorption activation energies (and their corresponding desorption temperatures) for the specific adsorption configurations analyzed. In contrast, an experimental TPD spectrum provides the temperature range over which species are desorbed by considering a plethora of adsorption configurations present in a real sample. Consequently, we would expect the calculated temperatures to belong to the corresponding experimental TPD signal range. Our theoretical predictions of T_{MDR} for the few adsorption cases considered fall within the wide experimental desorption peaks from [63].

Once validated the adsorption model, it is possible to discuss their contribution to the transduction. Observing Figure 18, can be deduced that, at the usual working temperatures (i.e., maximum sensor sensibility, from 150 to 250°C [64]), the relevant adsorption configurations for NO_2 are those related with $Sn_{InPlane}$ and $O_{InPlane}$ vacancies. Besides, $O_{Bridging}$ configurations contribute at higher temperatures. This is compatible with the charge variation of the adsorbed species (Δq): NO_2 over and in plane sites captures more charge than over a bridging site.

It is known that SO_2 avidly saturates NO_2 adsorption sites, reducing the sensing capability of SnO_2 [65]. In the present calculations, the strongest adsorptions within the cases studied correspond to SO_2. This theoretical behavior is compatible with the experimental evidence of poisoning. In particular, SO_2 adsorbs more strongly than NO_2 to vacant oxygen sites but, the difference in the calculated ΔE_{ads} values is smaller for $O_{BridgVac}$ related adsorptions (the higher temperature peak in the NO_2 TPD spectrum). This suggests that the poisoning strength depends on the adsorption site involved in the process. So, $SnO_2(110)$ in which the presence of $O_{BridgVac}$ dominates and there are few $O_{InPlaneVac}$ would appear to be a better sensor candidate as it would experience less poisoning. Linking this with the surface reduction stability described previously, it is clear that in order to avoid the massive apparition of $O_{InPlaneVac}$ the temperature of the sensing material should not exceed 480°C. If an occasional single $O_{InPlaneVac}$, is present below this temperature, adsorption onto such a site should be avoided to diminish the effect of the poisoning, and so, the sensing material should work at temperatures higher than 200°C which favors the desorption of NO_2 from an $O_{InPlaneVac}$. Finally, to obtain good sensing behavior over a large range of the target gas concentration, adsorption sites must be kept unsaturated. In other words, the sensing material should work at a high desorption rate temperature to achieve a steady state where the adsorption/desorption ratio is a function of concentration. Consequently, according to the NO_2 TPD spectrum, temperatures between 200 and 300°C do not

Table 2. Calculated adsorption energies (E_{ads}) for NOx and SO_2 on several adsorption sites of the $SnO_2(110)$ surface and maximum desorption rate temperature (T_{MDR}) estimated for the experimental conditions of [93]. Several surface terminations (Γ_0) from the stability analysis (fig. 12) were considered.

Adsorbate	Surf. term. (ΓO)	Adsorption site		ΔEads [eV]	TMDR [°C]		Δq [e-]
NO	0.0	$O_{Bridging}$		**−1.32**	198	(a)	−0.21
	0.0	$Sn_{InPlane}$		**−0.24**	52	(b)	−0.02
	−0.5	$O_{Bridging}$		**−1.18**	167	(c)	−0.24
	−0.5	$O_{Bridging\ Vac}$		**−0.42**	89	(d)	−0.05
	−1.0	$O_{Bridging\ Vac}$		**−0.98**	153	(e)	−0.10
NO$_2$	0.0	$O_{Bridging}$		**+1.51**	—		—
	0.0	$Sn_{InPlane}$		**−0.52**	94	(t)	+0.42
	−0.5	$O_{Bridging\ Vac}$	(single bonded)	**−2.31**	502	(u)	+0.31
	−0.5	$O_{Bridging\ Vac}$-$Sn_{InPlane}$		**+0.34**	—		—
	−1.0	$O_{Bridging\ Vac}$	(single bonded)	**−2.02**	424	(v)	+0.65
			(double bonded)	**−1.95**	400	(w)	+0.57
	−1.0	$O_{Bridging\ Vac}$-$Sn_{InPlane}$		**−2.11**	454	(x)	+0.68
	−0.5	$O_{InPlaneVac}$	(single bonded)	**−1.26**	178	(y)	+0.61
	−1.0	$O_{InPlaneVac}$	(double bonded)	**v0.74**	120	(z)	+0.92
SO$_2$	0.0	$O_{Bridging}$		**+1.72**	—		—
	0.0	$Sn_{InPlane}$		**−0.86**	128		+0.50
	−0.5	$O_{Bridging\ Vac}$	(single bonded)	**−2.05**	435		+0.43
	−0.5	$O_{Bridging\ Vac}$-$Sn_{InPlane}$		**+1.12**	—		—
	−1.0	$O_{Bridging\ Vac}$	(single bonded)	**+0.26**	—		—
			(doble bonded)	**−2.56**	606		+0.72
	−1.0	$O_{Bridging\ Vac}$-$Sn_{InPlane}$		**−2.97**	741		+0.95
	−0.5	$O_{InPlaneVac}$	(single bonded)	**−2.98**	748		+0.53

Source: Adapted and reprinted with permission from Ref.[58] J. D. Prades, et al., *J. Electrochem. Soc.* 154, H657 (2007). © 2007, The Electrochemical Society.

appear to be very promising. All these considerations suggest that to achieve the best adsorption conditions and diminish poisoning by SO_2, the optimum working temperatures are between 300°C to 450°C (left side of the high temperature desorption peak of NO$_2$).

To conclude, the described analysis of surface-gas interaction is a valuable tool to understand the main sensing features of metal oxide-based chemical sensors.

3. DFT MODELS AND RESULTS IN SENSING MATERIALS: DESIGN, CHARACTERIZATION AND CHEMISORPTION

As introduced in Section 1, materials that change their properties depending on the ambient gas can be used as gas sensing materials. Many metal oxides are suitable for detecting exhaust, hazardous, volatile organic gases, and so on, either reducing or oxidizing. For instance, all the following oxides show a gas response in their conductivity: Cr_2O_3, Mn_2O_3, Co_3O_4, NiO, CuO, CdO, MgO, SrO, BaO, In_2O_3, WO_3, TiO_2, V_2O_3, Fe_2O_3, GeO_2, Nb_2O_5, MoO_3, Ta_2O_5, La_2O_3, CeO_2, Nd_2O_3, and many others [66, 67, 68]. However, the most commonly used gas sensing materials are SnO_2, ZnO, and TiO_2 [69] so that we will center the following review sections on the theoretical studies of this materials. In the paradigmatic case of SnO_2 (which was one of the first considered and still is the most widely used material for these applications) there is an obvious close relationship between the gas sensitivity of oxides and their surface chemical activity and thus gas sensing applications and catalytic properties should be jointly considered. So, again, the theoretical study for sensing applications is mainly centered on the surface (*see* Section 2).

One aspect of the first principles analysis of surfaces is to elucidate the interaction between molecules and solid surfaces by studying well-defined systems as described in Section 2.5. As it becomes more visible that oxides often play an intricate role in chemical processes, surface studies of well-ordered oxides or bulk oxides surfaces are becoming more popular [100–102]. Recent surface studies of metal oxides, however, indicate that these surfaces can be rather complex [70, 71]. For the same oxide many different surface structures and compositions exist and the surface phase one obtains depends largely on the preparation conditions in surface science experiments. Consequently, it is assumable that during catalysis and gas sensing applications different local arrangements involving stoichiometry and microstructure could arise depending on the operation conditions (temperature, atmosphere, and so on). Not all oxide surfaces may be equally active and thus by tuning the operation conditions to favor one phase over the other better activity, selectivity, or gas sensing sensitivity may be obtained. Again, this decision can be assisted by the theoretical analysis of the interaction with molecules (Section 2.5) of several stable surface configurations (Section 2.3).

On the other hand, a great variety of self-assembled nanoscale materials have been recently discovered. Following the example of tin oxides, SnO nanodiskettes [72], SnO_2 nanobelts, and other nanoscopic materials [73] have been obtained. SnO_2 nanobelts have the bulk-like cassiterite structure and are only of the order of 10 to 100 nm in the cross-section and up to several mm in length. Their surfaces are low index bulk terminations and thus should exhibit similar properties to single crystal surfaces. A simple vapor phase transport growth can be employed to grow many of these tin oxide nanostructures. Besides, many non-isotropic nanostructured materials have gas sensing properties. This fact and their large surface to volume ratio make them promising materials for well defined, highly sensitive gas sensors. Again,
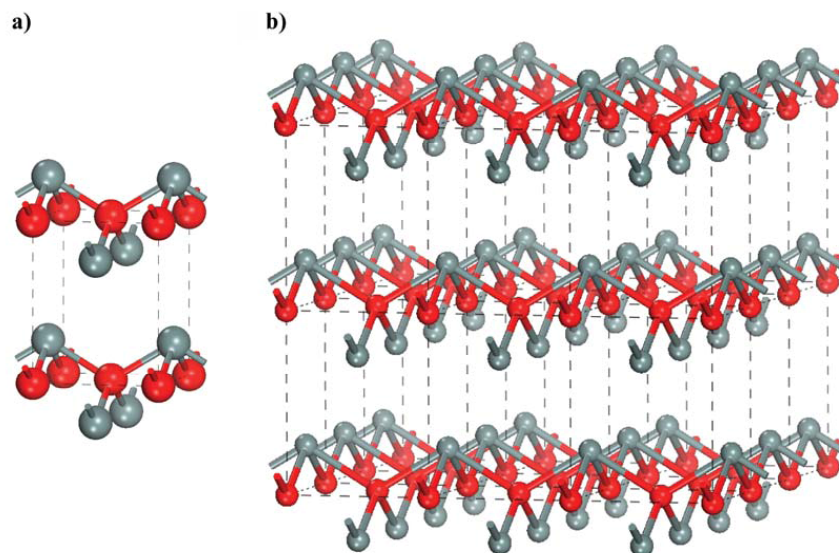
Figure 19. a) Ball and stick representation of the SnO$_2$-litharge unit cell. b) 3×3×2 supercell of the same phase showing the layered structure. Grey spheres represent Sn and red spheres represent O atoms.

even in the case of nanostructures, focus the theoretical study on the surface and the most stable shape of the nanostructured active metal oxides (Section 2.4).

3.1. SnO$_2$

The ab initio study of tin oxide has been motivated by its applications as oxidation catalyst, transparent conductor, and as the main solid state gas sensor material. In this section, we review some relevant first-principles works that describe the physical and chemical properties that make tin oxide a suitable material for sensing applications. The key for understanding many aspects of SnO$_2$ surface properties is the dual valence of Sn. The dual valence facilitates a reversible transformation of the surface composition from stoichiometric surfaces with Sn^{4+} surface cations into a reduced surface with Sn^{2+} surface cations depending on the oxygen chemical potential of the system. Additionally, this double valence is responsible of the stability of tin monoxide. For this reason, theoretical studies on the bulk electronic structure of both tin mono and dioxide are reviewed in Section 3.1.1. The rich variety of surface terminations for different environmental (working) conditions in tin oxide makes extremely important to know which of them are the most relevant and how their electron structure differs from the bulk. Section 3.1.2 is dedicated to review the theoretical findings on this topic. Finally, the interaction with gas molecules has been extensively studied and some of the main results regarding the most important target gases are presented in Section 3.1.3.

3.1.1. SnO and SnO$_2$ Bulk Properties

There are two main oxides of tin: the more stable stannic oxide (SnO$_2$) and the less stable stannous oxide (SnO). The existence of these two oxides reflects the dual valence of tin, with oxidation

states of 2+ and 4+. SnO is less characterized compared with SnO$_2$. For example, its electronic band gap is not accurately known but lies somewhere in the range of 2.5 eV to 3 eV. Thus SnO exhibits a smaller band gap than SnO$_2$, which is commonly quoted to be 3.6 eV. Also, there are no single crystals available that would facilitate more detailed studies of stannous oxide.

The crystal structure of stannous oxide (SnO) is shown in (Fig. 19). It has a tetragonal unit cell with the litharge structure, isostructural to PbO. The symmetry space group is P4/nmm and the lattice constants are a = b = 3.8029 Å and c = 4.8382 Å [74]. Each Sn and O atom is fourfold coordinated with a bond length of 2.23 Å. The structure is layered in the [001] crystallographic direction with a Sn$_{1/2}$–O–Sn$_{1/2}$ stack sequence with a gap between two adjacent Sn planes of 2.52 Å. The positive charge of the Sn^{2+} ions is screened by electron charge clouds between the Sn planes, thus reducing the Coulombic repulsion between adjacent Sn layers [108–110]. These charge clouds, or charge hats, arise from Sn$_{5s}$ electrons that do not participate in the bonding for Sn(II) and thus can be described as a lone pair.

The total density of states of SnO is characterized by four peaks labeled A–D in Figure 20(a) (from [75]). These four structures are mainly O$_{2p}$ states, which are hybridized with Sn-p and Sn-s states. Structure A corresponds mainly to hybridization with Sn$_{5s}$ states, structure B also has some 5s character, while structure C results from hybridization between O$_{2p}$ and Sn$_{5p}$ states. The last state D has significant 5s character. In contrast to SnO, SnO$_2$ does not exhibit any Sn$_{5s}$ character at the VBM. Figure 20(b) shows DOS calculations for SnO$_2$. It can be differentiated three energy regions. The VBM is mainly of O$_{2p}$ character, while the center region results form hybridization of Sn$_{5p}$ with O$_{2p}$, and only the bottom of the valence band has some Sn$_{5s}$ character.

SnO$_2$ is much better characterized than SnO$_2$, since stannic oxide (SnO$_2$) is the most abundant (i.e., stable) form of tin oxide and is the one of technological significance in gas sensing applications

Applications of DFT Calculations to Chemical Gas Sensors: Design and Understanding   **263**
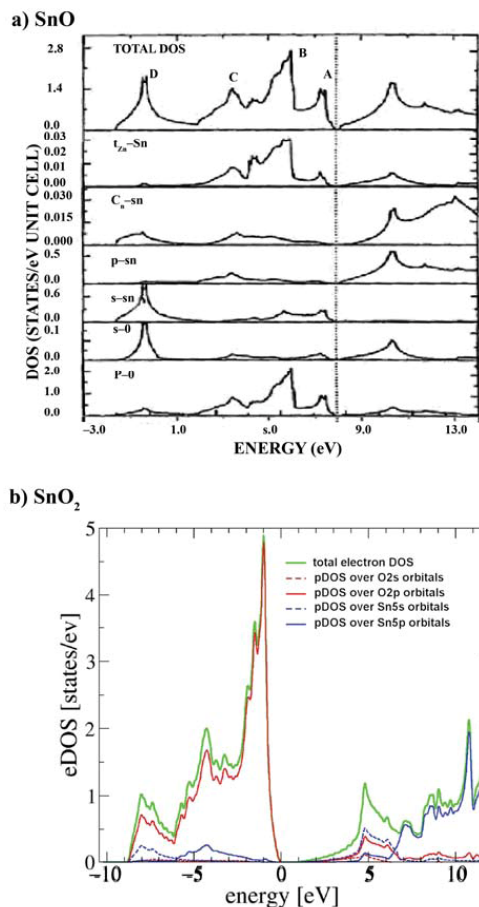
Figure 20. Density of states calculations for a) SnO (Reprinted with permission from [111], V. M. Jiménez et al., *Phys. Rev. B* 60, 11171 (1999). © 1999, American Physical Society.) and for b) SnO$_2$ (obtained from a DFT-LDA calculation). Labeled A-D features of the electron density of states of SnO are described in the text. pDOS stands for projected density of states.

and oxidation catalysts. As a mineral, stannic oxide is also called cassiterite (so called rutile) that has a tetragonal unit cell with a space-group symmetry of P4$_2$/mnm. The lattice constants are a = b = 4.7374 Å and c = 3.1864 Å [76]. In the bulk all Sn atoms are sixfold coordinated to threefold coordinated oxygen atoms. More details on this structure and its low index surfaces are given in Sections 2.1 and 2.3, respectively.

In addition to this tetragonal phase, there also exists a slightly more dense orthorhombic high pressure phase. Suito and co-workers [77] showed that in a pressure-temperature diagram the regions of tetragonal (lower pressure) and orthorhombic (higher pressure) phases can be separated by a straight line of the equation

$$p = 140.0 + 0.022T \qquad (72)$$

where the pressure p is given in kbar and the temperature T in °C.

Electrically, SnO$_2$ is a wide band-gap semiconductor that behaves as a good insulator in its stoichiometric form. Non-stoichiometric, in particular oxygen deficiency, makes it a conductor (n-type). Kiliç and Zunger [78] showed that the formation energy of oxygen vacancies and tin interstitials in SnO$_2$ is very low and thus these defects form readily, explaining the often observed high conductivity of pure, but non-stoichiometric, SnO$_2$. Defect levels for oxygen vacancies lie just 114 meV below the conduction band minimum (CBM) and thus can be easily thermally ionized. For Sn interstitials a level 203 meV above the CBM was found implying a spontaneous donation of electrons into the conduction band (n-type). This analysis for non-stoichiometric, pure SnO$_2$ suggests that the first two scenarios outlined above may be active.

Figure 20(b) shows the orbital character of the valence band and conduction band. It can be seen from this representation that for SnO$_2$ the empty Sn$_{5s}$ and O$_{2p}$ orbitals make up the bottom of the conduction band. A more detailed band structure calculation for SnO$_2$ is presented in Figure 21(a). With these general properties for the bulk electronic structure in mind we will turn to the electronic structure of stoichiometric and reduced SnO$_2$ low index surfaces later.

As a final remark, the electronic structure of bulk SnO$_2$ has been calculated for Sb as an impurity dopant [79]. The impurity atom has one valence electron more than the cations of the host lattice. Then, a donation of the extra electron into the conduction band upon substitutional replacement of a cation by the impurity dopant may be expected. Band structure calculations for Sb doped SnO$_2$ suggested (*see* Fig. 21(b)) the formation of a Sb$_{5s}$ like band in the SnO$_2$ band gap with a free electron-like character at the Γ-point. It was concluded that this band could be a half-filled metallic band and that additional thermal excitation into the Sn-like bands could increase the conductivity. However, these calculations were performed on a unit cell with a Sn$_3$SbO$_8$ composition, i.e. a much higher Sb concentration than is reasonable in real materials with Sb concentrations of a few tenths percent at most.

3.1.2. SnO$_2$ Surface Properties

The low energy surfaces of SnO$_2$ have been described in Section 2.3. Their surface energies with a termination that maintains the bulk stoichiometry have been calculated by several authors [116–121] and are summarized in Table 3.

For these bulk terminated SnO$_2$ surfaces, i.e., surfaces with surface-tin atoms in their bulk Sn^{4+} oxidation state, the (110) surface exhibits the lowest energy surface followed by the (100), (101), and (001) surfaces. The fact that the (110) surface is the lowest energy surface can be appreciated by investigating the crystallographic orientations of the bulk termination of single crystals or nanocrystals. In Figure 22, it is shown a photograph of a single crystal grown by a vapor phase transport technique. It is obvious that the {110} surfaces make up the majority of the surface area followed by the {100} faces and small {101} faces. No {001} faces are obsrved. Although this crystal does not necessarily represent an ideal crystal one would obtain from a Wulff's construction [80], it clearly demonstrates the preferential terminations of a SnO$_2$ single crystal.

Due to the double valence of tin atoms, it has been shown that both the stoichiometric Sn^{4+} and the reduced Sn^{2+} bulk terminations (*see* Fig. 23) are feasible and that the surface termination one obtains on these surfaces depends on the equilibrium conditions with the gas phase [81]. Details on this point will be given in the following sections.
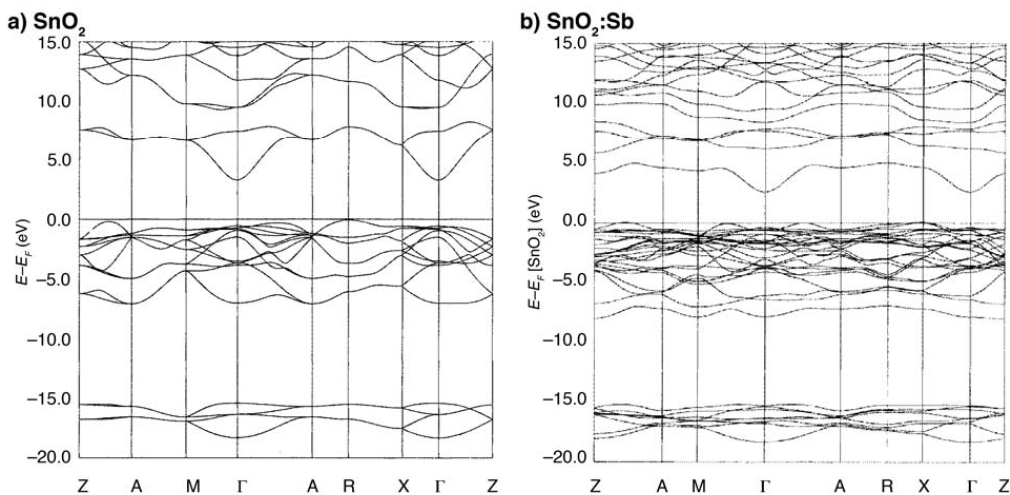
Figure 21. Band structure cluster calculations for a) SnO$_2$, b) Sb doped SnO$_2$. Reprinted with permission from [115], K. C. Mishra, et al., *Phys. Rev. B* 51, 13972 (1995). © 1995, American Physical Society.

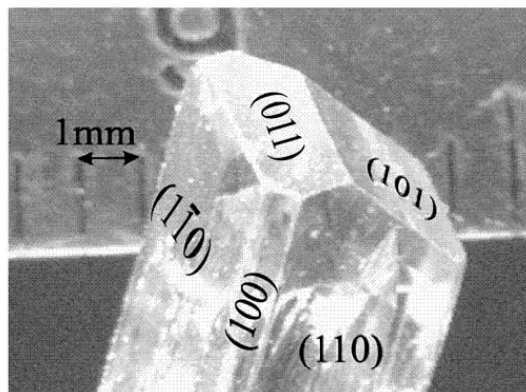### 3.1.2.a. Thermodynamic Surface Stability

Recent ab initio atomic thermodynamics calculations have been dealing with the compositional variations of oxide surfaces under various chemical potentials[124–128]. In these works the surface energies, that are functions of the chemical potential, are computed for different surface structures and compositions as described in Section 2.3. Therefore, different surface compositions have different surface energies for different oxygen chemical potentials (i.e., at a given partial pressure and temperature). Obviously, the thermodynamic stable surface is the one with the lowest energy at a given oxygen chemical potential. So that surface structure may change as a function of the chemical potential or, in the case of sensors, the working conditions. Consequently, the theoretical prediction of realistic surface models for different working conditions is an issue to be addressed for the latter study of surface molecule interactions.

For the low index surface orientations previously presented, the stoichiometric, i.e. SnO$_2$, bulk termination is the energetically favored surface only at high oxygen chemical potentials. At lower oxygen chemical potentials oxygen depleted surface phases become energetically favored (*see*, for example, Fig. 24). This is in agreement with the experimental LEIS studies that showed compositional transitions of the surfaces upon vacuum annealing [82]. In the following the structures and thermodynamic stability of different surface phases of the (110), (101) and (100) crystallographic surface orientations are presented.

The SnO$_2$(110) shows the most complex behavior of the three surface orientations presented. It has been found experimentally found that it reduces at the lowest temperature under vacuum, but a high degree of disorder observed in STM studies made it impossible to derive a reliable surface model [83]. Different reduced surface structures were evaluated by DFT calculations in order to find a likely surface structure for low oxygen chemical potential. These structures included the proposed [84] structures for 4×1 reconstruction with periodically removed in-plane oxygen atoms, various different arrangement of removed surface oxygen atoms, as well as constellations of threefold coordinated Sn atoms in non-bulk positions. For all these considered models the two structures that showed the lowest surface energies in some ranges of the oxygen chemical potential are, in one hand, the stoichiometric surface (at high oxygen potential, *see* Fig. 23(a)) and, on the other, a surface that in addition to removed bridging oxygen atoms also has every other row of in-plane oxygen atoms removed (at low oxygen chemical potential, *see* Fig. 23(c)). These structures were found independently by two research groups [85]. The dependence of the surface energy of this two surfaces on the oxygen chemical potential is shown in Figure 24. The reduced surface structure leaves threefold coordinated tin and oxygen atoms at the surface and a surface layer with SnO composition. Thus Sn is attaining a 2+ oxidation state. Furthermore, such a surface structure still exhibits a 1×1 unit cell. This surface phase becomes favored over the stoichiometric
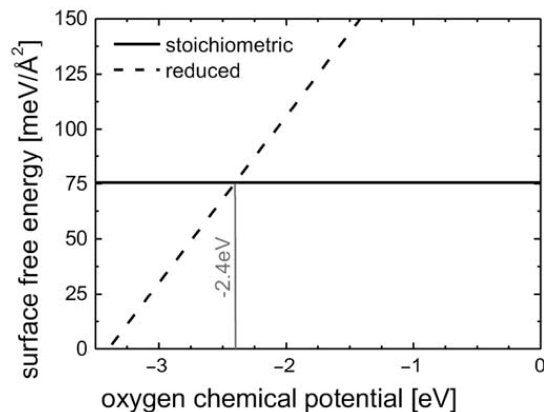
Table 3. Surface free energies of stoichiometric surfaces in SnO$_2$-cassiterite in J/m^2 calculated with different DFT approximations.

Surface orientation	B3LYP		GGA		LDA	
	Ref [117]	Ref [118]	Ref [58]	Ref [121]	Ref [122]	Ref [119, 120]
{110}	1.20	1.04	1.01	1.01	1.21	1.30–1.40
{100}	1.27	1.14	1.32	—	1.29	1.66–1.65
{101}	1.43	1.33	1.49	1.42	1.60	1.55
{001}	1.84	1.72	1.87	—	—	2.36

Applications of DFT Calculations to Chemical Gas Sensors: Design and Understanding   **265**

Figure 22. Photograph of a SnO_2 single crystal grown by a vapor phase transport technique. Reprinted with permission from [107], M. Batzill and U. Diebold, *Prog. Surf. Sci.* 79, 47 (2005). © 2005, Elsevier.


Figure 24. Dependence of the surface energy on the oxygen chemical potential for the different bulk termination: the stoichiometric and the reduced $SnO_2(110)$ surfaces. When oxygen chemical potential falls below –2.4 eV due to environmental conditions, the stoichiometric SnO_2 surface becomes unstable and should transform to reduced SnO_2 at the equilibrium. Data taken from [62].

surface at a chemical potential –2.4 eV. It is worth pointing out that the surface energy is lowest if every second row of in-plane surface oxygen atoms is removed instead of alternatingly removing oxygen atoms from adjacent rows. This thermodynamic result is consistent with vacancy formation energies calculated by Oviedo and Gillan [86]. They pointed out that the energy for oxygen vacancy formation is lowest for in-plane oxygen atoms if an entire oxygen row is removed. For such geometries, the formation energy was comparable to the energy that it takes to remove bridging oxygen atoms. Thus, the formation of in-plane oxygen vacancy rows does not exhibit a high formation energy, at the contrary to an intuitive feeling.

In other communications, based on the experimental results from Cox and co-workers [81], a half reduced surface with only bridging oxygen atoms removed (Fig. 23(b)) was often assumed. A detailed analysis of this surface termination is presented in Section 2.3 as well as other partially reduced surfaces.

The basic argument that surface structures that exhibit either a SnO or a SnO_2 composition are favored, also applies to the (100) and (101) surfaces. The difference between these surfaces and the (110) surface is, however, that in (100) and (101) the removal of
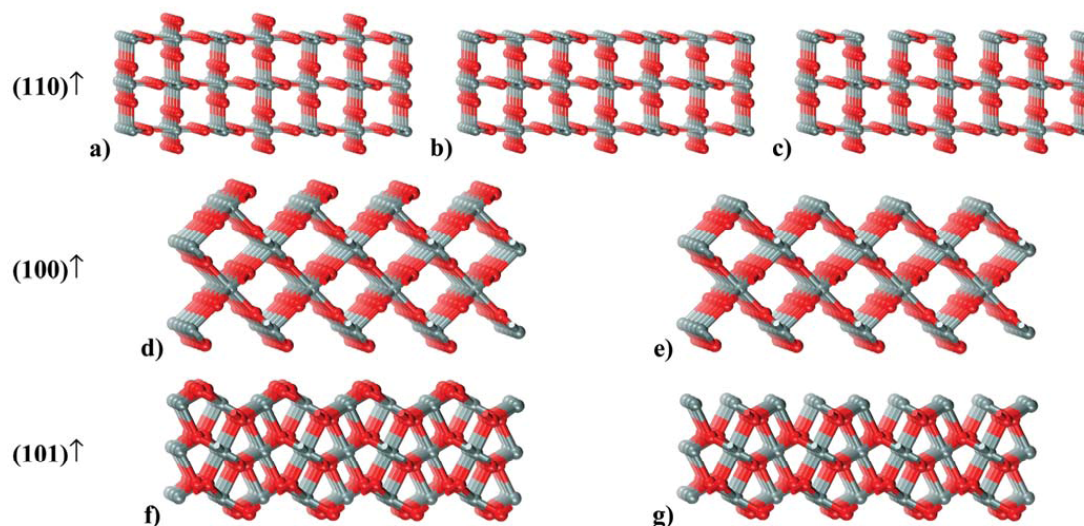
Figure 23. Ball-and-stick models of SnO_2 low index surfaces. a), d), and f) show bulk termination of the stoichiometric (110), (100), and (101) surfaces, respectively. b), e), and g) show surfaces with reduced oxygen concentration. These surfaces are obtained by removing twofold coordinated bridging oxygen rows from the stoichiometric surfaces. c) corresponds to a surface that, having removed bridging oxygen atoms, also has some rows of in-plane oxygen atoms removed.
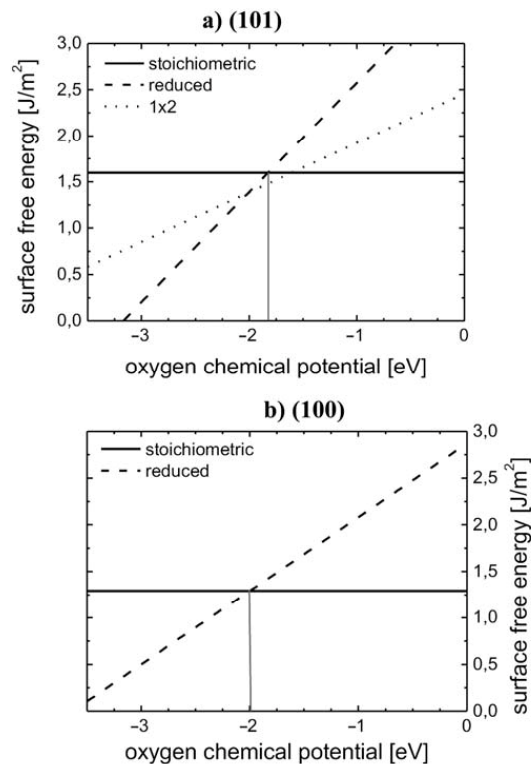
Figure 25. Surface energy as a function of the oxygen chemical potential for stoichiometric and reduced surfaces for a) the (100) and b) the (101) surfaces of SnO_2. Data taken from [62].

the twofold bridging oxygen atoms leaves threefold coordinated Sn atoms and a SnO-like surface layer. Thus simple bulk terminations of the crystal exist that have surface tin atoms in either the 4+ or 2+ oxidation state. Consequently, these two surfaces can convert from a SnO_2 stoichiometry to a SnO composition by removal of bridging oxygen atoms. The absence of significant surface reconstructions has been verified experimentally by LEED and STM. They show the same unit cell for reduced and oxidized surfaces. Relaxation of the two surface terminations for the (100) and (101) surfaces have been calculated by DFT. Somewhat, surprisingly, the reduced surfaces show less surface relaxations compared to the stoichiometric bulk terminations [85].

Experimental observation of a dual surface termination is confirmed by ab initio atomistic thermodynamic calculations of fully relaxed surfaces. Figure 25 shows that the oxygen-rich surfaces (see Fig. 23(d) for (100) and Fig. 23(f) for (101)) are preferred at high oxygen chemical potential, while the reduced surfaces (Fig. 23(e, g)). become favored if the oxygen chemical potential is reduced. According to this figure the (101) surface reduces at somewhat higher chemical potential (−1.8 eV) than the (100) surface (−2.1 eV).

3.1.2.b. Surface Electron Structure
Electron structure calculations have been performed for stoichiometric and reduced (110) surfaces[134–136]. For the stoichiometric

surface, i.e., a bulk terminated surface including bridging oxygen atoms, surface states above the top of the valence band have been predicted by calculations by Oviedo and Gillan [86], as well as by Mäki-Jaskari and Rantala [87]. It has been proposed that this surface state is formed by p-orbital electrons of the bridging oxygen atoms and results in a flat band about 0.8 eV above the bulk valence band maximum. Removal of bridging oxygen atoms causes formation of defect states within the band gap. At first, for low densities of bridging oxygen vacancies a separate peak at the bottom of the band gap appears. Eventually, with all the bridging oxygen atoms removed, a broad distribution of defect states fills the entire band gap associated with fourfold Sn^{2+} ions with in-plane oxygen p contribution [87, 88]. Further reduction of the surface by formation of in-plane oxygen vacancies has also been investigated. In this case, surface states with Sn^{2+} charge are formed [87], these states have a tendency to lie also in the band gap [88].

In Figure 26, reproduced from [85], the results from band structure calculations for three different bulk terminations are presented. The stoichiometric $SnO_2(110)$ surface exhibits surface states within the bulk band-gap region (Fig. 26(a)), in agreement with the above-mentioned calculations. These states are nearly flat, with one just above and the other 0.2–0.3 eV above the bulk VBM. The band structure calculations for a surface with removed bridging oxygen atoms only are also shown in Figure 26(b). Such a surface would have a strongly dispersed surface state that extends up to 2 eV above the bulk VBM at the M-point of the surface Brillouin zone. Other reported DFT calculations for the same surface structure show the same features. The electronic structure of the surface with bridging and in plane oxygen rows removed (Fig. 23(c)) is shown in Figure 26(c). This structure also exhibits surface bands in the bulk band-gap region, but they only extend less than 1 eV into the bulk band gap from the VBM in agreement with other works.

No band structure calculations for the (100) surface have been reported. The only reported band structure calculations for the (101) surface is shown in Figure 27(a) and (b) for the reduced and the stoichiometric surfaces, respectively from [85]. The binding energy in the calculations, which is set to 0eV, is referenced to the VBM. The bulk bands projected onto the (101) surface are indicated by the gray shaded area and surface states and resonances by the dotted lines. Similar to the band structure, calculations for the stoichiometric (110) surface calculations predict surface states distinct from the bulk-valence band for the stoichiometric (101) surface.

3.1.2.c. Dopants at the Surface
Important characteristics of doped tin oxide surfaces are surface conductivity and reactivity, for instance in the context of gas sensors [89, 90]. These properties can be strongly influenced by the amount, distribution and chemical state of Pd dopants in addition to associated deformation of the supporting SnO_2 surface[141–143]. The electronic conductance increase associated to the sensing function is explained to be a result of adsorbates or their products acting as donors and/or causing structural changes like decrease of oxygen content of the surface, which also cause a similar effect. Even in idealized cases, quantitative theoretical investigations of these properties is almost impossible. For instance, electronic conductivity of metal oxides is problematic because of different activated processes and scattering of charge carriers, which depend on external conditions and environment [91, 92] (e.g., oxygen partial pressure and different surface coatings).

Applications of DFT Calculations to Chemical Gas Sensors: Design and Understanding **267**
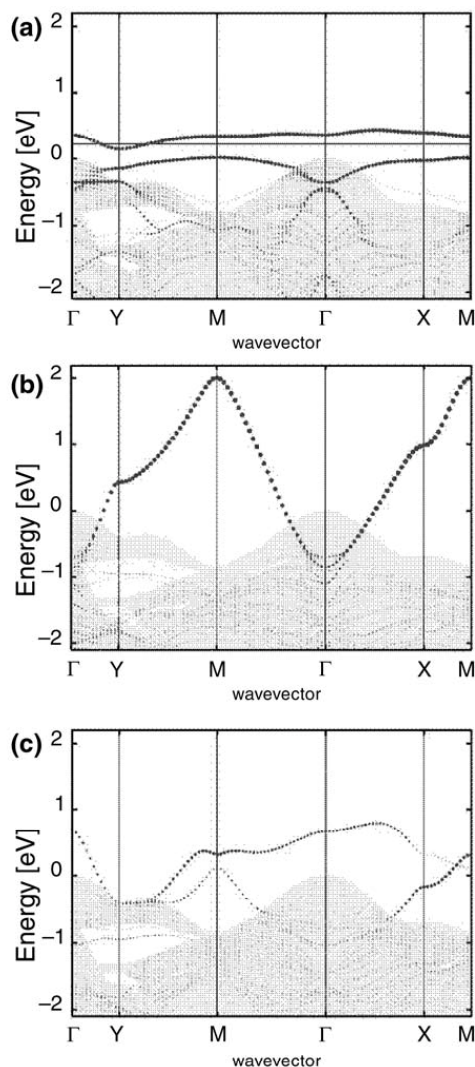
Figure 26. From top to bottom, surface band structure calculations for bulk terminations indicated in Figure 23(a), (b), and (c), respectively. Grey shaded area represents the projection of the bulk bands on the surface and red-dotted lines indicate the surface bands. Reprinted with permission from [132], M. Batzill et al., *Phys. Rev. B* 72, 165414 (2005). ©2005, American Physical Society.

Mäki-Jaskari and Rantala have shown in DFT calculations that Pd can adsorb to various anionic and cationic sites depending on surface reduction and external conditions [93]. At anionic sites Pd–Sn bond lengths significantly exceed Sn–O lengths in bulk and surface. They predicted that on perfect stoichiometric (110) support, clustering of Pd results, while on reduced surfaces, the palladium–metal oxide interaction may also cause deformations of the supporting surface layer by Pd substitution of surface layer atoms. Additionally, they observed that strong binding of Pd with
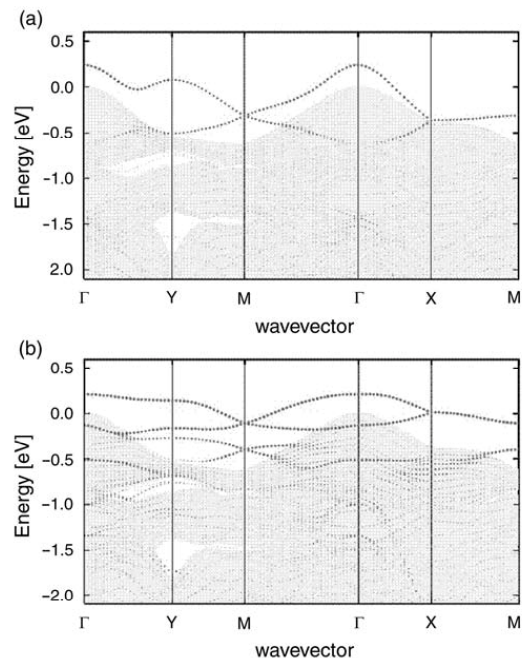
Figure 27. Band structure calculations for a) the reduced and b) the stoichiometric $SnO_2(101)$ surface (*see* Fig. 23(f) and (g), respectively). Grey shaded area represents the projection of the bulk bands on the surface and red-dotted lines indicate the surface bands. Reprinted with permission from [132], M. Batzill et al., *Phys. Rev. B* 72, 165414 (2005). ©2005, American Physical Society.

surface tin atoms can enhance release of oxygen from stoichiometric surface, which makes tin sites on surface more reactive. In the reduced surface containing Sn^{2+} type of ions has smaller band gap that was slightly below the gap of the Pd/SnO_2 surfaces considered. Surface in-plane oxygen vacancies were found to be preferred adsorption sites (E_{ads} below $-4eV$) for Pd adatoms, some of which are expected to be or become available in the case of oxygen deficient surfaces. Fourfold and fivefold coordinated surface tin atoms provided adsorption sites also. Binding was weaker at the stoichiometric (110), (100) and (101) surfaces than at the reduced (110) surfaces. In these cases, Pd is bound with bridging oxygen and/or surface tin atoms. The weak attraction between palladium adatoms can enhance the alignment and nucleation of Pd adatoms along [001] surface direction, especially in the case of stoichiometric (110) surface. Least coordinated (3 or 4) surface tin atoms of the reduced $SnO_2(110)$ surfaces were predicted to be preferred substitution sites of Pd among tin atoms. They proposed that, on one side the observed substitution reactions may be connected with the experimentally observed formation of tin alloy on Pd/SnO_{2-x} surface. On the other, once the continuous Pd rows has been formed, or the surface cations of Sn^{2+} or Pd^+ types are present at the surface with large density, the thin film conductivity can be increased due to the decrease of the band gap and de-localization of conduction band states. This may be associated with increased reactivity, over the stoichiometric surface and over the case in which some in-plane oxygen sites are occupied by Pd.

3.1.2.d. Surface Conclusion

It has been shown that a change in the oxygen chemical potential of the gas phase results in a shift in the surface phase diagram towards an oxygen rich or poor surface that implies the thermodynamic stability of one or other surface termination. Additionally, it has been shown that different surface terminations imply different surface electronic structure: the surface states for reduced SnO_2 surfaces and defect states at oxygen vacancies have been observed to lie low within the band gap for all three surfaces investigated. Since charge transfer to adsorbed molecules is responsible for the gas response, these changes of the surface electronic structure may play an intricate role in the gas sensing mechanism. So there can be expected altered molecule–surface interactions when modifying the working condition (i.e.: temperature and partial pressure of the surrounding gas). Finally, it has been remarked that theoretical works are helping to understand the great influence of dopants, such as Pd, at the surface of SnO_2 in gas sensing applications.

3.1.3. Molecule Adsorptions

Despite the importance of molecular interactions with SnO_2, in its applications as gas sensor and heterogeneous catalyst, relatively few experimental surface science studies of molecular adsorption and reactions on SnO_2 single crystals have been performed. Furthermore, most of these studies have been concentrated on the $SnO_2(110)$ surface where are also centered most of theoretical works. Much of this work has been performed by Cox and coworkers. In their studies they assumed simple bulk terminations with different oxygen concentration. However, it has been discussed in Section 3.1.2 that the surface structure of $SnO_2(110)$ can be quite complex. Nevertheless, many of the conclusions drawn by Cox and co-workers regarding surface-composition dependent reactivity are still valid. In the next sections we review some of the first-principles works on molecular reactions.

3.1.3.a. O2

Although there is evidence for complex oxygen/SnO_2 interactions, which are instrumental for triggering gas responses, there is little knowledge about specific adsorption geometries. Calculations were conducted in order to understand better the interaction of O_2 with SnO_2. The adsorption of O_2 on stoichiometric (110) [147–150] and (101) [94] surfaces as well as at oxygen vacancies has been theoretically investigated. Neutral O_2 adsorbs extremely weakly on stoichiometric SnO_2 surfaces, with calculated adsorption energies less than −0.02 eV for the (110) surface. However, at bridging-oxygen vacancies adsorption is strong. Dissociation of O_2 adsorbed at vacancy sites with one O atom filling the vacancy and the other adsorbing at neighboring five fold coordinated Sn sites has been shown to be exothermic for the (110) surface [95]. A thorough investigation of oxygen adsorption on stoichiometric and various reduced surfaces by DFT calculations was performed by Oviedo and Gillan. They confirmed that O_2 cannot adsorb exothermally on the stoichiometric (110) surface. Weak adsorption is possible at the fivefold coordinated Sn sites with an adsorption energy less than −0.4 eV. Much stronger adsorption is possible at bridging-oxygen vacancy sites with an adsorption energy of up to −1.8 eV. There was also evidence that a bridging oxygen vacancy can bind three O_2 molecules simultaneously, one at the vacancy site and two at the neighboring fivefold Sn sites.

Using a point-charge model, Yamaguchi et al. studied the stability of different oxygen anion species stabilized at bridging-oxygen vacancy sites at the (110) surface. They concluded that a low concentration of O^{-2} and O^- can be expected if considering the energy diagram for different oxygen species.

Mäki-Jaskari et al. studied the charge accumulation of oxygen species adsorbed on an ideal and defective $SnO_2(110)$ surface with excess charge by DFT calculations [95]. An excess charge of 10^{21}–10^{22} cm^{-3} influenced the oxygen surface chemistry of SnO_2 and allowed to model the ionosorption of oxygen. With additional charges, an O^- ion adsorbs at fivefold Sn sites, while without additional charges a O_2^{-2} complex is favorable. This latter structure is identical to the adsorption of O_2 at a bridging-oxygen vacancy site and can also be viewed as the initial step of oxygen adsorption. An energy of $2eV/O_{ads}$ is being released upon transformation of the initial adsorption geometry to the final geometry in the presence of excess charge.

For the $SnO_2(101)$ surface, DFT calculations showed that O_2 adsorbs at oxygen vacancy sites with a significant charge transfer forming an O^{-2} species [94].

Recently, Mazzone and Morandi [96] reported a quantum mechanical study of the adsorption properties of defective SnO_2 nanostructures based on a semi-empirical Hamiltonian. Crystalline SnO_2-cassiterite nanograins, with a size and shape comparable with the experimental ones, where considered. The results on the adsorption of both O_2 and CO show that the presence of the defects enhances the grain cohesion and favors adsorption. The conductance has a functional relationship with the structure and the defective state of the nanograins and its dependence on these quantities parallels the one of the binding energy.

3.1.3.b. NOx

A detailed DFT study on the adsorption of NO, NO_2 on the $SnO_2(110)$ surface is presented in Section 2.5 and reported in. There it is shown that the strongest adsorption of NO and NO_2 over $SnO_2(110)$ takes place over surface oxygen atoms and surface oxygen vacancies, respectively. From the point of view of the charge transfer, NO release charge to the surface while NO_2 captures it being this compatible with their respective reducing and oxidizing behavior.

Other DFT calculations of NO_2 adsorption on $SnO_2(101)$ were performed in view of an observed gas response of SnO_2 nanoribbons (or nanobelts) [94]. It was found that NO_2 adsorbs either with a single bond to a single fivefold coordinated Sn surface atom or in a bidentate structure to two Sn atoms. The difference in the binding energy between these two configurations is small implying that a bidentate bonded NO_2 molecule can easily break one bond, rotate around the remaining bond, and re-bond to another Sn atom. Thus NO_2 molecules are expected to be mobile at room temperature. If two NO_2 molecules meet at the surface an oxygen atom is transferred from an NO_2 molecule to the other forming strongly bidentate bonded NO_3 and a weakly bonded NO that may desorb from the surface. The NO_3 molecule is not expected to be mobile at room temperature. There is significant charge transfer from the SnO_2 substrates of −0.4 electrons to the NO_3 molecule. This should result in a drop of the conductivity of the nanoribbons. Nitrogen K-edge XANES spectra confirmed the presence of NO_2 and NO_3 at the surface of these nanoribbons with NO_3 being the dominant species [94].

Applications of DFT Calculations to Chemical Gas Sensors: Design and Understanding   **269**

3.1.3.c. CO

Melle-Franco and Pacchioni investigated the interaction of CO with the fivefold Sn site at the stoichiometric $SnO_2(110)$ surface by quantum-mechanical calculations [97]. Only CO adsorption with the C-end oriented to the surface was considered as the favored adsorption geometry. It was found that electrostatic effects play a dominant role in the interaction. Chemical bonding with charge donation from the CO 5σ level to the empty Sn states and CO polarization was also found. Unlike for TiO_2 [98] or Cu_2O [99, 100] no back donation from the oxide to the CO molecule was observed. Overall, the CO adsorption was rather weak with an adsorption energy of -0.25 eV.

Ciriaco et al. [101] calculated the influence of CO adsorption on the electronic structure of SnO_2. CO adsorption at Sn sites resulted in a shift of the Fermi level. They also discussed the possibility of abstraction of lattice oxygen to from CO_2 and found that this is a thermodynamically disfavored process.

Recent works of Mazzone and Morandi [96, 102] studied the adsorption of CO onto SnO_2-cassiterite clusters based on DFT calculations. Their results indicate the formation of a stable complex formed by the cluster, with an essentially unchanged shape, and by the deposited molecule which has a small displacement and rotation with respect to the incidence conditions. An extensive testing on the parameters needed by the DFT formulation indicated fluctuations of either the structural parameters or the structure of the allowed energy levels. Three sources for these effects were identified, i.e. the evaluation of the spin distribution, the choice of the correlation potential and the limited size of the basis sets.

3.1.3.d. CO_2

Cluster and periodic ab initio calculations showed that the stoichiometric $SnO_2(110)$ surface is rather unreactive towards CO_2 [103]. CO_2 interacts electrostatically with fivefold Sn cations with the molecular axis perpendicular to the surface. On the bridging oxygen atoms CO_2 is chemisorbed with the formation of a surface carbonate. However, this process is almost thermoneutral and the chemisorbed state is metastable.

3.1.3.e. H_2O

Water omnipresence and the consequently unavoidable "contamination" of any surface with water exposed to ambient conditions ensures continuous interest of surface scientists in the interaction of water with inorganic materials [104, 105]. The adsorption of water on tin-dioxide surfaces plays an important role for its applications as gas sensing material. For this application, device applications get considerably affected by the presence of water [106]. Furthermore, many gas sensors are intended to detect harmful gases in the environment under ambient conditions, and water is constantly present in these applications. In the use of SnO_2 gas sensors it was early recognized that SnO_2 was not just sensitive to inflammable gases but also was sensible to humidity [107].

Recently, DFT calculations have been performed in order to obtain a better fundamental understanding of water adsorption on the stoichiometric $SnO_2(110)$ surface as well as on the reduced and stoichiometric $SnO_2(101)$ surfaces. These studies are summarized in the following.

First principle DFT calculations show that (partial) dissociative adsorption on the stoichiometric (110) surface are favored. Goniakowski and Gillan found that for $SnO_2(110)$ dissociated water is the most stable configuration [108]. However, as pointed out by Lindan [109] because inter-molecular bonding was not explicitly addressed in these calculations these conclusions are of
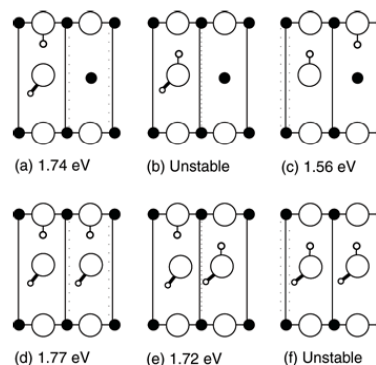

Figure 28. Schematic representation of the adsorption geometries of water on $SnO_2(110)$ by DFT calculations considered in [166]. Oxygen, tin and hydrogen are represented by large, small filled and small open circles respectively. Half coverage (top) and monolayer coverage (bottom) are considered. The presented adsorption energies are favorable to the adsorption and should be considered negative for coherence with the rest of the present text. Reprinted with permission from [166], P. J. D. Lindan, *Chem. Phys. Lett.* 328, 325 (2000). © 2000, Elsevier.

limited use [110]. Lindan studied half and full monolayer coverage of water and found that, in both cases, complete dissociation is the most energetically favored adsorption. However, while for half monolayer coverage no molecular adsorbed water was stable, at full coverage a half dissociated/half molecular adsorbed water geometry was found to exhibit an slightly lower adsorption energy compared to the fully dissociated structure. The considered adsorption geometries and the adsorption energies are shown in Figure 28. Bates [111] confirmed theoretically many of Lindan's conclusions for the full monolayer coverage on $SnO_2(110)$ and extended the studies using a larger surface unit cell.

Although all the theoretical studies point towards preferential dissociation of water on $SnO_2(110)$, experimental studies have ambiguously confirmed this conclusion. Gercher and Cox [112] performed UPS and TPD studies of water adsorption on $SnO_2(110)$ single crystals. Molecular desorption peaks at 200 and 300 K were observed and desorption at 435 K was attributed to OH disproportionation. In their study they found only 10–15% dissociated water on the stoichiometric, reduced (all bridging oxygen atoms removed) and highly defective surfaces (with in-plane oxygen vacancies). It was observed an increase in dissociation to about 35% on a less defective surface. This suggested that a limited number of in-plane vacancies promotes dissociation, but further increase in vacancies decreases the dissociation probabilities. A downward band bending of -0.1 eV was observed for water adsorption on stoichiometric $SnO_2(110)$ surfaces [113]. This implies an electron transfer from water to the sensing material and is consistent with the increase in conductivity of SnO_2 gas sensors in a humid atmosphere.

Water adsorption on the (101) surface was studied on both the stoichiometric and reduced bulk terminations by UPS measurements and DFT calculations [114]. A strong difference in the water adsorption was observed depending on the oxidation state of the surface. Adsorption studies at 110 K are shown in Figure 29 (a–c). It can be observed in the difference spectra (spectra that have the contribution of the clean surface subtracted from the
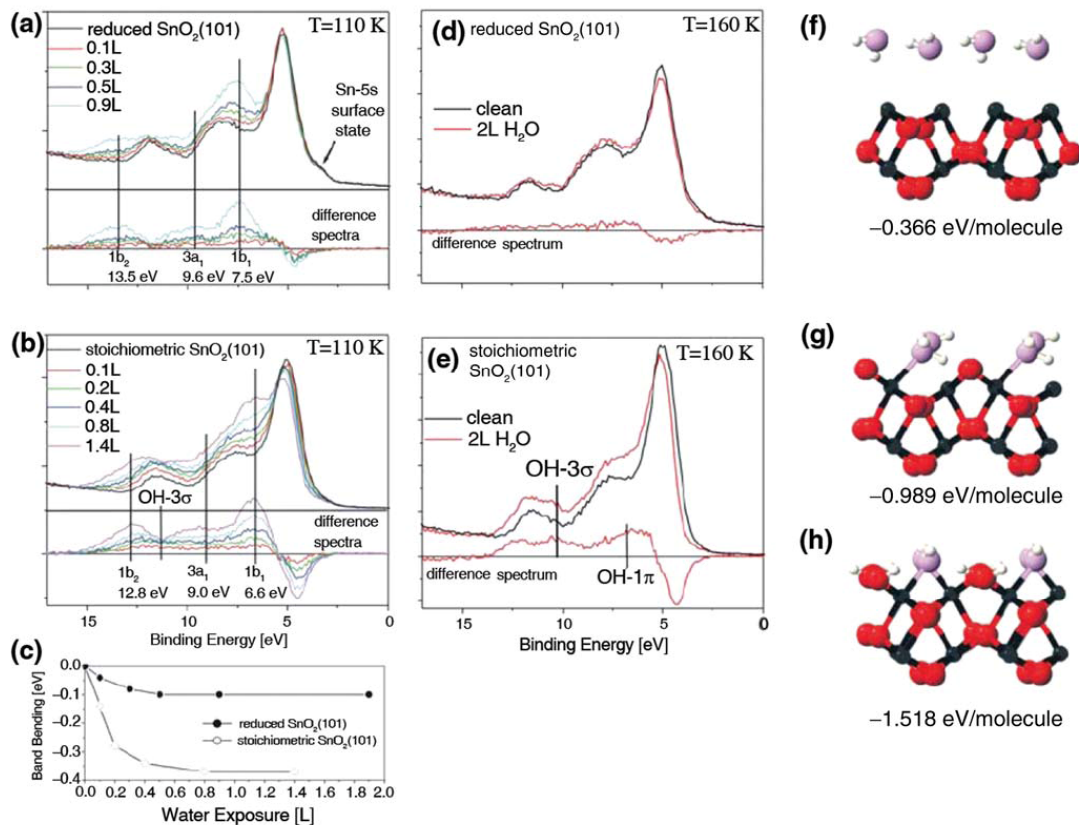
Figure 29. Water adsorption on the reduced and stoichiometric SnO$_2$(101) surface studied by UPS measurements and DFT calculations. Adsorption at 110 K is shown in (a)–(c) for the reduced surface (a) and stoichiometric surface (b). Band bending effects upon water exposure is plotted in (c) for the two surfaces. UPS measurements for water exposure at 160 K is shown in (d) for the reduced surface and in (e) for the stoichiometric surface. Only on the stoichiometric surface (e) adsorption and dissociation of water is observed at 160 K. Models of water adsorption derived from DFT calculations are shown in (f) for the reduced surface and (g) and (h) for the stoichiometric surface for molecular and dissociative water adsorption, respectively. Calculated adsorption energies are also shown. Reprinted with permission from [62], M. Batzill and U. Diebold, *Prog. Surf. Sci.* 79, 47 (2005). ©2005, Elsevier.

water exposed samples) weak additional features on the stoichiometric surface. These may be assigned to orbitals of OH from dissociated water. If water is adsorbed at higher temperatures (160 K), a stronger difference is observed between the two surfaces (Fig. 29(d–e)). At this temperature significant water adsorption is observed on the stoichiometric surface only. Furthermore, there is clear indication of dissociated water in the difference spectrum for the stoichiometric surface. In addition to valence band photoemission, band bending effects upon water adsorption was also investigated. Figure 29(c) shows that water adsorption at 110 K causes a much stronger downward band bending on the stoichiometric surface compared to the reduced surface. This is consistent with the notion that dissociated water causes most of the band bending and thus is responsible for the humidity gas response of SnO$_2$. DFT calculations verified the differences in the water adsorption on the reduced and stoichiometric SnO$_2$(101) surfaces. Figure 29(f–h) shows the results of these calculations. Only molecular water is stable and adsorbs weakly on the reduced surface. This is most likely because of the lack of surface oxygen

that could accept hydrogen. For the stoichiometric surface both molecular and dissociative adsorption is possible, however, dissociation is thermodynamically favored and exhibits the highest adsorption energy of the configurations considered.

3.1.3.f. SO$_2$

In Section 2.5, a DFT study on the interaction of SnO$_2$(110) with SO$_2$ is presented showing that the strongest adsorptions take place over surface oxygen vacancies and that their corresponding adsorption energies are stronger than in the case of NO$_2$. This result and the competence between SO$_2$ and NO$_2$ for similar adsorption sites seem to explain the poisoning by SO$_2$ of the NO$_2$ sensors based on SnO$_2$. Additional details on this work can be found reported in.

3.2. ZnO

ZnO properties make it well suited to applications in chemical gas sensing, UV light emitters, transparent high power electronics, surface acoustic wave devices, piezoelectric transducers and varistors.

Applications of DFT Calculations to Chemical Gas Sensors: Design and Understanding   271
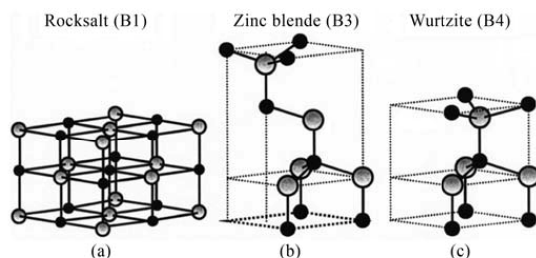
Figure 30. Stick and ball representation of ZnO crystal structures: a) cubic rocksalt (B1), b) cubic zinc blende (B3), and c) hexagonal wurtzite (B4). The shaded grey and black spheres denote Zn and O atoms, respectively. Reprinted with permission from [185], Ü. Özgür et al., *J. Appl. Phys.* **98**, 041301 (2005). ©2005, American Institute of Physics.
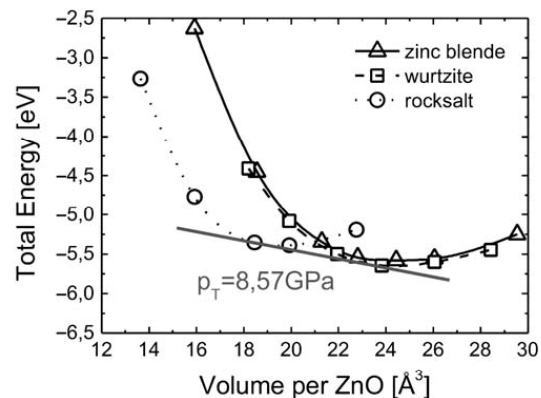

Figure 31. Total energy vs. volume (both per ZnO formula unit) for the three phases: zinc-blende (squares), wurtzite (diamonds), and rocksalt (circles). The zero of energy is the sum of the total energy of an isolated Zn and an isolated O atom. Data taken from [186].

The interest of ZnO in optical applications is due to ZnO several potential advantages, with respect to other commonly used materials like AlInGaN, including the commercial availability of bulk single crystals and the larger exciton binding energy (~60 meV for ZnO, ~25 meV for GaN). The latter property should translate to an even brighter light emission than that obtained with GaN photonics. Moreover, ZnO of reasonable quality can also be deposited at lower growth temperatures than GaN, leading to the possibility of transparent junctions on cheap substrates, such as glass. A short review of ZnO bulk phases and its electron structure is presented in Section 3.2.1.

An additional advantage of ZnO for optoelectronics is that it can be a good n-type (with and without dopping) and also p-type (with dopping) wide gap semiconductor: it is possible to obtain homojunctions of ZnO to produce UV light emitting diodes or light detectors. The n-type character of ZnO appears spontaneously, and in Section 3.2.2 we review some of the last DFT works dealing its intrinsic origin. On the other hand, many studies have been recently reported [172–178] to fabricate usable p-type ZnO. Of special interest is the codoping method proposed by Yamamoto and Hiroshi [115] and further developed by others [180–182]. It was found that by applying different forms of dopant sources which contain the same dopant chemical element may result in different types (n or p) of semiconductors. Some usual dopants, which have been studied theoretically with DFT tools, are H, N and P. In Section 3.2.3 we review some of these works.

As far as gas sensing properties of zinc oxide (nano-)crystals are concerned, they have been studied towards CO, CO_2, NO, NO_2, H_2S, HCHO, NH_3, H_2, ethanol and humidity. Complete reviews on the state of the art of ZnO based gas sensors and the production of well-terminated nanostructures can be found elsewhere [116, 117]. Before studying the theoretical interaction of ZnO with target molecules, a great effort has been dedicated to understand the stability and electron structure of ZnO low index surfaces. Details on main results on this topic, that are given in Section 3.2.4, imply the distinction between polar and non-polar surfaces. Finally, there exist only a few works dealing with interaction of ZnO with gas molecules that are summarized in Section 3.2.5.

3.2.1. Bulk Properties

Most of the group II-VI binary compound semiconductors crystallize in either cubic zinc-blende or hexagonal wurtzite

structure where each anion is surrounded by four cations at the corners of a tetrahedron, and vice versa. This tetrahedral coordination is typical of sp3 covalent bonding, but these materials also have a substantial ionic character.

ZnO is a II-VI compound semiconductor whose ionicity resides at the borderline between covalent and ionic semiconductor. The crystal structures shared by ZnO are wurtzite (B4), zinc blende (B3), and rocksalt (B1), as schematically shown in Figure 30 (from [118]). At ambient conditions, the thermodynamically stable phase is wurtzite. The zinc-blende ZnO structure can be stabilized only by growth on cubic substrates, and the rocksalt (NaCl) structure may be obtained at relatively high pressures.

The ground-state total energy of ZnO in wurtzite, zinc-blende, and rocksalt structures has been calculated as a function of unit-cell volume using a first-principles theory by several groups [186–189]. The total-energy data versus volume for the three phases are shown in Figure 31. The theoretical results predict that the wurtzite form is energetically preferable compared to zinc blende and rocksalt, which is compatible with the observations.

Wurtzite structure has a hexagonal unit cell with two lattice parameters, a and c, in the ratio of $c/a = \sqrt{8/3} = 1.633$ and belongs to the space group of $P6_3mc$. In an ideal wurtzite structure, the structure is composed of two interpenetrating hexagonal-close-packed (hcp) sublattices, each of which consists of one type of atom displaced with respect to each other along the threefold c-axis by the amount of $u = 3/8 = 0.375$ in fractional coordinates (the u parameter is defined as the length of the bond parallel to the c axis, in units of c). Each sublattice includes four atoms per unit cell and every atom of one kind (group-II atom) is surrounded by four atoms of the other kind (group VI), or vice versa, which are coordinated at the edges of a tetrahedron. In a real ZnO crystal, the wurtzite structure deviates from the ideal arrangement, by changing the c/a ratio or the u value. Lattice constants at room temperature determined by various experimental measurements and theoretical calculations are in good agreement [118, 119]. The lattice constants mostly range from 3.2475 to 3.2501 Å for the a parameter and from 5.2042 to 5.2075 Å for the c parameter. The c/a ratio and u parameter vary in a slightly wider range, from 1.593 to 1.6035 and from 0.383 to 0.3856, respectively.

Since the wurtzite structure described above does not present inversion symmetry, the crystal exhibits crystallographic polarity, which indicates the direction of the bonds, i.e., (0001) basal planes in the wurtzite structure differs from (000-1) planes. The convention is that the (0001) axis points from the face of the O plane to the Zn plane and is the positive z direction. Many properties of the material depend also on its polarity, for example, growth, etching, defect generation and plasticity, spontaneous polarization, and piezoelectricity. In wurtzite ZnO, besides the primary polar plane (0001) and associated direction <0001>, which are the most commonly used surface and direction for growth, many other secondary planes and directions exist in the crystal structure. This is discussed in detail in Section 3.2.4.

The electronic structure of zinc oxide has been investigated in some detail in several experiments (*see* [120] and references therein). Typically, the density of states reveals two primary bands between 0 and −10 eV (measured from the valence band maximum). The upper band is primarily derived from O 2p and Zn 4s orbitals, while the lower band arises almost only from Zn 3d electrons with a maximum between −7 eV and −8 eV [121]. From x-ray photoelectron spectra the mixture of Zn 3d states in the O 2p band has been determined to be about 9% indicating a small covalent contribution to bonding [122]. Zinc oxide displays a direct band gap of about 3.4 eV at the Γ-point.

The theoretical calculation of the band structure of ZnO mostly involve the LDA [194–197], which is complex because of the cationic 3d electrons. The calculated lattice constant underestimates the experimental values by as much as 18% for wurtzite ZnO if the 3d electrons are treated as core electrons, while inclusion of the 3d electrons in the valence band yields very accurate lattice constants. However, even if the 3d electrons are properly taken into account, the results of standard LDA calculations show distinct shortcomings, such as strongly underestimated band gap and overestimated occupied cationic 3d bands, which roughly reside 3 eV high in energy as compared to experiment. In addition, their interactions with the anion 2p valence bands are artificially enlarged, resulting in overestimated dispersion and bandwidth of the latter and shifting them unphysically close to the conduction bands. For example, the LDA underestimates the ZnO band gap to be as low as $E_g = 0.23$ eV, as opposed to the experimental $E_g = 3.37$ eV. Zakharov et al. [123] reported plane-wave GW method for a number of II-VI compounds. They simply treated the 3d electrons as core electrons and obtained very good results for the anion p valence bands and for the band-gap energies but it was not possible to make any assertion concerning the d-band positions. Recently, some groups reported GGA and GGA+U calculations of the band structure. A band diagram from Erhart et al. [124] and a detailed DOS from Jeffe et al. are reprinted in Figure 32. For further reference, the electronic band structure of the other phases of ZnO has also been studied by a number of researchers [125, 126].

3.2.2. Intrinsic Point Defects

The defect physics of ZnO has been extensively studied since many properties of zinc oxide are highly sensitive to point defects present in the material. Theoretically, a number of DFT calculations have been performed to elucidate the behavior of intrinsic[202–205], as well as extrinsic point defects [206–209] following the methodology described in Section 2.2. These cal-
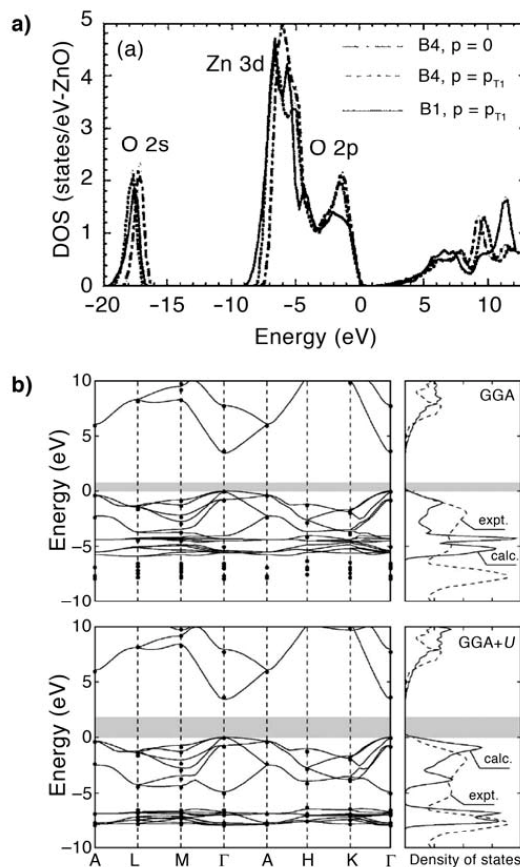

Figure 32. a) Total density of states (DOS) for ZnO in the B4 structure and the B1 structure calculated by DFT. Adapted and reprinted with permission from [187], J. E. Jaffe et al., *Phys. Rev. B* 62, 1660 (2000). © 2000, American Physical Society. b) Band structures obtained from density-functional theory calculations within the generalized-gradient approximation GGA (top) and using the GGA+U method (bottom). The conduction band states have been rigidly shifted to the experimental band gap. The small black circles represent data from self-interaction and relaxation corrected (SIRC) pseudopotential calculations [202]. In the plots on the right the solid and dashed lines show the calculated and experimental [191] density of states, respectively. The gray stripe shows the calculated band gap. Reprinted with permission from [199], P. Erhart et al., *Phys. Rev. B* 73, 205203 (2006). © 2006, American Physical Society.

culations are based on LDA or GGA which suffer from an underestimation of the band gap and an improper description of the band structure. The first shortcoming is intrinsic to the DFT method in general (*see* [127, 128]). The second problem is particularly pronounced for zinc oxide because GGA exchange-correlation potentials and self-interactions intrinsic to the LDA cause an energy level shift of the Zn 3d states. As a result, the calculations not only yield a band-gap error of more than 2 eV but also overestimate the covalence of the Zn-O bond. A direct comparison between data calculated within LDA or GGA-DFT

Applications of DFT Calculations to Chemical Gas Sensors: Design and Understanding **273**

Table 4. Calculated formation enthalpies (in eV) for point defects in bulk zinc oxide for zinc-rich and p-type conducting conditions ($\mu_e = 0$ eV, VBM. Different first principles methods and approximations have been used: DFT GGA and GGA+U [199]; DFT, GGA, ultrasoft PP [204]; DFT, LDA, ultrasoft PP [202]; DFT, LDA, norm-conserving PP [203]; and DFT, LDA, norm-conserving PP [205].

Defect type	Defect state	Ref. [199] GGA	Ref. [199] GGA+U	Ref. [204] GGA	Ref. [202] LDA	Ref. [203] LDA Uncorr.	Ref. [203] LDA Corr.	Ref. [205] LDA
$Zn_{i,oct}$	0	2.50	4.25	1.2	1.7	3.4	6.2	
	+1	0.98	1.69	>0.4	1.3	1.5	2.1	
	+2	0.33	0.02	−0.6	0.9	−0.2	−2.3	
V_O	0	1.00	1.71		0.0	1.5	2.4	0.9
	+1	0.26	0.71		0.2	0.8	1.5	
	+2	−0.48	−0.73	−0.9	−0.3	−0.5	−3.0	−0.5
$O_{i,db}$	0	4.61	4.70					5.1
	+1	4.76	4.59					5.1
	+2	5.36	5.08					5.2
$O_{i,db-rot}$	−2	7.70	8.79	8.2				7.2
	−1	6.51	7.08	>7.1	7.5			6.6
	0	4.87	4.96	6.0	6.5			5.2
	+1	5.07	4.91		6.5			5.3
	+2	5.67	5.41					5.4
$O_{i,oct}$	−2	7.84	8.97	7.8	7.8	7.4	9.7	7.4
	−1	6.65	7.33	6.9	6.8	6.4	10.4	6.7
	0	6.20	6.60	6.4	6.4	6.2	12.1	6.2
	+1	6.36	6.60		6.4			6.3
	+2	6.95	7.09					6.3
V_{Zn}	−2	6.32	7.06	5.1	6.6	5.8	10.1	5.9
	−1	5.57	5.96	5.0	5.8	5.7	10.1	5.8
	0	5.35	5.60	>5.1	6.0	5.8	10.6	6.0
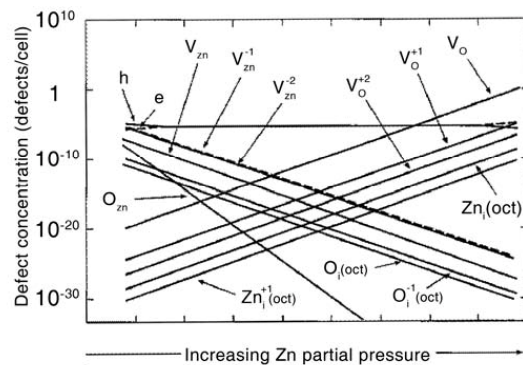
Figure 33. Intrinsic defect concentration at 1000 K. Conduction electrons are identified as "e" and holes as "h". Reprinted with permission from [202], A. F. Kohan et al., *Phys. Rev. B* 61, 15019 (2000). © 2000, American Physical Society.

and experiment is, therefore, severely hampered. This problem has been addressed in various ways. Zhang et al. proposed an empirical correction scheme based on a Taylor expansion of the formation enthalpies in the plane-wave cutoff energy [129]. The results can only be interpreted semiquantitatively since a profound physical motivation for this scheme is lacking. Kohan et al. discussed corrections based on the electronic structure of the defect configurations while other authors resorted to a qualitative discussion of their results.

If no correction is applied, the calculated formation enthalpies reported by different authors are comparable (*see* Table 4), whereas the various correction schemes lead to very different results. This

fact can be illustrated for the case of the oxygen vacancy. According to the data of Kohan et al. the ε(+2/0) transition for this defect should be located in the vicinity of the valence band maximum, while the corrected data by Zhang et al. predict the same transition to occur just below the conduction band minimum. Quantitatively more reliable calculations are required since it is difficult to assess the reliability of these predictions.

Regarding the dependence of concentration of point defects with respect to the partial pressure of Zn during the synthesis at a given temperature (i.e.: variations of the chemical potential of Zn or, conversely O), Kohan et al. shown (*see* Fig. 33) that high concentrations of Zn vacancies are reached at low partial pressure of Zn, and vice versa, high concentrations of O vacancies are reached at low partial pressures of oxygen.

Regarding the origin of the intrinsic n-type character of ZnO, Oba et al. highlighted that only the zinc interstitial (Zn_i) or the zinc antisite (Zn_O) can explain the n-type conductivity of undoped ZnO based on intrinsic defect stability calculations. However, the oxygen vacancy should be dominant under n-type conditions since it shows the lowest formation energy among the donor-type defects. This inconsistency could be a reason for the controversy on the native donor.

Similarly, Zhang et al. found that ZnO is n type at Zn-rich conditions because 1) the Zn_i is a shallow donor, supplying electrons; 2) its formation enthalpy is low for both Zn-rich and O-rich conditions, so this defect is abundant; and 3) the native defects that could compensate the n-type doping effect of Zn_i (interstitial O, O_i, and Zn vacancy, V_{Zn}), have high formation enthalpies for Zn-rich conditions, so these "electron killers" are not abundant. Additionally, they found that ZnO cannot be doped p-type via native defects (O_i, V_{Zn}) despite the fact that they are shallow (i.e., supplying holes at room temperature). This is because at both Zn-rich and O-rich conditions, the defects that could compensate
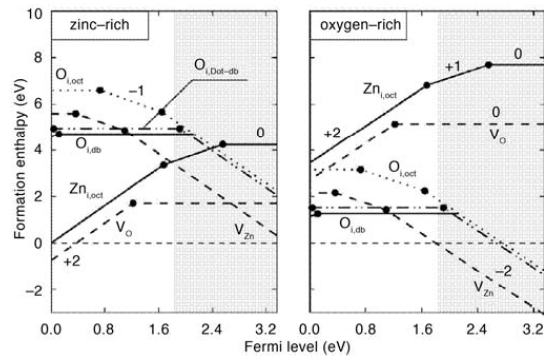
Figure 34. Variation of defect formation enthalpies with Fermi level under zinc-rich (left) and oxygen-rich (right) conditions as obtained from GGA+U calculations. Open and closed circles correspond to defects on the zinc and oxygen sublattices, respectively. The numbers in the plot indicate the defect charge state; parallel lines imply equal charge states. The gray shaded area shows the difference between the calculated band gap (1.83 eV) and the experimental (3.37 eV). Reprinted with permission from [199], P. Erhart et al., *Phys. Rev. B* 73, 205203 (2006). © 2006, American Physical Society.

p-type doping (V_O, Zn_i, Zn_O) have low formation enthalpies so these "hole killers" form readily.

According to other authors, the formation of defect complexes and/or unknown residual impurities (such as nitrogen substitutional N_O) is proposed to play central roles for the n-type conductivity of undoped ZnO. This is the case of Look et al. [130] how, based on molecular dymanics simulations, show that the Zn_i-N_O defect complex is a shallow donor with a sufficient binding energy to explain data.

Recently, Erhart et al. [124] reported an extensive work on ZnO intrinsic point defects, based on the GGA+U. This work partly confirms earlier calculations but reveals a larger number of transition levels (*see* Fig. 34): (1) For both the zinc interstitial as well as the oxygen vacancy, transition levels are close to the conduction band minimum. (2) The zinc vacancy shows a transition rather close to the valence band maximum and another one near the middle of the calculated band gap. (3) For the oxygen interstitials, transition levels occur both near the valence band maximum and the conduction band minimum.

3.2.3. Dopants

The possibility of doping ZnO to obtain wide-gap p-type semiconductor has great interest for different applications. For instance, using N_2 as the dopant source led to n-type conduction but NO_2 or NO led to p-type conduction; using P_2O_5 led to n-type conduction (poor reproducible p-type conduction also was reported) but Zn_3P_2 led to p-type conduction experimentally. Since the difference in oxygen chemical potential may be partially responsible for the above ZnO experiments, some DFT calculations were reported focusing on the relationship between oxygen chemical potential and electronic band gap structure. However, the underline mechanism that governs the above observed dopant behavior is still not clear. This problem has been explored from both DFT and chemical thermodynamic calculations.

Lee et al. studied the difficulty to obtain p-type ZnO with an N_2 doping source. They found that at low N doping levels using a normal N_2 source, O vacancies are the main compensating donors for N acceptors, while N acceptors are compensated via the formation of defect complexes with Zn antisites at high doping levels. When an active plasma N_2 gas is used to increase the N solubility, N acceptors are still greatly compensated by N_2 molecules at oxygen sites and N-acceptor–N_2 complexes, explaining the difficulty to achieve low-resistivity p-type ZnO. Recently, based on first-principles calculations, Marfaing et al. [131] proposed that efficient doping appears possible in various alternative ways: simultaneous incorporation of hydrogen as an interim compensating donor to be subsequently eliminated; use of a high activity dopant in the external phase (atomic N, NO) while preventing the formation of N_2-O compensating donors; planar doping for separate optimization of nitrogen incorporation and a defect-free crystal.

Van de Walle [132] reported strong theoretical evidences that hydrogen cats as a source of conductivity: it can incorporate in high concentrations and behaves as a shallow donor. This behavior is unexpected and very different form hydrogen's role in other semiconductors, in which it acts only as a compensating center and always counteracts the prevailing conductivity.

Yu et al. [133], indicate that it is unlikely to fabricate a usable p-type ZnO using P_2O_5 as dopant and predicted that Zn_3P_2 is a good dopant source under zinc rich growth conditions.

3.2.4. Surfaces

Theoretical investigations on ZnO-wurzite surfaces have been centered on the three low index surfaces (10–10), (11–20) and (0001).

The nonpolar (10–10) and (11–20) surfaces are obtained by cutting the crystal perpendicular to the hexagonal Zn and O layers (*see* Fig. 35). In both cases, for the (101–10) and the (11–20) planes, two equivalent surfaces are created so that always stoichiometric slabs with the same surface termination on top and at the bottom can be formed. The (10–10) surface geometry is sketched in Figure 35(a). Each surface layer contains one ZnO dimmer. The dimmers form characteristic rows along the (1–210) direction which are separated by trenches. The surface layers of the (11–20) surface are built up by two ZnO dimmers, which form zigzag lines along the surface (*see* Fig. 35(b)). The two dimmers are equivalent and are related by a glide plane symmetry. Cleaving the crystal perpendicular to the c axis (*see* Fig. 35(c)) always creates simultaneously a Zn- and an O-terminated polar (0001) and (000–1) surface, respectively. If we only consider cuts where the surface atoms stay threefold coordinated, all slabs representing polar surfaces are automatically stoichiometric and are inevitably Zn terminated on one side and O terminated on the other side so that each Zn-O double layer exhibits a dipole moment perpendicular to the surface with physical an computations consequences. More details on this point are given in Section 2.3.

The nonpolar (10–10) surface of ZnO has been the focus of several experimental and theoretical studies. However, the form of the relaxation of the surface atoms is still very controversial. Duke et al. [134] concluded from LEED analysis that the top-layer zinc ion is displaced downwards by $d_{Zn} = -0.45 \pm 0.1$ Å and likewise the top-layer oxygen by $d_O = -0.05 \pm 0.1$ Å, leading to a tilt of the Zn-O dimer of $12° \pm 5°$. No clear evidence for lateral
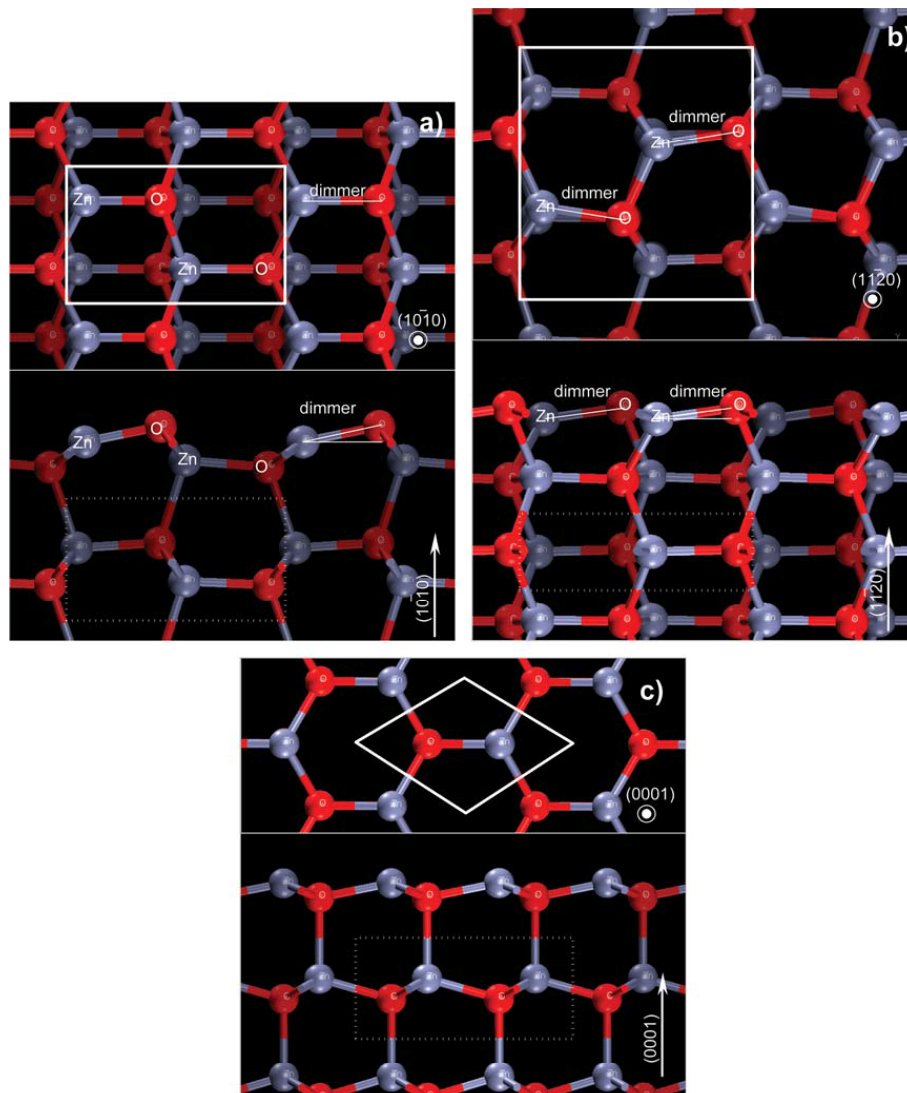
Figure 35. Solid rectangle marks the surface repetition unit. Dotted rectangle shows the thickness of a single surface layer: a surface unit one layer thick contains two ZnO dimmers (as in the bulk unit cell). a) Top and side views of the relaxed surface (10–10). Notice that the two dimmers are placed at different depths. b) Top and side views of the relaxed surface (11–20); in this case, both dimmers are in the same plane. c) Top and side views of the relaxed (0001) surface. a) and b) reprinted with permission from [231], J. D. Prades et al., *Thin Sol. Films* 515, 8670 (2007). © 2007, Elsevier.

distortions within the first layer or for second-layer relaxations were obtained. The strong inward relaxation of the Zn ion was later confirmed by Göpel et al. [135] in an angle-resolved photoemission experiment.

The first theoretical investigations of the (10–10) surface were done using empirical tight-binding (TB) models. With two very different TB models, Wang and Duke [136] found a strong displacement of $d_{Zn} = -0.57$ Å, whereas Ivanov and Pollmann [137] obtained an almost bulk-like surface geometry. A recent

calculation with atomistic potentials based on a shell model [138] predicted $d_{Zn} = -0.25$ Å and a rather strong upward relaxation of the second-layer Zn of +0.165 Å. Several ab initio studies (DFT-LDA) [139], Hartree-Fock (HF) [140] and a hybrid HF and DFT method using the B3LYP functional [141] employing Gaussian orbitals as basis functions to solve the electronic structure problem favor small inward relaxations of Zn and small tilts of the ZnO-dimers of 2° to 5°. However, it is questionable if these studies represent fully converged results. We found only

Table 5. Cleavage energy $E_{cleavage}$ (in J/m^2) for the different ZnO surfaces from several calculations reported in the literature.

Surface	(10–10)						(11–20)		(0001)/(000–1)		
Method	B3LYP	GGA	LDA	LDA	HF	Shell model	GGA	LDA	B3LYP	GGA	LDA
Ref.	[224,227]	[230]	[225]	[230]	[222]	[221]	[230]	[230]	[227]	[230]	[230]
$E_{cleavage}$ [J/m^2]	2.3	1.6	1.7	2.3	2.7	2.0	1.7	2.5	4.0	3.4	4.3

one DFT-LDA calculation using plane waves [142] where larger relaxations with a tilt of 11.7° were obtained.

The nonpolar (11–20) ZnO surface has been less frequently studied than its (10–10) counterpart. The two tightbinding models [136, 137] predicted the same relaxation behavior for the (11–20) as for the (10–10) surface: Wang and Duke [136] found a strong zinc displacement of $d_{Zn} = -0.54$ Å toward the bulk whereas the TB model of Ivanov and Pollmann [137] preferred an almost bulk-like surface structure. With a first-principles hybrid B3LYP method, Wander and Harrison [143] found much smaller relaxations for the (11–20) surface than for the (10–10) face, but not all degrees of freedom were relaxed in this study. To our knowledge there has been no quantitative experimental investigation.

Ab initio calculations on polar slabs [227–229] predict, consistently for both surface terminations, contractions for the first Zn-O double-layer distance, with a larger inward relaxation at the O-terminated surface.

In view of the above-discussed discrepancies between different experimental and theoretical investigations, Meyer and Marx provided a consistent set of fully converged calculations for the four main ZnO surfaces that solved this disagreement [144]. Additionally, they proposed that the polar surfaces can only be stable if a rearrangement of charges between the Zn- and the O-terminated surfaces takes place. In their calculations the polar surfaces were stabilized by allowing the electrons to move from the (000–1)-O to the (0001)-Zn surface, thereby quenching the internal electric field.

Concerning surface stability, Table 5 (reproduced from the work of Meyer and Marx [144]), reviews the main results on the cleavage energies of the low index surfaces. (Notice that, because of the polar surfaces, this comparison can not be made in terms of the surface free energy; *see* Section 2.3). Besides the discrepancies between the different approximations, it is clear that nonpolar (10-10) surface is the most stable face of ZnO with the lowest cleavage energy. But the energy of the (11–20) surface is only slightly higher. The cleavage energy for the polar surface is roughly a factor of 2 larger than for the nonpolar surfaces.

Regarding the surface electronic structure, less theoretical works have been reported. Prades et al. [145] predicted a very similar electron structure of the stoichiometric nonpolar surface with respect to the bulk. However, intragap levels (0.5eV above the valence band maximum) associated to oxygen vacancies were found (*see* Fig. 36).

3.2.5. *Molecule Adsorptions*

Besides the stability of ZnO surfaces at different chemical potentials of oxygen, several works have dealt with the interaction of ZnO low index surfaces with molecules of interest in gas sensing but, in all cases, polar surfaces where selected. In the following lines we review some of them.

The interaction of the polar ZnO(000–1) surface (O-terminated) with hydrogen and oxygen was studied by Meyer [146] by combining a thermodynamic formalism with first-principles
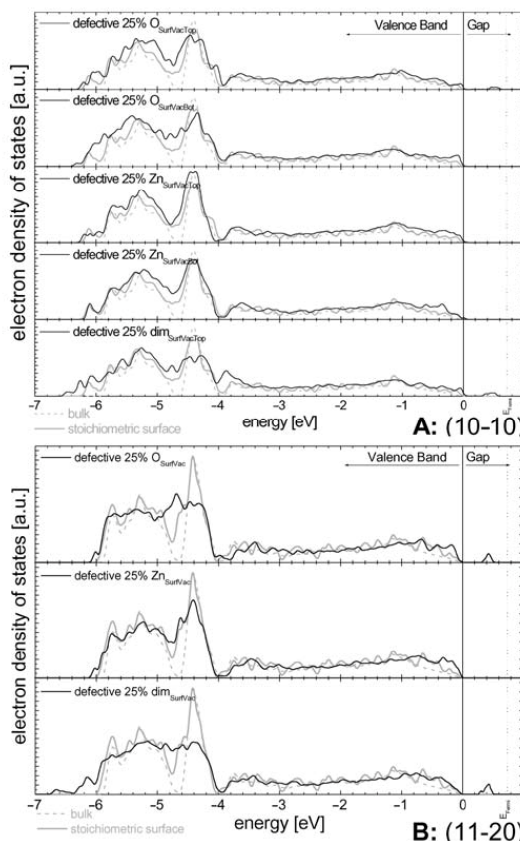
Figure 36. Electron density of states of stoichiometric and defective ZnO surfaces compared with the bulk: intragap levels 0.5 eV above the VBM only appear when outermost surface oxygen is removed. A) (10–10) surface B) (11–20) surface. Reprinted with permission from [231], J. D. Prades et al., *Thin Sol. Films* 515, 8670 (2007). © 2007, Elsevier.

density-functional calculations (their essential results are reprinted in Fig. 37). From this surface phase diagram they predicted that hydrogen is adsorbed at the (000–1)-O surface for a wide range of temperatures and H$_2$ partial pressures, including UHV conditions. This was also confirmed in a study of the CO adsorption on the polar ZnO surfaces [147] and is in agreement with observations of a HAS experiment of Kunat et al. [148].

They found a H binding energy of roughly 2.3eV per atom if molecular hydrogen dissociates and adsorbs at the clean O-terminated surface. Moreover, they predicted that in situations where both polar surface terminations are present (for example in powder samples) the dissociative adsorption of water with H and OH
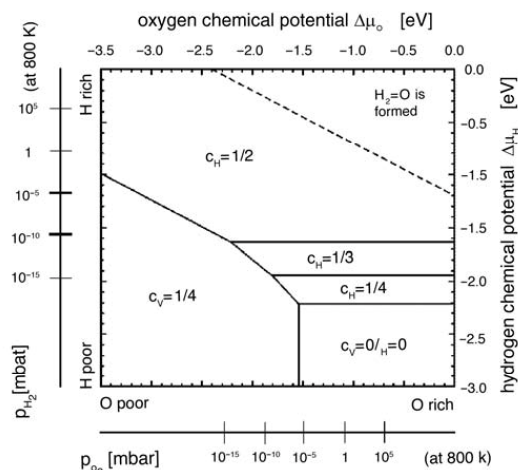
Figure 37. Phase diagram of the polar O-terminated (000–1) Surface in equilibrium with H_2 and O_2 particle reservoirs controlling the chemical potentials $\Delta\mu_H$ and $\Delta\mu_O$, based on selected superstructures as explained in the text [232]. The lowest-energy surface structures are labeled by the concentrations of oxygen vacancies c_V and hydrogen adatoms c_H. The upper right area indicates conditions under which H_2O condensates on the surface. Reprinted with permission from [232], B. Meyer, *Phys. Rev. B* 69, 045416 (2004). © 2004, American Physical Society.

groups being adsorbed at the O and Zn-terminated surface, respectively, is also energetically preferable. However, as soon as a coverage of ½ monolayer of hydrogen is reached, the energy gain of adsorbing more hydrogen on the (000–1)-O surface drops very rapidly with increasing hydrogen coverage. Therefore, no stable phases with more than 1/2 monolayer H coverage appear in the surface phase diagram. Particularly, a structure with a full monolayer of H as predicted in [148] seem not very likely to exist globally in thermodynamic equilibrium (which does not exclude a kinetic or local stabilization).

They predict it is possible to gradually remove the hydrogen from the surface and to form stable phases with less than 1/2 monolayer coverage of hydrogen by lowing hydrogen partial pressures and higher temperatures. Oxygen vacancies will be created if all hydrogen is removed as proposed by Kunat et al. [148]. However, they found that a surface with a vacancy concentration of 1/4 is much more stable than a missing-row structure where 1/3 of the oxygens have been removed. Finally, at higher oxygen partial pressures the O vacancies will be filled and the clean, defect-free O-terminated surface becomes the most stable structure.

Very recently, Cooke et al. [149] also calculated the stability of the non-polar surfaces under oxygen and hydrogen atmospheres. In each case, two terminations only are stable for a significant range of oxygen and hydrogen chemical potential: the pure stoichiometric surface and a surface covered in a monolayer of water. However, the mode by which the water adsorbs is different for the two surfaces considered. On the (10–10) surface (*see* Fig. 38(a)) hydrogen bonding can occur between adjacent chemiadsorbed water molecules because the close proximity of the water molecules and hence there is little difference in the stability of the hydrated and hydroxylated surface. In fact, the most stable surface occurs with a combination of dissociated and

undissociated water adsorption. In the case of the (11–20) surface (*see* Fig. 38(b)), only a hydrogen-bonding network can form when full dissociation has occurred.

Recently, Fink [150] studied the adsorption of H_2, CO and CO_2 on oxygen vacancies at the polar ZnO(000-1) surface based on cluster calculations. Regarding H_2, he identified 3 defects, namely V_{H2O}, V_O, and V_{OH2} which differ only by the number of H_2 molecules adsorbed at the defect site and proposed to judge their relative stability by a comparison of the total energies of $V_{H2O} + 2H_2$, $V_O + H_2$, and V_{OH2}. The lowest total energy was obtained for $V_O + H_2$. To remove a further H_2 molecule from the surface and obtain V_{H2O} costs 2.32 eV (2.16 eV). To add H_2 to the defect needs 1.35 eV (1.52 eV). For the numbers in brackets, zero point vibrations were corrected.

The latter result seems to contradict the DFT slab calculations of Meyer [146] who obtained very similar energies for the configurations $V_O + H_2$, and V_{OH2}. The hydrogenated defect was slightly lower in energy in his calculations. Considering the chemical potential of H_2, this would mean that it is possible to form a hydrogenated defect for very high H_2 pressures on the basis of the DFT slab calculations, while this configuration is never reached on the basis of the cluster calculations. The reason for the different results would be a difference in the description of the conduction band in the DFT slab calculations and the embedded cluster calculations. In the V_{H2O} and V_O defects, the valence band of ZnO is completely filled and the conduction band empty. The vacancy electrons of V_O occupy a local defect level. These states can be well described by an embedded cluster approach. The additional two electrons at the V_{OH2} defect have to occupy the conduction band. It is well known that the position of the conduction band is too low in DFT slab calculations without self-interaction correction [151] Therefore, the binding energy of the additional H_2 molecule will be overestimated in the slab calculations. So that, Fink assumed it is very unlikely that V_{OH2} can be lower in energy than $V_O + H_2$. He concluded that a hydrogenated defect can not be reached in experiment.

From the calculations on the adsorption of CO and CO_2, he assumed that electron rich defects can be refilled by the reaction: Vacancy + CO_2 → Surface + CO under catalytic conditions, though he did not now estimate the barrier heights of this reaction. CO can be bound with both ends at V_{H2O}, as observed already before [152] The adsorption of CO with the O end was in his calculations only possible at V_{H2O}, while it can bind with the C end at V_{OH} and at V_{OH2} with binding energies in the same order of magnitude. For a quantitative comparison of the binding energies he proposed it is necessary to perform high level wavefunction based ab initio calculations, since the energy differences between different adsorption geometries are very small.

Chaturvedi et al. [153] studied the interaction of SO_2 with polar surfaces of ZnO (both Zn and O terminated) by combining photoemission and molecular orbital techniques. They found that the chemistry of SO_2 on ZnO is complex, and oxygen is the active site. When SO_2 is dosed on ZnO at 100 K, a mixture of SO_3 and SO_4 species is formed on the surface. Theoretical calculations suggest that SO_2 adsorbs on an oxygen site to form SO_3, which later extracts an oxygen atom from the ZnO lattice to form SO_4. At 100 K, the energy available for this "extraction" is limited due to the low temperature of the system. Additionally, SO_2 dosed on ZnO at 300K forms surface SO_4 species that are stable up to temperatures above 500K. These SO_4 species decompose to form Zn-bonded S and ZnO.
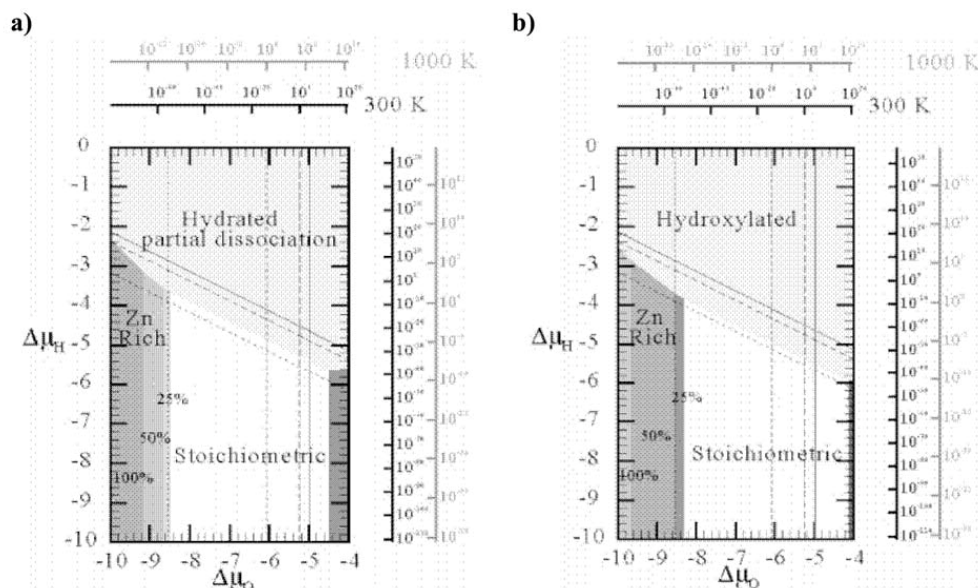
Figure 38. a) Calculated phase diagram of the structure of the ZnO (10–10) surface as a function of oxygen and hydrogen chemical potentials or partial pressures. The dotted vertical line on the left-hand side limits the stability domain of solid zincite with respect to metal zinc. The vertical lines on the right-hand side correspond to the condensation of oxygen into molecular O_2, at different temperatures (full 0 K, broken 298 and 1000 K). The diagonal lines correspond to the water/H_2 equilibrium (same temperature convention). The lower and left scales give the chemical potentials, in eV. The upper and right scales give the corresponding partial pressure at 298 and 1000 K, in bar. b) Calculated phase diagram of the structure of the ZnO (11–20) surface as a function of oxygen and Hydrogen chemical potentials or partial pressures. Same grayscale convention as before. Adapted and reprinted with permission from [235], D. J. Cooke et al., *J. Phys. Chem. B* 110, 7985 (2006). © 2006, American Chemical Society.

To conclude, Rodriguez et al. [154] studied the interaction of NO_2 with both polar ZnO surfaces by combining photoemission, XANES and DFT techniques. They concluded that NO_2 is a very good oxidizing agent for preparing ZnO from metallic zinc. Zn reacts more vigorously with NO_2 than metals such as Rh, Pd, or Pt which are typical DeNO$_x$ catalysts. At 300K, the main product of the reaction of NO_2 with polycrystalline ZnO is adsorbed NO_3 with little NO_2 or NO present on the surface of the oxide. No evidence was found for the full decomposition of the NO_2 molecule (i.e., no $NO_2 \rightarrow N + 2O$). The Zn $\leftrightarrow NO_2$ interactions on ZnO are strong and the Zn sites probably get oxidized and nitrated as a result of them. It appears that NO_2 is very efficient for fully oxidizing metal centers that are missing O neighbors in oxide surfaces. On zinc oxide, the nitrate species are stable up to temperatures near 700K. ZnO can be useful as a sorbent in DeNO$_x$ operations.

3.3. TiO$_2$

Titanium dioxide is used as gas sensor, as a photocatalyst, in solar cells for the production of hydrogen and electric energy, as white pigment (e.g., in paints and cosmetic products), as a corrosion-protective coating, as an optical coating, in electric devices such as varistors and in ceramics. It is important in earth sciences, plays a role in the biocompatibility of bone implants, finds applications in nanostructured form in Li-based batteries and electrochromic devices, and is being discussed as

a gate insulator for the new generation of MOSFETS and as a spacer material in magnetic spin-valve systems.

TiO_2 is not used as extensively as SnO_2 and ZnO in gas sensing applications, but it has received great attention an it its widely used as an oxygen gas sensor, e.g., to control the air/fuel mixture in car engines [241–243]. Two different temperature regimes are distinguished [155]. At low temperatures, addition of Pt leads to the formation of a Schottky-diode and a high sensitivity against oxygen [155]. At high temperatures, TiO_2 can be used as a thermodynamically controlled bulk defect sensor to determine oxygen over a large range of partial pressures. The intrinsic behavior of the defects responsible for the sensing mechanism can be controlled by doping with tri- and pentavalent ions.

Several review papers discuss the technical and scientific aspects of TiO_2 photocatalysis [245–248]. An extensive review of the surface science aspects of TiO_2 photocatalysis has been given by Linsebigler et al. [156].

Besides, TiO_2 is one of the most investigated metal oxides from the theoretical point of view. In Section 3.3.1, we review the most relevant results on TiO_2 bulk properties (including the two most relevant polymorphs rutile and anatase). After this, main works on the stability and the electron structure of rutile (110), (100), (001), and anatase surfaces are summarized in Sections 3.3.2 and 3.3.3. Finally, Section 3.3.4 presents the main theoretical results on the surface chemistry and molecular adsorption on TiO_2.

Applications of DFT Calculations to Chemical Gas Sensors: Design and Understanding
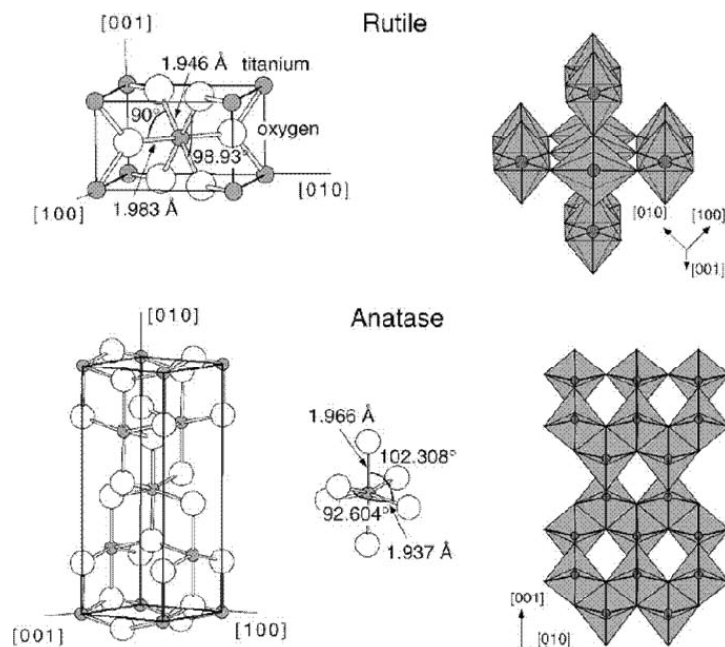
Figure 39. Bulk structures of rutile and anatase are shown. The tetragonal bulk unit cell of rutile has the dimensions, a = b = 4.584 Å, c = 2.953 Å, and the one of anatase a = b = 3.782 Å, c = 9.502 Å. In both structures, slightly distorted octahedra are the basic building units. The bond lengths and angles of the octahedrally coordinated Ti atoms are indicated and the stacking of the octahedra in both structures is shown on the right side. Reprinted with permission from [252], U. Diebold, *Surf. Sci. Rep.* 48, 53 (2003). © 2003, Elsevier.

3.3.1. Bulk Structure

Titanium dioxide crystallizes in three major different structures; rutile -so called cassiterite- (tetragonal, P4$_2$/mnm, a = b = 4.584 Å, c = 2.953 Å [157]), anatase (tetragonal, I4$_1$/amd, a = b = 3.782 Å, c = 9.502 Å) and brookite (rhombohedrical, Pbca, a = 5.436 Å, b = 9.166 Å, c = 5.135 Å) [158]. However, only rutile (stable) and anatase (metastable, but frequently found in nanograins) play any role in the applications of TiO$_2$ and are of great interest here as they have been studied with computational techniques. Their unit cells are shown in Figure 39 (from [159]). In both structures, the basic building block consists of a titanium atom surrounded by six oxygen atoms in slightly distorted octahedral configuration. In each structure, the two bonds between the titanium and the oxygen atoms at the apices of the octahedron are slightly longer. A sizable deviation from a 90° bond angle is observed in anatase. In rutile, neighboring octahedra share one corner along {110} directions, and are stacked with their long axis alternating by 90°. In anatase the corner-sharing octahedra form (001) planes. They are connected with their edges with the plane of octahedra below. In all these TiO$_2$ structures, the stacking of the octahedra results in threefold coordinated oxygen atoms.

3.3.1.a. Defects

The titanium–oxygen phase diagram is very rich with many stable phases with a variety of crystal structures (*see*, for example, [158]). In consequence, TiO$_2$ can be reduced easily. Bulk reduction and the resulting color centers are reflected in a pronounced color change of TiO$_2$ single crystals from initially transparent to light and, eventually, dark blue. These intrinsic defects result in n-type doping and high conductivity [159].

As has been remarked [160], bulk defects play a major role in a variety of surface phenomena where annealing to high temperatures is necessary, e.g., during the encapsulation of Pt [161]. The relationship between crystal color, conductivity, bulk defects as characterized by EPR measurements, and surface structure of rutile (110) has been investigated systematically by Diebold et al. [160]. The electric properties in dependence on the bulk defect concentration has been investigated in [162].

The bulk structure of reduced TiO$_{2-x}$ crystals is quite complex with different types of defects such as doubly charged oxygen vacancies, Ti^{3+} and Ti4+ interstitials, and planar defects. The defect structure varies with oxygen deficiency which depends on temperature, gas pressure, impurities, etc. Despite years of research, the question of which type of defect is dominant in which region of oxygen deficiency was subject to debate [162]. It was shown that the dominant type are Ti interstitials in the region from TiO$_{1.9996}$ to TiO$_{1.9999}$ [162].

3.3.2. Surface Structure

Based on total energy self-consistent ab initio calculations, Ramamoorthy et al. [163] studied the low index surfaces of TiO$_2$. Since they presented their surface free energy results in surface

Table 6. Surface free energies of low-index TiO_2-rutile surfaces. Normalized values to the lowest surface free energy $\tilde{E}_{surf}(110)$ are presented for comparison. Values taken from [256, 257].

Surface	LDA from [256]		GGA from [257]	
	E_{surf} [meV/a.u.^{2}]	$E_{surf}/E_{surf}(110)$	E_{surf} [J/m^2]	$E_{surf}/E_{suf}(110)$
{110}	15.6	1.00	0.50	1.00
{100}	19.6	1.26	0.69	1.38
{101}	24.4	1.56	1.03	2.06
{001}	28.9	1.85	1.25	2.50

Figure 40. The equilibrium shape of a macroscopic TiO_2 rutile crystal using the Wulff construction and the calculated surface energies of [256].

arbitrary units, it is not straightforward to compare them result with more recent works such as Perron et al. [164]. In any case, the former and the more recent calculations leads to the same conclusions (*see* Table 6). The (110) surface has the lowest surface energy, and the (001) surface the highest. This is also expected from considerations of surface stability, based on electrostatic and dangling-bonds arguments discussed previously for SnO_2(110) in Section 2.1. (Atomic models of these three rutile (cassiterite) surfaces agree equivalent to those reproduced for SnO_2 in Fig. 23.) The thermodynamic stability of the (100) surface was also considered, and was found to be stable with respect to forming (110) facets. The (001) surface was almost unstable with respect to the formation of macroscopic (1×1) (011) facets. The experimental results on the three low-index rutile surfaces discussed here fit rather well with the stability expected from these calculations: for rutile, the (110), (001) and (100) surfaces have been analyzed, with (110) being the most stable one. From the calculated energies [256] a three-dimensional (3D) Wulff plot was constructed (*see* Fig. 40). The Wulff construction [165] gives the equilibrium crystal shape of a macroscopic crystal.

For anatase, the (101) and the (100)/(010) surface planes are found in powder materials, together with some (001). The (101) surface was calculated to have the lowest surface energy, even lower than the rutile (110) surface [166].

Theoretical works on the stability of rutile and anatase low index surfaces are reviewed in the following sections. Section 3.3.3 is dedicated to the electron structure of such surfaces.

3.3.2.a. TiO_2-rutile(110)
The rutile (110) surface is the most stable crystal face and structure and stability of TiO_2(1 1 0)-(1×1) can be predicted with simple guidelines. Although the TiO_2(110) surface is very stable, it reconstructs and restructures at high temperatures under both oxidizing and reducing conditions.

Several groups have studied the relaxations of TiO_2(110) with total-energy calculations [256, 260–264]. Both linear combination of atomic orbitals (LCAOs) and plane-wave techniques were used. Either periodic or free-standing supercells with different numbers of layers were considered. Because of the localized nature of the Ti_{3d} electrons in the TiO_2 structure, plane-wave expansions are demanding. A rather high-energy cutoff needs to be used for convergence, and the functional for the LDA- or GGA-based calculations may also influence the results [167]. In addition, the thickness of the slab may play a role in the accuracy of the calculated geometry.

The directions of the calculated relaxations agree with the experimentally determined coordinates in (almost) all the theoretical papers. The quantitative agreement is not as good as one could expect from state-of-the art ab initio calculations, however. In particular, all the calculations find a much smaller relaxation
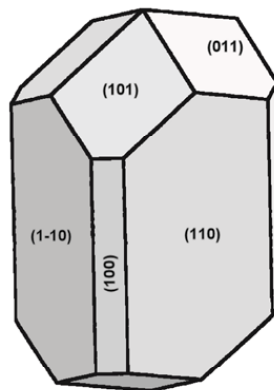
for the position of the bridging oxygen atom. As Harrison et al. pointed out, the extensive experience of calculations on bulk oxides which has been built up in recent years leads one to expect that DFT and HF calculations will reproduce experimental bond lengths to somewhat better than 0.1 Å. They proposed that a reason for this disagreement could be and strong anharmonic thermal vibrations at the TiO_2(110) surface since theoretical DFT and HF results are strictly valid only at zero temperature. However, discarding this explanation, it was found in molecular dynamics simulations using the Carr-Parrinello approach [168] that the average position in dynamic calculations is only relaxed by 0.05 Å rather than by 0.27 Å as previously found. It was suggested that the O atom might relax laterally so that it is displaced into an asymmetric position.

It is now well-known that adsorbates often have a significant influence on the "re-relaxation" of the surface. Computational studies, such as the one given in [169] for the adsorption of Cl, clearly show strong effects upon adsorption. Only a few experimental data exist so far. For example, Cu overlayers on TiO_2(110) cause the Ti atoms at the Cu/TiO_2(110) interface relax back to the original, bulk-like positions. The O atoms relax even stronger, which was attributed to Cu–O bonding [170].

3.3.2.b. TiO_2-rutile(100)
The rutile (100) surface has received considerably less attention than the (110) crystal face. This appears to be a strongly corrugated surface, with rows of bridging oxygen atoms at the outermost, (100)-oriented ridges. Indeed a (1×1)-terminated LEED pattern is observed on this surface after sputtering and annealing, and STM and non-contact AFM images are consistent with this model [171, 172].

Several theoretical calculations have determined likely relaxations of the (1×1) surface [163, 173, 174]. In [173], different theoretical approaches and basis sets were tested. All these calculations agree in the general displacements of the atoms, although the amount of relaxations differ somehow. As expected from symmetry, no relaxations occur along [001]. In the [100] direction only the fivefold coordinated Ti atoms show appreciable (downwards) relaxations [163]. Substantial relaxations occur along the [010] direction with the twofold coordinated and the threefold coordinated oxygen atoms moving in opposite

Applications of DFT Calculations to Chemical Gas Sensors: Design and Understanding 281

Table 7. Comparison of calculated surface formation energies for relaxed, unreconstructed TiO_2-anatase surfaces. Values taken from [276, 277].

Surface orientation	{101}	{100}	{001}	{110}
E_{surf} [J/m^2]	0.44	0.53	0.90	1.09

direction of the fivefold and sixfold coordinated Ti atoms. The net effect of these displacements is to increase the effective coordination of the fivefold coordinated Ti atoms [173]. No experimental data on relaxations of the $TiO_2(100)$-(1×1) surface exist.

3.3.2.c. TiO$_2$-rutile(001)
The least detailed structural information is available for the rutile (001) surface. Additional theoretical and experimental work could help to resolve the geometry of this surface would be quite valuable.

3.3.2.d. Vicinal TiO$_2$ Rutile Surfaces
Vicinal surfaces of TiO_2 have not been studied extensively. The most detailed investigation was performed on a $TiO_2(210)$ surface [175]. In a formal sense, $TiO_2(210)$ lies midways between (110) and (100), and is the most simple vicinal surface. Atomistic simulations, based on Coulombic interaction between ions and a short-range repulsive interaction, predicted an asymmetric sawtooth-like structure of the surface, consisting of {110} nanofacets. The width of each nanofacet is 1.5 times the width of the surface unit cell of the (110)-(1×1) structure (i.e. $3a/\sqrt{2}$). Each nanofacet terminates with a row of Ti atoms carrying bridging oxygen atoms. The surface energy of this structure is predicted to be 2.07 J/m^2. (This is to be compared to a surface energy of 1.78 J/m^2 derived using a similar calculation for $TiO_2(110)$ [175]).

3.3.2.e. TiO$_2$-anatase Surfaces
As far as anatase is concerned, typically, (101) and (100)/(010) surface planes are found, together with some (001) [166]. Several theoretical studies have predicted the stability of the different low-index anatase surfaces [166, 176, 177]. The (101) face is the thermodynamically most stable surface (*see* the calculated surface energies in Table 7 from [178, 179]). While it is difficult to obtain accuracy for surface energies numbers with DFT calculations, the relative surface energies in Table 7 should still be meaningful. The calculated Wulff shape of an anatase crystal, based on these values, compares well with the shape of naturally grown mineral samples (*see* Fig. 41). Interestingly, the average surface energy of an equilibrium-shape anatase crystal is smaller than the one of rutile [178, 179], which might explain the fact that nanoscopic TiO_2 particles are less stable in the rutile phase.

Woning and van Santen [180] also predicted, based on calculations of the electrostatic potential, that the rutile (110) surface can be reduced easier than the anatase (101) surface.

The stable, anatase (001) surface exhibits exclusively fivefold coordinated Ti atoms, as well as twofold and threefold coordinated oxygen atoms (*see* Fig. 42(a)). Calculations show that the corrugation increases somewhat upon relaxation, from 0.82 to 0.92 Å [166]. Based on first-principles calculations, Lazzeri and Selloni suggested the so-called 'added molecule (ADM)' structure (*see* Fig. 42(b, c) [181]. High-resolution STM and NC-AFM images are consistent with the ADM model [182]. Kinks and defects in the bright rows of the (1×4) structure as well as the faint lines between the bright lines (which would be at the location of
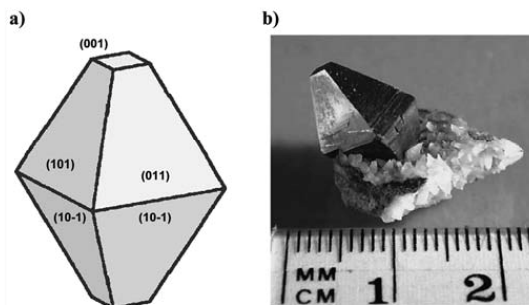
Figure 41. a) The equilibrium shape of a TiO_2 crystal in the anatase phase, according to the Wulff construction and surface energies calculated in [276]. b) Picture of an anatase mineral crystal reprinted with permission from [252], U. Diebold, *Surf. Sci. Rep.* 48, 53 (2003). © 2003, Elsevier.

the Ti(5) atoms) fit very well to the proposed model. The NC-AFM images show elevated features which are also consistent with these added features.

As seen from Table 7, the anatase (100) surface should be quite stable. While this plane is not a terminating face at an equilibrium-shape crystal, such planes are observed in powder materials.

3.3.2.f. Conclusion
Extensive theoretical work together with scanning probe techniques has helped to refine the understanding of surface relaxations. The level of detail on the atomic geometry of the $TiO_2(110)$ surface is certainly comparable to that of certain elemental semiconductors or metals. DFT calculations have helped in understanding the structure of TiO_2 surfaces, and have given a warning sign when structural models based on experimental observations were too simplistic.

One interesting theme is the interplay between surface structure and bulk defects in rutile; the presence of different structural features under exactly the same preparation conditions show its the importance in the reduction state of the crystal.

The expanding data base has made rutile TiO_2 a very popular model system for metal oxides. Nevertheless, there are still many open questions concerning the crystal structure of rutile surfaces as pointed out throughout this section. One interesting aspect is the advent of surface studies on anatase.

3.3.3. Surface Electron Structure
An excellent introduction to the (bulk) electronic structure of transition metal oxides was given by Cox [183]. This was followed up with a detailed discussion of the surface electronic structure in the book on oxide surfaces by Henrich and Cox [184]. Since publication of this book in 1994, much progress has been made in the theoretical understanding of TiO_2 surfaces. Increasingly powerful computational approaches have been used as is described in a large number of publications [256, 262, 263, 283–297]. The basic understanding of the structure of clean TiO_2 surfaces as given in [184] is still valid; so that here it is summarized briefly. In the following a distinction is made between stoichiometric surfaces, and oxygen-deficient, 'reduced'. Since defects are introduced rather easily in rutile, this distinction is made somewhat
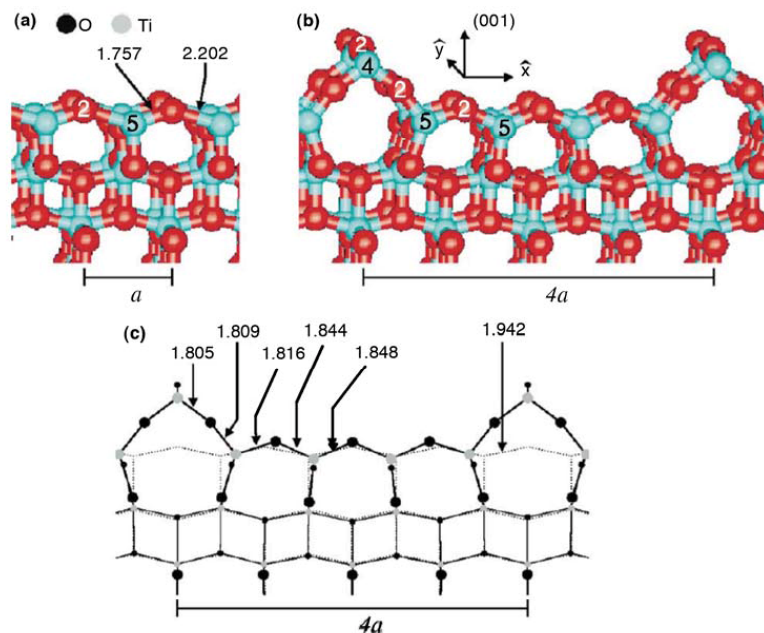
Figure 42. a) Relaxed (001)-(1×1) surface of anatase TiO_2. b) Relaxed structure of the 'ad-molecule' (ADM) model for the (1×4) reconstruction. c) Projection of the atomic positions of the ADM model on the plane perpendicular to the y direction. Dots with different sizes represent atoms belonging to different planes parallel to the figure. Dotted lines represent bonds in the ideally bulk-truncated surface. The length in Å of some surface bonds is indicated. a is the theoretical in-plane bulk lattice spacing (a = 3.786 Å). x and y correspond to the [001] and [010] directions. Reprinted with permission from [279], M. Lazzeri and A. Selloni, *Phys. Rev. Lett.* **87**, 266105 (2001). © 2001, American Physical Society.

arbitrarily. Almost every work that discusses clean TiO_2 surfaces is also concerned with reduced, defective surfaces.

3.3.3.a. Stoichiometric Surfaces
The electronic structure of TiO_2 has been calculated using a wide variety of theoretical approaches with varying degree of sophistication [256, 262, 263, 284–296, 298–304]. There is wide agreement that the surface electronic structure is not too different from that of the bulk. Except for non-stoichiometric surfaces, no surface states are observed or predicted (*see* below).

The occupied states are mostly O_{2p} derived, but exhibit a significant degree of covalency (*see* Fig. 43). The use of LDA vs. GGA in DFT, and the inclusion of spin-polarization, has been shown to cause little change in the overall features of the LDOS of stoichiometric surfaces. The hybridization of the Ti levels with oxygen are experimentally determined with resonant photoemission [185, 186]. When the photon energy is swept across the Ti_{3p} absorption edge, the photoemission cross-section for Ti_{3d}-derived states increases [187]. These resonances can be used for a qualitative estimate of Ti–O hybridization. Projected partial density of states have also been extracted from photoelectron diffraction measurements [188]. The iono-covalent character of the TiO_2(110) surface and of Ti_nO_m clusters with different sizes and charges has been studied by Albaret et al. [189]. On average, the Ti charge is close to +1.7 (as compared to the formal oxidation state of +4), and the oxygen charge is close to −0.85 (formal oxidation state of −2), with only small variations depending on the system. On the TiO_2(110) surface, the covalency of bonds
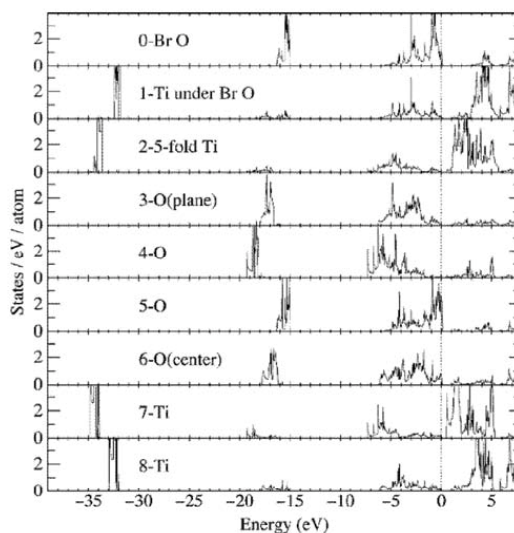
Figure 43. Mulliken projected densities of states of a three-layer slab of a stoichiometric TiO_2(110) surface. The atom indexes indicate the position in the supercell (*see* reference). Reprinted with permission from [295], A. T. Paxton and L. Thiên-Nga, *Phys. Rev. B* **57**, 1579 (1998). © 1998, American Physical Society.
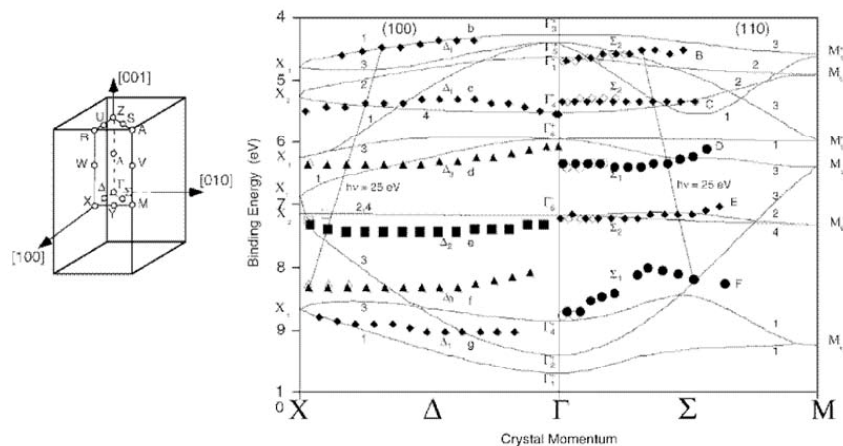
Figure 44. Calculated and experimental dispersions for rutile TiO_2 along the X–Γ–M directions of the reduced zone. The data were obtained from normal-emission spectroscopy from $TiO_2(110)$ and $TiO_2(100)$ surfaces. The final states bands for $h\nu = 25$ eV are also shown. Closed and open symbols represent emission from different Brillouin zones in the extended zone scheme. Experimental bands are labeled by the symmetry derived from dipole selection rules. Adapted and reprinted with permission from [311], P. J. Hardman et al., *Phys. Rev. B* 49, 7170 (1994). © 1994, American Physical Society.

between the bridging oxygen atom and the underlying sixfold coordinated Ti atoms is enhanced compared to other surface bonds. This is similar to a Mulliken charge analysis of the calculations by Paxton and Thiên-Nga.

While the calculations of the electronic structure of TiO_2 are abundant, only one photoemission experiment (where measured dispersions were related to the calculated band structure) has been reported [190] (*see* Fig. 44). Spectra were taken on a $TiO_2(110)$ and a $TiO_2(100)$ samples. Two angles of incidence for the photon beam were used. Because of the polarization of synchrotron, the identification of the symmetry of the valence band states based on selection rules was allowed. Such an assignment is critical, because the valence band in photoemission is broad and complex (Fig. 44). Photon energies below the Ti_{3p} to Ti_{3d} resonance have been used in the analysis. Very flat bands have been found in reasonable agreement with theory.

3.3.3.b. Reduced Surfaces

Annealing at high temperatures (or bombarding with electrons) creates point defects in the rows of bridging oxygen atoms and reduces the $TiO_2(110)$ surface. Figure 45 shows two typical photoemission spectra from the valence band region which exemplify the presence of oxygen vacancies. The solid line is from a (blue) $TiO_2(110)$ crystal after sputtering and annealing in UHV. The defect state in the band gap is visible. It shows almost no dispersion when the emission angle is changed [191]. The defect state disappears upon exposure to molecular oxygen gas at room temperature.

However, the defect state in the band gap is usually not reproduced in theoretical calculations. One possible reason was pointed out by Lindan et al. Spin-polarized DFT calculations of 'reduced' models system (where all the bridging oxygen atoms were removed, and the coordinates were relaxed) show localized band gap states formed by Ti_{3d} orbitals (*see* Fig. 46). In spin-paired calculations, this feature is generally not present in the band gap. The nature of the defect state is easily explained [184]. Removal of a neutral oxygen atom leaves behind two electrons

which previously occupied O_{2p} levels in the valence band. These states are no longer available, and the electrons go into the conduction band, the bottom of which is formed by Ti_{3d} states. Both, the neighboring fivefold and the sixfold Ti atoms receive an electron, and these electrons are unpaired.

Reduced TiO_2 is an n-type semiconductor, and band-bending effects accompany the adsorption of gases or metals. Figure 45 shows an example where such a band-bending effect is clearly visible. When oxygen vacancies are present, the extra electrons in the vacancies act as donor-like states that create an accumulation layer in the near-surface region. This causes a downward band bending. Only minimal changes occur in shape of the valence band after adsorption of oxygen in Figure 45, but there is a rigid shift of all peaks in the photoemission spectrum upwards by 0.2–0.3 eV. This is caused by a downwards shift of the Fermi level and an 'unbending' of the bands.

3.3.4. Molecule Adsorptions

Molecules and atoms adsorption, and their dissociation and/or reaction to other products, is certainly the most extensive area of study in TiO_2. In this review, we summarize the most relevant results on adsorption onto TiO_2 surfaces of molecules of interest in gas sensing applications. A more complete and detailed review of experimental an theoretical works on the interaction of TiO_2 with organic and inorganic molecules was elaborated by Diebold [159].

3.3.4.a. O₂

Because Ti is such a reactive element, oxygen-deficient surfaces are clearly expected to react with O_2. In many studies it has implicitly been assumed that oxygen exposure would just fill surface vacancies on TiO_2. In the mid 90's, the intricacies of the oxygen/defect interaction were investigated in more detail. Photocatalytic studies [313–315] as well as co-adsorption studies of water and ammonia with oxygen-predosed surfaces [316–318] revealed that the 'filling' of oxygen vacancies is not as simple as

a)

b)
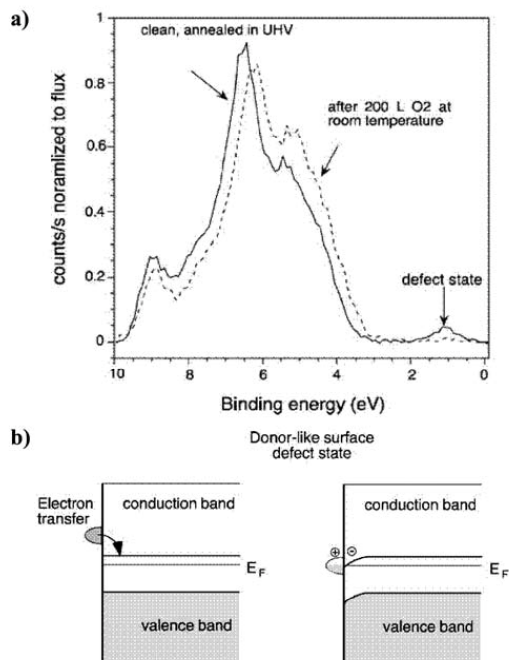
Figure 45. a) Photoemission spectra (hv=35 eV, normal emission) from the valence band region of a sputtered and UHV-annealed, clean TiO_2(110) surface. After adsorption of molecular oxygen at room temperature, the defect state in the band gap region disappears and the spectrum shifts by 0.2–0.3 eV to higher binding energy due to band bending. A Shirley background was subtracted from both spectra. b) Schematic diagram of the band-bending effect due to donor-like surface defect states. Surface oxygen vacancies create a defect state and electrons are donated to the system. A charge accumulation layer is created in the near-surface region and the bands in the n-type semiconducting TiO_2 sample bend downwards. Reprinted with permission from [312], Y. Aiura et al., *Physica B* 194–196, 1215 (1994). © 1994, Elsevier.

previously thought. The theoretical analysis of this complex situation was performed based on LDA first-principles calculations when discussing the stability of different surface relaxations.

More recently, Wendt et al. reported an study of the origin of various point defects on reduced rutile TiO_2(110)-(1×1) based on combining high-resolution scanning tunneling microscopy (STM) and DFT calculations [192]. By means of adsorption and desorption experiments using H_2O and O_2 as probe molecules they assigned the different features observed in STM images to bridging oxygen vacancies, oxygen atoms on surface Ti atoms, and single as well as pairs of hydroxyls on bridging oxygen rows. These experimental results were discussed in comparison to previous STM reports [320–322] where different assignments of the STM features were suggested. Based on DFT calculations they compared the interaction of water and oxygen with the reduced TiO_2(110) surface with the situation when these molecules encounter a perfect stoichiometric TiO_2(110) surface. These DFT calculations strongly support the assignments of the features observed experimentally by STM.
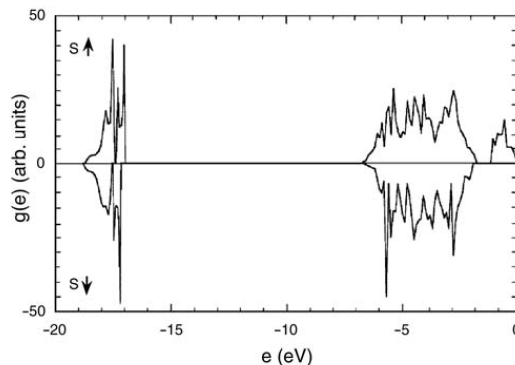
Figure 46. Densities of states g(e) for spin-up and spin-down electrons calculated for a stoichiometric TiO_2(110) surface after structural relaxations. Reprinted with permission from [284], P. J. D. Lindan et al., *Phys. Rev. B* 55, 15919 (1997). © 1997, American Physical Society.

In a recent work dealing with electroacceptor adsorbates on rutile-TiO_2(110) and MgO(100) surfaces, Ménétrey et al. showed that the adsorption of O_2 on a perfect surface is not very favorable since the surface is oxidized loosing the stoichiometry [193]. On the contrary, on the reduced surface restoring the stoichiometry is much more favorable. The consequence is not only on the strength of the adsorption; it also monitors the adsorption mode. They also concluded that the TiO_2 (110) surface is more active than MgO (100) and the adsorption mode changes from a balanced mode involving both Ti and O on the perfect surface to a mode involving only the cations and the vacancy in the defective surface. Coadsorption of ions preserving the global electroneutrality was observed to be favorable on perfect surfaces.

3.3.4.b. CO
Several authors studied the adsorption of CO on metal-promoted TiO_2 surfaces [324–332]. Of particular interest is the low-temperature oxidation of CO on nanosized, TiO_2-supported Au particles. In contrast to metal-promoted surfaces, the adsorption of CO on the clean TiO_2(110) surface has been far less investigated experimentally [194, 195, 196, 197], although this system has been treated theoretically by a number of groups [292, 337–344]. An early study by Göpel et al. [194,196] found oxygen vacancies to be special adsorption sites for H_2 and CO.

The adsorption of CO/TiO_2(110) has been treated with different computational techniques (*see* review of Diebold [159]). Adsorption with the C-end down is consistently found to be energetically much more favorable than the alternative orientation, where the CO molecule would bind with the O-end down. Throughout these calculations the C–O bond distances are rather similar, but the adsorption energies vary considerably, with the experimental value from [195] being on the lower end of the given range. The decrease in binding energy with higher coverage, caused by the onset of repulsive interaction between CO molecules, is reproduced in slab calculations. Experimentally, the C–O stretching mode of the adsorbed CO molecule shows a red shift compared to a free molecule [198]. The calculated values of the red shifts of the C–O stretching mode vary considerably. A quantitative comparison with experiment is difficult because of lack of reliable vibrational spectroscopy results on well-characterized,

Applications of DFT Calculations to Chemical Gas Sensors: Design and Understanding   **285**

single-crystalline rutile. However, the calculations seem to over-estimate the amount of this shift [198] with one exception. The $CO/TiO_2(110)$ system is a good test case for a refinement of computational techniques. Several authors explored systematically how these theoretical results are influenced by the embedding method of the clusters, the basis set, and various corrections [292, 337, 340–344].

Based on their TPD measurements, Linsebigler et al. [195] suggested that a CO moiety adsorbed close to an oxygen vacancy experiences an additional interaction with the vacancy that leads to a stronger bonding. Only one calculation found an increase in binding energy of CO at defect sites, in agreement with experiment [195]. However, this calculation was performed with a rather small, unrelaxed cluster.

3.3.4.c. N_2

The physisorption of N_2 was treated theoretically [199, 200]. According to cluster calculations the molecule physisorbs at TiO_2 surfaces in an end-on configuration. The high adsorption energy for zero coverages found experimentally was reproduced in these calculations. An interaction potential was constructed for N_2/TiO_2 clusters of various stoichiometries [200], and was used in Monte-Carlo calculations of N_2 adsorption at 77K [199]. For adsorption at low pressures (<1 Torr), every fivefold coordinated Ti site is occupied by one N_2 molecule; lateral repulsion between molecules causes an arrangement of N_2 in 1D zigzag chains. According to these calculations, the area covered by one N_2 molecule (19.2 and 9.6 $Å^2$ in the monolayer regime and multilayer regime, respectively) is quite different from the one usually used for determination of surface areas (16.2 $Å^2$).

3.3.4.d. NO

Nitrogen oxides (NO_x) are major contributors to acid rain and ground-level ozone pollution. TiO_2 is used to photocatalytically oxidize NO_x [201]. Molecular scale studies of NO adsorption on single-crystalline TiO_2 surfaces are useful for gaining an understanding of the underlying mechanisms [202, 203].

DFT slab calculations found as the favorable adsorption geometry a tilted NO molecule with the N-end down [202]. The calculations showed formation of N_2O_2 species for higher coverages which are bound much stronger than NO. In a previous TPD study [204], it was found that NO reacts reductively at the Ti^{3+} sites at oxygen vacancies to produce N_2O. The oxygen atoms in the adsorbate molecules are extracted by the TiO_2 surface and cause the oxidation of surface Ti^{3+} sites [204]. DFT calculations [202] showed that other molecules, such as N_2O or NO_2 bind weakly to the surface.

3.3.4.e. NO_2

The main product of the adsorption of NO_2 on $TiO_2(110)$ surface is surface nitrate, NO_3, with a small amount of chemisorbed NO_2 [205]. Photoemission data and DFT calculations suggest that this surface nitrate forms through a disproportionation process $2NO_{2,ads} \rightarrow NO_{3,ads} + NO_{gas}$ after adsorption at Ti sites. Because NO_2 is a big molecule, this result implies that substrate O vacancies and related defects migrate towards the surface in the presence of NO_2; a thesis that is supported by DFT calculations [205]. This is another example for the importance of subsurface defects for the surface chemistry of TiO_2. Such mechanisms are of remarkable importance in the prevention of environmental pollution when using an oxide for trapping or destroying NO_x species [205].

3.3.4.f. NH_3

Ammonia adsorbs molecularly on $TiO_2(110)$ as well as $TiO_2(001)$ surfaces at room temperature. This was confirmed in several experiments [353–356] as well as theoretical calculations [206]. It binds with the N-end down to the fivefold coordinated Ti sites.

3.3.4.g. H_2O

Water is probably the most important adsorbate at TiO_2 surfaces for many reasons since many of its applications are performed in an aqueous environment. Water vapor in the ambient interacts with TiO_2 surfaces, and surface hydroxyls can easily affect adsorption and reaction processes. The adsorption of water on TiO_2 has been of intense interest in recent years. Consequently, it has been investigated with a variety of experimental and theoretical techniques [159]. Recently, an excellent review article on water adsorption on solid surfaces was given by Henderson [207].

For the rutile (100) surface, there exist experimental and theoretical which agree that water can dissociate to some extent on perfect rutile (100) surfaces. Results from different spectroscopies generally indicate that water adsorbs both dissociatively and molecularly [359–362]. The sticking coefficient is unity at a sample temperature of 130K [208]. Adsorption/desorption occurs reversibly, i.e., molecular water is the only desorption product, and the surface generally does not become oxidized. Most theoretical results [176, 209], but not all of them [168], agree with the notion of initial dissociative adsorption, followed by molecular adsorption at higher coverages.

In the case of rutile (110), there is a considerable disagreement on the initial adsorption behavior of water, especially between theoretical and experimental studies despite the extensive work on water adsorption on rutile (110) reviewed by [159]. While most of the experimental results agree that H_2O does not dissociate on $TiO_2(110)$, except at defect sites, most theoretical studies predict dissociative adsorption. Calculations indicate that dissociation of the water molecule is energetically favored on the perfect $TiO_2(110)$ surface. Intermolecular H bonding was invoked to act as a stabilizing factor for a mixed dissociated/ molecular state [210, 211]. Other calculations point out that, while dissociative adsorption on rutile (110) is thermodynamically favored, it might be hindered by a potential barrier. One cluster calculation showed molecular adsorption [212], while many others, using a similar approach, predict dissociative adsorption. A recent DFT slab calculation by Norskov and co-workers [213] agrees with the experimental data (water dissociation is an endothermic and exothermic process on terraces and point defects, respectively), and it is argued that the configuration of the water molecules in test geometries plays an important role for the calculated energetics. A molecular dynamics simulation using the Carr–Parinello approach [168] found molecular adsorption on stoichiometric TiO_2 surfaces. However, these calculations do not reproduce other experimental results. Placing an H_2O molecule in a bridging oxygen vacancy did not lead to spontaneous dissociation on the $TiO_2(110)$ surface. Also, in [168] it was concluded that single OH groups are not stable on $TiO_2(110)$, in contradiction to recent STM data [213, 214].

The adsorption of water on anatase surfaces has so far been mostly studied theoretically. On the basis of DFT and first-principles molecular dynamics calculations, Selloni and co-workers [166] concluded that water adsorbs molecularly on anatase (101). Calculations of water adsorption on the anatase (001) surface [166, 176] predict dissociative adsorption but have yet to be confirmed by measurements.

4. CONCLUSIONS

The development of advanced gas sensing devices based on metal oxides requires the comprehension of the physical and chemical phenomena that occur in the interaction between the target gas molecules and the surface of the sensing materials.

Initially, this involves a detailed description of the active surfaces of the metal oxides from the point of view of both the atomic arrangement and the electronic structure. As we have shown, this is a first meeting point between experimental surface science studies and theoretical first-principles works.

After that, the size and shape of the sensing materials is also crucial to obtain better sensing performances and, again, theoretical works are helping to understand the synthesis methods of nanostructures. With this valuable knowledge, new synthesis possibilities are being opened to nanomaterials.

Finally, the ab initio study of concrete interactions between molecules and meaningful surfaces (as a result of previous stages of theoretical analysis of surface/shape stability) makes possible not only to reproduce and understand the well established adsorption and sensing behavior but also to propose new working methods to increases its performance such as different optimum working temperatures or the convenience of additives.

In this work, all these aspects have been reviewed for three of the most relevant metal oxides, such as SnO_2, ZnO and TiO_2, showing that part of great advances in the comprehension of metal oxides made in the last years are due to the complementation of experimental works with first-principles calculations. In the next years, the development of new theoretical approaches and methods of increased accuracy and performance together with new computational facilities will open new and exciting potential applications of theoretical first-principles calculations to eminently applied fields such as gas sensing.

ACKNOWLEDGMENTS

REFERENCES

1. W. H. Brattain and J. Bardeen, *Bell Systems Tech. J.* 32, 1 (1953).
2. T. Seiyama, A. Kato, K. Fujisishi, and M. Nagatoni, *Anal. Chem.* 34, 1052 (1962).
3. N. Taguchi, Japanese Patent 45–38200 (1962).
4. N. Taguchi, UK patent 1280809 (1970) and US patent 3631436 (1970).
5. G. Sberveglieri, *Sens. Actuators B* 23, 103 (1995).
6. W. Göpel and G. Reinhardt, "Metal oxide sensors: New devices through tailoring interfaces on the atomic scale," from Sensors Update,
   edited by H. Baltes, W. Göpel, and J. Hesse, VHC, Weinheim, 1996, Vol. 1.
7. G. Korotcenkov, *Mat. Sci. Eng. B* 139, 1 (2007).
8. W. Göpel, *Sens. and Actuators B* 18, 1 (1994).
9. W. Göpel and K.D. Schierbaum, "Chemical sensor based on catalytic reactions," from Handbook of Heterogeneous Catalysis, edited by E. Ertl, H. Knözinger, and J. Weitkamp, VCH, Weinheim, 1997.
10. P. Romppainen and V. Lantto, *J. Appl. Phys.* 63, 5159 (1988).
11. G. Blaustein, M. S. Castro, and C. M. Aldao, *Sens. Actuators B* 55, 33 (1999).
12. A. Cirera, A. Vilà, A. Diéguez, A. Cabot, A. Cornet, and J. R. Morante, *Sens. Actuators B* 64, 65 (2000).
13. A. Cirera, A. Cabot, A. Cornet, and J. R. Morante, *Sens. Actuators B* 78, 151 (2001).
14. Z. W. Pan, Z. R. Dai, and Z. L. Wang, *Science* 291, 1947 (2001).
15. F. Hernández-Ramírez, A. Tarancón, O. Casals, J. Rodríguez, A. Romano-Rodríguez, J. R Morante, S. Barth, S. Mathur, T. Y. Choi, D. Poulikakos, V. Callegari, and P. M. Nellen, *Nanotechnology* 16, 5577 (2006).
16. A. Kolmakov and M. Moskovits, *Annu. Rev. Mater. Res.* 34, 151 (2004).
17. P. Hohenberg and W. Kohn, *Phys. Rev.* 136, B864 (1964).
18. W. Kohn and L. J. Sham, *Phys. Rev.* 140, A1133 (1965).
19. Inorganic Crystal Structure Database, http://icsd.ill.fr/icsd/index.html (accessed March 2007).
20. A. A. Bolzan, C. Fong, B. J. Kennedy, and C. Howard, *Acta Cryst. B* 53, 373 (1997).
21. S. Lany and A. Zunger, *Phys. Rev. B* 72, 035215 (2005).
22. J. Oviedo, M. J. Gillan, *Surf. Sci.* 463, 93 (2000).
23. K. Reuter and M. Sheffler, *Phys. Rev. B* 65, 035406 (2002).
24. N.W. Ashcorft and N.D. Mermin, Solid state physics, CBS, Tokyo (1981).
25. J. E. Jaffe and A. C. Hess, *Phys. Rev. B* 48, 7903 (1993).
26. G. Makov and M. C. Payne, *Phys. Rev. B* 51, 4014 (1995).
27. F. Oba, S. R. Nishitani, S. Isotani, H. Adachi, and I. Tanaka, *J. Appl. Phys.* 90, 824 (2001).
28. V. Srikant and D. R. Clarke, *J. Appl. Phys.* 83, 5447 (1998).
29. G. A. Somorjai, Introduction to Surface Chemistry and Catalysis, Wiley, New York, 1994.
30. M. C. Payne, M. P. Teter, D. C. Allan, T. A. Arias, and J. D. Joannopoulos, *Rev. Mod. Phys.* 64, 1045 (1992).
31. J. Oviedo and M. J. Gillan, *Surf. Sci.* 467, 35 (2000).
32. W. Zhu and P. Wu, *Chem. Phys. Lett.* 396, 38 (2004).
33. P. W. Tasker, *J. Phys. C* 12, 4977 (1979).
34. B. Meyer and D. Marx, *Phys. Rev. B* 67, 035403 (2003).
35. P. Perrot, A to Z of Thermodynamics, Oxford University Press, New York, (1998).
36. M. W. Chase, NIST-JANAF Thermochemical Tables, American Chemical Society, Woodbury, (1998).
37. J. D. Prades, A. Cirera, and J. R. Morante, *J. Electrochem. Soc.* 154, H657 (2007).
38. K. Ellmer, *J. Phys. D: Appl. Phys.* 34, 3097 (2001).
39. D. F. Cox, T. B. Fryberger, and S. Semancik, *Phys. Rev. B* 38, 2072 (1988).
40. D. F. Cox, T. B. Fryberger, and S. Semancik, *Surf. Sci.* 227, L105 (1990).
41. M. Batzill and U. Diebold, *Prog. Surf. Sci.* 79, 47 (2005).
42. A. P. Alivisatos, *Science* 271, 933 (1996).
43. R. S. Berry, *Nature* 393, 212 (1998).
44. G. Wulff, *Z. Kristallogr.* 34, 449 (1901).
45. A. S. Barnard and P. Zapol, *J. Chem. Phys.* 121, 4276 (2004).
46. A. S. Barnard and L. A. Curtiss, *Rev. Adv. Mater. Sci.* 10, 105 (2005).
47. A. S. Barnard and P. Zapol, *J. Phys. Chem. B* 108, 18435 (2004).
48. A. S. Barnard, and P. Zapol, *Phys. Rev. B* 70, 235403 (2004).
49. A. S. Barnard, P. Zapol, and L. A. Curtiss, *J. Chem. Theory Comput.* 1, 107 (2005).
50. A. S. Barnard and L. A. Curtiss, *Nano Lett.* 5, 1261 (2005).

Applications of DFT Calculations to Chemical Gas Sensors: Design and Understanding $\qquad$ **287**

51. A. S. Barnard, Y. Xiao, and Z. Cai, *Chem. Phys. Lett.* 419, 313 (2006).
52. S. F. Boys and F. F. Bernardi, *Mol. Phys.* 19, 553 (1970).
53. J. Y. W. Seto, *J. Appl. Phys.* 46, 5247 (1975).
54. M. L. Tarng, *J. Appl. Phys.* 49, 4069 (1978).
55. J. Oviedo and M. J. Gillan, *Surf. Sci.* 490, 221 (2001).
56. C. G. Fonstad and R. H. Rediker, *J. Appl. Phys.* 42, 2911 (1971).
57. E. Thornton and P. Harrison, *J. Chem. Soc. Faraday Trans.* 71, 461 (1975).
58. A. Diéguez, Structural analysis for the improvement of SnO$_2$-based gas sensors, PhD thesis at the University of Barcelona, Barcelona, 1999.
59. W. Göpel, G. Rocker, and R. Feierabend, *Phys. Rev. B* 28, 3427 (1983).
60. T. S. Rantala, V. Lantto, and T. T. Rantala, *Sens. Actuators B* 18, 716 (1994).
61. J. Oviedo and M. J. Gillan, *Surf. Sci.* 513, 26 (2002).
62. H. A. Bethe, MIT Radiation Laboratory Report No. 43, 12 (1942).
63. F. Leblanc, L. Perier-Camby, G. Thomas, R. Gibert, M. Primet, and P. Gelin, *Sens. Actuators B* 62, 67 (2000).
64. W. Göpel and K. D. Schierbaum, *Sens. Actuators B* 26–27, 13 (1995).
65. B. Ruhland, T. Becker, and G. Muller, *Sens. Actuators B* 50, 85 (1998).
66. P. T. Moseley, *Sens. Actuators B* 6, 149 (1992).
67. W. Göpel and G. Reinhardt, "Metal oxide sensors: New devices through tailoring interfaces on the atomic scale," from Sensors Update, edited by H. Baltes, W. Göpel, and J. Hesse, Weinheim, 1996, Vol. 1.
68. Y. Shimizu and M. Egashira, *MRS Bull.* 24, 18 (1999).
69. Chemical sensors, in Proceedings of the International Meeting on Chemical Sensors, edited by T. Seiyama, K. Fueki, J. Shiokawa, S. Suzuki, Kodansha, Tokyo and Elsevier, Amsterdam, (1983).
70. W. Weiss and W. Ranke, *Prog. Surf. Sci.* 70, 1 (2002).
71. S. Surnev, M. G. Ramsey, and F.P. Netzer, *Prog. Surf. Sci.* 73, 117 (2003).
72. Z. R. Dai, Z. Wei Pan, and Z. L. Wang, *J. Am. Chem. Soc.* 124, 8673 (2002).
73. Z. L. Wang, *Adv. Mater.* 15, 432 (2003).
74. J. Pannetier and G. Denes, Acta Crystallogr., Sect. B: Struct. Crystallogr. *Cryst. Chem.* 36, 2763 (1980).
75. V. M. Jiménez, G. Lassaletta, A. Fernández, J. P. Espinós, F. Yubero, A. R. González-Elipe, L. Soriano, J. M. Sanz, and D. A. Papaconstantopoulos, *Phys. Rev. B* 60, 11171 (1999).
76. A. A. Bolzan, C. Fong, B. J. Kennedy, and C. J. Howard, *Acta Crystallogr. Sect. B—Struct. Sci.* 53, 373 (1997).
77. K. Suito, N. Kawai, and Y. Masuda, *Mater. Res. Bull.* 10, 667 (1975).
78. C. Kiliç and A. Zunger, *Phys. Rev. Lett.* 88, 095501 (2002).
79. K. C. Mishra, et al., *Phys. Rev. B* 51, 13972, (1995).
80. G. Wulff and Z. Kristallogr, 34, 449 (1901).
81. D. F. Cox, T. B. Fryberger, and S. Semancik, *Surf. Sci.* 224, 121 (1989).
82. D. F. Cox, T. B. Fryberger, and S. Semancik, *Phys. Rev. B* 38, 2072 (1988).
83. M. Batzill, K. Katsiev, and U. Diebold, *Surf. Sci.* 529, 295 (2003).
84. F. H. Jones, R. Dixon, J. S. Foord, R. G. Egdell, and J. B. Pethica, *Surf. Sci.* 376, 367 (1997).
85. M. Batzill, K. Katsiev, J. M. Burst, U. Diebold, A. M. Chaka, and B. Delley, *Phys. Rev. B* 72, 165414 (2005).
86. J. Oviedo and M. J. Gillan, *Surf. Sci.* 467, 35 (2000).
87. M. A. Mäki-Jaskari and T. T. Rantala, *Phys. Rev. B* 65, 245428 (2002).
88. I. Manassidis, J. Goniakowski, L. N. Kantorovich, and M. J. Gillan, *Surf. Sci.* 339, 258 (1995).
89. A. Cabot, J. Arbiol, J. R. Morante, U. Weimar, N. Barsan, and W. Gopel, *Sens. Actuators B* 70, 1 (2000).
90. A. Cabot, A. Dieguez, A. Romano-Rodriguez, J. R. Morante, and N. Barsan, *Sens. Actuators B* 79, 2 (2001).
91. P. A. Cox, Transition Metal Oxides: An Introduction to Their Electronic Structure and Properties, Clarendon Press, Oxford, (1992).
92. V. Brynzari, G. Korotchenkov, and S. Dimitriev, *Sens. Actuators B* 61, 143 (1999).
93. M. A. Mäki-Jaskari and T. T. Rantala, *Surf. Sci.* 537, 168 (2003).
94. A. Maiti, J. A. Rodriguez, M. Law, P. Kung, J. R. McKinney, and P. Yang, *Nano Lett.* 3, 1025 (2003).
95. M. A. Mäki-Jaskari, T. T. Rantala, and V. V. Golovanov, *Surf. Sci.* 577, 127 (2005).
96. A. M. Mazzone and V. Morandi, *Appl. Surf. Sci.* 253, 4010 (2007).
97. M. Melle-Franco and G. Pacchioni, *Surf. Sci.* 461, 54 (2000).
98. G. Pacchioni, A. M. Ferrari, and P. S. Bagus, *Surf. Sci.* 350, 159 (1996).
99. T. Bredow and G. Pacchioni, *Surf. Sci.* 373, 21 (1997).
100. T. Bredow, A. M. Marquez, and G. Pacchioni, *Surf. Sci.* 430, 137 (1999).
101. F. Ciriaco, L. Cassidei, M. Cacciatore, and G. Petrella, *Chem. Phys.* 303, 55 (2004).
102. A. M. Mazzone and V. Morandi, *Comput. Mat. Sci.* 38, 814 (2007).
103. M. Melle-Franco, G. Pacchioni, and A. V. Chadwick, *Surf. Sci.* 478, 25 (2001).
104. M. A. Henderson, *Surf. Sci. Rep.* 46, 1 (2002).
105. P. A. Thiel and T. E. Madey, *Surf. Sci. Rep.* 7, 221 (1987).
106. S. Zhang, Y. F. Zhu, and D. E. Brodie, *Sens. Actuators B* 12, 71 (1993).
107. J. F. Boyle and K. A. Jones, *J. Electron. Mater.* 6, 717 (1977).
108. J. Goniakowski and M. J. Gillan, *Surf. Sci.* 350, 145 (1996).
109. P. J. D. Lindan, *Chem. Phys. Lett.* 328, 325 (2000).
110. P. J. D. Lindan, N. M. Harrison, and M. J. Gillan, *Phys. Rev. Lett.* 80, 762 (1998).
111. S. P. Bates, *Surf. Sci.* 512, 29 (2002).
112. V. A. Gercher and D. F. Cox, *Surf. Sci.* 322, 177 (1995).
113. S. Semancik and D. F. Cox, *Sens. Actuatuators* 12, 101 (1987).
114. M. Batzill, W. Bergermayer, I. Tanaka, and U. Diebold, *Surf. Sci.* 600, L29 (2006).
115. T. Yamamoto and K.-Y. Hiroshi, *Jpn. J. Appl. Phys.* 38, L166 (1999).
116. E. Comini, *Anal. Chim. Acta.* 568, 28 (2006).
117. C. M. Lieber and Z. L. Wang, *MRS Bull.* 32, 99 (2007).
118. Ü Özgür, Ya. I. Alivov, C. Liu, A. Teke, M. A. Reshchikov, S. Doğan, V. Avrutin, S.-J. Cho, and H. Morkoç, *J. Appl. Phys.* 98, 041301 (2005).
119. R. R. Rever, *J. Appl. Phys.* 41, 5063 (1970).
120. R. Blachnik, J. Chu, R. R. Galazka, J. Geurts, J. Gutowski, B. Hönerlage, D. Hofmann, J. Kossut, R. Lévy, P. Michler, U. Neukirch, T. Story, D. Strauch, and A. Waag, Landolt-Börnstein: Numerical Data and Functional Relationships in Science and Technology, New Series, Springer, Heidelberg, 1999, Vol. III/41B.
121. M. Usuda, N. Hamada, T. Kotani, and M. van Schilfgaarde, *Phys. Rev. B* 66, 125101 (2002).
122. S. A. Leontiev, S. V. Koshtcheev, V. G. Devyatov, A. E. Cherkashin, and E. P. Mikheeva, *J. Struct. Chem.* 38, 725 (1997).
123. O. Zakharov, A. Rubio, X. Blasé, M. L. Cohen, and S. G. Louie, *Phys. Rev. B* 50, 10780 (1994).
124. P. Erhart, K. Albe, and A. Klein, *Phys. Rev. B* 73, 205203 (2006).
125. N. A. Hill and U. Waghmare, *Phys. Rev. B* 62, 8802 (2000).
126. J. E. Jaffe, R. Pandey, and A. B. Kunz, *Phys. Rev. B* 43, 14030 (1991).
127. M. S. Hybertsen and S. G. Louie, *Phys. Rev. Lett.* 55, 1418 (1985).
128. B. Arnaud and M. Alouani, *Phys. Rev. B* 62, 4464 (2000).
129. S. B. Zhang, S.-H. Wei, and A. Zunger, *Phys. Rev. Lett.* 84, 1232 (2000).
130. D. C. Look, G. C. Farlow, P. Reunchan, S. Limpijumnong, S. B. Zhang, and K. Nordlund, *Phys. Rev. Lett.* 95, 225502 (2005).
131. Y. Marfaing and A. Luzón, *Superlatt. Microstruct.* 38, 385 (2005).
132. C. G. Van de Walle, *Phys. Rev. Lett.* 85, 1012 (2000).
133. Z. G. Yu, H. Gong, and P. Wu, *Chem. Mater.* 17, 852 (2005).
134. C. B. Duke, R. J. Meyer, A. Paton, and P. Mark, *Phys. Rev. B* 18, 4225 (1978).
135. W. Göpel, J. Pollmann, I. Ivanov, and B. Reihl, *Phys. Rev. B* 26, 3144 (1982).
136. Y. R. Wang and C. B. Duke, *Surf. Sci.* 192, 309 (1987).
137. I. Ivanov and J. Pollmann, *Phys. Rev. B* 24, 7275 (1981).
138. L. Whitmore, A. A. Sokol, and C. R. A. Catlow, *Surf. Sci.* 498, 135 (2002).
139. P. Schröer, P. Kröger, and J. Pollmann, *Phys. Rev. B* 49, 17092 (1994).
140. J. E. Jaffe, N. M. Harrison, and A. C. Hess, *Phys. Rev. B* 49, 11153 (1994).

141. A. Wander and N. M Harrison, *Surf. Sci.* 457, L342 (2000).

142. A. Filippetti, V. Fiorentini, G. Cappellini, and A. Bosin, *Phys. Rev. B* 59, 8026 (1999).

143. A. Wander and N. M. Harrison, *Surf. Sci.* 468, L851 (2000).

144. B. Meyer and D. Marx, *Phys. Rev. B* 67, 035403 (2003).

145. J. D. Prades, A. Cirera, A. Cornet, and J. R. Morante, *Thin Sol. Films* 515, 8670 (2007).

146. B. Meyer, *Phys. Rev. B* 69, 045416 (2004).

147. V. Staemmler, K. Fink, B. Meyer, D. Marx, M. Kunat, S. Gil Girol, U. Burghaus, and C. Wöll, *Phys. Rev. Lett.* 90, 106102 (2003).

148. M. Kunat, S. Gil Girol, T. Becker, U. Burghaus, and C. Wöll, *Phys. Rev. B* 66, 081402 (2002).

149. D. J. Cooke, A. Marmier, and S. C. Parker, *J. Phys. Chem. B* 110, 7985 (2006).

150. K. Fink, *Phys. Chem. Chem. Phys.* 8, 1482 (2006).

151. J. P. Perdew and A. Zunger, *Phys. Rev. B* 23, 5048 (1981).

152. M. Kurtz, J. Strunk, O. Hinrichsen, M. Muhler, K. Fink, B. Meyer, and C. Wöll, *Angew. Chem. Int. Ed.* 44, 2790 (2005).

153. S. Chaturvedi, J. A. Rodriguez, T. Jirsak, and J. Hrbek, *J. Phys. Chem. B* 102, 7033 (1998).

154. J. A. Rodriguez, T. Jirsak, J. Dvorak, S. Sambasivan, and D. Fischer, *J. Phys. Chem. B* 104, 319 (2000).

155. U. Kirner, K. D. Schierbaum, W. Göpel, B. Leibold, N. Nicoloso, W. Weppner, D. Fischer, and W. F. Chu, *Sens. Actuators B* 1, 103 (1990).

156. A. L. Linsebigler, G. Lu, and J. T. Yates, Jr., *Chem. Rev.* 95, 735 (1995).

157. F. A. Grant, *Rev. Mod. Phys.* 31, 646 (1959).

158. G. V. Samsonov, The Oxide Handbook, IFI/Plenum Press, New York, 1982.

159. U. Diebold, *Surf. Sci. Rep.* 48, 53 (2003).

160. U. Diebold, M. Li, O. Dulub, E. L. D. Hebenstreit, and W. Hebenstreit, *Surf. Rev. Lett.* 5–6, 613 (2000).

161. O. Dulub, W. Hebenstreit, and U. Diebold, *Phys. Rev. Lett.* 84, 3646 (2000).

162. E. Yagi, R. Hasiguti, and M. Aono, *Phys. Rev. B* 54, 7945 (1996).

163. M. Ramamoorthy, D. Vanderbilt, and R. D. King-Smith, *Phys. Rev. B* 49, 16721 (1994).

164. H. Perron, C. Domain, J. Roques, R. Drot, E. Simoni, and H. Catalette, *Theor. Chem. Acc.* 117, 565 (2007).

165. A. Zangwill, Physics at Surfaces, Cambridge, (1988).

166. A. Vittadini, A. Selloni, F. P. Rotzinger, and M. Grätzel, *Phys. Rev. Lett.* 81, 2954 (1998).

167. D. R. Hamann, *Phys. Rev. B* 56, 14979 (1997).

168. W. Langel, *Surf. Sci.* 496, 141 (2002).

169. D. Vogtenhuber, R. Poducky, J. Redinger, E. L. D. Hebenstreit, W. Hebenstreit, and U. Diebold, *Phys. Rev. B* 65, 125411 (2002).

170. G. Charlton, P. B. Howes, C. A. Muryn, H. Raza, N. Jones, J. S. G. Taylor, C. Norris, R. McGrath, D. Norman, T. S. Turner, and G. Thornton, *Phys. Rev. B* 61, 16117 (2000).

171. H. Raza, C. L. Pang, S. A. Haycock, and G. Thornton, *Phys. Rev. Lett.* 82, 5265 (1999).

172. H. Raza, C. L. Pang, S. A. Haycock, and G. Thornton, Appl. *Surf. Sci.* 140, 271 (1999).

173. J. Muscat, N. M. Harrison, and G. Thornton, *Phys. Rev. B* 59, 2320 (1999).

174. P. J. D. Lindan, N. M. Harrison, J. M. Holender, M. J. Gillan, and M. C. Payne, *Surf. Sci.* 364, 431 (1996).

175. A. Howard, C. E. J. Mittchell, D. Morris, R. G. Egdell, and S. C. Parker, *Surf. Sci.* 448, 131 (2000).

176. A. Fahmi and C. Minot, *Surf. Sci.* 304, 343 (1994).

177. T. Bredow and K. Jug, *Surf. Sci.* 327, 398 (1995).

178. M. Lazzeri, A. Vittadini, and A. Selloni, *Phys. Rev. B* 63, 155409 (2001).

179. M. Lazzeri, A. Vittadini, and A. Selloni, *Phys. Rev. B* 65, 119901 (2002).

180. J. Woning and R. A. van Santen, *Chem. Phys. Lett.* 101, 541 (1983).

181. M. Lazzeri and A. Selloni, *Phys. Rev. Lett.* 87, 266105 (2001).

182. R. E. Tanner, A. Sasahara, Y. Liang, E. I. Altman, and H. Onishi, *J. Phys. Chem. B* 106, 8211 (2002).

183. P. A. Cox, Transition Metal Oxides—An Introduction to Their Electronic Structure Properties, Clarendon Press, Oxford, 1992.

184. V. E. Henrich and P. A. Cox, The Surface Science of Metal Oxides, Cambridge University Press, Cambridge, (1994).

185. Z. Zhang, S. P. Jeng, and V. E. Henrich, *Phys. Rev. B* 43, 12004 (1991).

186. U. Diebold, H. S. Tao, N. D. Shinn, and T. E. Madey, *Phys. Rev. B* 50, 14474 (1994).

187. E. Bertel, R. Stockbauer, and T. E. Madey, *Surf. Sci.* 141, 355 (1984).

188. R. Heise and R. Courths, *Surf. Sci.* 288, 658 (1993).

189. T. Albaret, F. Finocchi, and C. Noguera, *Faraday Discuss., Chem. Soc.* 114, 285 (1999).

190. P. J. Hardman, G. N. Raikar, C. A. Muryn, G. van der Laan, P. L. Wincott, G. Thornton, D. W. Bullett, and P. A. D. M. A. Dale, *Phys. Rev. B* 49, 7170 (1994).

191. Y. Aiura, Y. Nishihara, Y. Haruyama, T. Komeda, S. Kodaira, Y. Sakisaka, T. Maruyama, and H. Kato, *Physica B* 196, 1215 (1994).

192. S. Wendt, R. Schaub, J. Matthiesen, E. K. Vestergaard, E. Wahlström, M. D. Rasmussen, P. Thostrup, L. M. Molina, E. Lægsgaard, I. Stensgaard, B. Hammer, and F. Besenbacher, *Surf. Sci.* 598, 226 (2005).

193. M. Ménétrey, A. Markovits, and C. Minot, *J. Mol. Struct.: THEOCHEM* 808, 71 (2007).

194. W. Göpel, G. Rocker, and R. Feierabend, *Phys. Rev. B* 28, 3427 (1983).

195. A. Linsebigler, G. Lu, and J. T. Yates, Jr., *J. Chem. Phys.* 103, 9438 (1995).

196. G. Rocker and W. Göpel, *Surf. Sci.* 175, L675 (1986).

197. M. C. Torquemada, J. L. de Segovia, and E. Román, *Surf. Sci.* 337, 31 (1995).

198. K. Tanaka and J. M. White, J. Catal. 79, 81 (1983).

199. F. Rittner, B. Boddenberg, M. J. Bojan, and W. A. Steele, *Langmuir* 15, 1456 (1999).

200. F. Rittner, B. Boddenberg, R.F. Fink, and V. Staemmler, *Langmuir* 15, 1449 (1999).

201. S. Wang, B. Raman, D. H. Chen, K. Y. Li, and J. A. Colapret, *Chem. Oxid.* 5, 289 (1997).

202. D. C. Sorescu, C. N. Rusu, and J. T. Yates, *Jr., J. Phys. Chem. B* 104, 4408 (2000).

203. C. N. Rusu and J. T. Yates, Jr., *J. Phys. Chem.* B 105, 2596 (2001).

204. G. Lu, A. Linsebigler and J. T. Yates, Jr., *J. Phys. Chem.* 98 , 11733 (1994).

205. J. A. Rodriguez, T. Jirsak, G. Liu, J. Hrbek, J. Dvorak, and A. Maiti, *J. Am. Chem. Soc.* 123, 9597 (2001).

206. A. Markovits, J. Ahdjoudj, and C. Minot, *Surf. Sci.* 365, 649 (1996).

207. M. A. Henderson, *Surf. Sci. Rep.* 46, 1 (2002).

208. M. A. Henderson, *Surf. Sci.* 319, 315 (1994).

209. R. F. Nalewajski, A. M. Koester, T. Bredow, and K. Jug, *J. Mol. Catal.* 82, 407 (1993).

210. P. J. D. Lindan, N. M. Harrison, J. M. Holender, and M. J. Gillan, *Chem. Phys. Lett.* 261, 246 (1996).

211. P. J. D. Lindan, N. M. Harrison, and M. J. Gillan, *Phys. Rev. Lett.* 80, 762 (1998).

212. E. V. Stefanovich and T. N. Truong, *Chem. Phys. Lett.* 299, 623 (1999).

213. R. Schaub, P. Thostrup, N. Lopez, E. Lægsgaard, I. Stensgaard, J. K. Nørskov, and F. Besenbacher, *Phys. Rev. Lett. 87, 266104 (2001).*

214. I. M. Brookes, C. A. Muryn, and G. Thornton, *Phys. Rev. Lett. 87, 266103 (2001).*

T. Andreu, J. Arbiol, A. Cabot, A. Cirera, J.D. Prades, F. Hernandez-Ramirez, A. Romano-Rodriguez, J.R. Morante, *"Nanosensors: Controlling Transduction Mechanisms an the Nanoscale Using Metal Oxides and Semiconductors"* in *"Sensors Based on Nanostructured Materials"* (Ed. F. Arregui), chap. 5, pp. 79-129, Springer Science + Business Media (2009).

2

Chapter 5
Nanosensors: Controlling Transduction Mechanisms at the Nanoscale Using Metal Oxides and Semiconductors

Teresa Andreu, Jordi Arbiol, Andreu Cabot, Albert Cirera, Joan Daniel Prades, Francisco Hernandez-Ramírez, Alberto Romano-Rodríguez, and Joan R. Morante

5.1 Introduction

Nanotechnology is defined as the design and engineering of functional materials and devices through control of matter in dimensions of roughly 1–100 nm, where unique phenomena enable novel applications [1]. While nanotechnology allows us to take advantage of these exclusive phenomena and related properties, it offers us new possibilities and relationships among the different multidisciplinary effects. Nanotechnology not only occupies the fields of material science and engineering but also applies to fundamental physics, chemistry and biology. Figures 5.1–5.3 show examples of functional semiconductor nanostructures.

The design and engineering of materials at the nanometer scale can be achieved from two opposed directions: (a) the reduction of bulk dimensions of the material to the nanometer scale, which is known as the *top-down approach* and (b) the assembly of molecules and atoms into structures up to the nanometer scale, known as the *bottom-up approach.*

The scaling down performed in the microelectronics area during the last decades of the past century presents a clear example of the "top-down approach". Moore's law describes the evolution followed by the computing power of the silicon chips. This evolution is doubling every 18–24 months due to the increase in the number of transistors integrated by area unit. Nowadays, transistor sizes have already reached dimensions down to 50 nm. However, in the near future, integration would not be able to follow this law since it will no longer be possible to shrink dimensions due to the intrinsic material characteristics.

The bottom-up approach is a promising nanotechnology alternative to the extrapolation of the top–bottom methods inherited from the macroworld. During the last years, both top-down and bottom-up strategies have overlapped and coexisted, facilitating and accelerating the discovery of new functional materials. Organic and molecular-based transistors coming from the

T. Andreu
Department of Electronics, Faculty of Physics, University of Barcelona, Barcelona,
E-08028, Spain
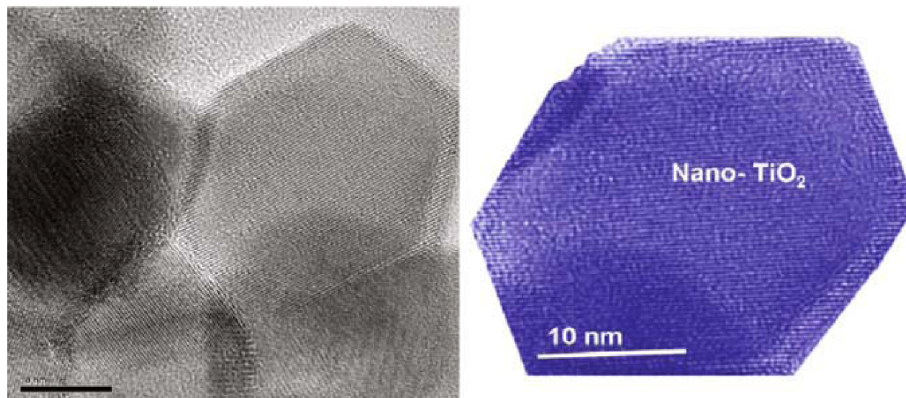
Fig. 5.1 Faceted TiO$_2$ anatase nanocrystals

bottom-up approach are overlapping with the options obtained from the top-down processes.

It is clear that all of these possibilities, developments or implementation of ideas dealing with the nanoworld require adequate tools and processes that allow us to measure, fabricate, characterize and, importantly, manipulate
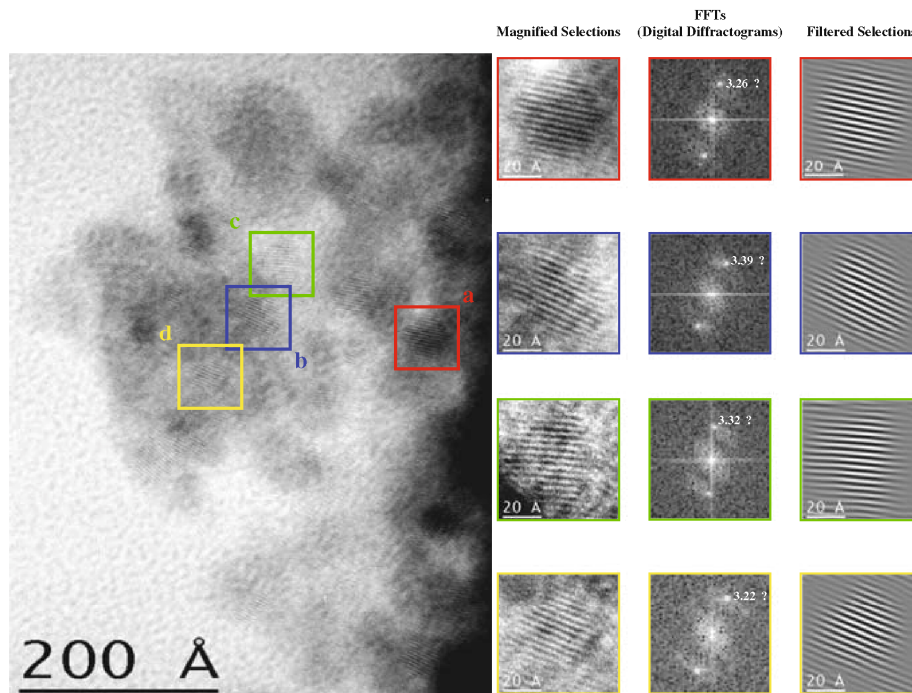
Fig. 5.2 HRTEM analysis of tiny distorted and non-faceted SnO$_2$ nanoparticles
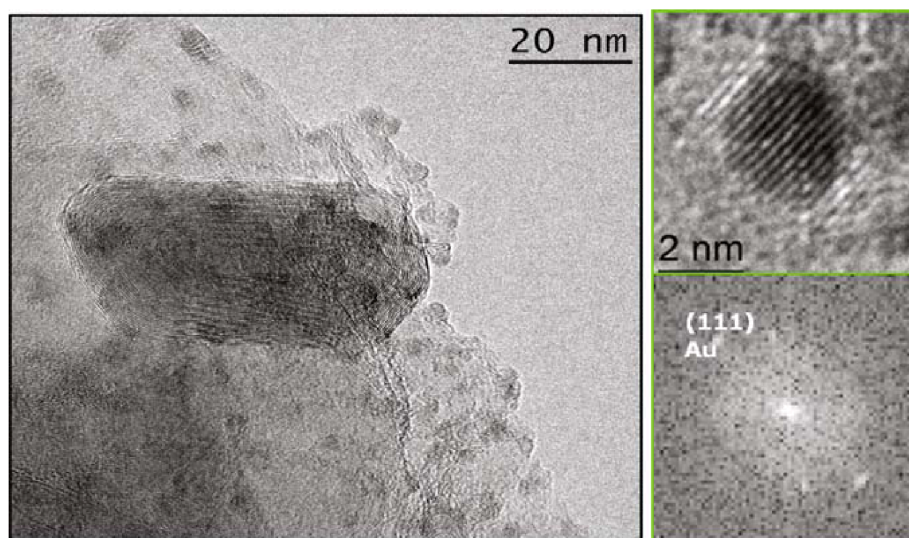
Fig. 5.3 Gold clusters decorating TiO_2 anatase nanoparticles

nanostructures. In fact, new instruments and techniques with nanoscale resolution are accelerating scientific knowledge and technological implementations that promote new challenges in miniaturization. In spite of the growing activities and efforts in this field – that are revealed by a high number of published activities, specialized conferences, workshops and patents – it must be kept in mind that the way for converting basic discoveries into marketable products is long and hard. However, the new options are so flashing, exciting and attractive that scientists, technologists, policy makers, entrepreneurs and high-tech enterprises are converging in their activities for launching a broad range of novel products reaping social benefits for a sustainable and intelligent ambient world where nanosensor devices will play an outstanding role.

Despite having such high expectations, it should be noted that, due to the lack of standardizations, nanotechnology is accompanied by many possible dangers. Many difficulties, hurdles and challenges have yet to be overcome. Among them, interfacing between the nanoworld and the macroworld or the effects of the nanomaterials on our health and on our environment are still relatively unclear.

5.2 Nanosensors

The motivation for having sensors is given by our needs of monitoring – receiving information – the environment around us and having the capability of using the obtained data, after processing it, for interacting again with our environment. So, it is through sensors that we connect with the world, in the same way humans use

their senses. The concept *sensor* is derived from the Latin word "sentire" which means perceive (or sense, which is not clear and hence we need to go to Latin). The word sensor denotes an entity that responds to external stimulus or "energy variation" by generating a functionally related output [2] as a measure, either directly or indirectly, of this information.

Sensors transduce information in the form of variations of different forms of energy, such as thermal, mechanical, optical, electrical, magnetic, radioactive, chemical or biochemical, into another form of energy. For example, the information about the kinetic energy in a mobile machine could be revealed by the increase of temperature due to the heat released by applying a disc brake. Nevertheless, as one of the main objectives is the processing of this information, in the same way human senses send the collected information to our brain, we typically are looking for a direct or indirect transduction from any energy form to a final electrical one, for example, if we use the resistance variation with the temperature for monitoring the kinetic energy information in the above-described case.

Although there is no totally accepted difference between *transducers* and *sensors*, and even both concepts are used as equivalent, the word sensor is mainly used when there is an electrical output signal. On the other hand, *detector* is reserved for those cases for which non-quantitative measurements are required but only sensitivity to an input signal is obtained.

Our present society has become characterized by the significant incorporation of the information technologies. These define the present century as that of the intelligent ambient thanks to the continuous development of sensors. As the needs for physical, chemical and biological recognition systems and transduction platforms grow very fast, sensor technology is continuously pushing up. Sensors are used in applications ranging from environmental monitoring, intelligent buildings and smart ambient; health care and medical diagnostic; industrial manufacturing, transport elements and automotive; defence and security; food control and agriculture and everything that can contribute to make our lives better, easier and safer as well as more sustainable to our world.

In such a scenario of increasing demand of sensors and of requested new applications, novel approaches for sensor technology are pursued and for it, nanotechnology is offering one of the most outstanding impacts on the basis of *small device sizes* – integration, miniaturization and low power consumption; *inexpensive* – capability for high production volume at low cost; *high efficiency* – controlled transduction mechanisms at the nanoscale tightening up homogeneity and uniformity; *long-term stability* – material properties improved and designed at the nanoscale and *improved sensor dynamic* – minimized time required for sensor response. In fact, the enhancement of the interactions taking place at the nanoscale enables the efficiency of the transduction mechanisms and, hence, the implementation of more advantageous sensors than the conventional ones.

Thus, bottom-up nanotechnology approach enables to design and synthesize novel materials with tailored properties adequate for the sensing processes that

cannot be imagined from top-down approaches or conventional microtechnologies. Due to these tailored properties, detection limits can be lowered – smaller quantities of samples – increasing the sensitivity. The small size, lightweight and high surface-to-volume ratios, Figs. 5.1–5.3, are the best candidates for improving the capability for transducing chemical and biological species or to have different electrical, magnetic, optical or phonon properties and even quantum effects.

Likewise, the better controlled transduction mechanisms may favour the sensor selectivity or, alternatively, improve its sensor performances. It is expected that nanostructured material with modified or functionalized surface may also assist in having greater selectivities. So, for example, biosensing applications are enhanced by specific surface functionalizations, Fig. 5.3. Nevertheless, one of the advantages is to use multiple nanosensor elements as active part of the macro-sensors that may compensate for the loss of performance of the individual nanosensor element.

Furthermore, the nanotechnological synthesis and processing open the option for tuning material properties and making them more stable by controlling its crystalline defects and surface orientation. Some of the micro/nanofabrication technologies are very mature and widely used, especially those used for the top-down approach, whilst others, more related with the bottom-up approach, are still in their early stages or waiting for tools for interfacing nano with macroworld that are needed for nanomanipulation, nanopatterning, nanolithographic machinery and other procedures driving knowledge towards application of nanodevices and their integration when needed. In this framework, the nanostructured material characteristics become the cornerstone of the possible nanosensor building and, hence, their synthesis methods are the clue for a successful development of nanotechnology.

5.3 Nanomaterial Synthesis for Sensing

Materials can be confined at the nanoscale level in 0D, 1D, 2D or 3D defining quantum dots, thin films, nanowires and/or nanoparticles. At the same time, they can adopt multitude of shapes, such as nanorods, nanospheres and nanocubes. These nanomaterials exhibit optical, thermal, mechanical, electrical and surface properties that are strongly dependent on their dimensions. The characteristic wavelength for phonons (10^1 nm) and visible photons (10^2 nm) is located at the nanometer scale. At the same time quantum effects are already observed at the 10^0 nm range and functional semiconductors have Debye lengths at or below the 10^1 nm scale. All these particularities of the nanoscale offer multiple new sensing processes. Furthermore, nanomaterials are also characterized by huge ratios of surface-to-bulk atoms. Then they could present phonon, photon or electron confinement effects that can be used for sensing processes but they also present interesting surface properties that

involve all the interactions of this unit with the ambient. All of these effects can be enhanced by engineering and acting on their dimensions, shapes and the own nature of these materials that can be metals, metal oxides, semiconductors or magnetic materials [3].

At the present, there is no generally available technology for using only one of these units as sensing elements because there is no easy way for connecting individually one of them or for getting the information facilitated for one of them. Therefore, for their application in sensing devices, these particles suspended in liquid or gas phase require, in general, their organization on substrates or their deposition as thin films. Furthermore, the possibility to add these nanomaterials into more complex assemblies including even organic materials gives rise to alternatives for novel applications, for example, in solar cells [4] or in biosensing [5, 6, 7].

There are numerous techniques and methods for synthesizing nanoparticles, although selection of one of them depends on the particle nature – metal, metal oxide, semiconductor, magnetic, etc.– its functionality and the surface to which they should be attached. The capability of these methods is directly related to its possibility to be applied with tight control of the conditions and parameters during synthesis [8]. The main difficulty is the general trend to easily aggregate or precipitate although stabilizing additives can change the growth, solubility and surface charge in such a way that particles are kept separated and suspended in the liquid. The use of reverse micelles as nanounit reaction is one of the most common methods in colloidal synthesis. Then nanomaterials are obtained via chemical reduction of metal ions or via coprecipitation reactions [9].

All of these techniques and processes offer a broad variety adapted to the final desired properties in the nanomaterials. Thus, it is well known that the magnetic softness/hardness is straightforwardly related to its magnetic exchange length that highlights the significant importance of the nanometric dimensions. As a consequence, there are many reported methods for the magnetic nanoparticles synthesis [10, 11]. Likewise, the synthesis of metallic nanoparticles has received much attention due to their inert nature and catalytic properties [12]. Moreover, their size and quantum confinement modify their light scattering and absorption several orders of magnitude more than other materials. Therefore, there are also a broad range of techniques for their synthesis [13, 14].

In this nanoparticle area, one of the most extended techniques is based on the named sol-gel technique [15] that involves the transition of a system from a liquid "sol" (usually colloidal) into a solid or "gel" phase through hydrolysis, polymerization and condensation steps. Generally, metal or metalloid elements surrounded by reactive ligands are used as precursors and among them metal alkoxides, aluminates, titanates or borates are commonly used in these processes. It is quite compatible with well-known methods for obtaining thin films on substrate such as spin coating, dip coating, spray coating or drop coating [16]. In fact, sol-gel is one of the most employed technologies for sensing applications using thin films

based on nanostructured materials [17] as it is advantageous from an economical point of view and at the same time offers easy options to investigate new compounds and nanomaterials [18]. Maybe one of the major inconveniences is the control of the postdeposition processes. Annealing parameters are critical for adequately removing organic additives used to adjust the viscosity or to control the stability of the suspension. Likewise, aside of the layer morphology – non-uniformities due to the cracks or holes formation – it can alter the final crystallization and grain growth as well as the adhesion to the substrate. Just to avoid many of these drawbacks, there are many efforts in other directions for obtaining thin films. So, Langmuir–Blodgett technique [19] gives to the nanomaterial synthesis community an interesting alternative for assembling 1D nanoscale building blocks, allowing final superstructures that depend on the fine-tuning of the compression process [20].

During these last years, its use has been increased together with other innovative techniques based on different variations of the chemical solution deposition [21, 22, 23] processes or just using nanotemplates [24] or even electrodeposition techniques that can or cannot be also combined with nano-templates. In fact, the use of a replica obtained from the solution filling of a previously synthesized silica nanotemplate allows to easily have 3D distribution of nanostructures after performing the thermal annealing inside the nanotem-plate and removing it by means of chemical etching processes [25, 26]. Their characteristics are according to the employed nanotemplate typically based on anodic aluminium oxides, Figs. 5.4 and 5.5, or silica [27], Figs. 5.6 and 5.7. One of them that deserves the attention of the sensing community is the surface faceting of these tiny or very small particles. In many cases, the minimization of the constitution energy involves a quasi-spherical shape without well-faceted surfaces. Then particles surfaces present more reactive centres and many of their properties become affected by these boundary conditions [28]: (i) phonon confinement and phonon propagation affecting the thermal conductivity; (ii) free charge scattering affecting electrical mobility; (iii) enhanced photon absorption by the high surface state density; (iv) surface built-in potential
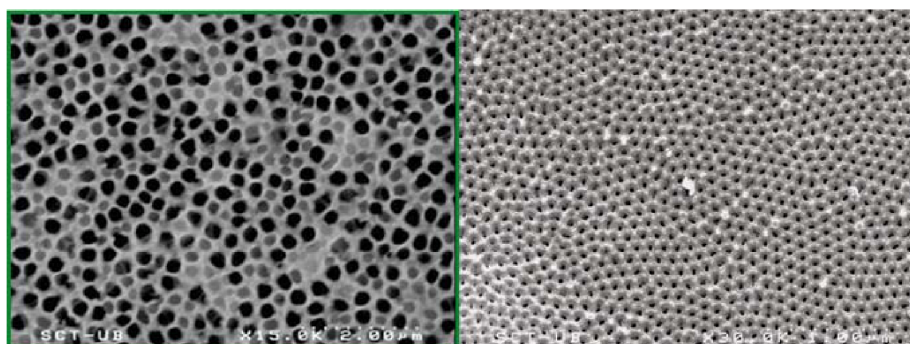
Fig. 5.4 SEM pictures of anodic aluminium oxides used as nanotemplates

Fig. 5.5 SnO$_2$ nanowires obtained by impregnation and calcinations of anodic aluminium oxide nanotemplates
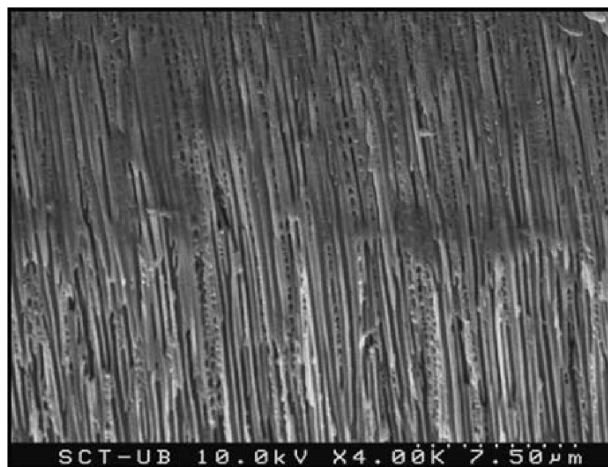
modifying the inner conduction channel at the nanostructure and (v) adsorption states affecting the interaction of the nanostructure with the surrounded ambient.

To overcome these possible drawbacks as well as to favour the possibility for individual electrical access, one of the options is the synthesis of the 1D nanostructures. These nanomaterials keep the surface-to-volume ratio quite large and besides they can also be deposited or used applying standard or low-cost nano and microtechnologies maintaining well-defined surface from a crystallographic point of view. They are almost free of crystallographic defect and they are almost perfect monocrystals. In the specialized literature, several names can be found concerning these 1D nanostructures that, in a general
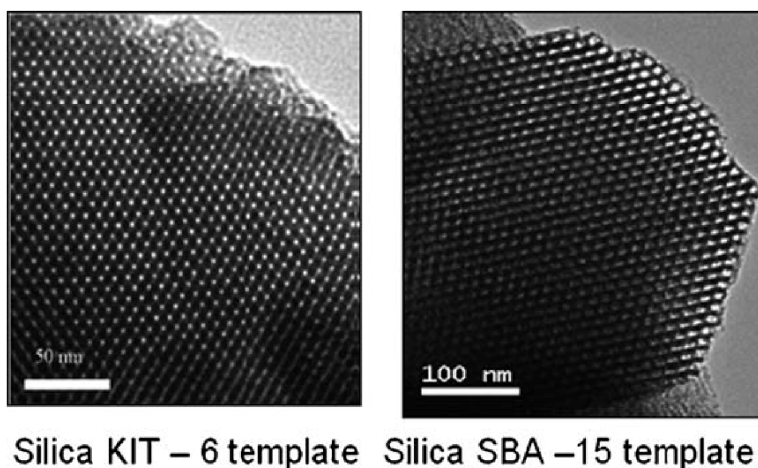
Silica KIT – 6 template   Silica SBA –15 template

Fig. 5.6 Examples of silica-based nanotemplates showing the regular porous distribution
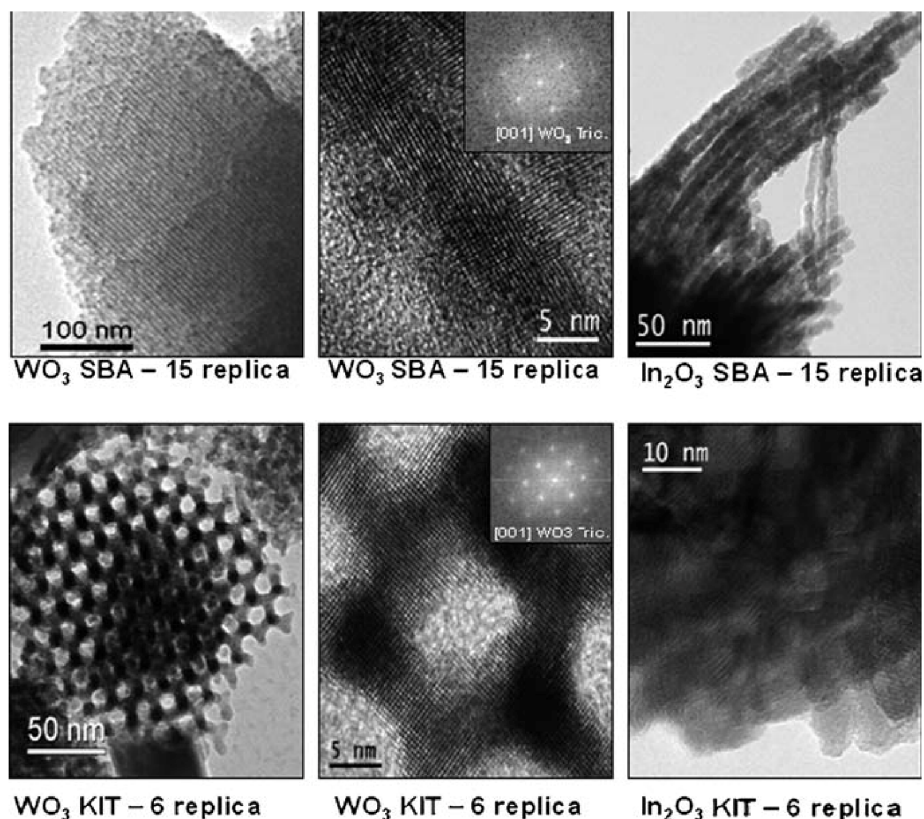
Fig. 5.7 Negative replica of different metal oxides obtained from silica nanotemplates

way, can be determined by its length L, width W and thickness T. If L is comparable to W or T they receive the name of *nanostick* [29] or *nanorod* [30]. If L is much larger than W or T, they receive the name of *nanowire* [31, 32] or *nanobelt* [33] according to the ratio W/T be less than or not greater than 5. A very particular case of these 1D nanostructures is that defined by the concept of *nanotube* [34]. It corresponds to one, SWNT, or several atomic planes, MWNT, that fold on themselves. The most well known are the carbon nanotubes but also many other materials like TiO_2, for example [35], have been reported as nanotubes.

Varied techniques have been proposed to grow these nanostructures on several substrates, Fig. 5.8. On one side there is the method based on the evaporation–condensation processes. In the pioneering work of Z.L. Wang and coworkers [36], these authors used commercially available nanopowders of metal oxides. They evaporated them using low-vacuum deposition conditions at temperatures much lower than their actual bulk evaporation and condensed them at lower temperature sites along the horizontal oven. Several initial theories have been proposed for explaining the growth mechanisms. But,
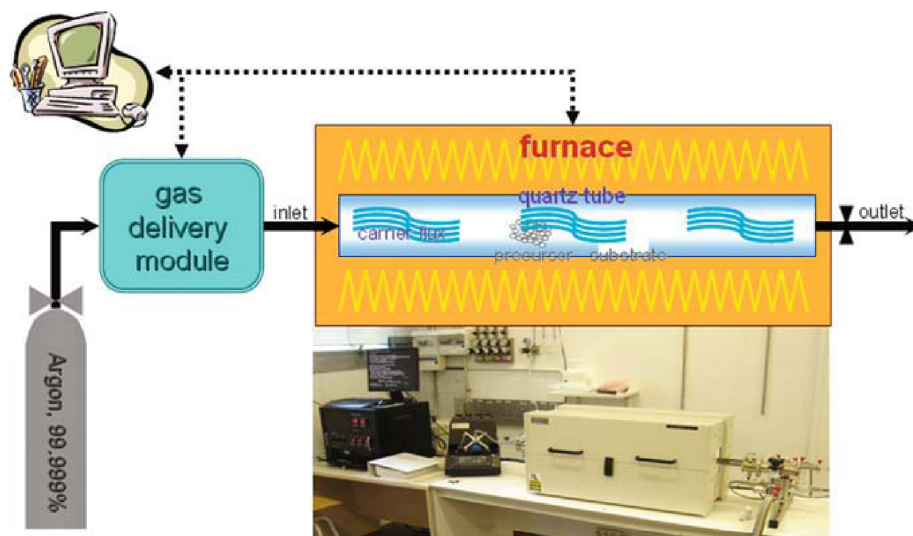
Fig. 5.8 Chemical vapour deposition reactor adapted to grow nanowires

up to now, they fail to describe a general model which can design the growth in different situations [37]. A variation of this method is based on the use of a second phase that helps in the condensation process on the surface. In fact, this second phase acts as a catalytic nucleation site [38]. Catalyst species are deposited on the substrate as a space distribution of small nanodroplets that at the growing temperature become liquids, Fig. 5.9. Each one acts as a trap for the growth species. The catalyst must be inert and the capture species are amalgamate or diluted, enhancing its deposition and growing in one direction limited by the wettability of the catalyst elements. One of the most currently used catalysts is gold even though other elements such as Cu, Ga, Fe, etc. have also been applied mainly for metal oxides and typical semiconductors as silicon or gallium arsenide for example, Figs. 5.10 and 5.11. Around these two principles, evaporation–condensation or vapour–liquid–solid, there is a plethora of variations using the well-known physical vapour deposition methods that based on conditions of solid–vapour transformation obtain nanostructured thin films. In this sense, molecular beam epitaxy-based techniques are one of the most promising options for growing nanowires. MBE grows at very-low deposition rate, few Angstrom by second, in ultra-high vacuum, allowing the control of the deposited material as well as the ideal growth conditions of Frank-van der Merwe [39]. Under these conditions, it is effective to force the growth of nanowires using adequate substrate with a catalytic seed distribution. Precisely, the ways used to obtain this distribution of nanocatalytic clusters, the selected substrate and the applied catalytic species define the broad variety of procedures that can be found in the specialized literature. Gold clusters have
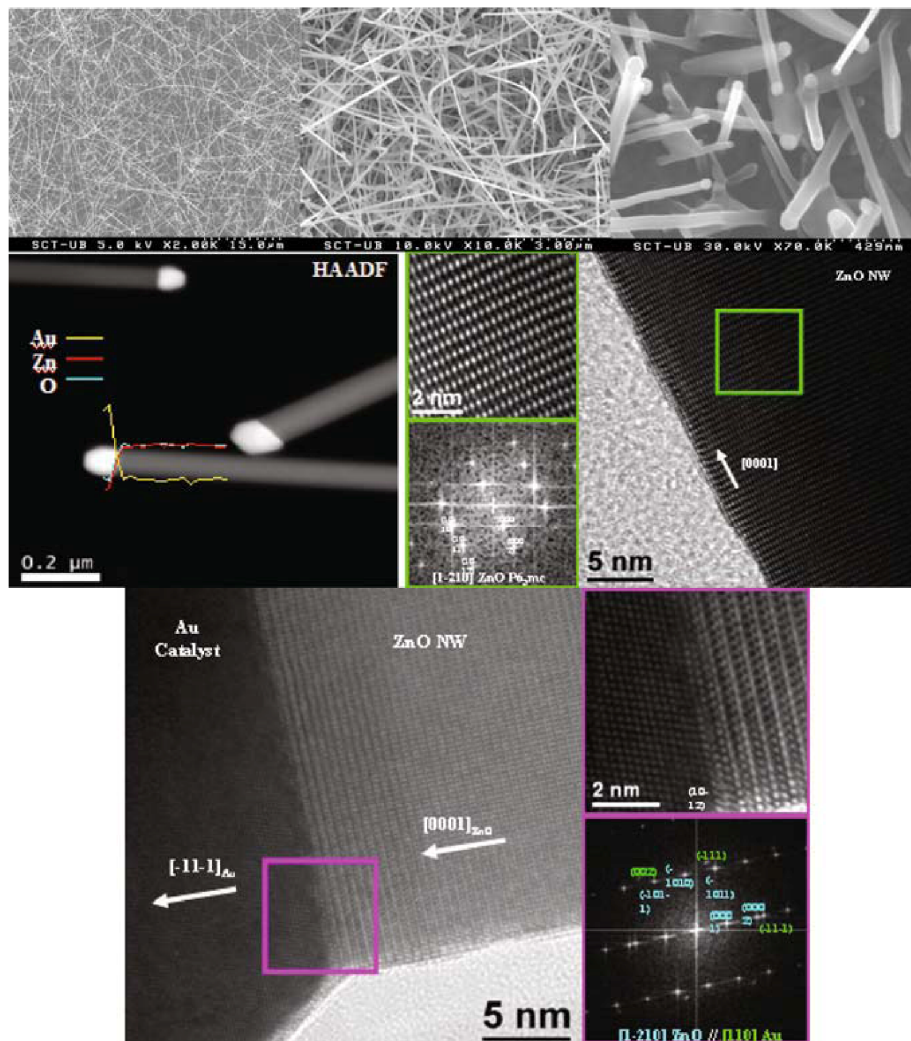
Fig. 5.9 SEM and HRTEM images of ZnO nanowires grown on SiO$_2$-coated silicon substrates

widely been used for growing many nanowires [40] but many other species have also been proposed [41]. For other materials, like GaAs, self-catalyst of Ga droplets has also been proposed [42]. Likewise, different patterning processes have been proved although the growth sites control the pattern [43, 44] and posterior nanomanipulation [45, 46] still needs much more efforts.

Moreover, all of these procedures are also pushing for controlling doping [47] and the formation of lateral or coaxial junctions [48] or heterostructures [49, 50] or even containing radial multiquantum wells [51], Fig. 5.12.
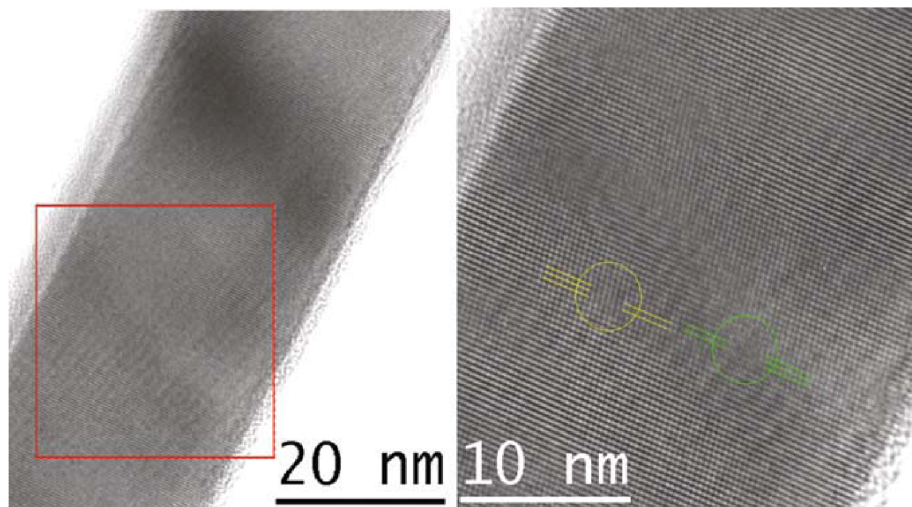
Fig. 5.10 High-resolution transmission microscopy images of a SnO_2 nanowire showing the presence of some dislocations

A totally different approach for obtaining nanowires from some material that can be had as foils or wafers is based on nanoelectrochemistry [52]. In this case, the doping is that previously existing in the starting substrate, which is an interesting advantage[28]. Essentially, for the case of silicon nanowires, the process is based on the electroless metal deposition [53] based on a FH solution that gives rise simultaneously to anodic and cathodic processes on the substrate surface [54].
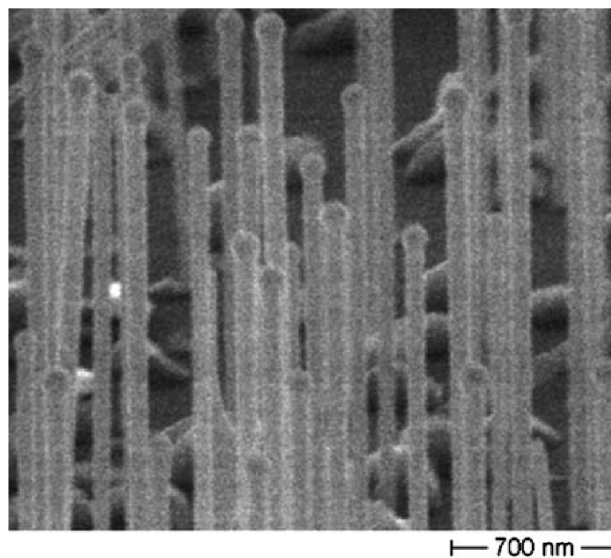
Fig. 5.11 GaAs nanowires obtained on SiO_2-coated (111)B GaAs wafers
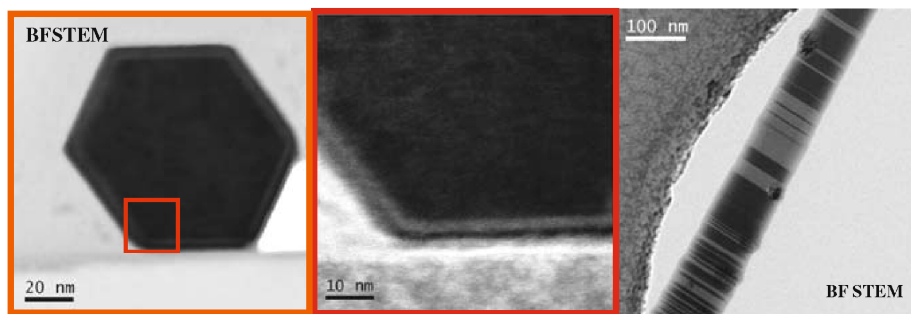
Fig. 5.12 (a) BFTEM image and (b) magnified detail of a GaAs NW with coaxial QWs [51]. (c) HRTEM image of an axial modulated nanowire showing a region with hetero-structures [41]

5.4 Nanosensing Mechanism Features

After all of these plethora of techniques, methods and procedures, finally, it is the control of the nanocrystals properties and performances that becomes more outstanding. Crystallographic structure and defects, impurities concentrations and distributions and surface characteristics determine (i) the phonon propagations and confinement, (ii) the charge transport and charge scattering mechanisms and (iii) the absorption and recombination processes as well as the optical confinement, Stokes shift and optical resonance. On the other hand, the surface properties and its functionalization reveal the solid–ambient interactions that define the chemical and biochemical sensing processes. As a consequence, the different sensing processes at nanoscale and, hence, the types of nanosensors can be classified using many different criteria. Thus, on a very general basis, it is standard to classify the nanosensors as (i) chemical, (ii) biochemical and (iii) physical sensors. These last ones include the optical, thermal, electrical, magnetic and mechanical sensors. However, here, we will focus on the more significant features taking place at the nanoscale mechanisms. Here, among many other possibilities and casuistry, we are going to consider only four nanosensor groups that concern mainly the more outstanding transduction mechanisms that nowadays have already developed significant nanosensor applications:

a) *Surface characteristics*. Chemical and biochemical nanosensors are mainly based on this type. Special attention must be paid to the *functionalized surface*-based sensors. In this group the charge transfer processes from the outer molecules towards the inner part of the solid nanomaterial through the surface is the most outstanding feature of these transduction mechanisms. It gives rise to nanosensors based on electrical interaction through the surface.

b) *Photons*. The photon interaction with the nanomaterial determines the optical-based nanosensors (photon absorptions, Stokes shifts, resonances,

luminescence pathways and so on). It gives rise to the development of nanosensors based on photon capture that are available for the photodetection at the nanoscale.

c) *Plasmon resonances.* Small variation of the dielectric constant defined at the nanoscale domain can easily modify the surface plasmon resonance. It gives rise to the development of nanosensors based on plasmon resonance that reveal the influence of the dielectric constant variations at the nanoscale.

d) *Mechanical properties.* The progressive scaling down of the mechanical structures allows having new significant relation among the different physical forces. It gives rise to the development of nanosensors based on mechanical resonances which present an important influence on its resonance values of the small mass changes taking place on these mechanical nanostructures.

Due to the small dimensions of the nanostructures, the models deduced for bulk cases are not more applicable, whilst the analyses of the sensing mechanism features require the application of new simulations and models of these nanostructures. So, a broad variety of methods starting from the classical calculations up to the most advanced quantum mechanical calculations have been developed during the last years [55, 56]. Properties such as energy of the structure, work function changes, binding energies as well as chemisorption and physisorption properties [57] of the surface can be calculated on the basis of the DFT (density functional theory) and wave methods. In spite of the huge effort performed in this area, there is still an important task to be done. Without this theoretical support, many of the experimental activities carried out are lacking complete scientific analysis. The knowledge advancement is fortunately very positive but it is not going fast enough.

5.5 Nanosensors Based on Electrical Interaction Through the Surface

It is well known that metal oxide materials due to their surface electronic structure present very interesting properties that give rise to interactions with the gas molecules, tin oxides being one of the most representative of these materials [58] although at the beginning ZnO was the metal oxide used for building the first solid state-based gas sensor. Many years ago, it was already pointed out that attention on tiny crystals of metal oxide semiconductors shows outstanding changes of their electric resistance upon exposure to reducing or oxidizing gases [59, 60, 61], Fig. 5.13. As found with pure SnO_2 devices, electric resistances in air as well as those under exposure to H_2 diluted in air began to increase sharply when the size of component SnO_2 grains decreased beyond a critical point (about 6 nm in diameter). In addition, sensor response to H_2 increased remarkably with decreasing size.

A similar size effect was also observed with the response of other metal oxide device sensors to oxidizing gases [62, 63, 64]. It was suggested that extension of
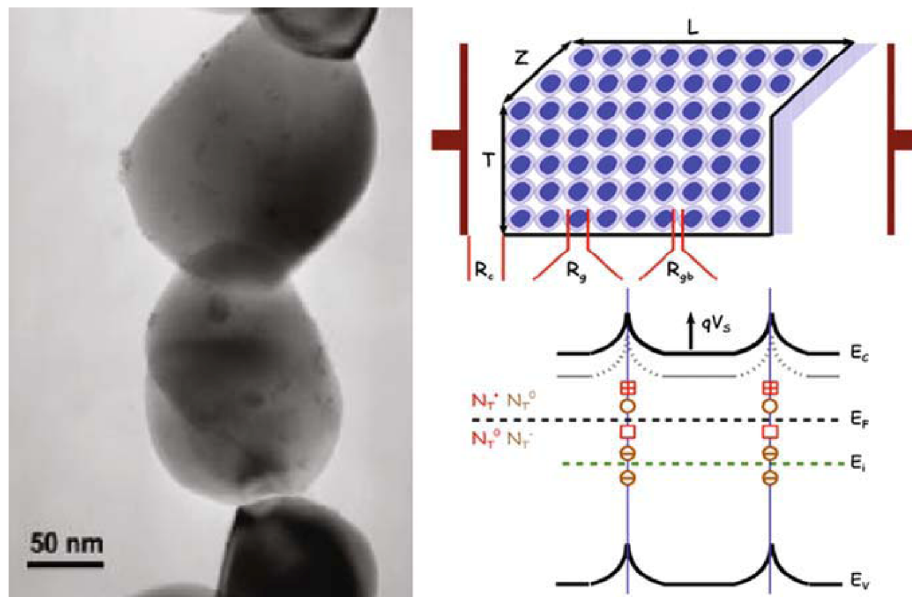
Fig. 5.13 Detail of the intergrain connectivity between nanocrystals and its electrical equivalent model considering grain, intergrain and electrode resistances

space charge layer to a whole region of component crystals could be responsible for such effects, though the precise mechanisms involved were left open. They also appear to be related to the surface characteristics [65]. Typically, porously sintered assemblies of these tiny crystals as thick or thin film layer [66] are used, Fig. 5.14. It is working as a 3D network of interconnected tiny crystals presenting the above-described electrical properties and hence contributing to the total 3D network equivalent resistance changes when the ambient composition is varied. This property has provided a base to develop semiconductor gas sensors
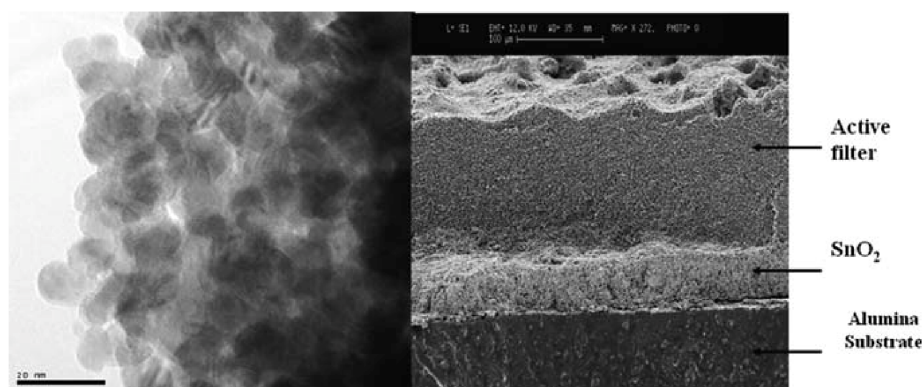
Fig. 5.14 Cross-section of a sensitive metal oxide layer based on nanocrystals

for use in various fields. Despite marvellous development, this type of gas sensors still has some basic problems on gas response left unsolved or not well understood like porosity influence, crystal grain boundary interconnections, surface crystal orientations and shapes and sizes of the component crystals. What will happen when the size minimized drastically up to the geometrical sizes are comparable with the depletion zone dimension, the free scattering-less length or the screening length?

What is representative of a solid state gas-sensing material is its capability for absorbing gas molecules according to their oxidizing or reducing character onto surface sites identified by their acidic or basic properties. So, for example, gases like O_2 and NO_2 are very well known to be adsorbed on oxide semiconductors to form anionic adsorbates. The most standard one is O_2 that is adsorbed as follows, see Fig. 5.15:

$$O_2 + 2e = 2O^-. \tag{5.1}$$

The equilibrium of this chemical process is expressed by

$$(K_{O2}P_{O2})^{1/2}[e] = [O^-]. \tag{5.2}$$

Here K_{O2} and P_{O2} are, respectively, the adsorption constant and the partial pressure of oxygen, and $[e]$ and $[O^-]$ are surface densities of free electrons and O^- adsorbates, respectively. One must observe that the former quantity determines resistance of the sensor device so that solving how it is related with P_{O2} is a central subject in semiconductor gas sensors. Although $[e]$ as well as $[O^-]$ are surface quantities, these are deeply associated with the bulk of the semiconductor.

In fact, this equation points out the adsorption equilibrium on a semiconductor and, as it is shown, it cannot be solved without considering the electronic equilibrium of the semiconductor. Therefore, the electronic equilibrium
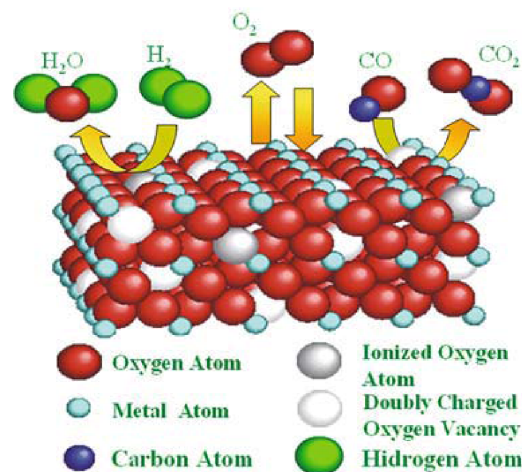
Fig. 5.15 Schematic of the surface interactions taking place on metal oxides

Oxygen Atom   Ionized Oxygen Atom

Metal Atom   Doubly Charged Oxygen Vacancy

Carbon Atom   Hidrogen Atom

depends not only on gas adsorption strength but also on shape and size of component crystals that determine the charge neutrality into the crystal. There-fore, the general aspects of the electronic equilibrium become straightforwardly connected with the chemical equilibrium and its description and analyses are harder as the crystal dimensions scale down to the nanoworld, and the applica-tion that was useful for larger crystals becomes no more acceptable.

It is known that, if there are traps of electrons on the surface of an n-type semiconductor, conduction electrons are transferred from the subsurface to the traps, leaving an electron-depleted layer behind.

This transfer continues until an electronic equilibrium is reached throughout all regions from surface to bulk. The simpler scheme of electron transfer for a plane surface is drawn in Fig. 5.16.

Conventionally it is assumed that donors are ionized completely and that all of the conduction electrons up to depth w are completely transferred to the surface (abrupt model). Under the latter assumption, density of surface charges, Q_{sc}, is nominally equal to $-qN_dW$, where q is elementary charge of electron and N_d is the density of donors in semiconductor. Under these conditions, electric potential, V, in the depletion region should satisfy the following Poisson's equation, where x is the depth from the surface and ε is the permittivity of semiconductor:

$$\mathrm{d}^2 V/\mathrm{d}x^2 = -q\mathrm{N}_d/\varepsilon. \qquad (5.3)$$

By introducing the boundary conditions that $\mathrm{d}V/\mathrm{d}x$ as well as V are zero at $x = W$, the above equation is solved to give the following depth profile of electric potential:

$$V(x) = -(qN_d/2\varepsilon)(x - W)^2. \qquad (5.4)$$
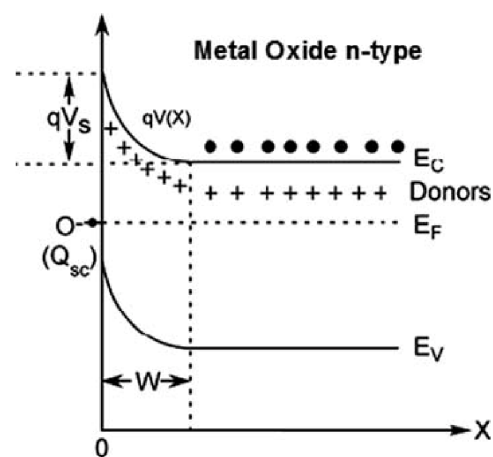
Fig. 5.16 Charge space zone scheme at the surface due to the interaction with the ambient

Potential energy of electron, $qV(x)$, as well as surface potential barrier height, qV_s, are directly obtained from the above equations:

$$qV/kT = (q^2 N_d/2\varepsilon kT)(x - W)^2 = (1/2)\{(x - W)/L_D\}^2, \qquad (5.5)$$

$$qVs/kT = (1/2)(W/L_D)^2. \qquad (5.6)$$

Here we have introduced an important quantity called Debye length, L_D, defined by $L_D = (q^2 N_d/\varepsilon kT)^{-1/2}$ for simplifying the expressions.

The surface chemical equilibrium can be solved now because the quantities involved have been made explicit with the properties of the underlying semiconductor.

$$[e] = N_d \exp(-qV_s/kT), \qquad (5.7)$$

$$[O^-] = -Q_{sc}/q = N_d W. \qquad (5.8)$$

Using these relations, chemical equilibrium can be rewritten as

$$(K_{O2}P_{O2})^{1/2}/L_D = (W/L_D) \exp((W/L_D)^2/2), \qquad (5.9)$$

and then resistance for the sensor device, R, can be estimated from the [e] values

$$R \sim \exp(qV_s/kT) \quad \text{or} \quad R \sim \exp((W/L_D)^2/2). \qquad (5.10)$$

In the presence of a reducing gas such as H_2 under fixed P_{O2}, $[O^-]$ is modulated by its surface reactions. Even in this case, once $[O^-]$ is properly estimated as a function of P_{H2}, then one can estimate the correlation between R and P_{H2}.

It should be remarked that the performed hypothesis for this calculation is only a coarse approximation. Actually, the used abrupt model is not necessarily rationalized. It ignores that conduction electrons are never perfectly absent in the depletion region but actually present rather abundantly in the vicinity of the border to the inner intact region. The phenomenon is called a distribution tail. This tailing eventually reduces Q_{sc} from that estimated above and also it over-estimates W and the bending potential qV_s. It becomes important as we are dealing with very tiny crystals for which the accurate dimensions are very significant. In this case, for example, there is no possibility for a non-limited P_{O2} increase because there is no room to extend W. When the absorption of gas molecules starts, electrons are depleted from surfaces – nanocrystal shapes are essential for a right description and it is not equivalently spherical, columnar or plate like – leaving the inner region intact, but subsequently the whole area including the central part is deprived of electrons thereafter achieving the condition of deep depletion shrinking the inner neutral part.

In spite of the existing classic models [67, 68], an accurate and completed theory which describes resistance and response of a semiconductor gas sensor using very tiny component crystals has still to be constructed. It must involve the combination of the chemical equilibrium on the surface of semiconductor with the electronic equilibrium inside. In fact, nanomaterials are one of the most promising alternatives for gas sensing. They represent the natural bridge between single molecules and macroscopic bulk materials. Their finite size and limited number of electronic states create a lot of restrictions for the transport mechanisms, specially for the charge conduction as the number of surface states can be comparable with that of the bulk. Then, their electrical behaviour is expected to present novel electrical and optical properties which can be used to fabricate nanodevices with improved capabilities [69]. This is the case of small nanowires where the area–volume ratio is easily maximized as the diameter size is decreased [70].

In this scenario, for small crystals, there are three paramount important findings that must be underlined: (i) how will the catalytic additive affect at the nanoscale level [71, 72, 73]? (ii) how much probable is it to achieve deep depletion conditions in the nanocrystal as partial pressure of adsorbing gas increases? and (iii) how much nanocrystals are needed to have a reliable sensing platform based on the surface interactions?

It is this last question that has arisen many requests for using nanotechnologies. In fact, in spite of the complexity of the mathematics models to find the equivalent impedance between two terminals to a 3D distribution of impedances, it is clear that the final value is proportional to that of a single element [74]. It tells us that we will have similar information just using only one of these nanostructures instead of an entangled bunch of them. In this case, no grain boundaries exist and, hence, the electrical transduction effects induced by the adsorbed gas molecules onto the surface of these nanowires can straightforwardly be revealed by the electrical magnitudes of these single nanocrystals. Several attempts for using only one of a few grains of metal oxide nanocrystals were already done by J. Tamaki et al. [75, 76, 77] using different gaps open in a gold electrode. Nevertheless, the lack of repetitiveness is still a challenge and the quality of contacts of gold/particle and among the particle seems not to be enough. On the contrary, this situation has moved the efforts from spherical-like nanocrystals towards the use of nanowires, nanotubes or structures based on them.

Unlike the small quasi-spherical nanoparticles with non-faceted surfaces, these nanostructured materials present well-defined crystallographic directions as crystal surfaces as well as looking like a perfect monocrystal. No grain boundaries are present. Therefore, the electrical transduction effects induced by the adsorbed gas molecules onto the surface of these nanostructures can straightforwardly be revealed by the electrical performances of these single nanostructures [78]. Moreover, as the gas molecules adsorption takes place at the surface, one of the most important issues for tailoring the sensor material response is the control of its active surface area. Many authors [59, 60, 61, 79]

have shown that there is a direct relationship between the active surface areas presented by the sensing material and the response given by the macroscopic sensor fabricated with these nanomaterials. According to these results, an increase of the surface area should involve an increase of the sensor response. This is the case of nanowires and 3D nanocrystal networks where the area–volume ratio is easily maximized as the diameter size is decreased, although as is discussed below it is needed to reduce a lot of the nanowire diameter to have high surface/volume ratio like it happens for the nanograins.

The majority of the experimental works show gas sensor based on multiple nanostructures or entangled bunch of nanowires, Fig. 5.17. A large number of these nanostructures are contacted and their electrical parameters estimated. However, only some equivalent mean values of these parameters are deter-mined due to the dispersion existing among the contacted nanostructures and the grain boundaries among them. In this scenario it is not straightforward to study the sensing mechanisms onto a single metal oxide nanocrystal, Fig. 5.18. To study gas-sensing mechanism onto one individual nanocrystal is still a challenge but it is required to reach a better knowledge of the electrical trans-port mechanisms which take place in these nanostructures. One of the reasons to explain this lack of experimental studies is that there are many difficulties in performing reliable electrical contacts on one individual nanostructure in a controlled fabrication process at the nanoscale level.

The most common techniques are optical and electron beam lithographies. Nevertheless, both techniques are multistep and time-consuming processes [80, 81], and they are difficult to tailor for each specific sample. For all these reasons, a complementary method based on FIB technique to the electron-based litho-graphy process has been proposed as one option which could, experimentally, help to solve problems related to more conventional contacting processes.
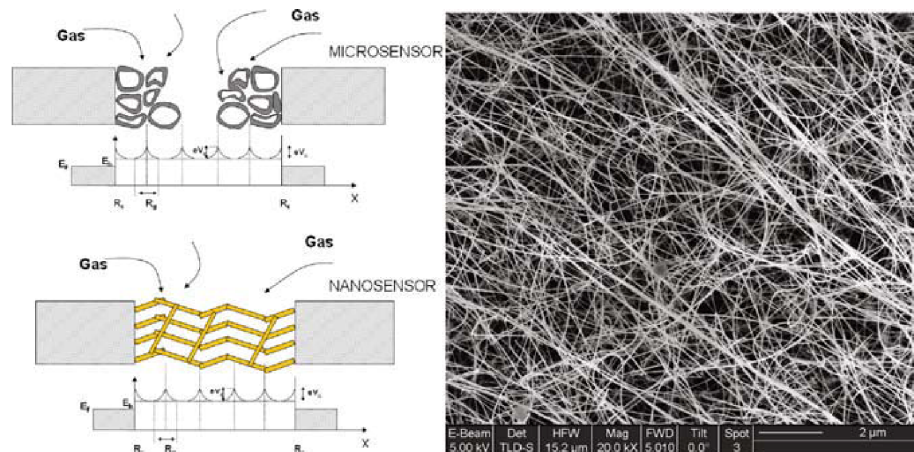
Fig. 5.17 Electrical scheme for entangled bunch of nanowires compared with that corresponding to a nanocrystal network

Fig. 5.18 Simplified electrical equivalent circuit to a resistance distribution corresponding to a nanostructure network
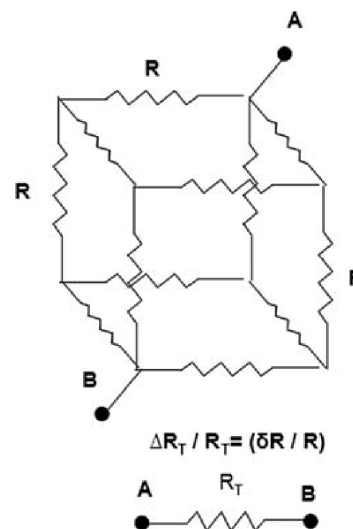
Focused ion beam (FIB) is a powerful technique developed during the late 1970s and the early 1980s for the patterning and, later, for the deposition of materials, with resolution in the tens of nanometer range, and commonly used in circuit edit, mask repair, microsystem technology processes and material characterization [82, 83, 84]. The basic principle of this technique is a focused ion beam of highly energetic particles that scans the sample's surface and sputters the material of the exposed area. The scanning can be performed, similarly to a SEM, using electrostatic lenses and, thus, the milling occurs without the need of masks. At the present time, gallium (Ga^+) ions are the most used particles in FIB technique due to the fact that gallium is a metallic element with a low melting temperature which allows the fabrication of long lifetime, high brightness and reliable liquid metal ion source (LMIS) required in FIB technique. Moreover, the element gallium is positioned in the centre of the periodic table (element number 31), so its momentum transfer capability is optimal for a wide variety of materials. On the contrary, lighter elements would be less efficient in milling heavier elements [82].

On the other hand, if a metal organic compound is introduced in the beam path with the help of a so-called gas delivery system by using a microneedle, decomposition occurs due to interaction of the compound with both secondary electrons and ions originated during the Ga^+ ion bombardment. Part of the compound can be deposited on the sample's surface (ion-assisted deposition) or can reactively assist the milling process (gas-assisted etching), while the rest is removed by the vacuum system. In this way, conductive and isolating materials can easily be deposited with FIB with nanometer precision. Although the purity of the deposition is generally lower as compared to conventional deposition techniques like CVD or PVD owing to contamination originated during the metal organic decomposition, the main advantage of this technique is its

flexibility and masks are not required. However, damage introduced in these materials by ion bombardment (Ga$^+$ ions accelerated to 30 kV, in our case) during fabrication of contacts has limited the use of this technique. Alternatively, it is possible to fabricate electrical contacts by using low ion currents in the proximity of the nanomaterials in order to reduce the damage. But, ion exposure is not thoroughly eliminated, and contacted nanomaterials are still modified [85].

At the present, the appearance of the so-called dual beam systems, a traditional FIB which incorporates a scanning electron microscope (SEM), has facilitated the use of FIB thanks to the possibility of acquiring electron images in situ, avoiding the damage caused by ions when imaging. Moreover, metal organic compounds can be also dissociated with the help of secondary electrons (SE), giving rise to electron beam-induced deposition (EBID) [86], electrons accelerated to 5 keV and methylcyclopentadienyl Pt (IV) trimethyl (PtC$_6$H$_{16}$) as gas precursor. Nevertheless, the number of SE produced by the primary electrons is smaller than that produced by Ga$^+$ ions, so the deposition rate is much lower in an electron beam-induced deposition [82].

Due to the fact that interaction between electrons and the sample is less destructive, performing an electron-assisted deposition on the nanostructure to be contacted and finishing the rest of the contact with the help of ions can avoid undesired surface damage and structure modification of the nanostructure. According to this procedure based on the combination of both electron- and ion-assisted deposition, metal oxide nanowires (NWs) and 3D nanocrystal networks can be contacted either in 2- or 4-probe configuration. The attempts of contacting nanomaterials using this method are still scarce and further research must be done in order to have a complete knowledge of the overall characteristics and performances of the electrical contacts [87, 88, 89].

The focused ion beam machine can be used to contact single nanostructures deposited previously and nano/micro manipulated onto a silicon wafer already processed to have an adequate distribution of microelectrodes. The manipulation defines a better placement of the nanostructure in front of the microelectrodes before proceeding with the Pt deposition. Then, four or two electron-deposited Pt contacts are performed, two or one, respectively, in each extreme. In this way, damage is strongly diminished and Ga$^+$ ions effects on the nanostructure are avoided. In fact, a couple of contacts are fabricated near each extreme of the nanostructure requiring much less than a half micron. The remaining nanostructure, of a significant length (more than several couples of microns), is released of any feature relative to the contact fabrication such as is shown in Figs. 5.19–5.21. Once the influence area due to the deposition is far away from the nanostructure, ion deposition methodology is used to extend the stripes to the pre-patterned contacts, Fig. Y, because the deposition time is much shorter than using the electron one. The electron and the Ga$^+$ ion beams are accelerated to 5 and 30 kV, respectively.
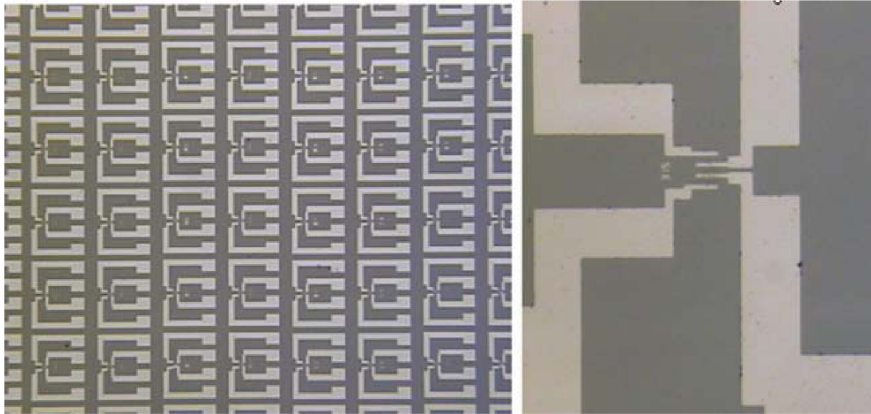
Fig. 5.19 Details of the four electrodes array patterned on a silicon wafer

Using this procedure, the previously presented nanostructures have been contacted in 2- and 4-probe configurations. This contact fabrication process for each nanometer-sized material takes more or less 2 h, limiting the application of this lithography technique in large-scale processes. On the other hand, its flexibility guarantees that it can be used for rapid prototyping, helping to solve some of the multistep-related problems of other nanolithography techniques.

Two- and four-probe V–I electrical measurements have been performed using a Keithley Source Measure Unit (SMU) 2400. These measurements at room temperature reveal that contact resistance contribution in 2-probe measurements is much more important than the nanowire resistance, Fig. 5.22.
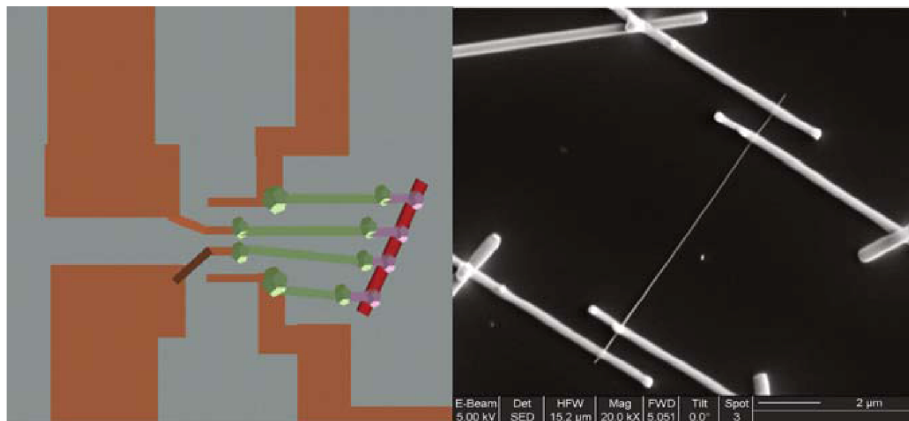
Fig. 5.20 (**a**) Schematic of the focused ion beam processes for obtaining four contacts using electron (pink) and ion (green) beams. (**b**) Image of a nanowire with four electrical connections
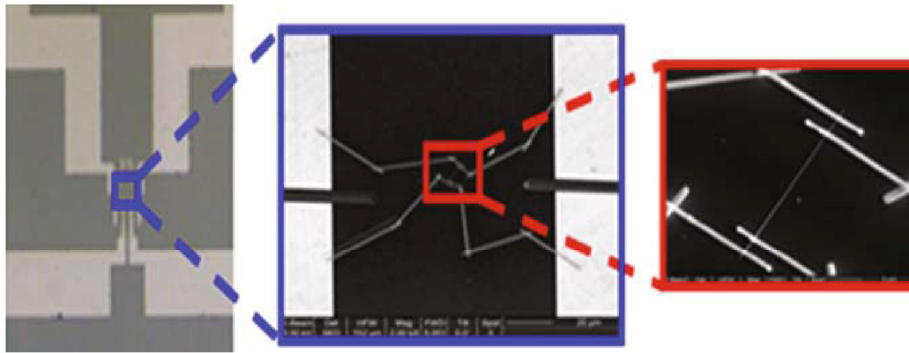
Fig. 5.21 Magnification from microscale to the nanoscale level for a connected individual nanowire

In some case, such contribution is even higher than 90% of total measured resistance, which range between some hundreds of kiloohms and some tens of megaohms. This huge difference between 2- and 4-probe measurements cannot be explained only by the sum of FIB-fabricated platinum stripes resistance and the contact resistance between them and pre-patterned gold microelectrodes since according to FIB platinum resistivity, lower resistance values would be expected (a few tens of kiloohms). So, the main part of the measured contact resistance is believed to be originated in the Pt–SnO_2 NW junction.

No degradation in this kind of contacts has been noticed after a long time of their fabrication, more than 4 weeks, and neither after applying constant current for several minutes. For example, good stability of the contacts performed on a nanowire has been observed after 1 month and no degradation after a current of 700 nA has been injected during 20 min.

All measured nanowires are destroyed at current densities below 10^{10} A/m^2, which is the critical current density value obtained for both ion- and electron-assisted deposition.

As has been said previously, due to the influence of the contact resistance to the final result, 4-probe electrical measurements are required if electrical parameters of nanostructure must be extracted. In order to determine the importance of this contact resistance contribution and as an example, the SnO_2 nanowire shown in Fig. 5.21 has been measured in both 2- and 4-probe electrical measurements. A resistance of $R = 12.53$ MΩ has been obtained under the first setup, while a resistance of $R = 1.93$ MΩ, see Fig. 5.22, has been obtained in the second case. These results point out clearly how the contribution of the contact impedance distorts the measurement of the nanostructure and even, sometimes, can be higher than the resistance of the nanostructure itself.

The extraction of the electrical parameters of the contacted nanowires is performed applying a simple model to estimate the material resistivity. Considering that these nanowires have a cylindrical cross-section, the resistivity can be calculated with the help of Eq. (5.11).
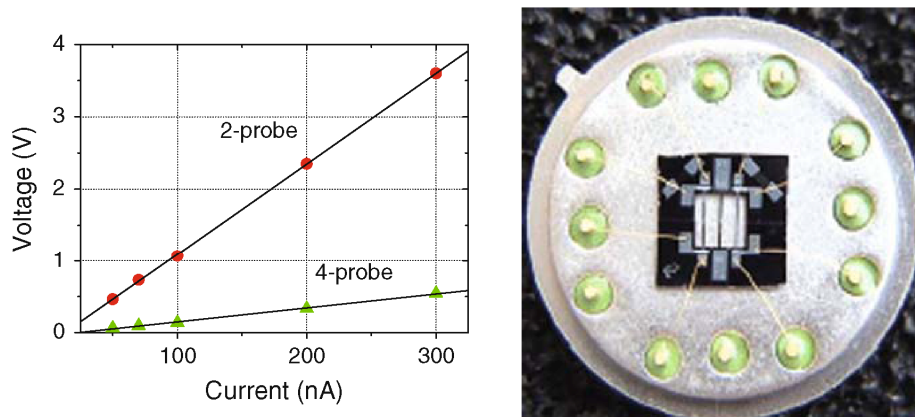
Fig. 5.22 Electrical measurements of a single nanowire using 2 or 4 probes on a silicon substrate die mounted on a TO packaging

$$R = \rho L / A = \rho L / \pi r^2, \tag{5.11}$$

where R is the measured resistance, ρ is the unknown resistivity, L is the length of the nanowire between the fabricated contacts and A is its cross-section, which can be determined if the radius, r, of the nanowire is measured.

Once a nanowire has been contacted, the dimensions L and r are measured in the SEM using XP-Annotate© software, which is available in the FIB work-station. This software compensates for the error introduced in the measurements when the sample is tilted.

In order to test the accuracy of this software, morphological characterization has been performed with an AFM working in tapping mode. It has been checked how platinum stripes have a roughness between 2 and 5 nm and their dimensions differ by less than 10% of the ones obtained with XP-Annotate©. So, the use of this software has been considered a reliable and fast method to determine dimensions (L and r) of the nanowires.

Once the dimensions and the resistance of the nanowires are known, the resistivity can be easily determined by applying Eq. (5.11). In the case of the SnO_2 nanowire of Fig. 5.21, a resistivity of $\rho = 50$ m$\Omega\cdot$cm has been found. The found value agrees with previous values of the literature related to NW studies of single SnO_2 crystals [90].

These contacts show excellent electrical stability as a function of time and applied current density. Therefore, they fulfil the requirements to fabricate nanodevices able to work for a long time. However, there is still an important feature to be discussed. It is the linearity of the electrical contact. These ones are symmetric but reveal a non-ohmic behaviour such as is shown in Fig. 5.23. This rectifying behaviour originates at the Pt–SnO_2 NW junctions.

This junction forms a Schottky barrier of height $\Phi_B = 0.75 \pm 0.10$ eV in the absence of interface states owing to the differences between the work function
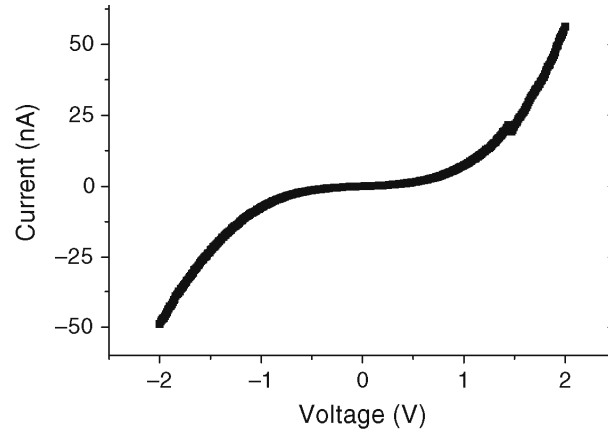
Fig. 5.23 Intensity versus applied voltage in a nanowire measured using 2-probe contact

of Pt ($\Phi_{Pt} = 5.65$ eV) and the electron affinity of SnO_2 ($\chi_{SnO2} = 4.9 \pm 0.1$ eV). This configuration can be described as a back-to-back Schottky-like circuit.

According to this assumption, the applied bias V must distribute as

$$V = V_a + V_d + V_{NW} + V_i, \tag{5.12}$$

where V_a is the voltage drop in the cables, gold microelectrodes and FIB-fabricated platinum stripes, V_d is the voltage drop in the direct-biased Pt–SnO_2 junction, V_{NW} is the voltage drop along the SnO_2 NW and V_i is the voltage drop in the reverse-biased junction. In this back-to-back Schottky-like configuration, the total current is limited by this reverse-biased junction, insert in figure A. The contact barrier height is reduced and the current increases with increasing bias according to

$$I = AA^{**}T^2 \exp\left(\frac{-q\phi_{BE}}{k_B T}\right), \tag{5.13}$$

where

$$\phi_{BE} = \phi_{B0} - \sqrt{\frac{qE}{4\pi\varepsilon_s}} - \frac{q}{\varepsilon_S}\sqrt{\frac{N_S \cdot d}{4\pi}}, \tag{5.14}$$

and

$$E = \sqrt{\frac{2qN_D}{\varepsilon_s}\left(V + \phi_{bi} - \frac{k_B T}{q}\right)}, \tag{5.15}$$

where A is the contact area, A^{**} is the effective Richardson constant, $_{BE}$ is the effective barrier height, $_{Bo}$ is the ideal barrier height in the absence of image force, E is the maximum electric field at the junction, ε_s and N_D are the dielectric

constant and doping concentration of SnO_2, N_s is the surface state density and $_{bi}$ is the built-in potential. If both the voltage drop in the direct-biased junction V_d and the voltage drop in the nanowire V_{NW} are supposed to be small compared with the voltage drop in the reverse-biased junction V_i, then, it can be considered, as first approximation, that all the applied voltage falls in this latter junction,

$$V_d + V_{NW} \leq V_i \Rightarrow V \approx V_i. \tag{5.16}$$

According to this assumption, $\ln(I)$ versus $V^{1/4}$ should be linear at all temperatures for which the model is valid. Rectifying $I–V$ curve values confirm that the back-to-back Schottky-like assumption can be very useful to describe the electrical response of these SnO_2 NWs at room temperature, Fig. 5.24.

The contact resistance presents an activation energy at room temperature, which is found depending on the nanowire, but over 200–250°C its value becomes, generally, already non-predominant. It is important if we keep in mind the gas sensor working temperatures. This behaviour can be explained assuming that some FIB-induced disorder is produced underneath the Pt contacts during the contact fabrication process, creating surface states used by electrons to overcome the barrier, even at low bias, considering multiphonon-assisted tunnel mechanisms. Another consequence of this contact resistance that must be taken into account as relevant in many experimental cases is the heat dissipation.

So, to avoid also the DC thermal effects due to the power dissipation, as well as to avoid any problem with the species migration through the structures, AC measurements can also be applied. AC impedance spectroscopy is a well-known and widely used technique in material science studies that can help us to
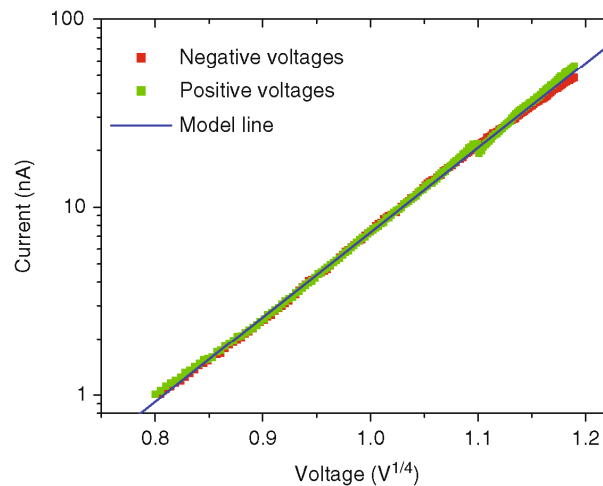
Fig. 5.24 Logarithmic plot of the intensity versus $V^{1/4}$

overcome these limitations. Moreover, AC impedance spectroscopy is known to be useful to characterize Schottky barriers originated in Pt–SnO_2 junctions.

For the AC measurements, an impedance analyser Solartron SI-1260 with a maximum working frequency of $f = 5$ MHz and an impedance analyser Gamry EIS300 with a maximum working frequency of $f = 300$ kHz can be used inside of a Faraday cage. As far as we know, these were the first attempts of performing 4-probe electrical measurement using AC impedance spectroscopy on a single nanowire [91].

For it, gas sensor nanodevices were fabricated following a bottom-up process based on the use of an individual SnO_2 nanowire based on DC [92] or on AC [93] measurements. These nanowires were grown by variations of the methods based on vapour–liquid–solid (VLS) mechanisms in evaporation/condensation or chemical vapour deposition processes that have been described elsewhere [94, 95, 96, 97]. In all the cases, under different growth conditions, it has been possible to have very excellent single nanocrystals as nanowires which present different crystallographic orientation and faceting, Fig. 5.25.

Electrical values reveal directly the consequences of the electrical transduction of the gas–solid interaction taking place at the nanowire surface. It can be seen in Fig. 5.26 for a nanowire of 50 nm diameter measured at 265°C in two atmospheres, nitrogen and dry synthetic air (80% N_2, 20% O_2). On the basis of these procedures, systematic measurements of the nanowire resistance in the bottom-up gas sensor nanodevices at different temperatures and atmospheres have been performed.

One of the most interesting results using metal oxide nanowires can be attained in the analysis of its resistance against the synthetic air and nitrogen atmospheres. It reveals a clear dependence on the diameter size according to (1/D) dependence, Fig. 5.27. It gives support to the model that assumes the existence of a space charge zone created by the adsorbed oxygen which is limiting the central area of the nanowire for electrical transportation.

So, adsorbed oxygen as well as the hydroxyl group modify the surface conditions for other gases and they must be considered before studying any gas-sensing process. Among the typical test gases used to evaluate sensor performances, carbon monoxide is the more studied and it presents, at the same time, simple transduction mechanisms. It is accepted that in the temperature range between 200 and 370°C, there is CO_2 formation from the adsorbed oxygen [98]. Ideally, it follows a well-reported mechanism. Therefore, CO is one of the most reported gases to evaluate the performances of the nanosensors based on single nanowires. Again, the main variation in the performed measures has been found related to the values of the diameter of the nanowire. It constitutes one of the most critical points, such as it is well accepted for nanograins. The possibility of getting nanosensors with high performances depends on it such as is shown by Fig. 5.28.

It corroborates the above-shown trends for the atmosphere change from nitrogen to synthetic air. So, a small amount of adsorbed molecules can easily bend the bands in the radial or coaxial direction. It limits the central zone of the
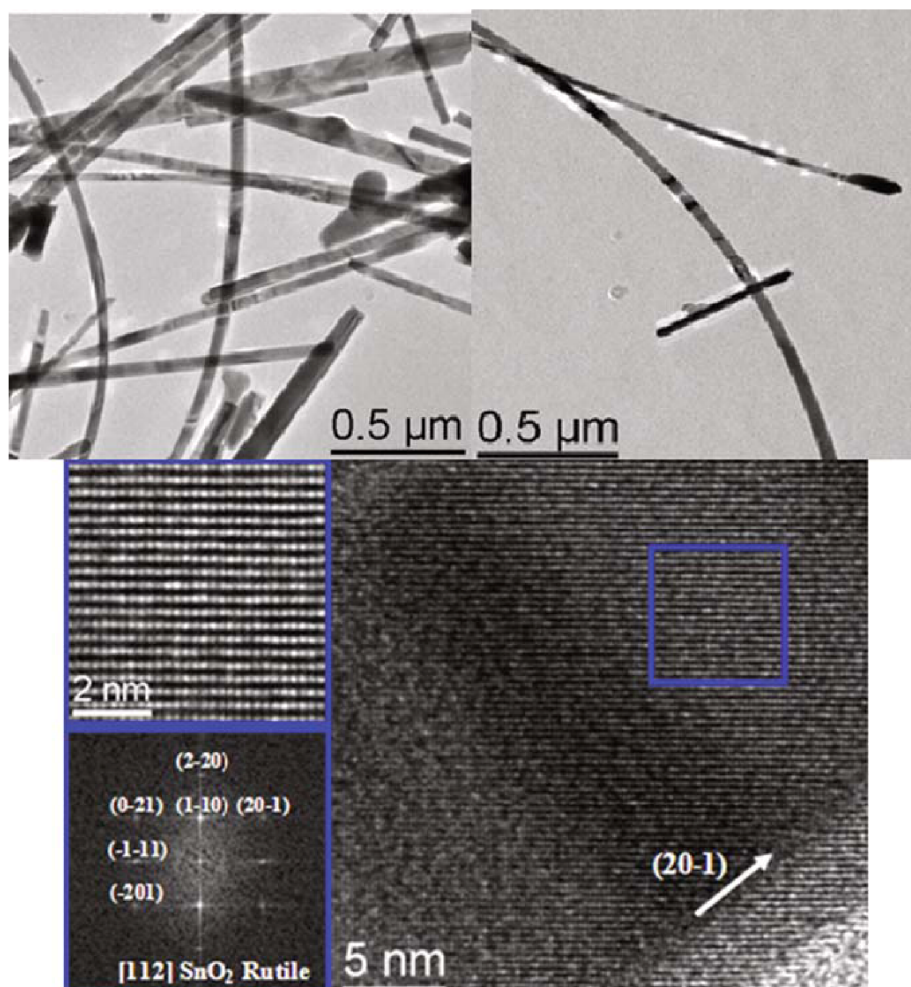
Fig. 5.25 SnO$_2$ nanowires

nanowire available for lateral transport and, as a consequence, the sample resistance is then a measure of the amount and type of gas. Obviously, it becomes significant as the transversal radius of this central zone is comparable to the dimensions of the surface space zone. Many references from the literature have reported about CO measures using individual nanowires. However, the reported sensor responses are, as it was discussed above, not important due to the large radius of the electrically contacted nanowires used in these references. In spite of the difficulties in their manipulation and contacts fabrication, values around 25 nm and below are needed to achieve higher sensor response than those reported for macroscopic gas sensor based on interconnected particles of only a few nanometers of diameter [99]. Nevertheless, it should be noted that using an individual nanowire as a single nanocrystal has more advantages from

Fig. 5.26 AC electrical measurements of a single SnO$_2$ nanowire under different gas atmospheres
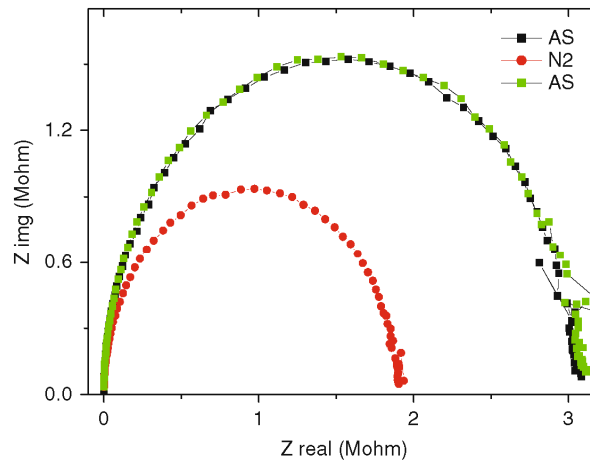
the point of view of stability, repetitivity and reliability as there are no grain boundaries. Moreover, there are well-defined crystallographic directions for the surfaces of the nanowire unlike the case of very small nanoparticles that usually present very reactive surface because they are not yet faceted surfaces [100]. Therefore, a single nanowire presents the characteristics of a monocrystal that fits much better with the stability requirements and long-term wearout claims.

So, maintaining small radius in the selected nanowires, the surface variation has a stronger influence on the nanowire resistance. Nevertheless, in spite of these interesting results, more detailed studies are still needed to achieve a complete mechanism views and to have a complete modelling of it, especially if it is possible to module the working temperature. Just this interest has focused the efforts to achieve the combination of individual nanowires and micromembranes with integrated heaters.
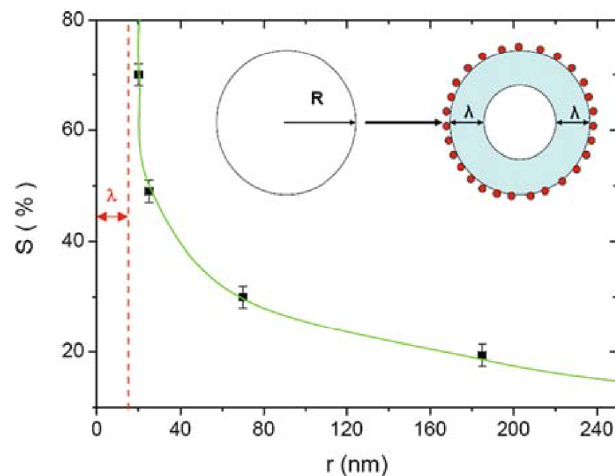
Fig. 5.27 Nanowire section size dependence of the electrical response from nitrogen to synthetic air atmosphere

Fig. 5.28 Sensor response for different sensing materials against the CO concentration (Commercial = nanocrystal of 10 nm, NW literature ≈ 200 nm)
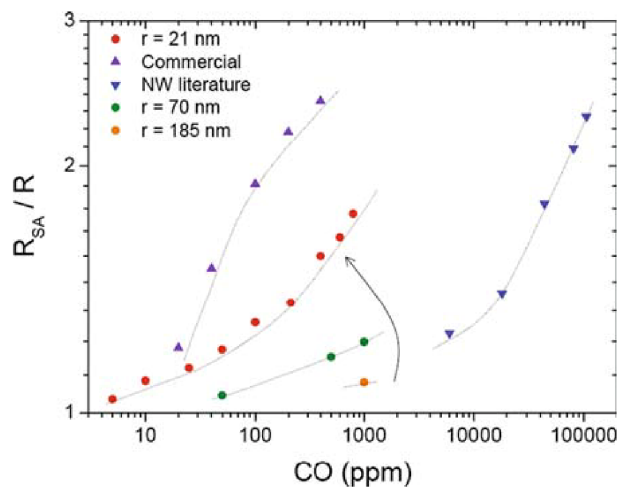
It is one of the most promising approaches for obtaining portable devices for gas sensing since their working temperature can effectively and easily be modulated. To the best of our knowledge, only a few attempts to use this fabrication methodology have been reported in the literature [101, 102]. On the other hand, some challenging issues like the electrical stability of the final devices based on single nanowires should also be solved prior to their large-scale application. Recently, portable gas sensor based on an individual SnO_2 nanowire has been reported [92], Fig. 5.29.

In this example, individual SnO_2 nanowires synthesized by chemical vapour deposition of a molecular precursor [Sn(OtBu)$_4$] were transferred onto suspended micromembranes with one integrated SnO_2:Sb heater and platinum interdigitated microelectrodes, Fig. 5.29a. Membranes were fabricated using silicon-on-insulator wafers. High-resolution TEM images showed single crystalline nanowires with dislocation-free bodies and a main growth direction of [100] and interplanar spacing in correspondence with the rutile structure of SnO_2 [103]. Nanowires were electrically contacted to platinum microelectrodes using a FEI Dual Beam Strata 235 FIB instrument equipped with a trimethyl methylcyclopentadienylplatinum ((CH_3)3$CH_3C_5H_4Pt$) injector to deposit platinum, following a nanolithography process, Fig. 5.29b. Two-probe DC measurements were performed with the help of an electronic circuit, Fig. 5.29c, designed to guarantee low current levels and avoid any undesired fluctuation.

This option reports the possibility of modulating the device temperature using the integrated heater. Although the temperature of these membranes was calibrated as a function of the power dissipated by the heater, accurate estimation of the effective temperature of nanowires is quite difficult since uncontrolled self-heating effects due to the existence of Schottky barriers and their conduction of charge carriers should always be considered [104]. The dynamic response of these devices was fast enough to reach complete thermal
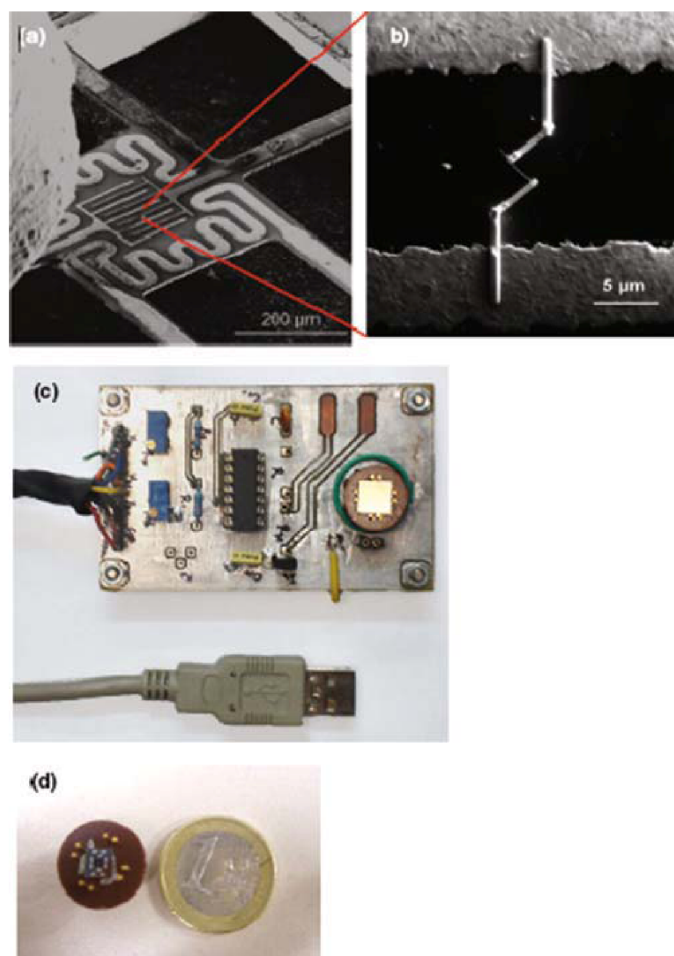
Fig. 5.29 Details of a gas-integrated nanosensor based on a single SnO_2 nanowire

stabilization after a few seconds of changing the power applied to the heater, demonstrating that the optimal working conditions can be easily modulated in a fast and controlled way. It facilitates its use as devices for monitoring this gas such as is shown by Fig. 5.30. This last result demonstrates that these devices could be used in the future as portable and reliable gas microsensors.

The sensing performances of these nanostructures can be enhanced by means of the adequate modification of the surface. It is well known that the presence of catalytic nanoclusters of different noble metals, such as gold and platinum, or inorganic compounds, such as CuO and CaO, has been widely reported to improve reactivity with some molecules. However, the modification of the surface wins a maximum significance when we are looking for the interaction with biomolecules. In this case, the interactions can cover a wide range from very strong covalent bonds to weak van der Waals interactions, Fig. 5.31.
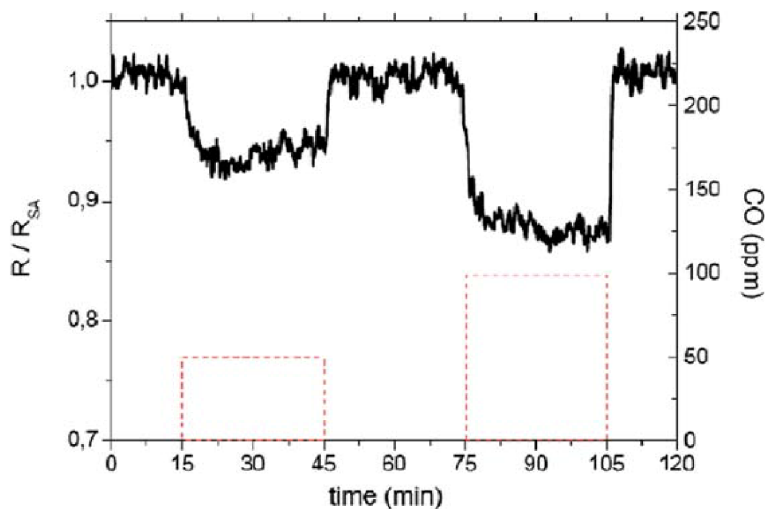
Fig. 5.30 Sensor response against CO of the integrated nanosensor shown in Fig. 29

Many organic compounds possess different functional groups such as amines (H_2N-R'), thiols (HS-R'), alcohol (OH-R'), phenol (OH-cycle-R') and carboxylic acids which are organic molecules that contain a carboxyl group (-C$=$O)- whose carbon atom is bonded to a hydroxyl group (-OH) as it happens, for example, in the methanoic acid, ethanoic acid or propanoic acid (R-COOH). So, these functional groups can be used to form covalent bonds on the target organic molecules where atoms forming this bond share pairs of electrons. Sometimes, this covalent coupling can be done directly on the surface of the sensing material, whereas in many other cases, other molecules named cross-links are needed to link one molecule to another. Likewise,
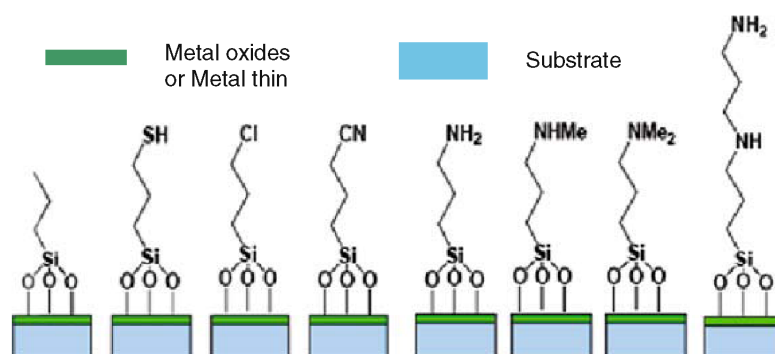
Fig. 5.31 Schematic of a typical functionalized surface

very often, the functional groups need to be energetically activated avoiding the deterioration of these biomolecules. In general, there are many functional groups but carboxylic acids (R-COOH) are frequently used. They can be covalently coupled with other functional groups to give rise to different bonds: (i) amides, R-CO-NH-R', (ii) thio ester R-CO-S-R', (iii) acyl ester R-CO-O-R' and (iv) aryl ester R-CO-O-cycle-R'. All of them allow fixing functional groups but often there is the problem about how to be fixed on the substrate that is typically based on silicon wafer (silicon dioxide films) or alternatively on metal layer or metal oxide materials. For it, self-assembling monolayers formation has become one of the most applied methodologies. Molecules with hydrophobic–hydrophilic nature, also named amphiphilic molecules, are used. These molecules consist of two different head and tail functional groups where one end sticks to the sensor surface and the other end interacts with the analyte biomolecules establishing a strong link. The alternative adsorption of different materials containing complementary charged or functional groups [105, 106] allows, layer by layer, to form ultra-thin layers with a level of control over the film composition and structure down to several nanometers [107]. Gold is a suitable substrate for forming SAMs since freshly deposited gold presents a high hydrophilic degree which facilitates the interaction with a thiol group. Alkane thiols, $HS-C_nH_{2n+1}$, are among the most used thiols for sensing applications due to the easy formation of a thiolate bond with the gold surface from an alcohol solution and the ordered alkane tail packaging because of the existing van der Waals among them. Other materials such as silver, platinum, copper can replace gold and alternatively silicon dioxide and many metal oxides can also be applied due to the oxygen bridged and hydroxyl groups on their surface that gives a strong hydrophilic character. Moreover, it also gives the possibility for using other compounds, silanol for example, as intermediate links between the substrate surface and the target analytes. On the other hand, other materials such as carbon present a strong hydrophobic character.

These surface modification protocols are usually applied to functionalize the nanoparticles or substrate surfaces in order to develop sensitive and highly stable biosensors. Furthermore, during the last years, this capability has been enhanced due to the use of the surface plasmon resonance effects, SPR, which supplies a powerful tool for the sensing procedure [108], mass sensors based on quartz crystal microbalance (QCM) or surface acoustic wave (SAW) devices. Likewise, these surface modification procedures have been enriched by incorporating antibodies, enzymes, nucleotides or DNA sequences [109]. Nevertheless, although the versatility of the biosensors as analytical tools has increased and the biosensors are used for continuous monitoring of vital biochemical parameters [110, 111], some applications remain limited by functional deterioration due to surface fouling by proteins and other biological components [112]. Nowadays, nanotechnology is bringing continuously new possibilities for biosensors construction and for developing novel electrochemical bioassays. So, new developments are combining the use of the

functionalized surface of carbon nanotubes or metal oxide (MO) nanowires as a gate electrode of the FET-like sensing structures [113]. Their advantages as conductive transducers are high surface area and accelerated electron transfer (ET) [114].

In spite of the very promising results, there are still many challenges due to the relatively inefficient interaction with biomolecules, low selectivity and interfacing activity with respect to specific analytes. The improvements can be directed at self-assembling a layer of specifically designed active molecules that make electrical communication between the analyte and the sensing surface (gate electrode in the case of FET scheme) more efficient, improve sensitivity and stability and even make the interfacing layer an active player in sensing mechanism [115]. The improvement of the functionalization steps and procedures becomes the right clue to have a reliable electrochemical communication between the analyte and the electrode surface with enhanced and controllable electron transfer mechanisms that still require much more effort for their understanding.

5.6 Nanosensors Based on Photon Capture: Photodetection at the Nanoscale

In this section, like in the previous one where the advantages of playing in the nanoscale for the electrical interaction through the surface has been shown, we want to discuss about the advantages of using nanosized materials in light-sensing applications. Therefore, our aim is not to present a detailed description of all the photodetection strategies and achievements but to emphasize the photodetection capability at the nanoscale. Detailed information on this topic can be found elsewhere [116, 117, 118]. The simplest strategy to electrically "transduce" the presence of light is the use of photoconductors. In such materials, the energy of the absorbed light is used to promote an electron from the valence band to the conduction band of the material (usually, a semiconductor) leaving behind a hole in a process known as photogeneration of charge pairs. Consequently, the conductance of the material decreases after exposure to light and, in first approach, the minimum detectable wavelength corresponds to the bandgap energy of the material. Since this essentially is a bulk process, what is the advantage of using nanosized materials (with high surface-to-volume ratio) instead of other conventional technologies such as thin films [119]?

Photoconductors, Fig. 5.32, based on individual nanowires, modelled as an arbitrary volume of length L, width W and thickness T can be studied using the fundamental principles ruling light carrier generation on semiconductors [120, 121, 122]. For simplicity, let us consider the case of extrinsic n-type semiconductors. In low-injection regime (i.e. under low illumination levels), the current

Fig. 5.32 Diagram of a metal oxide structure with an arbitrary volume of length L, width W and thickness T under a photon flux Φ_{ph}. Photocarrier generation is produced in the outer layer of the nanowire until depth α^{-1}
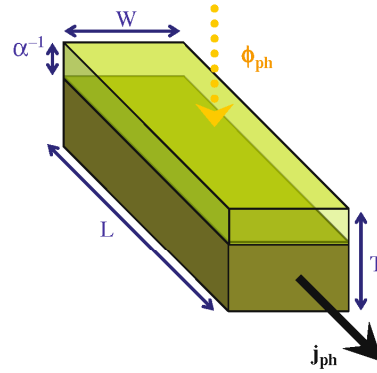
density j_{ph} corresponding to the photogenerated electrons is given by the following equation:

$$j_{ph} = q\,\frac{1}{L\,\alpha^{-1}}\,\beta\,\eta\,\tau\,\mu^*\,V\,\Phi_{ph}, \qquad (5.17)$$

where q is the elemental charge, L is the length of the nanowire, α is the absorption coefficient of the material at the wavelength of the incident light, β is the fraction of photons not reflected by the surface, η is the quantum efficiency of carrier generation by one photon, ι is the carrier lifetime, μ^* is the effective carrier mobility, V is the (external) applied voltage along the nanowire and Φ_{ph} is flux of photons impinging on the nanowire. Here we assumed a constant carrier generation profile until the depth α^{-1} and, according to Matthiessen's rule, μ^* can be broken down into the following factors [122]:

$$\frac{1}{\mu^*} = \frac{1}{\mu_B} + \frac{1}{\mu_S}, \qquad (5.18)$$

where μ_B and μ_S are the bulk and surface contribution.

To evaluate the total photogenerated current I_{ph}, which is the experimental response of real devices, one can assume that the nanowire is thick enough to absorb all the incident photons. That is to say,

$$T \geq \alpha^{-1}. \qquad (5.19)$$

Therefore, it can be deduced that thinner nanowires ($T < \alpha^{-1}$) will lead to lower photoresponses. On the contrary, the use of thicker nanowires ($T >> \alpha^{-1}$) will not imply a further enhancement of the response. To exemplify this, the penetration depth α^{-1} of near-UV photons (wavelength from 400 to 250 nm) in ZnO is almost constant at 50 nm [123]. Thus, ZnO nanowires with radii slightly above $r \approx 25$ nm should be used to maximize photoresponse to UV light in this

wavelength range. If the constant absorption profile approximation is maintained (light penetration depth α^{-1} and nanowire width T), photocurrent I_{ph} in nanowires which verify Eq. (5.19) is given by

$$I_{ph} = j_{ph}\left(\alpha^{-1} \, W\right) = q \, \frac{W}{L} \, \beta \, \eta \, \tau \mu^* \, V \Phi_{ph}, \qquad (5.20)$$

where three different contributions are clearly identified. The first one is related to geometric parameters of the device (W/WLL), the second one to the intrinsic properties of nanowires ($\beta\eta \, \iota\mu^*$) and the third one depends only on the working conditions ($V\Phi_{ph}$). The performance of these devices can be also analysed in terms of their photoconductive gain G_{ph}, which is defined as [121, 122,]

$$G_{ph} \equiv \frac{I_{ph}}{q \, F} \approx \frac{1}{L^2} \, \eta \, \tau \mu \, V, \qquad (5.21)$$

where the same type of contributions are identified.

Concerning the geometry of photodetectors, it is clear from Eq. (5.4) that I_{ph} is enhanced by increasing the width of photoactive area (W). Besides, I_{ph} and G_{ph} are also improved by decreasing the distance between the electrical contacts L (see Eqs. (5.20) and (5.21)). On the one hand, a convenient way to increase the area is using multinanowire-based configurations. These devices can be fabricated by means of self-assembly techniques, i.e. dielectrophoresis, to electrically contact large amounts of them in parallel [124, 125]. This fabrication methodology prevents parasitic effects arising from uncontrolled nanowire-to-nanowire contacts. It is noteworthy that according to Eq. (5.21), the photoconductive gain G_{ph} obtained with these multinanowire configurations is equivalent to that provided by one single nanowire, if all of them are identical. On the other hand, both I_{ph} and G_{ph} increase inversely with the distance between contacts L. Thus, this experimental parameter is critical to optimize the performance of final photodetectors. The lower limit for L will strictly depend on the precision of the nanolithography technique and other size-associated phenomena like diffraction, if L approaches the wavelength of photons, or uncontrolled degradation effects produced when the ruptured electric field of the metal oxide is overcome. To exemplify this last point, it can be roughly estimated that nanowires contacted between two electrodes separated by only 50 nm [126] and polarized at 5 V [127, 128] will be subjected to electric fields as high as 1 MV/cm.

As far as the intrinsic properties of nanowires are concerned, the dependence of I_{ph} with η, ι, μ^* and β must be also considered (see Eq. (5.20)). The quantum efficiency η determines the spectral response of photodetectors and was observed to increase orders of magnitude when photons with energies above the bandgap interact with these devices compared to typical responses obtained with sub-bandgap photons [129]. It is noteworthy that the bandgap edge of nanowires depends not only on the material but also on their dimensions [122,

130]. Thus, controlling the radii of nanowires is critical to tune the spectral sensitivity of the final devices. Photogenerated carrier lifetime ι is the second parameter directly related to the intrinsic properties of nanowires, and it is known to be higher in nanomaterials than bulk because of their large surface-to-volume ratio and the formation of deep-level surface states [121, 131]. In the case of semiconductor nanowires, it is generally accepted that photocarrier relaxation dynamics consists of an initial decay process in the nanosecond range, explained by the fast carrier thermalization and hole trapping by surface states, followed by a slow decay dependent on the surrounding atmosphere and the nanowire surface coating [128, 132, 133, 134, 135]. This second process, with characteristic times of seconds, dominates the final response of nanowire-based photodetectors. For this reason, the carrier lifetime contribution ι to the photo-response I_{ph} (see Eq. (5.20)) can be enhanced by controlling the surface inter-actions of this type of nanowires. The third parameter related to the intrinsic properties of nanowires is the electrical mobility μ^*, which is known to be dependent on their radii. To exemplify this with ZnO nanowires, mobility values ranging from 2 to 30 cm^2/Vs were reported for nanowires with radii below $r \approx 100$ nm [136, 137, 138, 139]. This diminished mobility tends to the bulk value ($\sim$200 cm^2/Vs) with thicker nanowires [128]. This behaviour is attributed to scattering and trapping of the electrons by surface defect states and becomes more important with thin nanowires, whose surface-to-volume ratio increases. In these circumstances, surface contribution μ_S to μ^* is signifi-cantly minimized (see Eq. (5.18)). Thus, nanowires as thick as possible are convenient to obtain optimal devices from a point of view of μ^* optimization. The limitation introduced by the dependence of μ^* with radius can be also overcome by coating the nanowires' surface with a passivation layer. Using the previous example, it was demonstrated that the mobility of ZnO nanowires dramatically increased using this fabrication strategy (up to 4,000 cm^2/Vs) [139]. The last intrinsic parameter of nanowires to be considered in this work is the fraction of photons not reflected by the surface of the metal oxide β, which was recently demonstrated to be lower in a wide spectrum range with photo-detectors based on aligned nanowires instead of thin films [140].

As far as the experimental conditions are concerned, it can be demonstrated from Eqs. (5.20) and (5.21) that photoresponse rises with applied voltage V and flux of photons Φ_{ph}, making it difficult to compare most of the reported results, since different experimental conditions were used in all these experiments [127, 128]. For this reason the photoconductive gain (Eq. (5.21)) can be expressed in a more convenient way

$$g_{ph} \equiv \frac{L^2 G_{ph}}{V} \approx \eta\, \tau\, \mu^*, \tag{5.22}$$

which is normalized and independent of the device geometry and the experi-mental conditions.

Besides the gain, the dynamic response of a photodetector is also important. The low-pass bandwidth is approximately $BW \approx (2\pi\tau)^{-1}$ and the normalized gain per bandwidth becomes

$$g_{ph}\text{BW} \approx \frac{\eta\,\mu^*}{2\pi}. \tag{5.23}$$

Therefore, mobility and quantum efficiency are the key parameters to determine the overall performance of a photodetector. Equations (5.22) and (5.23) show the fact that high photoconductive gains are achieved by increasing the carrier lifetime but this worsens the dynamic response.

Finally, it is illustrative to compare the performance already achieved using single nanowire photoconductors with thin film-based detectors [119]. We focused again in ZnO. In high-quality thin films mobility tends to the bulk value ($\sim$200 cm^2/Vs) [141]. The highest photoconductive gain reported with thin film photodetectors is $G_{ph\,lit}^{TF} = 1360$ [142]. Using the polarization and geometric conditions reported by the authors ($V_{ph\,lit}^{TF} = 5V$, $L_{ph\,lit}^{TF} = 10\mu$), the normalized photoconductive gain is $g_{ph\,lit}^{TF} = 3 \cdot 10^{-8}$m^2/V. This gain is clearly below the ones reachable with single ZnO nanowires in their present stage of development ($G_{ph\,lit}^{NW} = 5 \cdot 10^7$) [128]. However, if we estimate the overall performance with the normalized gain per bandwidth ($\tau_{lit}^{TF} \sim 1.5\mu s$) product we obtain $g_{ph\,lit}^{TF} = 3 \cdot 10^{-3}$m^{2}Hz/V to be compared with the best figure for a single nanowire photodetector ($g_{ph\,lit}^{NW} \cdot BW = 5 \cdot 10^{-8}$m^{2}Hz/V) [128]. Therefore, the high photogain currently achieved with individual nanowires is mainly associated with the longer lifetime of the photocarriers. In conclusion, nanowires can be used as photoconductors as an alternative to conventional technologies. However, we can only take advantage of their superior properties (high crystalline quality and extremely high mobility) if appropriate layout and operating conditions are considered. Some of these promising strategies are diminishing the distance between the electrical contacts, increasing the photoactive area or improving the electrical mobility of nanomaterials using surface coatings.

Besides photoconductors, there exist a number of other devices based on the photogeneration of charge pairs that are conventionally used in photodetection [119, 120, 121, 122]. Most of them are based on the charge separation of the photogenerated pairs (electron and hole) by a built-in electric field. In these cases the junction of different materials (metal–semiconductor, heterojunction and homojunction of semiconductors) is used to generate these built-in fields. In Fig. 5.33 we summarize some of them [119]. Recently, many of these configurations have been successfully obtained using nanowires (diodes in individual nanowires [143, 144], core–shell nanowires [145, 146], nanowire–wafer unions [147]) and open the door to further improvements in photodectection with nanowires.

Finally, similar nanostructures and devices can be also used in solar energy harvesting applications in which the same principle of separation of
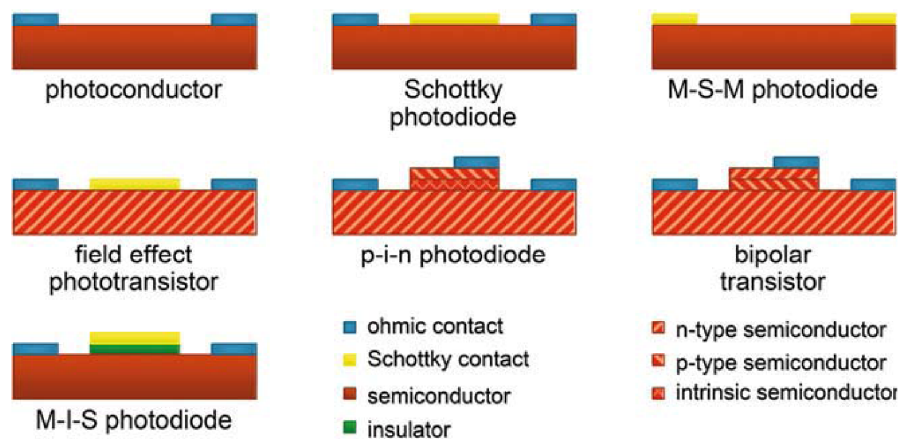
Fig. 5.33 Schematic structure of different semiconductor photodetectors suggested by [119]

photogenerated pairs can be used to provide power (voltage and current) to an external electrical load [122, 148. 149]. Particularly, the use of nanosized materials in cost-effective dye-sensitized solar cells is necessary to efficiently collect the charge generated by light in the organic dye layer [150, 151, 152]. Other promising achievements are the integration of a fully functional solar cell in one single nanowire [143, 144, 153].

5.7 Nanosensors Based on Plasmon Resonance: Influence of the Dielectric Constant Variations at the Nanoscale

Plasmons, collective oscillations of the free electron gas density, can be exploited for sensor purposes in two different ways: (i) as transducers of the measured magnitude into an optical signal or (ii) as enhancers of the spectroscopic signatures concerning the measured magnitude.

As a transducer, we take advantage of the sensitivity of the plasmon resonance to the very close dielectric environment that can be easily achieved by controlling it at the nanoscale domains that present a high surface/volume ratio enhancing the role played by the surface plasmon. This dependence to a highly localized dielectric environment, coupled with the use of metal nanoparticles as sensing probes, provides with a considerable spatial resolution to probe-based sensors taking advantage of this transduction mechanism. In this direction, silver and gold nanoparticles, having resonance frequencies in the visible region, have been used as single particle optical biochemical and chemical sensors [154, 155, 156]. Usually, dark field optical microscopy is used to analyse the resonance spectra of these single nanoparticles. Its resonance frequency is very sensitive to the adsorbants on its surface (Fig. 5.34).
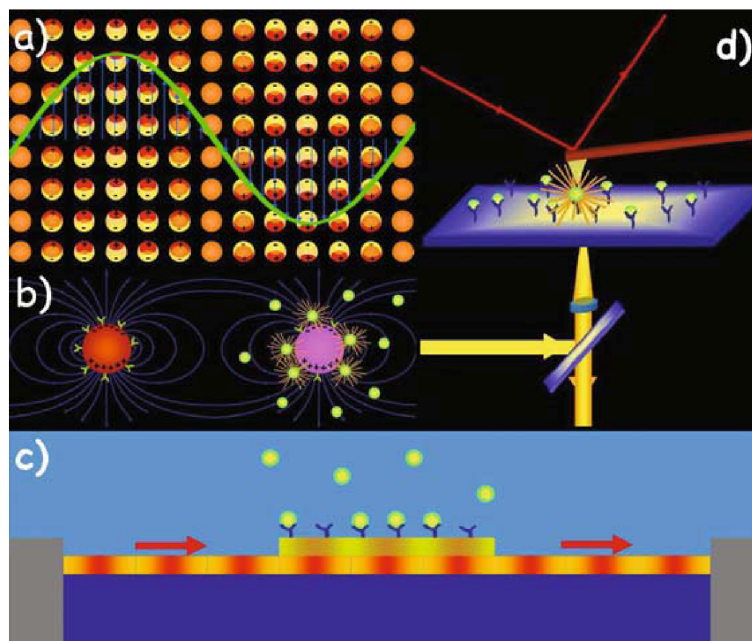
Fig. 5.34 Cartoons of the (a) plasmon generation in metal nanoparticles by an electromagnetic field, (b) modification of the plasmon resonance frequency of single nanoparticles due to the presence of the target analyte and enhancement of the optical signature of the species nearby the metal surface, (c) waveguide surface plasmon resonance sensor and (d) tip-enhanced Raman spectroscopy

Plasmon resonances are sensitive not only to the surrounding dielectric media but also to the shape, size and interaction between particles [157, 158]. While such dependences deteriorate the characteristics of nanoparticle arrays as plasmon resonance sensors, they can be used to measure geometric parameters at the nanometer scale [159]. As an example, interparticle distances, and thus molecular length, can be optically measured using metal nanoparticles linked by the entity for which distance needs to be measured. This plasmon molecular ruler can be used to further analyse the geometric parameters of suitable biological processes [160].

Probe-based sensors require somewhat demanding systems for signal discrimination and imaging. The analysis of the plasmon resonance spectra of single nanoparticles usually requires a dark field optical microscopy setup.

Further integrated plasmon resonance sensors can be obtained using metal thin films in place of independent nanoparticles. In this direction, a complete sensor can be fabricated by coupling a thin layer of gold or silver with an emitter and a receptor. Due to the different momentums of surface plasmon waves and light, the coupling of the electromagnetic waves with the surface plasmons on a metal thin film requires a special configuration. There are three coupling designs predominantly used: (a) the coupling using a prism (ATR method);

(b) coupling using an optical waveguide and (c) coupling using a grating coupler [161, 162, 163, 164].

In these devices, surface plasmon propagation constants strongly depend on the wavelength, showing a propagation maximum, that is a light absorption maximum, at a given resonance wavelength. The field of the surface plasmon waves generated at the metal/dielectric interface strongly decays into both media. Therefore, the resonance wavelengths, like on surface plasmons generated in nanoparticles, are highly sensitive to the very localized dielectric medium neighbouring the metal surface. Thus, changes on this dielectric constant, such as those associated with the presence of an analyte, can be precisely detected by measuring the intensity, the coupling angle or the wavelength of resonance coupling of the surface plasmon wave and light. Resonance peak positions not only are used to sense the presence of analytes but can be used to determine distances and even analyse biological processes thanks to the sensitivity of the plasmon resonance to interparticle distances [165, 166].

The very intense fields created at the resonance frequencies in the close vicinity of the metal nanostructures [167, 168, 169] can also be used as enhancers of the spectroscopic signatures of analytes attached or lying close to the metal surface [170, 171, 172]. Surface-enhanced Raman spectroscopy uses this extreme field enrichment to improve Raman sensitivity up to 10^{11} times [173, 174, 175]. This technique, which can be integrated using optic fibres [176] and potential in vivo usage [177, 178], finds its most intriguing feature on its potentially huge spatial resolution. The very localized enhancement obtained at the metal surfaces allows for the simultaneous topographic and spectroscopic analysis of the sample with a resolution at the nanometer scale when coupling the surface-enhanced Raman spectroscopy with an AFM provided with gold- or silver-coated tips [179]. So, the most interesting feature is its potential spatial resolution. In this direction, the coupling of the surface-enhanced Raman spectroscopy with an AFM using metal tips allows the simultaneous topographic and spectroscopic analysis of the sample [180].

5.8 Nanosensors Based on Mechanical Resonances: Influence of Small Mass Changes onto Nanostructures

At the nanoscale, small mechanical forces are involved which is a challenge for using them as transduction elements in a device [181]. But, nowadays, they are used in promising mechanical devices as they are quite sensitive to very small mass changes. For it, mechanical resonators offer a very promising standard alternative although it requires aligned and free-standing active elements at the nanoscale that are, at the present technology level, not straightforward or easy to obtain or to process, mainly due to the residual stress controls. Anyway, among many possible nanostructures, small cantilevers, which monitor the resonant frequency of the cantilever, are one of the most used sensitive mass detectors.

The theoretical mass sensitivity ($\delta m/\delta f$) of a rectangular cantilever can be calculated as

$$\Delta m/\delta f(kg/Hz) \approx 0.208 \,(k/f_0^3), \tag{5.24}$$

assuming that the spring constant k remains constant after the mass change and that the mass is evenly distributed on the cantilever. f_0 is the cantilever's resonant frequency and δf is the frequency shift of the cantilever. f_0 depends on the viscous medium in which it is vibrating due to viscous damping of the cantilever, and in vacuum f_0 will be equal to

$$f_{\text{vac}} = 0.162\sqrt{E/\rho}(w/l^2), \tag{5.25}$$

where ρ is the mass density of the cantilever material, E the Young's modulus and l and w the length and width of the cantilever.

Therefore, mass sensitivity increases as the resonant frequency increases too [182]. It depends inversely on the size. For a cantilever with a width, height and length of 1, 2 and 50 μm, respectively, $\delta m/\delta f$ is approximately 10–15 g/Hz. This equation also demonstrates that by decreasing the dimensions even further the mass sensor could theoretically detect single molecules and, of course, large proteins [183].

Normally, for a micron range size cantilever, the movement is detected by optical techniques where a laser is focused on and reflected from the cantilever surface. However, as the cantilever dimensions are decreased to nanometer scale, this method becomes difficult to apply and new readout techniques have been developed. Typically, the readout from nanometer-sized cantilevers has been rather complicated and the operation of the mass sensor has been limited to vacuum [184]. It is well known that due to the damping mechanism introduced by the air molecules at atmospheric pressure even more than two orders of magnitude in the Q-factor can exist.

New alternatives have presented a nanometer-sized cantilever with integrated capacitive readout, which offers a simple readout scheme that can be operated at atmospheric pressure and vacuum [185, 186]. In this option, by monolithic integration of the nanocantilever and CMOS circuitry, it has been shown that it is possible to increase both the functionality and the resolution of the sensor, allowing operation in more viscous media or functionalities like resonant frequency tracking and Q-factor enhancement. In this technological frame, these mass nanosensors are open for new applications that require the measurement of particle fluxes in high vacuum – i.e. an atom lithography system – or a high-sensitive gas sensor. Likewise, applications that need a high spatial resolution can also be obtained, i.e. the localized measurement of particle fluxes, something that is impossible with quartz microbalances [187, 188, 189].

As alternatives to these readout methods to overcome the difficulties inherent in the optical detection for very small cantilevers, AFM-based methods have been proposed on a cantilever actuated electrostatically by means of a driver electrode placed closely parallel to the cantilever. For it, the AFM is operated in a dynamic non-contact mode using oscillation amplitudes corresponding to a low-force regime. The dependence of the static cantilever deflection on DC voltage and of the oscillation amplitude on the frequency of the AC voltage is measured and the results are fitted by a simple non-linear electromechanical model [190]. Even though this method works well and is very precise, the resulting system complexity makes it difficult to use in portable low-cost devices. For these reasons, from a practical point of view, the straightforward measurement of the cantilever deflection by means of an electrical transducer integrated on the cantilever becomes more plausible and realistic but it needs the integration compatibility with on-chip electronics fabrication. It can be obtained if the cantilever deflection is measured by means of a piezoresistor integrated in the cantilever [191]. In fact, the use of cantilevers with submicrometer thickness and width in the micrometer range gives the possibility to have small spring constant and high force sensitivity that are the requirements for detecting small forces like those involved in molecular recognition experiments [192, 193, 194, 195]. A clear example of these options is given by the detection of antibody–antigen forces. For example, cantilevers with 2 µm thickness have been reported to have a spring constant $k \approx 4$ N/m. However, the forces to be measured for molecular detection are in the range of tens to hundreds of piconewton. Then, to obtain a deflection of 1 nm under a 10 pN load, the cantilever must have a small spring constant of $k \approx 0.01$ N/m. This spring constant can be achieved with a silicon microcantilever with small spring constants and high force sensitivity, which as we shall see requires transverse cantilever dimensions in the submicrometer range, which should be submicron in thickness and about 1 µm in width [196, 197].

Thus, for improving the system performances, it has been proposed by several groups to use a U-shaped structure for the cantilevers [198, 199] in which the piezoresistor uses the complete surface of the cantilever. This shape allows the minimization of the cantilever dimensions, especially its width. If $L >> w$, where L is the length of the cantilever and w the width of each leg, the U-shaped cantilever will behave as two identical separated rectangular cantilevers corresponding to the two legs. The classical beam theory for small deformations can be applied to calculate the stress in the rectangular cantilever for a given perpendicular force F applied to the tip. The stress can be used to calculate the output signal ΔV when the piezoresistor is connected in a half Wheatstone bridge with an identical reference cantilever resistor. Using these procedures, it has been probed that it is possible to fabricate cantilevers with lengths between 60 and 200 µm and leg widths between 2 and 10 µm with spring constants ranging from 1.02 to 0.006 N/m and the force sensitivities from 2.4 to 11.8 µV/nN that are given a resolution, within the parameter ranges used, of about 10 pN.

5.9 Summary

The improved knowledge and control of the transduction mechanisms at the nanoscale level has enabled and enhanced the ideas, designs and developments of nanosensors. There are many examples that have been reported during the last decades that cover all the fields of physical, chemical and biochemical areas. Nevertheless, advancements have been more relevant in some sensor types. Among them, some examples have been highlighted as representative of the nanoscience and nanotechnology contributions to the sensor field.

So, controlled performances of surface/volume-based sensors using a single nanocrystal as conductometric or transistor channel device have already been achieved and these sensors are applied in the chemical and biochemical fields using inorganic and organic materials. Surface properties control and their functionalizations become one of the most outstanding and challenging features for future developments.

On the other hand, the interaction of nanomaterials with photons of different energies at the nanoscale level is being used as one of the best scenarios for charge separation, charge collection and electrical or optical confinements. Likewise, the increase in some properties such as plasmon resonances at the nanoscale level has given rise to many options for new nanosensor applications based on the enhanced Raman mechanism of fundamental importance for sensing analytes.

Furthermore, mechanical resonances-based nanosensors have also been reported to bring a paramount importance for new highly mass-sensitive sensor.

There are many other options to take advantage of the mechanisms and properties at the nanoscale level, and in the immediate future their associated feasibility challenge will be solved on the basis of the nanotechnology advancements and nanoscience understandings.

References

1. http://www.nano.gov
2. W. Göpel, J. Hesse, and J.N. Zemel. *Sensor: A comprehensive survey*. VCH, Weinheim, Germany, 1991.
3. A.P. Alivisatos, *Science*, 271, 933–937 (1996).
4. K. Kalyanasundaram and M. Grätzel, *Curr Sci,* 66, 706–715 (1994).
5. W.J. Aston, *Biosens Bioelectron*, 7, 161–163 (1992).
6. S.P. Mohanty and E. Kougianos, *IEEE Potentials*, 25 (2), 35–40 (2006).
7. D. Erickson, S. Mandal, A.H.J. Yang, and B. Cordovez, *Microfluidics and Nanofluidics*, 4, 33–52 (2008).
8. M. Epifani, R. Diaz, J. Arbiol, E. Comini, N. Sergent, T. Pagnier, P. Siciliano, G. Faglia, and J.R. Morante, *Advanced Funct. Mater.* 16, 1488–1498 (2006).
9. M. Epifani, J. Arbiol, E. Pellicer, and J.R. Morante, *Chem. Mater.*, 19 (20), 4919–4924 (2007).
10. A.-H. Lu, E.L. Salabas, and F. Schüth, *Angew. Chem. Int. Ed.*, 46, 1222–1244 (2007).

11. X.-M. Lin and A.C.S. Samia, *J. Magn. Magn. Mater.*, 305, 100–109 (2006).
12. A. Cabot, A. Diéguez, A. Romano-Rodríguez, J.R. Morante, and N. Barsan, *Sensors Actuat. B*, 79, 98–106 (2001).
13. M.C. Daniel and D. Astruc, *Chem. Rev.,* 104, 293–346 (2004).
14. G. Schmid, *Chem. Rev.,* 92, 1709–1727 (1992).
15. A. Dieguez, A. Vila, A. Cabot, A. Romano-Rodriguez, J.R. Morante, J. Kappler, N. Barsan, U. Weimar, and W.Gopel, *Sensors Actuat. B-Chem.*, 68, 94–99, (2000).
16. J. Puigcorbe, A. Vila, J. Cerda, A. Cirera, I. Gracia, C. Cane, and J.R. Morante, *Sensors Actuat. A*, 97–98, 379–385 (2002).
17. J. Arbiol, Metal additive distribution in $TiO_2$and SnO_2 semiconductor gas sensor nanostructured materials. PhD Thesis Dissertation. University of Barcelona (2001) ISBN84-475-2636-4.
18. M. Epifani, E. Comino, J. Arbiol, E. Pellicer, P. Siciliano, G. Faglia, and J.R. Morante, *J. Phys. Chem*, 111 (37), 13967–13971 (2007).
19. I.R. Peterson, *J. Phys. D,* 23, 379–395 (1990).
20. P. Yang and F. Kim, *Chemphyschem,* 3, 503–506 (2002).
21. L. Vayssieres, *Adv. Mater.*, 15 (5), 464–466 (2003).
22. L. Vayssieres and M. Graetzel, *Angew. Chem. Int. Ed.*, 43, 3666–3670 (2004).
23. L. Vayssieres, *Appl. Phys. A*, 89 (1), 1–8 (2007).
24. E. Rossinyol, A. Prim, E. Pellicer, J. Rodríguez, F. Peiró, A. Cornet, J.R. Morante, B.Z. Tian, T. Bo, and D. Zhao, *Sens Actuat. B,* 126, 18–23 (2007).
25. A. Prim, E. Pellicer, E. Rossinyol, F. Peiró, A. Cornet, and J.R. Morante, *Adv. Funct. Mater.,* 17 (15), 2957–2963 (2007).
26. E. Rossinyol, A. Prim, E. Pellicer, J. Arbiol, F. Hernández- Ramírez, F. Peiró, A. Cornet, J.R. Morante, L.A. Solovyov, T. Bozhi, T. Bo, and D. Zhao, *Adv. Funct. Mater.,* 17, 1801–1806 (2007).
27. E. Rossinyol, E. Pellicer, A. Prim, S. Estrade, J. Arbiol, F. Peiró, A. Cornet, and J.R. Morante, *J. Nanoparticle Res.*, 10, 369–375 (2008).
28. A.I. Hochbaum, R. Chen, R. Díaz, W. Liang, E.. Garnett, M.G. Najarian, A. Majumdar, and P. Yang, *Nature*, 451, 163–167 (2008).
29. J. Arbiol, A. Cirera, F. Peiro, A. Cornet, J.R. Morante, J.J Delgado, and J.J Calvino, *Appl. Phys. Lett.*, 80, 329–31 (2002).
30. Y.S. Kim, S.C. Ha, K. Kim, H. Yang, S.Y Choi, Y.T Kim, J.T. Park, C.H. Lee, J. Choi, J. Paek, and K. Lee,. *Appl. Phys. Lett.,* 86, 213105 (2005).
31. Y. Cui, Q. Wei, H. Park, and C.M. Lieber, *Science,* 293, 1289–1292 (2001).
32. F. Hernández-Ramirez, J.D. Prades, A. Tarancon, S. Barth, O. Casals, R. Jiménez-Diaz, E. Pellicer, J. Rodriguez, M.A. Juli, A. Romano-Rodríguez, J.R. Morante, S. Mathur, A. Helwig, J. Spannhake, and G. Muller, *Nanotechnology,* 18, 495501–06 (2007).
33. E. Comini, G. Faglia, G. Sberveglieri, Z. Pan, and Z.L. Wang,. *Appl. Phys. Lett.*, 81, 1869 (2002).
34. S. Chopra, A. Pham, J. Gaillard, A. Parker, and A.M. Rao, *Appl. Phys. Lett.,* 80, 4632 (2002).
35. G.K. Mor, O.K. Varghese, C.A. Grimes, M.A. Carvalho, and M.V. Pishko, *J. Mater Res. ,* 19, 628–634 (2004).
36. Z.W. Pan, Z.R. Dai, and Z.L. Wang, *Science,* 291, 1947–1949 (2001).
37. M. Borgstrom, G. Immink, B. Ketelaars, R. Algra, and E. Bakkers, *Nature Nanotechnol.,* 2, 541–544 (2007).
38. R.S. Wagner and W.C. Ellis, *Appl. Phys. Lett.,* 4, 89–90 (1964).
39. E. Bauer and J. H. van der Merwe, *Phys. Rev. B*, 33, 3657–3671 (1986).
40. Y. Cui, Q. Wei, H. Park, and C. Lieber, *Science*, 293, 1289 (2001).
41. J. Arbiol, B. Kalache, P. Rocai Cabarrocas, J. R. Morante, and A Fontcuberta i Morral, *Nanotechnology,* 18, 305606–14 (2007).
42. A. Fontcuberta i Morral, C. Colombo, G. Abstreiteer, J. Arbiol, and J.R. Morante, *Appl. Phys. Lett.,* 92, 063112 (2008).

43. A.L. Giermann and C.V. Thompson, *Appl. Phys. Lett.*, 86, 121903 (2005).
44. W.K. Choi, T.H. Liew, H.G. Chew, F. Zheng, C.V. Thompson, Y. Wang, M.H. Hong, X. D. Wang, L. Li, and J. Yun, *Small*, 4, 330–333 (2008).
45. H.A. Pohl, *Dielectrophoresis: the behaviour of neutral matter in nonuniform electric field*, Cambridge University Press, Cambridge, UK (1978)
46. P.J. Burke, Encyclopedia of Nanoscience and Nanotechnology, In: H.S. Nalwa (Ed.) Vol 6 American Scientific Publishers, Los Angeles, CA 2004, pp 623–641.
47. Q. Wan, E. Dattoli, and W. Lu, *Small*, 4 (2008).
48. B. Tian, X. Zheng, T.J. Kempa, Y. Fang, N. Yu, G. Yu, J. Huang, and C.M. Lieber, *Nature*, 449, 885–890 (2007).
49. Z. Zhong, C. Yang, and C.M. Lieber, *Nanosilicon*, 176–216. (Ed. V. Kumar, Elsevier (2008)).
50. A. Vomiero, M. Ferroni, E. Comini, G. Faglia, and G. Sberveglieri, *Nano Lett.*, 7, 3553–3558 (2007).
51. A. Fontcuberta i Morral, D. Spirkoska, J. Arbiol, M. Heigoldt, J.R. Morante, and G. Abstreiter, *Small*, 4 (2008).
52. K.Q. Peng, Y.J. Yan, S.P. Gao, and J. Zhu, *Adv. Mater.*, 14, 1164–1167 (2002).
53. P. Gorostiza, M.A. Kulandainathan, R. Diaz, F. Sanz, P. Allongue, and J.R. Morante, *J. Electrochem. Soc.*, Society, 147, 1026 (2000).
54. P. Gorostiza, P. Allongue, R. Díaz, J.R. Morante, F. Sanz, *J.Phys.Chem. B*, 107, 6454–6461 (2003).
55. A.R. Leach, *Molecular modelling principles & applications.* Addison Wesley Publishing Company, USA (1997).
56. J.D. Prades, A. Cirera, and J.R. Morante, Quantum chemical calculations of surfaces and interfaces of materials, In: V.A. Basluk and P. Ugllengo (Eds.) American Scientific Publisher (2008).
57. J.D. Prades, A. Cirera, and J.R. Morante, *J. Electrochem. Soc.*, 154 (8), H675–H680 (2007).
58. M. Batzill and U. Diebold, *Prog. Surf. Sci.*, 79, 47 (2005).
59. C.N. Xu, J. Tamaki, N. Miura, and N. Yamazoe, *Chem. Lett.*, 1990(3), 441 (1990).
60. C.N. Xu, J. Tamaki, N. Miura, and N. Yamazoe, *Tech. Digest of 9th Sensor Symp.*, Tokyo, Japan, p.95 (1990).
61. C.N. Xu, J. Tamaki, N. Miura, and N. Yamazoe, *Sens. Actuat. B*, 3, 147 (1991).
62. J. Tamaki, Z. Zhang, K. Fujimori, M. Akiyama, T. Harada, N. Miura, and N. Yamazoe, *J. Electrochem. Soc.*, 141, 2208 (1994).
63. Y.- G. Choi, G. Sakai, K. Shimanoe, N. Miura, and N. Yamazoe, *Sens. Actuat. B*, 95, 258, (2003).
64. A. Cabot, J. Arbiol, E. Rossinyol, J.R. Morante, F. Chen, and M. Liu, *Electrochem. Solid State Lett.*, 7 (5), G93–G97 (2004).
65. M.N. Rumyantseva, A. Gaskov, N. Rosman, T. Pagnier, and J.R. Morante, *Chem. Mater.*, 17, 893–901 (2005).
66. A. Cabot, J. Arbiol, A. Cornet, J.R. Morante, F. Chen, and M. Liu, *Thin Solid Film*, 436, 64–69 (2003).
67. W. Gopel and K.D. Schierbaum, *Sens. Actuat. B*, 26, 1–12 (1995).
68. N. Barsan, D. Koziej, and U. Weimar, *Sens. Actuat. B*, 121, 18–35 (2007).
69. J. Jortner and C.N.R. Rao, *Pure Appl. Chem.*, 74, 1489–1783 (2002).
70. M. Law, J. Goldberger, and P. Yang. *Annu. Rev. Mater. Res.*, 34, 83–122 (2004).
71. A. Cabot, A. Diéguez, A. Romano-Rodríguez, J.R. Morante, and N. Barsan, *Sens. Actuat. B*, 79, 98–106, (2001).
72. A. Dieguez, A. Vila, A. Cabot, A. Romano-Rodriguez, J.R. Morante, J. Kappler, N. Barsan, U. Weimar, and W. Gopel, *Sens. Actuat. B-Chem.*, 68, 94–9, (2000).
73. J. Kappler, N. Barsan, U. Weimar, A. Dieguez, J.L. Alay, A. Romano-Rodríguez, J.R. Morante, W. Göpel, and Fresenius, *J. Anal. Chem.*, 361, 110–114 (1998).

74. http://mathforum.org/library/drmath/view/65234.html
75. J. Tamaki, J. Niimi, S. Ogura, and S. Konishi, *Sens. Actuat. B*, 117, 353–358 (2006).
76. J. Tamaki, A. Miyaji, J. Makinodan, S. Ogura, and S. Konishi, *Sens. Actuat. B*, 108, 202–206 (2005).
77. J. Tamaki, Y. Okochi, and S. Konishi, *Electrochemistry*, 74, 159–162 (2006).
78. F. Hernandez-Ramirez, Fabrication strategies and characterization of nanodevices fabricated with focused ion beam techniques. PhD Thesis Dissertation, University of Barcelona (2007).
79. G.J. Li and S. Kawi, *Matter. Lett.*, 34, 99–102 (1998).
80. P.A. Smith, C.D. Nordquist, T.N. Jackson, T.S. Mayer, B.R. Martin, J. Mbindnyo, and T.E. Mallouk, *Chem.-Eur. J.*, 8, 4355 (2002).
81. M.E. Toimil-Morales, E.M. Höhberger, C.H. Schaeflein, R.H. Blick, R. Neumann, and C. Trautmann, *Appl. Phys. Lett.*, 82, 2139 (2003).
82. "Focused ion beam technology, capabilities and applications". FEI Company (2004). Brochure available at (www.feicompany.com)
83. S. Reyntjens and R. Puers, *J. Micromech. Microeng.*, 11, 287–300 (2001).
84. S. Matsui and Y. Ochiai, *Nanotechnology*, 7, 247–258 (1996).
85. G. de Marzi, D. Iacopino, A.J. Quinn, and G. Redmond, *J. Appl. Phys.*, 96, 6 (2004).
86. L. Rotkina, J-F. Lin, and J. P. Bird, *Appl. Phys. Lett.*, 83, 4426 (2003).
87. F. Hernandez-Ramirez, O. Casals, J. Rodríguez, A. Vila, A. Romano-Rodriguez, J.R. Morante, M. Abid, S. Valizadeh, *Mat. Res. Soc., Symp. Proc., J* 5.2 (2005).
88. V. Gopal, V.R. Radmilovic, C. Daraio, S. Jin, P. Yang, and E. Stach, *Nano. Lett.*, 4, 2059 (2004).
89. A. Vila, F. Hernandez-Ramirez, J. Rodriguez, O. Casals, A. Romano-Rodriguez, J.R. Morante, and M. Abid, *Mater. Sci. Eng. C.*, 26, 1063–1066 (2006).
90. M. Law, H. Kind, B. Messe, F. Kim, and Y. Peidong, *Angew. Chem.*, 114, 2511 (2002).
91. F. Hernández-Ramírez, J. Rodríguez, O. Casals, E. Russinyol, A. Vilà, A. Romano-Rodríguez, J.R. Morante, and M. Abid, *Sens. Actuat. B*, 118, 98–203 (2006).
92. F. Hernandez-Ramirez, J.D. Prades, A. Tarancon, S. Barth, O. Casals, R. Jiménez–Diaz, E. Pellicer, J. Rodriguez, M.A. Juli, A. Romano-Rodriguez, J.R. Morante, S. Mathur, A. Helwig, J. Spannhake, and G. Mueller, *Nanotechnology*, 18, 495501–06 (2007).
93. F. Hernández-Ramírez, A. Tarancón, O. Casals, J. Arbiol, A. Romano-Rodríguez, and J.R. Morante, *Sens. Actuat. B*, 121, 30, 3–1 (2007).
94. Z.R. Dai, Z.W. Pan, and Z.L. Wang, *Adv. Funct. Mater.*, 13, 9–24 (2003).
95. R.S. Wagner and W.C. Ellis, *Appl. Phys. Lett.*, 4, 89–90, (1964).
96. Y. Ding, P.X. Gao, and Z.L. Wang, *J.Am. Chem. Soc.*, 126, 2066 (2004).
97. S. Mathur, S. Barth, H. Shen, J.-C. Pyun, and U. Werner, *Small*, 1, 7, 713–717 (2005).
98. S. Lenaerts, M. Honore, G. Huyberechts, J. Roggen, and G. Maes, *Sensor and Actuators B*, 18/19, 478 (1994).
99. A. Cabot, J. Arbiol, E. Rossinyol, J.R. Morante, F.L. Chen, M.L. Liu, *Electrochem. Solid State Lett.*, 7, G93 (2004).
100. M.N. Rumyantseva, A.M. Gaskov, N. Rossman, T. Pagnier, J.R. Morante, *Chem. Mater.*, 17, 893 (2005).
101. D. Li, Y. Wu, L. Shi, P. Yang, and A. Majumdar, *Appl. Phys.Lett.*, 83,14 (2003).
102. C. Yu, Nanomaterials characterization and bio-chemical sensing using microfabricated devices. Thesis Dissertation, University of Texas (2004).
103. S. Mathur, S. Barth, H. Shen, J.C. Pyun, and U. Werner, *Small*, 1, 713 (2005).
104. F. Hernandez-Ramrez, A. Tarancon, O. Casals, E. Pellicer, J. Rodrguez, A. Romano-Rodrguez, J.R. Morante, S. Barth, and S. Mathur, *Phys. Rev. B*, 76, 085429 (2007).
105. G. Decher, *Science*, 277, 1232–1237 (1997).
106. A. Ulman, *An introduction to ultra thin organic films from Langmuir Blodgett to self-assembly*. Academic Press, New York, USA (1991).

107. J. Zhang, Z.L. Wang, J. Liu, S. Chen, and G.Y. Liu, *Self assembled nanostructures*. Kluwer Academic/Plenum Publishing, New York, USA (2003).
108. M. La Barbera, *Science*, 289, 1882 (2000).
109. C.M. Niemeyer and C.A. Mirkin, *Nanobiotechnology: Concepts, applications and perspectives*. Wiley-VCH, Dortmund, Germany, (2004).
110. N. Wickramasinghe, S. Choudhary, and E. Geisler, *Int. J. Biomed. Eng. Technol.*, 1, 41–58 (2007).
111. S. Vikas and C. Pundir, *Sens. Trans.*, 82, 1405–1417 (2007).
112. D. Fraser, An introduction to in vivo biosensing: progress and problems, In: Fraser, D. (Ed.), *Biosensors in the body, continuous in vivo monitoring*. Wiley, London, 10–56 (1997).
113. M. Pumera, S. Sanchez, I. Ichinose, and J. Tang, *Sens. Actuat. B*, 123, 1195–1205 (2007).
114. X.-J. Huanga and Y.K. Choi, *Sens. Actuat. B*, 122, 659–671 (2007).
115. V. Chukharev, T. Vuorinen, A. Efimov, N.V. Tkachenko, M. Kimura, S. Fukuzumi, H. Imahori, and H. Lemmetyinen, *Langmuir*, 21, 6385–6391 (2005).
116. P. Avouris and J. Chen, *Mater. Today*, 9, 10, 46–54 (2006).
117. D.J. Sirbuly, M. Law, H.Q. Yan, et al., *J. Phys. Chem. B*, 109, 32, 15190–15213, (2005).
118. H.E. Maes, C. Claeys, R. Mertens, et al., *Adv. Eng. Mater.*, 3, 10781–787 (2001).
119. E. Monroy, F. Omnes, and F. Calle, *Semicond. Sci. Technol.*, 18, R33–R51 (2003).
120. A. Rose, *Concepts in photoconductivity and allied problems*. Interscience Publishers: New York (1963).
121. R.H. Bube, *Photoelectronic properties of semiconductors*. Cambridge University Press: Cambridge (1992).
122. S.M. Sze, *"Physics of semiconductor devices"*. John Wiley & Sons, Inc: New York (1981).
123. H. Yoshikawa and S. Adachi, *Jpn, J. Appl. Phys.*, 36, 10, 6237–6243, (1997).
124. S. Kumar, S. Rajaraman, R.A. Gerhardt, Z.L. Wang, and P.J. Hesketh, *Electrochim. Acta*, 51, 943–951, (2005).
125. J. Suehiro, N. Nakagawa, S. Hidaka, M. Ueda, K. Imasaka, M. Higashihata, T. Okada, and M. Hara, *Nanotechnology*, 17, 2567–2573 (2006).
126. This resolution value was taken as a rough approximation to the minimal feature of current lithography techniques.
127. H. Kind, H. Yan, B. Messer, M. Law, and P. Yang, *Adv. Mater.* (Weinheim, Germany) 14 (2), 158–160 (2002).
128. C. Soci, A. Zhang, B. Xiang, S.A. Dayeh, D.P.R. Aplin, J. Park, X.Y. Bao, Y.H. Lo, and D. Wang, *Nano Lett.*, 7 (4), 1003–1009, (2007).
129. X.G. Zheng, Q. Sh. Li, J.P. Zhao, D. Chen, B. Zhao, Y.J. Yang, L. Ch. Zhang, *Appl. Surf. Sci.*, 253, 2264–2267 (2006).
130. S. Mathur, S. Barth, H. Shen, J.-C. Pyun, and U. Werner, *Small*, 1, 77, 713–717 (2005).
131. J.S. Jie, W.J. Zhang, Y. Jiang, X.M. Meng, Y.Q. Li, and S.T. Lee, *Nano Lett.*, 6, 9, 1887–1892 (2006).
132. Z.Y. Fan, P.C. Chang, J.G. Lu, E.C. Walter, R.M. Penner, C.H. Lin, and H.P. Lee, *Appl. Phys. Lett.*, 85, 25, 6128–6130 (2004).
133. Y.W. Heo, B.S. Kang, L.C. Tien, D.P. Norton, F. Ren, J.R. La Roche, and S.J. Pearton, *Appl. Phys. A: Mater. Sci. Process.*, 80, 3, 497–499 (2005).
134. S.A. Studenikin, N. Golego, and M. Cocivera, *J. Appl. Phys.*, 87, 5, 2413–2421 (2000).
135. C.S. Lao, M.-C. Park, Q. Kuang, Y. Deng, A.K. Sood, D.L. Polla, Z.L. Wang, *J. Am. Chem. Soc.*, 129 (40), 12096–12097 (2007).
136. P.-C. Chang, C.-J. Chien, D. Stichtenoth, C. Ronning, and J.G. Lu, *Appl. Phys. Lett.*, 90, 113101 (3 pages) (2007).
137. Z.Y. Fan, D.W. Wang, P.C. Chang, W.Y. Tseng, J.G. Lu, *Appl. Phys. Lett.*, 85, 5923 (2004).

138. P. -C. Chang, Z. Fan, D. Wang, W.. - Y. Tseng, W. - A. Chiou, J. Hong, J.G. Lu, *Chem. Mater.*, 16, 5133–5137 (2004).
139. P. Chang, Z. Fan, C. Chien, D. Stichtenoth, C. Ronning, J.G. Lu, *Appl. Phys. Lett.*, 89, 133113 (2006).
140. L. Hu and G. Chen, *Nano Lett.* 7, 11, 3249–3252 (2007).
141. A. Ohtomo and A. Tsukazaki, *Semicond. Sci. Technol.*, 20, S1–S12 (2005).
142. Y. Liu, C.R. Gorla, S. Liang, N. Emanetoglu, Y. Lu, H. Shen, and M. Wraback, *J. Electron. Mater.*, 29, 69–74 (2000).
143. K. Q. Peng, Z.P. Huang, and J. Zhu, *Adv. Mater.*, 16, 73–76 (2004).
144. Chen Yang, Zhaohui Zhong, and Charles M. Lieber, 310, 1304–1307 (2005).
145. L.J. Lauhon, M.S. Gudiksen, D.Wang, and C.M. Lieber, *Nature*, 420, 57–61 (2002).
146. Y.-L. Chueh, L.-J. Chou, and Z.L. Wang, *Angew. Chem. Int. Ed.*, 45, 7773–7778 (2006).
147. B. Pradhan, S.K. Batabyal, and A.J. Pal, *Appl. Phys. Lett.*, 89, 233109,(2006).
148. M. Law, L.E. Greene, J.C. Johnson, R. Saykally, and P. Yang, *Nat. Mat.*, 4, 455 (2005).
149. X.D. Wang, J.H. Song, J. Liu, and Z.L. Wang, *Science*, 316, 102 (2007).
150. M. Gratzel, *Nature*, 414, 338 (2001), and B. O'Regan, M. Grätzel, *Nature*, 353, 737 (1991).
151. W.U. Huynh, J.J. Dittmer, and A.P. Alivisatos, *Science*, 295, 242 (2002).
152. L.E. Greene, M. Law, B.D. Yuhas, and P.D. Yang (2007). *J. Phys. Chem. Lett.*, 111,18451 (2007).
153. B. Tian, X. Zheng, T.J. Kempa, Y. Fang, N. Yu, G. Yu, J. Huang, and C.M. Liebre, *Nature*, 449, 885–889 (2007).
154. Chanda Ranjit Yonzon, Douglas A. Stuart, Xiaoyu Zhang, Adam D. McFarland, Christy L. Haynes, and Richard P. Van Duyne, *Talanta*, 67, 438–448 (2005).
155. Adam D. McFarland and Richard P. Van Duyne, *Nano Lett.*, 3, 1057 (2003).
156. J.J. Mock, David R. Smith, and Sheldon Schultz, *Nano Lett.*, 3, 485 (2003).
157. T.R. Jensen, M.D. Malinsky, C.L. Haynes, and R.P. Van Duyne, *J. Phys. Chem. B*, 104, 10549–10556 (2000).
158. J.J. Mock, M. Barbic, D.R. Smith, D.A. Schultz, and S. Schultz, *J. Chem. Phys.*, 116, 6755 (2002).
159. C. Sönnichsen, B.M. Reinhard, J. Liphardt, and A.P. Alivisatos, *Nature Biotechnol.*, 23, 741–745 (2005).
160. B.M. Reinhard, S. Sheikholeslami, A. Mastroianni, A.P. Alivisatos, and J. Liphardt, *Proc. Natl. Acad. Sci., USA* 104, 2667–2672 (2007).
161. J. Dostálek, J. Tyroký, J. Homola, E. Brynda, M. Skalský, P. Nekvindová, J. Pirkovác, J. Kvord, and J. Schröfele, *Sens. Actuat. B*: 76, 8–12 (2001).
162. J. Homola, Ivo Koudela b, and Sinclair S. Yee, *Sens. Actuat. B*, 54, 16–24 (1999).
163. J. Homola, S.S. Yee, and G. Gauglitz, *Sens. Actuat. B*, 54, 3–15 (1999).
164. J. Homola, *Anal. Bioanal. Chem.*, 377, 528–539 (2003) .
165. Carsten Sönnichsen, Björn M Reinhard, Jan Liphardt, and A Paul Alivisatos, *Nat. Biotechnol.*, 23, 741–745 (2005).
166. Björn M. Reinhard, Sassan Sheikholeslami, Alexander Mastroianni, A.P. Alivisatos, and Jan Liphardt, Use of Plasmon Rulers to Reveal the Dynamics of DNA Bending and Cleavage by Single EcoRV Restriction Enzymes, *Proc. Natl. Acad. Sci. USA* 104, 2667–2672 (2007).
167. E. Hao and G.C. Schatza, *J. Chem. Phys.*, 120, 1 (2004).
168. H. Xu, J. Aizpurua, M. Kall, and P. Apell, *Phys. Rev. E*, 62, 4318 (2000).
169. D.A. Genov, A.K. Sarychev, V.M. Shalaev, and Alexander Wei Resonant, *Nano Lett.*, 4, 1 (2004).
170. C.L. Haynes, C.R. Yonzon, X. Zhang, and R.P. Van Duyne, *J. Raman Spectrosc.*, 36, 471–484 (2005).
171. Z. Zhul, T. Zhu, and Z. Liu, *Nanotechnology*, 15, 357–364 (2004).
172. Zhong-Qun Tian, Bin Ren, and De-Yin Wu, *J. Phys. Chem. B*,, 106, 37 (2002).

173. Martin Moskovits, *J. Raman Spectrosc.*, 36, 485–496,(2005).
174. Katrin Kneipp, Yang Wang, Harald Kneipp, Lev T. Perelman, Irving Itzkan, Ramachandra R. Dasari, and Michael S. Feld, *Phys. Rev. Lett.*,, 78, 1667 (1997).
175. Shuming Nie and Steven R. Emory, *Science*,, 275, 1102 (1997).
176. David L. Stokes and Tuan Vo-Dinh, *Sens. Actuat. B: Chem.*, 69, 28–36 (2000).
177. Chanda Ranjit Yonzon, Christy L. Haynes, Xiaoyu Zhang, Joseph T. Walsh, Jr., and Richard P. Van Duyne, *Anal. Chem.*, 76, 78–85 (2004).
178. A. Stuart, Jonathan M. Yuen, Nilam Shah, Olga Lyandres, Chanda R. Yonzon, Matthew R. Glucksberg, Joseph T. Walsh, and Richard P. Van Duyne, *Anal. Chem.*, 78, 7211–7215 (2006).
179. Raoul M. Stöckle, Yung Doug Suh, Volker Deckert1, and Renato Zenobi, *Chem. Phys. Lett.*, 318, 131–136 (2000).
180. Raoul M. Stöckle, Yung Doug Suh, Volker Deckert1, and Renato Zenobi, *Chem. Phys. Lett.*, 318, 131–136 (2000).
181. V. Sazonova, Y. Yaish, H. Ustunel, D. Roundy, T.A. Arias, P.L. McEuen, *Nature*, 431, 284–287 (2004).
182. G. Abadal, Z.J. Davis, B. Helbo, X. Borrisé, R. Ruiz, A. Boisen, F. Campabadal, J. Esteve, E. Figueras, F. Pérez-Muranso, and N. Barniol, *Nanotechnology*, 12, 1–5 (2001).
183. J. Yang, T. Ono, and M. Esashi, *Sens. Actuat. B*, 82, 102–107,(2000).
184. A.N. Cleland and M.L. Roukes, *Appl. Phys. Lett.*, 69, 2653–2655 (1996).
185. Z.J. Davis, G. Abadal, B. Helbo, O. Hansen, F. Campabadal, F. Pérez-Murano, J. Esteve, E. Figueras, J. Verd, N. Barniol, and A. Boisen, *Sens. Actuat. A*, 105, 311–319 (2003).
186. A. Boisen, K. Birkelund, O. Hansen, and F. Grey, *J. Vac. Sci. Technol. B*, 16, 2977–2981 (1998).
187. P. Engels, S. Salewski, H. Levsen, K. Sengstock and W. Ertmer, *Appl. Phys. B*, 69, 407–412 (1999).
188. A.S. Bell, B. Brezger, U. Drodofsky, S. Nowak, T. Pfau, J. Stuhler,T.H. Schulze, and J. Mlynek, *Surf. Sci.*, 433–435, 40–47 (1999).
189. Z.J. Davis, G. Abadal, O. Kuhn, O. Hansen, F. Grey, and A. Boisen, *J. Vac. Sci. Technol. B*, 18, 612–616 (2000).
190. G. Abadala, Z.J. Davis, X. Borris!e, O. Hansen, A. Boisen, N. Barniol, F. P!erez-Murano, and F. Serra, *Ultramicroscopy*, 97,127–133 (2003).
191. C. Hagleitner, A. Hierlemann, D. Lange, A. Kummer, N. Kerness, O. Brand, and H. Baltes, *Nature*, 414, 293–296 (2001).
192. G.U. Lee, L.A. Chrisey, and R.J. Colton, *Science*, 266, 771–773 (1994).
193. M. Rief, M. Gautel, F. Oesterhelt, J.M. Fernandez, and H.E. Gaub, *Science*, 276, 1109 112 (1997).
194. J. Fritz, M.K. Baller, H.P. Lang, H. Rothuizen, P.Vettiger, E. Meyer, H.-J. Guntherodt, C.H. Gerber, and J.K. Gimzewski, *Science*, 288, 316–318 (2000).
195. F. Oesterhelt, D. Oesterhelt, M. Pfeiffer, A. Engel, H.E. Gaub, and D.J. Muller, *Science*, 288,143–146 (2000).
196. J.A. Harley, and T.W. Kenny, *Appl. Phys. Lett.*, 75, 289–291 (1999).
197. E.L. Florin, V.T. Moy, and H.E. Gaub, *Science*, 264, 415–417 (1994).
198. G. Villanueva, J. Montserrat, F.P_erez-Murano, G. Rius, and J. Bausells, *Microelectr. Eng.*, 73–74, 480–486 (2004).
199. P.A. Rasmussen, J. Thaysen, O. Hansen,, S.C. Eriksen, and A. Boisen, *Ultramicroscopy*, 97, 371–376 (2003).

Portable microsensors based on individual SnO$_2$ nanowires

F Hernandez-Ramirez[1,2,6]**, J D Prades**[1]**, A Tarancon**[1]**, S Barth**[3,4]**,
O Casals**[1]**, R Jiménez–Diaz**[1]**, E Pellicer**[1]**, J Rodriguez**[1]**, M A Juli**[1,2]**,
A Romano-Rodriguez**[1]**, J R Morante**[1]**, S Mathur**[3,4]**, A Helwig**[5]**,
J Spannhake**[5] **and G Mueller**[5]

[1] EME/IN²UB Departament d'Electrònica, Universitat de Barcelona, C/Martí i Franquès 1,
E-08028 Barcelona, Spain
[2] NTEC106 S.L., C/Mare de Déu dels Desemparats 12, E-08903 L'Hospitalet de Llobregat,
Spain
[3] Leibniz Institute of New Materials, Department of Nanocrystalline Materials and Thin Film
Systems, D-66123 Saarbruecken, Germany
[4] Department of Chemistry, Wuerzburg University, D-97074 Wuerzburg, Germany
[5] Department of Sensors, Electronics and Systems Integration, EADS Innovation Works,
D-81663, Muenchen, Germany

E-mail: fhernandezra@gmail.com

Abstract
Individual SnO$_2$ nanowires were integrated in suspended
micromembrane-based bottom-up devices. Electrical contacts between the
nanowires and the electrodes were achieved with the help of electron- and
ion-beam-assisted direct-write nanolithography processes. The stability of
these nanomaterials was evaluated as function of time and applied current,
showing that stable and reliable devices were obtained. Furthermore, the
possibility of modulating their temperature using the integrated microheater
placed in the membrane was also demonstrated, enabling these devices to be
used in gas sensing procedures. We present a methodology and general
strategy for the fabrication and characterization of portable and reliable
nanowire-based devices.

S Supplementary data are available from stacks.iop.org/Nano/18/495501

(Some figures in this article are in colour only in the electronic version)

1. Introduction

One-dimensional (1D) materials, such as metal oxide
nanowires, have attracted considerable attention because
of their potential applications in electronic devices [1].
Although much effort has been devoted to reaching a better
understanding of their novel and fundamental properties,
fabricated devices based on single 1D materials are still
scarce due to the difficulties related to their manipulation
and characterization [2]. Furthermore, the high cost of such
devices is still one important limitation to their industrial
application [3]. The combination of individual nanowires

and micromembranes with integrated heaters is one of the
most promising approaches for obtaining portable devices for
gas sensing, since their working temperature can be easily
modulated. To the best of our knowledge, only a few attempts
to use this fabrication methodology have been reported in
the literature [4, 5]. On the other hand, some challenging
issues like the electrical stability of the final devices based on
single nanowires should also be solved prior to their large-scale
application.

In this work, the integration of individual SnO$_2$ nanowires
with suspended micromembranes is presented. These
nanowires were attached to the microelectrodes by dual-
beam focused ion beam (FIB) nanolithography techniques,
following a process explained elsewhere [6]. Stable and

---

[6] Author to whom any correspondence should be addressed.

F Hernandez-Ramirez *et al*
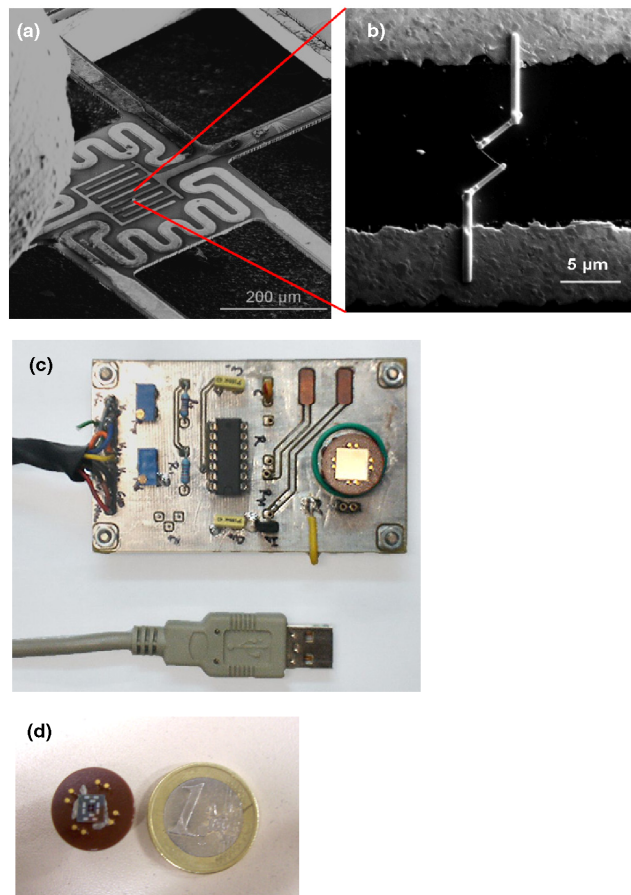
Figure 1. (a) SEM image of one suspended micromembrane with one integrated heater. The microneedle used during the nanolithography process to introduce the gas precursor inside the FIB chamber can be observed in the left part of the image. (b) A SnO_2 nanowire electrically contacted to the platinum microelectrodes. Dimensions: $L = 2.1$ μm (length) and $R = 35 \pm 5$ nm (radius). (c) Experimental set-up including the electronic circuit where all the measurements were performed next to its USB connector. (d) Micromembrane mounted on a TO8 placed next to a 1 Euro coin.

reliable devices were obtained and electrically characterized using an electronic circuit specially designed to avoid irreversible damage to both the nanowires and the FIB contacts by uncontrolled current fluctuations. The possibility of modulating the temperature of these devices with the help of the microheater integrated in the membranes was also evaluated. Fast and reproducible variations of the electrical resistance were observed as a function of the power applied to the heating system, showing that immediate temperature modulation can be produced in these devices. This capability facilitates their use in gas sensing procedures, where high temperatures are usually required. In this work, the electrical response of some of these devices to different gas species was monitored, demonstrating their feasibility as portable microsensors. The fabrication and measuring methodology presented here can be easily extended to other nanomaterials of interest.

2. Experimental section and results

Individual SnO_2 nanowires synthesized by chemical vapour deposition of a molecular precursor $[Sn(O^tBu)_4]$ [7] were transferred onto suspended micromembranes with one integrated SnO_2:Sb heater and platinum interdigitated microelectrodes (figure 1(a)). Membranes were fabricated using silicon-on-insulator wafers. High resolution TEM images showed single-crystalline nanowires with dislocation-free bodies and a main growth direction of [100] and interplanar spacing in correspondence with the rutile structure of SnO_2 [7]. Nanowires were electrically contacted to platinum microelectrodes using a FEI Dual-Beam Strata 235 FIB instrument equipped with a trimethyl-methylcyclopentadienyl-platinum $((CH_3)_3CH_3C_5H_4Pt)$ injector to deposit platinum [8], following a nanolithography process explained elsewhere (figure 1(b)) [6]. Two-probe dc measurements were performed with the help of an electronic circuit (figure 1(c))

2

J. D. Prades

F Hernandez-Ramirez *et al*

designed to guarantee low current levels and avoid any undesired fluctuation (see supporting information available at stacks.iop.org/Nano/18/495501) [9]. All the experiments were performed in a home-made chamber, where the gas flow was maintained between 50 and 200 ml min^{-1}. Accurate gas mixtures were prepared by combining different gases passed through mass flow controllers.

Figure 1(d) represents the comparison of a 1 Euro coin with an as-prepared microelectronic device to give an impression of the overall dimensions of the system.

Up to ten devices were fabricated using individual SnO$_2$ nanowires with lengths between 2 and 7 μm, and radii between 30 and 70 nm (figure 1(b)), which showed stable and reproducible electrical responses. Depending on the diameter of the nanowires, electrical resistances ranging between a few hundred kiloohms and a few megaohms were estimated. These data were in good correspondence to previously reported two-probe measurements on similar nanowires [6]. No significant degradation of the electrical performance of these devices was observed after 2 weeks of continued operation or after exposure to the laboratory atmosphere for additional 2 weeks, indicating that stable and reliable devices were obtained using the presented nanofabrication methodology. On the contrary, an important and fast degradation of the electrical response was always observed when current values above $I = 100 \mu$A were conducted through such devices. Self-heating effects lead to the destruction of nanowires and modification of the FIB-fabricated contacts. This latter effect can be partially explained by the evaporation of the carbon present in high concentrations (around 70%) in the FIB nanolithography processed contacts, caused by the decomposition of the metal organic precursor [10]. Botman *et al* recently reported that this change in FIB-fabricated platinum stripes is also observed after annealing them at temperatures above $T = 300$ °C, showing how important the local self-heating effects can be when high currents are applied to these nanostructures [11].

The possibility of modulating the device temperature using the integrated heater was also studied. Figure 2(a) shows the variation of the resistance of one nanowire with the power applied to the heater integrated into the membrane, and how the system recovers the initial value after switch off. Nevertheless a slight drift of the resistance baseline is observed when power pulses higher than $P = 90$ mW were applied (nominal temperature at the centre of the micromembrane higher than $T = 200$ °C) (figure 2(b)). The increase of the nanowire resistance tends to disappear after a few minutes without applying pulses, suggesting that this reversible effect could be directly related to uncontrolled modifications of the adsorbed species at the nanowire surface, mainly oxygen and water molecules [12, 13], when working under these experimental conditions.

Although the temperature of these membranes was calibrated as a function of the power dissipated by the heater, accurate estimation of the effective temperature of nanowires is quite difficult, since uncontrolled self-heating effects due to the existence of Schottky barriers and their conduction of charge carriers should always be considered [14]. For this reason, in this work merely dissipated power and nominal temperatures at the centre of the membrane are mentioned. The dynamic response of these devices was fast enough to reach
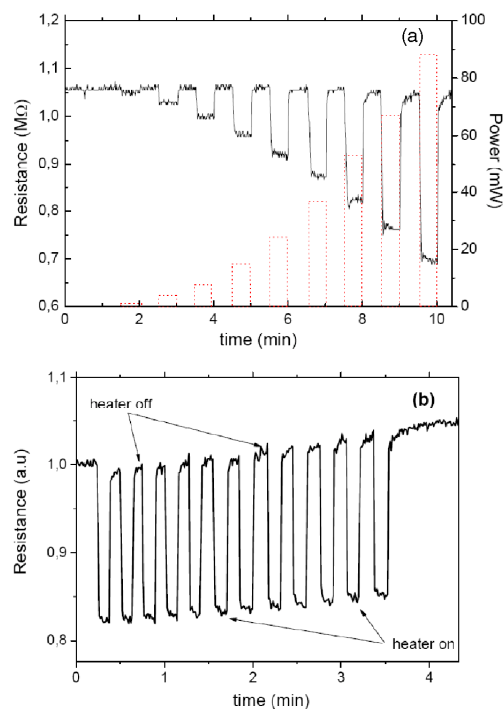
Figure 2. (a) Sensitivity of one SnO$_2$ nanowire ($L = 6.4 \mu$m, $R = 50 \pm 5$ nm) to increasing dissipated power by the heater. This experiment was performed in synthetic air. Increasing power (0–90 mV), directly related to temperature, leads to a decreasing nanowire resistance, demonstrating semiconductor characteristics. At the highest value, a nominal temperature of $T = 210$ °C is obtained in the centre of the micromembrane. (b) The reproducibility of variations in the nanowire resistance is demonstrated by turning the power source on and off several times ($P = 110$ mW, $T = 240$ °C). A small drift in the resistance baseline is observed when powers higher than 90 mW are dissipated in the membrane, probably originating from modification of adsorbed species at the nanowire surface.

complete thermal stabilization after a few seconds of changing the power applied to the heater (figure 2), demonstrating that the optimal working conditions can be easily modulated in a fast and controlled way.

Gas sensing experiments were performed to show the potential of these devices. It is well known that the electrical resistance of SnO$_2$ nanowires drops when changing from an oxygen-rich environment (e.g. synthetic air, SA) to a low pressure oxygen atmosphere (e.g. N$_2$ 99.999%), because of oxygen desorption from the surface of nanowires [12, 13]. Nevertheless, oxygen desorption is a slow process at room temperature with typical characteristic times of several hours [13], justifying why real devices always operate at higher temperatures. The electrical response of one SnO$_2$ nanowire at $T = 25$ °C is shown in figure 3(a), when N$_2$ was introduced into the chamber after signal stabilization in SA for several hours. With the heater switched off, only slight changes in the resistance were observed, while dissipating a power as low as $P = 17$ mW ($T = 60$ °C) these changes were enhanced.

3

F Hernandez-Ramirez *et al*

Figure 4. Response of one SnO_2 nanowire to different CO concentrations (50 and 100 ppm), when the membrane heater is switched on ($P = 56$ mW, $T = 120\,°C$). The dashed line indicates the CO pulses.
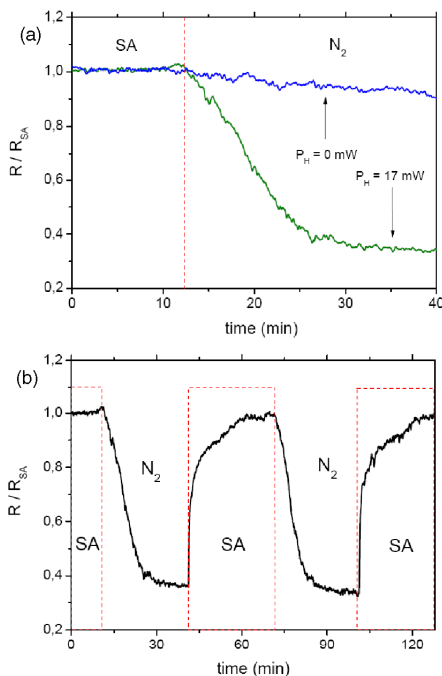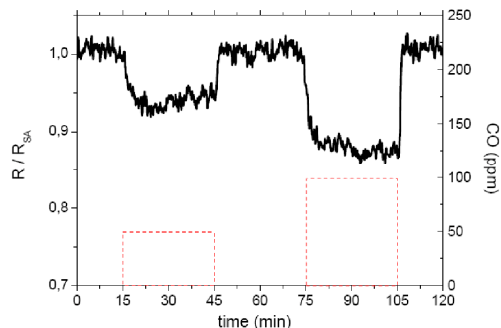

Figure 3. (a) Response of one SnO_2 nanowire to a change from synthetic air to nitrogen atmosphere at room temperature. Although a slight drop in the electrical resistance is observed in N_2 due to desorption of oxygen molecules from the nanowire surface, the dynamic response of this device is too slow for real sensing use when the heater is switched off ($P = 0$ mW). On the contrary, if the heater is activated ($P = 17$ mW, $T = 60\,°C$), a faster response is clearly observed, reaching electrical stabilization after approximately 30 min. The dashed line indicates the synthetic air pulse. (b) Response of one SnO_2 nanowire to synthetic air and nitrogen gas pulses at room temperature, when the membrane heater is switched on ($P = 17$ mW, $T = 60\,°C$). A repetitive drop in the electrical resistance is observed when N_2 is introduced into the chamber, recovering the initial value when a synthetic air flux is applied again. The dashed line indicates the synthetic air pulses.

Oxygen desorption was therefore improved and accelerated by the use of the heater, enabling the use of these devices in sensing applications (figure 3(b)). SnO_2 is usually employed for the detection of pollutant species like carbon monoxide (CO) [13, 15]. In this work we also report the possibility of using these devices for monitoring this gas. CO is a reducing gas which leads to a reversible reduction of SnO_2 resistance. By increasing the power dissipated by the heater ($P = 56$ mW, $T = 120\,°C$), since the optimal operating temperature is close to $T = 300\,°C$ [13], these devices were able to detect and discriminate two different CO concentrations (figure 4). This last result demonstrates that these devices could be used in the future as portable and reliable gas microsensors.

3. Conclusions

Individual SnO_2 nanowires were successfully contacted to microelectrodes on free-standing micromembranes by FIB nanolithography techniques. The electrical characterization was performed using an electronic circuit designed to prevent the destruction of such devices due to uncontrolled current fluctuations. Modulation of the device temperature was shown to be reproducible and fast due to the integrated heater on the micromembranes. The obtained devices showed stable and reproducible responses, demonstrating their potential as gas sensors. The nanofabrication and measuring methodologies presented here are both versatile processes which can be used to study other nanomaterials.

References

[1] Law M, Goldberger J and Yang P 2004 *Annu. Rev. Mater. Res.* **34** 151
[2] Chen Y, Zhu C, Cao M and Wang T 2007 *Nanotechnology* **18** 285502
[3] Wu Y and Yang P 2000 *Appl. Phys. Lett.* **77** 43
[4] Li D, Wu Y, Shi L, Yang P and Majumdar A 2003 *Appl. Phys. Lett.* **83** 14
[5] Yu C 2004 Nanomaterials characterization and bio-chemical sensing using microfabricated devices *Thesis Dissertation* University of Texas
[6] Hernandez-Ramirez F *et al* 2006 *Nanotechnology* **17** 5577
[7] Mathur S, Barth S, Shen H, Pyun J C and Werner U 2005 *Small* **1** 713
[8] Strata D B 235 *Product Data Sheet* FEI Company

4

F Hernandez-Ramirez *et al*

[9] Pescio E, Ridi A and Gliozzi A 2000 *Rev. Sci. Instrum.* **71** 1740

[10] Vilà A, Hernández-Ramírez F, Rodríguez J, Casals O, Romano-Rodríguez A, Morante J R and Abid M 2006 *Mater. Sci. Eng.* C **26** 1063

[11] Botman A, Mulders J J, Weemaes R and Mentink S 2006 *Nanotechnology* **17** 3779

[12] Kolmakov A and Moskovits M 2004 *Annu. Rev. Mater. Res.* **34** 83

[13] Hernandez-Ramirez F, Tarancon A, Casals O, Arbiol J, Romano-Rodriguez A and Morante J R 2006 *Sensors Actuators* B **121** 13

[14] Hernández-Ramírez F, Tarancón A, Casals O, Pellicer E, Rodríguez J, Romano-Rodríguez A, Morante J R, Barth S and Mathur S 2007 *Phys. Rev.* B **76** 085429

[15] Baraton M I and Merhari L 2002 *Mater. Trans.* **42** 1616
Comini E 2006 *Anal. Chim. Acta* **568** 28
Franke M E, Koplin T J and Simon U 2006 *Small* **2** 36

5

Supporting Information

The electrical characterization was performed with an electronic circuit sketched in Scheme A. This circuit can be simultaneously used either as voltage controlled low–current source or as resistance recorder. This study demonstrated that controlling the applied intensity is a crucial point in order to avoid the premature ageing of these devices due to uncontrolled self–heating effects. Similar circuits were previously reported for other applications where stable currents in the picoampere range are required [9].

As a current source, the circuit guarantees a constant current I_m through the resistance R_m, such as the SnO$_2$ nanowire. The current value depends on the regulation voltage V_{in}, the ratio R_1 / R_2 and the value of R as follows:

$$I_m = \frac{V_{in}}{R_1/_{R_2} \cdot R} \tag{1}$$

The operational amplifier A is configured as a voltage adder of the control voltage (V_{in}) and the output voltage of the circuit (V_{out}), ensuring a constant current I_m, independent on R_m variations. This last point assures that the measured nanowire will not be damaged after gas exposure, when significant changes in its electrical resistance are induced. Output voltage V_{out} is directly related to R_m by:

$$V_{out} = R_m \cdot I_m \tag{2}$$

As a resistance recorder, the operational amplifier B is a voltage follower that allows measuring V_{out} without interfering I_m value. Variations of I_m due to fluctuations of V_{in} can be avoided if $R_1 / R_2 \gg 1$. In our case, the selected R_1 / R_2 ratio was high enough to guarantee current fluctuations below 1 % of the I_m value.

Appropriate values of V_{in} and R allow to inject stable currents above I = 10 nA using precision resistors (tolerance below 0.1 %) and low input bias current amplifiers (< 100 pA). Current values up to I = 100 nA were found to preserve the integrity of the measured devices, as explained in the paper.

This circuit was controlled with a low–cost commercial 12–bit AD / DA converter board and a laptop. Voltages close to 5 V were high enough to bias and control the circuit. Therefore, the USB interface of a conventional computer could be used to perform all the presented measurements demonstrating ability to fabricate simple and portable electronics for controlled operation of device based on single nanowires.

Scheme A. Schematic diagram of the low-current source and resistance recording electronics: a constant current (I_m) is supplied to the nanowire (R_m) whose value is voltage-monitored (V_{out}). In the prototype developed for this work, the indicated components were used. With these values and voltages V_{in} < 50 mV, stable currents I_m < 100 nA were obtained.

3.2 Summary of Results

- The development of advanced chemical gas sensing devices based on metal oxides (MOXs) requires the comprehension of the physical and chemical phenomena that occur in the interaction between the gaseous molecules and the MOX surfaces. Firstly, this requires a detailed description and identification of the most active MOX surfaces and interaction sites. Second, the morphology of the sensing materials is also essential to obtain better sensing performances. Third, the study of specific interactions between molecules and surfaces (identified in the previous stages) makes possible not only to reproduce and understand the sensing mechanisms of these devices but also to propose new working methods to increase their performance. *Ab initio* atomistic calculations provide valuable information in the three fields (*Paper 1*).

- Nowadays, the development of novel theoretical approaches (with great accuracy and computational performance) based on well established theories like the Density Functional Theory (DFT), together with new computational facilities are opening new and exciting potential applications of theoretical *ab initio* calculations to eminently applied fields like gas sensing (*Paper 1*).

- The previous points justify the election of state-of-the-art DFT tools to perform the theoretical study of the gas–MOX interactions described in *Unit 1*.

- In the last years, nanowires have emerged as the building blocks of a new generation of sensor devices. These devices have shown outstanding properties, especially in chemical and light sensing applications. In the former field, the improvements are due to the high surface stability and high surface-to-volume ratio in nanowires. In the later, the high crystallinity of the nanowire is leading to excelent charge separation, collection and confinement properties. Consequently, the study of the gas and light interactions in individual nanowire offers an excellent scenario to comprehend the sensing properties of MOXs (*Paper 2*).

- The important advancements achieved in the last years in the synthesis, control, manipulation and electrical access to individual nanowires make possible today the here-proposed studies (*Paper 2*).

- At the beginning of this Ph.D work, there still existed important difficulties in the electrical characterization of individual nanowires. The tiny cross section of the nanowires makes them extremely sensitive to the Joule power dissipated by the current applied to them. This power was identified as the cause of degradation and failure in these devices (due to the so-called self-heating effect). At that moment, the power dissipated at the nanowires could only be controlled with expensive lab-class equipments. This fact hindered the future utilization of individual nanowires in real-life sensors. The here-presented electronic platform demonstrated that it is possible to operate these devices with low-cost consumer electronic components (*Paper* ♣). This platform was used during the development of this Ph.D work to perform great part of the measurements.

4. Results and Discussion

This chapter contains the most relevant results of this work and their discussion organized in 3 units, which correspond to the different areas developed by the author during his Ph.D. Specifically, the three units are:

- *Unit 1: Gas Molecules – MOX interaction*

- *Unit 2: Light – MOX interaction*

- *Unit 3: Simultaneous Gas – Light – MOX interaction*

The first two correspond to the theoretical modeling of two apparently independent interactions with MOX nanowires. Indeed, the gas–MOX interaction seems to occur only at the surface while the light–MOX one appears to be exclusively a bulk phenomenon. Results showed that both interactions are connected by the phenomena that take place at the outer shell of the nanowire and illustrate how important the role played by the surface in these nanomaterials is. Subsequently, the previous results were used to model the simultaneous interaction of gases and light with MOX nanowires. This final case resulted to be of great practical importance from the sensors technology point of view.

4.1 Unit 1: Gas Molecules – MOX interaction

Unit 1 is fully devoted to the study of the chemical processes that take place at the surface of MOX nanowires on the basis of *ab initio* atomistic calculations (described in *Chapter 3*). This unit is separated in sections concerning the atomistic calculations, the experimental assessment of the simulations and the proposal of alternative operational and theoretical approaches.

- *Unit 1.a   Ab initio atomistic modeling:* First, the most significant and realistic surface terminations and adsorption sites at the typical working temperatures of MOX–based sensors were determined. This is important because the arrangement of the oxygen atoms at the surface of MOXs (this involves concepts like oxygen vacancies and adsorbed oxygen atoms) varies at different temperatures and depends on their thermodynamic equilibrium with the oxygen content in air. Subsequently, their interaction with some relevant target gases was analyzed. Here we choose NO and NO_2. These toxic gases, which are produced in many combustion processes, are hazardous for the human health. Therefore, from the practical point of view, these gases are interesting in gas sensing and combustion control applications. Besides their practical relevance, the fact that these gases react at the surface of MOXs following first order processes makes this an specially attractive problem to start with *ab initio* calculations. Surprisingly, no theoretical work dealing with the interaction of NO and NO_2 with the most relevant surfaces of SnO_2 and ZnO [(110) for the former and the non-polar (10-10) and (11-20) for the later] was previously reported. This fact increases the interest of the here–presented research. For completeness, the effects of other interfering gases like SO_2 on the sensing properties of MOX towards NO and NO_2 were also studied. From the practical point of view, SO_2 is well–known because it poisons the sensors and their response can only be recovered after thermal treatments at high temperature. The results concerning SnO_2 are presented in two scientific articles (*Paper 3* and *Paper 4*) being the second the continuation and completion of the first. The case of ZnO is analyzed in *Paper 5*.

- ***Unit 1.b   Experimental validation – Novel sensing approaches enabled by the nanoscale:*** To validate part of the results presented in *Unit 1.a*, the conductometric response of well–faceted individual SnO_2 nanowires to NO_2 at different temperatures was measured (*Paper 6*). In first place, this result served to identify the adsorption sites (mainly surface oxygen vacancies) involved in the response to these gases. In second place, the technical challenges overcame to perform these measurements suggested a novel method to heat the sensing materials. *Paper 6* demonstrates that the current applied to the nanowire in order to measure thier conductance can be modulated to self-heat them up to the optimum temperatures to detect NO_2. As explained in the paper, this result represents not only an important step forward in sensor miniaturization but also a dramatic reduction of the power needed to operate them. In addition to this, the availability of microheaters integrated in the substrates used to fabricate the devices made possible to estimate the effective temperature reached by the nanowire in self-heating operation (*Papers 6* and *7*).

- ***Unit 1.c   On the connection between surface and bulk oxygen vacancies:*** On the one hand, the calculations presented in *Unit 1.a*, demonstrate the important role played in the gas response by the oxygen vacancies at the surface of MOXs. On the other hand, MOXs are spontaneously doped in nature by abundant intrinsic defects related to bulk oxygen vacancies. Therefore, a straightforward question was if there is any connection between surface and bulk oxygen vacancies. Experimental measurements of the long–term drifts in the conductance of individual SnO_2 and ZnO nanowires after sudden changes of the oxygen content in air suggested that the diffusion of oxygen atoms into the bulk of the nanowires is feasible, even at room temperature. In this section, a bulk–center model (complementary to the conventional surface–centered one) is proposed and validated experimentally. All these results are presented in *Paper 8*.

4.1.1 Papers

3.   J.D. Prades, A. Cirera, J.R. Morante, J.M. Pruneda, P. Ordejón, *"Ab initio study of NOx compounds adsorption on SnO₂ surface"* Sens. Actuators B-Chemical **126**, 99-110 (2007).

4.   J.D. Prades, A. Cirera, J.R. Morante, *"First-Principles Study of NO$_x$ and SO₂ Adsorption onto SnO₂(110)"* J. Electrochem. Soc. **154**, H675-H680 (2007).

5.   J.D. Prades, A. Cirera, J.R. Morante, *"Ab initio calculations of NO₂ and SO₂ chemisorption onto non-polar ZnO surfaces"* Thin Sol. Films, submitted (2008).

6.   J.D. Prades, R. Jimenez-Diaz, F. Hernandez-Ramirez, S. Barth, A. Cirera, A. Romano-Rodriguez, S. Mathur, J.R. Morante, *"Ultralow power consumption gas sensors based on self-heated individual nanowires"* Appl. Phys. Lett. **93**, 123110 (2008). Remarks: Selected for highlighted publication in the "V. Journal of Nanoscale Science & Technology" of the American Institute of Physics.

7.   J.D. Prades, R. Jimenez-Diaz, F. Hernandez-Ramirez, A. Cirera, A. Romano-Rodriguez, J.R. Morante, S. Barth, P. Jun, S. Mathur, *"An experimental method to estimate of the temperature of individual nanowires"* Int. J. Nanotechnol., accepted for publication (2008).

8.   F. Hernandez-Ramirez, J.D. Prades, A. Tarancon, S. Barth, O. Casals, R. Jimenez-Diaz, E. Pellicer, J. Rodriguez, J.R. Morante, M.A. Juli, S. Mathur, A. Romano-Rodriguez, *"Insight into the role of oxygen difussion into the sensing mechanisms of SnO₂ nanowires"* Adv. Funct. Mater. **18**, 2990-2994 (2008).

J.D. Prades, A. Cirera, J.R. Morante, J.M. Pruneda, P. Ordejón,
"Ab initio study of NOx compounds adsorption on SnO₂ surface"
Sens. Actuators B-Chemical **126**, 99-110 (2007).

3

Ab initio study of NO$_x$ compounds adsorption on SnO$_2$ surface

J.D. Prades [a,*], A. Cirera [a], J.R. Morante [a], J.M. Pruneda [b,c], P. Ordejón [b]

[a] *EME/CeRMAE/IN² UB, Departament d'Electrònica, Universitat de Barcelona, C/ Martí i Franquès 1, E-08028 Barcelona, Spain*
[b] *Institut de Ciències de Materials de Barcelona (ICMAB), CSIC, Campus de la UAB, E-08193 Cerdanyola del Vallès, Spain*
[c] *Department of Physics, University of California at Berkeley, Berkeley, CA 94720, USA*

Available online 28 November 2006

Abstract

An ab initio study of the adsorption processes on NO$_x$ compounds on (1 1 0) SnO$_2$ surface is presented with the aim of providing theoretical hints for the development of improved NO$_x$ gas sensors. From first principles calculations (DFT–GGA approximation), the most relevant NO and NO$_2$ adsorption processes are analyzed by means of the estimation of their adsorption energies. The resulting values and the developed model are also corroborated with experimental desorption temperatures for NO and NO$_2$, allowing us to explain the temperature-programmed desorption experiments. The interference of the SO$_2$ poisoning agent on the studied processes is discussed and the adsorption site blocking consequences on sensing response are analyzed.
© 2006 Elsevier B.V. All rights reserved.

Keywords: Ab initio; SnO$_2$; Gas sensor; NO; NO$_2$; SO$_2$; Poisoning

1. Introduction

Developing new solid-state gas sensors with improved properties carries with it an obvious close relationship between the sensing performance of the active materials and their surface chemical activity. The theoretical study of such surface–adsorbate interactions provides a valuable tool to get superior performances that are unattainable using only a trial-and-error approach together with a powerful analytic methodology to explain the experimental data.

Tin dioxide (SnO$_2$) plays a key role as one of the more representative sensing materials in solid-state gas sensors [1], presenting a significant surface reactivity with many important reducing (CO, NO) and oxidizing gases (O$_2$, NO$_2$) [2,3]. The present article deals with sensing mechanisms and processes concerning the detection of NO$_x$ using SnO$_2$. Detection of NO$_x$ is clearly important because it is a well-known environmental pollutant with harmful consequences for human health [4]. However, to explain the sensing behavior it is necessary to keep in mind that there exist interfering processes poisoning the surface [5] and that these can dramatically change the effective adsorp-

tions of the target species and, therefore, their eventual detection. In the case of the SnO$_2$ surface, SO$_2$ is one of the more relevant poison specimens [6]. Thus, in the present analysis, its effects have also been studied in order to point up the consequences of the poisoning process on the sensing mechanisms.

Nowadays, first-principles methodologies based on density functional theory (DFT) can provide precise calculations of the energetic and vibrational properties of the adsorption [7]. Moreover, faster codes and new computational facilities allow dealing with numbers of surface–adsorbate configurations in moderate computing times.

In this context, the aim of the present work is to provide theoretical hints for the development of improved NO$_x$ gas sensors using SnO$_2$ as the base sensing material. The surface orientation relevance is discussed, and the most significant adsorption sites of NO$_x$ are identified. Regarding SO$_2$ as poisoning specimen, its adsorption sites are located and the dependence of the poisoning effect with technologically accessible parameters is discussed.

2. Calculation details

The first-principles methodology we used is based on density functional theory [8,9] (DFT) as implemented in the SIESTA method [10,11]. We made use of the generalized gradient

---

* Corresponding author. Tel.: +34 93 40 39 147; fax: +34 93 40 21 148.
  E-mail address: dprades@el.ub.es (J.D. Prades).

approximation (GGA) for the exchange-correlation functional [12] and norm-conserving Troullier–Martins pseudo-potentials [13] in Kleinman–Bylander factorization form [14]. The solutions of the Kohn–Sham equations are expanded as a linear combination of atomic pseudo-wave-functions of finite range. For all atomic species double ζ plus polarization orbitals basis-sets were used. Total energy convergence is guaranteed below 10 meV, as is usual in this kind of calculations [15]. A real space mesh cut-off of 250 Ry and a reciprocal space grid cut-off of approximately 15 Å were used. The structural relaxations were done by means of a conjugate gradient minimization of the energy, until the forces on all the atoms were smaller than 0.04 eV/Å. No constraints were imposed in the relaxation, where forces were calculated as analytical derivatives of the total energy [16]. Spin polarization was also considered in the total energy computations, and basis set superposition error [17] (BSSE) was corrected in the calculated adsorption energies.

3. Results and discussion

3.1. Surface modeling

For a given material, the most common (and relevant) faceting orientation will have the lowest E_{surf} [18]. Therefore, the surface energies of several low-index facets of SnO_2–cassiterite (also known as rutile or tetragonal phase, space group $P4_2mnm$, lattice parameters $a = b = 4.74$ Å, $c = 3.19$ Å and two non-symmetry-equivalent atoms at (0.0, 0.0, 0.0)$_{Sn}$ and (0.305, 0.305, 0.0)$_O$ [2]) were calculated in order to select the surface on which the adsorption processes would be analyzed. The initially considered low-index orientations are (1 1 0), (1 0 0), (1 0 1) and (0 0 1), which are accepted as some of the most common SnO_2–cassiterite faceting surfaces [19]. E_{surf} values were evaluated following the procedure and definitions described in [19,20], and the results, compared with values from the literature, are shown in Table 1. Our calculated data are in acceptable agreement with the literature and provide confidence in the accuracy of the calculation framework used. TiO_2 results are shown for comparison with another cassiterite system where (1 1 0) is also the lowest energy surface [21]. Therefore, in the following sections, adsorption phenomena will be studied over this surface orientation.

3.2. Adsorption energy modeling

To be able to estimate the energy change involved in the process of adsorption of a molecule onto a clean surface, we built models of (1) the clean surface slab, (2) the molecule, and (3) the surface plus the molecule system. For all three of these models, total energy calculations were performed, allowing us to evaluate the total energy balance of the adsorption process (so called adsorption energy E_{ads}) as follows:

$$E_{Tinitial} = E_{T(clean\,surface)} + E_{T(molecule)},$$

$$E_{Tfinal} = E_{T(clean\,surface+molecule)},$$

$$E_{ads} = \Delta E_T = E_{Tfinal} - E_{Tinitial} \qquad (1)$$

Accordingly, a negative value of E_{ads} means that the adsorption is energetically favorable, it being possible for this to occur spontaneously without entropic considerations (DFT deals with the ground state at 0 K).

It is necessary to ensure the effective cancellation of errors between the large energies that appear in Eq. (1). For this, adequate conditions were considered [7]. It has been verified that, in our case, a two layer thick slab is enough to ensure the stability of the adsorption energy values. Additionally, to ensure that the adsorbed compound will not interact with periodic images of the supercell, a 12 Å vacuum thickness and a 2 × 1 supercell width were used.

Moreover, the adsorption analysis requires several complementary steps: location of possible surface adsorption sites, also considering vacant sites, molecular modeling and, finally, adsorption modeling of NO_x and SO_2 compounds.

Fig. 1 shows the slab model used for the adsorption on the SnO_2–cassiterite (1 1 0) surface. In order to obtain realistic values, surface relaxation was necessary (Fig. 1 also presents the relaxed slab). Surface relaxation shows how six-fold coordinated Sn atoms (Sn_{6c}) tend to move outside the surface plane, whereas five-fold coordinated Sn atoms (Sn_{5c}) tend to move inside. A similar behavior on (1 1 0) surface relaxation has been observed by other authors [22,23].

Two relevant adsorption sites appear to be a natural choice for the stoichiometric surface: a bridging site around bridging-oxygen [O_{Bridg}] and an inplane site around Sn_{5c} and the neighboring O_{3c} [$Sn_{InPlane}$]. In addition, O_{Bridg} appears at first glance, to be the most clear vacancy formation site [$O_{BridgVac}$] [15]. Consequently, two additional adsorption sites will be considered: a single O_{Bridg} vacancy (or a 50% reduced surface as long as there are only two non-equivalent O_{Bridg} atoms per slab) and a double O_{Bridg} vacancy site (or a 100% reduced surface). Finally, the adsorption of a molecule between an inplane Sn_{5c} and an O_{Bridg} vacancy [$O_{BridgVac}$–$Sn_{InPlane}$] was considered for NO_2 and SO_2.

Since a good description of the adsorbed molecules is necessary to obtain credible theoretical predictions, Table 2 presents the molecular models used and the obtained energetic and geometric parameters compared with those in the literature. It is worth noting that the agreement achieved is comparable with the commonly accepted discrepancy described in the literature [24].
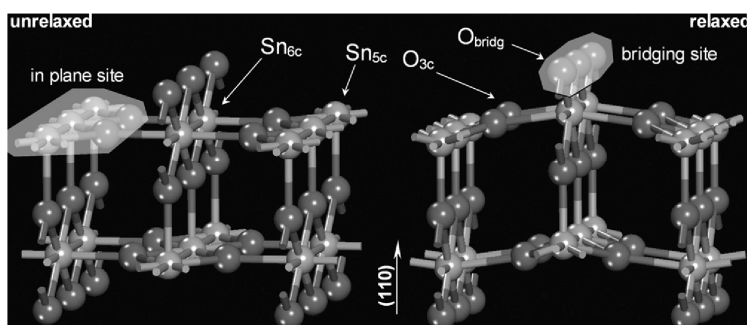
Table 1
Surface energy results for the considered SnO_2–cassiterite faceting orientations

Surface	E_{surf} (J/m^2)		
	SnO_2 GGA [this work], (<±0.20)	SnO_2 GGA [19], (<±0.20)	TiO_2 LDA [21]
(1 1 0)	1.01	1.04	0.89
(1 0 0)	1.32	1.14	1.12
(1 0 1)	1.49	1.33	1.39
(0 0 1)	1.87	1.72	1.65

Several references form the literature are given. Computational uncertainty is also shown when possible.

Fig. 1. Slab model of the SnO_2–cassiterite (1 1 0) surface. Relaxed and unrelaxed geometries are shown. Adsorption sites are highlighted and relevant surface atoms are identified.

Table 2
Energetic and geometric first-principles results of several molecules involved in the adsorptions considered in this work

Compound	Bond energy (eV)		Bond length (Å)		Angle (°)	
	This work	Reference [24]	This work	Reference	This work	Reference
O_2	5.90	6.23 (calc.), 5.23 (exp.)	1.24	1.18–1.21 [25]	–	–
N_2	9.47	10.55 (calc.), 9.47 (exp.)	1.12	1.09–1.11 [26]	–	–
NO	7.03	7.45 (calc.), 6.63 (exp.)	1.17	1.12–1.17 [27]	–	–
NO_2	5.54	–	1.23	1.20 [28]	132	133–134 [28]
SO_2	5.91	–	1.49	1.48 [29]	112	109 [29]

Table 3 summarizes the calculated E_{ads} of NO and NO_2 on the considered adsorption sites. Desorption temperature results are obtained by means of the well-known Redheat equation, which links the $|E_{ads}|$ of a process with its maximum desorption rate temperature (T_{MDR}) in a temperature-programmed desorption (TPD) experiment [30]. Adjusting parameters were set according to the experimental conditions of [31] where an experimental TPD spectrum can be found for NO and NO_2 desorption from SnO_2 (1 1 0) surface (Fig. 2).

We recall that our model only provides energies (and their corresponding desorption temperatures) for the concrete adsorption configurations analyzed. In contrast, an experimental TPD spectrum provides the temperature range at which a given specie is desorbed by considering a plethora of adsorption configurations present in the real sample. Consequently, we would expect the calculated temperatures to belong to the corresponding experimental TPD signal range. It is remarkable, therefore, how theoretical predictions of T_{MDR} for the few adsorption cases

Table 3
Calculated adsorption energies E_{ads} for NO_x on several adsorption sites of the SnO_2 (1 1 0) surface and maximum desorption rate temperature T_{MDR} estimated for the experimental conditions of [31]

Adsorbate	Surface state	Adsorption site	E_{ads} (eV)	T_{MDR} (°C)
	Stoichiometric slab	O_{Bridg}	−1.32	188 (a)
	Stoichiometric slab	$Sn_{InPlane}$	−0.24	52 (b)
NO	50% reduced slab	O_{Bridg}	−1.18	167 (c)
	50% reduced slab	O_{Bridg} + (SO_2 in $O_{BridgVac}$)	−1.28	– (#)
	50% reduced slab	$O_{BridgVac}$	−0.42	89 (d)
	100% reduced slab	$O_{BridgVac}$	−0.98	153 (e)
	Stoichiometric slab	O_{Bridg}	+1.51	–
	Stoichiometric slab	$Sn_{InPlane}$	−0.52	94 (v)
	50% reduced slab	$O_{BridgVac}$ (single bonded)	−2.31	502 (w)
NO_2	50% reduced slab	$O_{BridgVac}$–$Sn_{InPlane}$	+0.34	–
	100% reduced slab	$O_{BridgVac}$ (single bonded)	−2.02	424 (x)
	100% reduced slab	$O_{BridgVac}$ (double bonded)	−1.95	400 (y)
	100% reduced slab	$O_{BridgVac}$–$Sn_{InPlane}$	−2.11	454 (z)

Some configurations are not energetically favorable ($E_{ads} > 0$). Energetically favorable processes are labeled using letters in parentheses to identify them in Fig. 2. For NO, a configuration with presence of SO_2 (#) is considered for later discussion on poisoning. Notice that NO_2 adsorption on a 100% reduced slab can appear with two different configurations: bonding one single O atom of the molecule (single bonded) or bonding both (double bonded).

65
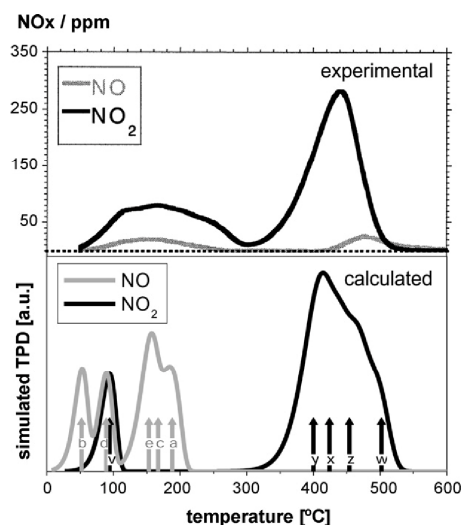
Fig. 2. (Top) Experimental TPD spectra of NO and NO_2 desorbing form a dehydroxylated SnO_2 (1 1 0) surface (reprinted from [31], with permission from Elsevier). (Bottom) Calculated TPD spectra for NO and NO_2 considering all the configurations detailed in Table 3. One TPD spectrum was simulated (by means of solving the rate expression for desorption kinetics [30,32]) for each adsorption configuration with the experimental parameters given in [31]. For every configuration the temperature corresponding to its maximum desorption rate is indicated with a labeled arrow (see labels and T_{MDR} values in Table 3). Total spectra were obtained as the summation of the normalized single configuration spectra.

Fig. 3. Adsorption energies E_{ads} of NO_2 and SO_2 as a function of the SnO_2 (1 1 0) surface reduction. Only stronger adsorptions and identical configurations are considered at every reduction percentage so a competitive situation is analyzed. Details on adsorption configurations of every data point is given in Tables 3 and 4. Dotted lines are plotted as visual aids.

considered fall within the wide experimental desorption peaks from [31].

Our results suggest that O_{Bridg} sites are the most energetically favorable for NO. This behavior is compatible with the observed fact that NO reduces the SnO_2, given that NO is expected to bond with a surface oxygen to be able eventually to remove it reducing the surface [1]. Instead, $O_{BridgVac}$ are involved in the energetically preferred adsorption sites for NO_2.

For these preferred adsorption sites, a dependency of the adsorption energy with the reduction state of the surface is observed. In both cases (NO and NO_2) surface reduction

seems to diminish slightly the adsorption energy on O_{Bridg} and $O_{BridgVac}$ sites, respectively.

It is important to note that the difference in the preferred adsorption sites between NO and NO_2 suggests that by generating vacant sites and adjusting their density, the adsorption feasibility of NO versus NO_2 on an eventual SnO_2-based gas sensor may be changed. This leads to a technological suggestion in the preparation of the sensing material.

Concerning the SO_2 adsorption, Table 4 summarizes the calculated E_{ads} of SO_2 on several sites. As for NO_2, the preferred adsorption sites also involve $O_{BridgVac}$ but, in this case, it seems that the more reduced the surface is, the stronger is the SO_2 adsorption that takes place. This different behavior with respect to the surface reduction percentage has dramatic consequences on the interference of SO_2 when trying to detect NO_2.

It is a known fact that SO_2 avidly saturates NO_2 adsorption sites, reducing the SnO_2 sensing capability [6]. In order to shed some light on this, Fig. 3 shows the E_{ads} values of the most energetically favorable adsorption configurations of NO_2 and SO_2 as a function of the surface reduction. At every reduction percentage, the same adsorption configuration is considered for both compounds, so a competitive situation is analyzed. It is confirmed that the strongest adsorption within the studied cases

Table 4
Calculated adsorption energies E_{ads} for SO_2 on several adsorption sites of the SnO_2 (1 1 0) surface and maximum desorption rate temperature T_{MDR} estimated for the experimental conditions of [31]

Adsorbate	Surface state	Adsorption site	E_{ads} (eV)	T_{MDR} (°C)
	Stoichiometric slab	O_{Bridg}	+1.72	–
	Stoichiometric slab	$Sn_{InPlane}$	−0.86	128
	50% reduced slab	$O_{BridgVac}$ (single bonded)	**−2.05**	435
SO_2	50% reduced slab	$O_{BridgVac}$–$Sn_{InPlane}$	+1.12	–
	100% reduced slab	$O_{BridgVac}$ (single bonded)	+0.26	–
	100% reduced slab	$O_{BridgVac}$ (doble bonded)	−2.56	606
	100% reduced slab	$O_{BridgVac}$–$Sn_{InPlane}$	−2.97	741

Notice that, in contrast with the NO_2 case, calculations show that SO_2 adsorption on a 100% reduced slab may only be spontaneous ($E_{ads} < 0$) in one single O bonding configuration. Some configurations are not energetically favorable ($E_{ads} > 0$).

J.D. Prades et al. / Sensors and Actuators B 126 (2007) 62–67

corresponds to SO_2, which is a theoretical behavior compatible with the experimental evidence of the poisoning effect.

It is also clear that SO_2 adsorbs stronger than NO_2 in stoichiometric and also in 100% reduced configurations. However, for intermediate surface reductions, NO_2 seems to be adsorbed stronger than SO_2. This suggests that the poisoning strength is dependant on the surface reduction state and may even be reduced for intermediate bridging-oxygen vacancy densities on the SnO_2 (1 1 0) surface. This again points out a technological hint for the preparation of the sensing material.

Regarding NO, it has been shown that its preferred adsorption sites are O_{Bridg}. Therefore, it may seem that there is no competitive behavior with SO_2. However, Table 3 shows how, for intermediate reductions, the adsorption of NO on O_{Bridg} under the presence of an SO_2 occupying an $O_{BridgVac}$ site (Table 3 case #) is slightly stronger than in the non-interacting (case c). These results suggest that in spite of the fact that the preferred adsorption sites for NO and SO_2 are different, a cross-influence may occur between both compounds, and this would merit further analysis.

4. Conclusions

A theoretical approach to the NO and NO_2 adsorption on SnO_2 (1 1 0) based on ab initio calculations has been presented. Bridging-oxygen sites and bridging-oxygen vacancy sites were identified as the most relevant adsorption sites for NO and NO_2, respectively. This difference may suggest that adjusting oxygen vacant sites density the adsorption feasibility of NO versus NO_2 on an eventual SnO_2-based gas sensor may be changed.

Regarding the poisoning by SO_2, bridging-oxygen vacancies seem to be the most favorable adsorption sites, suggesting a competitive behavior with NO_2. Theoretical trends indicate that NO_2 adsorption strength decreases with the surface reduction while for SO_2, it increases. Such a different evolution insinuates that the poisoning effect may be diminished by means of adjusting the SnO_2 surface reduction to intermediate values. In the case of NO, no competitive behavior with SO_2 is expected because of their preferred adsorption sites being different, but further study may be necessary to analyze an eventual cross-influence.

To conclude, under the light of the presented adsorption sites and their corresponding maximum desorption rate temperatures, one can see that adjusting the working conditions (i.e. working temperature) of an eventual SnO_2-based gas sensor will determine the reversibility of the adsorption at a given site. Working at temperatures around 300 °C, where the low desorption rate may ease the fast saturation of the adsorption sites thus spoiling the sensing properties, seems to be particularly problematic. In any case, to make theoretical predictions on the optimum working conditions of a real sensor, a more complex model is necessary, for example, one including the cross-influence of OH groups due to humidity.

Acknowledgements

References

[1] W. Göpel, K.D. Schierbaum, SnO_2 sensors: current status and future prospects, Sens. Actuators B: Chem. 26/27 (1995) 1–12.
[2] M. Batzill, U. Diebold, The surface and materials science of tin oxide, Prog. Surf. Sci. 79 (2005) 47–154.
[3] G. Sverveglieri, Recent developments in semiconducting thin-film gas sensors, Sens. Actuators B: Chem. 23 (1995) 103–109.
[4] A. Fritz, V. Pitchon, The current state of research on automotive lean NO_x catalysis, Appl. Catal. B: Environ. 13 (1997) 1–27.
[5] D.E. Williams, G.S. Henshaw, K.F.E. Pratt, Detection of sensor poisoning using self-diagnostic gas sensors, J. Chem. Soc., Faraday Trans. 91 (1995) 3307–3308.
[6] B. Ruhland, T. Becker, G. Muller, Gas–kinetic interactions of nitrous oxides with SnO_2 surfaces, Sens. Actuators B: Chem. 50 (1998) 85–94.
[7] K.M. Neyman, F. Illas, Theoretical aspects of heterogeneous catalysis: applications of density functional methods, Catal. Today 105 (2005) 2–16.
[8] P. Hohenberg, W. Kohn, Inhomogeneous electron gas, Phys. Rev. 136 (1964) B864–B871.
[9] W. Kohn, L.J. Sham, Self-consistent equations including exchange and correlation effects, Phys. Rev. 140 (1965) A1133–A1138.
[10] P. Ordejón, E. Artacho, J.M. Soler, Self-consistent order-N density-functional calculations for very large systems, Phys. Rev. B 53 (1996) R10441–R10444.
[11] J.M. Soler, E. Artacho, J.D. Gale, A. García, J. Junquera, P. Ordejón, D. Sánchez-Portal, The SIESTA method for ab initio order-N materials simulation, J. Phys.: Condens. Matter 14 (2002) 2745–2779.
[12] J.P. Perdew, K. Burke, M. Ernzerhof, Generalized gradient approximation made simple, Phys. Rev. Lett. 77 (1996) 3865–3868.
[13] N. Troullier, J.L. Martins, Efficient pseudopotentials for plane-wave calculations, Phys. Rev. B 43 (1991) 1993–2006.
[14] L. Kleinman, D.M. Bylander, Efficacious form for model pseudopotentials, Phys. Rev. Lett. 48 (1982) 1425–1428.
[15] J. Oviedo, M.J. Gillan, First-principles study of the interaction of oxygen with the SnO_2 (1 1 0) surface, Surf. Sci. 490 (2001) 221–236.
[16] D. Sánchez-Portal, P. Ordejón, E. Artacho, J.M. Soler, Density-functional method for very large systems with LCAO basis sets, Int. J. Quantum Chem. 65 (1997) 453–461.
[17] S.F. Boys, F.F. Bernardi, Calculation of small molecular interactions by differences of separate total energies—some procedures with reduced errors, Mol. Phys. 19 (1970) 553–566.
[18] A.S. Barnard, P. Zapol, Effects of particle morphology and surface hydrogenation on the phase stability of TiO_2, Phys. Rev. B 70 (2004) 235403–235416.
[19] J. Oviedo, M.J. Gillan, Energetics and structure of stoichiometric SnO_2 surfaces studied by first-principles calculations, Surf. Sci. 463 (2000) 93–101.
[20] W. Zhu, P. Wu, Surface energetics of hydroxyapatite: a DFT study, Chem. Phys. Lett. 396 (2004) 38–42.
[21] M. Ramamoorthy, D. Vanderbilt, R.D. King-Smith, First-principles calculations of the energetics of stoichiometric TiO_2 surfaces, Phys. Rev. B 49 (1994) 16721–16727.
[22] T.T. Rantala, T.S. Rantala, V. Lantto, Electronic structure of SnO_2 (1 1 0) surface, Mater. Sci. Semiconduct. Process. 3 (2000) 103–107.
[23] F.R. Sensato, R. Custódio, M. Calatayud, A. Beltrán, J. Andrés, J.R. Sambrano, E. Longo, Periodic study on the structural and electronic properties

of bulk, oxidized and reduced SnO_2 (1 1 0) surfaces and the interaction with O_2, Surf. Sci. 511 (2002) 408–420.

[24] S. Kurth, J.P. Perdew, P. Blaha, Molecular and solid-state tests of density functional approximations: LSD, GGAs, and meta-GGAs, Int. J. Quantum Chem. 75 (1999) 889–909.

[25] H. Dong, Y.-H. Ding, C.-C. Sun, Mechanism of $HCS + O_2$ reaction: hydrogen- or oxygen-transfer? Phys. Chem. Chem. Phys. 7 (2005) 3711–3715.

[26] H. Orita, N. Itoh, Adsorption of N_2 and N_2O on Ni(755) surface: ab initio periodic density functional study, Surf. Sci. 550 (2004) 166–176.

[27] Z.-G. Wei, X.-R. Huang, S.-W. Zhang, Y.-B. Sun, H.-J. Qian, C.-C. Sun, A theoretical study on the potential energy surface of the $3C_2 + NO$ reaction, J. Phys. Chem. A 108 (2004) 6771–6777.

[28] J.-X. Zhang, J.-Y. Liu, Z.-S. Li, C.-C. Sun, Theoretical study on reaction mechanism of the fluoromethylene radical with nitrogen dioxide, J. Comput. Chem. 25 (2004) 1888–1894.

[29] K. Sendt, B.S. Haynes, Role of the direct reaction $H_2S + SO_2$ in the homogeneous Claus reaction, J. Phys. Chem. A 109 (2005) 8180–8186.

[30] M.C. Desjonquères, D. Spanjard, Concepts in Surface Physics, 2nd ed., Springer, 1996.

[31] E. Leblanc, L. Perier-Camby, G. Thomas, R. Gibert, M. Primet, P. Gelin, NO_x adsorption onto dehydroxylated or hydroxylated tin dioxide surface. Application to SnO_2-based sensors, Sens. Actuators B: Chem. 62 (2000) 67–72.

[32] V.P. Zhdanov, B. Kasemo, Simulation of oxygen desorption from Pt(1 1 1), Surf. Sci. 415 (1998) 403–410.

Biographies

J.D. Prades was graduated in Physics at the University of Barcelona in 2005. Now he is PhD student in Department of Electronics of the same university. His current research is focused on first-principles modeling of electronic and vibrational properties of nanostructured metal oxides.

A. Cirera was graduated in Physics at the University of Barcelona in 1996. He received his PhD in 2000 from the University of Barcelona, developing new technologies and their characterization for tin oxide gas sensor devices. He is currently associate professor and works in the field of sensors and its simulation, as scientist and coordinator in several related industrial projects.

J.R. Morante was born in Mataró (Spain). At 1980 he received the PhD degree in Physics from the University of Barcelona. Since 1986 he is full professor of Electronics and director of the Electronic Materials and Engineering, EME, group. He has been dean of the Physics Faculty and academic advisor of the Electronic Engineering degree. He was director of the Electronics Department in the University of Barcelona which is associated unity to the Centre Nacional de Microelectronics at Bellaterra (Barcelona). Actually, he is research head of the EME group and co-director of the CEMIC, center of the Microsystems Engineering and director of the CeRMAE, reference center of advanced materials for energy from Generalitat of Catalunya. His activity is devoted to the electronic materials and technology, physics and chemical sensors, actuators, and microsystems. He has especial interest in nanoscience and micro- and nano-technologies. He has collaborated in international R&D projects as BRITE, GROWTH (micromechanics, microengineering, gas sensors, nanomaterials, etc.), ESPRIT, IST (advanced devices, sensors, actuators, microsystems, electronic systems, etc.), JOULE, ..., EUREKA, IBEROEKA and industrial projects. He is co-author of more than 400 works in international specialised journal and member of international committees and editorial boards in the field of electronic materials and technology, sensors & actuators and microsystems, and electronic systems. He has been distinguished with the research prize Narciso Monturiol and the "senior research distinction" award from the Generalitat of Catalunya (Spain).

J.M. Pruneda is Marie Curie Fellow between the Department of Physics at UC Berkeley and the ICMAB. Graduated in physics at Universidad de Oviedo in 1997, and got the PhD in 2002 (Oviedo). After 3 years as a research associate at the department of Earth Sciences in the University of Cambridge studying materials for nuclear waste immobilization, joined the group of P. Ordejón. Interest in materials for nanotechnology and spintronic.

P. Ordejón is a research professor at the ICMAB-CSIC, in Barcelona. He studied physics at the Universidad Autonoma de Madrid (Spain), where he obtained his PhD in science in 1987, and afterwards he did a 3 years postdoctoral stay at the University of Illinois at Urbana-Champaign (USA). His research has focused on the development and application of efficient methods for electronic structure calculations in large and complex systems, and techniques for large-scale atomistic simulations based on first-principles methods. He is Regional Editor of the journal Physica Status Solidi and was recently elected as Fellow of the American Physical Society.

J.D. Prades, A. Cirera, J.R. Morante,
"First-Principles Study of NOₓ and SO₂ Adsorption onto SnO₂(110)"
J. Electrochem. Soc. **154**, H675-H680 (2007).

4

First-Principles Study of NO$_x$ and SO$_2$ Adsorption onto SnO$_2$(110)

Joan Daniel Prades,[z] Albert Cirera, and Joan Ramon Morante

EME/CeRMAE/IN^{2}UB, Departament d'Electrònica, Universitat de Barcelona, C/ Martí i Franquès 1, 08028 Barcelona, Spain

An ab initio study of the adsorption of NO$_x$ and SO$_2$ onto SnO$_2$(110) surfaces is presented and related to gas-sensing applications. Using first-principles calculations density functional theory–generalized gradient approximation (DFT-GGA), the most relevant NO and NO$_2$ adsorptions were analyzed by estimating their adsorption energies. The resulting values were compared to experimental desorption temperatures for NO and NO$_2$. The adsorption of the poisoning agent SO$_2$ was also analyzed. Optimum SnO$_2$ working temperatures for minimum SO$_2$ poisoning in NO$_2$ sensing applications are discussed from the perspective of adsorption. In all cases, we observed that the surface reduction state has dramatic consequences on adsorption strength. An ab initio thermodynamics study is presented to analyze the stability of several surface oxygen configurations with respect to the ambient oxygen partial pressure and the temperature of the material.
© 2007 The Electrochemical Society. [DOI: 10.1149/1.2742295] All rights reserved.

Gas sensor performance depends on the surface chemical activity of the active materials. The theoretical study of surface-adsorbate interactions provides a valuable tool for understanding the chemistry of gas sensors. Chemical transduction involves many stages, including the adsorption of the target species and charge transfer from the compound to the sensing material. These processes must be studied to allow understanding of the sensing mechanism.

Tin dioxide (SnO$_2$) is one of the most common sensing materials in solid-state gas sensors.[1] It shows significant surface reactivity with reducing (CO,NO) and oxidizing gases (O$_2$,NO$_2$).[2,3] The present article deals with adsorptions involved in the detection of NO$_x$ using SnO$_2$. Detection of NO$_x$ is important because it is a toxic environmental pollutant.[4] However, to explain the behavior of sensors, we must keep in mind that certain processes may interfere with the sensor surfaces.[5] This interference can dramatically change the effective adsorptions of the target species and, therefore, their eventual detection. In the case of the SnO$_2$ surface, SO$_2$ is one of the most important poisons.[6] The present analysis therefore considers the effects of SO$_2$ to point out the consequences of poisoning on sensing mechanisms.

Several papers have dealt with the energetics and electron structure of stoichiometric and oxygen-defective SnO$_2$ surfaces.[7-11] The interaction of these surfaces with oxygen[12-14] and the presence of catalytic additives[15] have also been studied. To our knowledge, the interaction of NO$_x$ with SnO$_2$ has only been analyzed in the case of the (101) and (100) surface orientations in a study on nanobelts.[16]

Here we present a theoretical study of the interaction of NO$_x$ with SnO$_2$–cassiterite in its most common surface orientation, which is shown to be the (110)[2] even in nanostructures.[17] Surface stability with respect to orientation and oxidized-reduced termination is discussed, the most significant adsorption sites of NO$_x$ are identified and the energetics of the adsorption interaction are evaluated. We compare our results with data from desorption experiments where possible. The adsorption sites of SO$_2$ are located and we discuss the effects of poisoning using technologically accessible parameters, such as the working temperature of a hypothetical SnO$_2$-based gas sensor.

Calculation Details

The first-principles methodology we used is based on the density functional theory (DFT),[18,19] as implemented in the SIESTA code.[20,21] We used the generalized gradient approximation (GGA) for the exchange-correlation functional[22] and norm-conserving Troullier–Martins pseudo-potentials[23] in Kleinman–Bylander factorization form.[24] Solutions of the Kohn–Sham equations are expanded as linear combinations of atomic pseudo-wave-functions of finite range. For all atomic species double ζ plus polarization orbital basis-sets are used. Oxygen atoms were described by 6 valence electrons, nitrogen by 5, sulfur by 6, and tin atoms by 4 plus the corresponding pseudo-potential ion cores. We set a real space mesh cut-off[20,21] of 250 Ry to obtain total energies converged within 5 meV, which is more than sufficient for this kind of calculation.[7] In SIESTA, k-point sampling is controlled by the k-grid cut-off parameter defined as half the length of the smallest lattice vector of the supercell required to obtain the same sampling precision with a single k-point.[25] For bulk calculations, the total energy was converged to within 5 meV per six-atom unit cell with a k-grid cut-off of 10 Å that generates a 5 × 5 × 7 Monkhorst–Pack set.[26] In slab calculations, k-point sampling in the direction normal to the surface was not needed, and all calculations were performed with a 5 × 5 × 1 Monkhorst–Pack set generated with a 15 Å k-grid cut-off. Under these conditions, forces over atoms are converged to better than 0.004 eV/Å^2. We also considered spin polarization in the total energy computations, and corrected the basis set superposition error (BSSE)[27] in the calculated adsorption energies.

To deal with surface stability and adsorption energy calculations, we modeled all surface geometries as three-dimensionally periodic slab systems, generated from the relaxed bulk unit cell, with a vacuum width of 12 Å between surfaces to avoid interaction between periodic images of the slabs.[7-16]

Initially, to explore different possible adsorption sites, we performed calculations using slabs composed of two O(Sn$_2$O$_2$)O layers. For adsorption energy and structural calculations, we used slabs composed of five O(Sn$_2$O$_2$)O layers. Increasing slab thickness to seven layers had a negligible effect on energetics and surface relaxations (see Fig. 1a). This procedure was successfully used in previous works.[9,10,15] Furthermore, we analyzed the influence of supercell width and show that a 2 × 1 supercell provides converged adsorption energies (see Fig. 1b). Comparable supercell widths were previously employed in similar works.[16]

We introduced structural relaxations by means of conjugate gradient minimization of the energy, until the forces on all the atoms (calculated as analytical derivatives of the total energy[28]) were smaller than 0.04 eV/Å^2 (which is one order of magnitude greater than the estimated force convergence). In the relaxation of the slabs, supercell dimensions were kept constant and, as proposed by some authors,[7] we chose to impose no constraints to the atomic positions within the supercell. In the slab composed of 5 layers, the maximum displacement of the atoms in the middle layer was as small as 0.05 Å.

[z] E-mail: dprades@el.ub.es
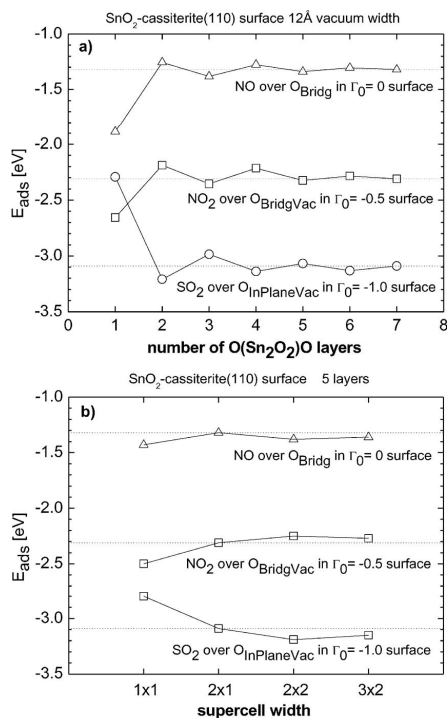
Figure 1. Adsorption energies, E_{ads}, of the three compounds studied (NO, NO_x, and SO_2) adsorbing to an SnO_2–cassiterite (110) surface with different terminations, as functions of (a) the number of $O(Sn_2O_2)O$ layers and (b) the supercell width.

Results and Discussion

Surface orientation stability.— It is commonly agreed that the facets of a crystal are those that minimize the surface free energy γ.[29] Consequently, for a given material, the most common (and relevant) facet orientation will have the lowest γ. Therefore, we calculated the surface energies of several low index facets of SnO_2–cassiterite, also known as rutile or tetragonal phase, space group $P4_2mnm$, lattice parameters $a = b = 4.74$ Å $c = 3.19$ Å and two non-symmetry-equivalent atoms at $(0.0,0.0,0.0)_{Sn}$ and $(0.305,0.305,0.0)_O$,[2] to select the surface on which the adsorption processes would be analyzed. The low-index orientations we considered initially were (110), (100), (101), and (001), which are accepted as some of the most common SnO_2–cassiterite faceting surfaces.[2,7]

Surface-free energy values were calculated following the procedure and definitions described in Ref. 7 and 30, and we compared the results with values from the literature in Table I. Our calculated data is in acceptable agreement with the literature. We based our study on the (110) orientation because it has the lowest surface free energy. TiO_2 results are shown for comparison with another cassiterite system whose (110) orientation also has the lowest surface energy.[31]

Figure 2 shows one of the slab models used for adsorption onto the SnO_2–cassiterite(110) surface. Figure 2 clearly shows that it is possible to distinguish between bridging oxygens (O_{Bridg}) and in-plane oxygens ($O_{InPlane}$).[9] When any one of these oxygen atoms is removed, a surface oxygen vacancy is generated. Henceforth, we will refer to these as $O_{BridgVac}$ and $O_{InPlaneVac}$, respectively.

Table I. Surface energy for the SnO_2—cassiterite facet orientations considered. Several references from the literature are given. Computational uncertainty is also shown where possible.

Surface	$E_{surf}[J/m^2]$		
	This work SnO_2 GGA $< \pm 0.20$	SnO_2 GGA [7] $< \pm 0.20$	TiO_2 [31]
(110)	1.01	1.04	0.89
(100)	1.32	1.14	1.12
(101)	1.49	1.33	1.39
(001)	1.87	1.72	1.65

Surface reduction–oxidation stability.— We followed the methodology for the interpretation of ab initio calculations on surface models in terms of oxidation, reduction thermodynamics described by Reuter and Scheffler.[32] Briefly, the most stable surface composition and geometry at a given temperature T and pressure P is the one that minimizes the surface-free energy $\sigma(T,P)$ given by

$$\sigma(T,P) = \gamma - \Gamma_O\mu_O(T,P)/A \qquad [1]$$

where $\Gamma_O = 1/2(N_O - 2N_{Sn})$ is the excess of oxygen in each surface (N_O and N_{Sn} are the number of oxygen and tin atoms in the outermost $O(Sn_2O_2)O$ layer, respectively), γ is the surface free energy at $\mu_O = 0$ (i.e., under the ground conditions of 0 K that are assumed in DFT), $\mu_O(T,P)$ is the oxygen chemical potential (that is given as a function of the temperature and the partial pressure of O_2[33]), and A is the area of the slab model. In this procedure, ab initio calculations provide estimations of γ which can be used to evaluate the surface-free energy (σ) of a particular surface termination (Γ_O) for a range of μ_O values that are functions of T and P. Two points must be considered to ensure that the μ_O values are physically meaningful: SnO_2 dissociates into $SnO + O_2$ at temperatures above $1500°C$[34] and, for gas sensing applications under ambient conditions, the oxygen partial pressure can be fixed at atmospheric conditions (i.e., ~ 0.21 bar). Therefore, we restrict μ_o to values from -2.7 eV (at $1500°C$ and 0.21 bar) to 0 eV (at $-273°C$).

Semancik and co-workers observed that simple heating of a stoichiometric SnO_2–cassiterite (110) surface under ultrahigh vacuum
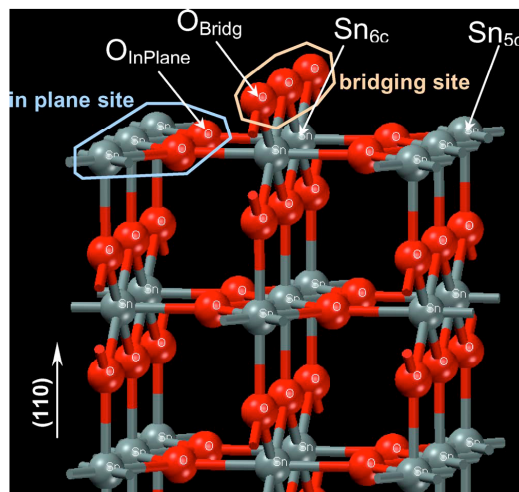
Figure 2. (Color online) Slab model of the SnO_2–cassiterite (110) surface. Adsorption sites are highlighted and relevant surface atoms are identified.
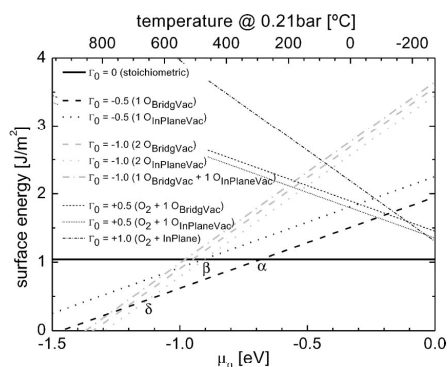
Figure 3. Surface-free energies for different terminations of the $SnO_2(110)$ surface as a function of the oxygen chemical potential. The top axis shows the corresponding O_2 gas temperature for atmospheric air equivalent conditions (i.e., oxygen partial pressure of ~ 0.21 bar).[32]

(UHV) to temperatures above 225°C leads to a loss of O_{Bridg} and the formation of bridging oxygen vacancies ($O_{BridgVac}$).[35,36] However, if the temperature is raised above 525°C, in-plane oxygen vacancies ($O_{InPlaneVac}$) can be produced, which usually form complex configurations with the presence of $O_{BridgVac}$ and $O_{InPlaneVac}$. As stated in Ref. 35, note that the given vacancy generation temperatures may depend on the particular samples used and the oxygen pressure. In any case, it is accepted that $O_{BridgVac}$ are generated at lower temperatures than $O_{InPlaneVac}$ and that the latter form more complex configurations.

Figure 3 shows straight line plots of $\sigma(\mu_O)$ for several surface terminations. It can be seen that for a single oxygen vacancy per slab unit ($\Gamma_O = -0.5$) $O_{BridgVac}$ becomes more stable than the stoichiometric configuration at 270°C, whereas $O_{InPlaneVac}$ does so at 480°C (points α and β). Thus, the thermodynamics of the formation of a single $O_{BridgVac}$ is fairly well explained by ab initio calculations but, with the model used, it is not possible to determine the threshold temperature above which a single $O_{InPlaneVac}$ will be more stable than an $O_{BridgVac}$. To study this point, and bearing in mind the complex configurations suggested in Ref. 35, we considered double oxygen vacancies per slab termination ($\Gamma_O = -1$). All of these complex configurations cross the single $O_{BridgVac}$ line at temperatures between 640 and 780°C (point δ).

In short, under ambient conditions, the stoichiometric surface configuration is the most stable (as we expected). When the temperature is raised above 270°C a single $O_{BridgVac}$ may form and even at higher temperatures (above 480°C) the formation of a single isolated $O_{InPlaneVac}$ is plausible. At temperatures above 640°C multiva-

cant configurations are the most probable. This predicted evolution is compatible with known behavior with slightly higher temperatures than under UHV conditions as expected due to the presence of ambient oxygen that may make vacancy generation more difficult. All of this suggests that temperature can be used to technologically adjust the surface oxygen vacancy type and concentration.

To give a more complete view of surface stability, we considered several oxidized configurations and, remarkably, these are metastables in the complete range of temperatures under atmospheric oxygen partial pressure. The difficulty in oxidizing the surface may arise from the fact that the cations in SnO_2 are already in their maximum oxidation states, which prevents the further addition of monatomic O^{2-} species to the surface.

We should stress that, because of the size of the slab used in our calculations (2×1 supercell), here we have compared only certain discrete degrees of oxidation-reduction of the surface. For example, in the case of $O_{BridgVac}$, $\Gamma_O = -0.5$ and $\Gamma_O = -1$ correspond to 50% and 100% reduction of the surfaces, but, in the real system, intermediate compositions may be stable under different pressure and temperature conditions. Slightly reduced surfaces could then be stable at temperatures lower than those estimated above.

Adsorption energy modeling.— To estimate the energy change involved in the process of adsorption of a molecule onto a clean surface, we built models of (*i*) the clean surface slab, (*ii*) the molecule, and (*iii*) the surface plus the molecule system. For all three of these models, total energy calculations were performed, allowing us to evaluate the total energy balance of the adsorption process (the so-called adsorption energy, E_{ads})

$$E_{Tinitial} = E_{T(clean\ surface)} + E_{T(molecule)}$$

$$E_{Tfinal} = E_{T(clean\ surface+molecule)}$$

$$E_{ads} = \Delta E_T = E_{Tfinal} - E_{Tinitial} \qquad [2]$$

A negative E_{ads} means that the adsorption is energetically favorable, and may occur spontaneously without entropic considerations (DFT deals with the ground state at 0 K).

The adsorption analysis requires several complementary steps: identification of possible surface adsorption sites (considering vacant sites), molecular modeling, and, finally, adsorption modeling of NO_x and SO_2.

Two relevant adsorption sites appear to be a natural choice for the stoichiometric surface: a bridging site and an in-plane site.[9] It seems clear that the latter involves not only oxygen atoms but also the corresponding Sn_{5c} atom. In addition, the adsorption to oxygen-removed sites (vacant sites) seems relevant, so $O_{BridgVac}$ and $O_{InPlaneVac}$ sites are considered.

A good description of the adsorbed molecules is necessary to obtain credible theoretical predictions, Table II gives the molecular models used and the energetic and geometric parameters obtained

Table II. Energetic and geometric first-principles-modeled parameters of several molecules involved in the adsorptions considered in this work. Reference values are from the literature.

Compound	Bond energy (eV)		Bond (Å)		Angle (°)	
	This work	Reference value[37]	This work	Ref.	This work	Ref.
O_2	5.90	6.23(calc.) 5.23(exp.)	1.24	1.18–1.21[38]	-	-
N_1	9.47	10.55(calc.) 9.47(exp.)	1.12	1.09–1.11[39]	-	-
NO	7.03	7.45(calc.) 6.63(exp.)	1.17	1.12–1.17[40]	-	-
NO_2	5.54	-	1.23	1.20[41]	132	133–134[41]
SO_2	5.91	-	1.49	1.48[42]	112	109[42]

Table III. Calculated adsorption energies, E_{ads}, for NO_x at several adsorption sites of the $SnO_2(110)$ surface and maximum desorption rate temperature T_{MDR} estimated for the experimental conditions of Ref. 44. Some configurations are not energetically favorable ($E_{ads} > 0$). Energetically favorable processes are labeled with letters in parenthesis to identify them in Fig. 4. For NO, a configuration in the presence of $SO_2(Y)$ is considered for later discussion on poisoning.

Adsorbate	Surface termination (Γ_O)	Adsorption site		E_{ads} (eV)	T_{MDR} (°C)	
NO	0.0	O_{Bridg}		−1.32	198	(a)
	0.0	$Sn_{InPlane}$		−0.24	52	(b)
	−0.5	O_{Bridg}		−1.18	167	(c)
	−0.5	$O_{Bridg}+SO_2$ in $O_{BridgVac}$		−1.28	-	(Y)
	−0.5	$O_{BridgVac}$		−0.42	89	(d)
	−1.0	$O_{BridgVac}$		−0.98	153	(e)
NO_2	0.0	O_{Bridg}		+1.51	-	
	0.0	$Sn_{InPlane}$		−0.52	94	(t)
	−0.5	$O_{BridgVac}$	(single bonded)	−2.31	502	(o)
	−0.5	$O_{BridgVac} - Sn_{InPlane}$		+0.34	-	
	−1.0	$O_{BridgVac}$	(single bonded)	−2.02	424	(v)
			(double bonded)	−1.95	400	(w)
	−1.0	$O_{BridgVac} - Sn_{InPlane}$		−2.11	454	(x)
	−0.5	$O_{InPlaneVac}$	(single bonded)	−1.26	178	(y)
	−1.0	$O_{InPlaneVac}$	(double bonded)	−0.74	120	(z)

compared with those in the literature. The agreement achieved is comparable with the commonly accepted discrepancy described in the literature.[37]

Table III summarizes calculated E_{ads} for NO and NO_2 and the adsorption sites considered. Adsorption temperatures were obtained by means of the well-known Redhead equation, which links the $|E_{ads}|$ of a process with its maximum desorption rate temperature (T_{MDR}) in a temperature-programmed desorption (TPD) experiment.[43] The adjusting parameters were set according to the experimental conditions of Ref. 44 where an experimental TPD spectrum can be found for NO and NO_2 desorption from an $SnO_2(110)$ surface (Fig. 4).
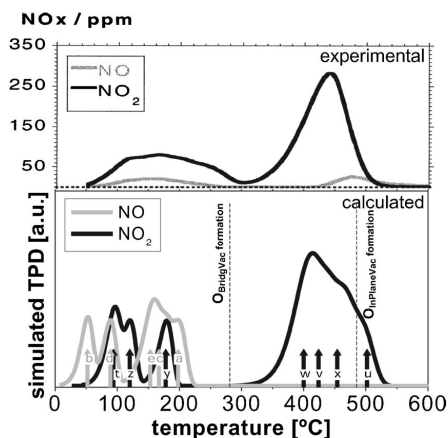
Figure 4. Top: Experimental TPD spectra for NO and NO_2 desorbing from a dehydroxylated $SnO_2(110)$ surface (reprinted from Ref. 44, with permission from Elsevier). Bottom: Calculated TPD spectra for NO and NO_2 considering all of the configurations detailed in Table III. One TPD spectrum was simulated (by means of solving the rate expression for desorption kinetics[43,45]) for each adsorption configuration with the experimental parameters given in Ref. 44. For every configuration, the temperature corresponding to the maximum desorption rate is indicated with a labeled arrow (see labels and T_{MDR} values in Table III). Total spectra are sums of the normalized single configuration spectra. Total intensities only serve as a visual guide as they are obtained from summing normalized intensities.

We recall that our model only provides energies (and their corresponding desorption temperatures) for the specific adsorption configurations analyzed. In contrast, an experimental TPD spectrum provides the temperature range over which species are desorbed by considering a plethora of adsorption configurations present in a real sample. Consequently, we would expect the calculated temperatures to belong to the corresponding experimental TPD signal range. Our theoretical predictions of T_{MDR} for the few adsorption cases considered fall within the wide experimental desorption peaks from Ref. 44.

Our results suggest that O_{Bridg} sites are the most energetically favorable for NO. This behavior is compatible with the observation that NO reduces SnO_2, given that NO is expected to bond with a surface oxygen and eventually to remove it, thus reducing the surface.[1] In contrast, energetically preferred adsorption sites for NO_2 are related to oxygen vacancies. Moreover, the TPD spectrum simulated for NO_2 suggests that the lower temperature peak could be associated with $O_{InPlaneVac}$ sites while the one at a higher temperature seems to be due to $O_{BridgVac}$.

Note that the difference between the preferred adsorption sites of NO and NO_2 indicates that by generating vacant sites and adjusting their density, the feasibility of adsorption onto SnO_2 of NO vs NO_2 may be changed.

Table IV summarizes the calculated E_{ads} for SO_2 at several sites. As for NO_2, the preferred adsorption sites involve oxygen vacancies but in this case it seems that the adsorption has a similar strength for both $O_{InPlaneVac}$ and $O_{BridgVac}$. This difference in behavior with regard to the oxygen vacancy type has dramatic consequences on the interference of SO_2 when trying to detect NO_2.

It is known that SO_2 avidly saturates NO_2 adsorption sites, reducing the sensing capability of SnO_2.[6] In the present calculations, the strongest adsorption within the cases studied corresponds to SO_2. This theoretical behavior is compatible with the experimental evidence of poisoning.

In particular, SO_2 adsorbs more strongly than NO_2 to vacant oxygen sites but the difference in the calculated E_{ads} values is smaller for $O_{BridgVac}$ related adsorptions (the higher temperature peak in the NO_2 TPD spectrum). This suggests that the poisoning strength depends on the adsorption site involved in the process. So $SnO_2(110)$ in which the presence of $O_{BridgVac}$ dominates and there are few $O_{InPlaneVac}$ would appear to be a better sensor candidate, as it should experience less poisoning. Linking this with the surface reduction stability described above, it is clear that to avoid the massive apparition of $O_{InPlaneVac}$ the temperature of the sensing material

Table IV. Calculated adsorption energies, E_{ads}, for SO$_2$ at several adsorption sites of the SnO$_2$(110) surface and maximum desorption rate temperature T_{MDR} estimated for the experimental conditions of Ref. 44. Note that, in contrast to the case of NO$_2$, our calculations show that SO$_2$ adsorption onto a 100% reduced slab may only be spontaneous ($E_{ads} < 0$) in one single O bonding configuration. Some configurations are not energetically favorable ($E_{ads} > 0$).

Adsorbate	Surface termination (Γ_O)	Adsorption site		E_{ads} (eV)	T_{MDR} (°C)
SO$_2$	0.0	O$_{Bridg}$		+1.72	-
	0.0	Sn$_{InPlane}$		−0.86	128
	−0.5	O$_{BridgVac}$	(single bonded)	−2.05	435
	−0.5	O$_{BridgVac}$ − Sn$_{InPlane}$		+1.12	-
	−1.0	O$_{BridgVac}$	(single bonded)	+0.26	-
			(double bonded)	−2.56	606
	−1.0	O$_{BridgVac}$ − Sn$_{InPlane}$		−2.97	741
	−0.5	O$_{InPlaneVac}$	(single bonded)	−2.98	748
	−1.0	O$_{InPlaneVac}$	(double bonded)	−3.09	770

should not exceed 480°C. If an occasional single O$_{InPlaneVac}$ is present below this temperature, adsorption onto such a site should be avoided to diminish the effect of the poisoning, and so the sensing material should work at temperatures higher than 200°C which favors the desorption of NO$_2$ from and O$_{InPlaneVac}$. Finally, to obtain good sensing behavior over a large range of the target gas concentration, adsorption sites must be kept unsaturated. In other words, the sensing material should work at a high desorption rate temperature to achieve a steady state where the adsorption/desorption ratio is a function of the concentration. Consequently, according to the NO$_2$ TPD spectrum, temperatures between 200 and 300°C do not appear promising.

All of these considerations suggest that to achieve the best adsorption conditions and diminish poisoning by SO$_2$, the optimum working temperatures are between 300 to 450°C (left side of the high-temperature desorption peak of NO$_2$).

The preferred adsorption sites for NO are O$_{Bridg}$. Therefore, it may seem that there is no competitive behavior with SO$_2$. However, Table III shows that, for intermediate reductions, the adsorption of NO onto O$_{Bridg}$ in the presence of an SO$_2$ occupying an O$_{BridgVac}$ site (Table III case Y) is slightly stronger than in the noninteracting case (case c). These results suggest that in spite of the predilection for different adsorption sites shown by NO and SO$_2$, a cross-influence may occur between the two compounds, and this would merit further analysis.

It is important to bear in mind that the previous discussion is centered around good behavior in the adsorption stage. This is only one stage in the chemical transduction and, therefore, it is necessary but not sufficient to guarantee a good sensing response.

Conclusions

We adopted a theoretical approach to study the NO and NO$_2$ adsorption onto SnO$_2$(110) based on ab initio calculations. Bridging oxygen sites and oxygen vacancy sites were identified as the most relevant adsorption sites for NO and NO$_2$, respectively. This difference suggests that by adjusting the oxygen vacancy site density the feasibility of NO vs NO$_2$ adsorption onto SnO$_2$ may be changed.

Oxygen vacancies seem to be the most favorable adsorption sites for poisoning by SO$_2$, suggesting competitive behavior with NO$_2$. Theoretical trends indicate that while SO$_2$ adsorption strength is almost independent of the oxygen vacancy type (bridging or in-plane), NO$_2$ adsorbs more strongly onto bringing than in-plane vacancies. Such a difference suggests that poisoning may be reduced if the working conditions make bridging oxygen vacancies the dominant adsorption site. Considering the surface reduction stability with respect to temperature under atmospheric oxygen partial pressure, and the experimental and ab initio modeled TPD spectra of NO$_2$, ideal SnO$_2$(110) surfaces present optimum adsorption activity for gas sensing applications with minimum poisoning at temperatures between 300 and 450°C. In the case of NO, no competitive behavior

with SO$_2$ was expected due to their predilection for different adsorption sites, but further study may be necessary to analyze cross-influences.

We have shown how ab initio modeling of surfaces and adsorptions can provide ideas for improving the performance of solid-state chemical sensors. Theoretical predictions regarding optimum working conditions for real sensors would require a more complex model including, for example, charge transfers between adsorbate and surface and the cross-influence of OH groups due to humidity.

References

1. W. Göpel and K. D. Schierbaum, *Sens. Actuators B*, **26/27**, 1 (1995).
2. M. Batzill and U. Diebold, *Prog. Surf. Sci.*, **79**, 47 (2005).
3. G. Sverveglieri, *Sens. Actuators B*, **23**, 103 (1995).
4. A. Fritz and V. Pitchon, *Appl. Catal., B*, **13**, 1 (1997).
5. D. E. Williams, G. S. Henshaw, and K. F. E. Pratt, *J. Chem. Soc., Faraday Trans.*, **91**, 3307 (1995).
6. B. Ruhland, T. Becker, and G. Muller, *Sens. Actuators B*, **50**, 85 (1998).
7. J. Oviedo and M. J. Gillan, *Surf. Sci.*, **463**, 93 (2000).
8. J. Oviedo and M. J. Gillan, *Surf. Sci.*, **467**, 35 (2000).
9. M. A. Mäki-Jaskari and T. T. Rantala, *Phys. Rev. B*, **64**, 075407 (2001).
10. M. A. Mäki-Jaskari and T. T. Rantala, *Phys. Rev. B*, **65**, 245428 (2002).
11. M. Batzill, K. Katsiev, J. M. Burst, U. Diebold, A. M. Chaka, and B. Delley, *Phys. Rev. B*, **72**, 165414 (2005).
12. J. Oviedo and M. J. Gillan, *Surf. Sci.*, **490**, 221 (2001).
13. J. Oviedo and M. J. Gillan, *Surf. Sci.*, **513**, 26 (2002).
14. F. R. Sensato, R. Custódio, M. Calatayud, A. Beltrán, J. Andrés, J. R. Sambrano, and E. Longo, *Surf. Sci.*, **511**, 408 (2002).
15. M. A. Mäki-Jaskari and T. T. Rantala, *Surf. Sci.*, **537**, 168 (2003).
16. A. Maiti, J. A. Rodriguez, M. Law, P. Kung, J. R. McKinney, and P. Yang, *Nano Lett.*, **3**, 1025 (2003).
17. J. Arbiol, A. Cirera, F. Peiró A. Cornet, J. R. Morante, J. J. Delgado, and J. J. Calvino, *Appl. Phys. Lett.*, **80**, 329 (2002).
18. P. Hohenberg and W. Kohn, *Phys. Rev.*, **136**, B864 (1964).
19. W. Kohn and L. J. Sham, *Phys. Rev.*, **140**, A1133 (1965).
20. P. Ordejón, E. Artacho, and J. M. Soler, *Phys. Rev. B*, **53**, R10441 (1996).
21. J. M. Soler, E. Artacho, J. D. Gale, A. Garcia, J. Junquera, P. Ordejón, and D. Sánchez-Portal, *J. Phys.: Condens. Matter*, **14**, 2745 (2002).
22. J. P. Perdew, K. Burke, and M. Emzerhof, *Phys. Rev. Lett.*, **77**, 3865 (1996).
23. N. Troullier and J. L. Martins, *Phys. Rev. B*, **43**, 1993 (1991).
24. L. Kleinman and D. M. Bylander, *Phys. Rev. Lett.*, **48**, 1425 (1982).

25. J. Moreno and J. M. Soler, *Phys. Rev. B*, **45**, 13891 (1992).
26. H. Monkhorst and J. Pack, *Phys. Rev. B*, **13**, 5188 (1976).
27. S. F. Boys and F. F. Bernardi, *Mol. Phys.*, **19**, 553 (1970).
28. D. Sánchez-Portal, P. Ordejón, E. Artacho, and J. M. Soler, *Int. J. Quantum Chem.*, **65**, 453 (1997).
29. A. S. Barnard and P. Zapol, *Phys. Rev. B*, **70**, 235403 (2004).
30. W. Zhu and P. Wu, *Chem. Phys. Lett.*, **396**, 38 (2004).
31. M. Ramamoorthy, D. Vanderbilt, and R. D. King-Smith, *Phys. Rev. B*, **49**, 16721 (1994).
32. K. Reuter and M. Scheffler, *Phys. Rev. B*, **65**, 035406 (2002).
33. M. W. Chase, *NIST-JANAF Thermochemical Tables*, American Chemical Society, Woodbury (1998).
34. K. Ellmer, *J. Phys. D*, **34**, 3097 (2001).
35. D. F. Cox, T. B. Fryberger, and S. Semancik, *Phys. Rev. B*, **38**, 2072 (1988).

36. D. F. Cox, T. B. Fryberger, and S. Semancik, *Surf. Sci.*, **227**, L105 (1990).
37. S. Kurth, J. P. Perdew, and P. Blaha, *Int. J. Quantum Chem.*, **75**, 889 (1999).
38. H. Dong, Y.-H. Ding, and C.-C. Sun, *Phys. Chem. Chem. Phys.*, **7**, 3711 (2005).
39. H. Orita and N. Itoh, *Surf. Sci.*, **550**, 166 (2004).
40. Z.-G. Wei, X.-R. Huang, S.-W. Zhang, Y.-B. Sun, H.-J. Qian, and C.-C. Sun, *J. Phys. Chem. A*, **108**, 6771 (2004).
41. J.-X. Zhang, J.-Y. Liu, Z.-S. Li, and C.-C. Sun, *J. Comput. Chem.*, **25**, 1888 (2004).
42. K. Sendt and B. S. Haynes, *J. Phys. Chem. A*, **109**, 8180 (2005).
43. M. C. Desjonquères and D. Spanjard, *Concepts in Surface Physics*, 2nd ed., Springer, Berlin (1996).
44. E. Leblanc, L. Perier-Camby, G. Thomas, R. Gibert, M. Primet, and P. Gelin., *Sens. Actuators B*, **62**, 67 (2000).
45. V. P. Zhdanov and B. Kasemo, *Surf. Sci.*, **415**, 403 (1998).

J.D. Prades, A. Cirera, J.R. Morante,
"Ab initio calculations of NO₂ and SO₂ chemisorption onto non-polar ZnO surfaces"
Thin Sol. Films, submitted (2008).

5

Ab initio calculations of NO_2 and SO_2 chemisorption onto non-polar ZnO surfaces

J. Daniel Prades*, Albert Cirera, and Joan R. Morante.

EME/XaRMAE/IN²UB, Departament d'Electrònica, Universitat de Barcelona, E-08028, Barcelona, Spain

RECEIVED DATE (automatically inserted by publisher); dprades@el.ub.es

Abstract: The authors present an *ab initio* study of NO_2 and SO_2 chemisorption onto non-polar ZnO(10-10) and ZnO(11-20) surfaces with the aim of providing theoretical hints for further developments in gas sensors. From first principles calculations (DFT-GGA approximation), the most relevant surface reduction scenarios are analyzed and, subsequently, considered in the chemisorption study. First, calculations indicate that NO_2 adsorbs avidly onto Zn surface atoms. This is compatible with the oxidizing character of NO_2. Second, the results also explain the sensor poisoning by SO_2 adsorption (since this molecule competes with NO_2 for the same adsorption sites) and indicate that poisoning can only be reverted at typical operation temperatures (T ≤ 700 ºC) in the case of stoichiometric ZnO(10-10) surfaces.

1. Introduction

Zinc oxide (ZnO) is a semiconductor metal oxide suited for a great variety of applications like chemical gas sensing, UV light emitters/detectors, transparent high-power electronics, surface acoustic wave devices, piezoelectric transducers and varistors [1-4].

As far as gas sensing properties are concerned, ZnO was the first metal oxide used in semiconductor gas sensing devices [5]. There are studies that demonstrate their response towards gases like CO, CO_2, NO, NO_2, SO_2, H_2S, HCHO, NH_3, H_2, ethanol and humidity [6,7]. Short later, the great stability and sensitivity of other materials such as SnO_2 and TiO_2 attracted the attention of the researchers [8,9]. For this reason, today we can find many computational studies devoted to the interaction of gaseous molecules with SnO_2 and TiO_2 [8-10], but only few theoretical works dealing with the interaction of ZnO with gases [11-18]. Complete reviews on the state-of-the-art of ZnO based gas sensors and their theoretical modeling can be found elsewhere [2,6-8]. In the last few years, ZnO has attracted again great interest [19] as a result of the development of the first nanowire synthesis techniques [20].

NO_2 is generated in combustion processes and has hazardous effects on the human health [21]. Consequently, its detection is an issue of major interest in the mainstream gas sensing applications. It can be easily detected measuring the modulation of the electrical conductance of metal oxides (like ZnO) when NO_2 molecules are trapped at their surface [6,7]. An important problem of this technology is that other interfering gases (like SO_2) have a poisoning effects on the sensors' response to NO_2 [6,7,9,10]. As previously stated, very few theoretical works studied the interaction between NO_2 and ZnO surfaces and only considered the interaction with ZnO polar surfaces (i.e. ZnO(000±1)) [18]. According to the work of Rodriguez et al. [18] on the interaction of NO_2 with polar ZnO surfaces, NO_2 is a very good oxidizing agent for preparing ZnO from metallic zinc. Zn sites reacts more vigorously with NO_2 than with other metals such as Rh, Pd, or Pt which are typical $DeNO_x$ catalysts. No evidence was found for the full decomposition of the NO_2 molecule (i.e., no $NO_2 \rightarrow N + 2O$). It appears that NO_2 is very efficient for fully oxidizing metal Zn centers that are missing O neighbors in oxide surfaces.

In contrast to this previous theoretical work [18], most of the nanowires used in recent gas sensing experiments expose lateral non-polar surfaces (i.e. ZnO(10-10) and ZnO(11-20)) [19,20]. Consequently, there is a lack of theoretical background to support the development of this gas sensing technology. Here we present an atomistic theoretical study on the interaction of NO_2 and SO_2 with the most stable (and relevant) non-polar surfaces of ZnO that may contribute to understand the chemistry and performance of ZnO-based gas sensors.

2. Computational Details

Our first-principles methodology was based on the density functional theory [22,23] (DFT) as implemented in the SIESTA code [24,25]. We made use of the generalized gradient approximation (GGA) for the exchange-correlation functional [26] and norm-conserving Troullier-Martins pseudopotentials [27] in the Kleinman-Bylander factorization form [28]. The solutions of the Khon-Sham equations were expanded as a linear combination of atomic pseudo-wave-functions of finite range. For all atomic species double ζ plus polarization orbitals basis-sets were used. Total energy convergence was guaranteed below 10 meV as usual in this kind of calculations [29]. To do so, a real space mesh cut-off of 250 Ry and a reciprocal space grid cut-off about 15 Å were used. The structural relaxations were done by means of a conjugate gradient minimization of the energy, until forces on all atoms were smaller than 0.04 eV/Å (which provided relaxed total energy values more stable than 10 meV). No constraints were imposed in the relaxation where forces were calculated as analytical derivatives of the total energy [30]. Spin polarization was considered in the total energy computations and basis set superposition error (BSSE) [31] was corrected in the calculated adsorption energies.

To deal with surface stability and adsorption calculations, we modeled all surface geometries as three dimensionally periodic slab systems, generated from the relaxed bulk unit cell, with a vacuum width of 12 Å between surfaces to avoid interaction between periodic images of the slabs. These slabs were constituted by 2x2 surface supercells to model different surface reduction percentages, and to ensure that the adsorbed compound do not interact with periodic images of the supercell.
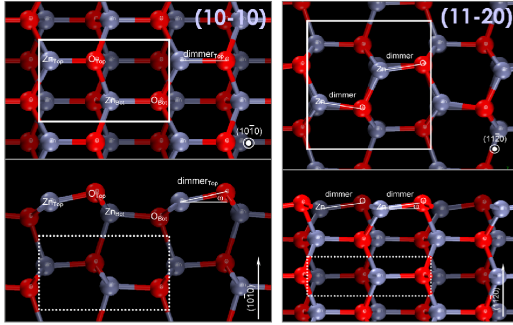
Figure 1: Top and side views of the non-polar ZnO(10-10) and ZnO(11-20) surfaces. In each case, squares limit the atoms contained in one single unit cell. Adsorption sites are highlighted and relevant surface atoms are identified.

3. Results and Discussion

3.1 Surface orientation stability

ZnO wurtzite structure belongs to the hexagonal system (space group P6$_3$mc, lattice parameters a = b = 3.25 Å and c = 5.20 Å), and two non-symmetry-equivalent atoms at $(1/3,2,0,0)_{Zn}$ $(1/3,2/3,0.3826)_o$ [2]. Wurtzite structure does not present inversion symmetry along ZnO(000±1), and consequently, the crystal exhibits crystallographic polarity. The non-polar ZnO(10-10) and ZnO(11-20) surfaces are the most abundant and studied from the surface science point of view [11,32-36].

Both non-polar surfaces are obtained by cutting the crystal perpendicular to hexagonal Zn and O layers. The (10-10) and (11-20) surface geometries are sketched in Fig. 1. Each layer of the (10-10) surface contains two Zn-O dimmers per repetition unit, at different depths (labeled as "Top" and "Bot" in Fig. 1). The (11-20) surface layers are formed by two Zn-O dimmers, which form *zig-zag* lines along the surface. In this case, the two dimmers are equivalent and in the same plane. Our estimates of the surface free energy values were 0.064 eV/Å^2 for (10-10) and 0.070 eV/Å^2 for (11-20). Therefore, the (10-10) surface orientation is slightly more stable than the (11-20). This result is compatible with previous calculations [36].

3.2 Surface reduction-oxidation stability

We followed the *ab initio* thermodynamics methodology proposed by Reuter and Scheffler [37] for the theoretical analysis of surface oxidization and reduction. This formalism enables to elucidate the most favorable surface configuration in equilibrium with the oxygen content in air at a given pressure and temperature (or, equivalently, a given oxygen chemical potential μ_O). Briefly, the most stable surface composition and geometry at a given temperature T and pressure P is the one that minimizes the surface-free energy $\sigma(T,P)$ given by

$$\sigma(T,P) = \gamma - \Gamma_0 \mu_0(T,P) / A \qquad (1)$$

where $\Gamma_0 = \frac{1}{2}(N_0 - N_{Zn})$ is the excess of oxygen in each surface (N_o and N_{Zn} are the number of oxygen and zinc atoms at the outermost layer), γ is the surface free energy at $\mu_0 = 0$ (i.e. under the ground conditions of 0K that are assumed in DFT), $\mu_0(T,P)$ is the oxygen chemical potential. A detailed description of this procedure and its applications can be found elsewhere [9,10].

The application of Eq. (1) to the oxygen defective ZnO non-polar surfaces indicates that, under thermodynamic equilibrium at P ~ 0.21 bar of atmospheric oxygen, heating above room temperature (T ~ 25°C) is required to remove the outermost oxygen atoms. Fig. 2 shows the results for different reduction percentages for both surfaces.

In the case of (10-10), reduction of O$_{Top}$ atoms becomes always more energetically favorable than reduction of O$_{Bot}$ atoms. In the first case (O$_{Top}$), slight surface reduction becomes favorable above 750°C while the second case (O$_{Bot}$) is possible above 1100°C. This is compatible with previously reported experiments [38].

Concerning (11-20), there is only one type of oxygen atoms at the outermost surface layer (see Fig. 1). In this case slight reduction takes place at temperatures above 550°C. Our results also indicate that higher reduction percentages are stable above 1000°C. Complete surface reduction is feasible above 1200°C.

In summary, only stoichiometric or slightly reduced surfaces are plausible scenarios at the operating temperatures of ZnO gas sensors (T ≤ 700°C) [6,7] and, consequently, only these two situations will be considered in the following sections.
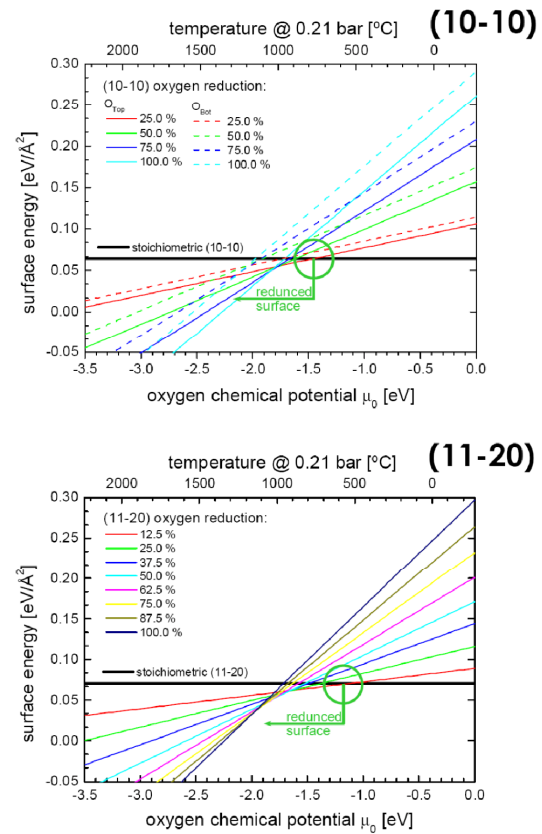
Figure 2: Surface free energies for different terminations of the non-polar ZnO(10-10) and ZnO(11-20) surfaces as a function of the oxygen chemical potential. The top axis shows the corresponding O$_2$ gas temperature for atmospheric air equivalent conditions (i.e.: oxygen partial pressure of P ~ 0.21 bar [39])

Table 1. Calculated adsorption energies E_{ads}, temperature of maximum desorption rate T_{MDR} and charge transfer Δq for NO_2 and SO_2 onto the ZnO(10-10) surface. "O_{Top}" and "Zn_{Top}" cases correspond to the stoichiometric surface. "Zn_{Top} + O_{Top} vac" corresponds to the slightly reduced surface (25% of O_{Top} oxygens). Schematic representations (side view) of the adsorption geometries are included.

(10-10)		E_{ads} [eV]		T_{MDR}[ºC]		Δq[e⁻]	
Site \ Adsorbate		NO_2	SO_2	NO_2	SO_2	NO_2	SO_2
O_{Top}		+0.02	-1.09	-	510	+0.01	+0.59
Zn_{Top}		-0.45	-1.08	50	502	+0.12	+0.10
Zn_{Top} + O_{Top} vac		-0.76	-0.61	273	165	+0.28	+0.15
Zn_{Top}		-0.66	-1.12	201	531	+0.14	+0.32
Zn_{Top} + O_{Top} vac		-1.10	-2.30	517	1378	+0.36	+0.79

Table 2. Calculated adsorption energies E_{ads}, temperature of maximum desorption rate T_{MDR} and charge transfer Δq for NO_2 and SO_2 onto the ZnO(11-20) surface. "O" and "Zn" cases correspond to the stoichiometric surface. "Zn + O vac" corresponds to the slightly reduced surface (12.5% of surface oxygens). Schematic representations (side view) of the adsorption geometries are included.

(11-20)		E_{ads} [eV]		T_{MDR}[ºC]		Δq[e⁻]	
Site \ Adsorbate		NO_2	SO_2	NO_2	SO_2	NO_2	SO_2
O		+0.15	-1.19	-	581	+0.05	+0.69
Zn		-0.58	-1.28	142	646	+0.15	+0.16
Zn + O vac		-0.79	-0.72	300	241	+0.23	+0.17
Zn		-0.55	-1.03	121	472	+0.18	+0.35
Zn + O vac		-0.94	-2.15	369	1273	+0.45	+0.70

3.3 Molecular adsorption modeling

In order to estimate the energy exchange involved in the adsorption process of a molecule onto a clean surface, we built models of (1) the clean surface slab, (2) the molecule, and (3) the surface slab with the molecule adsorbed. For all these three models, total energy calculations were performed allowing us to evaluate the total energy balance of the adsorptions process (so called adsorption energy E_{ads}) as:

$$E_{Tinitial} = E_{T(clean\ surface)} + E_{T(molecule)}$$
$$E_{Tfinal} = E_{T(clean\ surface+molecule)}$$
$$E_{ads} = \Delta E_T = E_{Tfinal} - E_{Tinitial} \qquad (2)$$

Accordingly, a negative value of E_{ads} means that the adsorption is energetically favorable, it being possible for this to occur spontaneously without entropic considerations [9,10]. To ensure the effective cancellation of errors between the large energies that appear in Eq. (2) adequate conditions were considered [40]. In our case, a 5 layer slab was enough to guarantee the stability of the adsorption energy values.

Desorption temperature estimations were obtained by means of the well-known Redhead equation, which relates $|E_{ads}|$ of a process to the maximum desorption rate temperature (T_{MDR}) in a temperature-programmed desorption (TPD) experiment [9,41].

The charge transferred to the adsorbate Δq was estimated by the usual Mulliken's population analysis of the molecule atoms before and after the adsorption. According to our definition, a higher and positive Δq implies a bigger charge captured by NO_2.

3.3.a (10-10) surface

Under the light of the previous results on surface stability (section 3.2), we only considered adsorptions on stoichiometric and slightly (25%) O_{Top} reduced ZnO(10-10) surfaces (Table 1).

In the case of stoichiometric surfaces, NO_2 tends to adsorb onto Zn sites. Slight surface reduction does not change the preferential adsorption site but the presence of surface oxygen vacancies increase the adsorption strength (and T_{MDR}) and the charge transfer (and the effect on the conductance of the sensor). In both cases there is a strong influence of the molecule orientation being the bi-dentate configuration (2 O atoms bonded to a surface Zn atom) the most stable one. All these results are compatible with the general trends reported by Rodriguez et al. [18]: NO_2 is an oxidizing agent that reacts vigorously with Zn atoms.

As far as SO_2 is concerned, our results indicate that this oxidizing molecule competes with NO_2 for the same adsorption

sites and adsorbs more avidly (specially in reduced surfaces, with T_{MDR} as high as 1273ºC). Only, in the case of stoichiometric surfaces, temperatures in the range of 550ºC would "clean" and "reset" the surface after poisoning by SO_2.

3.3.b (11-20) surface

The study of the thermodynamic stability of ZnO(11-20) revealed that the stoichiometric configuration is the most plausible up to 550ºC. Above this temperature slight reduction is also possible. For this reason we considered again only stoichiometric and slightly (12.5%) oxygen reduced ZnO(11-20) surfaces (Table 2).

Again, spontaneous adsorption take place only onto Zn atoms and these adsorptions are stronger onto reduced surfaces. In this case, $|E_{ads}|$ energies (and T_{MDR}) are lower than in (10-10) probably due to the zig-zag structure of (11-20) that creates local electric fields less favorable for the adsorption. This effect is also observed in the adsorption of SO_2, that competes again with NO_2 for the same adsorption sites).

Now, "cleaning" the stoichiometric (11-20) surface after SO_2 poisoning is not straightforward. "Resetting" would require temperatures around 650ºC but this could induce surface reduction which would increase the strength of the SO_2 adsorption.

4. Conclusions

An ab initio study of the adsorption of NO_2 and SO_2 onto non-polar ZnO(10-10) and ZnO(11-20) surfaces is presented. The (10-10) and (11-20) stoichiometric surfaces are stable up to 750 ºC and 550 ºC, respectively. At higher temperatures, a progressive reduction of the oxygen content of the outermost ZnO layer appears.

NO_2 adsorption takes place spontaneously onto the stoichiometric and slightly reduced terminations of both non-polar surfaces. In all cases, bi-dentate NO_2 adsorption onto Zn surface atoms are the preferred configurations. This is compatible with the oxidizing character of NO_2.

In both surfaces, SO_2 competes with NO_2 for the same adsorption sites, and in general, adsorbs more avidly. This result explains the poisoning by SO_2 of the sensing response of ZnO towards NO_2. According to our results, temperatures around 550ºC would be enough to revert the poisoning effect in stoichiometric (10-10) surfaces but temperatures above 1000ºC would be necessary to recover (11-20) surfaces.

Acknowledgement

References

[1] L. Schmidt-Mende et al., Materials Today **10** (2007) 40
[2] Ü. Özgür et al., J. Appl. Phys. **98** (2005) 041301
[3] D.P. Norton et al., Materials Today **7** (2004) 34
[4] G.-C. Yi et al., Semicond. Sci. Technol. **20** (2005) S22
[5] T. Seiyama et al., Anal. Chem. **34** (1962) 1052
[6] G. Eranna et al., Critical Rev. Sol. State and Mater. Sci. **29** (2004) 111
[7] E. Comini, Anal. Chim. Acta. **568** (2006) 28
[8] U. Diebold et al., App. Surf. Sci. **237** (2004) 336
[9] J. D. Prades et al. Chapter 13 in *"Quantum Chemical Calculations of Surfaces and Interfaces of Materials"*, Editors: V.A. Basiuk and P. Ugliengo. American Scientific Publishers (2008).
[10] (a) J. D. Prades et al., J. Electrochem. Soc. **154** (2007) H657; (b) J. D. Prades et al, Sensors and Actuators B **126** (2007) 6; (c) J. D. Prades et al., Sensors and Actuators B **126** (2006) 62
[11] B. Meyer, Phys. Rev. B **69** (2004) 045416.
[12] V. Staemmler et al., Phys. Rev. Lett. **90** (2003) 106102
[13] M. Kunat et al., Phys. Rev. B **66** (2002) 081402
[14] D. J. Cooke et al., J. Phys. Chem. B **110** (2006) 7985
[15] K. Fink, Phys. Chem. Chem. Phys. **8** (2006) 1482
[16] S. Chaturvedi et al., J. Phys. Chem. B **102** (1998) 7033
[17] J. D. Prades et al., Thin Sol. Films **515** (2007) 8670
[18] J. A. Rodriguez et al., J. Phys. Chem. B **104** (2000) 319
[19] C. M. Lieber et al., MRS Bull. **32** (2007) 99
[20] Z. W. Pan et al., Nature **291** (2001) 1947
[21] World Health Organisation. Information available in http://www.who.int/peh/air/Airqualitygd.htm
[22] P. Hohenberg et al., Phys. Rev. **136** (1964) B864
[23] W. Kohn et al., Phys. Rev. **140** (1965) A1133
[24] P. Ordejón et al., Phys. Rev. B **53** (1996) R10441
[25] J. M. Soler et al., J. Phys: Condens. Matter. **14** (2002) 2745
[26] J. P. Perdew et al., Phys. Rev. Lett. **77** (1996) 3865
[27] N. Troullier et al., Phys. Rev. B **43** (1991) 1993
[28] L. Kleinman et al., Phys. Rev. Lett. **48** (1982) 1425
[29] J. Oviedo et al., Surf. Sci. **490** (2001) 221
[30] D. Sánchez-Portal et al., Int. J. Quantum Chem. **65** (1997) 453
[31] S. F. Boys et al., Mol. Phys. **19** (1970) 553
[32] I. Ivanov et al., Phys. Rev. B **24** (1981) 7275
[33] P. Schröer et al., Phys. Rev. B **49** (1994) 092
[34] J. E. Jaffe et al., Phys. Rev. B **49** (1994) 153
[35] A. Filippetti et al.. Phys. Rev. B **59** (1999) 8026
[36] A. F. Kohan et al., Phys. Rev. B **61** (2000) 15019
[37] K. Reuter et al., Phys. Rev. B **65** 035406 (2002).
[38] W. Göpel et al., Phys. Rev. B **22** (1980) 6447
[39] M.W. Chase, *"NIST-JANAF Thermochemical Tables"*. American Chemical Society, Woodbury (1998).
[40] K.M. Neyman et al., Catalysis Today **102** (2005) 2
[41] M.C. Desjonquères et al., *"Concepts in Surface Physics"* 2nd ed. Springer (1996).

J.D. Prades, R. Jimenez-Diaz, F. Hernandez-Ramirez, S. Barth, A. Cirera, A. Romano-Rodriguez, S. Mathur, J.R. Morante,
"Ultralow power consumption gas sensors based on self-heated individual nanowires"
Appl. Phys. Lett. **93**, 123110 (2008).

6

Ultralow power consumption gas sensors based on self-heated individual nanowires

J. D. Prades,[1,a)] R. Jimenez-Diaz,[1] F. Hernandez-Ramirez,[1,2,a)] S. Barth,[3,b)] A. Cirera,[1]
A. Romano-Rodriguez,[1] S. Mathur,[3,4] and J. R. Morante[1]

[1]*EME/XaRMAE/IN²UB, Departament d'Electrònica, Universitat de Barcelona, C/ Martí i Franquès 1, Barcelona E-08028, Spain*
[2]*Electronic Nanosystems, S. L., Barcelona E-08028, Spain*
[3]*Nanocrystalline Materials and Thin Film Systems, Leibniz-Institute of New Materials, Saarbruecken D-66123, Germany*
[4]*Department of Inorganic Chemistry, University of Cologne, Cologne D-50939, Germany*

Dissipated power in metal oxide nanowires ($r_{NW} < 45$ nm) often causes important self-heating effects and as a result, undesired aging and failure of the devices. Nevertheless, this effect can be used to optimize the sensing conditions for the detection of various gaseous species, avoiding the requirement of external heaters. In this letter, the sensing capabilities of self-heated individual SnO_2 nanowires toward NO_2 are presented. These proof-of-concept systems exhibited responses nearly identical to those obtained with integrated microheaters, demonstrating the feasibility of taking advantage of self-heating in nanowires to develop ultralow power consumption integrated devices. © *2008 American Institute of Physics*. [DOI: 10.1063/1.2988265]

Nanowires have emerged as potential components of new devices and circuit architectures, due to their unique chemical and physical properties.[1-5] However, their small dimensions are responsible for self-heating effects caused by dissipated power while operating in electrical devices.[6] This leads to temperature gradients, which significantly reduce the lifetime of these components.[7] Nevertheless, applying well-controlled current values through individual nanowires[8] enables setting their effective temperatures to values appropriate for gas sensing applications.

In this letter, we demonstrate that self-heating in individual SnO_2 nanowires can be used to fabricate ultralow consumption gas sensors. These proof-of-concept devices exhibit responses to different concentrations of NO_2, nearly identical to those obtained with an external microheater. Therefore, energy-efficient metal oxide sensors suitable for mobile devices can be obtained using this intrinsic effect. Moreover, the combination of experiments with both technologies (self- or external heating) allows determining the effective temperature achieved during the measurements. The latter result is mandatory for further improvement of the future prototype performance.

Individual single-crystal SnO_2 nanowires, synthesized by catalyst supported chemical vapor deposition of a molecular precursor $[Sn(O^tBu)_4]$,[9] were transferred onto suspended silicon micromembranes equipped with an integrated SnO_2:Sb microheater and platinum interdigitated microelectrodes. Nanowires were electrically contacted to platinum microelectrodes by a lithography process using a FEI Dual-Beam Strata 235 FIB instrument combined with a trimethyl-methylcyclopentadienylplatinum $[(CH_3)_3CH_3C_5H_4Pt]$ injector to deposit platinum.[10] Two probe dc measurements were performed using an electronic circuit designed to guarantee

and control low current levels I_m (from 0.1 to 500 nA) and to avoid undesired fluctuation.[8] All the experiments were performed in a customized chamber, in which the gas flow was maintained at 200 ml min^{-1}. Accurate gaseous environments were provided by massflow controllers mixing synthetic air (SA) and NO_2 (10 ppm ± 1% in SA). Lab-class gases contained less than 5 ppm/V of C_nH_m and H_2O. Ten devices were fabricated using SnO_2 nanowires with lengths (L_{NW}) between 5 and 15 μm and radii (r_{NW}) between 35 and 45 nm, which showed reproducible electrical responses in experiments repeated along for four weeks. Herein, we use the following definition of the conductometric response (S) to NO_2

$$S(\%) = 100 \times \frac{R_{NO_2} - R_{SA}}{R_{SA}}, \qquad (1)$$

where R_{NO_2} is the steady value of the resistance of the nanowire exposed to NO_2 and R_{SA} is the reference resistance value in SA.

Response (S) of SnO_2 to NO_2 strongly depends on the operation temperature.[11] Thus, fast and reversible sensing is merely observed at temperatures above $T = 75$ °C, since the spontaneous desorption of this gas has a minimum thermal energy of $E_{des} \geq 0.52$ eV, which corresponds to a thermal desorption process active above $T \gtrsim 80$ °C.[12]

Individual SnO_2 nanowires exhibited low responses to NO_2 at room temperature ($T = 25$ °C) and probing currents below $I_m = 0.1$ nA without any noticeable recovery of the resistance baseline [Fig. 1(a)]. On the contrary, same devices displayed significant responses to NO_2 pulses (concentrations of 100 ppb–10 ppm) at higher I_m [Fig. 1(a)]. From a dynamic point of view, NO_2 sensing is a thermally activated process, and as a consequence, the higher the temperature T, the shorter is the residence time of the gas molecules on the SnO_2 surface.[13] Thus, shorter response (τ_r) and recovery times (τ_f) are expected with the increasing T.

a)Authors to whom correspondence should be addressed. Electronic addresses: dprades@el.ub.es and fhernandezra@gmail.com.
b)Present address: INRS-Énergie, Matériaux et Télécommunications, Université du Québec, Varennes, Canada.
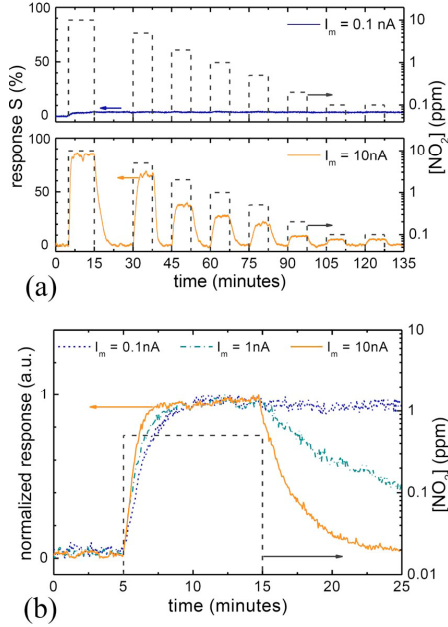
FIG. 1. (Color online) (a) Response S of a SnO$_2$ nanowire operated at two different current values (I_m=0.1 nA and I_m=10 nA) to NO$_2$ pulses of different concentrations. Both measurements were obtained without external heating sources. (b) Normalized responses to [NO$_2$]=0.5 ppm at three different current values I_m. In these three plots, the response S was normalized (from 0 to 1) to the corresponding S to NO$_2$ at each temperature: this transformation ease the comparison of the recovery dynamics in the same y-scale.

A similar behavior was observed in SnO$_2$ nanowires with the increasing I_m [Fig. 1(b)], suggesting a close relation between I_m and T. Due to the integrated microheater in these prototypes,[8] it was possible to validate this assumption and compare the response of the devices operated by either self- or external heating. Experimental results demonstrated that self-heated devices could reproduce the best performance achieved with the conventional approach [inset Fig. 2(a)]. The comparison of the responses (S) and recovery times (τ_f) obtained with the two operating conditions (Fig. 2) allowed a first and rough estimation of the effective temperature reached by the nanowire due to self-heating (Fig. 3), since nearly equivalent response curves were observed in both cases. According to Fig. 2, maximum response to this gas was monitored with I_m=10 nA, which was in good correspondence with the optimal working temperature reported in literature for NO$_2$ sensing with SnO$_2$ ($T \approx 175$ °C).[11]

The modulation of the gas response with T or I_m, shown in Fig. 2(a), is explained by the existence of manifold adsorption sites on the SnO$_2$ surface, all of them with different desorption energies (E_{des} from 0.52 to 1.26 eV) and charge exchange probability (Δq_{NO_2} from 0.42 to 0.96 electrons per NO$_2$ molecule).[12] We compared the experimental values of the desorption time τ_f to the residence time τ_{res} of different NO$_2$ states. Each state is defined by a specific desorption enthalpy ($-\Delta H_{des}=E_{des}$) and a mean residence time τ_{res}. These two parameters are related to Eq. (2),
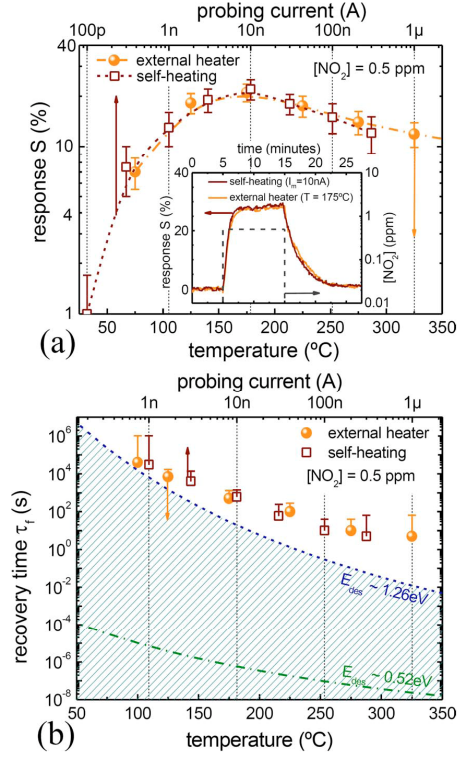

FIG. 2. (Color online) Response S of our SnO$_2$ nanowires operated in self-heating mode and with external microheater to [NO$_2$]=0.5 ppm. (a) Comparison of the responses obtained with both measuring methodologies. The similarities to the calibration-curve of the external heater were used to roughly estimate the effective temperature obtained by the nanowire due to self-heating. The maximum response to this gas with and without heater (I_m=10 nA) is the absolute equivalent (inset). (b) Similar correlation between the recovery times (τ_f). Dotted and dash-dotted lines correspond to the mean residence time (τ_{res}) of a NO$_2$ molecule onto an adsorption site (described by E_{des}) as a function of the temperature [see Eq. (2)]. Shaded area corresponds to forbidden recovery times.

$$\tau_{res} = \frac{1}{\nu_0}\exp\left(\frac{-\Delta H_{des}}{k_B T}\right),\qquad(2)$$

where ν_0 is the average desorption attempt frequency (around 10^{13} Hz),[13] k_B is the Boltzmann constant, and T is the absolute temperature. Figure 2(b) shows the residence time τ_{res} for the slowest and fastest desorption process with experimental τ_f values as function of the operation temperature. First, the longest τ_{res} (E_{des}=1.26 eV) is the lowest limit of τ_f, as expected, in the first and rough approximation, the complete recovery to the resistance baseline occurs only after desorption of the last molecules from their surfaces, which happens long after the mean residence time τ_{res}. Nevertheless, a more realistic approach to estimate the experimental recovery time τ_f should consider other effects, such as surface band bending effects on the adsorbate binding energy.[14] It is noteworthy that the τ_f values decrease with temperature, which qualitatively agrees with a thermally activated desorption process [Fig. 2(b)].

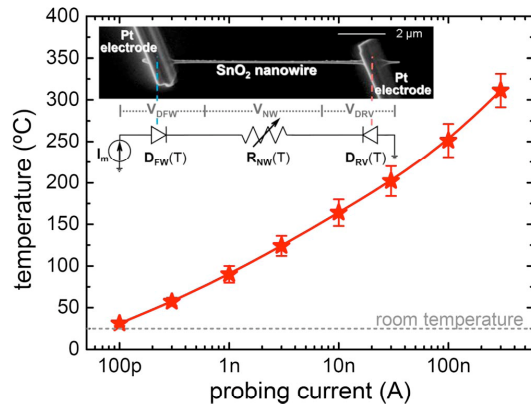From the electrical point of view, a SnO$_2$ nanowire and the two Pt–SnO$_2$ contacts can be modeled by two back-to-

FIG. 3. (Color online) Estimated temperature of the devices at different I_m. ($r_{nw} \sim 35$ nm) (inset) SEM image of a SnO_2 nanowire connected to two Pt microelectrodes fabricated with focused ion beam. The equivalent circuit of this structure corresponds to two back-to-back diodes (D_{FW} and D_{RV}) in series with the nanowire resistance (R_{NW}). These three components dissipate electrical power and contribute to the self-heating of the device.

back Schottky diodes in series with a resistance (Fig. 3).[7] These three components dissipate electrical power that contributes to the heating of the whole structure. In a first approximation, the voltage drop at the forward biased junction V_{DFW} is negligible, whereas the reverse biased contact contribution V_{DRV} is comparable to the voltage drop along the nanowire V_{NW}.[7,15] The dependence of these two last terms with the temperature together with the evaluation of the heat dissipation processes at the nanoscale makes modeling these self-heating effects rather complex.

The fact that the nanowire resistance may significantly change when exposed to the different concentrations of gas brings uncertainty to the sensor's response, opposite to conventional sensors, whose temperature remains constant during the operation. In our devices, these power variations were less than a factor of 1.8 under the optimum working conditions, and the dispersion of results obtained in all the experiments were fully comparable to those obtained with external microheaters (error bars in Figs. 2 and 3). In any case, this difficulty can be easily circumvented with appropriate calibrations of sensors.

It should be mentioned that these devices operated under optimal conditions for NO_2 sensing with less than 20 μW to both bias and heat them,[16] which is significantly lower than the 140 mW required for the external microheater.[17] This is an important step forward toward low power metal oxide gas sensing devices.

In summary, we have demonstrated that self-heating in metal oxide nanowires can be used to heat them and optimize their response to gases without the requirement of external heaters. These devices, which require extremely low power supply to come into operation, represent an important advance in power efficiency and miniaturization.

[1]Y. Cui, Q. Q. Wei, H. K. Park, and C. M. Lieber, Science **293**, 1289 (2001).

[2]R. Yasuda, H. Noji, M. Yoshida, K. Kinosita, and H. Itoh, Nature (London) **410**, 898 (2001).

[3]M. Law, H. Kind, B. Messer, F. Kim, and P. D. Yang, Angew. Chem., Int. Ed. **41**, 2405 (2002).

[4]M. Law, J. Goldberger, and P. Yang, Annu. Rev. Mater. Res. **34**, 83 (2004).

[5]S. V. N. T. Kuchibhatla, A. S. Karaoti, D. Bera, and S. Seal, Prog. Mater. Sci. **52**, 699 (2007).

[6]E. Pop, D. A. Mann, K. E. Goodson, and H. Dai, J. Appl. Phys. **101**, 093710 (2007).

[7]F. Hernandez-Ramirez, A. Tarancon, O. Casals, E. Pellicer, J. Rodríguez, A. Romano-Rodriguez, J. R. Morante, S. Barth, and S. Mathur, Phys. Rev. B **76**, 085429 (2007); T. Schwamb, B. R. Burg, N. C. Schirmer, and D. Poulikakos, Appl. Phys. Lett. **92**, 243106 (2008).

[8]F. Hernandez-Ramirez, J. D. Prades, A. Tarancon, S. Barth, O. Casals, R. Jimenez-Diaz, E. Pellicer, J. Rodriguez, M. A. Juli, A. Romano-Rodriguez, J. R. Morante, S. Mathur, A. Helwig, J. Spannhake, and G. Mueller, Nanotechnology **18**, 495501 (2007).

[9]S. Mathur, S. Barth, H. Shen, J.-C. Pyun, and U. Werner, Small **1**, 713 (2005); S. Mathur and S. Barth, ibid. **3**, 2070 (2007).

[10]F. Hernandez-Ramirez, A. Tarancon, O. Casals, J. Rodríguez, A. Romano-Rodriguez, J. R. Morante, S. Barth, S. Mathur, T. Y. Choi, D. Poulikakos, V. Callegari, and P. M. Nellen, Nanotechnology **17**, 5577 (2006).

[11]M. Batzill and U. Diebold, Prog. Surf. Sci. **79**, 47 (2005); A. Maiti, J. A. Rodriguez, M. Law, P. Kung, J. R. McKinney, and P. Yang, Nano Lett. **3**, 1025 (2003).

[12]J. D. Prades, A. Cirera, and J. R. Morante, J. Electrochem. Soc. **154**, H675 (2007); J. D. Prades, A. Cirera, J. R. Morante, J. M. Pruneda, and P. Ordejón, Sens. Actuators B **126**, 62 (2007).

[13]M. C. Desjonquères and D. Spanjaard, Concepts in Surface Physics, 2nd ed. (Springer, Berlin, 1996); V. P. Zhdanov and B. Kasemo, Surf. Sci. **415**, 403 (1998).

[14]A. Rothschild, Y. Komem, and N. Ashkenasy, J. Appl. Phys. **92**, 7090 (2002); A. Rothschild and Y. Komem, Sens. Actuators B **93**, 362 (2003).

[15]In our devices, the resistance of the reverse biased contact R_{DRV} =211 MΩ is not negligible compared to the resistance of the nanowire R_{NW}=76 MΩ [This results are extracted from Ref. 7].

[16]The electrical dissipated power P by Joule effect at an Ohmic device is given by $P = I^2 R$, where I is the current flowing through it and R is its electrical resistance. The maximum R we measured in our devices was $R_{max} \sim 300$ MΩ and the maximum current we applied was $I_{m\,max}$ =300 nA. Thus, the highest power dissipated at the device was P_{max} ~ 27 μW.

[17]According to the specifications given by the manufacturer (European Aeronautic Defense and Space Company, EADS N.V.), the suspended membranes we used (model IESSICA) require 140 mW to reach the maximum temperature achieved with self-heating ($I_{m\,max}$=300 nA corresponded to $T \approx 300$ °C).

J.D. Prades, R. Jimenez-Diaz, F. Hernandez-Ramirez, A. Cirera, A. Romano-Rodriguez, J.R. Morante, S. Barth, P. Jun, S. Mathur, *"An experimental method to estimate of the temperature of individual nanowires"* Int. J. Nanotechnol., accepted for publication (2008).

7

An experimental method to estimate of the temperature of individual nanowires

J. D. Prades[a,*], R. Jimenez-Diaz[a], F. Hernandez-Ramirez[b,*], A. Cirera[a], A. Romano-Rodriguez[a] and J. R. Morante[a,c]

[a]EME/XaRMAE/IN^{2}UB, Dept.d'Electrònica, Universitat de Barcelona,
   C/ Martí i Franquès 1, Barcelona, E-08028, Spain

[b]Electronic Nanosystems S. L., Barcelona, Spain

[c]Institut de Recerca en Energia de Catalunya (IREC)
   C/ Josep Pla 2, B3, Ground Floor, Barcelona, E-08019, Spain

[*]Corresponding authors e-mail: dprades@el.ub.es, fhernandezra@gmail.com

S. Barth[e], P. Jun[d] and S. Mathur[d]

[d]Department of Inorganic Chemistry,University of Cologne,
   Cologne, Germany

[e]Department of Chemistry, University College Cork, Cork, Ireland.

Abstract: In this paper, the authors present an effective experimental method to estimate the temperature of individual metal oxide nanowires that can be used to quantify the heating produced in conductometric or other operating conditions. The here-proposed method is based on the analysis of the recovery time of the nanowire's resistance after exposure to an gas pulse (0.5 ppm of NO_2 in dry air). It is reproducible with different devices always with uncertainties below ±20°C in the temperature range (70-300°C) studied herein. The exploration of alternative gases and nanolitography techniques may help to extend its working range its applicability to other materials. In any case, the opportunity to probe temperatures at the nanoscale opens the door to a number of fundamental and applied advancements in the field of nanotechnology.

Keywords: nanowire, self-heating, temperature, nanometrology, SnO2, NO2, gas sensor, FIB

Reference for publisher use only

2

Biographical notes:

Joan Daniel Prades was born in Barcelona in 1982. He graduated in physics at the Universitat de Barcelona in 2005 and now he is pursuing for the PhD degree in Department of Electronics of the same university. His current research is focused on first-principles modelling of electronic and vibrational properties of nanostructured metal oxides and on the experimental validation of these theoretical models.

Román Jiménez-Díaz was born in Barcelona in 1983. He received his degree in physics at the Universitat de Barcelona in 2007 and the Master degree in Electronic Engineering at the University of Barcelona in 2008 . Currently he is student of the doctor's degree program "electronic engineering and technology". His professional experience is related to the use of focused ion beam (FIB) lithography in the fabrication of metal oxide gas nanosensors.

Francisco Hernàndez-Ramírez was born in Barcelona in 1981. He received his degree in physics at the Universitat de Barcelona in 2002 and his Ph.D in 2007 at the same university. His professional experience is related to the use of focused ion beam (FIB) lithography in the fabrication of metal oxide gas nanosensors. Currently, he is CEO of Electronic Nanosystems, SL (e|nanos), an start-up company devoted to the development and commercialisation of nanotechnological products.

Albert Cirera Graduated in Physics at the University of Barcelona in 1996. He received his PhD in 2000 from the University of Barcelona, awarded with the extraordinary prize of the Universitat de Barcelona. He is permanent-staff Associate Professor at the Department of Electronics at the same university. His current research is involved in the IN^{2}UB (Nanoscience and Nanotechnology Intitute) and he leads the activities in Modelling for Nanoelectronics and Sensing Devices. He has published 40 papers in journals (h=14), about 100 papers in conferences, 3 book chapters and 3 patents. He leads 2 research and 2 industrial projects. Recently, his activity was recognized by the Intensification Research Program of the Universitat de Barcelona.

Albert Romano-Rodriguez is Professor in Electronics at the Universitat de Barcelona. His research activities are in the fields of characterization of semiconducting materials and processes, development of nano- and micromechanical devices and solid state gas sensors. He has started a strong involvement in the application of focused ion beam techniques in nanotechnology, with strong emphasis in the fabrication of nanocontacts to nanometre-sized materials. He is author or co-author of over 150 scientific and technical papers in these fields and has presented invited talks at different national and international conferences.

Joan Ramon Morante received the PhD degree in physics in 1980 from the Universitat de Barcelona. Since 1986 he is Full Professor of Electronics and Director of the Electronic Materials and Engineering (EME) group. Recently, he has been appointed Head of the Area of Materials of the Catalonia Institute for Energy Research (IREC). His activities have been centred in electronic materials and the validation of the technology and processes in materials, specially emphasizing semiconductor materials technology transfer, electronic ceramics, metallic oxides and sensing materials. Likewise, he has particular interest in nanosciences where he has specialized in the development of microsystems and integrated chemical sensors. He has published over 500 scientific papers, reviews and book chapters, several patents. He serves on the Steering and Organizing Committees of a number of international conferences.

An experimental method to estimate of the temperature of individual nanowires   3

Sven Barth was born in Neunkirchen, Germany in 1976. He received his chemistry diploma from the Saarland University, Saarbruecken in 2003 and his Ph.D in 2008 from the same university. His professional experience is related to the synthesis and characterization of nanoscaled metal oxides as well as metalorganic compounds. Currently, he is a postdoctoral fellow at UCC, Ireland, working on the formation of oxide and semiconductor nanostructures under high pressure conditions and their structural characterization.

Pan Jun was born in Gansu, China in 1981. He is a doctoral fellow at the University of Cologne. He has obtained is Masters in Engineering from the Central South University in China. His research interests focuses on the "Controlled Growth of Metal Oxide Nanowires for Device Applications" with emphasis on materials for energy applications.

Sanjay Mathur is the Chair Professor of Inorganic and Materials Chemistry at the University of Cologne, Cologne, Germany. He also leads the Division of CVD-PVD Technologies at the Leibniz Institute of New Materials in Saarbruecken, Germany. His research activities lies in the domain of Chemical Nanotechnology with focus on the molecule-based synthesis of functional inorganic nanostructures. He is Associate Editor of the journals Nanomaterials and Applied Ceramic Technology, and serves as the Editorial Board Member on Ceramics International and International Journal of Nanotechnology and Science of Advanced Materials. He has published over 120 scientific papers, reviews and book chapters, several patents and has delivered over 100 invited conference presentations. He is a member of the Inorganic Chemistry Division of the IUPAC and ISO Task Group on Nanotechnologies. He serves on the Advisory Committee of a number of international conferences.

1   Introduction

Nanowires have emerged as potential components of new devices and circuit architectures due to their unique chemical and physical properties [1-3]. On one hand, their high surface-to-volume ration makes them particularly attractive for sensing applications [1]. On the other, their crystalline properties (nanowires are well-faceted single-crystalline materials) makes them excellent systems to perform fundamental studies [2,3]. In both cases, controlling the experimental conditions, and particularly the temperature, is an issue of major interest. For example, the recovery of the photoresponse in metal oxide nanowires [4] and their response to gases [5,6] are thermally driven processes.

A widely used strategy to control the operating temperature of devices based on individual or bunches of nanowires is to establish a thermal equilibrium between the nanowire and a bulkier thermal source, such as a cryostat [7], a furnace [8], or a microheater [9]. However, the thermal equilibrium in nanowire based devices can be altered by the experimental conditions, such as the irradiation with photons [10] or the electrical measurements [4,8,11], leading to important temperature gradients. Precisely monitoring of these thermal variations, which are extremely localized in the nanowires, remains as an unsolved issue since conventional methods based on thermal probes or spectroscopic techniques [12] are not feasible at this scale. As a consequence these temperature effects are usually neglected and their actual impact on the device performance underestimated.

4

In this work, we present a methodology to estimate the temperature in individual metal oxide nanowires due to Joule self-heating. The strategy is based on the analysis of the temperature dependent device response to gaseous species. The opportunity to probe temperatures at the nanoscale could lead to progress in the fields of fundamental and applied nanotechnology.

2 Experimental section

Individual single-crystal SnO_2 nanowires, synthesized by catalyst supported chemical vapor deposition of a molecular precursor $[Sn(O^tBu)_4]$ [13], were transferred onto suspended silicon micromembranes equipped with an integrated SnO_2:Sb microheater and platinum interdigitated microelectrodes. Nanowires were electrically contacted to platinum microelectrodes by a lithography process using a FEI Dual-Beam Strata 235 FIB instrument combined with a trimethyl-methylcyclopentadienylplatinum $[(CH_3)3CH_3C_5H_4Pt]$ injector to deposit platinum [14].

Two and four probe DC measurements were performed using an electronic circuit designed to guarantee and control low current levels I_m (from 0.1 nA to 500 nA) and to avoid ANY undesired fluctuation [9].

Experiments were exclusively performed in a customized chamber (15 ml in volume), in which the gas flow was maintained at 200 ml min^{-1}. Accurate gaseous environments were provided by massflow controllers mixing dry synthetic air (SA) and NO_2 (10 ppm ±1% in SA). Lab-class gases contained less than 5ppm/V of C_nH_m and H_2O.

Ten devices were fabricated using SnO_2 nanowires with radii (r_{NW}) between 35 and 45 nm, which showed reproducible electrical responses in experiments repeated along 4 weeks.

3 Our proposal

It is well established that the power dissipated in individual nanowires by Joule effect may lead to important self-heating effects. In the case of semiconductor SnO_2 nanowires, this effect is evident in the decrease in the resistance values measured at different probing currents I_m (see Figure 1). However, the manifold intrinsic donor defects (with different activation energy) that cause the n-type semiconductor behaviour of SnO_2 [15], also complicate the relation between the variations in conductance values and changes in the temperature. Therefore, other strategies are mandatory.

SnO_2 is well know for conductometric responses to gases, which strongly depend on the operation temperature [15,16]. Specifically, the response S [17] to NO_2 presents a maximum between 150 and 225 °C, while the response τ_r and recovery τ_f times decrease monotonously with rising temperature (Figure 2.a and 2.b). The data follow approximately exponential decay laws [18] like

$$\tau_f \propto \exp\left(\frac{-\Delta H_{des}}{k_B T}\right) \tag{1}$$

where ΔH_{des} is the desorption enthalpy of the gaseous molecules from the surface, k_B is the Boltzmann's constant and T is the absolute temperature.

An experimental method to estimate of the temperature of individual nanowires   5

Therefore, while different temperatures may lead to the same S value, each τ_r or τ_f value can be unambiguously related to one single temperature. In addition, changes in S are in the range of percents while τ_r or τ_f can vary by orders of magnitude. In the following, we demonstrate that the analysis of the response dynamics is an appropriate method to estimate the nanowire temperature.

We observed that response times (τ_r) are faster than recovery times (τ_f) and, while τ_r values were comparable to the time needed to change the atmosphere inside the chamber (approximately 9 seconds) [19], all τ_f were above this value. Consequently, we will focus our discussion on the recovery transients (τ_f) in order to avoid any controversial interpretation of the dynamic measurements.

Figure 1 Nanowire resistance as function of the probing current I_m that causes self-heating. Resistance evolution displays a semiconductor behaviour, as expected for SnO_2. Measurements were performed in 4-probe configuration to avoid parasitic contact effects. (Inset) SEM micrograph of a nanowire with 4-probe contacts.
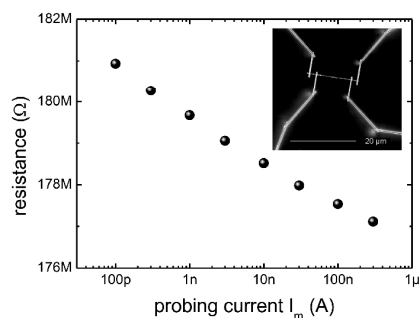
4. Results

To demonstrate the feasibility of our proposal, we measured the response of the nanowires to 10-minute-pulses of 0.5 ppm of NO_2 diluted in SA. First, we used probing currents I_m from 0.6 to 300 nA (values based on previous investigations [11]) to self-heat the nanowires and modulate their response. Subsequently, the experiment was repeated, with the same devices, using the microheaters integrated in the membranes to precisely set the nanowire temperature ($\pm5^{\circ}C$) based on the power-temperature calibrations provided by the membrane supplier [20]. The devices were operated at 75, 125, 225 and $325^{\circ}C$. In both cases, identical experimental conditions were maintained.

Comparison of both data sets (Figure 2.a and 2.b) allows the estimation of the nanowire temperature due to self-heating (T *.vs.* I_m calibration). The data displayed in Figure 2.b was also used to produce a T *.vs.* τ_f calibration-curve.

Figure 3 shows the result obtained with a test data set. These data point were acquired with ten different nanowires (r_{NW} = 40±5 nm) applying current values different than the ones used in the calibration set. Solid data points where obtained just measuring the fall time of the nanowire resistance (from 90% to 10% of the signal – Figure 4) after exposure to the gas pulse and using the T *.vs.* τ_f calibration-curve to estimate the temperature (solid grey line). Hollow data points indicate the deviation from the temperature calculated on the basis of the T *.vs.* I_m calibration. In all cases, the analysis

6

of τ_f allowed to estimate the nanowire temperature with a deviation lower than ± 20 °C. These results demonstrate that the correlation between T and τ_f can be reproduced, even with different devices.

Concerning the repeatability of this method, Figure 4 shows four records of the recovery of the nanowire resistance acquired weakly: differences were comparable to the noise of the measurements.

Figure 2 Response of SnO$_2$ nanowires operated in self-heating mode and with external microheater to [NO$_2$] = 0.5ppm. (a) Comparison of the responses S obtained with both methodologies. (b) Similar correlation between the recovery times τ_f. The similarities to the calibration-curve of the external heater were used to roughly estimate the effective temperature obtained by the nanowire due to self-heating.
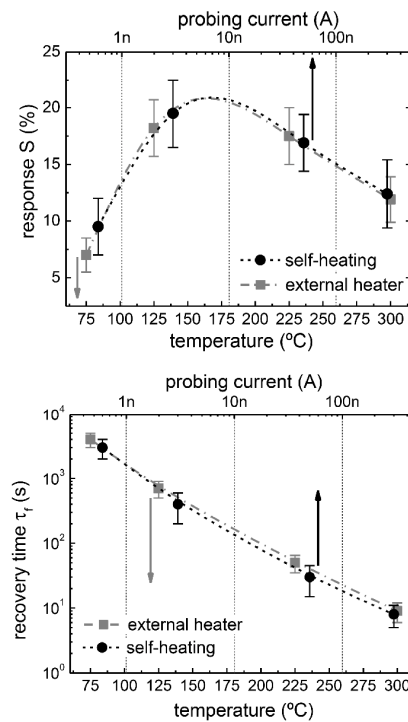
Figure 3   Validation of the here-proposed methodology with different nanowires and I_m values. Solid data points were obtained measuring τ_f (from 90% to 10% of the signal) and using the T .vs. τ_f calibration-curve (grey solid line) to estimate the temperature. Hollow data corresponds to the temperature predicted on the basis of the T .vs. I_m calibration. In all cases, deviations are bellow 20 °C.
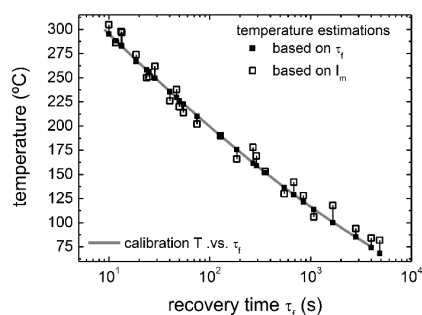
Figure 4   Resistance change due to the gas pulse measured at I_m = 8nA. The records were acquired weekly during four weeks: differences are comparable to the noise. The 90% to 10% signal decay time is indicated.
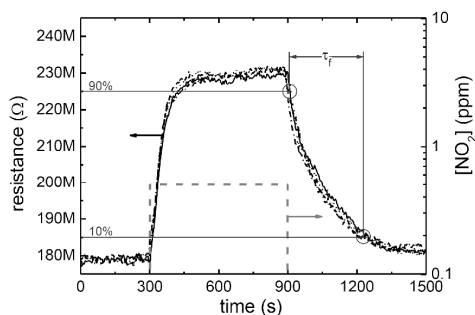
5. Discussion

The here-proposed method was tested for temperatures between 75 °C and 300 °C. The lower limit is due to the desorption temperature of NO_2 from the SnO_2 surface: reversible sensing is merely observed at temperatures above T = 75 °C, since the spontaneous desorption of this gas has a minimum thermal energy of $E_{des} \geq 0.52$ eV [21], which corresponds to a thermal desorption process active above T $\geq$ 80°C [18]. The upper limit is determined by the electrical degradation of the nanoelectrodes produced with FIB lithography [14]. In order to extend this range, other gases and other nanolithography processes should be explored in the future.

All metal oxides, various semiconductors and carbon nanotubes show significant conductometric response to NO_2 [1-3]. For this reason, this methodology can be easily

8

extended to other nanostructured materials. In any case, the selection of other gaseous species may help to further extend its applicability.

The possibility of using only one concentration of NO_2 enormously simplifies the implementation of this methodology and the concentration in the chamber is below the harmful limits for NO_2 [22].

From the signal processing point of view, the analysis of the 90%-10% fall time is very simple and insensitive to problems such as drifts in the baseline of the nanowire resistance.

Finally, the here-presented calibration of the self-heating effect warns about its importance even al low current operation. For instance, in SnO_2 nanowires of $r_{NW} \sim 35nm$, current values below the nA range are enough to heat them above 75°C. This result also suggests a critical revision of the previous electrical characterization works.

4. Conclusion

In summary, we provide an effective experimental method to estimate the temperature of individual nanowires that can be used to quantify the heating produced in conductometric or other operating conditions. The method is based on the analysis of the recovery time of the nanowire resistance after exposure to a gas pulse. For calibration purposes, also an external heating source is needed. These results pave the way for further developments in thermal control at the nanoscale.

Acknowledgements

References

1   Cui, Y., Wei, Q. Q., Park, H. K. and Lieber, C. M. (2001) 'Nanowire Nanosensors for Highly Sensitive and Selective Detection of Biological and Chemical Species', *Science*, Vol. 293, No. 5533, pp. 1289–1292.

2   Law, M., Goldberger, J. and Yang, P. (2004) 'Semiconductor nanowires and nanotubes', *Annu. Rev. Mater. Res.*, Vol. 34, pp. 83–122.

3   Kuchibhatla, S. V. N. T., Karaoti, A. S., Bera, D. and Seal, S. (2007) 'One dimensional nanostructured materials', *Progress Mater. Sci.*, Vol. 52, No. 5, pp. 699–913.

4   Prades, J. D., Hernandez-Ramirez, F., Jimenez-Diaz, R., Manzanares, M., Andreu, T., Cirera, A., Romano-Rodriguez, A. and Morante, J.R. (2008) 'The effects of electron–hole separation on the photoconductivity of individual metal oxide nanowires', *Nanotechnol.*, Vol. 19, No. 46, p. 465501.

An experimental method to estimate of the temperature of individual nanowires 9

5 Hernandez-Ramirez, F., Prades, J. D., Tarancon, A., Barth, S., Casals, O., Jimenez-Diaz, R., Pellicer, E., Rodriguez, J., Morante, J. R., Juli, M. A., Mathur, S. and Romano-Rodriguez, A. (2008) 'Insight into the Role of Oxygen Diffusion in the Sensing Mechanisms of SnO_2 Nanowires', *Adv. Funct. Mater.*, Vol. 18, No. 19, pp. 2990–2994.

6 Hernández-Ramírez, F., Tarancón, A., Casals, O., Arbiol, J., Romano-Rodríguez, A. and Morante, J.R. (2007) 'High response and stability in CO and humidity measures using a single SnO_2 nanowire', *Sens. Actuators B: Chem.*, Vol. 121, No. 1, pp. 3–17.

7 Mazzera, M., Zha, M., Calestani, D., Zappettini, A., Lazzarini, L., Salviati, G. and Zanotti, L. (2007) 'Low-temperature In_2O_3 nanowire luminescence properties as a function of oxidizing thermal treatments', *Nanotechnol.*, Vol. 18, No. 35, p. 355707.

8 Hernandez-Ramirez, F., Tarancon, A., Casals, O., Pellicer, E., Rodríguez, J., Romano-Rodriguez, A., Morante, J. R., Barth, S. and Mathur, S. (2007) 'Electrical properties of individual tin oxide nanowires contacted to platinum electrodes', *Phys. Rev. B*, Vol. 76, p. 085429.

9 Hernandez-Ramirez, F., Prades, J. D., Tarancon, A., Barth, S., Casals, O., Jimenez-Diaz, R., Pellicer, E., Rodriguez, J., Juli, M. A., Romano-Rodriguez, A., Morante, J. R., Mathur, S., Helwig, A., Spannhake, J. and Mueller, G. (2007) 'Portable microsensors based on individual SnO_2 nanowires', *Nanotechnol.*, Vol. 18, No. 49, p. 495501.

10 Prades, J. D., Arbiol, J., Cirera, A., Morante, J. R., Fontcuberta i Morral, A. (2007) 'Concerning the 506 cm^{-1} band in the Raman spectrum of silicon nanowires', *Appl. Phys. Lett.*, Vol. 91, No. 12, p. 123107.

11 Prades, J. D., Jimenez-Diaz, R., Hernandez-Ramirez, F., Barth, S., Cirera, A., Romano-Rodriguez, A., Mathur, S. and Morante, J. R., (2008) 'Ultra-low Power Consumption Gas Sensors Based On Self-heated Individual Nanowires', *Appl. Phys. Lett.*, Vol. 93, No. 12, p. 123110.

12 (a) Kip, B. J. and Meier, R. J. (1990) 'Determination of the Local Temperature at a Sample during Raman Experiments Using Stokes and Anti-Stokes Raman Bands', *Appl. Spectrosc.*, Vol. 44, No. 4, pp. 707–711. (b) Rassat, S. D. and Davis, E. J. (1990) 'Temperature measurement of single levitated microparticles using Stokes/anti-Stokes Raman intensity ratios', *Appl. Spectrosc.*, Vol. 48, No. 12, pp. 1498–1505.

13 (a) Mathur, S., Barth, S., Shen, H., Pyun, J.-C. and Werner, U. (2005) 'Size-Dependent Photoconductance in SnO_2 Nanowires', *Small*, Vol. 1, No. 7, pp. 713–717. (b) Mathur, S., and Barth, S. (2007) 'Molecule-Based Chemical Vapor Growth of Aligned SnO_2 Nanowires and Branched SnO_2/V_2O_5 Heterostructures', *Small*, Vol. 3, No. 12, pp. 2070–2075.

14 Hernandez-Ramirez, F., Tarancon, A., Casals, O., Rodríguez, J., Romano-Rodriguez, A., Morante, J. R., Barth, S., Mathur, S., Choi, T. Y., Poulikakos, D., Callegari, V. and Nellen, P. M. (2006) 'Fabrication and electrical characterization of circuits based on individual tin oxide nanowires', *Nanotechnol.*, Vol. 17, No. 22, pp. 5577–5583.

15 Batzill, M. and Diebold, U. (2005) 'The surface and materials science of tin oxide', *Prog. Surf. Sci.*, Vol. 79, pp. 47–154.

16 Maiti, A., Rodriguez, J. A., Law, M., Kung, P., McKinney, J. R. and Yang, P. (2003) 'SnO_2 Nanoribbons as NO_2 Sensors: Insights from First Principles Calculations', *Nano Lett.*, Vol. 3, No. 8, 1025–1028.

17 Herein, we use the following definition of the conductometric response (S) to NO_2: $S(\%) = 100 \times (R_{NO2} - R_{SA})/(R_{SA})$ where R_{NO2} is the steady value of the resistance of the nanowire exposed to NO_2 and R_{SA} is the reference resistance value in synthetic air (SA).

18 Desjonquères, M. C. and Spanjaard, D. (1998) *Concepts in Surface Physics*, Springer, Berlin.

19 In our experimental setup, the gas flow (200 ml min^{-1}) only needs 9 seconds to completely refill 3 times the test chamber (15 ml in volume). This criterion is enough to consider that the composition of the atmosphere inside the chamber is has completely changed after this time.

20 The membranes (model IESSICA) were manufactured, calibrated and supplied by EADS, N.V. (European Aeronautic Defence and Space Company).

10

21   (a) Prades, J. D., Cirera, A. and Morante, J. R. (2007) 'First-Principles Study of NO_x and SO_2 Adsorption onto $SnO_2(110)$', *J. Electrochem. Soc.*, Vol. 154, No. 8, pp. H675–H680. (b) Prades, J. D., Cirera, A., Morante, J. R., Pruneda, J. M. and Ordejón, P. (2007) 'Ab initio study of NO_x compounds adsorption on SnO_2 surface', *Sens. Actuators B: Chem.*, Vol. 126, No. 1, pp. 62–67.

22   World Health Organization (WHO). Information available at http://www.who.int/peh/air/Airqualitygd.htm

Asunto: Re: Paper submission certificate
De: VAYSSIERES Lionel <VAYSSIERES.Lionel@nims.go.jp>
Fecha: Tue, 09 Dec 2008 10:55:26 -0800
Para: "J.Daniel Prades García" <dprades@el.ub.es>

```
Dear Mr Prades Garcia,
It is my pleaure to announce that your invited paper entitled " An experimental method to estimate
of the temperature of individual nanowires" is accepted for publication for the
special issue of the International Journal of Nanotechnology dedicated to Transparent Conducting
Oxides.
With my regards,
The editor

*******************************************************************************************
Dr. Lionel Vayssieres
Nanomaterials Senior Scientist and R&D Consultant
Editor-in-chief of the International Journal of Nanotechnology
http://www.inderscience.com/ijnt

National Institute for Materials Science
International Center for Materials NanoArchitectonics
Nanomaterials and Biomaterials Research Building
Namiki 1-1, Tsukuba, Ibaraki 305-0044 JAPAN
Phone: +81 298-513-354 ext. 8781
Cell: +81 90-4629-1972
Research Lab: +81 298-513-354 ext. 8414
Admin. Assistant: +81 298-513-354 ext. 8620
Fax: +81 298-604-706
Vayssieres.Lionel@nims.go.jp

Lawrence Berkeley National Laboratory
Chemical Sciences Division, MS 70A-1150
One Cyclotron Road, Berkeley, CA 94720 USA
Phone: +1 (510) 486-4654,
Cellphone: +1 (510) 710-9433
Fax: +1 (510) 486-5596
LVayssieres@lbl.gov
*******************************************************************************************
```

8

FULL PAPER

ADVANCED FUNCTIONAL MATERIALS

Insight into the Role of Oxygen Diffusion in the Sensing Mechanisms of SnO₂ Nanowires**

By *Francisco Hernandez-Ramirez, Joan Daniel Prades, Albert Tarancon, Sven Barth, Olga Casals, Roman Jimenez-Diaz, Eva Pellicer, Jordi Rodriguez, Joan Ramon Morante, Miguel Angel Juli, Sanjay Mathur,* and *Albert Romano-Rodriguez**

The role of oxygen diffusion in the response of individual SnO₂ nanowires to this gas is studied. Different oxygen partial pressures lead to strong changes of their electrical resistance, even at room temperature. Since surface models fail to explain the experimentally observed long-term resistance transients, it is necessary to make a description of the interaction mechanisms between oxygen species and SnO₂ nanowires by taking ion diffusion into account. Our model correctly describes the experimentally measured dependence of the nanowire resistance with oxygen partial pressure, and it can be applied to the characterization of other metal oxide materials.

1. Introduction

Metal oxide nanowires are attracting a great attention in different applications due to their novel properties.[1–6] In particular, chemical sensing is favored by their high surface-to-volume ratio.[4] In the last years, many groups have devoted their efforts to determine the ultimate sensing capabilities of these nanomaterials[1–9] and to obtain theoretical models able

[*] Prof. A. Romano-Rodriguez, Dr. F. Hernandez-Ramirez, J. D. Prades, Dr. A. Tarancon, O. Casals, R. Jimenez-Diaz, Dr. E. Pellicer,[+] J. Rodriguez, Prof. J. R. Morante, M. A. Juli
EME/XaRMAE/IN²UB Departament d'Electrònica, Universitat de Barcelona
C/Martí i Franquès 1, 08028 Barcelona (Spain)
E-mail: aromano@el.ub.es
Dr. F. Hernandez-Ramirez, M. A. Juli
NTEC106 S.L.
C/Mare de Déu dels Desemparats 12,
08903 L'Hospitalet de Llobregat (Spain)
Dr. S. Barth, Prof. S. Mathur
Department of Nanocrystalline Materials and Thin Film Systems
Leibniz Institute of New Materials
66123 Saarbrücken, (Germany)
Dr. S. Mathur
Institute of Inorganic Chemistry, University of Cologne
97074 Würzburg (Germany)
[+] Present address: Departament de Fisica, Universitat Autonoma de Barcelona, Bellaterra 08193, Spain

to describe their experimental responses.[3,4,6] On the other hand, present nanofabrication techniques enable the development of new prototypes which combine metal oxide nanowires with well-established microelectronic technologies.[10,11] In this context, the characterization of tin oxide (SnO₂) nanowires is important to develop a new generation of metal oxide gas sensors, since this material is one of the most promising for sensing applications.[12–14] SnO₂ is a large band-gap (3.6 eV) semiconductor whose electrical properties can be adjusted for multiple uses by the incorporation of dopant ions[15] and catalytic additives.[16] In the past, their physico-chemical properties and sensing performances were extensively studied,[17,18] demonstrating the commercial relevance of SnO₂-based devices. SnO₂ nanowires are currently used as the building blocks of a new generation of gas sensors, and their properties are being examined in detail.[3,4,6,8,9,19]

In this study, the interaction between oxygen species and individual SnO₂ nanowires was analyzed. As surface models are not enough to explain the changes of nanowires' electrical resistance R_{NW} with different oxygen partial pressures, oxygen diffusion into the bulk is proposed to be the responsible for the long – term drifts of R_{NW} after exposing the nanowires to changes of the oxygen partial pressure in air. Similar analyses were successfully reported in the past to justify drift processes in SnO₂ thick and thin film sensors.[20–26] The results obtained with SnO₂ were corroborated by ZnO nanowires.

2. Results and Discussion

2.1. Description of Oxygen Sensing with the Surface Model

Oxygen sensing in SnO₂ nanowires is generally considered as a pure surface effect.[4] The adsorption of oxygen species at the nanowires creates a depleted region close to their external shell which reduces the conduction channel through them and

**ADVANCED
FUNCTIONAL
MATERIALS**

FULL PAPER

increases the overall electrical resistance R_{NW}.[3,4,7] According to this assumption, R_{NW} in nitrogen (N₂) and synthetic air (SA) is given by,

$$R_{NW-N_2} = \frac{\rho L}{\pi r^2} \qquad (1)$$

$$R_{NW-SA} = \frac{\rho L}{\pi(r-\lambda)^2} \qquad (2)$$

where ρ is the SnO₂ resistivity, L the nanowire length, r the nanowire radius and λ the width of the depletion layer. Here, electrical mobility μ inside the nanowire is assumed not to be modified by the sensing process. Then the response S (in percentage) of one SnO₂ nanowire to N₂-SA-N₂ pulses depends on the radius as,

$$S(\%) = \left[\frac{R_{NW-SA} - R_{NW-N_2}}{R_{NW-SA}}\right] \cdot 100 = \left[\frac{r^2 - (r-\lambda)^2}{r^2}\right] \cdot 100 \qquad (3)$$

Responses of our devices (Fig. 1) at $T = 573$ K were fitted to Equation 3 (Fig. 2)[27] and a depletion layer of width $\lambda = 10$ nm was estimated, which is in good agreement with literature data.[7,28]

If thin nanowires $(r \to \lambda)$ are studied, we approach to the deep depletion condition (also called in the literature flat band situation[4]), in which surface phenomena entirely modify the bulk properties (i.e., the number of free electrons N_d) and thus Equation 3 can be rewritten as,[4,29]

$$S(\%) = \left[\frac{R_{NW-SA} - R_{NW-N_2}}{R_{NW-SA}}\right] \cdot 100 = \left[\frac{N_{d-N_2} - N_{d-SA}}{N_{d-N_2}}\right] \cdot 100$$
$$= \frac{N_d'}{N_{d-N_2}} \cdot 100 \qquad (4)$$

where N_{d-N_2} and N_{d-SA} are the number of free electrons inside the nanowire in N₂ and SA atmosphere, respectively, and N_d', their difference. According to this model, the number of reactions involving charge transfer merely depends on the intrinsic properties of the surface. In this case, Equation 4 is modified as,

$$S(\%) = \frac{N_d'}{N_{d-N_2}} \cdot 100 = \frac{n_s(2\cdot\pi\cdot r\cdot L)}{n_d(\pi\cdot r^2\cdot L)} \cdot 100 = \left(\frac{2\cdot n_s}{n_d}\right)\frac{1}{r} \cdot 100 \qquad (5)$$

where n_s is the concentration of sites in which charge transfer takes place and n_d is the free electron concentration. Fitting the experimental data obtained with our thinnest nanowires $(r \approx 20$ nm) to Equation 5 and taking a value of $n_d = 5\cdot\times 10^{19}$ cm⁻³[30], a value of $n_s = (4.4 \pm 0.2)\times 10^{13}$ cm⁻² was found. The number of sites involving charge transfer at
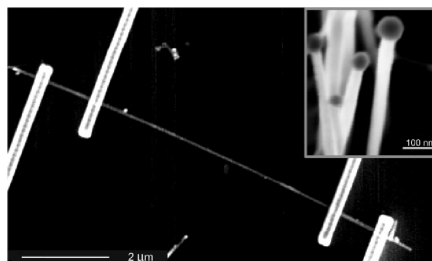

Figure 1. SnO₂ nanowire electrically contacted with FIB nanolithography techniques. The inset shows a high magnification SEM image of the SnO₂ nanowires. The gold particles used as catalytic element during the synthesis are visible at their tip.

the nanowire surface is assumed to be proportional to the total number of surface sites η_s available in SnO₂,

$$n_s = \theta \cdot \eta_s \qquad (6)$$

where θ is the fraction of sites contributing to the gas response.[4,29] A maximum of one site per surface unit cell in SnO₂ was found in theoretical examinations.[31] Consequently, η_s can be estimated as the reciprocal of the area of the surface unit cell. For the most stable surface orientations in SnO₂,[32] η_s has an average value of 5×10^{14} sites cm⁻² and, consequently, charge transfer takes place merely at 10% of all available sites ($\theta \approx 0.1$), which is in agreement with
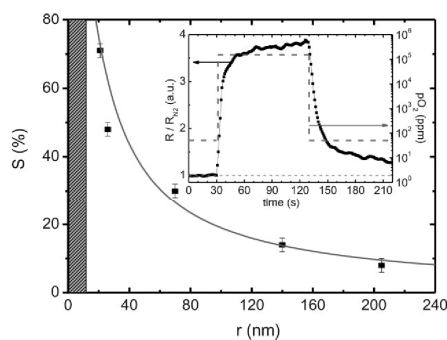
Figure 2. Response S of SnO₂ nanowires to synthetic air/nitrogen pulses as function of their radii. Higher responses are clearly observed with diminishing dimensions. Sensor response is defined as $S = 100 (R_{SA} - R_{N2})/R_{SA}$. (Inset) Typical response to synthetic air of a SnO₂ nanowire with $r \approx 20$ nm at $T = 573$ K. A slow drift of the electrical resistance is observed after the initial and fast increase of R_{NW} and during the last part of the recovery process.

literature values.[4,29] This is further justified by the Weisz limitation, which considers the electrostatic repulsion forces among adsorbed species.[33]

Albeit this model foretells the significant characteristics of the response of SnO$_2$ nanowires to oxygen, it is unable to explain long-term drifts of the resistance R$_{NW}$ values which are observed after the exposure of these nanomaterials to oxygen-rich atmospheres (inset in Fig. 2). The drift becomes important with thick nanowires and is highly dependent on the temperature. At normal working conditions ($T \approx 573$ K)[9,18] the steady state is reached after several minutes, whereas at room temperature ($T = 298$ K) it can take several hours, even for the thinnest nanowires ($r \approx 20$ nm), before complete stabilization of R$_{NW}$ is obtained (Fig. 3). Similar behavior was reported in the past with thin film SnO$_2$ sensors.[20–26]

2.2. Description of Oxygen Sensing Using the Diffusion Model

It is well established that SnO$_2$ is an n-type semiconductor due to its oxygen deficiency.[34] In undoped material, oxygen

vacancies $V_O^{\bullet\bullet}$ are compensated by conduction electrons (e').[21] Therefore, the oxygen exchange equilibrium can be written as (using the Kröger–Vink notation),

$$O_o^X \leftrightarrow V_o^{\bullet\bullet} + 2e' + \frac{1}{2}O_2 \qquad (7)$$

And the corresponding mass action law for Equation 7 as,

$$K_o = [V_o^{\bullet\bullet}] \cdot [e'] \cdot p(O_2)^{1/2} \qquad (8)$$

where $p(O_2)$ is the oxygen partial pressure, K_o is the respective mass action constant and square brackets indicate concentrations. Equation 8 and the electroneutrality condition imply a dependence of R$_{NW}$ on the oxygen partial pressure as,[20,21,35]

$$R_{NW} \propto \sigma^{-1} \propto p(O_2)^n \qquad (9)$$

with the nanowire conductivity and $n = 1/6$ for undoped SnO$_2$, if oxygen ions migrate into the bulk of the nanowires. The kinetics of this process is ruled by the chemical diffusion coefficient of oxygen in SnO$_2$, which is given by,[20,21,35]

$$D(T) = D_o \exp\left(\frac{-E_a}{kT}\right) \qquad (10)$$

where E_a is an activation energy and k the Boltzmann constant. Thus, the characteristic time τ before reaching the steady-state can be roughly estimated with the following expression,[20,21,35]

$$\tau = \frac{L^2}{D(T)} \qquad (11)$$

where L is the characteristic length of the diffusion path (see Supporting Information). Considering Equation 11, it can be
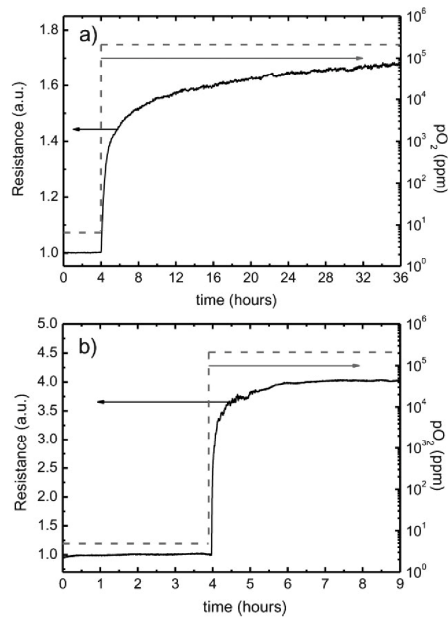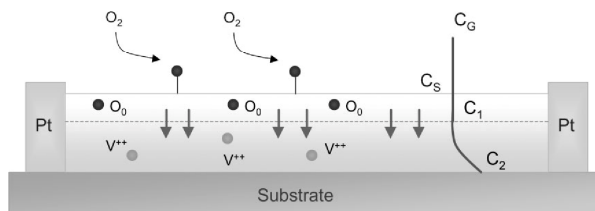

Figure 3. Response of two SnO$_2$ nanowires to a quick change of the oxygen partial pressure. a) SnO$_2$ nanowire with $r \approx 75$ nm at $T = 550$ K. Stabilization of R$_{NW}$ is not observed after 34 hours. b) SnO$_2$ nanowire with $r \approx 20$ nm at room temperature ($T = 298$ K). Stabilization of R$_{NW}$ takes a few hours. In the steady-state, oxygen diffusion into the bulk is completed.
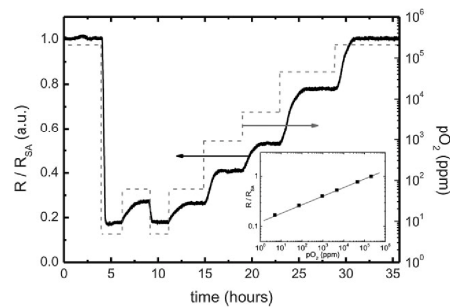
Figure 4. Response of one SnO$_2$ nanowire with $r \approx 20$ nm to increasing oxygen partial pressure at room temperature ($T = 298$ K). Resistance is normalized to the experimental value in synthetic air environment. (Inset) log–log plot of resistance as function of oxygen partial pressure. A linear behavior of slope $n = 1/6$ is observed.

F. Hernandez-Ramirez et al. / Oxygen Diffusion for SnO_2 nanowire Sensors

ADVANCED FUNCTIONAL MATERIALS

FULL PAPER

Figure 5. One-dimensional model of oxygen diffusion in nanowires. According to the surface model, adsorbed oxygen creates a depletion region close to the surface (red dashed line) and then a fast change of R_{NW} is observed. The new equilibrium between oxygen in the environment, C_G, and the concentration of oxygen at both the nanowire surface, C_S, and its external shell, C_1, creates a gradient with the inside C_2 favoring ion migration into the bulk. This diffusion is associated with long-term drifts of R_{NW}.

claimed that on a very long time scale, diffusion in SnO_2 occurs even at room temperature.[36]

In order to determine the exponent value n, in our nanowires (see Eq. 9), the relative change of R_{NW} was measured after a quick change of the oxygen partial pressure at $T = 573\,K$ and $T = 298\,K$ (Fig. 3). Thin nanowires ($r \approx 20\,nm$) were used to reduce the time to reach stabilization. A value close to $n = 1/6$ was estimated in the experiments ($n_{exp} = 0.156 \pm 0.007$).

The diffusion coefficient D at these two temperatures was $D_{573K} \approx 10^{-13}$ cm^2 s^{-1} and $D_{298K} \approx 10^{-15}$ cm^2 s^{-1} (see Supporting Information), in correspondence with reported values for SnO_2 single crystals.[20,21,37]

To check the validity of our results, SnO_2 nanowires were exposed to increasing oxygen partial pressures at $T = 298\,K$ (Fig. 4) and the experimental values of R_{NW} were fitted as function of $p(O_2)$ (inset in Fig. 4), exhibiting a slope of $n \approx 1/6$.

Identical experiments at room temperature ($T = 298\,K$) with ZnO nanowires were reported in the literature.[38] In the present study, we repeated oxygen diffusion experiments with these metal oxide nanowires ($T = 298\,K$), estimating a value of $n \approx 1/2$ for this material (see Supporting Information). This result corresponds to a diffusion process based on interstitial mechanisms, which is typical for ZnO.[39,40]

All these results can be explained using a one-dimensional model which combines surface phenomena and oxygen diffusion into the bulk of nanowires (Fig. 5). Immediately after the exposure to oxygen, adsorbed species at the surface compensate surface vacancies, leading to a fast increase of R_{NW} (inset in Fig. 2). This change is understood by the surface model as a widening of the depleted layer at the external shell of the nanowires. Later, ions migrate into the bulk compensating oxygen vacancies $V_O^{\bullet\bullet}$ in the material. This second step is responsible for the long-term drifts of R_{NW}, whose length depends on the nanowire radius and the temperature (inset in Fig. 3). In the steady-state, oxygen sensing becomes a bulk process. Although our approach provides a simple and intuitive explanation of drifts in R_{NW}, other phenomena might be required in further optimizations of the model, like charge mobility near the surface of nanowires or the existence of mobile donor species.[41]

The here-presented methodology can be extended to the study of other metal oxide nanowires and gas sensing processes involving a variation of the oxygen partial pressure. However, it does not explain the sensing mechanisms of other gas species diluted in synthetic air, like CO, since the oxygen partial pressure is almost constant.[9]

3. Conclusions

The resistivity of SnO_2 nanowires is highly dependent on the oxygen partial pressure of the surrounding atmosphere, even at room temperature. Although surface models describe most of the sensing characteristics of these nanomaterials, they do not explain long-term drift processes in the response of individual SnO_2 nanowires to oxygen. In this study, the contribution of ion diffusion into the bulk is considered, enabling a realistic description of the sensing phenomena present in nanomaterials. Furthermore, it is demonstrated that some of their intrinsic parameters can be estimated using the formalism describing ion diffusion in solids. This analysis is general and can be extended to study other metal oxides. In this work, it has been applied to ZnO. Furthermore, the presented methodology can be applied to other gases in which the partial pressure of oxygen plays an important role in the sensing mechanism.

4. Experimental

ADVANCED FUNCTIONAL MATERIALS

F. Hernandez-Ramirez et al. / Oxygen Diffusion for SnO$_2$ nanowire Sensors

low current levels and avoid undesired fluctuations, inside a home-made chamber following a methodology explained in detail elsewhere.[9,11]

[1] Y. Cui, Q. Q. Wei, H. K. Park, C. M. Lieber, *Science* **2001**, *293*, 1289.
[2] M. Law, H. Kind, B. Messer, F. Kim, P. D. Yang, *Angew. Chem. Int. Ed.* **2002**, *41*, 2405.
[3] M. S. Arnold, P. Avouris, Z. W. Pan, Z. L. Wang, *J. Phys. Chem. B* **2003**, *107*, 659.
[4] A. Kolmakov, M. Moskovits, *Annu. Rev. Mater. Res.* **2004**, *34*, 151.
[5] Z. Y. Fan, D. W. Wang, P. C. Chang, W. Y. Tseng, J. G. Lu, *Appl. Phys. Lett.* **2004**, *85*, 5923.
[6] A. Kolmakov, D. O. Klenov, Y. Lilach, S. Stemmer, M. Moskovits, *Nano Lett.* **2005**, *5*, 667.
[7] S. Dmitriev, Y. Lilach, B. Button, M. Moskovits, A. Kolmakov, *Nanotechnology* **2007**, *18*, 055707.
[8] V. V. Sysoev, J. Goschnick, T. Schneider, E. Strelcov, A. Kolmakov, *Nano Lett.* **2007**, *7*, 3182.
[9] F. Hernandez-Ramirez, A. Tarancon, O. Casals, J. Arbiol, A. Romano-Rodriguez, J. R. Morante, *Sens. Actuators B* **2007**, *121*, 3.
[10] D. C. Maier, S. Semancik, B. Button, E. Strelcov, A. Kolmakov, *Appl. Phys. Lett.* **2007**, *91*, 063118.
[11] F. Hernandez-Ramirez, J. D. Prades, A. Tarancon, S. Barth, O. Casals, R. Jimenez-Diaz, E. Pellicer, J. Rodriguez, M. A. Juli, A. Romano-Rodriguez, J. R. Morante, S. Mathur, A. Helwig, J. Spannhake, G. Mueller, *Nanotechnology* **2007**, *18*, 495501.
[12] G. Korotcenkov, *Mater. Sci. Eng. B* **2007**, *139*, 1.
[13] G. Korotcenkov, *Sens. Actuators B* **2005**, *107*, 209.
[14] N. Yamazoe, *Sens. Actuators B* **2005**, *108*, 2.
[15] a) S. Mathur, S. Barth, H. Shen, J.-C. Pyun, U. Werner, *Small* **2005**, *1*, 713. b) S. Mathur, S. Barth, *Small* **2007**, *3*, 2070.
[16] J. Arbiol, A. Cirera, F. Peiro, A. Cornet, J. R. Morante, J. J. Delgado, J. J. Calvino, *Appl. Phys. Lett.* **2002**, *80*, 329.
[17] M. Batzill, U. Diebold, *Prog. Surf. Sci.* **2005**, *79*, 47.
[18] N. Barsan, D. Koziej, U. Weimar, *Sens. Actuators B* **2007**, *121*, 18.
[19] F. Hernandez-Ramirez, A. Tarancon, O. Casals, J. Rodríguez, A. Romano-Rodriguez, J. R. Morante, S. Barth, S. Mathur, T. Y. Choi, D. Poulikakos, V. Callegari, P. M. Nellen, *Nanotechnology* **2006**, *17*, 5577.
[20] B. Kamp, Ph. D. Thesis, Max-Planck-Institut für Festkörperforschung, Stuttgart **2002**.
[21] B. Kamp, R. Merkle, J. Maier, *Sens. Actuators B* **2001**, *77*, 534.
[22] J. Jamnik, B. Kamp, R. Merkle, J. Maier, *Solid State Ionics* **2002**, *150*, 157.
[23] B. Kamp, R. Merkle, R. Lauck, J. Maier, *J. Solid State Chem.* **2005**, *178*, 3027.
[24] G. Blaustein, M. S. Castro, C. M. Aldao, *Sens. Actuators B* **1999**, *55*, 33.
[25] M. A. Ponce, M. S. Castro, C. M. Aldao, *Mater. Sci. Eng. B* **2004**, *111*, 14.
[26] V. V. Kissine, S. A. Voroshilov, V. V. Sysoev, *Thin Solid Films* **1999**, *348*, 304.
[27] The value of R_{NW} in oxygen-rich atmosphere was measured after the initial and fast rise (approximately at $t = 60$ s in Fig. 2 inset). This change of R_{NW} is explained by surface effects. Error bars come from both sample statistics and the difficulty to discriminate where ion diffusion into the bulks begins.
[28] E. Comini, V. Guidi, C. Malagu, G. Martinelli, Z. Pan, G. Sberveglieri, Z. L. Wang, *J. Phys. Chem. B* **2004**, *108*, 1882.
[29] Y. Zhang, A. Kolmakov, Y. Lilach, M. Moskovits, *J. Phys. Chem. B* **2005**, *109*, 1923.
[30] F. Hernandez-Ramirez, A. Tarancon, O. Casals, E. Pellicer, J. Rodríguez, A. Romano-Rodriguez, J. R. Morante, S. Barth, S. Mathur, *Phys. Rev. B* **2007**, *76*, 085429.
[31] a) J. Oviedo, M. J. Gillan, *Surf. Sci.* **2001**, *490*, 221; b) M. A. Mäki-Jaskari, T. T. Rantala, G. G. Golovanov, *Surf. Sci.* **2005**, *577*, 127.
[32] J. D. Prades, A. Cirera, J. R. Morante, *J. Electrochem. Soc.* **2007**, *154*, H675.
[33] P. B. Weisz, *J. Chem. Phys.* **1953**, *21*, 1531.
[34] K. Kilic, A. Zunger, *Phys. Rev. Lett.* **2002**, *88*, 095501.
[35] J. Maier, Festkörper-Fehler und Funktion: Prinzipien der Physikalischen Festkörperchemie, Teubner Studienbücher Chemie, Teubner, Stuttgart. **2000**.
[36] Y. Min, Ph. D. Thesis, Massachusetts Institute of Technology **2003**.
[37] G. N. Advani, *Int. J. Electron.* **1980**, *48*, 403.
[38] J. Liu, P. Gao, W. Mai, C. Lao, Z. L. Wang, R. Tummala, *Appl. Phys. Lett.* **2006**, *89*, 063125.
[39] J. J. Wortman, J. W. Harrison, H. L. Honbarrier, J. Yen, *Thin Film Oxygen Partial Pressure*, NASA CR-1941, Washington, DC **1972**.
[40] P. Bonasewicz, W. Hirschwald, G. Neumann, *Phys. Status Solidi a* **2006**, *97*, 593.
[41] S. Rantala, V. Lantto, *Surf. Sci.* **1996**, *352*, 765.

Submitted to **ADVANCED FUNCTIONAL MATERIALS**

Supporting Information

Determining the diffusion mechanisms in ZnO nanowires

ZnO nanowires synthesized via a CVD method[a] were contacted by FIB techniques (Fig.A).[b] To evaluate the mechanism of ion diffusion in their bulk, the resistance of some of these nanowires was monitored as function of the oxygen partial pressure (Fig.B) at room temperature (T = 298 K). The following experimental dependence was found in all the experiments,

$$R_{NW} \propto \sigma^{-1} \propto p(O_2)^n \qquad\qquad\qquad\qquad (i)$$

with n = 1 / 2. This result is in agreement with reported values for ZnO single crystals,[c,d] and justified by the existence of ion diffusion based on interstitial mechanisms.[c, e] The diffusion coefficient D at T = 298 K was estimated using the formula, [f, g]

$$D(T) = \frac{L^2}{\tau} \qquad\qquad\qquad\qquad (ii)$$

where L is the characteristic length of the diffusion path and t the characteristic time before reaching the steady-state. For a nanowire-based sensor and a one-dimensional diffusion model, L may be the diameter F of the nanowire (see Fig.4). In figure B, the response of a ZnO nanowire with r = 110 nm (F = 220 nm) stabilizes after t = 34 h approximately. Therefore, a value of D $\approx 10^{-15}$ cm^2 / s is determined in agreement with reported values for the diffusion coefficient in ZnO at this temperature (10^{-15}-10^{-17} cm^2 / s).[h]
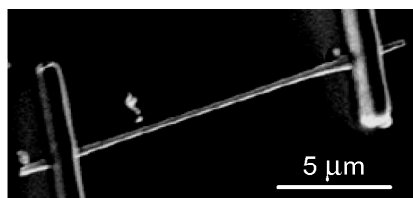
Figure A. ZnO nanowire of length L = 13 μm and radius r = 110 nm electrically contacted with FIB-techniques.
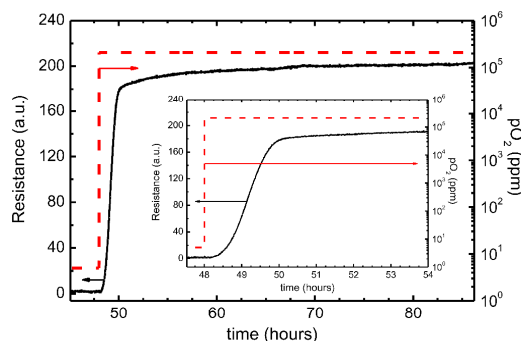
Figure B. Response of an individual ZnO nanowire (Fig.A) to a sudden change of the partial pressure of oxygen (T = 298 K). The nanowire was in low oxygen pressure for 48 hours to ensure initial stabilization. Signal stabilization to the steady-state is takes several hours. (Inset) Detail of the resistance transition from low to high oxygen partial pressure.

References

[a] Z. L. Wang, *J. Phys.: Condens. Mater*. **2004**, 16, R829.
[b] F. Hernandez-Ramirez, A. Tarancon, O. Casals, J. Rodriguez, A. Romano-Rodriguez, J. R. Morante, S. Barth, S. Mathur, T. Y. Choi, D. Poulikakos, V. Callegari and P. M. Nellen, *Nanotechnology* **2006**, 17, 5577.
[c] P. Bonasewicz, W. Hirschwald and G. Neumann, *Physica Status Solidi (a)* **2006**, 97, 593.
[d] J. J. Wortman, J. W. Harrison, H. L. Honbarrier, J. Yen. "Thin Film Oxygen Partial Pressure", NASA CR-1941, Washington, D. C. **1972.**
[e] A. Claret Soares Sabioni. *Solid State Ionics* **2004**, 170, 145.
[f] B. Kamp, R. Merkle, R. Lauck, J. Maier, *J. Solid State Chem*. **2005**, 178, 3027.
[g] An accurate estimation of the diffusion coefficient requires more complex studies where the Fick's law is taken into account. For a detailed explanation see [d] and [h].
[h] J. Liu, P. Gao, W. Mai, C. Lao, Z. L. Wang, R. Tummala, *Appl. Phys. Lett*. **2006,** 89, 063125.

4.1.2 Summary of Results

Unit 1.a   Ab initio atomistic modeling

- The *ab initio* study of the surface stability of SnO_2-cassiterite revealed that the most abundant and relevant surface orientation is the (110), which is in accordance with previous experimental works (*Papers 3* and *4*). Therefore, the subsequent studies were centered on this facet.

- In order to model realistic atomic arrangements, we explored the feasibility of different surface configurations based on the *ab initio* thermodynamics methodology. Under ambient conditions, the stoichiometric surface configuration is the most stable one. When the temperature is raised above 270°C a single O_{Bridg} vacancies may form and even at higher temperatures (above 480°C) the formation of a single isolated $O_{InPlane}$ vacancies is possible. At temperatures above 640°C multivacant configurations are the most probable (*Papers 3* and *4*). These theoretical predictions (which are in agreement with previous experimental works) together with the typical working and annealing temperatures of MOX–based sensors indicate that the partially reduced surface terminations must be considered in order to model realistic gas–surface interactions.

- As a consequence of the previous results, the surface oxygen vacancies were included to model the interaction of NO, NO_2 and SO_2 with the SnO_2(110). These calculations indicated that:

  - *NO* adsorption takes place onto oxygen sites in stoichiometric surfaces.
  - *NO_2* essentially interacts with oxygen vacancy sites (reduced surfaces).
  - *SO_2* competes with NO_2 for the same adsorption sites and it is harder to desorb thermally.

  These results are compatible with the expected oxidizing/reducing characters of each gas and explain the poisoning effect. Moreover, the comparison of the desorption energies involved in all these processes is in accordance with Temperature Programmed Desorption (TPD) experiments (*Papers 3* and *4*).

- Similar results were obtained with ZnO: the most stable surface terminations were the non-polar (10-10) and (11-20) ones of the wurtzite phase, it was necessary to consider the role played by the surface oxygen vacancies and NO_2 interacted preferentially with surface metallic sites (oxygen vacancy sites) competing with SO_2 (*Paper 5*).

Unit 1.b Experimental validation – Novel sensing approaches enabled by the nanoscale

- The conductometric response towards NO_2 of individual nanowires operated at different temperatures with microheaters revealed that the optimum working temperatures (T ~ 175°C) correspond to interactions with in plane sites of the $SnO_2(110)$ surface (according to the simulations of the TPD spectra) (*Paper 6*). Specific DFT calculations explained this: the charge captured by NO_2 upon absorption onto in plane sites is higher than any other (see *Paper 15* for more details).

- Similar responses towards NO_2 were reproduced heating the nanowires by means of the power dissipated by the applied current. As previously presented (*Paper ♣*), our experimental setup allowed controlling the probing current applied to the nanowires and thus, controlling the magnitude of the self-heating effect up to temperatures close to 350°C (*Paper 6*). Besides the enormous progress in terms of miniaturization, this novel approach reduces dramatically the power needed to operate these sensors to few tens of microwatt. This result opens the door to a new generation of ultralow power consumption gas sensor devices.

- Another consequence of the previous result was the proposal of an innovative experimental method to estimate the temperature at the nanowire's scale. This is based on the comparison of the dynamic response to gases of the nanowire operated with external heaters and with self-heating (*Paper 7*).

Unit 1.c   On the connection between surface and bulk oxygen vacancies

- The fact that the long-term drifts in the responses of MOX nanowires to sudden changes in the oxygen content in air vary with the nanowire's radii, compelled us to consider the influence of additional bulk effects in their response to gases. All the experimental evidences were compatible with the occurrence of oxygen diffusion into the bulk of MOX nanowires (even at room temperature). This result remarks the importance of the diffusion effects in MOX, which are frequently neglected, and indicates that these effects should be taken into account in further modeling of MOX gas sensors (*Paper 8*).

4.2 Unit 2: Light – MOX interaction

Unit 2 is fully devoted to the study of the photon–metal oxide (MOX) interactions on the basis of the principles that rule the charge transport properties in semiconductors. The unit is separated in sections concerning the critical analysis of the potential of individual MOX nanowires in light sensing applications and the study and theoretical modeling of the phenomena that limit their dynamic response.

- *Unit 2.a   Understanding photodetectors based on nanowires.* The opportunity to use a single crystal of a wide bandgap semiconductor for UV light detection experiments is attractive both from the technical and from the fundamental points of view. The superior crystalline quality is expected to provide excellent performances and opens the door to ideal experimental conditions for research. Individual metal oxide nanowires offer this exceptional experimental scenario. In this section, the photoconductive response of pristine ZnO and SnO_2 nanowires is studied. An exhaustive analysis of the factors that influence their response is presented. The technological issues that can improve their response are also identified. All these results are presented in *Paper 9.*

- *Unit 2.b.   Understanding the long-term photoconductive states*. The analysis presented in the previous section highlighted the poor dynamic response to light of MOX nanowires and preliminary identified its cause: the electron-hole separation effects that take place near the nanowire's surface. In this section, the problems concerning the long-term persistence of the photoconductivity in MOX nanowires are presented in detail and modeled on the basis of the results obtained in *Unit 1*. Several strategies to minimize this inconvenient effect are also proposed and tested (*Paper 10*).

4.2.1 Papers

9. J.D. Prades, R. Jimenez-Diaz, F. Hernandez-Ramirez, L. Fernandez-Romero, T. Andreu, A. Cirera, A. Romano-Rodriguez, A. Cornet, J.R. Morante, S. Barth, S. Mathur, *"Toward a systematic understanding of photodetectors based on individual metal oxide nanowires"* J. Phys. Chem. C **112**, 14639-14644 (2008). <u>Remarks:</u> Included in the three Most Read Papers of J. Phys. Chem. C during 2008.

10. J.D. Prades, F. Hernandez-Ramirez, R. Jimenez-Diaz, M. Manzanares, T. Andreu, A. Cirera, A. Romano-Rodriguez, J.R. Morante, *"The effects of electron-hole separation on the photoconductivity of individual metal oxide nanowires"*, Nanotechnol. **19**, 465501 (2008). <u>Remarks:</u> Highlighted as "Article of Interest" by Nanotechnology.

J.D. Prades, R. Jimenez-Diaz, F. Hernandez-Ramirez, L. Fernandez-Romero, T. Andreu, A. Cirera, A. Romano-Rodriguez, A. Cornet, J.R. Morante, S. Barth, S. Mathur, *"Toward a systematic understanding of photodetectors based on individual metal oxide nanowires"* J. Phys. Chem. C **112**, 14639-14644 (2008).

9

Toward a Systematic Understanding of Photodetectors Based on Individual Metal Oxide Nanowires

Joan Daniel Prades,*,† Roman Jimenez-Diaz,† Francisco Hernandez-Ramirez, Luis Fernandez-Romero,† Teresa Andreu,† Albert Cirera,† Albert Romano-Rodriguez,† Albert Cornet,† Joan Ramon Morante,† Sven Barth,‡ and Sanjay Mathur*,‡,§

EME/XaRMAE/IN²UB, Departament d'Electronica, Universitat de Barcelona, C/ Marti i Franques 1, Barcelona, E-08028, Spain, Nanocrystalline Materials and Thin Film Systems, Leibniz-Institute of New Materials, Saarbruecken, D-66123, Germany, and Department of Inorganic Chemistry, University of Cologne, Cologne, D-50939, Germany

Received: May 20, 2008; Revised Manuscript Received: July 3, 2008

We present a set of criteria to optimize photodetectors based on n-type metal oxide nanowires and a comparison methodology capable of overcoming the present lack of systematic studies dealing with such devices. The response of photoconductors is enhanced following different fabrication strategies, such as diminishing the distance between the electrical contacts, increasing the width of the photoactive area, or improving the electrical mobility of the nanomaterials. The validity of the theoretical background is verified by experimental results obtained with devices based on ZnO nanowires. The performances of our devices show that the normalized gain of single ZnO nanowire-based photodetectors exceeds those of thin films.

Introduction

Metal oxide nanowires are gaining growing interest as photodetectors due to their potential applications in gas sensing and optoelectronics.[1] Although preliminary works revealed promising results,[1-11] further research is necessary in order to reach complete control of their photosensing properties. Among all n-type metal oxide nanomaterials, photoresponses of ZnO and SnO_2 nanowires have been widely studied;[1-11] however, the lack of well-established fabrication methodologies and standardized procedures obfuscates a comparison of experimental results. For instance, photoconductive gains (G_{ph}) ranging from 10^2 to 10^8 [4,9,10] and response times (τ) between milliseconds and hours were reported for ZnO nanowires,[1,2,4,7,10] which possibly result from different experimental conditions and device geometry used in all of these studies. Here, we present some systematic strategies for enhancing the response of photodetectors based on nanowires and a methodology for the facile comparison of the measured photoresponses. These strategies are fundamental to the potential of this technology in real devices and applications.
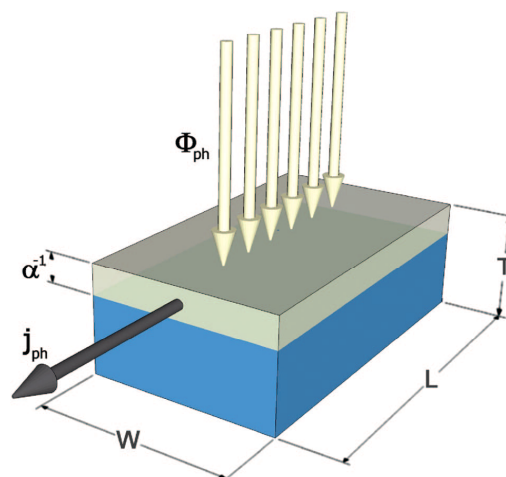
Experimental Methods

ZnO nanowires were fabricated via a vapor-phase carbothermal transport process inside an Atomate's chemical vapor deposition (CVD) system. The source material was a 1:1 molar mixture of commercial ZnO (metal basis, 99.99%) and graphite powder (crystalline, 300 mesh, 99%) from Alfa Aesar. Gold nanoparticles were used as catalytic islands on thermally oxidized Si wafers.[12] Uniform nanowires were obtained with mean radius $<r> = 90 \pm 15$ nm and lengths up to 30 μm. Some of them were electrically contacted to platinum microelectrodes using a FEI Dual-Beam Strata 235 FIB instrument

Figure 1. Diagram of a metal-oxide structure with an arbitrary volume of length *L*, width *W*, and thickness *T*, under a photon flux Φ_{ph}. Photocarrier generation is induced in the upper layer of the structure until a depth α^{-1} and leads to photoconduction (j_{ph}) under polarization.

following a nanolithography process explained elsewhere.[13-15] Electrical measurements were performed with the help of a self-made electronic circuit designed to ensure low current levels and to avoid undesired fluctuations[16] inside a homemade chamber. Photoresponse was excited using both UV LEDs and a UV lamp. UV LEDs were centered on $\lambda = 340 \pm 10$ nm and $\lambda = 385 \pm 15$ nm (Seoul Optodevices T9F34C and Purple-Hi E1L5M-4P0A2), whereas the UV lamp was a HAMAMATSU LC8 light source with a type[−01] Hg−Xe lamp enhanced for the line at $\lambda = 365$ nm. Light intensity impinging on the nanowires was determined with the help of a thermopile detector

* Corresponding authors: dprades@el.ub.es, s.mathur@uni-koeln.de.
† Universitat de Barcelona.
‡ Leibniz-Institute of New Materials.
§ University of Cologne.

(FieldMax-TOP). Up to 10 devices based on single ZnO nanowires were fabricated, and their photoresponses were studied as a function of different experimental parameters to validate the theoretical discussion. Two-probe I–V measurements revealed symmetric responses in great accordance with results published elsewhere.[17] The effective voltage drop along the nanowires was determined by decoupling the rectifying contact from the purely resistive contribution of the nanowires following the procedure described elsewhere.[17] To evaluate the role of surface contribution on the photoresesponse of these devices, some samples were coated with a 475 ± 50 nm thick layer of PMMA (2 wt % poly (methyl methacrylate) in dichloromethane) by spin coating. All experiments were performed in real air atmosphere.

Results and Discussion

1. Theoretical Background. Photodetectors based on single n-type metal oxide nanowires, modeled as an arbitrary volume of length L, width W, and thickness T (Figure 1), can be studied using the fundamental principles ruling light carrier generation on semiconductors.[18] Thus, current density j_{ph} is given by the following equation,

$$j_{ph} = q\Delta n_{ph}v \tag{1}$$

where q is the elemental charge, Δn_{ph} is the concentration of generated carriers, and v is their velocity. Δn_{ph} can be also written as shown in eq 2,

$$\Delta n_{ph} = \frac{\eta F}{V_{ph}}\tau \approx \frac{\eta F}{\alpha^{-1}WL}\tau \tag{2}$$

where η is the quantum efficiency of carrier generation by one photon, F is the absorption rate of photons, τ is the carrier lifetime, and V_{ph} is the photogeneration volume (Figure 1).

The approximation in eq 2 assumes a constant carrier generation profile until the depth α^{-1}, where α is the absorption coefficient of the metal oxide at one fixed wavelength (see the Supporting Information). Δn_{ph} and τ are also related through the following continuity equation,[18]

$$\frac{\partial \Delta n_{ph}}{\partial t} = g_{ph} - \frac{\Delta n_{ph}}{\tau} \tag{3}$$

where g_{ph} is the generation rate of charge carriers under illumination. Assuming that the concentration of electrons Δn_{ph} is independent of τ, the photocurrent dynamics at the rising (time constant τ_r) and falling (time constant τ_d) edges are given by (see Supporting Information),

$$i_{ph}(t) = I_{ph}(1 - e^{-t/\tau_r}) \tag{4}$$

$$i_{ph}(t) = I_{ph}e^{-t/\tau_d} \tag{5}$$

where I_{ph} is the photocurrent at the steady-state. However, if an external field E is applied parallel to the longitudinal axis of ohmic nanowires, then the velocity of carriers (v) can be expressed in terms of the applied voltage (V) using the following formula,

$$v = \mu^* E = \frac{\mu^* V}{L} \tag{6}$$

where μ^* is the effective carrier mobility. According to the Matthiessen's rule, μ^* can be divided into the bulk (μ_B) and surface (μ_S) contribution according to eq 7.[18]

$$\frac{1}{\mu^*} = \frac{1}{\mu_B} + \frac{1}{\mu_S} \tag{7}$$

The absorption rate of photons F when metal oxide nanowires are exposed to a flux of Φ_{ph} photons can be also expressed by eq 8,

$$F = \beta\Phi_{ph}WL \tag{8}$$

where β is the fraction of photons not reflected by the surface, and WL is the effective area of one nanowire (see Figure 1). Therefore, using eqs 2, 6, and 8, current density j_{ph} can be rewritten as eq 9

$$j_{ph} = q\frac{1}{L\alpha^{-1}}\beta\eta\tau\mu^* V\Phi_{ph} \tag{9}$$

To evaluate the total photogenerated current I_{ph}, which is the experimental response of real devices, we assume that nanowires are thick enough to absorb all the incident photons. That is to say,

$$T \geq \alpha^{-1} \tag{10}$$

Therefore, it can be deduced that thinner nanowires ($T < \alpha^{-1}$) will lead to lower photoresponses. On the contrary, the use of thicker nanowires ($T \gg \alpha^{-1}$) will not imply a further signal enhancement. For instance, the penetration depth α^{-1} of near-UV photons (wavelength from 400 to 250 nm) in ZnO is almost constant at 50 nm.[19] Thus, ZnO nanowires with radii slightly above $r \approx 25$ nm should be used to maximize photoresponse to UV-light in this wavelength range.

If the constant absorption profile approximation is maintained, photocurrent I_{ph} in nanowires that satisfy eq10 is given by eq 11,

$$I_{ph} = j_{ph}(\alpha^{-1}W) = q\frac{W}{L}\beta\eta\tau\mu^* V\Phi_{ph} \tag{11}$$

where three different contributions are clearly identified. The first one is related to geometric parameters of the device (W/L), the second one to the intrinsic properties of nanowires ($\beta\eta\tau\mu^*$) and the third one only depends on the experimental conditions ($V\Phi_{ph}$). The performance of these devices can be also analyzed in terms of their photoconductive gain G_{ph}, which is defined in eq 12,[18]

$$G_{ph} \equiv \frac{I_{ph}}{qF} \approx \frac{1}{L^2}\eta\tau\mu V \tag{12}$$

where identical types of contributions are involved.

2. Experimental Validation and Discussion. *2.1. Geometrical Aspects.* Concerning the geometry of photodetectors, eq 11 implies enhanced I_{ph} with increasing width (W) of the photoactive area. To verify this, the responses of single ZnO nanowires and lamellae were compared.[20] ZnO lamellae were randomly obtained during the synthesis process of ZnO nanowires when the density of catalytic gold nanoparticles is very high (Figure 2). Other authors have postulated that the origin of these structures could be related to variations of the oxygen concentration during synthesis.[20] ZnO lamellae presented thicknesses (T) comparable to the diameter of the nanowires ($2r \approx 220$ nm), but their widths (W) were up to 10 times larger, allowing us to confirm the enhancement of I_{ph} with increasing photoactive areas (Figure 2a). To compare the UV photosensing performances of individual ZnO nanowires with ZnO lamellae, identical conditions were used in all experiments ($\Phi_{ph} = 3.3 \times 10^{18}$ ph m^{-2}

Photodetectors Based on Individual Metal Oxide Nanowires
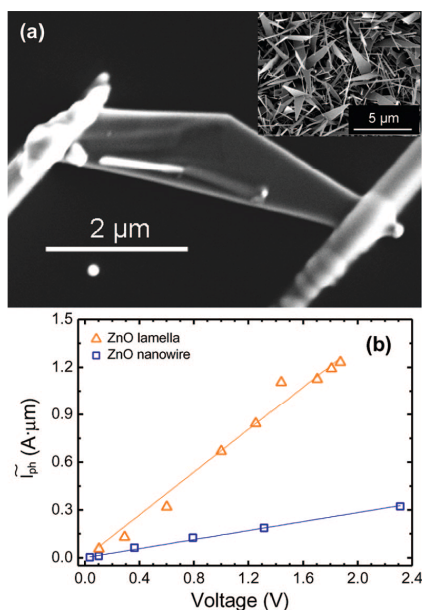
Figure 2. (a) ZnO lamella of length $L_L = 3.9$ μm and average width around $W_L \approx 1000$ nm contacted with FIB nanolithography techniques. (Inset) SEM image of the mixture of ZnO nanowires and ZnO lamellae obtained after the synthesis process. (b) Normalized photoresponse $\tilde{I}_{ph}$ to the distance between electrical contacts L of one ZnO lamella and one ZnO nanowire ($L_{NW} = 13$ μm) under identical conditions ($\Phi_{ph} = 3.3 \times 10^{18}$ ph m^{-2} s^{-1}; $\lambda = 340 \pm 10$ nm). I_{ph} is higher with the lamella due to a larger value of W.

s^{-1}; $\lambda = 340 \pm 10$ nm) and a comparable photocurrent ($\tilde{I}_{ph}$) value is obtained by normalization to the interelectrode distances (L).

$$\tilde{I}_{ph} = \frac{I_{ph}}{1/L} \qquad (13)$$

The photoresponse [Figure 2] obtained with a nanowire was 4.7 times lower than the one measured with the lamella shown in Figure 2a. The average width of this lamellar structure was $W_L \approx 1000$ nm, whereas the nanowire showed $W_L \approx 220$ nm in diameter ($W_L/W_{NW} \approx 4.5$). In accordance to eq 11, the higher active area of ZnO lamellae caused enhanced photocurrent values $\tilde{I}_{ph}$ as predicted by geometrical factors and shown by the presented values ($W_L/W_{NW} \approx \tilde{I}_{ph(L)}\tilde{I}_{ph(NW)}$).

Another convenient way to increase the width of the photoactive area is using multi-nanowire-based configurations. These devices can be realized by self-assembly techniques, such as dielectrophoresis, to electrically contact large amounts of nanowires in parallel.[21,22] This fabrication methodology prevents parasitic effects arising from uncontrolled nanowire−nanowire contacts, and the resulting devices admit higher currents (with simpler conditioning electronics) without damaging the nanowires[16] (see the Supporting Information). It is noteworthy that, according to eq 12, the photoconductive gain G_{ph} obtained with these multi-nanowire configurations is equivalent to the gain provided by one single nanowire, if all of them are identical.

The distance between contacts (L) also determines the response of the photodetector since both I_{ph} and G_{ph} increase inversely with this parameter. L not only influences the photocapture area (WL) but also determines the effective electric
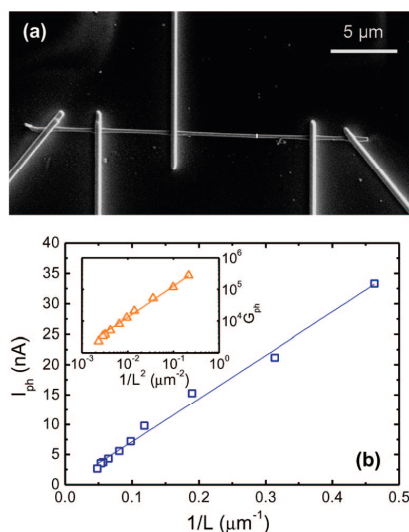
Figure 3. (a) ZnO nanowire with radius $r = 90 \pm 10$ nm contacted to five contacts fabricated with FIB nanolithography techniques. (b) Photoresponse I_{ph} and photoconductive gain G_{ph} (inset) of the ZnO nanowire as a function of the distance L between electrical contacts obtained with $\Phi_{ph} = 3.3 \times 10^{18}$ ph m^{-2}s^{-1}, $\lambda = 340 \pm 10$ nm, and $V = 1$ V.

field (E) inside the nanowire due to the bias voltage (V) applied externally. Indeed, this second aspect dominates the overall contribution of L to the photoresponse (see eqs 11 and 12). The dependence of I_{ph} and G_{ph} on L was experimentally confirmed by fabricating five electrical contacts separated at different distances on an individual ZnO nanowire (Figure 3a), and measuring the UV photoresponse between different pairs of electrodes. It was experimentally found that I_{ph} and G_{ph} increase inversely with the distance between contacts L, in accordance with eqs 11 and 12 (Figure 3b). Therefore, it can be concluded that higher-gain photodetectors are obtained by diminishing this fabrication-related parameter. The lower limit for L will strictly depend on the precision of the nanolithography technique and other size-associated phenomena such as diffraction, if L approaches the wavelength of photons, or uncontrolled degradation effects produced when the rupture electrical field of the metal oxide is overcome (see the Supporting Information). To exemplify the later point, it can be roughly estimated that nanowires contacted between two electrodes with a separation of only 50 nm[23] and polarized at 5 V[1,10] will be subjected to electrical fields as high as 1 MV/cm.

2.2. Intrinsic Properties of the Semiconductor. In addition to geometrical factors, the dependence of I_{ph} on intrinsic material properties, such as η, τ, μ^* and β, have to be considered (see eq 11). The spectral response of photodetectors is determined by the quantum efficiency η, which was observed to increase by up to 3 orders of magnitude when photons with energies above the bandgap interact with these devices, compared to typical responses obtained with sub-bandgap photons.[24] The variation of quantum efficiency η as a function of incident light wavelength (λ) was investigated. In Figure 7, it is demonstrated how I_{ph} scaled up when above-bandgap photons ($\lambda = 340 \pm 10$ nm) interacted with a single ZnO nanowire-based device, compared to low I_{ph} response obtained with sub-bandgap photons ($\lambda = 385 \pm 15$ nm). This result shows the importance of tuning the bandgap of such photodetectors to select their
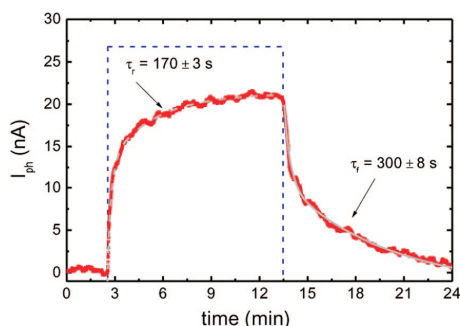
Figure 4. Dynamic behavior of the photoresponse I_{ph} measured with an individual ZnO nanowire when a UV pulse is applied (dashed line) ($\Phi_{ph} = 3.3 \times 10^{18}$ ph m^{-2} s^{-1}; $\lambda = 340 \pm 10$ nm; $V = 1$ V). The response fits with theoretically deduced exponential laws and exhibits time constants of $\tau_r = 170 \pm 3$ s and $\tau_d = 300 \pm 8$ s.

active/blind spectral regions.[11,18,24] It is noteworthy that the bandgap edge of nanowires depends not only on the material but also on their dimensions.[11,18] Thus, controlling the radii of nanowires is critical to tune the spectral sensitivity of the final devices.

The photogenerated carrier lifetime (τ) is the second parameter directly related to the intrinsic properties of nanowires, which is known to be higher in nanomaterials compared to bulk due to the large surface-to-volume ratio and the formation of deep level surface states.[18,25] For metal oxide nanowires, it is generally accepted that photocarrier relaxation dynamics consists of an initial decay process in the nanosecond range, explained by the fast carrier thermalization and hole-trapping by surface states, followed by a slow decay dependent on the surrounding atmosphere and the nanowire surface coating.[3,4,26,27] This second process, with characteristic time constants in seconds, dominates the final response of nanowire-based photodetectors. For this reason, the carrier lifetime contribution τ to the photoresponse I_{ph} (see eq 11) can be modified by controlling the surface interactions of this type of nanowires. Time-resolved measurements allowed us to estimate the rising time constant τ_r and falling time constant τ_d exhibited by our devices (Figure 4). The evolution in time ($i_{ph}(t)$) was in accordance with the theoretical model (eqs 4 and 5), whereby values close to a few minutes were found.

The third parameter related to the intrinsic properties of nanowires is the electrical mobility μ^*, which is known to be dependent on their radii. In the case of ZnO, mobility values ranging from 2 to 30 cm^2/(V s) were reported for nanowires with radii below $r \approx 100$ nm.[28–31] The diminished mobility increases up to the bulk value ($\sim$200 cm^2/(V s)) in thicker nanowires.[10] This behavior is attributed to scattering and trapping of the electrons by surface defect states and becomes more significant in thin nanowires possessing higher surface-to-volume ratios. Thus, thicker nanowires are convenient to obtain optimal devices for μ^* optimization due to minimized surface contributions μ_S (eq 7). The limitation introduced by the dependence of μ^* with radius can be also circumvented by passivating the nanowire surface, which is reported to dramatically increase the mobility of ZnO nanowires (up to 1.000 cm^2/(V s)).[31–34]

It was demonstrated that the mobility of ZnO nanowires dramatically increased (up to $\sim$1.000 cm^2/(V s)) with Si$_3$N$_4$/SiO$_2$,[31] polyimide,[32] poly(methyl methacrylate) (PMMA),[33] and polyacrylonitrile[34] coatings. Therefore, we covered some devices
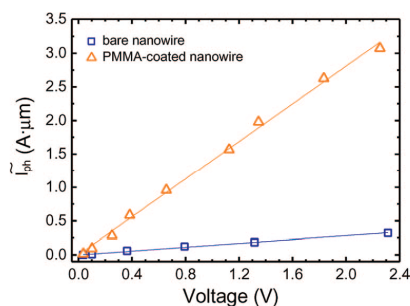
Figure 5. Photoresponse ($\tilde{I}_{ph} \equiv IL$) normalized to the distance between electrical contacts L of one single ZnO nanowire ($L_{NW} = 13$ μm) before and after coating with PMMA under identical illumination ($\Phi_{ph} = 3.3 \times 10^{18}$ ph m^{-2} s^{-1}; $\lambda = 340 \pm 10$ nm). $\tilde{I}_{ph}$ is higher after coating due to surface passivation induced higher μ^*.
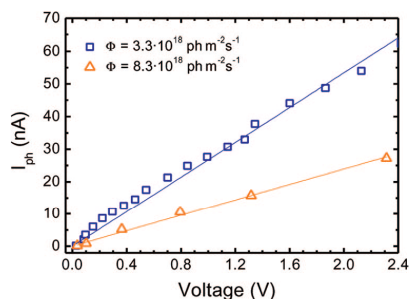
Figure 6. Linear dependency of photoresponses I_{ph} on the applied voltage V of an individual ZnO nanowire (under two different photon fluxes Φ_{ph}).
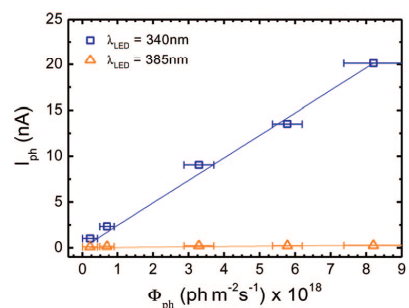
Figure 7. Photoresponse I_{ph} of an individual ZnO nanowire under different photon fluxes Φ_{ph} at constant polarization voltage ($V = 1$ V). A linear dependence between these two parameters is experimentally observed. Remarkably, photoresponse I_{ph} is highly dependent on the energy of the incident photons.

with PMMA by spin coating after eliminating the surface contamination with oxygen plasma. The passivation layers were approximately 500 nm thick, and presented high UV transparency (optical transmittance above 92% from 300 to 800 nm) and extremely low conductance (below 0.1 nS) independent of the illumination. The photoresponse of these devices was $\sim$9.5 times higher after coating (see Figure 5). To elucidate this point, the mobility of the nanowires[15] before and after passivation were estitmated to be $\mu^* \approx 3-5$ cm^2/(V s) and $\mu^*_{(PMMA)} \approx 40-53$ cm^2/(V s), respectively. This improvement in the nanowire mobility (factor of $\sim$10) and the high transmittance of the PMMA layer explain the increased photoresponse according to eq 11.

Photodetectors Based on Individual Metal Oxide Nanowires

The last intrinsic parameter of nanowires to be considered in this work is the fraction of photons (β) not reflected by the surface of the metal oxide, which was recently demonstrated to be lower in photodetectors based on aligned nanowires compared to thin films.[35]

2.3. Working Conditions. As far as the experimental conditions are concerned, it can be expected from eqs 11 and 12 that photoresponse raises linearly with applied voltage V and flux of photons Φ_{ph}. Figures 6 and 7 demonstrate the linear increase in device response in dependence to the two parameters and UV-light according to theory. This feature complicates comparing most of the reported results, since different experimental conditions were used in these experiments.[1–10] For this reason we propose a more generic way to express eq 12,

$$g_{ph} \equiv \frac{L^2 G_{ph}}{V} \approx \eta \tau \mu^* \qquad (14)$$

which is a normalized photoconductive gain, independent of the device geometry and the experimental conditions.

Apart from the photoconductive gain, the dynamic behavior of these devices is also important for optimizing real devices. Their low-pass bandwidth can be defined as $BW \approx (2\pi\tau)^{-1}$. Thus, the normalized gain per bandwidth becomes

$$g_{ph}BW \approx \frac{\eta \mu^*}{2\pi} \qquad (15)$$

From equation 15, it can be observed that the quantum efficiency η and mobility μ^* are the key parameters to evaluate the overall performance of these photodetectors.

3. Comparison to State-of-the-art Devices. To substantiate and validate the performances of our nanowire-based devices, the photoresponse values were critically compared with previously reported results. Soci et al.[10] recently reported photoconductive gain values of $G_{ph,lit} = 5 \times 10^7$ in devices with $L_{lit} = 1$ μm and $<r>_{lit} = 110$ nm polarized at $V_{lit} = 5$ V for equivalent illumination conditions, which is much higher than the typical G_{ph} values measured in our experiments. For example, $G_{ph} = 6 \times 10^3$ was obtained with $V = 1$ V, $L \approx 13$ μm, and $r \approx 110$ nm. However, an accurate comparison of these two devices can be only achieved if the photoconductive gain G_{ph} is rewritten as shown in equation 14. If g_{ph} is calculated, we find that $g_{ph,lit} = 10^{-5}$ m²/V and $g_{ph} = 10^{-6}$ m²/V, showing that the literature value is only 1 order of magnitude higher than ours. This discrepancy can be explained considering the mobility μ^* and lifetime τ_d of nanowires. On one hand, our ZnO nanowires have response time constants close to $\tau \approx 300$s (Figure 4) and exhibited mobility values of ~3 cm²/(V s), which was estimated following a procedure described elsewhere.[15] On the other hand, Soci and co-workers reported $\tau_{lit} \approx 33$ s and $\mu^*_{lit} \approx 270$ cm²/(V s), whose product ($\tau_{lit}\mu^*_{lit}$) is a factor 10 time higher than ours ($\tau\mu^*$), which justifies the divergence of values in g_{ph} (see eq 14). Fully consistent results were obtained with the rest of devices under test, demonstrating that gain normalization of photodetectors to the geometry and polarization conditions is necessary for adequate comparison. Moreover, comparison of g_{ph} values allows the determination of which intrinsic properties of the photoactive material must be improved to enhance the performance of future devices. For example, according to the experimental results, the electron mobility μ^* should be improved in our case. From all of these results, it can be concluded that the experimental responses obtained with photodetectors based on single nanowires are precisely modeled by the here-summarized theoretical approach.

Finally, the same methodology was applied to compare the photoresponse of ZnO nanowires and ZnO thin films.[36] In general, higher photocurrent values I_{ph} were obtained with larger grains,[37–41] due to increasing mobility which approaches bulk behavior (~200 cm²/(V s)) in high-quality thin films,[42] with typical photoconductive gain values of $G_{ph,lit}^{TF} = 1360$.[38] Using the polarization and geometric conditions reported by the authors ($V_{ph,lit}^{TF} = 5$ V; $L_{ph,lit}^{TF} = 10$ μ), the normalized photoconductive gain was found to be $g_{ph,lit}^{TF} = 3 \times 10^{-8}$ m²/V, whose value is clearly lower than the one reported with single ZnO nanowires. On the contrary, the normalized gain per bandwidth of ZnO thin films is significantly higher ($g_{ph,lit}^{TF}BW = 3 \times 10^{-3}$ m² Hz/V) than that obtained with ZnO nanowires ($g_{ph,lit}^{NW}BW = 5 \times 10^{-8}$ m² Hz/V[10]), if $\tau_{lit}^{TF} \approx 1.5$ μs.[38] Comparing this result with eqs 14 and 15, it is concluded that the higher photogain achieved with individual nanowires is mainly associated to the longer lifetime of the photocarriers, which increases at the expense of diminishing dynamic response.

Conclusions

We presented in detail the principles ruling the response of UV photodetectors based on metal oxide nanowires. Different design and fabrication strategies to enhance their performances were identified and discussed, such as controlling their geometry or tuning the intrinsic electrical properties of nanowires. Most of them were validated with experimental results obtained with photodetectors based on single ZnO nanowires. Finally, a rigorous methodology to compare different devices was presented, overcoming the present lack of systematic study in this field. On the basis of this methodology we conclude that current photodetectors based on single ZnO nanowires achieve better normalized gains (up to 3 orders of magnitude) with slower response compared with thin film devices.

Supporting Information Available: (I) Photogeneration theory details: nonuniform absorption and transient solution and (II) self-heating effects on nanowires. This information is available free of charge via the Internet at http://pubs.acs.org.

References and Notes

(1) Kind, H.; Yan, H.; Messer, B.; Law, M.; Yang, P. *Adv. Mater.* **2002**, *14*, 158–160.

(2) Keem, K.; Kim, H.; Kim, G. T.; Lee, J. S.; Min, B.; Cho, K.; Sung, M. Y.; Kim, S. *Appl. Phys. Lett.* **2004**, *84*, 4376–4378.

(3) Fan, Z. Y.; Chang, P. C.; Lu, J. G.; Walter, E. C.; Penner, R. M.; Lin, C. H.; Lee, H. P. *Appl. Phys. Lett.* **2004**, *85*, 6128–6130.

(4) Heo, Y. W.; Kang, B. S.; Tien, L. C.; Norton, D. P.; Ren, F.; La Roche, J. R.; Pearton, S. J. *Appl. Phys. A: Mater. Sci. Process.* **2005**, *80*, 497–499.

(5) Kumar, S.; Gupta, V.; Sreenivas, K. *Nanotechnology* **2005**, *16*, 1167–1171.

(6) Hsu, C. L.; Chang, S. J.; Lin, Y. R.; Li, P. C.; Lin, T. S.; Tsai, S. Y.; Lu, T. H.; Chen, I. C. *Chem. Phys. Lett.* **2005**, *416*, 75–78.

(7) Law, J. B. K.; Thong, J. T. L. *Appl. Phys. Lett.* **2006**, *88*, 133114.

Prades et al.

(8) Luo, L.; Zhang, Y. F.; Mao, S. S.; Lin, L. W. *Sens. Actuators, A* **2006**, *127*, 201–206.

(9) Suehiro, J.; Nakagawa, N.; Hidaka, S.; Ueda, M.; Imasaka, K.; Higashihata, M.; Okada, T.; Hara, M. *Nanotechnology* **2006**, *17*, 2567–2573.

(10) Soci, C.; Zhang, A.; Xiang, B.; Dayeh, S. A.; Aplin, D. P. R.; Park, J.; Bao, X. Y.; Lo, Y. H.; Wang, D. *Nano Lett.* **2007**, *7*, 1003–1009.

(11) (a) Mathur, S.; Barth, S.; Shen, H.; Pyun, J. C.; Werner, U. *Small* **2005**, *1*, 713–717. (b) Mathur, S.; Barth, S. *Small* **2007**, *3*, 2070–2075.

(12) Wang, Z. L. *J. Phys.: Condens. Matter* **2004**, *16*, R829−R858.

(13) Hernández-Ramírez, F.; Rodríguez, J.; Casals, O.; Russinyol, E.; Vilà, A; Romano-Rodríguez, A.; Morante, J. R.; Abid, M. *Sens. Actuators, B* **2006**, *118*, 198–203.

(14) Hernández-Ramírez, F.; Tarancón, A.; Casals, O.; Rodríguez, J.; Romano-Rodríguez, A.; Morante, J. R.; Barth, S.; Mathur, S.; Choi, T. Y.; Poulikakos, D.; Callegari, V.; Nellen, P. M. *Nanotechnology* **2006**, *17*, 5577–5583.

(15) Hernandez-Ramirez, F.; Tarancon, A.; Casals, O.; Pellicer, E.; Rodriguez, J.; Romano-Rodriguez, A.; Morante, J. R.; Barth, S.; Mathur, S. *Phys. Rev. B* **2007**, *76*, 085429.

(16) Hernandez-Ramirez, F.; Prades, J. D.; Tarancon, A.; Barth, S.; Casals, O.; Jiménez-Diaz, R.; Pellicer, E.; Rodriguez, J.; Juli, M. A.; Romano-Rodriguez, A.; Morante, J. R.; Mathur, S.; Helwig, A.; Spannhake, J.; Mueller, G. *Nanotechnology* **2007**, *18*, 495501.

(17) Zhang, Z.; Yao, K.; Liu, Y.; Jin, C.; Liang, X.; Chen, Q.; Peng, L. M. *Adv. Funct. Mater.* **2007**, *17*, 2478–2489.

(18) (a) Rose, A. *Concepts in Photoconductivity and Allied Problems*; Interscience Publishers: New York, 1963. (b) Sze, S. M. *Physics of Semiconductor Devices*; John Wiley & Sons, Inc: New York, 1981. (c) Bube, R. H. *Photoelectronic Properties of Semiconductors*; Cambridge University Press: Cambridge, 1992.

(19) Yoshikawa, H.; Adachi, S. *Jpn. J. Appl. Phys* **1997**, *36*, 6237–6243.

(20) Wang, Z. L. *Mat. Today* **2004**, 26–33.

(21) Kumar, S.; Rajaraman, S.; Gerhardt, R. A.; Wang, Z. L.; Hesketh, P. J. *Electrochim. Acta* **2005**, *51*, 943–951.

(22) Suehiro, J.; Nakagawa, N.; Hidaka, S.; Ueda, M.; Imasaka, K.; Higashihata, M.; Okada, T.; Hara, M. *Nanotechnology* **2006**, *17*, 2567–2573.

(23) This resolution value was taken as a rough approximation to the minimal feature of current lithography techniques.

(24) Zheng, X. G.; Li, Q. Sh.; Zhao, J. P.; Chen, D.; Zhao, B.; Yang, Y. J.; Zhang, L. Ch. *Appl. Surf. Sci.* **2006**, *253*, 2264–2267.

(25) Jie, J. S.; Zhang, W. J.; Jiang, Y.; Meng, X. M.; Li, Y. Q.; Lee, S. T. *Nano Lett.* **2006**, *6*, 1887–1892.

(26) Studenikin, S. A.; Golego, N.; Cocivera, M. *J. Appl. Phys.* **2000**, *87*, 2413–2421.

(27) Lao, C. S.; Park, M. C.; Kuang, Q.; Deng, Y.; Sood, A. K.; Polla, D. L.; Wang, Z. L. *J. Am. Chem. Soc.* **2007**, *129*, 12096–12097.

(28) Chang, P. C.; Chien, C. J.; Stichtenoth, D.; Ronning, C.; Lu, J. G. *Appl. Phys. Lett.* **2007**, *90*, 113101.

(29) Fan, Z. Y.; Wang, D. W.; Chang, P. C.; Tseng, W. Y.; Lu, J. G. *Appl. Phys. Lett.* **2004**, *85*, 5923.

(30) Chang, P. C.; Fan, Z.; Wang, D.; Tseng, W. Y.; Chiou, W. A.; Hong, J.; Lu, J. G. *Chem. Mater.* **2004**, *16*, 5133–5137.

(31) Chang, P.; Fan, Z.; Chien, C.; Stichtenoth, D.; Ronning, C.; Lu, J. G. *Appl. Phys. Lett.* **2006**, *89*, 133113.

(32) Park, W. I.; Kim, J. S.; Yi, G.-C.; Bae, M. H.; Lee, H.-J. *Appl. Phys. Lett.* **2004**, *85*, 5052–5054.

(33) Hong, W.-K.; Kimm, B.-J.; Kim, T.-W.; Jo, G.; Song, S.; Kwon, S.-S.; Yoon, A.; Stach, E. A.; Lee, T. *Colloids Surf. A* **2008**, *313−314*, 378–382.

(34) He, J. H.; Lin, Y. H.; McConney, M. E.; Tsuruk, V. V.; Wang, Z. L.; Bao, G. *J. Appl. Phys.* **2007**, *102*, 084303.

(35) Hu, L.; Chen, G. *Nano Lett.* **2007**, *7*, 3249–3252.

(36) Monroy, E.; Omnes, F.; Calle, F. *Semicond. Sci. Technol.* **2003**, *18*, R33−R51.

(37) Takahashi, Y.; Kanamori, M.; Kondoh, A.; Minoura, H.; Ohya, Y *Jpn. J. Appl. Phys* **1994**, *33*, 6611–6615.

(38) Liu, Y.; Gorla, C. R.; Liang, S.; Emanetoglu, N.; Lu, Y.; Shen, H.; Wraback, M. *J. Electron. Mater.* **2000**, 29.

(39) Basak, D.; Amin, G.; Mallik, B.; Paul, G. K.; Sen, S. K. *J. Cryst. Growth* **2003**, *256*, 73–77.

(40) Liu, M.; Kim, H. K. *Appl. Phys. Lett.* **2004**, *84*, 173–175.

(41) Liu, J.; Xia, Y.; Wang, L.; Su, Q.; Shi, W. *Appl. Surf. Sci.* **2006**, *253*, 5218–5222.

(42) Ohtomo, A.; Tsukazaki, A. *Semicond. Sci. Technol.* **2005**, *20*, S1−S12.

JP804614Q

Supporting Information:

I) Photogeneration theory details: non-uniform absorption and transient solution

ZnO and SnO$_2$ are n-type semiconductors [I, II] due to the donor character of their intrinsic defects [III, IV]. Photo-current I_{ph} generated by incident light can be theoretically modelled with the help of the continuity equation describing the photo-generated excess of minority carriers $\Delta p_{ph}(\vec{r},t)$ in the low injection regime [12]. That is to say,

$$\frac{\partial \Delta p_{ph}}{\partial t} = g_{ph} - \frac{\Delta p_{ph}}{\tau_p} + D_p \nabla^2 \Delta p_{ph} \qquad \text{(i)}$$

where g_{ph} is the pair generation rate per volume unit, τ_p is the hole lifetime and D_p the hole diffusion constant. If the x – axis and z – axis are considered to be parallel and perpendicular to the longitudinal direction of the nanowire (L and T dimensions in figure 1 of the main text) and the illumination is assumed to be uniform and parallel to the z – axis, the following simplifications can be introduced in equation (i),

$$\nabla^2 \Delta p_{ph} = \frac{\partial^2 \Delta p_{ph}}{\partial z^2} \qquad \text{(ii)}$$

$$g_{ph} \equiv g_{ph}(z) \qquad \text{(iii)}$$

$$\Delta p_{ph}(\vec{r},t) = \Delta p_{ph}(z,t) \qquad \text{(iv)}$$

In general, photo-generation across the section of the nanowire will be non – uniform. In this case, $g_{ph}(z)$ is generally described as,

$$g_{ph}(z) = \alpha \, \eta \, \beta \, \Phi_{ph} \, e^{-\alpha z} \qquad \text{(v)}$$

1

where α is the light absorption coefficient of the metal oxide at the incident wavelength, η is the quantum efficiency of pairs generation by one photon, β is the fraction of photons not reflected by the surface and Φ_{ph} is the flux of incident photons. Therefore, the steady excess of minority carriers along z is obtained by solving the following equation,

$$0 = \alpha \, \eta \, \beta \, \Phi_{ph} \, e^{-\alpha z} - \frac{\Delta p_{ph}(z)}{\tau_p} + D_p \frac{\partial^2 \Delta p_{ph}(z)}{\partial z^2} \qquad \text{(vi)}$$

If all excess carriers are extracted at $z = T$ [12], the solution of equation (vi) can be approximated by,

$$\Delta p_{ph}(z) = \frac{\tau_p \, \eta \, \beta \, \Phi_{ph}}{\alpha \, L_p^2} \left[\alpha \, L_p e^{-z/L_p} - e^{-\alpha z} \right] \qquad \text{(vii)}$$

where $L_p \equiv \sqrt{D_p \tau_p}$ is the diffusion length of minority carries. The previous approximation is valid only if $\alpha^2 L_p^2 \gg 1$. In the case of ZnO, α^{-1} of near UV photons (wavelength from *400* to *250 nm*) is almost constant at *50 nm* [13] and L_p is estimated to be above *2 μm* [IV]. Thus, the product $\alpha^2 L_p^2 \sim 1600 \gg 1$ verifies this restriction.

In quasi-neutral conditions, ($\Delta p_{ph}(z) \approx \Delta n_{ph}(z)$), the photo-generated current density j_{ph} along the x-axis at depth z can be expressed as,

$$j_{ph}(z) = q \, \Delta n_{ph}(z) \, v \qquad \text{(viii)}$$

where q is the elemental charge and v the carrier velocity. To obtain the photo-generated current I_{ph} through the section of the nanowire ($W \cdot T$) (see figure 1), the following integral must be evaluated,

$$I_{ph} = \int_{WxT} \overrightarrow{j_{ph}} \cdot \overrightarrow{ds} = W \int_0^T j_{ph}(z) \, dz \qquad \text{(ix)}$$

obtaining,

2

$$I_{ph} = q\,W\,v\,\frac{\tau_p\,\eta\,\beta\,\Phi_{ph}}{\alpha\,L_p^2}\left\{\alpha\,L_p^2\left(e^{-T/L_p}-1\right)-\frac{1}{\alpha}\left(e^{-\alpha T}-1\right)\right\} \qquad (x)$$

If the thickness of the nanowire fulfils,

$$\alpha^{-1} < T < L_p \qquad (xi)$$

and v is expressed as,

$$v - \frac{\mu^* V}{L} \qquad (xii)$$

where μ^* is the electron mobility, V the applied voltage and L is the length of the nanowire, equation (x) becomes,

$$I_{ph} = q\,\frac{W}{L}\,\beta\,\eta\,\tau\,\mu^* V\,\Phi_{ph} \qquad (xiii)$$

This expression is identical to equation 11, which was obtained assuming a constant generation profile until α^{-1}. Therefore, it can be concluded, in first approximation, that the existence of a non – uniform absorption profile would not modify the results presented here.

Let us also analyze the evolution in time of the photo-generated carriers Δp_{ph}. As we have demonstrated, uniform adsorption profile can be assumed without loss of generality. Therefore, equation (i) can be rewritten as

$$\frac{\partial \Delta p_{ph}}{\partial t} = g_{ph} - \frac{\Delta p_{ph}}{\tau_p}\,. \qquad (xiv)$$

The steady solution ($\partial \Delta p_{ph}/\partial t = 0$) of this equation is given by,

$$\Delta p_{ph} = g_{ph}\tau_p \qquad (xv)$$

3

which corresponds to equation 2, if we assume quasi-neutral conditions ($\Delta p_{ph} \approx \Delta n_{ph}$), electron-hole recombination in pairs ($\tau_p = \tau_n = \tau$) and $g_{ph} = \eta \, F / V_{ph}$, where η is the quantum efficiency of pairs generation by one photon, F the absorption rate of photons, and V_{ph} the photo-generation volume.

If the light is turned on at $t = 0$ and $\Delta p_{ph}(0) \approx \Delta n_{ph}(0) = 0$, the transient solution of equation (xiv) is,

$$\Delta n_{ph}(t) = g_{ph}\tau_p \left(1 - e^{-t/\tau_p} \right)$$
(xvi)

Since $i_{ph}(t)$ is proportional to $\Delta n_{ph}(t)$, an exponential raise of $i_{ph}(t)$ is predicted by turning on the light source before reaching the steady state (equation xv). On the other hand, if the light is turned off at $t = 0$, the transient solution of equation xiv is,

$$\Delta n_{ph}(t) = g_{ph}\tau_p \, e^{-t/\tau}$$
(xvii)

assuming a complete extinction of the charge excess long time after turning off the light: $\Delta p_{ph}(t\to\infty) \approx \Delta n_{ph}(t\to\infty) = 0$. Now, $i_{ph}(t)$ relaxes exponentially when turning off the light source as proposed in equation 4.

The time scale of these two processes are determined by the lifetime τ, which can be estimated from time resolved measurements of I_{ph}. This is the procedure we followed in this work. Lifetime τ may differ in raise and decay processes due to charge separation and trapping effects [12].

References:

[I] Özgür, Ü.; Alivov, Y. I.; Liu, C.; Teke, A.; Reshchikov, M. A.; Doğan, S.; Avrutin, V.; Cho, S. J.; Morkoç, H. *J. Appl. Phys.* **2005**, *98*, 041301.

[II] Batzill, M.; Diebold, U. *Prog. Surf. Sci.* **2005**, *79*, 47–154.

[III] Erhart, P.; Klein, A.; Albe, K. *Phys. Rev. B* **2005**, *72*, 085213.

4

[IV] Kiliç, C.; Zunger, A. *Phys. Rev. Lett.* **2002**, *88*, 095501.

[IV] Lopatiuk-Tirpak, O.; Chernyak, L.; Xiu, F. X.; Liu, J. L.; Jang, S.; Ren, F.; Pearton, S. J.; Gartsman, K.; Feldman, Y.; Osinsky A.; Chow, P. *J. Appl. Phys.* **2006**, *100*, 086101.

5

II) Self – heating effects on nanowires:

Dissipated power P in nanowires increases their temperature T due to Joule heating effect, as described by the authors elsewhere [14]. If individual nanowires are used as photodetectors, one critical parameter to preserve their integrity is the current I [19]. It was experimentally demonstrated that high power UV pulses dramatically increase photocurrent I_{ph} (figure I), leading to an irreversible degradation of these devices by melting (figure II).
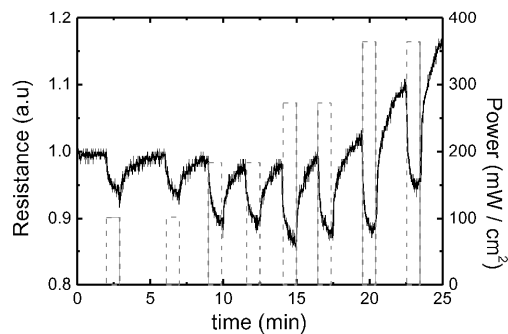
Figure I. Photoresponse of a SnO_2 nanowire [11] as function of fast UV pulses. The UV lamp was used in this experiment. It can be observed how the nanowire does not recover the resistance baseline with increasing UV intensity. (Dashed lines indicate UV pulses).
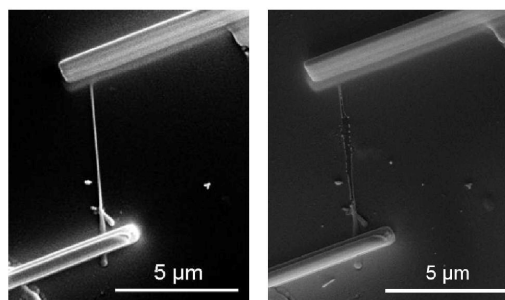
Figure II. SnO_2 nanowire before (left) and after (right) applying a UV light pulse of P = 365 mW/cm^2. The nanowire is completely destroyed after the measurement due to self-heating effects.

6

J.D. Prades, F. Hernandez-Ramirez, R. Jimenez-Diaz, M. Manzanares, T. Andreu, A. Cirera, A. Romano-Rodriguez, J.R. Morante,
"The effects of electron-hole separation on the photoconductivity of individual metal oxide nanowires",
Nanotechnol. **19**, 465501 (2008).

10

The effects of electron–hole separation on the photoconductivity of individual metal oxide nanowires

J D Prades[1,3]**, F Hernandez-Ramirez**[1,2,3]**, R Jimenez-Diaz**[1]**,
M Manzanares**[1]**, T Andreu**[1]**, A Cirera**[1]**, A Romano-Rodriguez**[1] **and
J R Morante**[1]

[1] EME/XaRMAE/IN[2]UB, Departament d'Electrònica, Universitat de Barcelona,
C/ Martí i Franquès 1, E-08028 Barcelona, Spain
[2] Electronic Nanosystems S L, Barcelona, Spain

E-mail: dprades@el.ub.es and info@e-nanos.com

Abstract
The responses of individual ZnO nanowires to UV light demonstrate that the persistent
photoconductivity (PPC) state is directly related to the electron–hole separation near the
surface. Our results demonstrate that the electrical transport in these nanomaterials is influenced
by the surface in two different ways. On the one hand, the effective mobility and the density of
free carriers are determined by recombination mechanisms assisted by the oxidizing molecules
in air. This phenomenon can also be blocked by surface passivation. On the other hand, the
surface built-in potential separates the photogenerated electron–hole pairs and accumulates
holes at the surface. After illumination, the charge separation makes the electron–hole
recombination difficult and originates PPC. This effect is quickly reverted after increasing either
the probing current (self-heating by Joule dissipation) or the oxygen content in air (favouring
the surface recombination mechanisms). The model for PPC in individual nanowires presented
here illustrates the intrinsic potential of metal oxide nanowires to develop optoelectronic
devices or optochemical sensors with better and new performances.

Ⓢ Supplementary data are available from stacks.iop.org/Nano/19/465501

(Some figures in this article are in colour only in the electronic version)

1. Introduction

Methods for the synthesis of nanomaterials have undergone a huge improvement in recent years [1, 2], providing researchers with nanowires with high surface-to-volume ratio and excellent crystalline properties [3, 4]. Their electrical characterization is a direct way to gain a deep comprehension of some of the phenomena typical of the nanoscale, which originate due to the overexposure of the bulk of nanomaterials to surface effects [5–7]. To date, a large majority of works have focused on the study of nanowire bundles [8], but uncontrolled parasitic effects between nanowires has made obtaining any conclusive result difficult [9]. The constant improvement of nanofabrication techniques is slowly changing

this situation, enabling the appearance of many works dealing with individual nanowires, whose electrical characterization is extremely helpful in evaluating transport phenomena in single-crystal structures [10].

Among nanowires, metal oxide ones are excellent candidates for evaluating the influence of surface effects on the bulk properties of nanomaterials, since they are highly reactive to their surrounding atmosphere [11]. This property has attracted an increasing interest in integrating them as building blocks of new nanodevices, such as gas sensors or optoelectronic devices [6, 7]. Zinc oxide (ZnO) nanowires are versatile metal oxide nanomaterials which have been successfully tested in different fields [12], such as chemical [3] and biological sensing [13], optoelectronics [6, 7], energy harvesting [14], and ultraviolet (UV) photodetection [15–19].

---

[3] Authors to whom any correspondence should be addressed.

                                    1

Chapter 4

J D Prades *et al*

In this last case, they even exhibit higher photoconductive gains [18, 19] than equivalent devices based on thin film technologies [20].

The effects of UV light on ZnO are more complex than a simple band-to-band photoresponse [15–19], since a persistent increase of the electrical conductivity is often induced which lasts for a long time after the exposure to UV [21–30] and requires a post-treatment of the sample to recover the initial value. The origin of this persistent photoconductivity (PPC) phenomenon is still controversial. On the one hand, some authors relate PPC to either intrinsic or extrinsic point defects which exhibit metastable charge states [21–23]. On the other hand, others claim that the origin is the electron–hole separation related to the surface properties of metal oxides [24–27, 29, 30]. Thus, a widely accepted description has not yet been presented [23].

In this paper, the strong influence of surface effects on the transport phenomena of nanomaterials has been used to evaluate the PPC effect in individual ZnO nanowires and demonstrate its surface origin. Unlike previous works, here, the use of a single nanowire has allowed us to exclude other influences and experimentally simplify the analysis. We have studied the influence of the surface recombination mechanisms on PPC via the effective mobility and the density of free carriers. Moreover, the PPC recovery at different working conditions (probing currents and atmospheres) has also been studied in detail. Based on these results, a model for PPC in a single nanowire is presented, and different strategies to minimize or even block the PPC in ZnO are outlined, enabling the design of nanowire-based photodetectors free of this undesirable effect.

2. Experimental details

ZnO nanowires [3] (see supporting information available at stacks.iop.org/Nano/19/465501) were dispersed in propylene glycol and deposited onto an insulating SiO_2 chip with pre-patterned Au/Ti/Ni microelectrodes. Then, some of them were electrically contacted to the microelectrodes in four-probe configuration with an FEI Dual-Beam Strata 235 focused ion beam (FIB) machine equipped with a metal–organic precursor to deposit Pt strips (figure 1) [31], following a methodology designed to minimize structural modification during the fabrication process [9]. The electrical response of the final devices was evaluated inside a home-made chamber specially designed to illuminate the sample at the same time then different atmospheres were applied with the help of gas mass-flow controllers. The light power impinging on this sample (λ_{ph} = 340 ± 10 nm)[4] was estimated with a photodiode located beside it[5]. A home-made electronic circuit designed to guarantee that low current

[4] The ZnO nanowires were synthesized with a commercial Atomate's CVD system. The source material was a 1:1 molar mixture of ZnO (metal basis 99.99%) and graphite powder provided by Alfa Aesar. Crystalline nanowires with average radii $\langle r_{NW} \rangle$ = 90 ± 15 nm and lengths up to L_{NW} = 30 μm were obtained [3]. High-resolution TEM images showed well-faceted single-crystalline nanowires with dislocation-free bodies grown along the [0001] direction (see supporting information available at stacks.iop.org/Nano/19/465501).
[5] Seoul Optodevices model T9F34C.
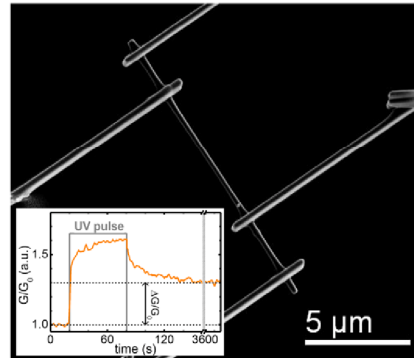
Figure 1. ZnO nanowire of length L_{NW} = 13 μm and radius r_{NW} ∼ 95 nm electrically contacted with FIB nanolithography techniques. The inset shows evidence of PPC in these nanowires: the conductance baseline was not fully recovered after switching off the light.

levels I_m (from 0.1 to 250 nA) were applied during the experiments was used [32], and parasitic effects of the metal-nanowire contacts were avoided by performing four-probe DC measurements [10] (see supporting information available at stacks.iop.org/Nano/19/465501). Fifteen of these devices exhibited stable characteristics without any noticeable degradation after three weeks of continuous operation. All the experiments were performed in either synthetic air (SA) or nitrogen (N_2). Finally, some of them were passivated with a 470 nm thick PMMA layer deposited by spin coating. This layer was UV transparent and electrically insulating (see supporting information available at stacks.iop.org/Nano/19/465501).

3. Experimental results and discussion

3.1. Evidence of PPC in individual ZnO nanowires

Non-illuminated ZnO nanowires (length L_{NW} = 13 μm and radius r_{NW} ∼ 95 nm) in oxygen-rich atmospheres exhibited conductance values of $G_{0(SA)}$ = 59 ± 6 nS, which are in agreement with reported data [15–19] (see supporting information available at stacks.iop.org/Nano/19/465501). No significant photoresponse was observed with impinging photons with energies $h\nu$ below the bandgap of ZnO (E_{gap} = 3.37 eV [33]) (see supporting information available at stacks.iop.org/Nano/19/465501). In contrast, photons with higher energies led to an important increase of the electrical conductance of the nanowires. This result confirms that photoconduction in ZnO nanowires is mainly originated by band-to-band electron–hole pair generation in their bulk. Dynamic measurements showed that the conductance baseline was not fully recovered after switching off the light, demonstrating the existence of PPC in these nanomaterials (see the inset in figure 1).

2

J. D. Prades
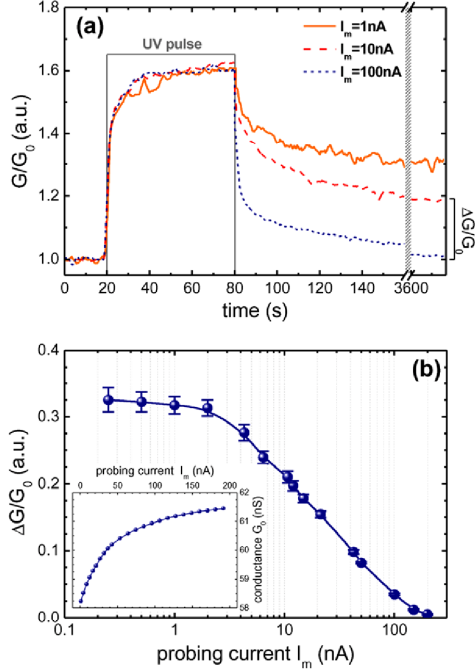
Figure 2. (a) Relative conductance change (G/G_0) of a ZnO nanowire under illumination (60 s UV pulse, photon flux $\Phi_{ph} = 3.3 \times 10^{18}$ m^{-2} s^{-1}, wavelength $\lambda_{ph} = 340 \pm 10$ nm) acquired at three different current levels (I_m) in synthetic air. The axis break shows the conductance 1 h later. (b) Dependence of the PPC with the probing current I_m in synthetic air. The magnitude of the PPC ($\Delta G/G_0$) was determined as described in the text. The PPC values and error bars shown in the figure are the mean and the standard deviation of the results obtained with ten different samples. The dependence of the conductance in the dark (G_0) with the probing current is shown in the inset. The conductance rise demonstrates the self-heating of the nanowires during the measurement, in accordance with the semiconductor character of ZnO.

3.2. Influence of the probing current on PPC

It was experimentally found that the intensity of PPC is directly related to the probing current (I_m) applied to the nanowires (figure 2). The recovery of the conductance G of a ZnO nanowire after a 60 s UV pulse at different I_m is shown in figure 2(a). Here, the relative persistence of the conductance was defined as

$$\frac{\Delta G}{G_0} = \frac{G_{1\,h} - G_0}{G_0} \tag{1}$$

where G_0 was the initial value in darkness and $G_{1\,h}$ the value 1 h after the pulse.

The PPC effect fully disappeared 1 h after illuminating the sample with $I_m > 100$ nA. In contrast, the PPC did not vanish with lower I_m, reaching a maximum with $I_m < 1$ nA (figure 2(b)). These two different behaviours are an indirect proof of the well-known dependence of PPC on temperature [21, 25, 26, 34], since nanodevices reach high temperatures due to the dissipated electrical power when they
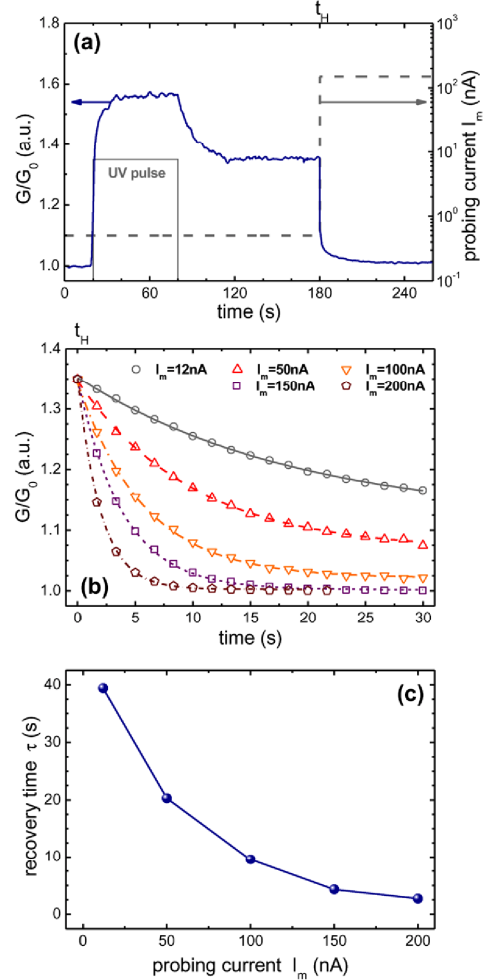
Figure 3. Recovery of the PPC stimulated by high probing current values. (a) G/G_0 record. A 60 s UV pulse was applied to a ZnO nanowire in low-current conditions ($I_m = 0.5$ nA). After the stabilization of the PPC (at t_H), the conductance recovery was stimulated by increasing the probing current ($I_m = 150$ nA). (b) Analysis of the recovery transients for different I_m. The experimental data points were fitted to exponential decay laws (lines) to estimate the recovery time constants τ. (c) The PPC recovery time constant τ as function of the probing current I_m.

come into operation. To validate this assumption, the recovery of G in a ZnO nanowire showing PPC was stimulated with a sudden increase of I_m from 0.5 to 150 nA (figure 3(a)). Transient responses in good correspondence with exponential decays were found in all the experiments (figure 3(b)). The higher the probing current I_m that was applied to the nanodevices, the faster the recovery time that was observed (figure 3(c)). Equivalent responses were monitored in SA and N$_2$. Thus, the modulation of I_m is proposed as a simple and

3

fast methodology to control PPC, despite it not shedding any light on the origin of PPC in ZnO. It goes without saying that an accurate estimation of the temperature reached by the nanowire due to Joule self-heating would provide valuable information about the activation energies of the states related to PPC, but this point remains a complex experimental issue [35].

3.3. On the origin of PPC in ZnO nanowires

There are two opposite models which describe PPC in ZnO. The first claims that this phenomenon is related to metastable bulk defects located between shallow and deep energy levels [21–23]. According to this assumption, oxygen vacancies can be excited to a metastable charged state after a structural relaxation. In these states, the recapture of electrons is prevented by a thermally activated barrier [21]. The second maintains that PPC is a pure surface effect related to the capture of electrons by surface states [26, 27, 29], which arise with the generation of oxygen vacancies by UV light [24, 26, 30]. This process is also reverted by temperature-assisted adsorption of oxygen species [26–28]. In these two theoretical approaches, if electron–hole pairs are spatially separated, their recombination rate is significantly reduced, giving rise to PPC.

3.3.1. Evaluation of surface effects in PPC. To clarify the origin of PPC, individual ZnO nanowires were used to take advantage of the overexposure of their bulk to surface effects. $I_m = 1$ nA was always applied, and the experiments were systematically repeated in both SA and N_2 (with 50 ppm of residual O_2). Conductance modulation curves were represented in terms of $\{(G/G_0) - 1\}$ to facilitate the comparison of the different recovery transients.

In figure 4(a), G_0 of a ZnO nanowire was respectively $G_{0(SA)} = 59 \pm 6$ nS and $G_{0(N_2)} = 110 \pm 10$ nS in SA and N_2. UV illumination gave rise to photoresponses 4.2 times higher in N_2 than in SA. Equivalent responses were monitored with the rest of nanowires, confirming that surface interaction mechanisms dominate the UV photoresponse and PPC. To decouple the bulk and surface phenomena, some of the nanowires were passivated with PMMA. Previous works proposed that coating ZnO with polymers not only prevents the interaction of its surface with gases, but it also passivates the electron states of metal oxides associated to dangling bonds located at the surface [19, 36–38]. The conductance in darkness of the coated sample ($G_{0(PMMA)} = 1400 \pm 120$ nS) was 24 times higher than in SA ($G_{0(SA)} = 59 \pm 6$ nS), whereas the photoresponse was found to increase 12 times in comparison to the response in SA.

3.3.2. Modelling PPC in ZnO nanowires. The electrical properties of metal oxide nanowires are strongly influenced by the environment. In general, oxygen molecules in air absorb onto their surface, trapping conduction electrons from the bulk [39]. This process leads to the appearance of a negative charge distribution fixed at the surface, which is generally described with an upward band-bending [39]. In the
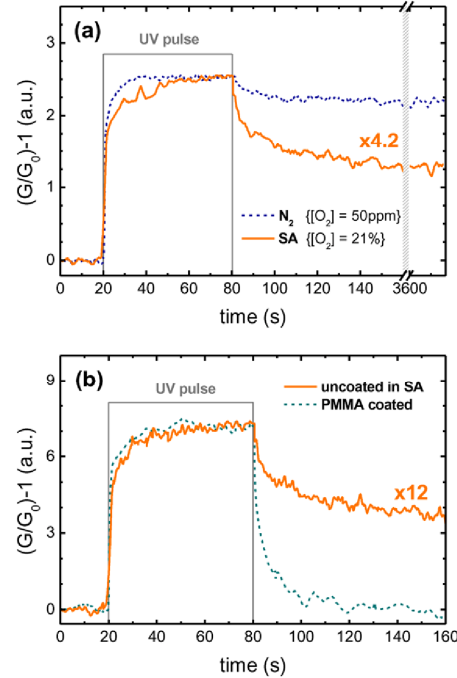
Figure 4. Relative conductance $\{(G/G_0) - 1\}$ of a ZnO nanowire with a 60 s UV pulse (photon flux $\Phi_{ph} = 3.3 \times 10^{18}$ m^{-2} s^{-1}, wavelength $\lambda_{ph} = 340 \pm 10$ nm) acquired at low probing current conditions ($I_m = 1$ nA). Solid-orange plots were rescaled (multiplying the data by ×4.2 and ×12, respectively) to ease the comparison of the recovery processes. (a) Two different atmospheres were used: synthetic air (SA) and nitrogen (N_2). The oxygen concentration was $[O_2]_{SA} = 210\,000$ ppm and $[O_2]_{N2} = 50$ ppm, respectively. The response to the UV pulse in N_2 was 4.2 times larger than in SA. (b) Relative conductance $\{(G/G_0) - 1\}$ of a ZnO nanowire with the same UV pulse before and after coating the nanostructure with PMMA. Response to the UV pulse after coating was 12 times larger than before.

steady state, this phenomenon reduces the effective conduction channel along the nanowires and modulates G as [40, 41]

$$G = |e| n_0 \mu \frac{\pi (r_{NW} - \lambda)^2}{L_{NW}} \qquad (2)$$

where G is the conductance of a nanowire of radius r_{NW} and length L_{NW}, e the fundamental charge, n_0 the concentration of free carriers, μ their electrical mobility, and λ the width of the depletion layer, which depends on the chemisorbed species.

In oxygen-rich atmospheres, λ grows, and thus lower electrical conductance is observed. In contrast, thinner λ occurs with low pressure oxygen atmospheres and higher conductance values are obtained [40]. This prediction is in agreement with our experimental data:

$$G_{0(PMMA)} = 1400\,\text{nS} \gg G_{0(N_2)} = 110\,\text{nS} > G_{0(SA)} = 59\,\text{nS}. \qquad (3)$$

4

The λ value in SA for ZnO nanowires can be estimated by solving the Poisson equation [41],

$$V_b = \frac{|e|n_0}{4\varepsilon_0\varepsilon_r}[(2r_{NW}^2 - \lambda^2) - 2(r_{NW} - \lambda)^2$$
$$\times \log(r_{NW}/(r_{NW} - \lambda))]. \qquad (4)$$

For $r_{NW} \sim 95$ nm, $\lambda \approx 35$ nm was found, considering a typical barrier of $V_b \sim 0.55$ eV [41], $n_0 = 4 \times 10^{17}$ cm^{-1} [10] (see supporting information available at stacks.iop.org/Nano/19/465501), and the relative dielectric constant of ZnO ($\varepsilon_r = 8.65$ [42]). This λ value is also in good correspondence with the literature value [41].

In fact, this simple model explains the modulation of G in N$_2$ and SA (up to a factor 2.5)[6], but it fails with the huge change observed in PMMA-coated samples (a factor of 12). In this case, the contribution of the electrical mobility must be taken into account as well, since high mobility values have been reported in coated nanowires due to the reduction of electron scattering at their surfaces [19, 36–38]. Following a methodology explained in detail elsewhere [10] (see supporting information available at stacks.iop.org/Nano/19/465501), the electrical mobility of both coated and uncoated ZnO nanowires in SA was estimated ($\mu_{(SA)} = 5 \pm 2$ cm^2 V^{-1} s^{-1} and $\mu_{(PMMA)} = 53 \pm 8$ cm^2 V^{-1} s^{-1}). This difference (a factor of 10) explains the variation of G between the two experiments (see equations (2) and (3)).

Under illumination, UV photons generate electron–hole pairs in the bulk of the nanowires. After a few seconds, the photoresponse (ΔG_{ph}) reaches a steady state in which the recombination and the generation rates are equal (figures 5(a) and (b)). Thus, the excess numbers of n and p carriers (Δn and Δp) is given by [43]

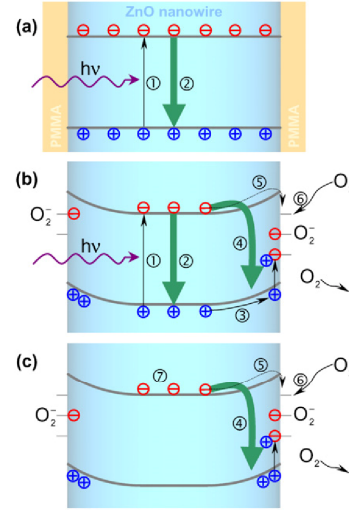$$\Delta G_{ph} \propto \Delta n = \Delta p = g\tau \qquad (5)$$

where g is the photogeneration rate of carriers per volume unit and τ their mean lifetime. If the number of recombination mechanisms is large, τ can be roughly estimated with the help of Mathiessen's rule [43],

$$\frac{1}{\tau} = \sum_j \frac{1}{\tau_j}. \qquad (6)$$

Some authors claim the existence of two different mechanisms which steer the photoresponse in metal oxides [28, 29, 44]. The former one is a fast band-to-band recombination in their bulk with characteristic times in the nanosecond range (figure 5(a)) [13]. The latter, which becomes dominant in nanosized materials[7], is highly dependent on the existence of chemisorbed oxygen molecules at their surfaces, since

Figure 5. (a) Flat-band situation. When the material is illuminated with above-bandgap photons the ① *photogeneration of electron–hole pairs* equals the ② *band-to-band recombination mechanism*, reaching steady conductance values. This case corresponds to the bulk material and also to the nanowires passivated with PMMA. (b) If band-bending near the surface is considered, an additional mechanism appears due to charge separation by this built-in potential: ③ *holes tend to accumulate near the surface* and recombine with electrons in an ④ *oxygen-assisted surface recombination mechanism*. ⑤ *Temperature* and ⑥ *adsorption of oxygen* by electron capture facilitates the access of the electrons to the surface. (c) When the illumination is switched off, the bulk-like recombination mechanism rapidly extinguishes holes in the inner part of the nanowire. The remaining unpaired electrons are responsible for the ⑦ *persistent photoconductivity situation*, which can only be reverted by favouring the ⑧ *oxygen-assisted surface mechanism*.

holes discharge oxygen species from the surface by indirect electron–hole recombination mechanisms (figure 5(a)) [44]. Thus, equation (5) can be rewritten as

$$\Delta G_{ph} \propto \Delta n = \Delta p = \frac{g}{1/\tau_{bulk} + 1/\tau_{surf}} \qquad (7)$$

where τ_{bulk} and τ_{surf} are the lifetimes of the photocarriers recombined in the bulk and at the surface. In oxygen-rich environments, surface recombination is favoured and lower ΔG_{ph} values are produced. In contrast, this mechanism is blocked in coated samples, explaining the experimental trend of measured photoresponses (figure 4),

$$\Delta G_{ph(PMMA)} > \Delta G_{ph(N_2)} > \Delta G_{ph(SA)}. \qquad (8)$$

When the light is switched off, the two recombination mechanisms swiftly contribute to recover the initial carrier concentration in the nanowires. Nevertheless, the built-in potential near the surface caused by oxygen adsorption separates the photogenerated pairs: holes accumulate at the outer shell of the nanowire and electrons remain together in the inner part. This photogenerated effect prevents the

---

[6] According to equation (2), the maximum conductance (G_{MAX}) of the nanowire corresponds to the case of a null depleted layer ($\lambda = 0$). The formation of a depleted layer of thickness λ results in a decrease of the conductivity (G_{min}). The change in the conductivity due to the formation of this depleted layer is thus $G_{MAX}/G_{min} = (r_{NW})^2/(r_{NW} - \lambda)^2$. In our case, $r_{NW} = 95$ nm, $\lambda = 35$ nm and $G_{MAX}/G_{min} = 2.5$.

[7] The contribution of surface mechanisms is especially important in the case of nanowires because their diameters are significantly lower than the diffusion length of carriers in ZnO ($L_{ZnO} \sim 1~\mu$m) [33].

5

recombination of a fraction of the pairs, whereby PPC is observed after the UV pulse (figure 5(c)). Thereby $\Delta G/G_0$ will strongly depend on the oxygen content in air. That is to say, the higher this experimental parameter is the more efficient recombination through the surface is, and the less important the PPC becomes (figure 4(a)). In the particular case of PMMA-coated samples, nanowires approach the so-called flat-band conditions[8] and thus, no charge separation takes place, favouring a complete recovery of the conductance baseline in the dark (figure 4(b)).

If the temperature increases, carriers gain thermal energy and they can easily overcome the built-in potential. In this case, PPC is not observed (figure 2).

According to first-principles calculations, oxygen in air (O_2) undergoes a dissociative chemisorption at the surface oxygen vacant (VO) sites in ZnO non-polar surfaces [45, 46], by filling the VO with one O atom originating from the adsorbate. This dissociation of O_2 is exothermic and barrierless, and may even occur spontaneously at room temperature. This result suggests that VO sites are the surface sites at which oxygen-assisted recombination of electrons and holes take place. From the point of view of the electron states, we demonstrated that VO sites are associated to surface states with energy 0.5 eV above the valence-band edge [47].

The model proposed here only assumes the existence of a built-in potential to justify the charge pair separation and hole accumulation near the surface of the material. Since this feature is common to other metal oxides, the model can be easily extended to other materials with similar PPC effects [48]. This model does not take into account the large number of bulk charge states located within the band gap of ZnO [33] with a strong influence in many applications, such as gas sensing [33]. Other simplifications that may limit the model are those related to the flat-band approximation in coated samples. These simplifications may prevent the explanation of the few-seconds kinetics to reach the steady state, which is experimentally observed even when the samples are coated with PMMA.

4. Conclusions

The study of persistent photoconductivity (PPC) in individual ZnO nanowires demonstrated that the electrical transport properties in these nanomaterials are determined by the surface in two different ways. On the one hand, the effective mobility and the available free carriers (μ and n_o) are controlled by the surface recombination mechanisms assisted by the oxidizing molecules in air. On the other hand, the photoconductance G is modified by the changes in the size of the depletion layer (λ).

In particular, PPC essentially depends on the built-in surface potential originated by the surface charges. Under UV illumination, this built-in potential induces electron–hole separation, and hole accumulation at the surface. Once the light is switched off, the accumulated charges need recombination

paths to be drained, and PPC appears if these paths are not available.

It is experimentally observed that PPC recovery times are linked with the availability of recombination paths. We observed that PPC was quickly reverted after increasing either the probing current (self-heating by Joule dissipation) or the oxygen content in air (favouring the surface recombination mechanisms). These experimental results and the proposed model helped us to elucidate the origin of the PPC in nanostructures. Thus, PPC can be completely blocked by heating the final devices or passivating their surfaces. It is noteworthy that PMMA coatings totally blocked the PPC, overcoming one of the main limitations of integrating ZnO and other metal oxides in a new generation of optoelectronic nanodevices.

Acknowledgments

References

[1] Fan H J, Werner P and Zacharias M 2006 *Small* **2** 700–17
[2] Law M, Goldberger J and Yang P 2004 *Annu. Rev. Mater. Res.* **34** 83–122
[3] Wang Z L 2004 *J. Phys.: Condens. Matter* **16** R829–58
[4] Mathur S, Barth S, Shen H, Pyun J-C and Werner U 2005 *Small* **1** 713–7
    Mathur S and Barth S 2007 *Small* **3** 2070–5
[5] Chang P-C, Chien C-J, Stichtenoth D, Ronning C and Lu J G 2007 *Appl. Phys. Lett.* **90** 113101
[6] Lieber C M and Wang Z L 2007 *MRS Bull.* **32** 99–104
[7] Patolsky F, Timko B P, Zheng G and Lieber C M 2007 *MRS Bull.* **32** 142–9
[8] Yang M-R, Chu S-Y and Chang R-C 2007 *Sensors Actuators* B **122** 269–73
[9] Hernandez-Ramirez F *et al* 2006 *Nanotechnology* **17** 5577–83
[10] Hernandez-Ramirez F, Tarancon A, Casals O, Pellicer E, Rodriguez J, Romano-Rodriguez A, Morante J R, Barth S and Mathur S 2007 *Phys. Rev.* B **76** 085429
[11] Law M, Kind H, Messer B, Kim F and Yang P D 2002 *Angew. Chem. Int. Edn* **41** 2405–8
[12] Heo Y W, Norton D P, Tien L C, Kwon Y, Kang B S, Ren F, Pearton S J and LaRoche J R 2004 *Mater. Sci. Eng.* R **47** 1–47
[13] Wang J X, Sun X W, Wei A, Lei Y, Cai X P, Li C M and Dong Z L 2006 *Appl. Phys. Lett.* **88** 233106
[14] Wang Z L and Song J H 2006 *Science* **312** 242–6
[15] Kind H, Yan H, Messer B, Law M and Yang P 2002 *Adv. Mater.* **14** 158–60
[16] Fan Z Y, Chang P C, Lu J G, Walter E C, Penner R M, Lin C H and Lee H P 2004 *Appl. Phys. Lett.* **85** 6128–30
[17] Law J B K and Thong J T L 2006 *Appl. Phys. Lett.* **88** 133114
[18] Soci C, Zhang A, Xiang B, Dayeh S A, Aplin D P R, Park J, Bao X Y, Lo Y H and Wang D 2007 *Nano Lett.* **7** 1003–9
[19] Prades J D, Jimenez-Diaz R, Hernandez-Ramirez F, Fernandez-Romero L, Andreu T, Cirera A, Romano-Rodriguez A, Cornet A, Morante J R, Barth S and Mathur S 2008 *J. Phys. Chem.* C **112** 14639

8 Surface passivation implies that there are no gas molecules chemisorbed onto the ZnO surface [19, 36–38]. In this situation, no charge is trapped at the nanowire's surface and no band-bending occurs. This obviously is a drastic approximation.

6

J D Prades *et al*

[20] Liu Y, Gorla C R, Liang S, Emanetoglu N, Lu Y, Shen H and Wraback M J 2000 *J. Electron. Mater.* **29** 69–74

[21] Lany S and Zunger A 2005 *Phys. Rev.* B **72** 035215

[22] Janotti A and Van de Walle C G 2005 *Appl. Phys. Lett.* **87** 122102

[23] Nayak J, Kasuya J, Watanabe A and Nozaki S 2008 *J. Phys.: Condens. Matter* **20** 195222

[24] Melnick D A 1957 *J. Chem. Phys.* **26** 1136–46

[25] Sheinkman M K and Shik A Y 1976 *Sov. Phys.—Semicond.* **10** 128–48

[26] Studenikin S A, Golego N and Cocivera M 2000 *J. Appl. Phys.* **87** 2413–21

[27] Sharma P, Sreenivas K and Rao K V 2003 *J. Appl. Phys.* **93** 3963–70

[28] Li Q H, Gao T, Wang Y G and Wang T H 2006 *Appl. Phys. Lett.* **86** 123117

[29] Reemts J and Kittel A 2007 *J. Appl. Phys.* **101** 013709

[30] Claflin B, Look D C and Norton D R 2007 *J. Electron. Mater.* **36** 442–5

[31] Hernandez-Ramirez F, Rodriguez J, Casals O, Russinyol E, Vila A, Romano-Rodriguez A, Morante J R and Abid M 2006 *Sensors Actuators* B **118** 198–203

[32] Hernandez-Ramirez F *et al* 2007 *Nanotechnology* **18** 495501

[33] Özgür Ü, Alivov Ya I, Liu C, Teke A, Reshchikov M A, Doğan S, Avrutin V, Cho S-J and Morkoç H 2005 *J. Appl. Phys.* **98** 041301

[34] Look D C 1983 *Semicond. Semimet.* **19** 75–170

[35] Prades J D, Jimenez-Diaz R, Hernandez-Ramirez F, Barth S, Cirera A, Romano-Rodriguez A, Mathur S and Morante J R 2008 *Appl. Phys. Lett.* **93** 123110

[36] Park W I, Kim J S, Yi G-C, Bae M H and Lee H J 2004 *Appl. Phys. Lett.* **85** 5052–4

[37] He J H, Lin Y H, McConney M E, Tsukruk V V, Wang Z L and Bao G 2007 *J. Appl. Phys.* **102** 084303

[38] Hong W K *et al* 2008 *Nano Lett.* **8** 950–6
Hong W K, Kim B-J, Kim T-W, Jo G, Song S, Kwon S-S, Yoon A, Stach E A and Lee T 2008 *Colloids Surf.* A **313/314** 378–82

[39] Arnold M S, Avouris P, Pan Z W and Wang Z L 2003 *J. Phys. Chem.* B **107** 659–63

[40] Hernandez-Ramirez F, Prades J D, Tarancon T, Barth S, Casals O, Jimenez-Diaz R, Pellicer E, Rodriguez J, Morante J R, Juli M A, Mathur S and Romano-Rodriguez A 2008 *Adv. Funct. Mater.* **18** 1

[41] Comini E, Guidi V, Malagu C, Martinelli G, Pan Z, Sberveglieri G and Wang Z L 2004 *J. Phys. Chem.* **108** 1882–87

[42] Bhargava B 1997 *Properties of Wide Bandgap II–VI Semiconductors* (London: Inspec)

[43] Sze S M 1981 *Physics of Semiconductor Devices* (New York: Wiley)

[44] Lin Y, Wang D, Zhao Q, Li Z, Ma Y and Yang M 2006 *Nanotechnology* **17** 2110–5

[45] An W, Wu X and Zeng X C 2008 *J. Phys. Chem.* C **112** 5747–55

[46] Yan Y and Al-Jassim M M 2005 *Phys. Rev.* B **72** 235406

[47] Prades J D, Cirera A, Morante J R and Cornet A 2007 *Thin Solid Films* **515** 8670–3

[48] Geraldo V, Scalvi L V A, Morais E A, Santilli C V, Miranda P B and Pereira T J 2005 *J. Eur. Ceram. Soc.* **25** 2825–8

7

Charge separation effects in the photoconductivity of individual MOX nanowires   12

A. Supporting information

A.1 Synthesis, morphology and structure of the ZnO nanowires
ZnO nanowires were fabricated via a vapor-phase carbothermal transport process inside an Atomate's chemical vapour deposition (CVD) system. The source material was a 1:1 molar mixture of commercial ZnO (metal basis, 99.99%) and graphite powder (crystalline, 300 mesh, 99%) from Alfa Aesar. Gold nanoparticles were used as catalytic islands on amorphous alumina substrates. Uniform and crystalline nanowires were obtained with mean radius $<r_{NW}> = 90\pm15$ nm and lengths up to L = 30 μm (Figure I). High resolution TEM images showed well-faceted single crystalline nanowires with dislocation free bodies grown along the [0001] direction (Figure II).
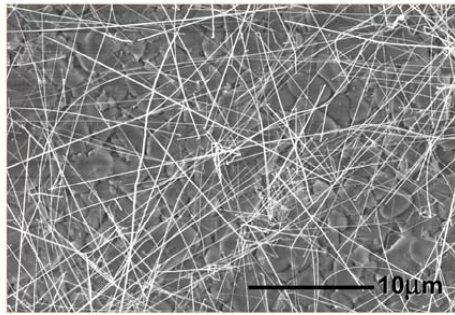
Figure I. SEM micrograph of the as grown ZnO nanowires. Nanostructures with mean radius r_{NW} = 90±15 nm and lengths up to 30 μm were obtained.
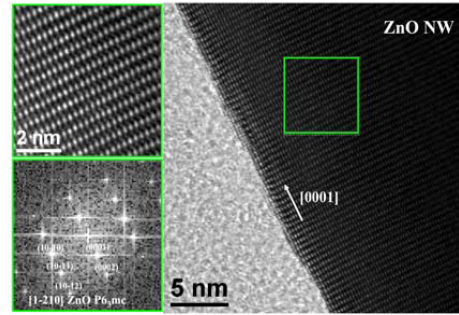
Figure II. HRTEM analysis of a ZnO nanowire. Crystalline and dislocation-free ZnO grow along the [0001] direction. Surface roughness is less than 3 monolayers. *Thanks are due to Dr. J. Arbiol.*

A.2 Electrical I(V) characteristics
The nanowires' I(V) characteristics measured in 2 and 4–probe configurations are shown in figure III. In the 2–probe case, we observed a symmetric non-linear characteristic corresponding to two back-to-back Schottky diodes in series with the resistance of the nanowire (1/G). The conduction through the metal-semiconductor (Pt/ZnO) junction is properly described by thermoionic emission and interface states assisted tunnelling (TE+TuSA) [a,b]. According to this model, the voltage drop across the hole structure in 2–probe configuration ($V_{(2-p)}$) is [a,b]

$$V_{(2-p)} = V_{diode} + V_{NW} = \left(\frac{ln\,I - \beta}{\alpha(n)}\right)^4 + \frac{I}{G(n,\mu)} \qquad (i)$$

where I is the current, G is the conductance of the nanowire and α and β are parameters of the TE+TuSA model for the voltage drop at the reverse biased diode (V_{diode}). It is noteworthy that α and G are analytic functions dependent on the free carriers concentration n and the mobility μ. Thus, fitting the experimental curve to equation (i) it is possible to estimate G and also decouple n and μ. A detailed explanation of this procedure can be found elsewhere [a]. In dark ($_0$) and synthetic air (SA), the conductance of our nanowires was $G_{0(SA)} = 60 \pm 8$ nS and the correspondent carrier concentration and mobility were $\mu_{(SA)} = 5 \pm 2$ cm^2 V^{-1} s^{-1} and $n_0 = 4\cdot10^{17}$ cm^{-1}.
In the case of 4-probe measurements, we observed a linear characteristic only due to the resistance of the nanowire. From the slope of this plot we estimated the conductance in dark of the nanowire in $G_{0(SA)} = 59\pm6$ nS which was in accordance with the previous estimation. The measurements reported in the main text were performed in 4-probe configuration to avoid the interfering effect form the contacts.

Charge separation effects in the photoconductivity of individual MOX nanowires   13
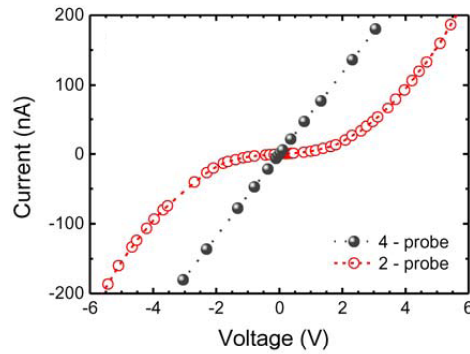
Figure III. I(V) characteristics of a single ZnO nanowire acquired in 2 and 4-probe configurations in dark conditions. Lines represent the mathematical fitting to estimate the values described in the text.

A.3 Wavelength photoresponse threshold in ZnO nanowires

To stimulate the photoresponse in ZnO nanowires, we used a set of LEDs [c] of energies hν above and below the bandgap of this semiconductor (E_{gap}(ZnO) = 3.37eV [d]). In figure IV we show the fully-ohmic **I(V)** characteristics under illumination at different energies. For hν below the E_{gap}(**ZnO**), photocurrent increase in less than 5%, while for hν above E_{gap}(**ZnO**), the photoresponse is about 160%. This indicates that photoconduction is essentially due to band-to-band electron-hole pairs generations. From the technological point of view, this results also suggest that ZnO nanowires are almost visible-blind UV photodetectors with flat response in the near-UV region. For this reason, we centre our study in the source at hν = 3.64eV (340nm).
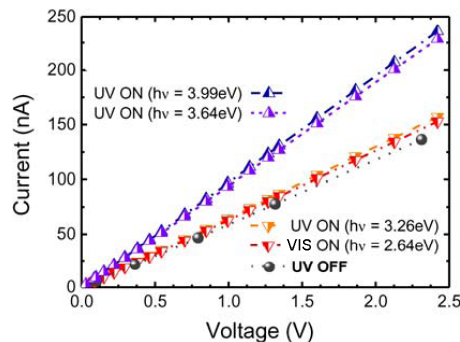
Figure IV. 4-probe I(V) characteristics of a single ZnO nanowire at different illumination conditions. Significant photoresponse is only obtained with photon energies above E_{gap}(ZnO) = 3.36eV. All measurements were acquired under photon flux Φ_{ph} = 3.3·10^{18} m^{-2}s^{-1}.

A.4 UV transmittance and conductance of PMMA layers

To evaluate the transparency of PMMA to UV light, transmittance spectroscopy experiments were performed on PMMA layers of thickness (475 ± 50) nm deposited over fused silica substrates (figure V). In figure VI, the transmittance spectrum of one of these layers is shown, after subtracting the silica contribution. Transmittances values above 90% were obtained for wavelengths from 250 nm to 800 nm.

Charge separation effects in the photoconductivity of individual MOX nanowires   14

Chips with pre-patterned microelectrodes were also coated in order to estimate the conductance and photoresponse of these PMMA layers. Typical conductance values were always below 0.1 nS, and any significant change was observed after UV illumination (figure VII).
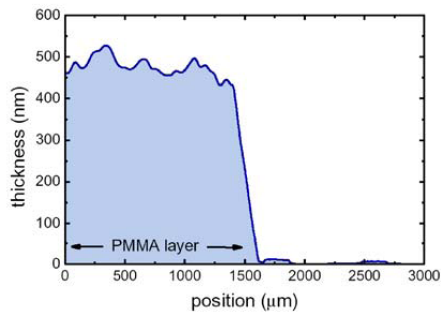
Figure V. Perfilometry profile of a cracked layer of PMMA deposited onto a silica substrate.
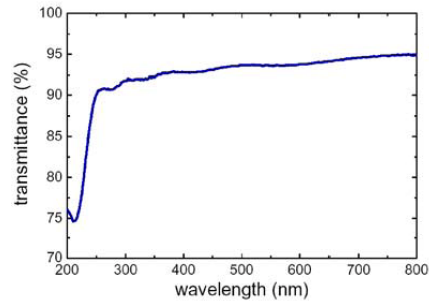
Figure VI. Transmittance spectrum of a PMMA layer. Contribution from the silica substrate was corrected.
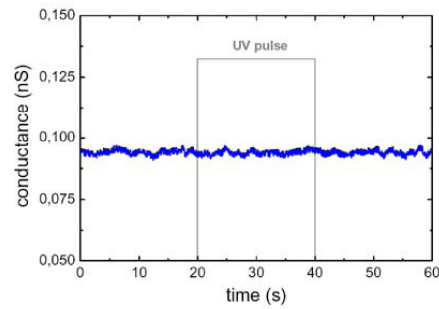
Figure VII. 4-probe measurement of the conductance of a PMMA layer. No response to UV light was observed.

4.2.2 Summary of Results

Unit 2.a   Understanding photodetectors based on nanowires

- The factors that determine the response of photoconductor devices based on individual nanowires were identified using the general principles that rule the electron–hole generation and transport in semiconductors (*Paper 9*). The here–proposed strategies were validated with customized devices.

   - Firstly, the layout of the devices was shown to be important: the optimum layout corresponds to thick nanowires with extremely short interelectrode distances. This is a consequence of the fact that the optimum photon–MOX interaction essentially is a bulk process.

   - Second, we demonstrated that the performance of these devices strongly depends on the working conditions (essentially, the bias voltage and the density of photons). A rigorous methodology to compare different devices was presented, overcoming the present lack of systematic in the studies of this field.

   - Third, the semiconductor properties intrinsic of the nanowires are different to those of the bulk material. Specifically, the mobility is lower and the carrier lifetime is larger. The former worsens the electron transport properties in nanowires while the latter boosts the photoresponse (up to 3 orders of magnitude with respect to alternative technologies). However, this improvement in the magnitude of the response spoils its dynamics. Both effects are related to surface phenomena: mobility is reduced by electron scattering with the nanowire's surface states (which are more accessible due to the large surface-to-volume ratio) and carrier lifetime, dominated by band-to-band recombinations, is enlarged by the built in potential near the nanowire's surface that separates electrons and holes and hampers their recombination.

Unit 2.b.   Understanding the long-term photoconductive states

- The effects of the enlarged carrier lifetime in MOX nanowires give rise to persistent photoconductivity (PPC) states after switching off the illumination. Under certain experimental conditions, these effects are especially dramatic –may even last for hours– and ruin the utility of these materials as photodetectors. However, this situation is extremely useful to gain deeper insight into the role played by the surface in the transport properties of the nanowires (*Paper 10*).

- The dependence of the PPC on the temperature and the atmosphere around the nanowire was fully explained by the following model (*Paper 10*). Under UV illumination, the built-in potential near the surface of the MOX nanowires induces electron–hole separation and hole accumulation at the surface. Once the light is switched off, the accumulated charges need recombination paths to be drained, and PPC appears if these paths are not available. It was experimentally observed that PPC recovery times are linked with the availability of recombination paths. We also observed that PPC was quickly reverted after increasing either the probing current (self-heating by Joule dissipation) or the oxygen content in air (which favors the surface recombination mechanisms).

- Therefore, PPC can be completely blocked by heating the final devices or passivating their surface states (*Paper 10*). It is noteworthy that PMMA coatings totally blocked the PPC and improved the carrier mobility, overcoming one of the main limitations to integrate ZnO, and other metal oxides, in a new generation of optoelectronic detectors.

- The result obtained so far (*Unit 1* and *Unit 2*) revealed a close connection between gas and light interaction in nanowires due to the dominant role played by the surface. This fact stimulated the author to model their combined interaction. These results are presented in the next unit.

4.3 Unit 3: Simultaneous Gas – Light – MOX interaction

Unit 3 is dedicated to the study of the combined molecule – photon – metal oxide (MOX) interactions on the basis of the concepts developed in the two previous units. The unit is separated in two sections. The first concerns the attractive gas sensing capabilities of MOXs enabled by the irradiation with UV photons. The second is devoted to the analysis of the luminescence produced in MOX, which is closely related to the gas active sites at the MOXs' surface.

- *Unit 3.a   Photoactivated detection of oxidizing molecules.* Illumination makes possible detecting oxidizing gaseous molecules with conductometric MOX gas sensors at room temperatures. Besides the number of potential applications of this sensing approach, there is a little known about the precise gas sensing mechanisms activated by the presence of photons. In this section, the effects of the illumination conditions (i.e.: photon flux and energy) on the response towards gases of individual SnO_2 nanowires are studied in detail (*Paper 11*). Combining these experimental results with the previous theoretical findings about the interaction of NO_2 with SnO_2 (*Unit 1*), a model that quantitatively explains these phenomena is postulated (*Paper 12*).

- *Unit 3.b   Detection of surface oxygen vacancies with luminescence analysis.* After confirming the key role of surface oxygen vacancies in the gas sensing activity of MOXs (*Unit 1* and *Unit 3.a*), we pursued to identify an experimental procedure to determine their presence. In this section the additional energy states introduced in the band gap of SnO_2 and ZnO by the presence of surface oxygen vacancies are correlated with their visible luminescence signal (*Paper 13* and *Paper 14*). This experimental method to probe the surface atomic arrangement is successfully applied to a variety of MOX samples (*Paper 13* and *Paper 14*) and used to predict their sensing performances (*Paper 15*).

4.3.1 Papers

11. J.D. Prades, R. Jimenez-Diaz, F. Hernandez-Ramirez, S. Barth, J. Pan, A. Cirera, A. Romano-Rodriguez, S. Mathur, J.R. Morante, *"High performance UV light-operated gas sensors based on individual SnO_2 nanowires for room temperature applications"* Appl. Phys. Lett., submitted (2008).

12. J.D. Prades, R. Jimenez-Diaz, F. Hernandez-Ramirez, M. Manzanares, T. Fischer, J. Pan, T. Andreu, A. Cirera, A. Romano-Rodriguez, S. Mathur, J.R. Morante, *"On the Role of the Illumination Conditions in the Performance of Room Temperature Gas Sensors Based on Individual SnO_2 Nanowires"* Chem. Mater., submitted (2008).

13. J.D. Prades, J. Arbiol, A. Cirera, J.R. Morante, M. Avella, L. Zanotti, E. Comini, G. Faglia, G. Sberveglieri, *"Defect study of SnO_2 nanostructures by cathodoluminescence analysis: Application to nanowires"* Sens. Actuators B-Chemical **126**, 6-12 (2007).

14. J.D. Prades, A. Cirera, J.R. Morante, A. Cornet, *"Ab initio insights into the visible luminescent properties of ZnO"* Thin Sol. Films **515**, 8670-8673 (2007).

15. M. Epifani, J.D. Prades, E. Comini, E. Pellicer, M. Avella, P. Siciliano, G. Faglia, A. Cirera, R. Scotti, F. Morazzoni, J.R. Morante, *"The role of surface oxygen vacancies in the NO_2 sensing properties of SnO_2 nanocrystals"* J. Phys. Chem. C **112**, 19540-19546 (2008).

J.D. Prades, R. Jimenez-Diaz, F. Hernandez-Ramirez, S. Barth, J. Pan, A. Cirera, A. Romano-Rodriguez, S. Mathur, J.R. Morante, *"High performance UV light-operated gas sensors based on individual SnO2 nanowires for room temperature applications"* Appl. Phys. Lett., submitted (2008).

11

High performance UV light-operated gas sensors based on individual SnO2 nanowires for room temperature applications

J. D. Prades[1,]*, R. Jimenez-Diaz[1] , F. Hernandez-Ramirez[1,2], S. Barth[3,⊥], J. Pan[3,4],

A. Cirera[1], A. Romano-Rodriguez[1], S. Mathur[3,4], J. R. Morante[1]

[1] *EME/XaRMAE/IN[2]UB, Dept.d'Electrònica, Universitat de Barcelona, Barcelona, Spain*

[2] *Electronic Nanosystems S. L., Barcelona, Spain*

[3] *Nanocrystalline Materials and Thin Film Systems, Leibniz-Institute of New Materials, Saarbruecken, Germany*

[4] *Department of Inorganic Chemistry, University of Cologne, Cologne, Germany*

Abstract: We demonstrate that illuminating metal oxide gas sensors with ultra-violet light is a viable alternative to activate chemical reactions at their surface without the necessity of heating them. Here, the performance of individual monocrystalline SnO_2 nanowires to NO_2 at room temperature as function of the flux and the energy of photons is studied. The results reveal that nearly identical responses, similar to thermally activated sensor surfaces, can be achieved by choosing the optimal illumination conditions. This finding paves the way to the development of conductometric gas sensors operating at room temperature.

Metal oxide (MOX) gas sensors have found extensive applications in process control industries and environmental monitoring [1]. The major technical limitation in their usage is the high operating temperatures essential for gas detection and sensing [2]. Illuminating these sensors with ultra-violet (UV) light is a viable alternative to activate chemical reactions at their surface without the necessity of heating them [3], which would significantly reduce explosion hazards and improve device life-time. The preliminary studies on the role of impinging photons on the final performance of these devices indicate their application potential [4]. In this letter, we report the response of monocrystalline SnO_2 nanowires to NO_2 at room temperature as function of the flux and the energy of photons. The results demonstrate that nearly identical responses, similar to thermally activated sensor surfaces, can be achieved by choosing the optimal experimental conditions.

NO_2 gas, generated in combustion processes is hazardous to human health [5], and can be detected by using resistive-type sensors in which the modulation of the electrical conductance of the sensing material relates to the amount of adsorbed NO_2 molecules [6]. According to first-principles calculations [7] and Temperature Programmed Desorption experiments [8], NO_2 molecules adsorb onto SnO_2 surface oxygen vacancies (OV) with typical desorption energies above $E_{des} \geq 0.52$ eV, which corresponds to a thermal desorption process only active above $T \geq 80^{\circ}C$ [9]. Thus, at room temperature ($T = 25\ ^{\circ}C$) NO_2 desorption barely takes place and no recovery of the device baseline is observed. For this reason, SnO_2 sensors are typically operated at temperatures above 150 °C in order to guarantee a fast molecular desorption and full recovery of the sensor surface [6].

Monocrystalline SnO_2 nanowires synthesized by catalyst supported chemical vapor deposition of a molecular precursor $[Sn(O^tBu)_4]$ [10] were transferred onto suspended silicon membranes equipped with an integrated SnO_2:Sb microheater and Pt interdigitated electrodes [11]. Nanowires were electrically contacted following FIB-assisted nanolithography procedure [12] (Figure 1.a). A set of monochromatic LEDs with different photon energies ($E_{ph} = 4.00 \pm 0.05$ eV to $E_{ph} = 0.75 \pm 0.01$ eV) were used to illuminate the devices, and light power impinging on the nanowires was estimated through a photodiode placed adjacent to the samples. Four-probe DC measurements were performed inside a customized chamber with gas flow maintained at 200 ml·min⁻¹.

An accurate gaseous environment (mixtures of synthetic air (SA) and NO_2) in the sample chamber was ensured using mass-flow controllers. Ten devices were fabricated using SnO_2 nanowires with lengths (L_{NW}) between 5 and 15 microns, and radii (r_{NW}) between 35 and 45 nm. Stable and reproducible responses were observed even after 4 weeks of continuous measurements illustrating the reversibility of photo-activated process and its application to a new device concept.
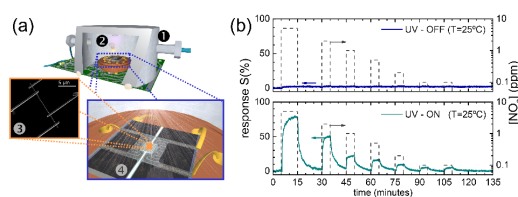
Figure 1. (Color Online) **(a)** Schematic representation of the here-proposed device. The sensor is contained in ❶ a gas tight measurement chamber with ❷ embedded light sources. Photons are used to photoexcite the ❸ nanowire contacted onto ❹ a microchip. **(b)** Response S of a SnO2 nanowire, operated in dark and UV illuminated ($E_{ph} = 3.67 \pm 0.05$ eV, $\Phi_{ph} = 30 \cdot 10^{22}$ ph m⁻² s⁻¹), to NO_2 pulses of different concentration. Both

---

⊥ Current affiliation: Department of Chemistry, University College Cork, Cork, Ireland

measurements were obtained without external heating sources at room temperature (T = 25°C).

Under dark (non-illuminated) conditions, nanowires exhibited extremely low responses S [13] to NO_2 at T = 25 °C without any noticeable recovery of the resistance baseline as evident in Figure 1.b. On the contrary, the same devices displayed significant and reversible responses to NO_2 pulses (concentrations from 100 ppb to 10 ppm) with characteristic response and recovery time constants of only a few minutes under constant UV illumination (Figure 1.b). It is noteworthy that sensor response to NO_2 scaled up with the energy of the impinging photons (Figure 2.a and 2.b). The dependence of the response S of these devices on E_{ph} is directly related to the capacity of photons to transfer energy to adsorbed NO_2 molecules, which facilitate their desorption from the SnO_2 surface. If $E_{ph} > E_{gap}$, the sensor recovery time τ is minimized and the gas response S maximized, suggesting that band-to-band photoexcited pairs contribute to a fast desorption of NO_2 adsorbates after their separation by the surface built-in potential [14] (Figure 2.a and 2.b).

On the other hand, it was experimentally found that a modulation of the response S is a function of both the photon flux Φ_{ph} and the gas concentration $[NO_2]$. To explain this connection, the influence of oxygen in air was taken into account. In principle, oxygen molecules tend to adsorb at OV even at room temperature [15], capturing less electrical charge than the NO_2 counterparts [7]. Thus, it can be asserted that NO_2 and O_2 molecules compete for the same adsorption sites (OV) during the gas sensing experiments. Under ambient conditions, the surface of SnO_2 is initially covered with oxygen ions in equilibrium with molecules in air, remaining only a small fraction of OV sites available for NO_2. This situation explains the weak and non-reversible response S which is experimentally found after the exposure of nanowires to this gas. Under illumination, photons partially desorb oxygen species from the surface, leaving more OV sites available for NO_2 molecules. The new steady state based on the dynamic balance between adsorption and desorption of oxygen and NO_2 molecules explains the higher response S of the devices. The fact that S displays a maximum at different flux of photons Φ_{ph} as function of the gas concentration $[NO_2]$ supports the here-proposed mechanism (Figure 2.c). However, a detailed theoretical analysis of the balance rate equations of the NO_2 and oxygen populations at the nanowire surface will be published elsewhere. In a first approximation, the optimum response of these sensors for a given Φ_{ph} and $[NO_2]$ corresponds to a state in which the amount of NO_2 molecules at the nanowire surface is maximized since the flux is high enough to desorb oxygen creating new OV, but still low enough to prevent a massive desorption of NO_2 by impinging photons. This is corroborated by the fact that the maximum S displaces to higher Φ_{ph} with increasing $[NO_2]$. Thermal heating effects [16] due to illumination were not observed according to previous calibrations in similar devices [17].

The performance of these prototypes was also compared to those operated with an external heater (Figure 2.d). Their calibration curves revealed non-linear responses to different $[NO_2]$ with a strong dependence on Φ_{ph}. Low Φ_{ph} values worsened their sensitivity [18] compared to their heated counterparts, especially at high $[NO_2]$ due to the low concentration of available OV sites for molecule adsorption. On the contrary, high Φ_{ph} exhibited extremely poor responses for low $[NO_2]$ (Figure 2.d). Nevertheless, it was possible to obtain both linear behavior in a broad range of gas concentration (nearly two orders of magnitude) and responses fully equivalent to the heated

ones by adjusting Φ_{ph} for each $[NO_2]$ range (Figure 2.d). This result agrees with our theoretical discussion.
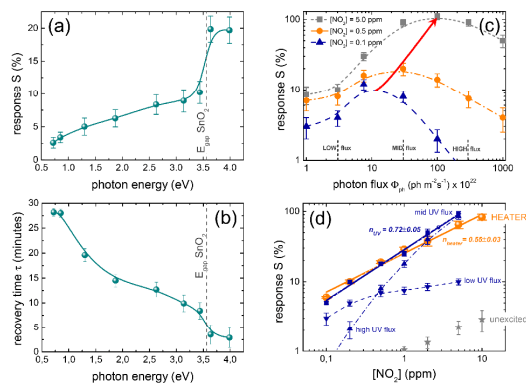
Figure 2. (Color Online) **(a)** Sensor response S and **(b)** recovery time τ to 0.5 ppm of NO_2 pulse in SA under illumination with different photon energies at constant photon flux (Φ_{ph} = $30 \cdot 10^{22}$ ph m^{-2} s^{-1}). **(c)** Sensor response S to 3 concentrations of NO_2 versus the flux of photons (E_{ph} = 3.67 ± 0.05 eV). The maximum response clearly depends on both the gas concentration and the flux of photons. **(d)** Comparison of the sensor response when operated with conventional heating and UV illumination. The selection of the appropriate photon flux leads to sensors' performances comparable to those of conventional heated sensors.

In summary, we have shown that UV illumination of tin oxide nanowires can be used to enhance their response towards oxidizing gaseous species, like NO_2, at room temperature. The final performance of these devices is strongly influenced by the flux and energy of impinging photons, but under the appropriate illumination conditions responses comparable with those obtained with resistively heated sensors are monitored, enabling their use in manifold early-warning applications [5]. This result paves the way to the development of conductometric gas sensors operating at room temperature.

References

[1] (a) F. Röck, N. Barsan, and U. Weimar. Chem. Rev. **108**, 705 (2008).(b) A. Kolmakov, and M. Moskovits. Annu. Rev. Mater. Res. **34**, 151 (2004).

[2] (a) A. Diéguez, A. Vilà, A. Cabot, A. Romano-Rodríguez, J.R. Morante, J. Kappler, N. Barsan, U. Weimar, W. Göpel, Sens. Actutators B **68**, 94 (2000). (b) N. Barsan, D. Koziej, and U. Weimar. Sens. and Actuators B. **121**, 18 (2007).

[3] (a) P. Camagni, G. Faglia, P. Galinetto, C. Perego, G. Samoggia, and G. Sberveglieri, Sens. Actuators B **31**, 99 (1996). (b) E. Comini, L. Ottini, G. Faglia, and G. Sberveglieri, IEEE Sensors J. **4**, 17 (2004).

[4] M. Law, H. Kind, B. Messer, F. Kim, and P. Yang, Angew. Chem. Int. Ed. **41**, 2405 (2002).

[5] (a) World Health Organisation. Information available in http://www.who.int/peh/air/Airqualitygd.htm (b) US Department of Labour, Occupational Safety & Health Administration, information available in http://www.osha.gov/

[6] M. Batzill, and U. Diebold, Prog. Surf. Sci. **79**, 47 (2005).

[7] (a) J. D. Prades, A. Cirera, and J. R. Morante, J. Electrochem. Soc. **154**, H675 (2007). (b) J. D. Prades, A. Cirera, J. R. Morante, J. M. Pruneda, and P. Ordejón, Sens. Actuators B **126**, 62 (2007).

[8] E. Leblanc, L. Perier-Camby, G. Thomas, R. Gibert, M. Primet, and P. Gelin, Sens. Actuators B **62**, 67 (2000).

[9] (a) M. C. Desjonquères, and D. Spanjaard, "Concepts in Surface Physics", 2nd ed.; Springer: Berlin, 1996. (b) V. P. Zhdanov, and B. Kasemo, Surf. Sci. **415**, 403 (1998).

[10] (a) S. Mathur, S. Barth, H. Shen, J.-C. Pyun, and U. Werner, Small **1**, 713 (2005). (b) S. Mathur, and S. Barth, Small **3**, 2070 (2007).

[11] F. Hernandez-Ramirez, J. D. Prades, A. Tarancon, S. Barth, O. Casals, R. Jimenez-Diaz, E. Pellicer, J. Rodriguez, M. A. Juli, A. Romano-Rodriguez, J. R. Morante, S. Mathur, A. Helwig, J. Spannhake, and G. Mueller, Nanotechnol. **18**, 495501 (2007).

[12] F. Hernandez-Ramirez, A. Tarancon, O. Casals, J. Rodríguez, A. Romano-Rodriguez, J. R. Morante, S. Barth, S. Mathur, T. Y. Choi, D. Poulikakos, V. Callegari, and P. M. Nellen, Nanotechnol. **17**, 5577 (2006).

[13] We use the following definition of the conductometric response (S) to NO_2: $S(\%) \equiv 100 \times (R_{NO2} - R_{SA})/(R_{SA})$ where R_{NO2} is the steady value of the resistance of the nanowire exposed to NO_2 and R_{SA} is the reference resistance value in synthetic air (SA).

[14] J D Prades, F Hernandez-Ramirez, R Jimenez-Diaz, M Manzanares, T Andreu, A Cirera, A Romano-Rodriguez and J R Morante, Nanotechnol., in press (2008).

[15] (a) J. Oviedo, and M.J. Gillan, Surf. Sci. **409**, 211 (2001). (b) M. Habgood, and N. Harrison, Surf. Sci. **602**,1072 (2008).

[16] (a) F. Hernandez-Ramirez, A. Tarancon, O. Casals, E. Pellicer, J. Rodríguez, A. Romano-Rodriguez, J.R. Morante, S. Barth, and S. Mathur, Phys. Rev. B **76**, 085429 (2007). (b) T. Schwamb, B. R. Burg, N. C. Schirmer, and D. Poulikakos, Appl. Phys. Lett. **92**, 243106 (2008).

[17] J. D. Prades, R. Jimenez-Diaz , F. Hernandez-Ramirez, S. Barth, A. Cirera, A. Romano-Rodriguez, S. Mathur, and J. R. Morante, Appl. Phys. Lett. **93**, 123110 (2008).

[18] *Sensitivity* is defined as the slope n of the log(S) – log ($[NO_2]$) plot.

Asunto: APL: MS #L08-09622 Receipt of New Manuscript
De: rempel@anl.gov
Fecha: Fri, 10 Oct 2008 18:15:49 UT
Para: dprades@el.ub.es

```
Dear Mr. Prades,

On October 10, 2008, we received your manuscript, referenced below:

Title:  "High performance UV light-operated gas sensors based on individual SnO2 nanowires
for room temperature applications"
Author: Joan Daniel Prades, Roman Jimenez-Diaz, Francisco Hernandez-Ramirez, Sven Barth,
Jun Pan, Albert Cirera, Albert Romano-Rodriguez, Sanjay Mathur, and Joan Morante.

Your manuscript has been assigned the Manuscript #L08-09622.  It is now being entered into
the peer-review process.

You may check on the status of your manuscript by accessing the Live Manuscripts folder
and selecting the "Check Manuscript Status" link at the following URL:
<http://apl.peerx-press.org/cgi-bin/main.plex?el=A5M5DaA2A7BHLe4J7A9T4nAJmfW2n8Spg8PofZUAZ>


(You may need to copy/paste the complete URL into your browser's address/location bar, if
clicking on it within your email reader doesn't work.)

You will receive another email when we have secured the review reports that the Editors
need to arrive at their evaluation and decision about publication.

Thank you for submitting your interesting work to Applied Physics Letters.

If you have any questions, feel free to contact us at apl@anl.gov.

Sincerely,

Laura Rempel
Staff
Applied Physics Letters
```

J.D. Prades, R. Jimenez-Diaz, F. Hernandez-Ramirez, M. Manzanares, T. Fischer, J. Pan, T. Andreu, A. Cirera, A. Romano-Rodriguez, S. Mathur, J.R. Morante, *"On the Role of the Illumination Conditions in the Performance of Room Temperature Gas Sensors Based on Individual SnO₂ Nanowires"* Chem. Mater., submitted (2008).

12

On the Role of the Illumination Conditions in the Performance of Room Temperature Gas Sensors Based on Individual SnO$_2$ Nanowires

J. Daniel Prades*[1], Roman Jimenez-Diaz[1], Francisco Hernandez-Ramirez[1,2], Marta Manzanares[1],

Thomas Fischer[3], Jun Pan [3,4], Teresa Andreu[1], Albert Cirera[1], Albert Romano-Rodriguez[1],

Sanjay Mathur[3,4], and Joan R. Morante[1]

[1]EME/XaRMAE/IN[2]UB, Dept. d'Electrònica, Universitat de Barcelona, E-08028, Barcelona, Spain

[2]Electronic Nanosystems, S.L., E-08028, Barcelona, Spain

[3]Nanocrystalline Mater. and Thin Film Systems, Leibniz-Institute of New Materials, D-66123, Saarbruecken, Germany

[4]Department of Inorganic Chemistry, University of Cologne, D-50939, Cologne, Germany

*Corresponding author: dprades@el.ub.es

RECEIVED DATE

A quantitative model to elucidate the role of impinging photons on the final performance light-activated gas sensor devices. The model provides deep insight about how to control the gas response which paves the way to the development of low consumption conductometric gas sensors operated at room temperature.
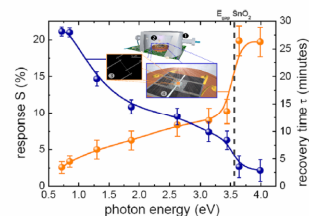
1

Abstract: The authors present a quantitative model to elucidate the role of impinging photons on the final performance light-activated gas sensor devices. The model is based on the competition between oxygen molecules in air and oxidizing target gases (like NO_2) for the same adsorption sites: the surface oxygen vacancies (VO). The model fairly reproduced the experimental measurements of both the steady and the dynamic response of the nanowires. The quantitative results indicate (1) that, at room temperature, NO_2 adsorbs onto OV sites in SnO_2 more avidly than oxygen, (2) the flux of photons and the NO_2 concentration determine the partition of the two gas populations at the surface, and (3) the band-to-band generation of electron-hole pairs seems to play a significant role on the photodesorption process. The model provides deep insight about how to control the gas response which paves the way to the development of low consumption conductometric gas sensors operated at room temperature.

Keywords: photoexcited gas sensor, NO_2, SnO_2, nanowire, adsorption, desorption

2

Introduction

Gas detection, either for health or environmental purposes, is a major area of application for metal oxide nanowires. Their high surface-to-volume ratio makes their electrical properties extremely sensitive to surface-adsorbed molecules [1]. From the technical point of view, chemical nanosensors are interesting because of their potential to detect extremely low concentrations of chemicals [2] on low power platforms [3] small enough to be used on a microchip [4]. From the scientific point of view, the study of individual nanowires provides deeper insight into the gas–surface interactions due to their high surface-to-volume ratio and excellent crystalline and surface properties [5,6].

Nevertheless they have to be maintained at high operating temperatures to perform the task of gas sensing [7]. The illumination of these sensors with ultra-violet (UV) light is considered an alternative way to activate chemical reactions at their surface without heating them [8], enabling a significant reduction of explosion hazard [9]. We recently demonstrated that the response of light-excited devices is nearly identical to those obtained heating if the optimal experimental conditions are used [10]. However, there are only descriptive and qualitative studies of the role of impinging photons on the final performance of these devices [9]. Here, we present a quantitative model based on the competition between oxygen molecules in air and oxidizing target gases (like NO_2) for the same adsorption sites. We demonstrate that it is possible to adjust the steady balance of this competition by tuning the photons' flux and energy and thus, controlling the gas response. This explains the role of photons in this type of sensors and paves the way to the development of low consumption conductometric gas sensors operated at room temperature.

Experimental methods

Individual single-crystal SnO_2 nanowires, synthesized by catalyst supported chemical vapor deposition of a molecular precursor [$Sn(O^tBu)_4$] [6], were transferred onto suspended silicon micromembranes equipped with an integrated SnO_2:Sb microheater and platinum interdigitated microelectrodes. Nanowires were electrically contacted by a lithography process using a FEI Dual-Beam Strata 235 FIB

3

instrument [11] combined with a trimethyl-methylcyclopentadienylplatinum [(CH$_3$)$_3$CH$_3$C$_5$H$_4$Pt] injector to deposit platinum. A set of monochromatic LED sources (photon energies from E$_{ph}$ = 4.00 ± 0.05 eV to 0.75 ± 0.01 eV) were used to illuminate the devices. The light power impinging on the nanowire (λ = 340 ± 10 nm) was estimated with a photodiode located beside it. Four-probe DC measurements were performed to avoid parasitic contacts effects [12] using an electronic circuit designed to guarantee and control low current levels I_m (*0.1 nA*) and to prevent undesired fluctuation [4] and self-heating effects [3]. All the experiments were performed in a customized chamber, in which the gas flow was maintained at *200 ml min^{-1}*. Accurate gaseous environments were provided by massflow controllers mixing synthetic air (SA) and NO$_2$ (*10 ppm ±1%* in SA). Lab-class gases contained less than *5ppm/V* of C$_n$H$_m$ and H$_2$O. Ten devices were fabricated using SnO$_2$ nanowires with lengths (L_{NW}) between *5* and *15 µm*, and radii (r_{NW}) between *35* and *45 nm*, which showed reproducible electrical responses in experiments repeated along 4 weeks. Herein, we use the following definition of the conductometric response (S) to NO$_2$:

$$S(\%) = 100 \times \frac{R_{NO_2} - R_{SA}}{R_{SA}} \tag{1}$$

where R_{NO2} is the steady value of the resistance of the nanowire exposed to NO$_2$ and R_{SA} is the reference resistance value in synthetic air (SA).

Results and discussion

1. Summary of experimental results

In the following lines, we summarize the key experimental results that motivated the here-proposed model. A detail description of this experimental work can be found elsewhere [10].

   (a)   Under dark conditions, nanowires exhibited extremely low responses S to NO$_2$ at T = 25 °C without any noticeable recovery of the resistance baseline. On the contrary, the same devices displayed significant and reversible responses to NO$_2$ pulses (concentrations from 100 ppb to

4

10 ppm) with characteristic response and recovery time constants of only a few minutes under constant UV illumination.

(b) The sensor response to NO_2 scaled up with the energy of the impinging photons E_{ph}: if $E_{ph} > E_{gap}$, the sensor recovery time τ is minimized and the gas response S maximized (Figure 1.a).

(c) The maximum S depends not only on the flux of the photons impinging on the nanowire Φ_{ph} but also on the concentration of analyte $[NO_2]$. Specifically, S displaces to higher Φ_{ph} with increasing $[NO_2]$ (Figure 1.b).

(d) Their calibration curves revealed non-linear responses to different $[NO_2]$ with a strong dependence on Φ_{ph} (Figure 1.c). Low Φ_{ph} values worsened their sensitivity [13] compared to their heated counterparts, especially at high $[NO_2]$. On the contrary, high Φ_{ph} exhibited extremely poor responses for low $[NO_2]$. Nevertheless, it was possible to obtain both linear behavior in a broad range of gas concentration (nearly two orders of magnitude).

The fact that light induce a recovery of the base line after exposure to gases (a) suggest that photons play an important role on the desorption of NO_2 molecules form the surface of SnO_2 probably via band-to-band photoexcited pairs (b). However, to explain the increase in the response S (a), other effects must be taken into account such as the competition with other reactive gaseous molecules present during the measurements. In the following sections, we demonstrate this assumption explains the rest of the experimental evidences ((c) and (d)).

5
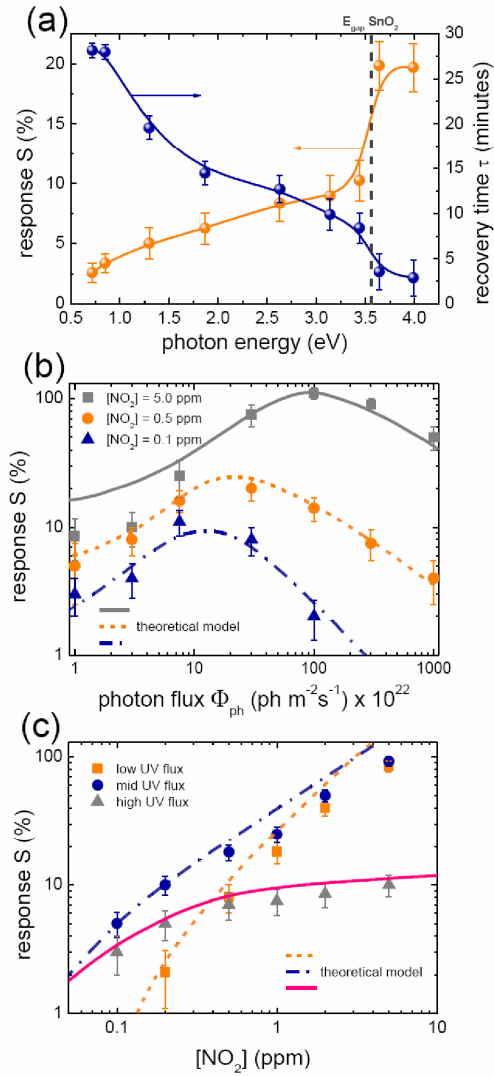
Figure 1. (a) Dependence on the sensors performance (response S and recovery time τ) on the energy of impinging photons. **(b)** Sensor response S versus the flux of impinging UV photons (E_{ph} = 3.67 ± 0.05 eV) for three different concentrations of NO_2. **(c)** Sensor response S versus the concentration of NO_2 for three fluxes of UV photons (E_{ph} = 3.67 ± 0.05 eV): $\Phi_{ph\,low} = 3 \cdot 10^{22}\ ph\ m^{-2}\ s^{-1}$, $\Phi_{ph\,mid} = 30 \cdot 10^{22}\ ph\ m^{-2}\ s^{-1}$, and $\Phi_{ph\,high} = 300 \cdot 10^{22}\ ph\ m^{-2}\ s^{-1}$). In (b) and (c), lines represent the values predicted by the here-proposed model.

6

2. Theoretical model

2.1 NO$_2$ and oxygen adsorption sites onto SnO$_2$ surface

NO$_2$ is a gas hazardous to health [14] which is generated in combustion processes. It can be detected measuring the modulation of the electrical conductance of MOXs, such as SnO$_2$, when NO$_2$ molecules are trapped at their surface [15]. According to first-principles calculations [16] and Temperature Programmed Desorption experiments [17], NO$_2$ molecules adsorb onto SnO$_2$ surface oxygen vacancies (OV) with typical desorption energies above E$_{des}$ ≥ 0.52 eV, which corresponds to a thermal desorption process only active above T ≥ 80ºC [18]. Thus, at room temperature (T = 25 ºC) NO$_2$ desorption barely takes place and no recovery of the device baseline is observed. For this reason, SnO$_2$ sensors are typically operated at temperatures above T = 150 ºC in order to guarantee a fast molecular desorption and fully regeneration of the sensor surface [7].

According to experimental [15] and theoretical works [19], oxygen molecules tend to adsorb at OV even at room temperature [15], capturing less electrical charge than the NO$_2$ counterparts [16].

2.2 Adsorption-desorption rate equation and steady conditions

Based on the previous data it can be asserted that NO$_2$ and O$_2$ molecules compete for the same adsorption sites (OV) during the gas sensing experiments. According to this picture, under ambient conditions, the surface of SnO$_2$ is initially covered with oxygen species in equilibrium with molecules in air, remaining only a small fraction of OV sites available for NO$_2$. This situation explains qualitatively the weak and non-reversible response S which is experimentally found after the exposure of nanowires to this gas. Under illumination, photons partially desorb oxygen species from the surface, leaving more OV sites available for NO$_2$ molecules. The new steady state based on the dynamic balance between adsorption and desorption of oxygen and NO$_2$ molecules explains the higher response S of the devices.

In order to demonstrate the validity of this assumption we analyzed in detail the balance rate equations of the NO$_2$ and oxygen populations at the nanowire surface to check the validity of this assumption. We made the following general assumptions:

7

(I)   Surface consists on a set of adsorption sites in a regular arrangement. Specifically, these sites are the surface oxygen vacancies (OV) with a maximum concentration of $\Lambda = 5\cdot10^{18}$ $sites/m^2$ [20]. Changes in the operating conditions (i.e. temperature, oxygen partial pressure) are small enough to do not modify this maximum values.

(II)   There are always gas molecules available in the environment at their corresponding concentration [NO_2] and [O].

(III) The adsorption of oxygen (i.e. the recombination of an OV site with an environmental oxygen O) leads to a situation equivalent to a non-reduced site.

(IV)   Oxygen and NO_2 compete for these adsorption sites and only 1 single molecule can be absorbed at each site at a time. The surface density of adsorbed oxygens and NO_2 are n_O and n_{NO2}, respectively. If the concentration of free adsorption sites (the ones available for further adsorptions) is n_{VO} the following identity applies at any time:

$$\Lambda = n_{OV} + n_O + n_{NO_2} \tag{2}$$

where Λ is the maximum density of adsorption sites (OV).

(V)   We assume that there is no additional chemical reactions after chemisorption of NO_2 in an OV site.

Under illumination and heating, the surface density of both species will obey the following rate equations

$$\frac{dn_{NO_2}}{dt} = c_{NO_2}(T)\cdot n_{OV}\cdot[NO_2] - \left(e_{NO_2}(T) + \sigma_{NO_2}\Phi_{ph}\right)\cdot n_{NO_2}$$
$$\frac{dn_O}{dt} = c_O(T)\cdot n_{OV}\cdot[O_2] - \left(e_O(T) + \sigma_O\Phi_{ph}\right)\cdot n_O \tag{3}$$

Explicitly, for each specie ($X = O$; NO_2), the adsorption rate is proportional $c_X(T)$ to the density of free adsorption sites n_{OV} and to the concentration of the adsorbates in air [X]. Desorption can be produced by two different excitation sources. The thermally activated desorption that is proportional $\{e_X(T)\}$ to the already adsorbed molecules n_X. The photoactivated desorption is proportional $\{\sigma_X\}$ to the

8

flux of incident photons Φ_{ph} and to the adsorbed molecules n_X. Notice that all adsorption and desorption constants ($c_X(T)$ and $e_X(T)$) depend on the temperature T.

Combining (2) and (3), the concentration of adsorbed molecules can be determined as a function of time. The steady state solution, which corresponds to the steady response of the sensors, can be solved just considering

$$\frac{dn_{NO_2}}{dt} = \frac{dn_O}{dt} = 0 \ . \tag{4}$$

2.3 Electrical response of an individual nanowire

The resistance of an ohmic nanowire (of length l_{nw} and radius r_{nw}) along its axis can be expressed as [21]

$$R_{nwX} = \rho \frac{l_{nw}}{\pi(r_{nw} - \lambda_X)^2} \tag{5}$$

where λ_X is the thickness of the depleted layer at the outer part of the nanowire that depends on the adsorbed molecules at the surface. Here, we assume that there is no influence of the gas on neither the mobility or the free carrier concentration of the material. It is widely accepted [22] that λ_X depends on the charges fixed at the surface Δq_X by adsorbates chemisorbed in density n_X as follows

$$\lambda_X \propto \sqrt{\Delta q_X \cdot n_X} = \alpha\sqrt{\Delta q_X \cdot n_X} \tag{6}$$

where α is the proportionality constant. In particular, the previous expression takes the following form for SA and NO_2 diluted in SA atmospheres

$$\begin{aligned} \lambda_{SA} &= \alpha_{(SA)}\sqrt{\Delta q_O \cdot n_{O,(SA)}} \\ \lambda_{NO_2/SA} &= \alpha_{(NO_2/SA)}\sqrt{\Delta q_O \cdot n_{O,(NO_2/SA)} + \Delta q_{NO_2} \cdot n_{NO_2}} \end{aligned} \ . \tag{7}$$

Notice that the prefactor α and the concentration of adsorbed oxygen n_O may depend on the presence of NO_2 in air. For this reason we have distinguished between the pure SA case and the NO_2/SA mixed case. In order to maintain the simplicity of the following analytical equations,

9

(VI)   we assume that nor α nor nO change dramatically by the presence of NO2 in SA. In this circumstances, equation (6) results in

$$\lambda_{SA} = \alpha \sqrt{\Delta q_O \cdot n_O}$$

$$\lambda_{NO_2/SA} = \alpha \sqrt{\Delta q_O \cdot n_O + \Delta q_{NO_2} \cdot n_{NO_2}} = \alpha \sqrt{\Delta q_O \cdot n_{O)}} \sqrt{1 + \frac{\Delta q_{NO_2} \cdot n_{NO_2}}{\Delta q_O \cdot n_O}} \qquad (8)$$

Based on the previous derivations, the response of the nanowire to varying concentrations of NO_2 in SA is

$$S_{NO_2/SA} = \frac{R_{nw\,NO_2/SA} - R_{nwSA}}{R_{nwSA}} = \frac{(r_{nw} - \lambda_{SA})^2}{(r_{nw} - \lambda_{NO_2/SA})^2} - 1 = \frac{\left(r_{nw} - \alpha \sqrt{\Delta q_O \cdot n_O}\right)^2}{\left[r_{nw} - \alpha \sqrt{\Delta q_O \cdot n_O} \sqrt{1 + \frac{\Delta q_{NO_2}}{\Delta q_O} \frac{n_{NO_2}}{n_O}}\right]^2} - 1$$

$$(9)$$

2.4 Steady response under UV illumination at room temperature

First, based on ab initio calculations [16,23] and spectroscopy measurements [24], we previously concluded that n_{OV} can be modified annealing the samples at well defined temperature and oxygen partial pressures. Thus, near room temperature, the density of surface oxygen vacancies will be strongly influenced by the previous history of the sample. Instead, under illumination, *UV photons would be able to desorb oxygen from the surface* and leading to illumination-dependant n_{OV}, even at room temperature. For this reason,

(VII)   we assume that under UV illumination, oxygen desorption is essentially activated by light.

Second, according specific to DFT calculations [16], NO_2 adsorption may occur spontaneously at room temperature but *NO2 desorption is an exothermic process with typical desorption temperatures above 75ºC*. Consequently,

(VIII)   we also assume that, under UV illumination, the desorption of NO_2 near room temperature is only a light activated process.

10

These two additional approximations are equivalent to

$$e_{NO_2}(\sim 300K) << \sigma_{NO_2} \Phi_{ph}$$
$$e_O(\sim 300K) << \sigma_O \Phi_{ph} \qquad .$$

$$(10)$$

Combining equations (2), (3), (4), (9) and (10) we can find the long-term steady response of the nanowire to NO$_2$ in SA as a function of the illumination and the concentration of gas.

$$S([NO_2],\Phi_{ph}) = \frac{\left[r_{nw} - \alpha \sqrt{\Delta q_O \cdot \dfrac{\Lambda \sigma_{NO_2}[O_2]_{SA} c_O}{\sigma_O[NO_2]c_{NO_2} + \sigma_{NO_2}([O_2]_{SA} c_O + \Phi_{ph}\sigma_O)}}\right]^2}{\left[r_{nw} - \alpha \sqrt{\Delta q_O \cdot \dfrac{\Lambda \sigma_{NO_2}[O_2]_{SA} c_O}{\sigma_O[NO_2]c_{NO_2} + \sigma_{NO_2}([O_2]_{SA} c_O + \Phi_{ph}\sigma_O)}} \sqrt{1 + \dfrac{\Delta q_{NO_2}}{\Delta q_O} \dfrac{c_{NO_2}}{\sigma_{NO_2}} \dfrac{\sigma_O}{c_O} \dfrac{[NO_2]}{[O_2]_{SA}}}\right]^2} -$$

$$(11)$$

The corresponding expressions for n_{NO2} and n_O are,

$$n_{NO_2} = \frac{\sigma_O[NO_2]c_{NO_2}}{\sigma_O[NO_2]c_{NO_2} + \sigma_{NO_2}([O_2]_{SA} c_O + \Phi_{ph}\sigma_O)}\Lambda$$

$$n_O = \frac{\sigma_{NO_2}[O_2]_{SA} c_O}{\sigma_O[NO_2]c_{NO_2} + \sigma_{NO_2}([O_2]_{SA} c_O + \Phi_{ph}\sigma_O)}\Lambda$$

$$(12)$$

2.4.a Discussion

Let us now compare the response predicted by the model with the response observed experimentally (see Figures 1.b and 1.c). Concerning the dependence of the response on the gas concentration, we first notice that the term

$$\sqrt{1 + \frac{\Delta q_{NO_2}}{\Delta q_O} \frac{c_{NO_2}}{\sigma_{NO_2}} \frac{\sigma_O}{c_O} \frac{[NO_2]}{[O_2]_{SA}}}$$

$$(13)$$

corresponds to the additional widening of the depleted shell of the nanowire due to its exposition to NO$_2$. As anticipated experimentally, the higher the gas concentration [NO$_2$] the higher the term (13) and also the higher the photoresponse S. On the contrary, the S becomes zero in absence of NO$_2$, as expected.

11

The high concentration regime is particularly interesting since we observed a saturation of the photoresponse (d). Experimentally, this corresponds to high [NO$_2$] compared to the flux Φ_{ph}, for example, 5ppm at low flux conditions (Figure 1.c). Remarkably our model also predicts this feature:

$$\lim_{[NO_2]\to+\infty} \frac{\partial S}{\partial[NO_2]} = 0 \quad . \tag{14}$$

As far as the flux of photons is concerned, experiments (c) revealed that the maximum response can be found at different flux values $\Phi_{ph\ MAX}$ depending on [NO$_2$]. There is one single positive and non trivial value of Φ_{ph} at which S reaches its maximum value:

$$\Phi_{ph\,MAX} = \frac{c_{NO_2}}{\sigma_{NO_2}}[NO_2] + \frac{c_O}{\sigma_O}[O_2]_{SA} \quad . \tag{15}$$
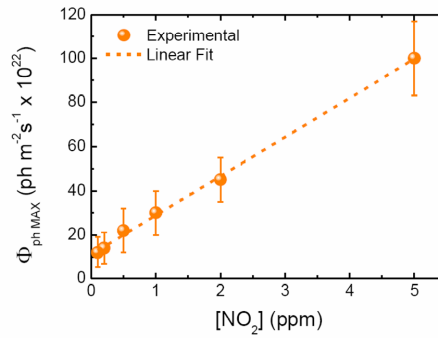
Figure 2. Flux value for a maximum response $\Phi_{ph\ MAX}$ versus the concentration of NO$_2$. The linear relation predicted by the model is observed.

The position of this maximum grows linearly with the concentration of NO$_2$ and the zero offset depends on the content of oxygen. We found a great accordance between this prediction and the experimental results (see Figure 2). By fitting equation (15) to the experimental data, we estimated the c/σ ratios for both gases.

$$\frac{c_{NO_2}}{\sigma_{NO_2}} = (1.77 \pm 0.03)\cdot 10^{23}\ m^{-2}s^{-1}ppm^{-1}$$
$$\frac{c_O}{\sigma_O} = (5.33 \pm 0.04)\cdot 10^{17}\ m^{-2}s^{-1}ppm^{-1} \tag{16}$$

12

We interpret this dependence as follows. The incident photons are used to activate two processes, namely, generation of NO_2 adsorption sites (desorption of oxygens and creation of OV) and desorption of NO_2. The former process tends to increase the photoresponse while the latter tends to decrease it. The optimum flux of photons $\Phi_{ph\ MAX}$ just balance both processes resulting in a maximum photoresponse. Certainly, this balanced flux will increase if any adsorption or desorption rate of NO_2 or oxygen increase (numerators and denominators respectively).

From this point of view, let us analyze the maximum and minimum values of n_{NO2}, n_O and n_{OV} in the whole range of Φ_{ph}. In dark conditions ($\Phi_{ph} \to 0$) the maximum surface density of adsorbates is reached and the minimum is achieved in high-flux conditions ($\Phi_{ph} \to \infty$). Applying these two conditions to equations (1) and (11) we obtain the particular ranges predicted by the model:

$$\text{for} \quad \Phi_{ph} \quad \text{from} \quad \infty \quad \text{to} \quad 0$$

$$0 \leq n_{NO_2}(\Phi_{ph}) \leq \frac{\sigma_O [NO_2] c_{NO_2}}{\sigma_O [NO_2] c_{NO_2} + \sigma_{NO_2} [O_2]_{SA} c_O} \Lambda$$

$$0 \leq n_O(\Phi_{ph}) \leq \frac{\sigma_{NO_2} [O_2]_{SA} c_O}{\sigma_O [NO_2] c_{NO_2} + \sigma_{NO_2} [O_2]_{SA} c_O} \Lambda \tag{17}$$

$$\Lambda \geq n_{OV}(\Phi_{ph}) \geq 0$$

Combining equations (12) and (15) we evaluate the specific surface densities of adsorbates (n_X) at the optimum illumination conditions ($\Phi_{ph\ MAX}$)

$$n_{NO_2}(\Phi_{ph\ MAX}) = \frac{1}{2} \frac{\sigma_O [NO_2] c_{NO_2}}{\sigma_O [NO_2] c_{NO_2} + \sigma_{NO_2} [O_2]_{SA} c_O} \Lambda$$

$$n_O(\Phi_{ph\ MAX}) = \frac{1}{2} \frac{\sigma_{NO_2} [O_2]_{SA} c_O}{\sigma_O [NO_2] c_{NO_2} + \sigma_{NO_2} [O_2]_{SA} c_O} \Lambda \tag{18}$$

$$n_{OV}(\Phi_{ph\ MAX}) = \frac{1}{2} \Lambda$$

that correspond to the central values of the previous ranges. According to the model, the maximum response corresponds to a surface where half of the available sites OV are occupied by NO_2 or O. The partition of these two populations depends on their particular adsorption and desorption rates. Figure 3 shows the corresponding plots for the case of $[NO_2] = 0.5$ppm. Surprisingly, to maximize the overall

13

response, half of the OV sites must remain empty. This is due to the coupling between the two adsorbed populations expressed in equations (2) and (3).
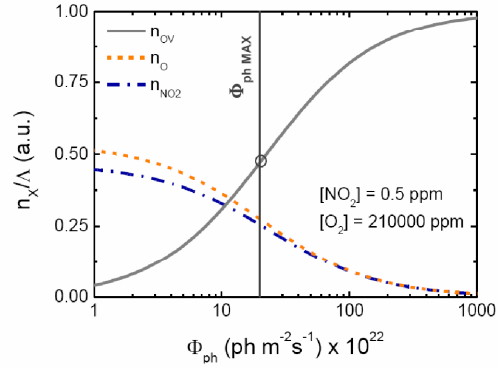
Figure 3. Surface density of adsorbates (n_{NO2} and n_O) and free adsorption sites (n_{VO}) versus the photon flux for 5ppm of NO_2 in SA. Surface densities are normalized to the density of surface sites Λ. At the optimum flux conditions $\Phi_{ph\ MAX}$, half of the sites are vacant and the rest are occupied by NO_2 and oxygen molecules.

Finally, to be able to compare the response predicted in (11) with the experimental data of Figures 1.b and 1.c, we still need to determine, in addition to the c/σ ratios, the charge capture rate $\Delta q_{NO2}/\Delta q_O$ and the prefactor α. According to our DFT calculations [25], the average charge captured by an NO_2 molecule adsorbed onto an oxygen vacancy site in the $SnO_2(110)$ surface is (1.6 ± 0.3) e^-. In these calculations, we considered more than 40 adsorption scenarios [25]. As far as the charge captured by oxygen is concerned, it was recently estimated to be around (0.9 ± 0.3) e^- onto oxygen vacant sites [19]. These theoretical estimations results in an average value $\Delta q_{NO2}/\Delta q_O = 1.8$. According to equation (8), to estimate the prefactor α we only need the previous theoretical prediction of Δq_O, the mean density of adsorbed oxygen ($n_O \approx 10^{18}$ m^{-2}) and the typical experimental value of λ_{SA} for SnO_2 nanowires in SA ($\lambda_{SA} \sim 10nm$) [21,26]. This results in $\alpha \approx 10^{-17}$ $m^2/\sqrt{e}$-.

With all these results, we compared the plots of the predicted response with the experiment (see Figures 1.b and 1.c). The here-proposed model fairly reproduces the experimental points. The major

14

differences are observed at low Φ_{ph} and high [NO_2]: these conditions maximize the neat absorption rate of NO_2 limiting the validity of the approximation (V). In these circumstances, the model underestimates the density of adsorbed oxygens n_O and overestimates the overall response S.

2.6 Dynamic response under UV illumination at room temperature

We also verified that the here-presented model explains the dynamic response to sudden changes of *[NO₂]*. To avoid any controversial interpretation of the dynamic measurements we will center our discussion in the recovery transients [27].

Let us assume steady conditions under illumination at a given *[NO₂]*. In this circumstances (*t = 0s*), the NO_2 in air is suddenly removed (*[NO₂] = 0*). At this point, the surface density of adsorbed NO_2 and oxygen will be *$n_{NO2}(0)$* and *$n_O(0)$* in accordance with equations (13). As time goes by, photons remove the adsorbed NO_2 and the surface evolves towards a new steady situation (with higher density of adsorbed oxygens) that only depends on the adosprtion/desorpion rates of oxygen under illumination. With this initial conditions, the evolution in time of the densities of adsorbed molecules of each specie can be obtained solving equations (2) and (3) with the approximations of equation (10). The result is

$$
\begin{aligned}
n_{NO_2}(t) &= n_{NO_2}(0) \cdot \exp\left(-\sigma_{NO_2} \Phi_{ph}\, t\right) \\
n_O(t) &= \left\{ n_O(0) - \frac{c_O\,[O_2]_{SA}}{\Phi_{ph}} \cdot \left[\frac{n_{NO_2}(0)}{\sigma_{NO_2}-\sigma_O} + \frac{\Lambda}{\sigma_O} \right] \right\} \cdot \exp\left(-\sigma_O \Phi_{ph}\, t\right) + \\
&\quad + \frac{c_O\,[O_2]_{SA}}{\Phi_{ph}} \frac{n_{NO_2}(0)}{\sigma_{NO_2}-\sigma_O} \cdot \exp\left(-\sigma_{NO_2} \Phi_{ph}\, t\right) + \frac{c_O\,[O_2]_{SA}\,\Lambda}{\sigma_O\,\Phi_{ph}}
\end{aligned}
\tag{19}
$$

As expected, long time after removing the NO_2, the model predicts a complete desorption of this gas and a new steady value of *n_O* (higher than the initial one) which corresponds to the balance between the adsorption (numerator) and desorption (denominator) rates of oxygen under illumination.

$$
\begin{aligned}
n_{NO_2}(t \to \infty) &= 0 \;\leq\; n_{NO_2}(0) \\
n_O(t \to \infty) &= \frac{c_O\,[O_2]_{SA}\,\Lambda}{\sigma_O\,\Phi_{ph}} \;\geq\; n_O(0)
\end{aligned}
\tag{20}
$$

Combining the evolution in time of the adsorbed populations with equations (5) and (8), the evolution in time of the resistance of the nanowire is

15

$$R_{nw}(t) = \rho \frac{l_{nw}}{\pi\left(r_{nw} - \alpha\sqrt{\Delta q_O \cdot n_O(t) + \Delta q_{NO_2} \cdot n_{NO_2}(t)}\right)^2} =$$

$$= \rho \frac{l_{nw}}{\pi\left(r_{nw} - \alpha\sqrt{\Delta q_O \dfrac{c_O [O_2]_{SA} \Lambda}{\sigma_O \Phi_{ph}} - A\cdot\exp\left(-\sigma_O\Phi_{ph}\,t\right) + B\cdot\exp\left(-\sigma_{NO_2}\Phi_{ph}\,t\right)+}\right)^2} \quad (21)$$

Reordering terms we define the square of the thickness of the depleted shell λ^2 as follows

$$\lambda^2(t) \equiv \left[r_{nw} - \sqrt{\frac{\rho\, l_{nw}}{\pi\, R_{nw}(t)}}\right]^2 = \Delta q_O\,\alpha^2\,\frac{c_O [O_2]_{SA} \Lambda}{\sigma_O \Phi_{ph}} - A\alpha^2\cdot\exp\left(-\sigma_O\Phi_{ph}\,t\right) + B\alpha^2\cdot\exp\left(-\sigma_{NO_2}\Phi_{ph}\right.$$

$$(22)$$

where the first term is the steady value of $\lambda^2(t)$ long time after removing NO_2

$$\lambda^2(t\to\infty) = \Delta q_O\,\alpha^2\,\frac{c_O [O_2]_{SA} \Lambda}{\sigma_O \Phi_{ph}} \quad (23)$$

and, therefore,

$$\lambda^2(t) - \lambda^2(\infty) = -A\alpha^2\cdot\exp\left(-\sigma_O\Phi_{ph}\,t\right) + B\alpha^2\cdot\exp\left(-\sigma_{NO_2}\Phi_{ph}\,t\right). \quad (24)$$

where have made explicit the negative sign of the oxygen's contribution to the transient. This expression corresponds to a two exponential decay law which can be fitted to the experimental decay (see Figure 4.a). Thanks to the different sign of the two contributions, each time constants can be unambiguously attributed to each adsorbate. Specifically, the recovery constant of each population is inversely proportional to the flux of photons (from equation (19)):

$$\begin{aligned}\tau_{NO_2} &= \frac{1}{\sigma_{NO_2}\Phi_{ph}} \\ \tau_O &= \frac{1}{\sigma_O\,\Phi_{ph}}\end{aligned} \quad . \quad (25)$$

In Figure 4.b we show the recovery time constants as function of $1/\Phi_{ph}$. This plot reveals great accordance with the model (equation (25)) and allows us to estimate the cross sections σ_{NO2} and σ_O:

$$\begin{aligned}\sigma_{NO_2} &= (40\pm10)\text{pm}^2 \\ \sigma_O &= (30\pm10)\text{pm}^2\end{aligned} \quad (26)$$

16

The resulting values are comparable within the experimental accuracy. Therefore, we conclude that the difference of 5 orders of magnitude in the c_X/σ_X rates observed previously (equation (16)) is essentially due to the difference in the adsorption rate constants of both gases. In other words, at room temperature, NO_2 adsorbs onto OV sites in SnO_2 more avidly than oxygen.
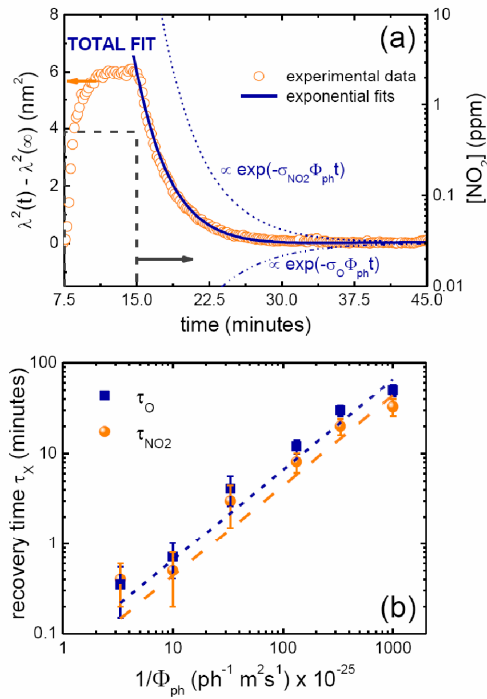
Figure 4. (a) Recovery transient after applying a NO_2 pulse of *0.5 ppm* under illumination *($E_{ph} = 3.67 \pm 0.05$ eV , $\Phi_{ph} = 30 \cdot 10^{22}$ ph m^{-2} s^{-1})*. We represented the evolution in time of the widh of the depleted layer based on the calculation proposed in equation (22). In this case, the radius of the nanowire was $r_{nw} = 45$ *nm*, the distance between electrodes $l_{nw} = 2$ *µm* and the resistivity $\rho = 0.0216$ *Ω m* [12.a]. The experimental data point where fitted with a tow exponential law (solid line). As predicted by the model, while the contribution from NO_2 decays (dashed line), the contribution form oxygen increase (dash-dot line).   **(b)** Recovery time constants of the two exponential contributions versus the inverse of the photon flux for pulses of *0.5ppm* of NO_2.

17

2.7 Effects of the photon energy

So far, we only considered monochromatic light with photon's energy above the band gap of the semiconductor ($E_{gap \, SnO2}$ = 3.57eV). We observed that the energy of this UV light is enough to produce desorption of NO_2 and oxygen but the ultimate cause of these desorptions has not yet been elucidated.

To clarify this point we studied the effect of the photon's energy on the response to NO_2 under illumination. Figure 1.a shows the response S to $[NO_2]$ = 0.5ppm as function of the photon energy hv. All measurements were performed under the same flux of photons (Φ_{ph} = 30·10^{22} ph m^{-2} s^{-1}). The response to NO_2 clearly increases with the energy of the photons. This is in accordance with the fact that the response in dark conditions is almost insignificant. It is noteworthy that the trend varies abruptly for energies above the band gap of SnO_2. This is suggesting that the band-to-band generation of electron-hole pairs plays a significant role on the photodesorption process.

Figure 1.a shows the recovery times τ after the exposure of the nanowire to $[NO_2]$ = 0.5ppm as function of the photon energy E_{ph}. The general trend is that the energy of the photons accelerates the recovery of the baseline but three different regimes can be distinguished. First, the recovery time decays abruptly for photons above 1.25eV and again for photons above 3.5eV. The first energy is comparable to the energy needed to thermally desorb an NO_2 molecule from an $O_{InPlane}$ site, the second one is similar to the bandgap of SnO_2. The first decay indicates that photodesorption of NO_2 is similar to the thermal desorption: the higher the photon/thermal energy, the lower the mean residence time of the molecules onto the surface and the faster the desorption and recovery of the sensor. The second abrupt decay of τ suggest again that the band-to-band generation of electron-hole pairs plays a significant role on the photodesorption process. The coexistence in the nanowire of photogenerated pairs and a built-in potential near the surface typical of metal oxides leads to a free carrier separation process and holes accumulation at the surface of the nanowire. These accumulated holes may ease the desorption of the oxidizing molecules (NO_2 and oxygens) by recombining with the electrons trapped at these adsorbates.

It goes without saying that these results indicate the cross sections σ_{NO2} and σ_O are implicit functions of the photon's wavelength.

18

Conclusions

We presented a quantitative model to elucidate the role of impinging photons on the final performance light-activated gas sensor devices. The model is based on the competition between oxygen molecules in air and oxidizing target gases (like NO_2) for the same adsorption sites: the surface oxygen vacancies (VO). This assumption was expressed in terms of the balance rate equations of the NO_2 and oxygen populations at the nanowire surface. The model fairly reproduced the experimental measurements of both the steady and the dynamic response of the nanowires. First, the quantitative results indicate that, at room temperature, NO_2 adsorbs onto OV sites in SnO_2 more avidly than oxygen. Second, the flux of photons and the NO_2 concentration determine the partition of the two gas populations at the surface. Third, the band-to-band generation of electron-hole pairs seems to play a significant role on the photodesorption process. The model also show how to adjust the steady balance of this competition by tuning the photons' flux and energy and thus, controlling the gas response which paves the way to the development of low consumption conductometric gas sensors operated at room temperature.

19

References

[1] Y. Cui, Q. Q. Wei, H. K. Park, and C. M. Lieber, Science 293, 1289 (2001). (b) R. Yasuda, H. Noji, M. Yoshida, K. Kinosita, and H. Itoh, Nature 410, 898 (2001).

[2] S. V. N. T. Kuchibhatla, A. S. Karaoti, D. Bera, and S. Seal, Progress Mater. Sci. 52, 699 (2007).

[3] J. D. Prades, R. Jimenez-Diaz , F. Hernandez-Ramirez, S. Barth, A. Cirera, A. Romano-Rodriguez, S. Mathur, and J. R. Morante, Appl. Phys. Lett. 93, 123110 (2008).

[4] F. Hernandez-Ramirez, J. D. Prades, A. Tarancon, S. Barth, O. Casals, R. Jimenez-Diaz, E. Pellicer, J. Rodriguez, M. A. Juli, A. Romano-Rodriguez, J. R. Morante, S. Mathur, A. Helwig, J. Spannhake, and G. Mueller, Nanotechnol. 18, 495501 (2007).

[5] Wang Z L 2004 J. Phys.: Condens. Matter. 16 R829-58

[6] Mathur S, Barth S, Shen H, Pyun J-C and Werner U 2005 Small 1 713-17 (b) Mathur S and Barth S 2007 Small 3 2070-5

[7] A. Diéguez, A. Vilà, A. Cabot, A. Romano-Rodríguez, J.R. Morante, J. Kappler, N. Barsan, U. Weimar, W. Göpel, Sens. Actutators B 68, 94 (2000). (b) N. Barsan, D. Koziej, and U. Weimar. Sens. and Actuators B. 121, 18 (2007).

[8] P. Camagni, G. Faglia, P. Galinetto, C. Perego, G. Samoggia, and G. Sberveglieri, Sens. Actuators B 31, 99 (1996). (b) E. Comini, L. Ottini, G. Faglia, and G. Sberveglieri, IEEE Sensors J. 4, 17 (2004).

[9] M. Law, H. Kind, B. Messer, F. Kim, and P. Yang, Angew. Chem. Int. Ed. 41, 2405 (2002).

[10] J. D. Prades, R. Jimenez-Diaz , F. Hernandez-Ramirez, A. Cirera, A. Romano-Rodriguez, J. R. Morante, S. Barth, J. Pan, and S. Mathur, J. Am. Chem. Soc. submitted.

20

[11] F. Hernandez-Ramirez, A. Tarancon, O. Casals, J. Rodríguez, A. Romano-Rodriguez, J. R. Morante, S. Barth, S. Mathur, T. Y. Choi, D. Poulikakos, V. Callegari, and P. M. Nellen, Nanotechnol. 17, 5577 (2006).

[12] F. Hernandez-Ramirez, A. Tarancon, O. Casals, E. Pellicer, J. Rodríguez, A. Romano-Rodriguez, J. R. Morante, S. Barth, and S. Mathur, Phys. Rev. B 76, 085429 (2007). (b) T. Schwamb, B. R. Burg, N. C. Schirmer, and D. Poulikakos, Appl. Phys. Lett. 92, 243106 (2008).

[13] Sensitivity is defined as the slope n of the $\log(S) - \log([NO2])$ plot.

[14] World Health Organisation. Information available in http://www.who.int/peh/air/Airqualitygd.htm (b) US Department of Labour, Occupational Safety & Health Administration, information available in http://www.osha.gov/

[15] M. Batzill, and U. Diebold, Prog. Surf. Sci. 79, 47 (2005).

[16] J. D. Prades, A. Cirera, and J. R. Morante, J. Electrochem. Soc. 154, H675 (2007). (b) J. D. Prades, A. Cirera, J. R. Morante, J. M. Pruneda, and P. Ordejón, Sens. Actuators B 126, 62 (2007).

[17] E. Leblanc, L. Perier-Camby, G. Thomas, R. Gibert, M. Primet, and P. Gelin, Sens. Actuators B 62, 67 (2000).

[18] M. C. Desjonquères, and D. Spanjaard, "Concepts in Surface Physics", 2nd ed.; Springer: Berlin, 1996. (b) V. P. Zhdanov, and B. Kasemo, Surf. Sci. 415, 403 (1998).

[19] J. Oviedo, and M.J. Gillan, Surf. Sci. 409, 211 (2001). (b) M. Habgood, and N. Harrison, Surf. Sci. 602,1072 (2008).

[20] This is the mean value for fully reduced $SnO2$ surfaces corresponding to the 4 most stable low index surface orientations of the cassiterite phase: (110), (101), (111) and (001). (Ref.[15])

21

[21] Hernandez-Ramirez, F.; Prades, J. D.; Tarancon, A.; Barth, S.; Casals, A.; Jimenez-Diaz, R.; Pellicer, E.; Rodriguez, J.; Morante, J. R.; Juli, M. A.; Mathur, S.; Romano-Rodriguez, A., Adv. Funct. Mater. 18, 1 (2008).

[22] Yamazoe, N; Shimanoe, K. Sens. Actuators B 2008, 128, 566.

[23] J. D. Prades, A. Cirera, and J. R. Morante, Chapter 13 in "Quantum Chemical Calculations of Surfaces and Interfaces of Materials", Editors: V.A. Basiuk and P. Ugliengo. American Scientific Publishers (2008).

[24] Prades, J. D.; Arbiol, J.; Cirera, A.; Morante, J. R.; Avella, M.; Zanotti, L.; Comini, E.; Faglia, G.; Sberveglieri, G. Sens. Actuators B 2007, 126, 6

[25] M. Epifani, J. D. Prades, E. Comini, E. Pellicer, M. Avella, P. Siciliano, G. Faglia, A. Cirera, R. Scotti, F. Morazzoni, and J. R. Morante, J. Phys. Chem. C, submitted.

[26] Kolmakov, M. Moskovits, Annu. Rev. Mater. Res. 2004, 34, 151.

[27] In our experimental setup, the gas flow (200 sccm) only needs 0.4 minutes to completely refill 5 times the test chamber (15ml in volume). This criterion is enough to consider an steady gas composition inside the chamber and is the limit of the fastest dynamic we can measure in our set up. We have observed that the response times are faster than recovery times. Response times were clearly below 0.4 minutes while all recovery time were above this value.

22

J.D. Prades, J. Arbiol, A. Cirera, J.R. Morante, M. Avella, L. Zanotti, E. Comini, G. Faglia, G. Sberveglieri,
"Defect study of SnO₂ nanostructures by cathodoluminescence analysis: Application to nanowires"
Sens. Actuators B-Chemical **126**, 6-12 (2007).

13

Defect study of SnO$_2$ nanostructures by cathodoluminescence analysis: Application to nanowires

J.D. Prades [a,*], J. Arbiol [a,b], A. Cirera [a], J.R. Morante [a], M. Avella [c], L. Zanotti [d],
E. Comini [e], G. Faglia [e], G. Sberveglieri [e]

[a] *EME/CeRMAE/IN^{2}UB, Departament d'Electrònica, Universitat de Barcelona, C/ Martí i Franquès, 1, E-08028 Barcelona, Spain*
[b] *TEM-MAT, Serveis Científicotècnics, Universitat de Barcelona, C/ Martí i Franques 1, E-08028 Barcelona, Spain*
[c] *Departamento de Física de la Materia Condensada, Universidad de Valladolid,*
Paseo del Prado de la Magdalena s/n Valladolid, Spain
[d] *IMEM-CNR, Parco Area delle Scienze 37/A, 43010 Fontanini, Parma, Italy*
[e] *Sensor Lab., INFM, Brescia University, Via Valotti 9, 25133 Brescia, Italy*

Available online 9 November 2006

Abstract

Defects in SnO$_2$ nanowires have been studied by cathodoluminescence, and the obtained spectra have been compared with those measured on SnO$_2$ nanocrystals of different sizes in order to reveal information about point defects not determined by other characterization techniques. Dependence of the luminescence bands on the thermal treatment temperatures and pre-treatment conditions have been determined pointing out their possible relation, due to the used treatment conditions, with the oxygen vacancy concentration. To explain these cathodoluminescence spectra and their behavior, a model based on first-principles calculations of the surface oxygen vacancies in the different crystallographic directions is proposed for corroborating the existence of surface state bands localized at energy values compatible with the found cathodoluminescence bands and with the gas sensing mechanisms. CL bands centered at 1.90 and 2.20 eV are attributed to the surface oxygen vacancies 100° coordinated with tin atoms, whereas CL bands centered at 2.37 and 2.75 eV are related to the surface oxygen vacancies 130° coordinated. This combined process of cathodoluminescence and ab initio calculations is shown to be a powerful tool for nanowire defect analysis.
© 2006 Elsevier B.V. All rights reserved.

Keywords: SnO$_2$; Cathodoluminescence; Nanostructure; Nanowire; Oxygen vacancy; Ab initio

1. Introduction

Tin dioxide (SnO$_2$) plays a key role in solid state gas sensors [1]. So a lot of experimental work has been done in order to characterize SnO$_2$ not only from the technological point of view as a sensor of different gases [2] but also from the materials science standpoint [3] so as to achieve improved performances by means of a better knowledge of the synthesized materials. The vacancy defects investigation deserves special attention as they have been clearly related to conductive and sensing properties of metal oxides [2]. This article will deal with the analysis of point defects using cathodoluminescence (CL) spectra of nanostructured SnO$_2$, as this technique reveals complementary information about radiative transitions related to these point defects that is not determined by other characterization techniques.

This experimental procedure is not new. Since the mid-1970s, however, few works have been published presenting the CL spectra of SnO$_2$ with different morphologies [4–7]. In all known cases, several bands between 1.9 and 2.6 eV have been reported but there still remains some uncertainty on their origin [6]. However, there are no systematic and detailed works considering nanowires and their comparison with nanoparticles of different sizes.

On the other hand, first-principles methodologies based on the density functional theory (DFT) now provide precise calculations of the energetic properties of bulk materials and their surfaces in moderate computing times [8]. Consequently, it is attractive to link theoretical findings with unclearly interpreted experimental results in order to attain better materials knowledge with a straightforward technological application, such as a fast and low cost defect detection.

* Corresponding author. Tel.: +34 93 40 39 147; fax: +34 93 40 21 148.
E-mail address: dprades@el.ub.es (J.D. Prades).

The aim of this article is to show how CL, with its notable spatial resolution, can be methodologically combined with the ab initio calculation and applied to analyze the role played by the surface oxygen vacancy defects in nanostructured SnO_2.

First, data from the literature about intra-gap energy levels and new DFT calculations are reported and discussed. Second, CL spectra of liquid pyrolysis synthesized SnO_2 nanoparticles with different grain sizes are presented and four different bands are identified. On the basis of these experimental results, a model is proposed. Finally, this model is applied to the surface oxygen vacancy defect detection of two different samples of SnO_2 nanowires.

2. Experimental details

The cathodoluminescence measurements (CL) were carried out in a Gatan XiCLone system attached to a JEOL JSM-820 scanning electron microscope. The collected luminescence was analyzed by a 300-line grating monochromator and detected by a Peltier cooled CCD, whose spectral range covers [200,1200] nm (around [6.2,1.0] eV). The CCD records the whole spectrum at once in the selected spectral window, thus reducing the measuring times. The system is equipped with a cryostat that allows low temperature measurements.

The measurements were carried out at liquid nitrogen temperature (~ 80 K). The excitation beam conditions for the SnO_2 powders were 20 kV for accelerating voltage and ~ 40 nA for beam current. The nanowires were measured with an accelerating voltage of 10 kV and a beam current of approximately ~ 5 nA. Details on sample synthesis are given below.

The structural and morphological characterization of some of our samples was carried out by means of transmission electron microscopy (TEM) and selected area electron diffraction (SAED). In order to obtain the high-resolution TEM (HRTEM) results we used a Jeol 2010F field emission gun microscope, which works at 200 kV and has a point-to-point resolution of 0.19 nm. To improve the contrast and resolution of our images, minimizing the chromatic aberration inherent in HRTEM micrographs, we obtained the images by filtering the electron zero loss peak, using a Gatan Image Filter (GIF 2000).

3. Results and discussion

3.1. Intra-gap energy levels of SnO_2

For SnO_2, it is established the abundance of shallow donor levels mainly located between 0.15 and 0.30 eV below the conduction band minimum (CBM). Henceforth, we will refer to these levels as bulk shallow levels. According to electro-physical study data, ionized oxygen vacancies in tin dioxide form shallow donor levels with an energy of ~ 0.03 and ~ 0.15 eV below the bottom of the CBM [9–11]. In electron spin resonance measurements, other authors have observed the existence of donor levels from ~ 0.15 up to ~ 0.30 eV underneath the CBM [12]. Note that the literature only shows how, for a given sample, one (or several) discreet levels are placed around this 0.15 eV broad energy region but does not suggest the existence of a continu-
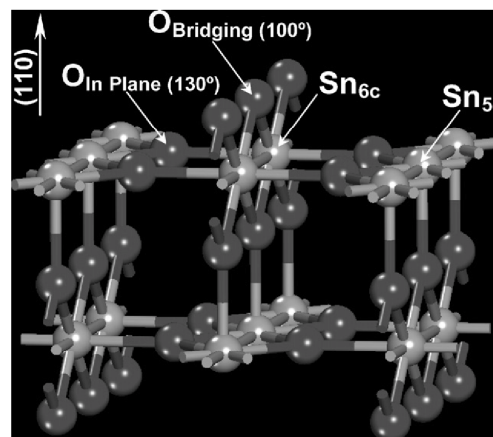
Fig. 1. SnO_2-cassiterite (1 1 0) surface model. Most relevant atoms are indicated. Note how $O_{Bridging}$ coordinates forming a 100° angle with six-fold coordinated tin atoms (Sn_{6c}) while $O_{InPlane}$ forms a different angle of 130° with Sn_{5c} and Sn_{6c}.

ous band 0.15 eV wide. In what follows, the level at ~ 0.03 eV will not be considered as long as it is indistinguishable from the CBM with the computational techniques and the experimental results shown below. In terms of luminescence, the existence of these bulk shallow levels means that when a SnO_2 sample is excited not only the very bottom states of the CBM but also the bulk shallow levels are populated, all those levels being the initial possible state of an eventual radiative recombination.

As far as the surface is concerned, there is much less previous data in the literature. However, these surface defects are relevant in determining the gas sensing mechanisms, especially in tiny nanostructured materials where the surface characteristics stand out clearly. Initially, we will center the discussion on the (1 1 0) surface that is considered the most common faceting orientation [13]. Fig. 1 shows the atomic arrangement on the SnO_2-cassiterite (1 1 0). A striking feature of this surface is the presence of so-called 'bridging' oxygen atoms (O_{Bridg}). These coordinate with their first neighboring tin atoms, forming an angle of 100°. It has been observed that simple heating of a stoichiometric SnO_2-cassiterite (1 1 0) surface to temperatures above 225 °C leads to loss of O_{Bridg} and the formation of oxygen bridging vacancies ($O_{BridgVac}$) [14,15]. According to the literature, if the temperature is raised above 525 °C, in-plane oxygen vacancies ($O_{InPlaneVac}$) can be formed [14]. Such a vacancy coordinates with neighboring Sn atoms forming an angle of 130°. It is worth noting that, as stated in ref. [14], the given vacancy generation temperatures may be dependent on the particular samples used.

At this point, we recall that real samples are not only faceted with (1 1 0) surfaces; therefore, a plethora of different oxygen vacancy sites over different surface orientations arise. In fact, deeper analysis shows that there are only two relevant surface oxygen vacant configurations: those that coordinate forming and angle of 100° ($O_{BridgVac}$ in the case of the (1 1 0) surface) and those of 130° ($O_{InPlaneVac}$). In order to investigate the band struc-

8   *J.D. Prades et al. / Sensors and Actuators B 126 (2007) 6–12*

Table 1
Ab initio results of oxygen vacancy levels over the top of the valence band

Surface	Sn-coordination angle (°)	$O_{vacancy}$ energy level over valence band (eV) (±0.05)
(1 1 0)	100 (bridging)	1.38
	130 (in-plane)	0.94
(1 0 0)	100	1.42
(1 0 1)	130	0.86
(0 0 1)	130	0.90

The computational accuracy was established to be better than 0.05 eV. Consequently, the presented results arise with two families of solutions with average values approximately at 1.40 and 0.90 eV above the maximum of the valence band.

ture consequences of the surface vacancies formation, ab initio simulations of several low index surfaces of SnO_2-casiterite were performed.

The first-principles methodology used in the present calculations is based on the density functional theory [16,17] (DFT) as implemented in the SIESTA code [18,19]. We make use of the generalized gradient approximation (GGA) for the exchange-correlation functional [20]. For all atomic species, double ζ plus polarization orbital basis-sets were used. Total energy convergence is guaranteed below 10 meV as is usual in this kind of calculations [21]. A real space mesh cut-off of 250 Ry and a reciprocal space grid cut-off of approximately 15 Å were used. The structural relaxations were done by means of a conjugate gradient minimization of the energy, until the forces on all the atoms were smaller than 0.04 eV/Å (which provides relaxed total energy values more stable than 10 meV). No constraints were imposed on the relaxation, where the forces were calculated as analytical derivatives of the total energy [22]. The convergence of the present results was verified for slabs thicker that two stoichiometric layers, 2 × 1 bulk unit cells wide and with 7 Å of vacuum spacing.

The initially considered low-index orientations are (1 1 0), (1 0 0), (1 0 1) and (0 0 1), which are accepted as some of the most common faceting surfaces of SnO_2-cassiterite [13]. It is worth noting that 100° coordinated oxygens are present on (1 1 0) and (1 0 0) surfaces and 130° coordinated oxygens appear in surfaces (1 1 0), (1 0 1) and (0 0 1). For all these cases, electron densities of states were computed for stoichiometric and reduced surface (i.e. without and with the oxygen vacancy). In all cases, the vacancy formation implies the creation of allowed states near the top of the valence band (energetic positions are given in Table 1). In summary, it is clear that two families of levels appear: one due to 100° coordinated vacancies at approximately 1.40 eV above the valence band and a second, due to 130° coordinated, at 0.90 eV. Finally, it is worth pointing out that this description in terms of coordination angles seems general enough to describe the rich surface vacancies casuistic, independently on the surface orientation (or the particle morphology).

3.2. Nanocrystalline powder CL spectrum

Fig. 2 shows the acquired CL spectra obtained using samples of SnO_2-cassiterite nanocrystalline particles prepared by liquid
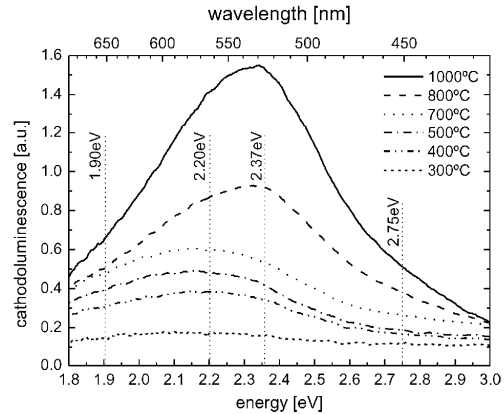
Fig. 2. CL spectra of SnO_2 nanocrystalline particles thermally treated at temperatures ranging from 300 to 1000 °C. All spectra were acquired under the same experimental conditions: acceleration voltage of 20 kV and beam current of ~40 nA with the sample cooled at ~80 K. It is remarkable how emission increases with the sample treatment temperature. The approximate centers of the four fitted bands are shown; fitting details are given in Table 2.

pyrolysis. This synthesis technique involves thermal treatment of a microdrop of tin chloride solution deposited onto a polished substrate [23]. Samples analyzed in this study were treated for 24 min at stabilization temperatures ranging from 300 to 1000 °C. More details on this particular samples synthesis and characterization can be found in ref. [24].

Table 2 presents the corresponding fitting data of the CL spectra. It is a remarkable feature that the CL signal increases

Table 2
Gaussian deconvolution parameters of the spectra shown in Fig. 2

Temperature (°C)	Grain size (nm)	Center (eV)	FWHM (eV)	Height (a.u.)
1000	46.7	2.76	0.28	0.21
		2.37	0.37	1.00
		2.19	0.38	0.70
		1.87	0.22	0.38
800	22.9	2.74	0.26	0.10
		2.38	0.34	0.50
		2.20	0.35	0.36
		1.87	0.23	0.14
700	16.9	2.19	0.50	0.38
		1.90	0.21	0.12
500	8.4	2.20	0.46	0.32
		1.87	0.29	0.10
400	7.0	2.21	0.46	0.24
		1.89	0.23	0.07
300	–	2.18	0.46	0.06
		1.94	0.21	0.01

Notice that these results reveal the existence of four different bands at approximately 1.90, 2.20, 2.37 and 2.75 eV. Also observe that the two higher energy bands (in italics) only appear at temperatures above 700 °C. Gain sizes estimated by XRD analysis and corroborated by TEM observation are given when available.
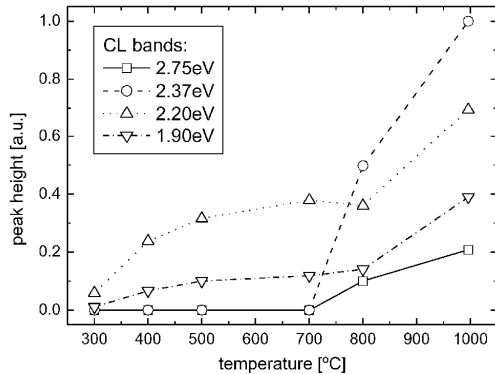
Fig. 3. Evolution with the sample thermal treatment temperature of the intensity of the four peaks fitted to the spectra shown in Fig. 2 (numerical values are given in Table 2). Remarkably, there is a general tendency that shows an increase of all contributions with the treatment temperature. Besides, the increase is even stronger for temperatures above 700 °C appearing two new contributions at 2.37 and 2.75 eV.

with the treatment temperature. According to these results, it is possible to identify four different contributions centered at 1.90, 2.20, 2.37 and 2.75 eV. The two lower energy bands appear in all samples whereas the two higher ones emerge at temperatures above 700 °C (see Fig. 3).

In light of the theoretical vacancy analysis presented above and the SnO$_2$ experimental spectra evolution, it is possible to sketch a fairly simple model. Fig. 4 shows schematically the energetic intra-gap positions of the bulk shallow levels and the two kinds of surface oxygen vacancies (100° and 130° coordinated). According to this, the four recombinations from conduction band and bulk shallow levels to the surface vacancy levels would arise four mean energy values compatible with the
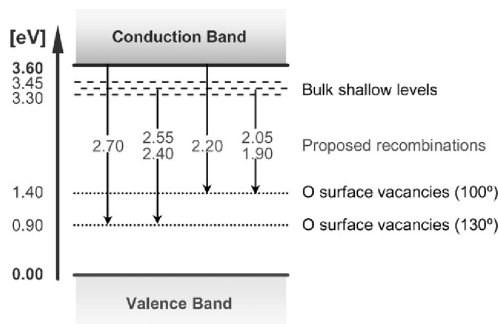
Fig. 4. Schematic representation of the intra-gap levels of SnO$_2$ corresponding to bulk shallow levels and oxygen surface vacancies. For clarity, energy zero was set at the top of the valence band. Recombinations compatible with the acquired CL spectra are shown. In the case of recombinations from bulk shallow levels (which are located within a 0.15 eV wide energy region) the two extreme values are given. From now on, we will consider the average values of the four proposed transitions: 2.70, 2.48, 2.20 and 1.98 eV but keeping in mind the uncertainty in the energy of shallow levels. It is also worth remembering that the computational accuracy of the oxygen surface vacancy levels was estimated at ±0.05 eV.

bands found experimentally within the computational accuracy (±0.05 eV): 1.98, 2.20, 2.48 and 2.70 eV.

Linking these four bands with their contribution to the spectra as a function of the sample treatment temperature, one could propose that: (1) bulk shallow levels are present at all temperatures as long as their energy level is the origin of the recombination of at least one band (1.90 eV) in all samples; (2) at lower temperatures, 100° coordinated oxygen vacancies are present whereas the apparition of 130° oxygen vacancies begins above 700 °C.

Regarding the first proposal, it is worth noting that, as discussed above, bulk shallow levels are commonly present in SnO$_2$ in the studied range of treatment temperatures (this is, for example, the case of bulk oxygen vacancies).

Finally, and concerning the second proposal, it is congruent with the vacancy formation evolution previously described, where 130° coordinated vacancies are harder to generate by heating than the 100° coordinated ones. In this sense, it should be remarked that, based only on a particular set of samples, strongly setting a fixed threshold temperature for the production of one kind of surface vacancy or another seems difficult.

3.3. Nanowires CL spectrum

Unlike nanoparticles, nanowires present better defined crystallographic surfaces and, depending on their geometric dimensions, the role played by surface oxygen vacancies becomes more essential for determining their electrical characteristics as well as their gas sensing mechanisms. Therefore, for understanding the nanowire properties and their applications as gas nanosensors, it is also basic to verify the role of these oxygen surface vacancies. In this context, the previous experimental and analytical procedure was also applied to different SnO$_2$ nanowires with different surface oxygen vacancy configuration.

The deposition of SnO$_2$ nanowires was performed in a tubular furnace with either quartz or alumina tubes. The deposition system was equipped with a vacuum pump in order to obtain a pressure lower than 1 mbar, and mass flow controllers in order to inject a controllable amount of gas carrier during the deposition.

Two different deposition procedures were pursued. In the first one (A-type nanowires), tin monoxide was used as source material, allowing lower working temperatures. Tin monoxide is placed at the center of the quartz tube and the alumina substrates are positioned in the lower temperature region; then, the system is pumped and the temperature is raised to 300 °C in vacuum. A subsequent temperature ramp to 900 °C is imparted, keeping a 100 sccm flux of Ar/H$_2$ at 300 mbar in order to prevent the oxidation of tin monoxide. At temperatures higher than 750 °C, the dissociation of tin monoxide into tin and tin dioxide takes place and leads to a complete dissociation. The carrier gas transports tin vapors and, due to the lower temperature of the substrates, there is a condensation in liquid droplets with dimensions ranging from tens of nanometers to microns. The temperature is then slowly decreased to 870 °C and an Ar/O$_2$ flux is introduced. Oxygen reacts with tin droplets and forms SnO$_2$ nuclei, which then develop in elongated nanocrystals. Finally, the system is cooled to room temperature.

10   *J.D. Prades et al. / Sensors and Actuators B 126 (2007) 6–12*
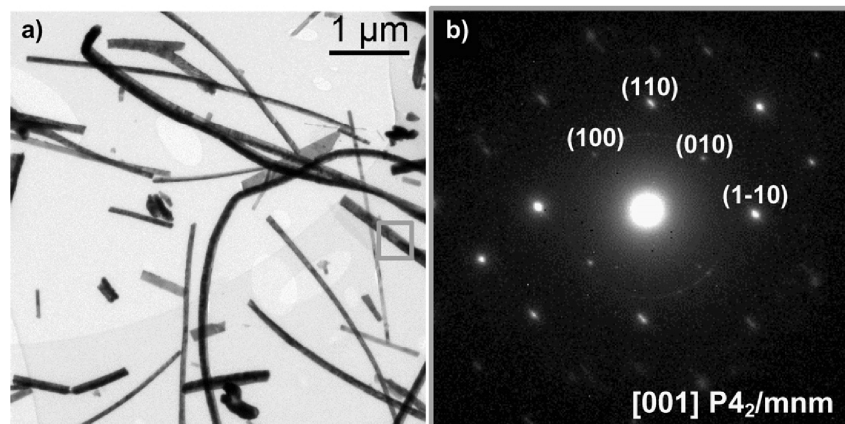
Fig. 5. (a) General bright field TEM view of the SnO_2 A-type nanowires. (b) SAED pattern of the area squared in (a).

For the second deposition procedure (B-type nanowires), tin dioxide powder was used as source material: tin dioxide is place at the center of the alumina tube at 1370 °C and a flux of 75 sccm of Ar is used as gas carrier at a pressure of 100 mbar. Tin oxide nanowires are collected at temperatures ranging from 430 to 470 °C.

Notice that whereas A-type nanowires are finally grown and collected at temperatures above 700 °C, B-type nanowires are collected at temperatures around 450 °C. These final thermal conditions determine the final surface vacancy configuration of the wires.

The presented nanowires were observed with SEM and TEM. A-type samples present nanostructures with widths ranging from 20 to 200 nm, while lengths of up to 200 μm are found. The example micrograph shown in Fig. 5a was captured by means of bright-field TEM (BFTEM). At this point, we obtained selected area electron diffraction (SAED) patterns from several nanowire-like structures in order to determine their structural composition. A SAED example is shown in Fig. 5b, corresponding to the diffraction pattern obtained on the squared area in Fig. 5a. A priori, SAED results confirmed our previous X-ray diffraction (XRD) analysis, where a clear SnO_2 cassiterite ($P4_2$-mnm) structure seemed to be mainly present in our samples. As regards B-type sample, it presents well-formed wire structures with widths from 50 to 1500 nm and lengths of over 100 μm. Fig. 6 shows a representative SEM view. By means of HRTEM, we found that the SnO_2 cassiterite nanowires observed in sample A mainly grow along the [1 0 1] direction, with lateral facets defining a square prism corresponding to {0 1 0} and {1 0 −1} planes. However, in the case of B samples, we found that the SnO_2 cassiterite nanowires crystallize along the [0 1 0] direction while the lateral most favorable facets, attending to HRTEM analysis, are the {2 0 0}, {1 0 1} and {1 0 −1}, defining a hexagonal prism morphology. Nevertheless, both structures differ from those Pd doped SnO_2 cassiterite nanowire-like structures reported previously [25], which grew along the [0 0 1]

direction, and had a square prism morphology with {1 1 0} and {1 −1 0} lateral facets.

CL spectra of both kinds of SnO_2 nanowires are shown in Fig. 7, while fitting values are presented in Table 3. Notably, both CL spectra somehow present a mixture of the four previously presented CL emissive bands. Comparing both spectra, it is remarkable that B-type sample (450 °C) clearly exhibits CL emission with contributions of four bands, whereas A-type sample (700 °C) only shows contributions of the higher energy bands. According to the previously described model, these experimental facts can be understood as follows: (1) both samples seem to present bulk shallow levels; (2) B-type sample may contain both kinds of surface oxygen vacancies, whereas
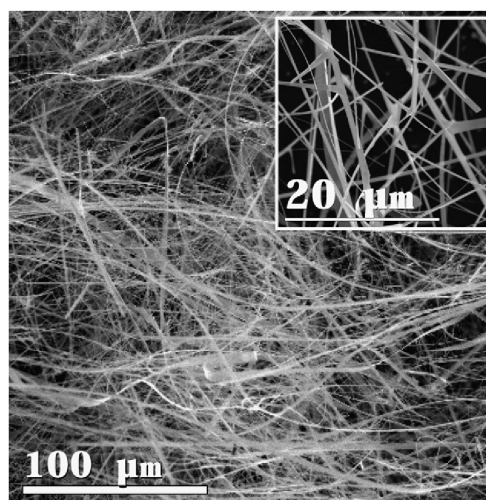
Fig. 6. General SEM view of the B-type sample. *Inset*: Detail SEM view of the same sample.

Fig. 7. CL spectra of SnO$_2$ nanowires synthesized with two different methods. All spectra were acquired under the same experimental conditions: accelerating voltage of 10 kV and beam current of ~5 nA with the sample cooled at ~80 K. The approximate centers of the four fitted bands are shown; fitting details are given in Table 3.

Table 3
Gaussian deconvolution parameters of the spectra shown in Fig. 7

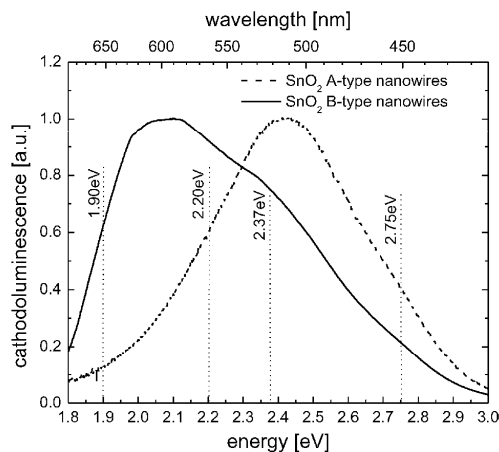| Sample	Center (eV)	FWHM (eV)	Height (a.u.)
B-type	2.72	*0.31*	*0.35*
	2.38	*0.29*	*0.67*
	2.17	0.27	1.00
	1.95	0.18	0.47
A-type	*2.76*	*0.20*	*1.00*
	2.42	*0.46*	*0.54*

Notice that for B-type sample it was possible to identify contributions of the four identified bands, whereas in the A-type sample only contributions of the two bands possibly related to 130° coordinated oxygen vacancies (in italics) were detected.

A-type sample only shows evidence of 130° coordinated oxygen vacancies.

Remarkably, the fact that it is mainly A-type nanowires that present the hardest to produce kind of vacancies (130 °C coordinated), whereas B-type nanowires present a dominant contribution of 100° coordinated vacancies, seems compatible with the final synthesis temperatures of both samples. As mentioned before, a fixed, well-defined temperature threshold for the production of one kind of vacancy or the other seems hard to establish, since it is strongly related to the experimental synthesis and thermal treatment procedures.

4. Conclusions

A model based on first-principles calculations was proposed to explain the cathodoluminescence spectra obtained using nanocrystalline SnO$_2$ powders treated at different temperatures and using different nanowires. According to this, four experimental bands centered at 1.90, 2.20, 2.37 and 2.75 eV were identified and related to recombinations from the conduction band and bulk shallow levels to levels near the top of the valence band corresponding to surface oxygen vacancies (100° and 130° tin atoms coordinated). Significant difference in the energy formation of both types of surface oxygen vacancies explains the appearance of these bands. Whereas 100° tin coordinated oxygen surface vacancy is related to 1.90 and 2.20 eV bands; the 130° tin coordinated oxygen surface vacancy is related to 2.37 and 2.70 eV bands. This appears to be significant in the gas interaction mechanisms and, hence, in the gas sensor performances of these nanostructured materials.

Acknowledgements

References

[1] W. Göpel, K.D. Schierbaum, SnO$_2$ sensors: current status and future prospects, Sens. Actuators B, Chem. 26–27 (1995) 1–12.
[2] G. Sverveglieri, Recent developments in semiconducting thin-film gas sensors, Sens. Actuators B, Chem. 23 (1995) 103–109.
[3] M. Batzill, U. Diebold, The surface and materials science of tin oxide, Prog. Surf. Sci. 79 (2005) 47–154.
[4] D.F. Crabtree, Cathodoluminescence of tin oxide doped with europium, J. Phys. D 7 (1974) L17–L21.
[5] D.F. Crabtree, Cathodoluminescence of tin oxide doped with terbium, J. Phys. D 7 (1974) L22–L26.
[6] D. Maestre, A. Cremades, J. Piqueras, Cathodoluminescence of defects in sintered tin oxide, J. Appl. Phys. 95 (2004) 3027–3030.
[7] D. Maestre, A. Cremades, J. Piqueras, Growth and luminescence properties of micro- and nanotubes in sintered tin oxide, J. Appl. Phys. 97 (2005) 044316 (4 pages).
[8] D. Sanchez-Portal, P. Ordejon, E. Canadell, Computing the properties of materials from first principles with SIESTA, Struct. Bonding 113 (2004) 103–170.
[9] Y.S. He, J.C. Campbell, R.C. Murphey, N.F. Arendt, J.S. Swinnea, Electrical and optical characterization of SbSnO$_2$, J. Mater. Res. 8 (1993) 3131–3134.
[10] S. Samson, C.G. Fonstad, Defect structure and electronic donor levels in stannic oxide crystals, J. Appl. Phys. 44 (1973) 4618–4621.
[11] C.G. Fonstad, K.H. Rediker, Electrical properties of high-quality stannic oxide crystals, J. Appl. Phys. 42 (1971) 2911–2918.
[12] Y. Mizokawa, S. Nakamura, ESR and electric conductance studies of the fine-powdered SnO$_2$, Jpn. J. Appl. Phys. 14 (1975) 779–804.
[13] J. Oviedo, M.J. Gillan, Energetics and structure of stoichiometric SnO$_2$ surfaces studied by first-principles calculations, Surf. Sci. 463 (2000) 93–101.
[14] D.F. Cox, T.B. Fryberger, S. Semancik, Oxygen vacancies and defect electronic states on the SnO$_2$(1 1 0)-1 × 1 surface, Phys. Rev. B 38 (1988) 2072–2083.
[15] D.F. Cox, T.B. Fryberger, S. Semancik, Preferential isotopic labeling of lattice oxygen positions on the SnO$_2$(1 1 0) surface, Surf. Sci. 227 (1990) L105–L108.

12   *J.D. Prades et al. / Sensors and Actuators B 126 (2007) 6–12*

[16] P. Hohenberg, W. Kohn, Inhomogeneous electron gas, Phys. Rev. 136 (1964) B864–B871.

[17] W. Kohn, L.J. Sham, Self-consistent equations including exchange and correlation effects, Phys. Rev. 140 (1965) A1133–A1138.

[18] P. Ordejón, E. Artacho, J.M. Soler, Self-consistent order-N density-functional calculations for very large systems, Phys. Rev. B 53 (1996) R10441–R10444.

[19] J.M. Soler, E. Artacho, J.D. Gale, A. García, J. Junquera, P. Ordejón, D. Sánchez-Portal, The SIESTA method for ab initio order-N materials simulation, J. Phys: Condens. Matter 14 (2002) 2745–2779.

[20] J.P. Perdew, K. Burke, M. Ernzerhof, Generalized gradient approximation made simple, Phys. Rev. Lett. 77 (1996) 3865–3868.

[21] J. Oviedo, M.J. Gillan, First-principles study of the interaction of oxygen with the $SnO_2(1\,1\,0)$ surface, Surf. Sci. 490 (2001) 221–236.

[22] D. Sánchez-Portal, P. Ordejón, E. Artacho, J.M. Soler, Density-functional method for very large systems with LCAO basis sets, Int. J. Quantum Chem. 65 (1997) 453–461.

[23] A. Cirera, A. Diéguez, R. Diaz, A. Cornet, J.R. Morante, in: Proceedings of Eurosensors XII, Southampton, UK, Sens. Actuators B 58 (1999) 360.

[24] A. Cirera, A. Cornet, J.R. Morante, S.M. Olaizola, E. Castaño, J. Gracia, Comparative structural study between sputtered and liquid pyrolysis nanocrystaline SnO_2, Mater. Sci. Eng. B 69–70 (2000) 406–410.

[25] J. Arbiol, A. Cirera, F. Peiró, A. Cornet, J.R. Morante, J.J. Delgado, J.J. Calvino, Optimization of tin dioxide nanosticks faceting for the improvement of palladium nanocluster epitaxy, Appl. Phys. Lett. 80 (2002) 329–331.

Biographies

J.D. Prades graduated in physics at the University of Barcelona in 2005. Now he is PhD student in Department of Electronics of the same university. His current research is focused on first-principles modeling of electronic and vibrational properties of nanostructured metal oxides.

J. Arbiol graduated in physics at the University of Barcelona in 1997 received his European PhD in physics in 2001, and obtained the PhD Extraordinary Award of the Electronics Department. He joined the Electronics Department in 1997, and in 2000 he was appointed as assistant professor in this department. His current research activities are centered in the structural, compositional and morphological characterization of nanosized materials and devices by means of TEM related techniques (HRTEM, EELS, EFTEM, Z-contrast, electron tomography).

A. Cirera graduated in physics at the University of Barcelona in 1996. He received his PhD in 2000 from the University of Barcelona, developing new technologies and their characterization for tin oxide gas sensor devices. He is currently associate professor and works in the field of sensors and its simulation, as scientist and coordinator in several related industrial projects.

J.R. Morante was born in Mataró (Spain). In 1980, he received the PhD degree in physics from the University of Barcelona. Since 1986, he is full professor of electronics and Director of the Electronic Materials and Engineering, EME, group. He has been dean of the physics faculty and academic advisor of the electronic engineering degree. He was Director of the Electronics Department in the University of Barcelona, which is associated unity to the Centre Nacional de Microelectronics at Bellaterra (Barcelona). Actually, he is research head of the EME group and co-director of the CEMIC, Center of the Microsystems Engineering and Director of the CeRMAE, reference center of advanced materials for energy from Generalitat of Catalunya. His activity is devoted to the electronic materials and technology, physics and chemical sensors, actuators and microsystems. He has especial interest in nanoscience and micro&nanotechnologies. He has collaborated in international R&D projects as BRITE, GROWTH (micromechanics, microengineering, gas sensors, nanomaterials, ...), ESPRIT, IST (advanced devices, sensors, actuators, microsystems, electronic systems, ...), JOULE, ..., EUREKA, IBEROEKA and industrial projects. He is co-author of more than 400 works in international specialized journal and member of international committees and editorial boards in the field

of electronic materials and technology, sensors&actuators and microsystems and electronic systems. He has been distinguished with the research prize Narciso Monturiol and the "senior research distinction" award from the Generalitat of Catalunya (Spain).

M. Avella graduated and obtained his PhD in 2000 at the Universidad de Valladolid, Spain. He belongs to the research staff of the Dpt. Fisica Materia Condensada. In 1992, he started his research in this department, collaborating in the development of an equipment of spatially resolved photocurrent for semi-insulating InP:Fe characterization. He is currently involved in the scanning electron microscopy (SEM) and cathodoluminescence (CL) measurements for characterization on semiconductor materials (GaAs, ZnO, InP, ternary and quaternary alloys, ...) and devices (laser diodes, photonic crystals, ...). He is also skilled to work with other additional techniques, such as micro-Raman spectroscopy, AFM, EDS X-ray microanalysis and phase stepping microscopy (PSM). He has participated in more than 12 international research projects and industry contracts. The scientific results were published in more than 60 papers in international journals and over 50 international conferences.

L. Zanotti was born on 15th July 1944. He has been graduated from the University of Bologna in 1969 with a specialization in chemistry. He is one of the founders of MASPEC Institute of the Italian National Council of Research and has been working there since 1970. Since 1983, he is head of the Technology Department at MASPEC. His research has been carried out mainly in the field of semiconductor compounds for use in micro and opto-electronics, infrared detectors and photovoltaic cells and in the field of inorganic/organic materials for non-linear optical application. His activity has been centered around: inorganic synthesis, purification procedures, impurity and compositional-inhomogeneity analysis, crystal growth of binary, ternary and multinary compounds from the melt, vapor and solution, defect (chemical etching) analysis, electrical and optical characterization. He is director of MASPEC (presently IMEM Institute) since 1987, is author of well over 150 scientific papers, reviews, patents in the field of material science and technology.

E. Comini was born on November 21st, 1972 and she received her degree in physics at the University of Pisa in 1996. She received her PhD in material science at the University of Brescia. She is presently working on chemical sensors with particular reference to deposition of thin films by PVD technique and electrical characterization of MOS thin films. In 2001, she has been appointed assistant professor at the University of Brescia.

G. Faglia was born in 1965 and has received an MS degree from the Polytechnic of Milan in 1991 with a thesis on gas sensors. In 1992, he has been appointed as a researcher by the Thin Film Lab at the University of Brescia. He is involved in the study of the interactions between gases and semiconductor surfaces and in gas sensors electrical characterization. In 1996, he has received the PhD degree by discussing a thesis on semiconductor gas sensors. In 2000, he has been appointed as associate professor in experimental physics at University of Brescia. During his career, Guido Faglia has published more than 50 articles on International Journals with referee.

G. Sberveglieri was born on 17th July 1947, and received his degree in physics from the University of Parma, where, starting in 1971, his research activities on the preparation of semiconducting thin film solar cells was conducted. He has been appointed as the associate professor at the University of Brescia in 1987. In the following year, he established the Thin Film Laboratory afterwards called Gas Sensor Laboratory, which is mainly devoted to the preparation and characterization of thin film chemical sensors. He has been the Director of the GSL since 1988. In 1994, he was appointed as full professor in physics, first at the Faculty of Engineering of University of Ferrara and then in 1996, at the Faculty of Engineering of University of Brescia. He is a referee of the journals Thin Solid Films, Sensors and Actuators, Sensors and Materials, etc., and is a member of the Scientific Committee of Conferences on Sensor and Materials Science. During his 25 years of scientific activities, Giorgio Sberveglieri has published more than 140 papers on international reviews; he has presented more than 50 oral communications to International Congresses and numerous oral communications to National Congresses.

J.D. Prades, A. Cirera, J.R. Morante, A. Cornet,
"Ab initio insights into the visible luminescent properties of ZnO"
Thin Sol. Films **515**, 8670-8673 (2007)

14

Ab initio insights into the visible luminescent properties of ZnO

Joan Daniel Prades *, Albert Cirera, Joan Ramon Morante, Albert Cornet

EME/CeRMAE/IN²UB, Departament d'Electrònica, Universitat de Barcelona, C/ Martí i Franquès, 1, E-08028 Barcelona, Spain

Abstract

The luminescence spectrum of ZnO exhibits, besides a UV band-edge recombination line, a broad visible band around 2.2–2.4 eV whose origin has not been satisfactorily established. Recently, analysis of the luminescence of nanostructured materials with high surface-to-volume ratios has led some authors to suggest that the band could be related to surface states. This work presents a novel ab initio study of the most relevant ZnO surfaces and their intrinsic point defects. It reveals the existence of intragap surface states 0.5 eV above the valence band maximum. If additional bulk defect levels are considered, several bulk-to-surface transitions are compatible with the observed visible luminescence.
© 2007 Elsevier B.V. All rights reserved.

Keywords: ZnO; Luminescence; Surface; Oxygen vacancy; Ab initio; DFT

1. Introduction

ZnO is a particularly attractive material for luminescent nanoparticle applications due to its wide band gap (3.37 eV), large exciton binding energy (60 meV), low refractive index (1.9), resistance to high-energy irradiation, stability to intense ultraviolet (UV) illumination, and low toxicity. Its luminescence spectrum exhibits, besides a UV band-edge recombination line, a broad visible band around 2.2–2.4 eV whose origin has not been totally established [1,2]. Numerous authors have related it to a large number of bulk defects such as oxygen vacancies [3], antisites [4], or impurities [5]. Analyzing the luminescence in nanostructured materials of high surface-to-volume ratio, some other authors suggest that it could be related to surface states [6–8].

This work presents a novel ab initio study of the most relevant ZnO surfaces and their intrinsic defects and discusses the plausibility of a surface origin of the luminescent band from the point of view of first principles calculations. It shows that ab initio modeling of materials is a powerful tool for interpreting luminescence results.

2. Calculation details

The first-principles methodology we used is based on density functional theory [9,10] (DFT) as implemented in the SIESTA code [11,12]. We used the generalized gradient approximation (GGA) [13] and norm-conserving Troullier–Martins pseudo-potentials [14]. For all atomic species double ζ plus polarization orbitals basis-sets were used. A real space mesh cut-off of 300 Ry and a reciprocal space grid cut-off of approximately 15 Å were used. Structural relaxation was achieved (with no constraints imposed) by means of a conjugate gradient minimization of the energy, until the forces on all the atoms were less than 0.04 eV/Å. This methodology was successfully applied in previous works [15,16].

All the surface calculations were represented by periodically repeated slabs consisting of up to 8 atomic layers and separated by a 9 Å vacuum. To simulate the underlying bulk structure, the slab lattice constant in the direction parallel to the surface was always set equal to its theoretical equilibrium bulk value. 2×2 supercells were used to model defective surfaces (see Fig. 1).

3. Results and discussion

The choice of surface orientation is crucial to the meaning of ZnO surface models. Experimental observation of faceting orientations in ZnO–wurzite crystals – hexagonal phase, space group P6₃mc, lattice parameters $a=b=3.25$ Å, $c=5.20$ Å and two nonsymmetry-equivalent atoms at $(1/3,2/3,0.0)_{Zn}$ and $(1/3,2/$

---

* Corresponding author. Tel.: +34 93 40 39 147; fax: +34 93 40 21 148.
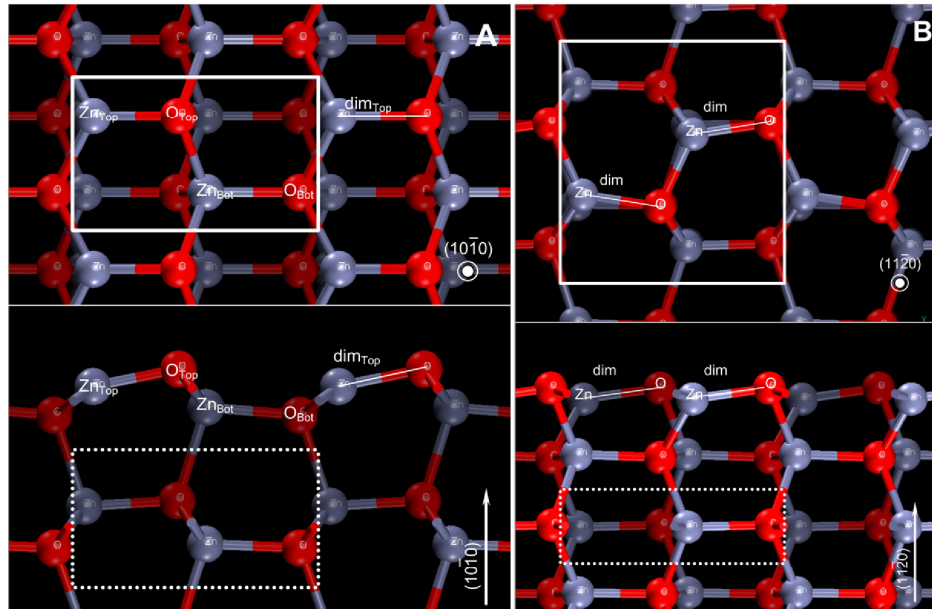*E-mail address:* dprades@el.ub.es (J.D. Prades).

Fig. 1. Solid rectangle marks the surface repetition unit. Dotted rectangle shows the thickness of a single surface layer: a surface unit one layer thick contains two ZnO dimers (as in the bulk unit cell). (A) Top and side views of the relaxed surface (10−10). Notice that the two dimers are placed at different depths ("Top" and "Bot" labels). (B) Top and side views of the relaxed surface (11−20); in this case, both dimers are in the same plane.

$3,0.3826)_O$ [2] – shows that the (10−10) and (11−20) surfaces are the most abundant (and thus the most relevant for our analysis). Both nonpolar surfaces are obtained by cutting the crystal perpendicular to hexagonal Zn and O layers. The (10−10) surface geometry is sketched in Fig. 1A. Each layer of this surface contains two dimers per repetition unit, at different depths (labeled as "Top" and "Bot" in Fig. 1A). The (11−20) surface layers are formed by two ZnO dimers, which form zigzag lines along the surface (Fig. 1B). In this case, the two dimers are equivalent and in the same plane.

Surface free energy values have been estimated at 0.064 eV/Å^2 for (10−10) and 0.070 eV/Å^2 for (11−20). Consequently, the (10−10) surface orientation is slightly more stable than the (11−20). This result is compatible with previous calculations [17].

If the visible luminescence implies radiative recombinations of energies lower than the band gap of ZnO, some kind of intragap level must be involved. Initially it could be thought that the stoichiometric surfaces present intragap levels due to the dangling bonds generated when cleaving the surface. In order to clarify this point, the electron density of states (eDOS) of the bulk and of the two surface orientations were computed (Fig. 2). The clear conclusion is that there are no significant differences between the bulk and the surface eDOS in the intragap region, so that the stoichiometric ZnO surfaces are not involved in the visible luminescence.

It is worth noting that we estimated the band gap in our calculation as 1.36 eV (usually underestimated in DFT-GGA calculations) placing the Fermi level 0.68 eV above the valence band maximum (VBM). Therefore, as DFT is a ground state theory, the only meaningful electron states are those located below the Fermi level [18]. For that reason, we limited the eDOS plot to the first eV above the VBM.

The variations in the visible luminescent band have been independently observed by different authors in samples of different sizes and also after different surface treatments [6−8]. It is therefore reasonable to assume the cause is intrinsic to the surface of ZnO. We considered three different kinds of intrinsic surface defects: oxygen vacancies ($O_{SurfVac}$), zinc vacancies ($Zn_{SurfVac}$) and combined dimer vacancies ($dim_{SurfVac}$). Again, notice that only in the case of the (10−10) surface can a distinction be made between the outermost oxygen atoms and the inner ones; hence the distinction between top ("Top") and bottom ("Bot") for that surface.

As well as the stoichiometric surface, Fig. 2 shows the eDOS of 25% defective surfaces. This reduction percentage is a compromise between convergence of the results and computing time: lower reduction percentages (more isolated surface defects) require wider surface models and this dramatically increases the computing time. We verified the convergence of the results with respect to the distribution and concentration of surface oxygen vacancies for models larger than 2×2 surface units.

From Fig. 2 it is clear that only surface defects related to the removal of the outermost oxygen atoms create acceptor levels just above the VBM (the generation of a $dim_{SurfVac}$ implies the creation of an $O_{SurfVac}$). In all cases, these acceptor levels are located 0.5 eV above the VBM. If the Fermi level is positioned
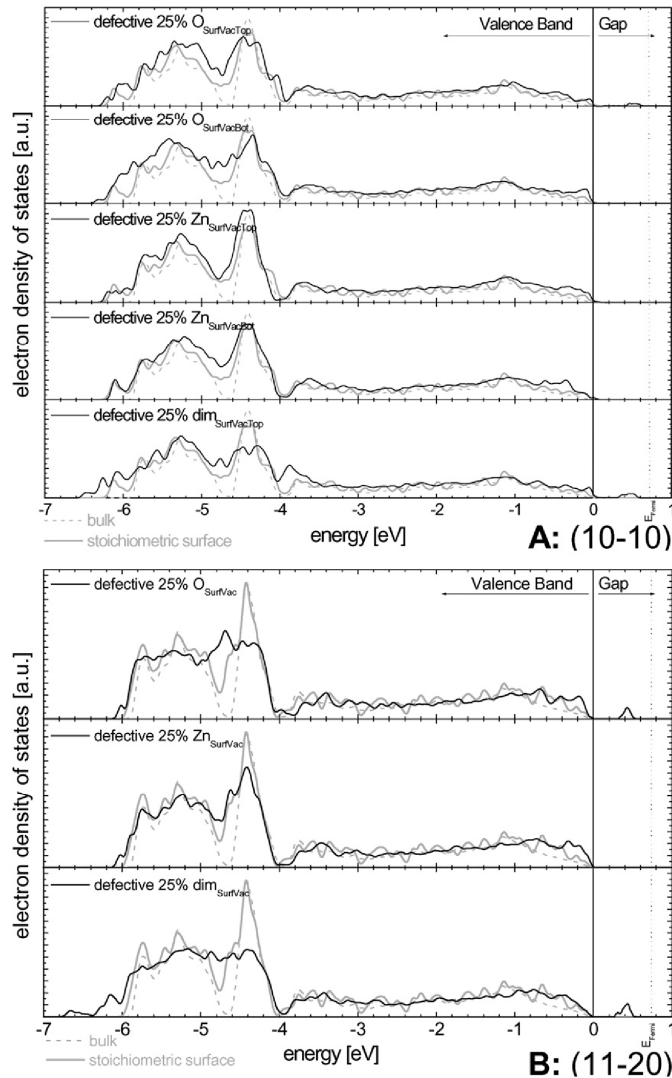
Fig. 2. Electron density of states of stoichiometric and defective ZnO surfaces compared with the bulk: intragap levels 0.5 eV above the VBM only appear when outermost surface oxygen is removed. (A) (10–10) surface; Top/Bot distinction is necessary. Intragap levels only appear when $O_{SurfVacTop}$ are removed. (B) (11–20) surface.

at 0.68 eV, these levels are occupied in the ground state and, therefore, their energy position is properly predicted by DFT. The apparition of acceptor levels associated with the generation of surface oxygen vacancies has been reported for other semiconducting metal oxides [16].

We have shown that surface oxygen vacancies are the only studied intrinsic surface defect that introduces intragap levels. Therefore, we have discussed their stability under atmospheric pressure following the methodology for the thermodynamic interpretation of ab initio calculations on surface models de-

scribed by Reuter and Scheffler [19]. This analysis reveals that the stoichiometric surface configuration is the most stable, as expected. At temperatures above 560–690 °C single $O_{SurfVac}$ can be formed and the reduction rate increases with increasing temperature, reaching total surface reduction above 1000 °C. Thus, reduced surfaces can exist at ambient temperatures but as metastable configurations. This predicted evolution is compatible with the known behavior described by W. Göpel and coworkers, who estimated that the massive generation of surface oxygen vacancies would begin above 700 °C [20]. The
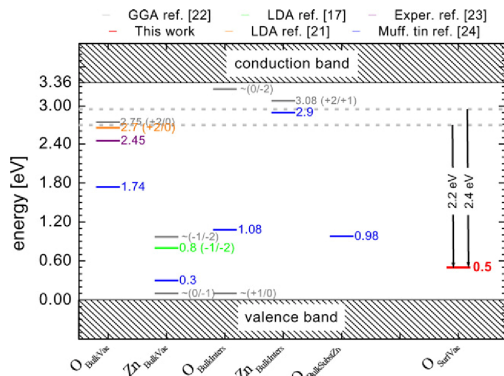
Fig. 3. Intrinsic point defect levels in ZnO from the literature. Results are taken from DFT calculations (GGA and LDA approximations), muffin tin calculations and experimental work. Transitions from some bulk defect levels to surface defect levels are compatible with the visible luminescence of ZnO (black arrows).

present result can be seen as a technological heating rule to adjust the surface reduction of an active material.

Recombination from the conduction band minimum (CBm) to the predicted surface state 0.5 eV above VBM involves an energy of 2.86 eV, which is not compatible with the observed visible luminescence. Therefore, other intrinsic bulk defects could be the initial state for an eventual recombination (Fig. 3). According to recent DFT calculations [21,22] and experimental work [23], bulk oxygen vacancies ($O_{BulkVac}$), introduce donor levels around 0.7 eV below CBm (previous and less precise muffin tin calculations are given as a reference [24]). Zinc vacancies ($Zn_{BulkVac}$) lead to acceptor levels at a range of energies from the very top of the valence band [22] to about 0.9 eV above VBM [17,22]. This spread appears to be related to different charge states of the $Zn_{BulkVac}$. Interstitial oxygen ($O_{BulkInters}$) could give rise to both donor and acceptor levels very close to the band edges due to different charge states [22]. Two papers also predict the generation of acceptor levels at about 0.3 eV below the CBm by zinc interstitials ($Zn_{BulkInters}$) [22,24]. Finally, oxygen atoms in a zinc substitutional position ($O_{BulkSubstZn}$) seem to introduce acceptor levels [24].

It is clear that bulk defect levels could be the initial state of recombinations with final state at the surface defect levels (see Fig. 3). Such transitions involve energy values compatible with the visible luminescence observed. In particular, transitions from $O_{BulkVac}$ to $O_{SurfVac}$ involve energies of around 2.2 eV and transitions from $Zn_{BulkInters}$ to $O_{SurfVac}$ involve energies of about 2.4 eV. It is therefore possible that the visible luminescence of ZnO has some kind of surface origin, but uncertainties in some of the reported energetic positions of the intrinsic bulk defects must be taken into account.

4. Conclusions

The valence band of stoichiometric surfaces does not present significant differences from the bulk valence band, neither does

it introduce intragap levels. Furthermore, only surface oxygen vacancies in the outermost layer of the material give rise to acceptor levels 0.5 eV above VBM. Finally, it has been shown that the energy differences involved in recombinations from bulk defect donor levels to surface oxygen vacancy acceptor levels are compatible with the observed visible luminescence. A surface origin of ZnO visible luminescence is therefore theoretically conceivable, but further work is needed.

References

[1] M.R. Phillips, O. Gelhausen, E.M. Goldys, Phys. Status Solidi 201 (2004) 229.
[2] Ü. Özgur, Ya.I. Alivov, C. Liu, A. Teke, M.A. Rechchikov, S. Dogan, V. Avrutin, S.-J. Cho, H. Markoç, J. Appl. Phys. 98 (2005) 041301.
[3] K. Vanheusden, C.H. Seager, W.L. Warren, D.R. Tallant, J.A. Voigt, Appl. Phys. Lett. 68 (1996) 403.
[4] B. Lin, Z. Fu, Y. Jia, Appl. Phys. Lett. 79 (2001) 943.
[5] N.Y. Barces, L. Wang, L. Bai, N.C. Giles, L.E. Halliburton, G. Cantwell, Appl. Phys. Lett. 81 (2002) 943.
[6] M.H. Huang, Y. Wu, H. Feick, N. Tran, E. Weber, P. Yang, Adv. Mat. 13 (2001) 113.
[7] B.D. Yao, Y.F. Chan, N. Wang, Appl. Phys. Lett. 81 (2002) 757.
[8] V.A.L. Roy, A.B. Djuristic, W.K. Chan, J. Gao, H.F. Lui, C. Surya, Appl. Phys. Lett. 83 (2003) 141.
[9] P. Hohenberg, W. Kohn, Phys. Rev. 136 (1964) B864.
[10] W. Kohn, L.J. Sham, Phys. Rev. 140 (1965) A1133.
[11] P. Ordejón, E. Artacho, J.M. Soler, Phys. Rev. B 53 (1996) R10441.
[12] J.M. Soler, E. Artacho, J.D. Gale, A. García, J. Junquera, P. Ordejón, D. Sánchez-Portal, J. Phys., Condens. Matter 14 (2002) 2745.
[13] J.P. Perdew, K. Burke, M. Ernzerhof, Phys. Rev. Lett. 77 (1996) 3865.
[14] N. Troullier, J.L. Martins, Phys. Rev. B 43 (1991) 1993.
[15] J.D. Prades, A. Cirera, J.R. Morante, J.M. Pruneda, P. Ordejón, Sens. Actuators, B, article (in press), doi:10.1016/j.snb.2006.10.040.
[16] J.D. Prades, J. Arbiol, A. Cirera, J.R. Morante, M. Avella, L. Zanotti, E. Comini, G. Faglia, G. Sbervegglieri, Sens. Actuators, B, article (in press), doi:10.1016/j.snb.2006.10.014.
[17] A.F. Kohan, G. Ceder, D. Morgan, C.G. Van de Walle, Phys. Rev. B 61 (2000) 15019.
[18] R.O. Jones, O. Gunnarsson, Rev. Mod. Phys. 61 (1989) 3.
[19] K. Reuter, M. Scheffler, Phys. Rev. B 65 (2002) 035406.
[20] W. Göpel, U. Lampe, Phys. Rev. B 22 (1980) 6447.
[21] C.G. Van de Walle, Physica B 308–310 (2001) 899.
[22] P. Erhart, K. Albe, A. Klein, Phys. Rev. B 73 (2006) 205203.
[23] F.H. Leiter, H.R. Alves, A. Hofstaetter, D.M. Hofmann, B.K. Meyer, Phys. Status Solidi 226 (2001) R4.
[24] B. Lin, Z. Fu, Y. Jia, Appl. Phys. Lett. 79 (2001) 943.

M. Epifani, J.D. Prades, E. Comini, E. Pellicer, M. Avella, P. Siciliano, G. Faglia, A. Cirera, R. Scotti, F. Morazzoni, J.R. Morante,
"The role of surface oxygen vacancies in the NO₂ sensing properties of SnO₂ nanocrystals"
J. Phys. Chem. C **112**, 19540-19546 (2008).

15

The Role of Surface Oxygen Vacancies in the NO₂ Sensing Properties of SnO₂ Nanocrystals

Mauro Epifani,*,† Joan Daniel Prades,‡ Elisabetta Comini,§ Eva Pellicer,‡ Manuel Avella,‖ Pietro Siciliano,† Guido Faglia,§ Albert Cirera,‡ Roberto Scotti,⊥ Franca Morazzoni,⊥ and Joan Ramon Morante‡

Consiglio Nazionale delle Ricerche, Istituto per la Microelettronica ed i Microsistemi (C.N.R.-I.M.M.), via Monteroni, I-73100 Lecce, Italy, EME/XaRMAE/IN²UB, Departament d'Electrònica, Universitat de Barcelona, C.\ Martí i Franquès 1, E-08028 Barcelona, Spain, CNR-INFM and Dipartimento di Chimica e Fisica per l'Ingegneria e i Materiali, SENSOR, Università di Brescia, via Valotti 9, Brescia, Italy, Departamento de Física de la Materia Condensada, Universidad de Valladolid, Paseo del Prado de la Magdalena, Valladolid, Spain, and Dipartimento di Scienza dei Materiali, Università degli Studi di Milano-Bicocca, via R. Cozzi 53, 20125 Milano, Italy

Received: June 4, 2008; Revised Manuscript Received: September 30, 2008

SnO₂ nanocrystals were prepared by injecting a hydrolyzed methanol solution of SnCl₄ into a tetradecene solution of dodecylamine. The resulting materials were annealed at 500 °C, providing 6−8 nm nanocrystals. The latter were used for fabricating NO₂ gas sensing devices, which displayed remarkable electrical responses to as low as 100 ppb NO₂ concentration. The nanocrystals were characterized by conductometric measurements, X-ray photoelectron spectroscopy (XPS), electron paramagnetic resonance (EPR), and cathodoluminescence (CL) spectroscopy. The results, interpreted by means of molecular modeling in the frame of the density functional theory (DFT), indicated that the nanocrystals contain topographically well-defined surface oxygen vacancies. The chemisorption properties of these vacancies, studied by DFT modeling of the NO₂/SnO₂ interaction, suggested that the in-plane vacancies facilitate the NO₂ adsorption at low operating temperatures, while the bridging vacancies, generated by heat treatment at 500 °C, enhance the charge transfer from the surface to the adsorbate. The behavior of the oxygen vacancies in the adsorption properties revealed a gas response mechanism in oxide nanocrystals more complex than the size dependence alone. In particular, the nanocrystals surface must be characterized by enhanced transducing properties for obtaining relevant gas responses.

Introduction

The use of semiconducting metal oxide (MOX) nanocrystals was suggested at the beginning of the 90's by Yamazoe and co-workers[1] as a powerful way for improving the performances of chemoresistive gas-sensors. The high response of nanocrystal-based sensors was predicted and experimentally demonstrated by the same authors. They explained the sensitivity in terms of enhanced modulation of the charge depletion layer due to the interaction with the surrounding gases. Since then, intensive efforts were devoted to the development of metal oxide nanostructure-based gas-sensors, and an increasing number of papers appeared in the literature. This fact confirms the potential of nanosized metal oxides in gas-sensing applications, either as 0-D nanocrystals[2] or as 1-D nanostructures,[3] such as nanobelts and nanowires. In a recent work,[4] we developed a wet chemical synthetic route for the preparation of metal oxide nanocrystals (mainly SnO₂, In₂O₃, Pd-SnO₂) employed as base materials for chemoresistive sensors.[5] Remarkable performances toward a broad range of gaseous analytes were obtained, which in the following will be focused on the SnO₂ sensing response toward NO₂, significantly high at low temperatures (25−100 °C). Thus we obtained a direct confirmation of the potential of nanosized

oxides for improved gas sensors. On the other hand, when comparing our results with other literature reports, it appeared that the sensing properties span a very broad range, depending on the processing route, the thermal history, morphology of the material, and so on. This spread in the results cannot be fully explained by the dependence of the gas response on the particle size. It could be indeed a rough approximation to consider the nanometric size as a tool to improve the sensing properties, totally skipping the nature of the surface adsorption processes. This difficulty explicitly appears by referring to the classical expressions for the charge depletion depth w formed in the oxide grain upon gas adsorption:[6]

$$w = L_D(2\beta V_S)^{1/2} \qquad (1)$$

where L_D is the Debye length, V_s the surface potential barrier, and $\beta = q/kT$, where q is the electron charge, k the Boltzmann constant, and T the temperature. The interest for oxide nanocrystals in gas-sensing stems from the possibility of having w comparable to the grain size and hence large relative electrical resistance change upon exposure to the gases. As the V_S value depends on the charge density established upon interaction with the gas, the value of w, for a given material and grain size, could span a whole range, depending on the surface capability of adsorbing gaseous species. This fact has to be carefully considered to achieve a deeper insight into the diverse sensing results of metal oxide nanocrystals and to rationally design their use in sensing devices.

* E-mail: mauro.epifani@le.imm.cnr.it.
† Istituto per la Microelettronica ed i Microsistemi.
‡ Universitat de Barcelona.
§ Università di Brescia.
‖ Universidad de Valladolid.
⊥ Università degli Studi di Milano-Bicocca.

NO$_2$ Sensing Properties of SnO$_2$ Nanocrystals

J. Phys. Chem. C, Vol. 112, No. 49, 2008 **19541**

It is generally proposed[6] that the NO$_2$ sensing at low operating temperatures, where we have obtained the highest responses, is due to NO$_2$ chemisorption and to the consequent charge depletion of the sensing material following the reaction:

$$NO_2(g) + e^- \rightleftharpoons NO_2^-(ads) \tag{2}$$
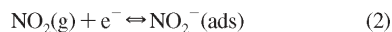
Thus the case of NO$_2$ is particularly amenable to the study of the adsorption properties of the sensing materials. The aim of this work is just to demonstrate the relevance of the surface oxygen vacancies in NO$_2$ adsorption on nanocrystalline SnO$_2$ and in the related sensing properties. First of all, the chemical nature of the nanocrystal surface was established by conductometric measurements, XPS, EPR, CL spectroscopy, and DFT modeling. The presence of a strongly reduced surface was evidenced, characterized by very well topographically defined oxygen vacancies. The latter were used as an input in the ab initio DFT modeling of the SnO$_2$/NO$_2$ interaction. It was observed that the calculated adsorption energy and the charge transfer to adsorbed NO$_2$ were strongly enhanced by such oxygen vacancies. Since the NO$_2$-sensing mechanism is based onto the gas adsorption on the nanocrystals surface and the related charge transfer phenomena,[6] direct correlation between the NO$_2$ response and the surface oxygen vacancies could be established. It was concluded that the nanometer size regime may be not sufficient by itself to justify high gas response, if not coupled with well defined surface reception properties.

Experimental Section

SnO$_2$ nanocrystals were prepared by a general procedure based on the injection of metal oxide sols into a hot (160 °C) solution of dodecylamine in tetradecene, as fully described in previous work.[4] After 3 h from the injection step, the nanocrystals were extracted from the synthesis pot and dried at 80 °C. Then, they were heat-treated up to 500 °C in synthetic air in order to eliminate the organic residuals. After the heat treatment, the size of nanocrystals did not increase substantially, reaching the final value of about 6 nm.

The substrates for the processing of sensing devices were precut alumina plates (2 × 2 mm^2) onto whose back and front were deposited platinum heaters and titanium/platinum electrodes, respectively, by lithographic techniques. Powder suspensions were prepared by dispersing 4−6 mg of the heat-treated nanocrystals in 1−1.5 mL of methanol. Drops of the suspensions (about 4 μL) were deposited onto the substrates, waiting for complete evaporation of the solvent before depositing the next drop. Gold wires were bonded to the electrodes and heaters before the drop-coating step.

The flow-through technique was used to test the electrical properties of the thin films. A constant flux of synthetic air of 0.5 L/min was used as gas carrier. All the measurements were carried out in a temperature-stabilized sealed chamber at 20 °C under controlled humidity. The operating temperatures of the sensors were varied between 25 and 300 °C using the platinum heating meander integrated in the alumina substrate. The conductance was studied as a function of operating temperature and oxygen concentration using certified bottles with oxygen diluted in nitrogen. Electrical characterization was carried out by volt-amperometric technique at constant voltage, equal to 1 V, measuring the current through a picoammeter.

XPS (X-ray photoelectron spectroscopy) data were collected with a Physical Electronics 5500 spectrometer at a pressure of 6 × 10^{-9} Torr. Aluminum Kα X-rays were produced with an energy of 1486.6 eV and natural line width of 0.9 eV. All the spectra were fitted to reach the right carbon position (284.5 eV).

The spectra were fitted with Gaussian−Lorentzian functions (80−20% respectively) and considering a Shirley baseline. Analyses were done both before and after Ar-ion sputtering for 1 min.

The cathodoluminescence measurements were carried out in a Gatan XiCLone system attached to a JEOL JSM-820 scanning electron microscope. The collected luminescence was analyzed by a 300-line grating monochromator and was detected by a Peltier cooled CCD, with a spectral range from 200 to 1200 nm. The system is equipped with a cryostat that allows low temperature measurements. The measurements were carried out at liquid nitrogen temperature ($\sim$80 K). The excitation beam conditions were 20 kV for accelerating voltage and $\sim$40 nA for beam current.

Electron paramagnetic resonance (EPR) spectra were recorded by using a conventional Bruker EMX spectrometer operating at the X band frequency and magnetic field modulation of 100 kHz, with a microwave power of 5 mW and a modulation amplitude of 10 or 3 G. The g values were calculated by comparison with diphenylpicrylhydrazyl (DPPH) ($g = 2.0036$). Powdered samples were put into a quartz apparatus suitable for both gas flow interaction and EPR measurements. CO was used as a probe molecule. The following gas treatment sequence was adopted: (1) SnO$_2$, previously heat-treated at 500 °C, as described before, was treated in dry air stream (30 cm^{3}min^{-1}) for 90 min at 400 °C; (2) CO(600 ppm)/Ar mixture was passed over SnO$_2$ (30 cm^{3}min^{-1}) for 30 min at the same temperature. After each thermal gas treatment, the samples were quenched at room temperature (in about 5 min), and EPR spectra were recorded at 113 K, under the same atmosphere.

The first-principles methodology used in the present work was based on density functional theory[7,8] (DFT) as implemented in the SIESTA code.[9,10] We used the generalized gradient approximation (GGA) for the exchange-correlation functional (PBE96)[11] and norm-conserving Troullier−Martins pseudopotentials.[12] Solutions of the Kohn−Sham equations were expanded as linear combinations of atomic pseudo wave functions of finite range. For all atomic species, double ζ plus polarization orbital basis-sets were used. Oxygen atoms were described by six valence electrons, nitrogen by five, and tin atoms by four plus the corresponding pseudopotential ion cores. To deal with surface stability and adsorption energy calculations, we modeled all surface geometries as three dimensionally periodic slab systems, generated from the relaxed SnO$_2$−cassiterite[13] bulk unit cell, composed of five O(Sn$_2$O$_2$)O layers with a vacuum width of 12 Å between surfaces to avoid interaction between periodic images of the slabs.[14−16] This procedure was successfully used in previous work.[16−20] We set a real space mesh cutoff[9,10] of 250 Ry and a 5 × 5 × 1 Monkhorst-Pack set[21] to obtain total energies converged within 5 meV per six-atom unit cell, which is suitable for this kind of calculation.[14−16] Under these conditions, forces over atoms converged to better than 0.004 eV/Å^2. We also considered spin polarization in the total energy computations and corrected the basis set superposition error[22] (BSSE) in the calculated adsorption energies. We introduced structural relaxations by means of conjugate gradient minimization of the energy, until the forces on all the atoms were smaller than 0.04 eV/Å^2. In the relaxation of the slabs, supercell dimensions were kept constant and, as proposed by some authors, no constraints were imposed to the atomic positions within the supercell. In the slab composed of five layers, the maximum displacement of the atoms in the middle layer was as small as 0.05 Å.

Epifani et al.
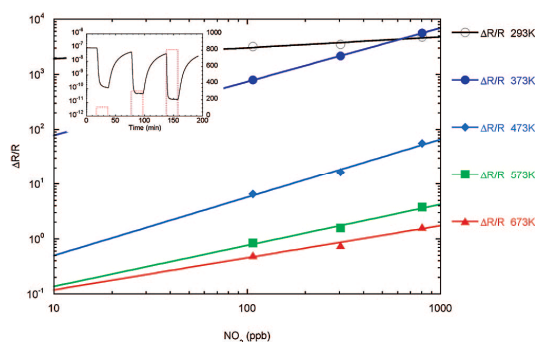
Figure 1. Calibration of SnO$_2$-based sensors to NO$_2$ at various operating temperatures. The inset shows a dynamic response curve measured at an operating temperature of 373 K.

Results

1. Review of NO$_2$ Sensing Properties. As shown in Figure 1, the main results concerning the NO$_2$ sensing properties of SnO$_2$ nanocrystals are the following[4,5] (we recall that the sensor response is defined as $(R_G - R_0)/R_0$, where R_G is the electrical resistance upon exposure to the gaseous analyte, and R_0 is the electrical resistance in pure synthetic air):

1. At 293 K, a huge response of more than 3 orders of magnitude was obtained toward as low as 100 ppb NO$_2$ concentrations.

2. At 373 K, the response decreased to about 3 orders of magnitude for the same concentration.

3. At 473 K, the response substantially dropped but still remained relatively high (about 70).

4. Beyond 473 K, the response decreases to values lower than unity.

2. The Chemical State of the Nanocrystals. (a) Conductance Measurements. Electrical characterization of the prepared nanomaterials was carried out by conductance measurements using different oxygen concentrations. These measurements were undertaken for characterizing the surface reactivity toward oxygen, since the oxygen adsorption is commonly invoked to explain the sensing mechanisms of metal oxides.[23] The results are reported in Figure 2 for SnO$_2$ nanocrystals heat-treated at 500 °C. At temperatures above 293 K, the increase in the oxygen concentration from 0 to 10% results in a remarkable conductance decrease.

The conductance drop is enhanced at higher temperatures, spanning a range of about 2 orders of magnitude. The current variation occurs upon injection of 10% O$_2$ and is more pronounced from 473 K. In this range of temperatures, ionosorption of atomic oxygen is known to be favored, while the adsorption of molecular oxygen is favored at lower temperatures.[23] We conclude that the surface reactions with ionosorbed oxygen control the electrical properties.

(b) Surface Chemical Composition by XPS. SnO$_2$ nanocrystals were analyzed by XPS both before and after Ar-ion sputtering. The survey spectra in Figure 2 show that they are chemically pure; even after sputtering no differences were seen in samples, except for the intensity of the C 1s signal. In fact, it is less than 0.5 atomic % after surface sputtering and confirms that the C presence is mainly due to adventitious surface contamination. The Cl moieties in SnO$_2$ nanocrystals disappear after the heat treatment at 500 °C. It is very important to observe that the O/Sn atomic ratio, obtained from the spectra analysis, is about 1.2, indicating a strongly reduced surface, if compared

with the theoretical ratio of 2 for SnO$_2$. The reason for the strongly reduced sample stoichiometry was suggested in the previous description of the synthesis process.[4] It appeared that during the heat treatment a carbon layer is formed at the surface of the sample, so providing a strongly reducing environment. Figure 3

(c) EPR Assessment of the Surface Reduction. The reaction of gaseous analytes with SnO$_2$ can be monitored by EPR spectroscopy in terms of the subsequent formation of paramagnetic centers. It was demonstrated[24] that the reaction of CO follows the equations:

$$CO + O_O \Leftrightarrow V_O + CO_2 \qquad (3)$$

$$V_O \Leftrightarrow V_O^\bullet + e^- \qquad (4)$$

where V_O is a *shallow* neutral oxygen vacancy, O_O an oxide anion in a regular lattice site, and $V_O^\bullet$ is a singly ionized, paramagnetic oxygen vacancy. EPR investigation was performed on nanocrystalline SnO$_2$ to detect the formation and the reactivity of such shallow defects, after thermal annealing and successive reaction with the gas. CO was used as a probe molecule, according to procedure reported in the Experimental Section, at 400 °C.

The sample heat-treated at 500 °C after the synthesis shows a very weak isotropic signal at $g = 1.91$ attributed to paramagnetic monoionized oxygen vacancies $V_O^\bullet$,[24] which do not change after further annealing in air at 400 °C (Figure 4a). After successive reaction with CO (600 ppm)/Ar at 400 °C, no new paramagnetic vacancies are formed (Figure 4b). These results do not follow the general trends observed in other work.[24] Residual $V_O^\bullet$, already present in the 500 °C heat-treated SnO$_2$ and after further treatment at 400 °C in air, are not reactive and are more likely located in the lattice far from the surface. The difficult formation of further paramagnetic species after treatment with CO at 400 °C is closely related to the peculiar surface chemistry evident in our samples. In particular, the absence of CO interaction with the sample surface is in agreement with the presence of a strongly reduced surface, as demonstrated by the electrical, XPS, CL, and simulation results: further reduction by CO is hindered for thermodynamic reasons, implying an energetically unlikely surface configuration.

(d) Investigation of the Surface Structure: Cathodoluminescence Measurements on the SnO$_2$ Nanocrystals. For investigating the surface states in low-conductive systems, cathodoluminescence (CL) is one of the best suited techniques.[17,18,25] It was shown in previous work[17] that the visible CL spectrum of SnO$_2$ is dominated by a broad signal composed of four different contributions centered around 1.90, 2.20, 2.37, and 2.75 eV (from now on I, II, III, and IV, respectively). On the basis of DFT calculations, these bands were assigned to radiative recombinations from the minimum of the conduction band and the SnO$_2$-intrinsic bulk shallow levels toward intragap states near the top of the valence band corresponding to surface oxygen vacancies. For the most common low index surfaces of SnO$_2$−cassiterite (namely (110), (100), (101), and (001)), the calculations revealed two families of states corresponding to two different angles between the oxygen site and the first neighboring tin atoms. Following the usual notation for the SnO$_2$(110)−cassiterite surface (which is the most stable, abundant, and deeply studied facet), the bands I and II were related to bridging oxygen vacancies (O$_{BridgVac}$) whereas the bands III and IV were attributed to in-plane oxygen vacancies (O$_{InPlaneVac}$). These results are summarized in Figure 5.

This model explained the CL spectra of a full set of SnO$_2$ nanomaterials obtained by different synthetic methods and
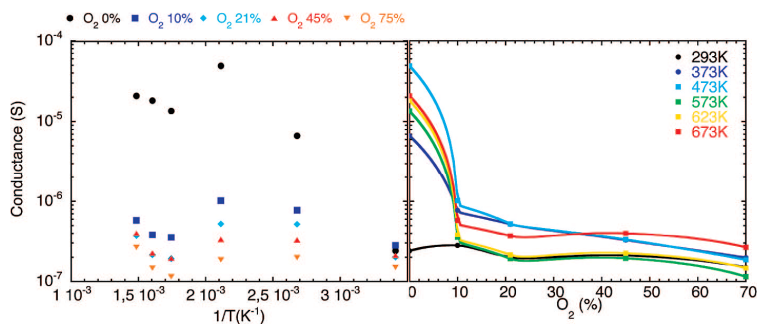
Figure 2. Electrical conductance data of SnO$_2$ nanocrystals as a function of $1/T$ for various oxygen concentrations (left), and the same data plotted as a function of the oxygen concentrations (right).
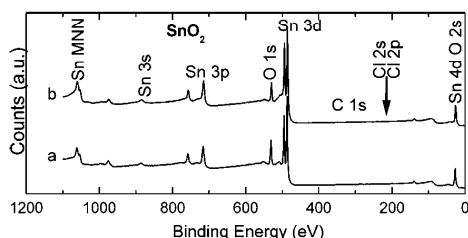
Figure 3. XPS survey spectra of SnO$_2$ nanocrystals heat-treated at 500 °C, measured on (a) the as-prepared sample and (b) after sputtering with Ar^{3+} ions. The spectra have been vertically shifted for clarity.
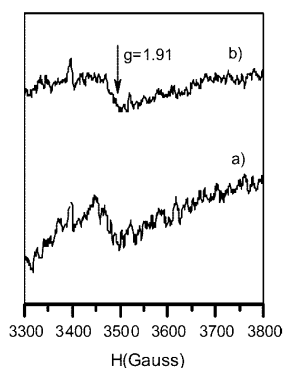
Figure 4. EPR spectra measured on SnO$_2$ nanocrystals under the following conditions: (a) after annealing in air at 400 °C; (b) after treatment with CO(600 ppm)/Ar at 400 °C.

Figure 5. (Top) Slab model of the SnO$_2$−cassiterite (110) surface. Bridging and in-plane oxygen sites are identified. (Bottom) Schematic representation of the intragap levels of SnO$_2$ corresponding to bulk shallow levels and oxygen vacancies at the surface. For clarity, energy zero has been set at the top of the valence band (VBM). Recombinations compatible with the CL spectra are shown.

processing.[17] We then applied the model to our samples. At the top of Figure 6, the CL spectra of the SnO$_2$ nanocrystals dried at 80 °C are shown, together with the fitting of the band by the four components previously described. In the nanocrystals heat-treated at 500 °C, the CL signal shape undergoes modifications due to the relative intensity changes of the single components, in particular the components I and II grow in intensity with respect to the components III and IV (Figure 6, bottom panel). According to the previous model, the change corresponds to an increase in the radiative recombination involving the O$_{BridgVac}$⁻ related state. Thus, it appears that both types of surface oxygen vacancies are present in the as prepared (dried at 80 °C) sample and that the thermal treatment at 500 °C mainly produced O$_{BridgVac}$.

Ab initio thermodynamics[19] helped us clarify why the generation of O$_{BridgVac}$ is favored, by discussing the energetic

requirements for the oxygen vacancy production at 500 °C in synthetic air. We followed the methodology described by Reuter and Scheffler[26] to elucidate the most favorable surface configuration in equilibrium with the oxygen content in air at a given pressure and temperature (or, equivalently, a given oxygen chemical potential μ_O). This methodology consists of applying a minimum energy criterion to the surface energy versus μ_O plots of every relevant surface configuration. In Figure 7 we report these plots for the stoichiometric, the O$_{Bridg}$ reduced and O$_{InPlane}$ reduced surface terminations. The most stable surface configuration after heat treatment at 500 °C, and therefore the most likely, corresponds to a reduced surface due to O$_{BridgVac}$ generation. This prediction agrees with previous theoretical[27,28] and experimental work[29] in which O$_{BridgVac}$ generation was observed at temperatures ranging from 225 to 525 °C.

(e) Summary: a Strongly Reduced SnO$_2$ Surface with Well Defined Defects Distribution. The results presented in the previous sections concur to define the picture of a strongly reduced nanocrystal surface, with an oxygen substoichiometry dictated by the heat treatment step. The substoichiometry is

Epifani et al.
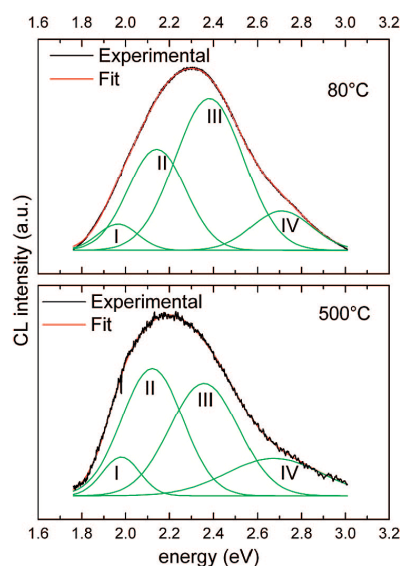
Figure 6. CL spectra measured on SnO_2 nanocrystals heated at the indicated temperatures, together with the fitting (green bands) with the components described in the text.
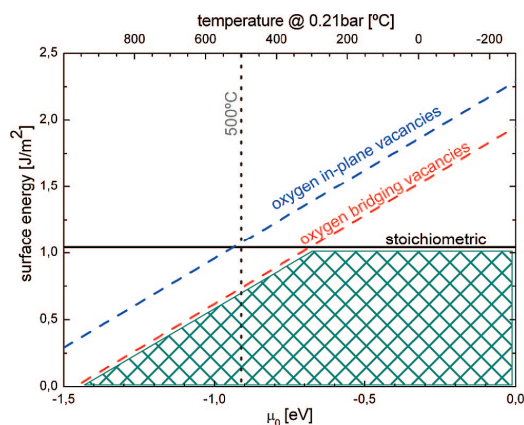
Figure 7. Surface free energies for three different terminations of the $SnO_2(110)$ surface as a function of the oxygen chemical potential. The top axis shows the corresponding O_2 gas temperature for synthetic air equivalent conditions (i.e., oxygen partial pressure of ~0.21 bar). Shaded area is limited by the minimum energy configuration at different air temperatures. At 500 °C (the experimental thermal treatment temperature) the most energetically favorable configuration is the surface reduction by generation of surface bridging vacancies ($O_{BridgVac}$).

directly indicated by the XPS results, while EPR data show that the surface reduction has occurred to a remarkable extent, so that further reduction is not allowed. The electrical conductance data (Figure 2) show that the reaction of gaseous oxygen with the nanocrystal surface is extremely favored. We have already mentioned that the data imply a prevalence of oxygen ionosorption. Now, this result can be interpreted as an indication of the adsorbing activity of the oxygen vacancies. In particular, it is known that bridging oxygen vacancies can strongly bond oxygen species.[30] Finally, the CL data allowed a careful identification of the involved oxygen vacancies, present as both bridging and

in plane species. The former are generated in the heat-treated nanocrystals, for thermodynamic reasons.

Discussion

The main question to answer is whether it is possible to find a correlation between the properties shown in sections 1 and 2, related to NO_2 sensing, and the surface chemical state. The possible link is suggested by the NO_2 sensing mechanism reported in the introduction, which implies NO_2 adsorption and subsequent increase of the electrical resistance. Because the oxygen vacancies make the SnO_2 surfaces strongly amenable to oxygen ionosorption, it is necessary to ask whether the oxygen vacancies may influence also the NO_2 adsorption and what is the effect of the adsorption onto the charge distribution in the nanocrystals. This task was accomplished by DFT simulation of the NO_2 adsorption onto SnO_2 surfaces in the presence of variable concentration of oxygen vacancies.

First of all, it is known from previous work on the simulation of temperature-programmed desorption (TPD) data[19,20] that NO_2 tends to adsorb onto $SnO_2(110)$ $O_{InPlane}$ and $O_{BridgVac}$ sites. The former site was found to be related to the low temperature TPD band (from 50 to 300 °C) while the latter site was responsible for the TPD signal from 350 to 500 °C. The very large responses to NO_2 at room temperature or 100 °C, reported in the section 1 of the Results, would then indicate that the sensing-promoting sites are the $O_{InPlane}$ vacancies. On the other hand, we have shown in the previous sections that the heat treatment at 500 °C stimulates the generation of vacancies related to O_{Bridg} sites. In order to obtain further insight into the sensing performances, it is necessary to solve this apparent contradiction. Hence, we studied the influence of the reduction percentage on the surface−adsorbate interaction from first principles. For the most relevant adsorption configurations reported previously,[19,20] and detailed in the Supporting Information, we calculated both the strength of the adsorption (the adsorption energy E_{ads}) and the resulting charge transfer ($\Delta q(NO_2)$) between the NO_2 molecule and the substrate. To model the changes in the surface reduction percentage, we removed from the atomistic models an increasing number of O_{Bridg}. It can be shown that only about a 10% of the available adsorption sites are effectively occupied by NO_2[31] (this is justified by the Weisz limitation,[32] which takes into account the electrostatic repulsion forces among the adsorbed species). To reach equivalent occupancies, we used a 3 × 3 supercell. With this model, occupancies of 11% onto $O_{BridgVac}$ were studied. At every reduction percentage all non-symmetry-equivalent vacancy distributions around the adsorbate were considered.

In Figure 4 we report the computed E_{ads} and $\Delta q(NO_2)$ for adsorption at lower temperatures (NO_2 onto an $O_{InPlane}$ site). Exothermic adsorption energies are assumed as negative E_{ads} values, and charge transfers refer to the adsorbate (positive $\Delta q(NO_2)$ means electron capture by the NO_2 molecule).

Thus, more negative E_{ads} energy means stronger adsorption, and a higher $\Delta q(NO_2)$ implies a bigger charge captured by NO_2. The calculations predict that reduction slightly favors the adsorption (maximum of a 20% in energy) and *almost doubles* the charge transfer to the adsorbate. From the point of view of the gas response, the effectiveness of the sensing sites is determined by (1) the continuous adsorption and desorption processes (which are determined by the analyte concentration, the energetics of the interaction, and the working temperature), and (2) the net charge exchange between the metal oxide and adsorbate (which determines the electrical response). Our results demonstrate that the surface reduction influences both the energy exchange and the charge transfer between surface and analyte.

NO$_2$ Sensing Properties of SnO$_2$ Nanocrystals
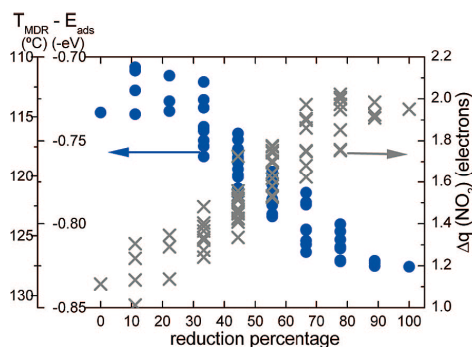
Figure 8. Influence of the reduction percentage (only due to O$_{BridVac}$ generation) on the energetics and charge transfers of NO$_2$ adsorption onto an O$_{InPlane}$ site[19] at the SnO$_2$(110) surface. The adsorption energy (E_{ads}) and the corresponding maximum desorption rate temperature (T_{MDR}) are represented in the left axis. T_{MDR} were calculated by solving the Redhead[33,34] equation with the experimental conditions reported elsewhere.[35] The charge transferred to the adsorbate Δq(NO$_2$) was estimated by the usual Mulliken's population analysis of the molecule atoms before and after the adsorption.

Concretely, the effect of removing O$_{Bridg}$ atoms from the SnO$_2$ (110) surface on the NO$_2$ adsorption onto O$_{InPlane}$ sites is a slight modification of the desorption temperatures and a strong increase of the charge trapped by this adsorbate. A strong influence on the sensor performance by the O$_{BridgVac}$ generation (by thermally treating the SnO$_2$ nanoparticles) then appears. For completeness, in the Supporting Information a plot similar to Figure 8 is reported but related to the adsorption onto the O$_{BridgVac}$ sites. Effects similar to those observed for the O$_{InPlane}$ sites are observed, despite the O$_{BridgVac}$ sites that are active at higher operating temperatures, as mentioned above.

Comparison with Other Work. The importance of the surface oxygen vacancies is further highlighted by comparison with other work. The computational approach to the understanding of the adsorption and gas-sensing properties of SnO$_2$ is well-known,[36] and recent results in the case of NO$_2$ sensing have been published.[15] In such work, the authors have extensively studied the adsorption of NO$_2$ onto various sites and in different configurations. The main results were the following: on *defect-free* surfaces, current drop by NO$_2$ adsorption is expected, due to NO$_2$ interaction with surface Sn atoms, and in particular upon formation of a bridging nitrate groups. When oxygen vacancies are introduced in the model, an enhanced conductance drop is expected upon interaction of oxygen with the *oxygen vacancies* and the neighboring Sn atoms, and the same behavior is expected for NO$_2$. In this work, we reported, both from an experimental and computational point of view, a significant current drop upon interaction of the SnO$_2$ nanocrystals with NO$_2$. Moreover, in Figure 2 a similar, large conductance drop is reported for interaction of the SnO$_2$ sample with oxygen. The observed trends are in agreement with results from ref 15 (where the authors simulate vacancies on (10-1) surfaces). This comparison shows that a careful computational approach is fundamental in unraveling the complex sensing phenomena. On the other hand, the distance of the computational models from the real operating conditions requires the simulation work to be constantly backed up by well-defined experimental data, in order to have a constant check of how much realistic the computational results can be.

Conclusions

The NO$_2$ sensing properties of SnO$_2$ nanocrystals have been investigated by comparing the experimental surface chemistry with the DFT modeling of the adsorption properties. It was found that the heat-treatment conditions (500 °C in air) favored the formation of surface oxygen vacancies, as demonstrated by electrical, XPS, EPR, and cathodoluminescence (CL) measurements and the CL-related DFT modeling. In particular, an increase of the bridging oxygen vacancies was observed, and the surface reduction effect on the NO$_2$ adsorption was studied by DFT modeling. It appeared that the interaction of NO$_2$ with the surface occurs through the oxygen vacancy sites, and that the presence of bridging oxygen vacancies strongly enhances the charge transfer from the surface to NO$_2$. Thus the achievement of remarkable gas-sensing properties was concluded to be not only a function of the small oxide grain but also of suitable surface-reception properties, which in the case of NO$_2$ we have related to oxygen vacancies.

Supporting Information Available: Plots of the relevant adsorption configurations for NO$_2$ and plot of the influence of the reduction percentage (only due to OBrigVac generation) on the energetics and change transfers of NO$_2$ adsorption onto an OBrigVac site. This material is available free of charge via the Internet at http://pubs.acs.org.

References and Notes

(1) (a) Chaonan Xu, C.; Tamaki, J.; Miura, N.; Yamazoe, N. *Sens. Actuators B* **1991**, *3*, 147. (b) Yamazoe, N. *Sens. Actuators B* **1991**, *5*, 7.

(2) (a) Vuong, D. D.; Sakai, G.; Shimanoe, K.; Yamazoe, N. *Sens. Actuators B* **2005**, *105*, 437. (b) Ruiz, A. M.; Cornet, A.; Shimanoe, K.; Morante, J. R.; Yamazoe, N. *Sens. Actuators B* **2005**, *108*, 34. (c) McCue, J. T.; Ying, J. Y. *Chem. Mater.* **2007**, *19*, 1009. (d) Chiu, H.-C.; Yeh, C.-S. *J. Phys. Chem. C* **2007**, *111*, 7256. (e) Erades, L.; Grandjean, D.; Nayral, C.; Soulantica, K.; Chaudret, B.; Menini, P.; Parret, F.; Maisonnat, A. *New J. Chem.* **2006**, *7*, 1026.

(3) (a) Comini, E. *Anal. Chim. Acta* **2006**, *568*, 28; this reference includes an exhaustive list of 1-D based gas sensors. (b) Kolmakov, A.; Zhang, Y.; Cheng, G.; Moskovits, M. *Annu. Rev. Mater. Res.* **2004**, *34*, 151. (c) McAlpine, M. C.; Ahmad, H.; Wang, D.; Heath, J. H. *Nat. Mater.* **2007**, *6*, 379. (d) Polleux, J.; Gurlo, A.; Barsan, N.; Weimar, U.; Antonietti, M.; Niederberger, M. *Angew. Chem., Int. Ed.* **2006**, *45*, 261. (e) Rout, C. S.; Govindaraj, A.; Rao, C. N. R. *J. Mater. Chem.* **2006**, *16*, 3936. (f) Du, N.; Zhang, H.; Chen, B.; Ma, X.; Liu, Z.; Wu, J.; Yang, D. *Adv. Mater.* **2007**, *19*, 1641.

(4) Epifani, M.; Díaz, R.; Arbiol, J.; Comini, E.; Sergent, N.; Pagnier, T.; Siciliano, P.; Faglia, G.; Morante, J. R. *Adv. Funct. Mater.* **2006**, *16*, 1488.

(5) (a) Epifani, M.; Comini, E.; Diaz, R.; Arbiol, J.; Siciliano, P.; Sberveglieri, G.; Morante, J. R. *Sens. Actuators B* **2006**, *118*, 105. (b) Epifani, M.; Diaz, R.; Arbiol, J.; Comini, E.; Sergent, N.; Pagnier, T.; Siciliano, P.; Faglia, G.; Morante, J. R. *Sens. Actuators B* **2007**, *126*, 163. (c) Epifani, M.; Comini, E.; Arbiol, J.; Pellicer, E.; Siciliano, P.; Faglia, G.; Morante, J. R. *J. Phys. Chem. C* **2007**, *111*, 13967. (d) Epifani, M.; Arbiol, J.; Pellicer, E.; Comini, E.; Siciliano, P.; Faglia, G.; Morante, J. R. *Cryst. Growth Des.* **2008**, *8*, 1774.

(6) Yamazoe, N.; Shimanoe, K. *Sens. Actuators B* **2008**, *128*, 566.

(7) Hohenberg, P.; Kohn, W. *Phys. Rev.* **1964**, *136*, B864.

(8) Kohn, W.; Sham, L. J. *Phys. Rev.* **1965**, *140*, A1133.

(9) Ordejón, P.; Artacho, E.; Soler, J. M. *Phys. Rev. B* **1996**, *53*, R10441.

(10) Soler, J. M.; Artacho, E.; Gale, J. D.; García, A.; Junquera, J.; Ordejón, P.; Sánchez-Portal, D. *J. Phys.: Condens. Matter* **2002**, *14*, 2745.

(11) Perdew, J. P.; Burke, K.; Ernzerhof, M. *Phys. Rev. Lett.* **1996**, *77*, 3865.

Epifani et al.

(12) Troullier, N.; Martins, J. L. *Phys. Rev. B* **1991**, *43*, 1993.

(13) Bolzan, A. A.; Fong, C.; Kennedy, B. J.; Howard, C. J. *Acta Crystallogr., Sect. B: Struct. Sci.* **1997**, *53*, 373.

(14) Oviedo, J.; Gillan, M. J. *Surf. Sci.* **2002**, *513*, 26.

(15) Maiti, A.; Rodriguez, J. A.; Law, M.; Kung, P.; McKinney, J. R.; Yang, P. *Nano Lett.* **2003**, *3*, 1025.

(16) Batzill, M.; Katsiev, K.; Burst, J. M.; Diebold, U.; Chaka, A. M.; Delley, B. *Phys. Rev. B* **2005**, *72*, 165414.

(17) Prades, J. D.; Arbiol, J.; Cirera, A.; Morante, J. R.; Avella, M.; Zanotti, L.; Comini, E.; Faglia, G.; Sberveglieri, G. *Sens. Actuators B* **2007**, *126*, 6.

(18) Prades, J. D.; Cirera, A.; Morante, J. R.; Cornet, A. *Thin Solid Films* **2007**, *515*, 8670.

(19) Prades, J. D.; Cirera, A.; Morante, J. R. *J. Electrochem. Soc.* **2007**, *154*, H675.

(20) Prades, J. D.; Cirera, A.; Morante, J. R.; Pruneda, J. M.; Ordejón, P. *Sens. Actuators B* **2007**, *126*, 62.

(21) Monkhorst, H.; Pack, J. *Phys. Rev. B* **1976**, *13*, 5188.

(22) Boys, S. F.; Bernardi, F. F. *Mol. Phys.* **1970**, *19*, 553.

(23) Barsan, N.; Schweizer-Berberich, M.; Gopel, W. *Fresenius J. Anal. Chem* **1999**, *365*, 287, and references therein.

(24) (a) Canevali, C.; Chiodini, N.; Di Nola, P.; Morazzoni, F.; Scotti, R.; Bianchi, C. L. *J. Mater. Chem* **1997**, *7*, 997. (b) Canevali, C.; Chiodini, N.; Morazzoni, F.; Scotti, R. *J. Mater. Chem.* **2000**, *10*, 773. (c) Armelao, L.; Barreca, D.; Bontempi, E.; Morazzoni, F.; Canevali, C.; Depero, L. E.; Mari, C. M.; Ruffo, R.; Scotti, R.; Tondello, E. *Appl. Magn. Reson.* **2002**, *22*, 89.

(25) (a) Huang, M. H.; Wu, Y.; Feick, H.; Tran, N.; Weber, E.; Yang, P. *Adv. Mater.* **2001**, *13*, 113. (b) Yao, B. D.; Chan, Y. F.; Wang, N. *Appl. Phys. Lett.* **2002**, *81*, 757.

(26) Reuter, K.; Scheffler, M. *Phys. Rev. B* **2002**, *65*, 035406.

(27) Oviedo, J.; Gillan, M. J. *Surf. Sci.* **2000**, *467*, 35.

(28) Duan, Y. *Phys. Rev. B* **2008**, *77*, 045332.

(29) (a) Cox, D. F.; Fryberger, T. B.; Semancik, S. *Phys. Rev. B* **1988**, *38*, 2072. (b) Cox, D. F.; Fryberger, T. B.; Semancik, S. *Surf. Sci.* **1990**, *227*, L105.

(30) Batzill, M.; Diebold, U. *Prog. Surf. Sci.* **2005**, *79*, 47. in particular pp. 122−124.

(31) Hernandez-Ramirez, F.; Prades, J. D.; Tarancon, A.; Barth, S.; Casals, A.; Jimenez-Diaz, R.; Pellicer, E.; Rodriguez, J.; Morante, J. R.; Juli, M. A.; Mathur, S.; Romano-Rodriguez, A. *Adv. Funct. Mater.* **2008**, *18*, 2990. (, DOI: 10-1002/adfm.200701191).

(32) Weisz, P. B. *J. Chem. Phys.* **1953**, *21*, 1531.

(33) Desjonquères, M. C.; Spanjaard, D. *Concepts in Surface Physics*, 2nd ed.; Springer: Berlin, 1996.

(34) Zhdanov, V. P.; Kasemo, B. *Surf. Sci.* **1998**, *415*, 403.

(35) Leblanc, E.; Perier-Camby, L.; Thomas, G.; Gibert, R.; Primet, M.; Gelin, P. *Sens. Actuators B* **2000**, *62*, 67.

(36) Batzill, M.; Diebold, U. *Prog. Surf. Sci.* **2005**, *79*, 47, in particular pp 120−132 and references therein.

SUPPORTING INFORMATION

The role of surface oxygen vacancies in the NO$_2$ sensing properties of SnO$_2$ nanocrystals

Mauro Epifani,[,1] Joan Daniel Prades,[2] Elisabetta Comini,[3] Eva Pellicer,[2] Manuel Avella,[4] Pietro Siciliano,[1] Guido Faglia,[3] Albert Cirera[2] and Joan R. Morante[2]*

[1]Consiglio Nazionale delle Ricerche - Istituto per la Microelettronica ed i Microsistemi (C.N.R.-I.M.M.), via Monteroni, I-73100 Lecce, Italy;

[2]EME/XaRMAE/IN[2]UB, Departament d'Electrònica, Universitat de Barcelona, C. Martí i Franquès 1, E-08028 Barcelona, Spain;

[3]CNR-INFM and Dip. Chimica e Fisica per l'Ingegneria e i Materiali, SENSOR, Università di Brescia, via Valotti 9, Brescia, Italy;

[4]Departamento de Física de la Materia Condensada, Universidad de Valladolid, Paseo del Prado de la Magdalena, Valladolid, Spain
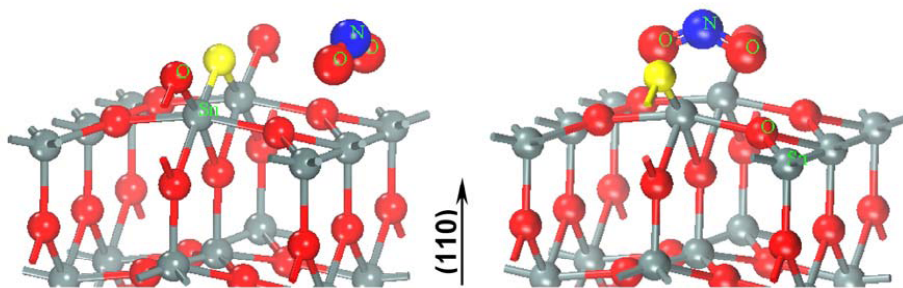
Figure S1: Most relevant adsorption configurations for modeling the NO$_2$ adsorption onto SnO$_2$(110) surface. Left: NO$_2$ adsorption onto O$_{InPlane}$ site. Right: NO$_2$ adsorption onto O$_{BridgVac}$ site. In each case, the type of atoms which were removed to model the surface reduction effect (O$_{Bridge}$ only) are highlighted in yellow.

1
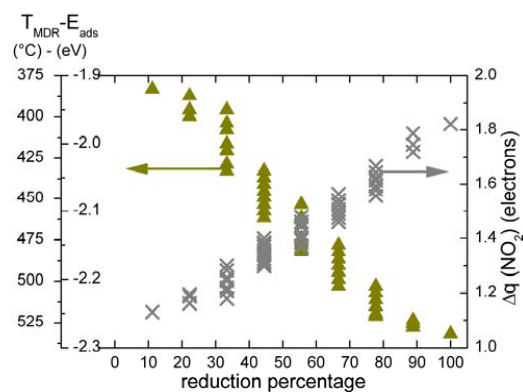
Figure S2 Influence of the reduction percentage (only due to $O_{BrigVac}$ generation) on the energetics and charge transfers of NO_2 adsorption onto an $O_{BrigVac}$ site[19] at the $SnO_2(110)$ surface. The adsorption energy (E_{ads}) and the corresponding maximum desorption rate temperature (T_{MDR}) are represented in the left axis. T_{MDR} were calculated by solving the Redhead[30-31] equation with the experimental conditions reported elsewhere.[32] The charge transferred to the adsorbate $\Delta q(NO_2)$ was by the usual Mulliken's population analysis of the molecule atoms before and after the adsorption.

2

4.3.2 Summary of Results

Unit 3.a   Photoactivated detection of oxidizing molecules

- The results presented in *Paper 11* demonstrate that UV illumination of tin oxide nanowires can be used to enhance their response towards oxidizing gaseous species (like NO_2) at room temperature. In addition to this, this work revealed that the final performance of these devices is strongly influenced by the flux and energy of impinging photons, but under the appropriate illumination conditions, responses comparable with those obtained with resistively heated sensors can be obtained, enabling their use in manifold early-warning applications. This result opens the door to the development of conductometric gas sensors operating at room temperature with a number of advantages, for example, in applications in explosive environments. The analysis of the power needed to operate these devices with Light Emitting Diodes indicates that it is comparable to the power requirements of state-of-the-art microheaters.

- The fact that light induces a recovery of the baseline after exposure to NO_2 suggests that photons play an important role in the desorption of NO_2 molecules form the surface of SnO_2, probably via band-to-band photoexcited pairs. However, to explain the increase in the response, other effects must be taken into account such as the competition with other reactive gaseous molecules present during the measurements (like the oxygen in air). These assumptions are compatible with the results about the NO_2 interaction with the surface of SnO_2 presented in *Unit 1.a*.

- The here–proposed model is based on the competition between the oxygen molecules in air and the oxidizing target gases (NO_2 in this case) for the same adsorption sites (*Paper 12*). The quantitative agreement with the experiments, demonstrates that it is possible to adjust the steady balance of this competition by tuning the photons' flux and energy and thus, controlling the gas response. This explains the role of photons in this type of sensors and paves the way to the development of low consumption conductometric gas sensors operated at room temperature. From the fundamental point of view this finding goes beyond the previous qualitative and vague descriptions of this phenomena available in the literature.

Unit 3.b   Detection of surface oxygen vacancies with luminescence analysis

- The results presented so far have in common the importance of the arrangement of the oxygen atoms at the surface of MOX nanowires, and specially the surface oxygen vacancies. The study with *ab inito* methods of the intragap electron states associated to these vacancies indicates that they are compatible with the recombination energies of the visible luminescence of MOXs.

- Calculations demonstrate that the energetic position of these levels depended on the geometry of the surface oxygen vacancies and therefore different luminescent bands must be exclusively related to specific oxygen vacancy geometries at the surface. This proposal stands for different MOX like SnO_2 (*Paper 13*) and ZnO (*Paper 14*). We confirmed the validity of our proposal with full series of independently treated samples. Recently, our results are being supported by the works of other authors that are reaching to similar conclusions [a,b,c,d].

- The utility of this experimental tool to analyze the surface termination of MOXs materials and predict their gas sensing performance was also demonstrated. SnO_2 nanoparticles of few nanometers in radii were thermally annealed to produce surface oxygen vacancies in order to enhance their response to gases (NO_2) (*Paper 15*). The analysis of the luminescence allowed tracking the generation of different types of vacancies. This materials design process was directed by the results presented in the previous units and it is an example of how to utilize *in silico* design of functional materials.

[a] F. Trani, M. Causà, D. Ninno, G. Cantele, V. Barone, "Density functional study of the oxygen vacancies at the SnO_2 surface and subsurface sites" Phys. Rev. B **77**, 245410 (2008).

[b] S. Letteri, A. Setaro, C. Baratto. E. Comini, G. Faglia, G. Sverveglieri, P. Maddalena, *"On the mechanism of photoluminescence quenching in tin dioxide by NO_2 adsorption"* New. J. Phys. **10**, 043013 (2008).

[c] N. L. Marana, V. M. Longo, E. Longo, J. B. L. Martins, J. R.Sambrano, *"Electronic and structural properties of the (10-10) and (11-20) ZnO surfaces"* J. Phys. Chem. A **112**, 8958-8963 (2008).

[d] C. Ton-That, M. R. Phillips, M. Foley, S. J. Moody, A. P. J. Stampfl, *"Surface electronic properties of ZnO nanoparticles"* Appl. Phys. Lett. **92**, 261916 (2008).

[e] Z. Q. Fang, B. Claflin, D. C. Look, "Effects of annealing in N_2 ambient on traps and persistent conduction in hydrothermally grown ZnO" J. Appl. Phys. **103**, 073714 (2008).

5. Conclusions

These are the main conclusions of this Ph.D Dissertation.

1. The interaction of gaseous molecules and light with metal oxides (MOXs) has been modeled applying the *ab initio* DFT formalism and the laws that rule the charge transport, generation and recombination in semiconductors, respectively.

    1.a In the field of gas sensors, the interaction with gases of interest from the theoretical and practical points of view, like NO, NO_2 and SO2, has been studied in detail. The mechanisms that produce the conductometric responses in MOXs towards these gases have been determined. Strategies to improve these responses and experimental methods to asses the influence of the surface termination on the performance of the sensors have been proposed. Moreover, it has been demonstrated that, in addition to the mere surface effects, other bulk effects must be taken into account in order to achieve a complete modeling of the gas – MOX interactions.

1.b   In the field of UV light sensors, the key parameters that determine the magnitude of the photoresponse in the nanowires together with the facts that restrain its dynamics have been identified. This allowed analyzing in detail the persistent photoconductive states in individual nanowires.

In summary, these findings have made possible to advance in the understanding of the functioning of these devices.

2.   Experimental tools and devices conceived to retrieve to the conductometric response of individual MOX nanowires in specifically designed experiments have been developed. The access to this valuable experimental scenario has allowed validating most of the conclusions and predictions obtained with the previous models.

3.   As far as the influence of the features characteristic of the nanowires in their performances as sensors is concerned, the following conclusions were reached.

3.a   On the one hand, the large surface-to-volume ratio and the surface stability of the nanowires are beneficial in gas sensing applications. The first provides higher responses by reducing the thickness of the nanowires. The second improves the stability and reversibility of this response to gases.

3.b   On the other hand, in spite of the fact that the crystalline quality of the nanowires can enhance the electrical transport and photogeneration properties, the importance of the surface effects in these nanomaterials hampers this possibility. Firstly, the electron mobility in nanowires worsens by the influence of the surface states. Second, the electric fields associated to the depleted region near the nanowires' surface (which explain the good response to gases) introduce additional charge separation phenomena that interfere with the photoresponse. In any case, strategies to reduce these surface effects and improve the performance of the nanowires as photodetectors (such as the surface passivation with PMMA) have been proposed and tested.

All in all, shows that taking advantage of the *a priori* beneficial properties of the nanowires is not straightforward, and to do so, a deeper understanding of the phenomena that take place in the nanowires is necessary.

4.   Based on the previous results, alternative methods to operate the nanowire based sensors have been conceived, implemented and tested.

   4.a   We have shown that it is possible to use controlled UV light fluxes to activate, at room temperature, the conductometric response of individual MOX nanowires towards oxidizing gases such as NO_2. A theoretical model that allows determining the optimum working conditions has been proposed. This result opens the door to the development of gas sensors operating at room temperature that may be suitable for explosive environments.

   4.b   We have also shown that it is possible to take advantage of the self-heating effect in nanowires caused by their tiny cross-section. In a controlled way, this effect allows warming the nanowires to the optimum temperature for gas detection (up to 350ºC) dissipating only few tens of microwatt. This represents not only a breakthrough in sensors miniaturization (since it is not necessary to include an external heater) but also it is a huge reduction of the power needed to operate these devices.

These results open the door and pave the way to a new generation of sensing devices based on the novel and promising properties of the nanowires.

Appendix A. Scientific Curriculum

JUAN DANIEL PRADES GARCIA
Born in April 2nd of 1982 in Barcelona, Spain.

Specialization (UNESCO codes): Electronics (3307) / Materials Science
Current position: Ph.D student at the Department of Electronics of the Universitat de Barcelona. Pursuing for the Ph.D Degree with the Dissertation *"Modelling of the Chemical and Light Interactions in Individual Metal Oxide Nanowires for Sensing Applications"*. Advisor: Dr. Albert Cirera Hernández

A.1 Academic Degrees

1. **MASTER** in NANOSCIENCE and NANOTECHNOLOGY.
    Master Thesis *"First-principles study of NO_x and SO_2 adsorption onto $SnO_2(110)$ and SnO_2 nanoparticles"*. Average qualification 9.50/10.00
    Universitat de Barcelona (Barcelona, 2007)

2. **DEGREE** in PHYSICS with final qualification of Extraordinary Award.
    Average qualification: 3.16/4.00
    Universitat de Barcelona (Barcelona, 2005)

3. **ENGINEER** in ELECTRONICS pending of Final Project
    Universitat de Barcelona (Barcelona, to be presented in June 2009)

4. BACHELOR GRADUATED with honors.
    Col·legi Casp – Sagrat Cor de Jesús, (Barcelona, 2000)

A.2 Publications

Papers in indexed journals

1. J.D. Prades, J. Arbiol, A. Cirera, J.R. Morante, A. Fontcuberta i Morral, *"Concerning the 506 cm⁻¹ band in the Raman spectrum of silicon nanowires"* Appl. Phys. Lett. **91**, 123107 (2007).

2. A. Fontcuberta i Morral, J. Arbiol, J.D. Prades, A. Cirera, J.R. Morante, *"Synthesis of Silicon Nanowires with Wurtzite Crystalline Structure by Using Standard Chemical Vapor Deposition"* Adv. Mater. **19**, 1347-1351 (2007).

3. J.D. Prades, A. Cirera, J.R. Morante, *"First-Principles Study of NO_x and SO_2 Adsorption onto $SnO_2(110)$"* J. Electrochem. Soc. **154**, H675-H680 (2007).

4. J.D. Prades, A. Cirera, J.R. Morante, J.M. Pruneda, P. Ordejón, *"Ab initio study of NOx compounds adsorption on SnO_2 surface"* Sens. Actuators B-Chemical **126**, 99-110 (2007).

5. F. Hernandez-Ramirez, J.D. Prades, A. Tarancon, S. Barth, O. Casals, R. Jimenez-Diaz, E. Pellicer, J. Rodriguez, M.A. Juli, A. Romano-Rodriguez, J.R. Morante, S. Mathur, A. Helwig, J. Spannhake, G. Mueller, *"Portable microsensors based on individual SnO_2 nanowires"* Nanotechnol. **18**, 495501 (2007). Remarks: Cover paper on December 12th of 2007 in Nanotechnology.

6. J.D. Prades, J. Arbiol, A. Cirera, J.R. Morante, M. Avella, L. Zanotti, E. Comini, G. Faglia, G. Sberveglieri, *"Defect study of SnO_2 nanostructures by cathodoluminescence analysis: Application to nanowires"* Sens. Actuators B-Chemical **126**, 6-12 (2007).

7. J.D. Prades, A. Cirera, J.R. Morante, A. Cornet, *"Ab initio insights into the visible luminescent properties of ZnO"* Thin Sol. Films **515**, 8670-8673 (2007).

8. F. Hernandez-Ramirez, J.D. Prades, A. Tarancon, S. Barth, O. Casals, R. Jimenez-Diaz, E. Pellicer, J. Rodriguez, J.R. Morante, M.A. Juli, S. Mathur, A. Romano-Rodriguez, *"Insight into the role of oxygen diffusion into the sensing mechanisms of SnO_2 nanowires"* Adv. Funct. Mater. **18**, 2990-2994 (2008).

9. J.D. Prades, A. Cirera, J.R. Morante, *"Ab initio calculations of NO_2 and SO_2 chemisorption onto non-polar ZnO surfaces"* Thin Sol. Films, submitted (2008).

10. J.D. Prades, R. Jimenez-Diaz, F. Hernandez-Ramirez, S. Barth, A. Cirera, A. Romano-Rodriguez, S. Mathur, J.R. Morante, *"Ultralow power consumption gas sensors based on self-heated individual nanowires"* Appl. Phys. Lett. **93**, 123110 (2008). Remarks: Selected for highlighted publication in the "V. Journal of Nanoscale Science & Technology" of the American Institute of Physics.

11. J.D. Prades, R. Jimenez-Diaz, F. Hernandez-Ramirez, A. Cirera, A. Romano-Rodriguez, J.R. Morante, S. Barth, P. Jun, S. Mathur, *"An experimental method to estimate of the temperature of individual nanowires"* Int. J. Nanotechnol., accepted for publication (2008).

12. J.D. Prades, R. Jimenez-Diaz, F. Hernandez-Ramirez, L. Fernandez-Romero, T. Andreu, A. Cirera, A. Romano-Rodriguez, A. Cornet, J.R. Morante, S. Barth, S. Mathur, *"Toward a systematic understanding of photodetectors based on individual metal oxide nanowires"* J. Phys. Chem. C **112**, 14639-14644 (2008). Remarks: Included in the three Most Read Papers of J. Phys. Chem. C during 2008.

13. J.D. Prades, F. Hernandez-Ramirez, R. Jimenez-Diaz, M. Manzanares, T. Andreu, A. Cirera, A. Romano-Rodriguez, J.R. Morante, "The effects of electron-hole separation on the photoconductivity of individual metal oxide nanowires", Nanotechnol. 19, 465501 (2008). Remarks: Highlighted as "Article of Interest" by Nanotechnology.

14.   M. Epifani, J.D. Prades, E. Comini, E. Pellicer, M. Avella, P. Siciliano, G. Faglia, A. Cirera, R. Scotti, F. Morazzoni, J.R. Morante, *"The role of surface oxygen vacancies in the NO$_2$ sensing properties of SnO$_2$ nanocrystals"* J. Phys. Chem. C **112**, 19540-19546 (2008).

15.   J.D. Prades, R. Jimenez-Diaz, F. Hernandez-Ramirez, S. Barth, J. Pan, A. Cirera, A. Romano-Rodriguez, S. Mathur, J.R. Morante*, "High performance UV light-operated gas sensors based on individual SnO$_2$ nanowires for room temperature applications"* Appl. Phys. Lett., submitted (2008).

16.   J.D. Prades, R. Jimenez-Diaz, F. Hernandez-Ramirez, M. Manzanares, T. Fischer, J. Pan, T. Andreu, A. Cirera, A. Romano-Rodriguez, S. Mathur, J.R. Morante, *"On the Role of the Illumination Conditions in the Performance of Room Temperature Gas Sensors Based on Individual SnO$_2$ Nanowires"* Chem. Mater., submitted (2008).

17.   M. Epifani, J.D. Prades, E. Comini, A. Cirera, P. Siciliano, G. Faglia, J.R. Morante, *"Chemoresistive sensing of light alkanes with SnO$_2$ nanocrystals: a DFT-based insight"* Phys. Chem. Chem. Phys., submitted (2008).

18.   J. Arbiol, S. Estradé, J.D. Prades, A. Cirera, F. Furtmayr, C. Stark, A. Laufer, M. Stutzmann, M. Eickhoff, M.H. Gass, A.L. Bleloch, F. Peiró, J.R. Morante, *"Triple-Twin Domains in Mg doped GaN Wurtzite Nanowires: Structural and Electronic Properties of this Zinc-Blende-like Stacking"* Crystal Growth & Design, submitted (2008).

19.   F. Hernandez-Ramirez, J.D. Prades, R. Jimenez-Diaz, A. Romano-Rodriguez, T. Fischer, S. Mathur, J.R. Morante, *"On the Properties of Individual Metal Oxide Nanowires and the Scaling Down of Chemical Sensors"*, Phys. Chem. Chem. Phys., submitted (2008).

Book chapters

20.   J.D. Prades, R. Orlando, A. Cirera, *"First-Principles Calculations of the Structural Stability of Si Nanowires"* in *"Science and Supercomputing in Europe"*, pp. 663-667, CINECA Consorzio Interuniversitario / HPC Europe (2007).

21.   J.D. Prades, A. Cirera, J.R. Morante, *"Applications of DFT Calculations to Chemical Gas Sensors: Desing and Understanding"* in *"Quantum Chemical Calculations of Surfaces and Interfaces of Materials"* (Ed. V. A. Basiuk and P. Ugliengo), chap. 13, pp. 243-288, American Scientific Publishers: Valencia CA (2008).

22.   T. Andreu, J. Arbiol, A. Cabot, A. Cirera, J.D. Prades, F. Hernandez-Ramirez, A. Romano-Rodriguez, J.R. Morante*, "Nanosensors: Controlling Transduction Mechanisms an the Nanoscale Using Metal Oxides and Semiconductors"* in *"Sensors Based on Nanostructured Materials"* (Ed. F. Arregui), chap. 5, pp. 79-129, Springer Science + Business Media (2009).

23.   F. Hernandez-Ramirez, J.D Prades, S. Barth, A. Romano-Rodriguez, S. Mathur, A. Tarancón, O. Casals, R. Jimenez-Diaz, J. Rodríguez, E. Pellicer, M.A. Juli, T. Andreu, S. Estrade, E. Rossinyol, J.R. Morante, *"Fabrication of Nanodevices Based on Individual SnO$_2$ Nanowires and Their Electrical Characterization"* in *"Metal Oxide Nanostructures and Their Applications"* (Ed. Ahmad Umar), in press, American Scientific Publishers: Valencia CA (2009).

A.3 Contributions in Conferences

- Conference: *Material Science and Technology 2007 Conference and Exhibition*
  Location: Detroit (USA) Year: 2007
  Type of contribution: **Invited**
  Authors: A. Romano-Rodriguez, F. Hernandez-Ramirez, A. Tarancon, O. Casals, J. D. Prades, J. R. Morante, S. Barth, S. Mathur
  Title: *Fabrication Strategies and Electrical Characterisation of Nanodevices Usign Focused Ion Beam Techniques*

- Conference: *12th International Meeting on Chemical Sensors (IMCS) 2008*
  Location: Columbus OH (USA) Year: 2008
  Type of contribution: **Invited**
  Authors: Hernandez-Ramirez, F.; Prades, J.D.; Jimenez-Diaz, R.; Romano-Rodriguez, A.; Morante, J.R.; Barth, S.; Mathur, S.; Helwig, A.; Spannhake, J.; Mueller, G.
  Title: *MEMS hotplates sensors based on single metal oxide nanowires*

- Conference: *Semiconductor Gas Sensors (SGS) 2008*
  Location: Zakopane (POLAND) Year: 2008
  Type of contribution: **Invited**
  Authors: Prades, J.D.; Cirera, A.;. Morante, J.R.
  Title: *Applications of atomistic calculations to chemical gas sensing*

- Conference: *Materials Science and Engineering (MSE) 2008*
  Location: Nürnberg (GERMANY) Year: 2008
  Type of contribution: **Invited**
  Authors: Romano-Rodriguez, A.; Hernandez-Ramirez, F.; Jimenez-Diaz, R.; Prades, J.D.; Casals, O.; Pellicer, E.; Tarancon, A.; Barth,S.; Mathur, S.
  Title: *Individual Metal Oxide Nanowire: Fundamental Properties and Device Applications*

- Conference: *Materials Science and Engineering (MSE) 2008*
  Location: Nürnberg (GERMANY) Year: 2008
  Type of contribution: **Invited**
  Authors: Romano-Rodriguez, A.; Prades, J.D.; Jimenez-Diaz, R.; Cirera, A.; Casals, R.; Morante, J.R.; Illa, X.; Barth, S.; Hernandez-Ramirez, F., Mathur, S.
  Title: *Individual Zinc Oxide Nanowires as UV Photodetectors*

- Conference: *Semiconductor Gas Sensors (SGS) 2008*
  Location: Zakopane (POLAND) Year: 2008
  Type of contribution: **Oral**
  Authors: Prades, J.D.; Hernandez-Ramirez, F.; Jimenez-Diaz, R.; Cirera, A.; Romano-Rodriguez, A.; Morante, J.R.
  Title: *Portable gas sensing device based on individual metal oxide nanowires*

- Conference: *IEEE Sensors 2008*
  Location: Lecce (ITALY) Year: 2008
  Type of contribution: **Oral**
  Authors: Prades, J.D.; Cirera, A.; Morante, J.R.
  Title: *Applications of atomistic calculations to chemical gas sensing*

- Conference: *IEEE Sensors 2008*
  Location: Lecce (ITALY) Year: 2008
  Type of contribution: **Oral**
  Authors: Epifani, M.; Prades, J.D.; Comini, E.; Pellicer, E.; Avella, M.; Siciliano, P.; Faglia, G.; Cirera, A.; Scotti, R.; Morazzoni, F.; Morante, J.R.
  Title: *The role of oxygen vacancies in the sensing properties of SnO_2 nanocrystals*

- Conference: *European Materials Research Society - 2006 Spring Meeting*
  Location: Nice (FRANCE) Year: 2006
  Type of contribution: **Oral**
  Authors: Prades, J. D.; Cirera, A.; Morante, J. R.; Pruneda, J. M.; Ordejón, P.
  Title: *Theoretical study of NOx compounds absorption paths over low index SnO_2 surfaces*

- Conference: *European Materials Research Society - 2006 Spring Meeting*
  Location: Nice (FRANCE) Year: 2006
  Type of contribution: **Oral**
  Authors: Prades, J. D.; Arbiol, J.; Cirera, A.; Morante, J. R.; Avella, M.; Zanotti, L.; Comini, E.; Faglia, G.; Sberveglieri, G.
  Title: *Defect study of SnO_2 nanostructures by CL analysis: application to nanowires.*

- Conference: *V International Workshop on Semiconductor Gas Sensors*
  Location: Ustrón (POLAND) Year: 2006
  Type of contribution: **Oral**
  Authors: Prades, J. D.; Cirera, A.; Morante, J. R.
  Title: *Gas sensors design from ab initio modeling: NO_x in SnO_2*

- Conference: *1st International Symposium on Transparent Conducting Oxides*
  Location: Hersonissos, Crete (GREECE) Year: 2006
  Type of contribution: **Oral**
  Authors: Prades, J. D.; Cirera, A.; Morante, J. R.
  Title: *Ab initio study of luminescent properties of ZnO*

- Conference: *European Materials Research Society - 2007 Spring Meeting*
  Location: Strasbourg (FRANCE) Year: 2007
  Type of contribution: **Oral**
  Authors: Prades, J.D.; Arbiol, J.; Cirera, A.; Morante, J.R.; Fontcuberta i Morral, A.
  Title: *In situ Raman study of laser-annealed Si nanowires.*

- Conference: *European Materials Research Society - 2007 Spring Meeting*
  Location: Strassbourg (FRANCE) Year: 2007
  Type of contribution: **Oral**
  Authors: Prades, J. D.; Cirera, A.; Avella, M.; Jiménez, J.; Morante, J. R.
  Title: *Cathodoluminescence analysis of thermal and mechanical treatment effects on SnO_2*

- Conference: *15th Annual International Conference on Composites Engineering*
  Location: Haikou (CHINA) Year: 2007
  Type of contribution: **Oral**
  Authors: Prades, J. D.; Cirera, A.; Fernández, L.; Cornet, A.; Morante, J.R.
  Title: *Modeling of the interactions of SnO_2 with NO and NO_2*

- Conference: *Materials Research Society (MRS) – Spring Meeting 2008*
  Location: San Francisco (USA) Year: 2008
  Type of contribution: **Oral**
  Authors: Prades, J.D.; Jimenez-Diaz, R.; Hernandez-Ramirez, F.; Barth, S.; Casals, O.; Tarancon, A.; Andreu, T.; Juli, M.A.; Cirera, A.; Cornet, A.; Perez-Rodriguez, A.; Mathur, S.; Romano-Rodriguez, A.; Morante, J.R.
  Title: *Extraction of the electrical parameters of individual metal oxide nanowires using two-point probing to FIB-fabricated platinum electrodes*

- Conference: *Materials Research Society (MRS) – Spring Meeting 2008*
  Location: San Francisco (USA) Year: 2008
  Type of contribution: **Oral**
  Authors: Jimenez-Diaz, R.; Hernandez-Ramirez, F.; Juli, M.A.; Prades, J.D.; Barth, S.; Casals, O.; Andreu, T.; Tarancon, A.; Morante, J.R.; Pellicer, E.; Helwig, A.; Spannhake, J.; Mueller, G.; Mathur, S.; Romano-Rodriguez, A.
  Title: *Design and Fabrication of a Portable Prototype of Gas Sensor and UV Photodetector based on Individual Semiconductor Nanowires*

- Conference: *European Materials Research Society (eMRS) – Spring Meeting 2008*
  Location: Strasbourg (FRANCE) Year: 2008
  Type of contribution: **Oral**
  Authors:Prades, J.D.; Jimenez-Diaz, R.; Hernandez-Ramirez, F.; Fernandez-Romero,L.; Andreu,T.; Cirera, A.; Romano-Rodriguez, A.; Cornet, A.; Morante, J.R.; Barth, S.; Mathur, S.
  Title: *Towards optimized photodetectors based on individual ZnO nanowires*

- Conference: *European Materials Research Society (eMRS) – Spring Meeting 2008*
  Location: Strasbourg (FRANCE) Year: 2008
  Type of contribution: **Oral**
  Authors: Prades, J.D.; Hernandez-Ramirez, F.; Jimenez-Diaz, R.; Manzanares, M.; Cirera, A.; Romano-Rodriguez, A.; Pérez-Rodríguez, A.; Cornet, A.; Morante, J.R.
  Title: *Measuring persistent photoconductivity in individual ZnO nanowires*

- Conference: *Eurosensors 2008*
  Location: Dresden (GERMANY) Year: 2008
  Type of contribution: **Oral**
  Authors: Prades, J.D.; Jimenez-Diaz, R.; Hernandez-Ramirez, F.; Illa, X.; Andreu, T.; Cirera, A.; Romano-Rodriguez, A.; Cornet, A.; Morante, J.R.; Barth, S.; Mathur, S.
  Title: *Platform And Electronic Interface For Photo Sensor Devices Based On Individual Nanowires*

- Conference: *2nd International Sympossium on Transparent Conductive Oxides (IS-TCO)*
  Location: Hersonissos, Crete (GREECE) Year: 2008
  Type of contribution: **Oral**
  Authors: Prades, J.D.; Jimenez-Diaz, R.; Hernandez-Ramirez, F.; Fernandez-Romero, L.; Andreu, T.; Cirera, A.; Romano-Rodriguez, A.; Cornet, A.; Morante, j.R.; Barth, S.; Mathur, S.
  Title: *Strategies for the optimization of photodetectors based on individual ZnO nanowires*

- Conference: *Jornada Catalana de SuperComputació 2005*
  Location: Tarragona (SPAIN) Year: 2005
  Type of contribution: **Poster**
  Authors: Prades, J. D.; Cirera, A.; Morante, J. R.
  Title: *Propietats electròniques i vibracionals de l'SnO₂ nanoestructurat*

- Conference: *Modeling in Solid State Chemistry 2006*
  Location: Torino (ITALY) Year: 2006
  Type of contribution: **Poster**
  Authors: Prades, J.D.; Cirera, A.; Morante, J.R.; Pruneda, J.M.; Ordejón, P.
  Title: *Ab initio study of NO_x compounds adsorption on SnO_2 surface*

- Conference: *XXII Trobades Científiques de la Mediterrània*
  Location: Maó (SPAIN) Year: 2006
  Type of contribution: **Poster**
  Authors: Prades, J. D.; Arbiol, J.; Cirera, A.; Morante, J. R.; Avella, M.; Zanotti, L.;Comini, E.; Faglia, G.; Sberveglieri, G.
  Title: *Defect study of SnO_2 nanowires by cathodoluminescence analysis and ab initio modeling*

- Conference: *NanoMem Course 2008*
  Location: Patras (GREECE) Year: 2008
  Type of contribution: **Poster**
  Authors: Prades, J.D.; Hernandez-Ramirez, F.; Jimenez-Diaz, R.; Manzanares, M.; Cirera, A.; Romano-Rodriguez, A.; Pérez-Rodríguez, A.; Cornet, A.; Morante, J.R.
  Title: *Measuring and understanding persistent photoconductivity in individual ZnO nanowires*

- Conference: 12th International Meeting on Chemical Sensors (IMCS) 2008
  Location: Columbus OH (USA) Year: 2008
  Type of contribution: **Poster**
  Authors: F. Hernandez-Ramirez, J. D. Prades, R. Jimenez-Diaz, A. Romano-Rodriguez, J. R. Morante, S. Barth, S. Mathur
  Title: *Highly – sensitive gas sensors based on single SnO₂ nanowires*

- Conference: *Materials Science and Engineering (MSE) 2008*
  Location: Nürnberg (GERMANY) Year: 2008
  Type of contribution: **Poster**
  Authors: R. Jimenez-Diaz, J. D. Prades, F. Hernandez-Ramirez, O. Casals, A. Tarancon, E. Pellicer, J. Rodriguez, J. R. Morante, M. A. Juli, A. Romano-Rodriguez, S. Barth, S. Mathur, A. Helwig, J. Spannhake, G. Müller
  Title: *Single-nanowire based portable gas-sensors and photodetectors*

- Conference: *Junior Euromat 2008*
  Location: Lausanne (SWITZERLAND) Year: 2008
  Type of contribution: **Poster**
  Authors: R. Jimenez-Diaz , J.D. Prades, F. Hernandez-Ramirez, A. Romano-Rodriguez
  Title: *Characterization of Semiconductor Nanowires and Their Integration in Novel Devices*

- Conference: *ASEVA Workshop 08 - Iber Red en Micro y Nano tecnologías (Ibernam)*
  Location: Salamanca (SAPIN) Year: 2008
  Type of contribution: **Poster**
  Authors: Jimenez-Diaz, R.; Prades, J.D.; Hernandez-Ramirez, F.; Barth, S.; Casals, O.; Romano-Rodriguez, A.; Morante, J.R.; Mathur, S.
  Title: *Integration of Metal Oxide Nanowires in Electronic Devices for Gas Sensing and UV Photodetection*

A.4 Participations in Projects

Research projects

- Title of the Project: "*Sensores de gas con selectividad mejorada para componentes del Gas Natural mediante capas zeolíticas como absrobentes y filtros*"
  Project number: MAT-00-0494-P4-03
  Funded by: CICY - Comisión Interministerial de Ciencia y Tecnología (CICYT)
  Period: July 2004 - November 2004
  Main researcher: Prof. Jesús Marcos Santamaría Ramiro
  Advisor: Dr. Albert Cirera Hernàndez

- Title of the Project: "*Nano-structured solid state gas sensors with superior performances*" (NANOS4)
  Project number: MMP4-CT-2003-001528
  Program: NANO - NANOS. VIè Programa Marc. Nanotechnologies and nanosciences
  Funded by: EUUN - Unión Europea
  Main researcher: Prof. Juan Ramón Morante Lleonart
  Period: August 2005 – December 2006
  Advisor: Dr. Albert Cirera Hernàndez

- Title of the Project: "*Síntesis de nanomateriales y estudio de su interacción con diferentes gases para su aplicación en dispositivos sensores*" (MAGASENS)
  Project number: NAN2004-09380-C04
  Program: AENN - Acción Estratégica de Nanociencia y Nanotecnología
  Funded by: MEDU - Ministerio de Educación y Ciencia
  Main researcher: Dr. Alejandro Pérez Rodríguez
  Period: from August 2005
  Advisor: Dr. Albert Cirera Hernàndez

- Title of the Project: *"Materiales Nanoestructurados Avanzados como Limitadores Activos Soportados en Sensores Amperométricos de Tecnología Planar para Aplicaciones MedioAmbientales y optimización de Combustion"*
  Project number: CIT-030000-2007-36
  Funded by: MEDU - Ministerio de Educación y Ciencia
  Main researcher: Dr. Albert Cirera Hernàndez
  Period: from 2007
  Advisor: Dr. Albert Cirera Hernàndez

- Title of the Project: *"Sensores Avanzados basados en Nanoestructuras de oxidos metálicos" (n-MOSEN)*
  Project number: MAT2007-66741-C02-01
  Program: NNMA - Programa Nacional de Materiales
  Funded by: MEDU - Ministerio de Educación y Ciencia
  Main researcher: Prof. Albert Cornet Calveras
  Period: from October 2007
  Advisor: Dr. Albert Cirera Hernàndez

- Title of the Project: *"Nanowire arrays for multifunctional chemical sensors" (NAWACS)*
  Project number: NAN2006-28568-E
  Program: AENN - Acción Estratégica de Nanociencia y Nanotecnología
  Funded by: MEDU - Ministerio de Educación y Ciencia
  Main researcher: Prof. Juan Ramón Morante Lleonart
  Period: from December 2006
  Advisor: Dr. Albert Cirera Hernàndez

Contract projects with companies

- Title of the Project: *"Simulació i Modelització de Sensors de Gas"*
  Company: **Francisco Albero, S.A.**
  Project leader: Albert Cirera Hernàndez
  Period: from 2007

- Title of the Project: *"Estudi i optimització d'algorismes i arquitectures de dilució per a nous sistemes de dilució de gasos amb aplicació a calibratge d'analitzadors de gasos"*
  Company: **Gometrics, S.L.**
  Project leader: Albert Cirera Hernàndez
  Period: from 2007

A.5 Experience with Scientific Equipments and Techniques

- **Ab initio DFT** codes: SIESTA, CRYSTAL, CASTEP, ...

- **Supercomputing** facilities: *MareNostrum Supercomputer* (Barcelona Supercomputing Center - Centro Nacional de Supercomputación) and *Supercomputing Center of Catalonia facilities* (CESCA)

- Growth of nanowires with **Chemical Vapor Depositon** techniques (Dept. Electronics, Universitat de Barcelona).

- **Intrumentation for nanoelectronics** (Dept. Electronics, Universitat de Barcelona).

- Raman spectroscopy (SCT, Universitat de Barcelona)

- Scanning Electron Microscopy (SCT, Universitat de Barcelona)

- Cathodoluminescence analysis (Universidad de Valladolid)

A.6 Other Merits

Specialization courses

- MSSC School 2006 "Ab inition Modelling in Solid State Chemistry"
  Director: Prof. Roberto Dovesi (University of Torino)
  Dates: 09/03/2006 - 09/03/2006

- Summer School on Theoretical and Computational Chemistry "Introduction to electronic structure calculations using SIESTA"
  Director: Pablo Ordejón (ICMAB, CSIC)
  Dates: 06/16/2007 - 06/20/2007

- NanoMemPro - Marie Courie Action course "Nanostructured materials, membrane modeling and simulation"
  Director: V. Burganos (ICEHT-FORTH)
  Dates: 06/18/2008 - 06/27/2008
  Remarks: Attendance granted via the competitive program *"Marie Courie Actions Grants (EU-FP6)"*

Other activities

- **Founder** of *"Electronic Nanosystems, S.L."*: start-up company devoted to the development of innovative products based on nanotechnology. Year: 2008

- **Solvay Award** to the *Best Business Idea* for the project *Electronic Nanosystems*. Year: 2008

- **Guest Editor** for the Special Issue "*Nanowires for Sensing: Fundamental Mechanisms, Devices, and Prospects*" of the indexed journal *"Journal of Sensors"*. Year: 2008.

- **Member** of the *"Materials Research Society"*

Appendix B. Resum en català

Modelització de les interaccions de gasos i llum amb nanofils individuals d'òxids metàl·lics per a aplicacions com a sensors

B.1 Introducció

Els òxids metàl·lics (MOXs) són materials excel·lents per a un gran nombre d'aplicacions en el camp dels sensors [1,2]. Les seves propietats de volum es corresponen a les d'un semiconductor de banda prohibida ample, dopat per la presència de defectes puntuals intrínsecs (relacionats amb els àtoms d'oxigen) [3]. Les seves propietats de superfície estan determinades per l'existència d'estats superficials, que actuen com a centres tant acceptadors com donadors d'electrons [4], fortament influïts per la presència de molècules quimiadsorbides [5]. Aquestes propietats físiques i químiques (juntament amb el seu baix cost) els fan especialment adequats per a la detecció de la llum ultraviolada i gasos [2]. Entre aquests materials, l'òxid de zinc (ZnO) [6] i el diòxid d'estany (SnO_2) [7] han atret gran atenció en tots dos camps de la tecnologia de sensors.

Avui en dia, la disponibilitat de nanofils de MOX [8,9] i la possibilitat d'emprar-los en dispositius funcionals [10,11] obre la porta a una més profunda comprensió de les interaccions que donen lloc a la seva resposta com a sensors. Aquesta tesi està completament dedicada a la model·lització teòrica i l'avaluació experimental d'aquests

processos en nanofils individuals. L'elecció d'aquests nanomaterials ha estat motivada per les atractives característiques que presenten tant des del punt de vista de la ciència de materials i com des del punt de vista del desenvolupament de dispositius.

Motivacions des del punt de vista de la ciència de materials.

La ciència de materials està exercint un paper central en el desenvolupament de nous i millors dispositius sensors. En molts casos, aquestes millores no es basen en una estratègia d'assaig-i-error sinó que els principals avenços es veuen impulsats per una comprensió més profunda dels mecanismes i processos que donen als materials la seva funcionalitat [12]. La modelització teòrica de les propietats dels materials és la força motriu que impulsa i guia aquest coneixement. Existeix una enorme base teòrica per explicar bona part de les propietats dels materials. Des de la física de l'estat sòlid i la física de semiconductors [13] fins a la química quàntica [14], totes les teories fan certes hipòtesis sobre la morfologia, l'estructura i l'ordre dels materials que s'han de tenir en compte quan les seves prediccions es comparen amb els experiments. Dit d'una altra manera, la validació experimental de les prediccions teòriques requereix un cert control sobre les propietats estructurals dels espècimens estudiats. Els recents progressos en la síntesi d'una gran varietat de nanomaterials [15,16] i el desenvolupament de tècniques de nanomanipulació i nanocaracterització [16,17] fan possible dur a terme estudis fonamentals amb nanofils individuals que eren inimaginables fa pocs anys. A banda dels nous fenòmens relacionats amb la nanoescala [18], les propietats estructurals dels nanofils són també extraordinàries (*Figura B.1*). D'una part, els nanofils són materials monocristal·lins [8,9,15,16]. Aquesta és, precisament, una de les principals aproximacions assumides en la física de l'estat sòlid i la física de semiconductors (sòlid cristal·lí infinit amb condicions periòdiques de contorn o Teorema de Block [13]). De l'altra part, els nanofils estan delimitats per superfícies ben definides ordenades a nivell atòmic [8,9]. Com es descriu a la secció *B.5*, aquesta és la l'aproximació clau dels models atomístics que descriuen les interaccions gas-superfície.

Per tot això, la possibilitat d'estudiar un de sol d'aquests nanofils obre les portes a situacions experimentals que estan molt a la vora de les idealitzacions assumides en els models teòrics. Treure partit d'aquesta possibilitat és una de les raons que va motivar el present treball.
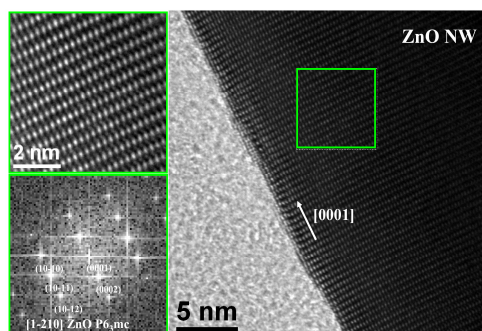
Figura B.1. Anàlisi per microscòpia electrònica de transmissió d'alta resolució (HRTEM) d'un dels nanofils de MOX emprats en aquest treball. Es pot observar com el material que forma el nanofil (ZnO) és monocristal·lí amb una rugositat superficial de menys de 2 monocapes. *Imatge cortesia del Dr. J. Arbiol.*

Motivacions des del punt de vista dels dispositius sensors.

Les tendències actuals en tecnologia de sensors porten a integrar l'electrònica de control i el material sensor en sistemes microelectrònics [19]. Això implica reduir al màxim la quantitat de material necessari per a la detecció amb la única limitació de permetre'n l'accés elèctric. En els darrers anys, la possibilitat de controlar, manipular i contactar nanofils individuals de MOXs ha fet possible estudiar nanodispositius [10,16,17,20], que estan molt a la vora dels límits d'integrabilitat. Fins a ara, l'ús de partícules i policristalls han estat les millors opcions per a emprar MOXs en dispositius funcionals de baix cost [2,21]. No obstant això, la naturalesa aleatòria de la xarxa de cristallets i la importància dels efectes de frontera de gra [3] fan molt complex l'estudi dels mecanismes de transducció amb aquests dispositius. Resultats recents han demostrat que, en les condicions apropiades [10], la conducció al llarg dels nanofils és una situació relativament senzilla que permet obtenir una millor comprensió sobre la relació entre el transport i els fenòmens de transducció (*Figura B.2*). A més a més, en aplicacions de sensat dominades pels fenòmens de superfície (com ara els sensors químics de gas), l'ús de nanomaterials en millora la resposta, a causa de la seva gran relació superfície-volum [22]. El fet de disposar de nanofils amb superfícies estables i ben definides, també en millora la estabilitat i reversibilitat de la resposta [11,22]. En aplicacions on la detecció és un procés eminentment de volum, (tals com la detecció de la llum), l'ús de nanofils monocristal·lins en millorar l'eficiència de les interaccions fotó-electró [23].

Malgrat que encara resten per resoldre molts reptes tecnològics que dificulten l'aplicació dels nanofils en sensors per a la vida real [20], l'estudi d'aquests dispositius està contribuint a desvetllar noves propietats que podran ser explotades en el futur. L'exploració d'aquestes perspectives també ha encoratjat aquest treball.
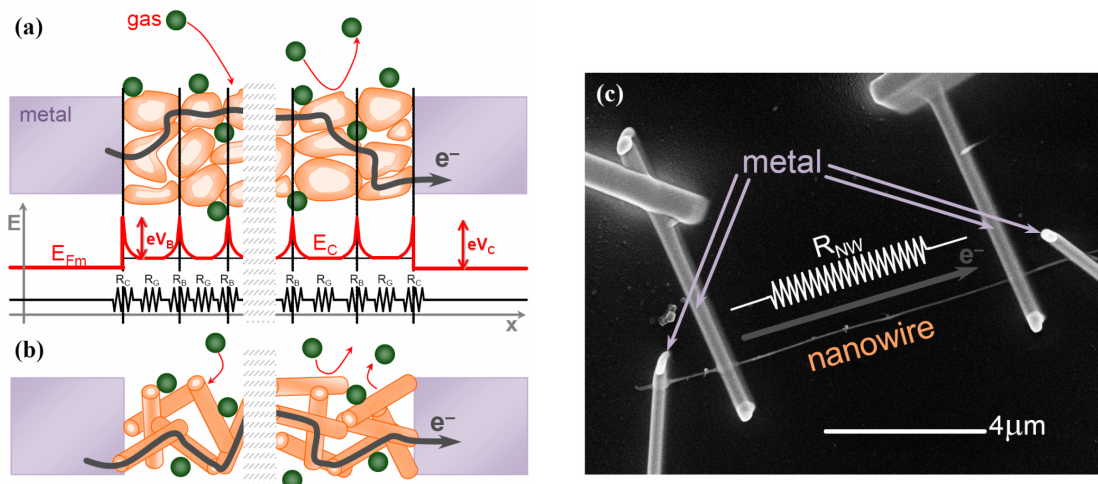
Figura B.2. Representació esquemàtica de sensors químics basats en nanopartícules i nanofils de MOX. **(a)** En el cas d'una capa de nanopartícules, el flux d'electrons ha de travessar una xarxa aleatòria de cristallets de mida i forma arbitraris. Des del punt de vista de l'energia dels electrons, aquests han de superar una sèrie de barreres de potencial. La influència del gas sobre l'alçada d'aquestes barreres determina la resposta dels sensors. Des del punt de vista elèctric, la situació és equivalent a una xarxa arbitraria de resistències que corresponen als contactes metall-semiconductor (R_C), les fronteres de gra (R_O) i els cristalls de MOX (R_G). **(b)** En el cas de grapats de nanofils, la situació és essencialment la mateixa. **(c)** En canvi, en el cas de nanofils individuals en configuració de 4 puntes, la resposta conductomètrica només és deguda als canvis en el canal de conducció al llarg del nanofil (R_{NW}). En aquestes condicions de mesura, els efectes paràsits de les interfícies metall-semiconductor s'han eliminat. *Imatge SEM cortesia de R. Jiménez-Díaz.*

Per concloure aquesta introducció, crec que les paraules d'un home savi poden resumir millor l'esperit d'aquest treball. El 29 de desembre de 1959, Richard P. Feynman, més tard guardonat amb el Premi Nobel de Física, va donar la seva famosa conferència *"There's plenty of room at the bottom"* en una trobada de l'American Physical Society a Caltech. Segons les seves pròpies paraules, *"Aconseguiríem un gran avanç en els camps de la química i la biologia si desenvolupéssim la capacitat tècnica de veure i actuar a un nivell atòmic – en qualsevol cas aquesta es una capacitat que desenvoluparem tard o d'hora".* Sóc conscient que encara estem molt lluny d'aquesta magnífica visió i només m'atreveixo a dir que aquest treball pot contribuir humilment al seu assoliment.

B.2 Guió del resum

Els **articles científics** objecte d'avaluació en aquesta tesi doctoral es llisten en la següent secció (*B.3 Llistat d'articles*)

Els **objectius** que han guiat aquest treball de tesi es resumeixen en la *B.4 Objectius.*

Els aspectes més rellevants de les **metodologies** utilitzades per l'autor durant el doctorat es presenten en la tercera secció d'aquest capítol (*B.5 Metodologia*). Això inclou informació detallada sobre els càlculs atomístics realitzats, sobre la utilització de nanopartícules i nanofils de MOX en dispositius sensors i sobre la plataforma electrònica desenvolupada per fer d'interfície amb aquests dispositius. Tots els detalls es presenten tal i com han estat publicats en 2 capítols de llibre i en 1 article científic.

Els **resultats** d'aquest treball i llur **discussió** (*B.6 Resultats i discussió*) estan organitzats en 3 unitats, que corresponen a les diferents àrees desenvolupades per l'autor durant el doctorat. Les unitats s'organitzen de manera que s'inclou una breu introducció al tema, seguidament es citen els articles publicats en revistes científiques que contenen els resultats i, finalment, es presenta un resum de les conclusions més significatives de cada unitat. Les unitats són les següents:

Unitat 1: Interacció gas - MOX. Aquesta unitat està dedicada a l'estudi dels processos químics que tenen lloc a la superfície de nanofils de MOX. Per fer-ho es van emprar càlculs *ab initio* per determinar les configuracions superficials més realistes a les temperatures típiques de treball. Posteriorment, el mateix marc teòric es va utilitzar per analitzar la seva interacció amb alguns gasos (principalment NO i NO_2) encara no explorats del punt de vista atomístic a la literatura. Aquestes conclusions teòriques es varen validar experimentalment amb nanofils individuals. Com a resultat d'aquestes troballes es van proposar i explorar altres maneres d'operar aquests sensors basats en nanofils de MOX que suposen un gran avenç quan a eficiència energètica. Els resultats d'aquesta unitat van ser publicats a 6 articles científics.

Unitat 2: Interacció llum - MOX. En aquesta unitat s'estudia la fotoresposta de nanofils de MOX en base als principis que regeixen les propietats de transport en semiconductors. La informació obtinguda en la unitat anterior sobre les interaccions superficials amb gasos, s'utilitzen per explicar els estats de fotoconductivitat persistent que limiten el rendiment dels nanofils de MOX com a detectors de llum. Tots aquests resultats han estat confirmats experimentalment i s'han publicat en 2 articles científics.

Unitat 3: Interacció simultània gas - llum - MOX. Els resultats obtinguts en les dues unitats anteriors s'utilitzen per proposar, modelitzar, implementar i validar un enfocament alternatiu per operar aquests sensors químics. Es basa en la fotoactivació de les interaccions de superfície. A més d'això, es demostra que la influència de la disposició atòmica en la superfície dels MOXs en la seva luminescència pot ser emprada per analitzar el acabat atòmic superficial d'aquest materials. Els resultats d'aquesta unitat van ser publicats en 5 articles científics.

En la última secció (*B.7 Conclusions*) es presenten les **conclusions** més significatives d'aquesta tesi doctoral.

L'autor espera sincerament que aquesta estructura, que és relativament nova en el Departament d'Electrònica de la Universitat de Barcelona, facilitarà la comprensió dels resultats que aquí es presenten.

B.3 Llistat d'articles

Només les publicacions que figuren en aquesta llista seran considerades per l'avaluació d'aquesta tesi doctoral. Podeu trobar una còpia a la **Pàgina** que s'indica. Una llista completa de les publicacions de l'autor actualitzada a desembre de 2008 es pot trobar en el seu CV (*Appendix A. Currículum científic*).

1. J.D. Prades, A. Cirera, J.R. Morante, *"Applications of DFT Calculations to Chemical Gas Sensors: Desing and Understanding"* in *"Quantum Chemical Calculations of Surfaces and Interfaces of Materials"* (Ed. V. A. Basiuk and P. Ugliengo), chap. 13, pp. 243-288, American Scientific Publishers: Valencia CA (2008). ISBN: 1-58883-138-8. **Pàgina 27**

2. T. Andreu, J. Arbiol, A. Cabot, A. Cirera, J.D. Prades, F. Hernandez-Ramirez, A. Romano-Rodriguez, J.R. Morante*, "Nanosensors: Controlling Transduction Mechanisms an the Nanoscale Using Metal Oxides and Semiconductors"* in *"Sensors Based on Nanostructured Materials"* (Ed. F. Arregui), chap. 5, pp. 79-129, Springer Science + Business Media (2009). ISBN: 978-0-387-77752-8. **Pàgina 73**

3. J.D. Prades, A. Cirera, J.R. Morante, J.M. Pruneda, P. Ordejón, *"Ab initio study of NOx compounds adsorption on SnO_2 surface"* Sens. Actuators B-Chem. **126**, 99-110 (2007). **Pàgina 141**

4. J.D. Prades, A. Cirera, J.R. Morante, *"First-Principles Study of NO_x and SO_2 Adsorption onto $SnO_2(110)$"* J. Electrochem. Soc. **154**, H675-H680 (2007). **Pàgina 147**

5. J.D. Prades, A. Cirera, J.R. Morante, *"Ab initio calculations of NO_2 and SO_2 chemisorption onto non-polar ZnO surfaces"* Thin Sol. Films, submitted (2008). **Pàgina 153**

6. J.D. Prades, R. Jimenez-Diaz, F. Hernandez-Ramirez, S. Barth, A. Cirera, A. Romano-Rodriguez, S. Mathur, J.R. Morante, *"Ultralow power consumption gas sensors based on self-heated individual nanowires"* Appl. Phys. Lett. **93**, 123110 (2008). **Pàgina 157**

7. J.D. Prades, R. Jimenez-Diaz, F. Hernandez-Ramirez, A. Cirera, A. Romano-Rodriguez, J.R. Morante, S. Barth, P. Jun, S. Mathur, *"An experimental method to estimate of the temperature of individual nanowires"* Int. J. Nanotechnol., accepted for publication (2008). **Pàgina 161**

8. F. Hernandez-Ramirez, J.D. Prades, A. Tarancon, S. Barth, O. Casals, R. Jimenez-Diaz, E. Pellicer, J. Rodriguez, J.R. Morante, M.A. Juli, S. Mathur, A. Romano-Rodriguez, *"Insight into the role of oxygen diffusion into the sensing mechanisms of SnO_2 nanowires"* Adv. Funct. Mater. **18**, 2990-2994 (2008). **Pàgina 171**

9. J.D. Prades, R. Jimenez-Diaz, F. Hernandez-Ramirez, L. Fernandez-Romero, T. Andreu, A. Cirera, A. Romano-Rodriguez, A. Cornet, J.R. Morante, S. Barth, S. Mathur, *"Toward a systematic understanding of photodetectors based on individual metal oxide nanowires"* J. Phys. Chem. C **112**, 14639-14644 (2008). **Pàgina 181**

10. J.D. Prades, F. Hernandez-Ramirez, R. Jimenez-Diaz, M. Manzanares, T. Andreu, A. Cirera, A. Romano-Rodriguez, J.R. Morante, *"The effects of electron-hole separation on the photoconductivity of individual metal oxide nanowires"* Nanotechnol. **19**, 465501 (2008). **Pàgina 193**

11. J.D. Prades, R. Jimenez-Diaz, F. Hernandez-Ramirez, S. Barth, J. Pan, A. Cirera, A. Romano-Rodriguez, S. Mathur, J.R. Morante*, "High performance UV light-operated gas sensors based on individual SnO_2 nanowires for room temperature applications"* Appl. Phys. Lett., submitted (2008). **Pàgina 207**

12. J.D. Prades, R. Jimenez-Diaz, F. Hernandez-Ramirez, M. Manzanares, T. Fischer, J. Pan, T. Andreu, A. Cirera, A. Romano-Rodriguez, S. Mathur, J.R. Morante, *"On the Role of the Illumination Conditions in the Performance of Room Temperature Gas Sensors Based on Individual SnO_2 Nanowires"* Chem. Mater., submitted (2008). **Pàgina 211**

13. J.D. Prades, J. Arbiol, A. Cirera, J.R. Morante, M. Avella, L. Zanotti, E. Comini, G. Faglia, G. Sberveglieri, *"Defect study of SnO_2 nanostructures by cathodoluminescence analysis: Application to nanowires"* Sens. Actuators B-Chem. **126**, 6-12 (2007). **Pàgina 233**

14. J.D. Prades, A. Cirera, J.R. Morante, A. Cornet, *"Ab initio insights into the visible luminescent properties of ZnO"* Thin Sol. Films **515**, 8670-8673 (2007). **Pàgina 241**

15. M. Epifani, J.D. Prades, E. Comini, E. Pellicer, M. Avella, P. Siciliano, G. Faglia, A. Cirera, R. Scotti, F. Morazzoni, J.R. Morante, *"The role of surface oxygen vacancies in the NO_2 sensing properties of SnO_2 nanocrystals"* J. Phys. Chem. C **112**, 19540-19546 (2008). **Pàgina 245**

B.4 Objectius

Els principals objectius d'aquesta tesi doctoral es poden resumir de la següent manera:

1. Comprendre i modelitzar el funcionament dels sensors conductomètrics basats en nanofils individuals d'òxids metàl·lics. Aquí s'inclouen aplicacions tant en el camp dels sensors de gas com en el dels detectors de llum.

2. Aprofitar les característiques pròpies dels nanofils com ara la gran relació superfície-volum, l'alta qualitat cristal·logràfica, o l'estabilitat superficial per tenir accés a situacions experimentals ben definides i properes als models.

3. Avaluar, en quina mesura les anteriors característiques dels nanofils són avantatjoses en aplicacions de sensat de gas i de llum. Tanmateix, determinar quines altres propietats dels nanofils poden ser avantatjoses en el camps aquí tractats.

4. Explorar, en base als resultants anteriors, aproximacions alternatives quan a la manera d'operar els sensors basats en nanofils individuals i avaluar-ne les prestacions de cara a futures aplicacions.

B.5 Metodologia

En les tesis basades en un compendi d'articles, no es necessari incloure un capítol dedicat a les tècniques i metodologies emprades durant el doctorat. Per les raons que es detallen a continuació, l'abutor ha considerat convenient incloure la informació relativa a determinats mètodes teòrics i experimentals. Com es habitual, els detalls de la resta de les tècniques es donen en la secció experimental de cada article.

En primer lloc, el fet que durant aquest treball de doctorat s'hagin iniciat les activitats en càlculs *ab initio* al Departament d'Electrònica ha motivat l'autor a descriure en detall els fonaments teòrics i els aspectes de procedimentals del formalisme escollit: la Teoria del Funcional Densitat (DFT). Aquestes informació es presenta en forma d'un capítol de llibre. L'autor agraeix al Prof. P. Ugliengo la seva invitació a escriure aquest capítol, i espera que el seu contingut sigui especialment útil per a les activitats futures del grup en aquest àmbit.

En segon lloc, les activitats experimentals desenvolupades en aquest treball de doctorat van aprofitar l'amplia experiència del grup en la síntesi, caracterització, manipulació i fabricació de nanomaterials i nanodispositius. Els detalls d'aquesta experiència es resumeixen en un capítol de llibre que recull les activitats del grup. L'autor d'aquesta tesi agraeix al Prof. J.R. Morante, al Prof. A. Romano-Rodríguez, i la resta de co-autors la voluntat de compartir la seva experiència i encoratjar-lo a contribuir en aquest capítol.

En tercer lloc, a més de la resta de resultats científics presentats en aquesta tesi (*Capítol 4*), l'autor vol presentar la seva modesta contribució als avanços tecnològics i metodològics del grup. Per aquest motiu es presenta una plataforma electrònica que serveix d'interfície amb els dispositius basats en nanofils. Aquesta eina ha estat àmpliament utilitzada en el desenvolupament de les activitats experimentals que es presenten en aquesta tesi. Els detalls sobre la plataforma es presenten en un article científic que no es considerarà per l'avaluació del treball de l'autor (ja que va ser avaluat en la tesi doctoral d'un altre coautor). L'autor agraeix al Dr. F. Hernández-Ramírez, la seva amable invitació a participar en aquest treball.

Les publicacions associades que contenen la informació metodològica són les següents.

1. J.D. Prades, A. Cirera, J.R. Morante, *"Applications of DFT Calculations to Chemical Gas Sensors: Desing and Understanding"* in *"Quantum Chemical Calculations of Surfaces and Interfaces of Materials"* (Ed. V. A. Basiuk and P. Ugliengo), chap. 13, pp. 243-288, American Scientific Publishers: Valencia CA (2008).

2. T. Andreu, J. Arbiol, A. Cabot, A. Cirera, J.D. Prades, F. Hernandez-Ramirez, A. Romano-Rodriguez, J.R. Morante, *"Nanosensors: Controlling Transduction Mechanisms an the Nanoscale Using Metal Oxides and Semiconductors"* in *"Sensors Based on Nanostructured Materials"* (Ed. F. Arregui), chap. 5, pp. 79-129, Springer Science + Business Media (2009).

♣   F. Hernandez-Ramirez, J.D. Prades, A. Tarancon, S. Barth, O. Casals, R. Jimenez-Diaz, E. Pellicer, J. Rodriguez, M.A. Juli, A. Romano-Rodriguez, J.R. Morante, S. Mathur, A. Helwig, J. Spannhake, G. Mueller, *"Portable microsensors based on individual SnO_2 nanowires"* Nanotechnol. **18**, 495501 (2007).

Resum dels resultats més importants

- El desenvolupament de tecnologies avançades amb dispositius detectors de gas basats en òxids metàl·lics (MOXs) requereix la comprensió dels fenòmens físics i químics que ocorren en la interacció entre les molècules de gas i les superfícies dels MOXs. En primer lloc, això requereix la descripció detallada i la identificació de les superfícies més actives. En segon lloc, la morfologia dels materials detectors també és crucial per obtenir millors respostes. En tercer lloc, l'estudi de les interaccions específiques entre les molècules i les superfícies (identificades en les etapes anteriors) fa possible no només reproduir i comprendre els mecanismes de la transducció que es donen en aquests dispositius, sinó també proposar nous mètodes de treball per augmentar-ne el rendiment. Els càlculs *ab initio* poden proporcionar informació valuosa ens tots tres àmbits.

- Avui en dia, el desenvolupament de nous formalismes sobre la base de teories ben establertes com la teoria del funcional densitat (DFT), juntament amb les noves instal·lacions de computació intensiva estan obrint noves i emocionants possibilitats d'aplicar càlculs teòrics *ab inito* a camp eminentment aplicats com

el dels sensors de gas. Els punts anteriors justifiquen l'elecció d'eines DFT per realitzar l'estudi teòric de les interacció gas-MOX tal i com es descriu a la *Unitat 1.*

- En els darrers anys, els nanofils han sorgit com els blocs de construcció d'una nova generació de dispositius sensors. Aquests dispositius han demostrat tenir bones propietats, en especial en els camps del sensat químic i de llum. En el primer, les millores es deuen a l'alta superfície-volum i l'estabilitat superficial dels nanofils. En el segon camp, l'alta cristal·linitat dels nanofils dona lloc a excel·lents propietats de separació, col·lecció i confinament de càrrega. En conseqüència, l'estudi de les interaccions de la llum i el gas amb nanofils individuals resulta ser una eina òptima per comprendre els mecanismes de detecció. Els principals avenços aconseguits en els darrers anys en la síntesi, el control, la manipulació i l'accés elèctric a nanofils possibiliten els estudis aquí proposats.

- Al inici d'aquest treball de doctorat, encara existien importants dificultats en la caracterització elèctrica de nanofils individuals. La minúscula secció dels nanofils fa que siguin extremadament sensibles a la potencia Joule dissipada pel corrent que se'ls hi aplica. Aquesta potència dissipada és causa de degradació en aquests dispositius. En aquells moments, la potència dissipada en els nanofils només podia ser controlada amb costosos equips de laboratori. Aquest fet dificultava la utilització dels nanofils en futures aplicacions reals. La plataforma electrònica que aquí s'ha presentat ha permès demostrar que es possible operar aquests dispositius amb molt baix consum energètic i emprant components de baix cost. Aquesta plataforma s'ha utilitzat intensivament durant el desenvolupament d'aquest doctorat i ha permès realitzar bona part de les mesures.

B.6 Resultats i discussió

Aquest capítol conté els resultats i discussions més rellevants d'aquest treball. S'ha organitzat en 3 unitats, que corresponen a les diferents àrees desenvolupades per l'autor. En concret, aquestes tres unitats són les següents:

- *Unitat 1: Interacció gas - MOX*
- *Unitat 2: Interacció llum - MOX interacció*
- *Unitat 3: Interacció simultània gas - llum - MOX*

Les dues primeres corresponen a la modelització teòrica de dues interaccions, aparentment independents, en nanofils de MOX. De fet, la interacció gas-MOX sembla tenir lloc només al a superfície mentre que la llum-MOX sembla ser un fenomen exclusivament de volum. Els resultats que aquí es presenten varen demostrar que totes dues estan relacionades pels processos que tenen lloc vora la superfície dels nanofils. L'objectiu de la tercera unitat és il·lustrar la importància de la superfície en tot allò que té a veure amb els nanofils tot modelitzant la interacció simultània de gasos i llum amb nanofils de MOX.

B.6.1 Unitat 1: Interacció gas - MOX

La Unitat 1 està plenament dedicat a l'estudi dels processos químics que tenen lloc a la superfícies dels nanofils de MOX basant-se en càlculs ab initio (tal i com es descriu en el la secció *B.5*). Aquesta unitat està dividida en seccions relatives als càlculs atomístics, la seva validació experimental i la proposta d'alternatives quan a modes de funcionament i enfocaments teòrics.

Unitat 1.a   Simulació atomística amb mètodes ab initio

En primer lloc, s'han determinat les terminacions superficials i els llocs d'adsorció més rellevants a les temperatures de treball típiques dels MOXs. Això és important perquè la disposició dels àtoms d'oxigen en la superfície dels MOXs (això implica conceptes com els de vacant d'oxigen) varia a diferents temperatures i depèn de l'equilibri termodinàmic amb el contingut d'oxigen en l'aire. Posteriorment, la seva interacció amb alguns gasos rellevants va ser analitzada. Aquí, s'ha seleccionat el NO i el NO_2. Aquests gasos tòxics, que es produeixen en molts processos de combustió, són perillosos per a la salut humana. Per tant, des del punt de vista pràctic, aquests gasos són interessants en sensors de gas de

combustió i aplicacions de control i seguretat. A més a més, el fet que aquests gasos reaccionen a las superfícies de MOXs seguint processos de primer ordre fan d'aquest un problema especialment atractiu per començar amb els càlculs *ab initio*. Sorprenentment, al inici d'aquesta tesi, encara no s'havia publicat cap treball teòric relatiu a la interacció de NO i NO_2 amb les superfícies de SnO_2 i ZnO més rellevants [la (110) del primer i les no-polars (10-10) i (11-20) del segon]. Aquest fet augmenta l'interès de la recerca que aquí es presenta. Per completitud, els efectes de la interferència d'altres gasos com el SO_2 en la detecció de NO i NO_2 amb MOX també van ser estudiats. Des del punt de vista pràctic, el SO_2 és ben conegut perquè els enverina els sensors i fa que la seva resposta només es pugui recuperar amb tractaments tèrmics a elevades temperatures. Els resultats relatius al SnO_2 es presenten en dos articles científics (*Articles 3* i *4*) essent el segon la continuació i finalització del primer. El cas del ZnO s'analitza en l'*Article 5*. Les referències complertes a aquests documents són les següents:

3. J.D. Prades, A. Cirera, J.R. Morante, J.M. Pruneda, P. Ordejón, *"Ab initio study of NOx compounds adsorption on SnO₂ surface"* Sens. Actuators B-Chemical **126**, 99-110 (2007).

4. J.D. Prades, A. Cirera, J.R. Morante, *"First-Principles Study of NOx and SO₂ Adsorption onto SnO₂(110)"* J. Electrochem. Soc. **154**, H675-H680 (2007).

5. J.D. Prades, A. Cirera, J.R. Morante, *"Ab initio calculations of NO₂ and SO₂ chemisorption onto non-polar ZnO surfaces"* Thin Sol. Films, submitted (2008).

Resum dels resultats més importants

- L'estudi *ab initio* de l'estabilitat superficial del SnO_2-cassiterita va revelar que la orientació superficial més rellevant i més abundant és la (110), en correspondència amb les evidències experimentals (*Articles 3* i *4*). Per tant, els estudis posteriors es varen centrar en aquesta faceta.

- Per tal de modelitzar ordenacions atòmiques realistes, s'ha explorat la rellevància de diferents arranjaments atòmics superficials mitjançant tècniques de termodinàmica *ab initio*. A temperatura ambient, la superfície estequiomètrica és la configuració més estable. Quan la temperatura s'eleva per sobre de 270°C, es poden formar vacants O_{Bridg} i a temperatures encara més altes (per sobre de 480ºC) la formació de vacants $O_{InPlane}$ és la dominant. A temperatures superiors

a 640ºC configuracions multivacants són les més probables (*Articles 3* i *4*). Aquestes prediccions teòriques (que estan d'acord amb anteriors resultats experimentals), indiquen que les superfícies parcialment reduïdes s'han de tenir en compte de cara a la modelització de les interaccions amb gas.

- Com a conseqüència dels resultats anteriors, les superfícies amb vacants d'oxigen varen ser incloses en el model de la interacció de NO, NO_2 i SO_2 amb la $SnO_2(110)$. Aquests càlculs indiquen que:

  - El NO s'adsorbeix als oxigens de superfícies estequiomètriques.

  - El NO_2 fonamentalment interactua amb les vacants d'oxigen (superfícies reduïdes).

  - El SO_2 competeix amb el NO_2 pels mateixos llocs d'adsorció i és més difícil de desorbir tèrmicament.

  Aquests resultats són compatibles amb el caràcter oxidant/reductor dels gasos anteriors i pot explicar els efectes d'enveriment. D'altra banda, la comparació de les energies de desorció obtingudes per tots els processos estudiats estan en consonància amb els resultats d'experiments de TPD (*Articles 3* i *4*).

- Quan al ZnO, s'han obtingut resultats similars: les superfícies més estables són les no polars (10-10) i (11-20) en la fase wurtzita, cal considerar el paper de les vacants d'oxigen superficials i el NO_2 interactua preferentment amb els llocs metàl·lics (llocs vacants d'oxigen) competint amb el SO_2 (*Article 5*).

Unitat 1.b   Validació experimental - Nous mètodes de detecció en la nanoescala

Per a validar part dels resultats presentats a la *Unitat 1.a*, es va mesurar la resposta conductomètrica al NO_2 en nanofils individuals de SnO_2 (*Article 6*) . En primer lloc, aquest resultat va servir per identificar els llocs d'adsorció que participen en la resposta a aquests gasos. En segon lloc, els reptes tècnics que va caldre superar per realitzar aquestes mesures varen inspirar un nou mètode per escalfar el material sensor. L'*Article 6* demostra que el corrent aplicat al nanofil amb l'objectiu de mesurar-ne la conductivitat pot ser emprat per escalfar el nanofil fins a les temperatures de treball òptimes per detectar gasos. Com s'explica en l'article, aquest resultat representa no només un extraordinari pas endavant en la miniaturització de sensors, sinó també una dràstica

reducció de la potència necessària per fer-los funcionar. A més d'això, la disponibilitat de microcalefactors integrats en els substrats utilitzats va fer possible mesurar la temperatura assolida pel nanofil mitjançant l'autoescalfament (*Articles 6* i *7*). Les referències complertes a aquests dos documents són les següents:

6.   J.D. Prades, R. Jimenez-Diaz, F. Hernandez-Ramirez, S. Barth, A. Cirera, A. Romano-Rodriguez, S. Mathur, J.R. Morante, *"Ultralow power consumption gas sensors based on self-heated individual nanowires"* Appl. Phys. Lett. **93**, 123110 (2008).

7.   J.D. Prades, R. Jimenez-Diaz, F. Hernandez-Ramirez, A. Cirera, A. Romano-Rodriguez, J.R. Morante, S. Barth, P. Jun, S. Mathur, *"An experimental method to estimate of the temperature of individual nanowires"* Int. J. Nanotechnol., accepted for publication (2008).

Resum dels resultats més importants

- L'estudi amb microcalefactors i nanofils individuals ha revelat que la resposta a NO_2 òptima s'obté a temperatures entorn a T~175ºC i que això correspon a interaccions a llocs d'interacció $O_{InPlane}$ de la superfície (110) de l'SnO_2 (d'acord amb les simulacions dels espectres de TPD) (*Article 6*). Càlculs DFT específics han permès confirmar això: la càrrega capturada per el NO_2 adsorbit en els llocs $O_{InPlane}$ és més gran que en qualsevol altre lloc dels estudiats (vegeu l'*Article 15* per a més detalls).

- S'ha aconseguit també reproduir les respostes a NO_2 obtingudes amb microcalefactors simplement emprant l'efecte d'autoescalfament. Com ja s'ha presentat (*Article* ♣), el dispositiu experimental emprat permet controlar el corrent aplicat als nanofil i, per tant, modular la magnitud de l'autoescalfament fins a temperatures pròximes a 350ºC (Article 6). A més dels enormes progressos en termes de miniaturització, aquest nou enfocament redueix dràsticament la potència necessària per fer funcionar aquests sensors a unes quantes desenes de microwatts. Aquest resultat obre la porta a una nova generació de dispositius sensors de gas de ultrabaix consum.

- Una altra conseqüència de l'anterior resultat va ser la proposta d'un mètode experimental innovador per estimar la temperatura a escala de nanofils.

Aquest es basa en la comparació de la resposta dinàmica dels nanofils a gasos tot fent-los funcionar amb microcalefactors o amb autoescalfament (Article 7).

Unitat 1.c   Sobre la relació entre les vacants d'oxigen superficial i de volum

D'una banda, els càlculs presentats a la *Unitat 1.a*, demostren l'important paper que exerceix la presència de vacants d'oxigen en la superfície dels MOXs en la seva resposta a gasos. D'altra banda, els MOXs són materials semiconductors que presenten dopatge intrínsec degut a l'abundància de defectes puntuals relacionats amb els àtoms d'oxigen. Per tant, una simple qüestió era si hi ha alguna relació entre els defectes d'oxigen del interior del material i els defectes a la superfície (vacants)? Mesures experimentals de les derives a llarg termini de la conductància tant en nanofils de SnO_2 com de ZnO en canviar abruptament el contingut d'oxigen ambiental suggereixen que la difusió d'àtoms d'oxigen a traves del interior dels nanofils de MOX és factible. En aquesta secció, es mostra com la descripció dels fenòmens de sensat, que sovint es centra només en la superfície del material, pot ser complementada tenint en compte altres efectes que ocorren en el seu interior. Tots aquests resultats es presenten en l'*Article 8*.

8.   F. Hernandez-Ramirez, J.D. Prades, A. Tarancon, S. Barth, O. Casals, R. Jimenez-Diaz, E. Pellicer, J. Rodriguez, J.R. Morante, M.A. Juli, S. Mathur, A. Romano-Rodriguez, *"Insight into the role of oxygen difussion into the sensing mechanisms of SnO_2 nanowires"* Adv. Funct. Mater. **18**, 2990-2994 (2008).

Resum dels resultats més importants

- Les derives a llarg termini en la conductivitat de nanofils de MOX a causa de canvis sobtats en la concertació d'oxigen depenen del seu radi. Aquest fet, i la resta d'evidències experimentals, són compatibles amb processos de difusió d'oxigen a d'interior dels nanofils. S'ha demostrat que aquests efectes de difusió són importants fins i tot a temperatura ambient, i per tant, cal tenir-los en compte quan es discuteixen els mecanismes que fan possible la detecció de gasos amb MOXs (*Article 8*).

B.6.2 Unitat 2: Interacció llum - MOX

La *Unitat 2* està plenament dedicada a l'estudi de les interaccions fotó - MOX en base a les propietats de transport en semiconductors. La unitat està dividida en seccions sobre l'anàlisi crítica de les possibilitats dels nanofils individuals en aplicacions de detecció de llum i l'estudi i modelització dels fenòmens que en limiten la resposta dinàmica.

Unitat 2.a   Comprenent els fotodetectors basats en nanofils

L'oportunitat d'utilitzar un únic nanofil semiconductor de gap ample per a la detecció de llum ultraviolada és atractiva tant des del punt de vista tècnic com fonamental. La qualitat cristal·lina dels nanofils resulta una situació ideal per investigar fenòmens de fotoresposta elèctrica. En aquesta secció, s'estudia la resposta de fotoconductors basats en nanofils de ZnO i SnO2. En particular, es presenta un anàlisi exhaustiu dels factors que influeixen en aquesta resposta així com dels principals problemes que presenta. Tots aquests resultats es presenten en l'*Article 9.*

9.   J.D. Prades, R. Jimenez-Diaz, F. Hernandez-Ramirez, L. Fernandez-Romero, T. Andreu, A. Cirera, A. Romano-Rodriguez, A. Cornet, J.R. Morante, S. Barth, S. Mathur, *"Toward a systematic understanding of photodetectors based on individual metal oxide nanowires"* J. Phys. Chem. C **112**, 14639-14644 (2008).

Resum dels resultats més importants

- Els factors que determinen la resposta dels dispositius fotoconductors basats en nanofils individuals han estat identificats usant els principis generals que regeixen la generació de parells de càrrega i el transport en semiconductors (*Article 9*). Les estratègies per controlar-los que aquí es proposen s'han validat amb dispositius fets a mida

  - En primer lloc, s'ha demostrat que la geometria del dispositiu és important: el disseny òptim correspon a nanofils gruixuts i distàncies entre elèctrodes molt curtes. Això és un reflex del fet que la interacció fotons-MOX és un fenomen principalment de volum.

  - En segon lloc, s'ha demostrat que el rendiment d'aquests dispositius depèn en gran mesura de les condicions de treball (en essència, la tensió

aplicada i la densitat de fotons). Amb l'objectiu de superar la manca de sistemàtica en els estudis fets fins ara en aquest camp, s'ha presentat una rigorosa metodologia per comparar els diferents dispositius.

- En tercer lloc, les propietats semiconductores dels nanofils són ben diferents dels les propietats dels materials més extensos. En concret, la mobilitat és menor i la vida mitja dels portadors és major. La primera empitjora el transport d'electrons en els nanofils mentre que el segon en millora la fotoresposta (fins a 3 ordres de magnitud respecte a altres tecnologies). Tanmateix, aquesta millora en la magnitud de la resposta n'empitjora la dinàmica. Ambdós efectes estan relacionats amb els fenòmens de superfície: la mobilitat es veu reduïda per les múltiples col·lisions i dispersions que pateixen els electrons amb els estats de superfície dels nanofils (ja que són més accessibles a causa de la gran superfície-volum) i la vida mitja dels portadors augmenta a causa del potencial de deplexió vora la superfície dels nanofils que separa els parell electró-forat i n'obstaculitza la recombinació.

Unitat 2.b   Comprenent els estats de fotoconductivitat persistent

L'anàlisi presentat a la secció anterior va posar de relleu la pobre resposta dinàmica a la llum dels nanofils de MOX i en va determinar preliminarment la causa: els processos de separació l'electró-forat que tenen lloc prop de la superfície dels nanofils. En aquesta secció, els problemes relatius a la persistència a llarg termini de la fotoconductivitat en nanofils de MOX es presenten en detall i s'elabora un model basat en part en els resultats de la *Unitat 1*. Diverses estratègies per minimitzar aquest efecte no desitjat es proposen i demostren en l'*Article 10*.

10.   J.D. Prades, F. Hernandez-Ramirez, R. Jimenez-Diaz, M. Manzanares, T. Andreu, A. Cirera, A. Romano-Rodriguez, J.R. Morante, *"The effects of electron-hole separation on the photoconductivity of individual metal oxide nanowires"*, Nanotechnol. **19**, 465501 (2008).

Resum dels resultats més importants

- L'augment del temps de vida mitja dels portadors en els nanofils de MOXs pot arribar a donar lloc a situacions de fotoconductivitat persistent (PPC). Sota certes condicions experimentals, aquests efectes són especialment dramàtics, podent arribar a durar hores, i poden arruïnar la utilitat d'aquests materials com fotodetectors. No obstant això, aquesta situació és extremadament útil per obtenir una informació més profunda sobre el paper que juga la superfície en el transport elèctric en nanofils (*Article 10*).

- La dependència de la PPC amb la temperatura a la que es troba el nanofil i la composició de l'atmosfera que l'envolta queda plenament explicada pel següent model (*Article 10*). Sota il·luminació UV, el potencial proper a la superfície dels nanofils de MOX indueix la separació dels parell electró-forat, acumulant els segons a la superfície del material. Una vegada que la llum s'apaga, els forats acumulats necessiten trobar-se amb els electrons per recombinar-se i ser drenats. Si aquests camins no estan disponibles apareix la PPC. Es va observar experimentalment que la recuperació de la PPC esta associada a un augment de la temperatura del nanofil o a l'exposició a una atmosfera rica en oxigen. El primer permet l'aproximació de les poblacions d'electrons i forats deguda a l'augment de l'energia dels portadors lliures i el segon proporciona vies de recombinació addicionals mediades pels oxigens quimiadsorbits.

- Així doncs, els efectes de la PPC es poden bloquejar completament simplement escalfant els nanofils o bé passivant-ne els estats de superfície (*Article 10*). Per exemple, els recobriments amb PMMA bloquejen la PPC i milloren la mobilitat en els nanofils. D'aquesta manera s'ha superat una de les principals limitacions per emprar nanofils de ZnO (i d'altres òxids metàl·lics) com a fotodetectors.

- Els resultats obtingut fins al moment (*Unitats 1* i *2*) van posar de manifest una estreta relació entre les interaccions del gas i de la llum amb els nanofils. Això es degut a la importancia de la superfície en aquests materials. Aquest fet va estimular l'autor a treballar en la modelització de la seva interacció combinada. Aquests resultats es presenten en la unitat següent.

B.6.3 Unitat 3: Interacció simultània gas - llum - MOX

La *Unitat 3* es dedica a l'estudi de les interaccions combinades de molècules, fotons i òxids metàl·lics (MOX) en base als conceptes desenvolupats en les dues unitats anteriors. La unitat està dividida en dues seccions. La primera es refereix a la atractiva possibilitat de detectar gasos tot fotoactivant els òxids metàl·lics. La segona està dedicada a l'anàlisi de la luminescència provinent dels MOXs i la seva relació amb els llocs d'adsorció de gasos oxidants.

Unitat 3.a   Detecció de molècules oxidants mitjançant fotoactivació

La irradiació amb llum ultraviolada fa possible la detecció de molècules gasoses tot mesurant la conductivitat d'òxids metàl·lics a temperatura ambient. Malgrat les atractives possibilitats que ofereix aquest mètode de detecció, es sap ben poc sobre el mecanismes que activa la presència dels fotons. En aquesta secció, els efectes de les condicions d'il·luminació (és a dir: el flux i la energia dels fotons) sobre la resposta als gasos de nanofils de SnO_2 són estudiats en detall (*Article 11*). Combinant aquests resultats experimentals amb les conclusions teòriques anteriors sobre la interacció de NO_2 amb SnO_2 (*Unitat 1*), es postula un model que explica quantitativament aquest fenomen (*Article 12*).

11.   J.D. Prades, R. Jimenez-Diaz, F. Hernandez-Ramirez, S. Barth, J. Pan, A. Cirera, A. Romano-Rodriguez, S. Mathur, J.R. Morante*, "High performance UV light-operated gas sensors based on individual SnO2 nanowires for room temperature applications"* Appl. Phys. Lett., submitted (2008).

12.   J.D. Prades, R. Jimenez-Diaz, F. Hernandez-Ramirez, M. Manzanares, T. Fischer, J. Pan, T. Andreu, A. Cirera, A. Romano-Rodriguez, S. Mathur, J.R. Morante, *"On the Role of the Illumination Conditions in the Performance of Room Temperature Gas Sensors Based on Individual SnO2 Nanowires"* Chem. Mater., submitted (2008).

Resum dels resultats més importants

- Els resultats presentats en l'*Article 11* demostren que la il·luminació UV de nanofils d'òxid d'estany es pot utilitzar per a millorar-ne la resposta cap a espècies gasoses oxidants, com el NO_2, a temperatura ambient. A més d'això, aquest treball va revelar que el rendiment final d'aquests dispositius està fortament

influït pel flux i la energia dels fotons que hi incideixen. En les condicions adequades d'il·luminació, es poden obtenir respostes comparables a les de dispositius calefactats convencionals. Aquest resultat obre la porta al desenvolupament de sensors de gas conductomètrics que operin a temperatura ambient amb una sèrie d'avantatges, per exemple, en aplicacions en entorns explosius. L'anàlisi de la potència necessària per fer funcionar aquests dispositius amb díodes emissors de llum (LED) indiquen que és comparable als requisits de potència del microcalefactors.

- El fet que la llum indueix una recuperació de la línia de base després de l'exposició al NO_2, suggereixen que els fotons juguen un paper important en la desorció de molècules de NO_2, probablement a través de parells fotogenerats banda-banda. Tanmateix, per explicar l'augment en la resposta, altres efectes s'han de tenir en compte, com la competència amb altres molècules presents durant les mesures (com ara l'oxigen en l'aire). Aquestes hipòtesis són compatibles amb els resultats sobre la interacció de l'NO_2 amb la superfície del SnO_2 presentats en la *Unitat 1.a*.

- El model que aquí es presenta es basa en la competència entre les molècules d'oxigen en l'aire i els gasos oxidants (com NO_2) pels mateixos llocs d'adsorció (*Article 12*). L'acord quantitatiu amb els experiments, ha demostrat que és possible ajustar el balanç d'adsorció i desorció controlant el flux de fotons i així ajustar la resposta al gas. Tot plegat, explica el paper dels fotons en aquest tipus de sensors i facilita la tasca de desenvolupar sensors conductomètrics de baix consum operats a temperatura ambient. Des del punt de vista fonamental, aquesta troballa va més enllà de la descripció d'aquest fenomen, vaga i qualitativa, que es pot trobar a la literatura.

Unitat 3.b Detecció de les vacants d'oxigen superficials mitjançant luminescència.

Després de confirmar el paper clau de les vacants d'oxigen superficials en la detecció de gasos amb MOXs (*Unitat 1* i *Unitat 3.a*), es va treballar en un procediment experimental per determinar-ne la presència. En aquesta secció, els nivell energètics dins la banda prohibida que introdueixen les vacants d'oxigen superficials es correlacionen amb la luminescència del SnO_2 i el ZnO (*Article 13* i *Article 14*). Aquest mètode experimental

permet conèixer l'acabat superficial dels MOX (*Article 13* i *Article 14*) i pot ser utilitzat per predir-ne el funcionament com a sensors (*Article 15*).

13. J.D. Prades, J. Arbiol, A. Cirera, J.R. Morante, M. Avella, L. Zanotti, E. Comini, G. Faglia, G. Sberveglieri, *"Defect study of SnO_2 nanostructures by cathodoluminescence analysis: Application to nanowires"* Sens. Actuators B-Chemical **126**, 6-12 (2007).

14. J.D. Prades, A. Cirera, J.R. Morante, A. Cornet, *"Ab initio insights into the visible luminescent properties of ZnO"* Thin Sol. Films **515**, 8670-8673 (2007).

15. M. Epifani, J.D. Prades, E. Comini, E. Pellicer, M. Avella, P. Siciliano, G. Faglia, A. Cirera, R. Scotti, F. Morazzoni, J.R. Morante, *"The role of surface oxygen vacancies in the NO_2 sensing properties of SnO_2 nanocrystals"* J. Phys. Chem. C **112**, 19540-19546 (2008).

Resum dels resultats més importants

- Els resultats presentats fins ara tenen en comú el important paper que juga la disposició dels àtoms d'oxigen en la superfície dels nanofils de MOXs, i especialment, les vacants d'oxigen superficials. L'estudi mitjançat mètodes *ab initio* dels estats electrònics associats a aquestes vacants indica que són compatibles a les recombinacions radiatives que donen lloc a la luminescència visible dels MOXs.

- Els càlculs demostren que la posició enèrgica d'aquests nivells depèn de la geometria de les vacants d'oxigen i, per tant, les diferents bandes de la luminescència es deuen, necessàriament, a diferents geometries de les vacants. Això s'ha confirmat amb diferents MOXs com el SnO_2 (*Article 13*) i el ZnO (*Article 14*) i amb sèries de mostres independents i tractades de forma diferent. Recentment, els nostres resultats estan essent recolzats per altres autors que estan arribant a conclusions similars [a,b,c].

- La utilitat d'aquesta eina experimental per analitzar l'acabament superficial dels MOXs i predir-ne el rendiment com a detectors de gas també ha estat demostrada. La resposta de nanopartícules de SnO_2 s'ha millorat mitjançant tractaments tèrmics que han introduït vacants d'oxigen (*Article 15*). L'anàlisi de la luminescència ha permès realitzar el seguiment de la generació de

diferents tipus de vacants. Tots els passos d'aquest procés varen ser guiats pels resultats teòrics presentats en els apartats anteriors i son un bon exemple de com escometre el disseny *in silico* de materials funcionals.

[a] N. L. Marana, V. M. Longo, E. Longo, J. B. L. Martins, J. R.Sambrano, *"Electronic and structural properties of the (10-10) and (11-20) ZnO surfaces"* J. Phys. Chem. A **112**, 8958-8963 (2008).

[b] C. Ton-That, M. R. Phillips, M. Foley, S. J. Moody, A. P. J. Stampfl, *"Surface electronic properties of ZnO nanoparticles"* Appl. Phys. Lett. **92**, 261916 (2008).

[c] Z. Q. Fang, B. Claflin, D. C. Look, "Effects of annealing in N_2 ambient on traps and persistent conduction in hydrothermally grown ZnO" J. Appl. Phys. **103**, 073714 (2008).

B.7 Conclusions

Aquestes són les principals conclusions d'aquesta tesi doctoral:

1. S'han modelitzat les interacció de molècules gasoses i llum amb òxids metàl·lics emprant, respectivament, els formalismes *ab initio* DFT i les lleis de transport, generació i recombinació de càrregues en semiconductors.

   1.a En el camp dels sensors de gas, s'ha aprofundit en les interaccions amb gasos d'interès teòric i pràctic com el NO, el NO_2 i el SO_2. S'han determinat els mecanismes que donen origen a la resposta conductomètrica envers a aquests gasos, s'han proposat maneres de millorar-la i mètodes experimentals basats en l'anàlisi de la luminescència per avaluar la influencia de la superfície del nanofil en la seva resposta a gasos. Tanmateix, s'ha demostrat que per assolir una modelització complerta de les interaccions entre gasos i òxids metal·lis cal tenir en compte altres efectes que van més enllà de la mera interacció superficial.

   1.b En el camp dels sensors de llum ultraviolada, s'han identificat els paràmetres que determinen la magnitud de la fotoresposta en nanofils així com els que en limiten la seva dinàmica. Això ha permès analitzar en detall els estats de fotoconductivitat persistent en nanofils individuals.

Tot plegat a permès aprofundir en la comprensió del funcionament d'aquests dispositius.

2. S'han desenvolupat eines experimentals i dispositius per poder accedir a la resposta conductomètrica de nanofils individuals d'òxids metàl·lics en experiments dissenyats específicament. La disponibilitat d'aquest escenari avantajós ha permès validar bona part de les conclusions i prediccions dels anteriors models.

3. Quan a la influència de les característiques pròpies dels nanofils en aplicacions de sensat, s'ha observat el següent.

   3.a D'una banda, que la gran relació superfície volum i l'estabilitat superficial pròpies dels nanofils són profitoses per a la detecció de gasos. La primera proporciona majors respostes en reduir el gruix dels nanofils mentre que la segona en millora l'estabilitat i la reversibilitat.

   3.b D'altra banda, que si bé la qualitat cristal·logràfica dels nanofils pot millorar-ne les propietats de transport elèctric i de fotogeneració de parells electró-forat, la importància dels efectes de superfície limiten aquesta possibilitat. En primer lloc, la mobilitat dels nanofils empitjora per la influencia de la superfície. En segon lloc, els camps elèctrics associats a la deplexió propera a la superfície (i que expliquen la bona resposta a gasos d'aquests materials) introdueixen fenòmens addicionals de separació de càrrega que interfereixen en la fotoresposta. No obstant això, s'han proposat i validat estratègies (com el passivat superficial amb PMMA) que redueixen els efectes de superfície i milloren les propietats dels nanofils com a fotodetectors.

   Tot plegat mostra que l'aprofitament de les propietats *a priori* avantatjoses que presenten els nanofils no és immediat i que, per fer-ho, cal avançar en la comprensió dels fenòmens que s'hi donen.

4. A partir dels resultats anteriors, s'han ideat, implementat i testat mètodes d'operació alternatius que treuen partit de les particulars característiques dels nanofils.

   4.a S'ha provat que es possible emprar fluxos controlats de llum ultravioleta per activar, a temperatura ambient, la resposta conductomètrica a gasos

oxidants com l'NO$_2$ en nanofils individuals. Tanmateix, s'ha proposat un model pel seu funcionament que permès determinar-ne les condicions òptimes de treball. Aquest resultat obre les portes al desenvolupament de sensors de gas que operin a temperatura ambient i puguin ser adequats per atmosferes explosives.

4.b S'ha demostrat que és possible treure partit de l'efecte d'autoescalfament Joule degut a la minúscula secció transversal dels nanofils. De forma controlada, aquest efecte permet escalfar els nanofils a temperatures de treball òptimes per a la detecció de gasos (fins a uns 350ºC) dissipant potències de tan sols desenes de microwatts. Això suposa no només un gran avenç quan a miniaturització de sensors (ja que no es necessari incloure un calefactor extern) sinó que suposa una reducció enorme de la potencia necessària per fer funcionar aquests sensors.

Tots aquests resultants obren les portes i aplanen el camí cap a una nova generació de dispositius sensors basats en les novedoses i prometedores propietats dels nanofils.

B.8 Referències

[1] S. Maekawa, T. Tohyama, S.E. Barnes, S. Ishihara, W. Koshibae, G. Khaliullin, *"Physics of Transition Metal Oxides"*, Springer Series in Solid-State Sciences, vol. 144 (2004).

[2] J.L.G. Fierro, "*Metal Oxides: Chemistry and Applications"*, CRC Press: Boca Raton FL (2006).

[3] D.M. Smyth, *"The Defect Chemistry of Metal Oxides"*, Oxford University Press: Oxford (2000).

[4] V.E. Henrich, P.A. Cox, *"The Surface Science Of Metal Oxides"*, Cambridge University Press: Cambridge (1996).

[5] E.H. Nicollian, J. R. Brews *"MOS (Metal Oxide Semiconductor) Physics and Technology"*, John Wiley & Sons: New Jersey (1982).

[6] Ü. Özgür, Y. I. Alivov, C. Liu, A. Teke, M. A. Reshchikov, S. Dogan, V. Avrutin, S.-J. Cho, H. Morkoç, *"A comprehensive review of ZnO materials and devices"* J. Appl. Phys. **98**, 041301 (2005).

[7]   M. Batzill, U. Diebold, *"The surface and materials science of tin oxide"* Prog. Surf. Sci. **79**, 47-154 (2005).

[8]   Z.L. Wang, *"Zinc oxide nanostructures: growth, properties and applications"* J. Phys.: Condens. Matter **16**, R829-R858 (2004).

[9]   S. Mathur, S. Barth, H. Shen, J.-C. Pyun, U. Werner, *"Size-Dependent Photoconductance in SnO₂ Nanowires"* Small **1**, 713-717 (2005). (b) S. Mathur, S. Barth, *"Molecule-Based Chemical Vapor Growth of Aligned SnO₂ Nanowires and Branched SnO₂/V₂O₅ Heterostructures"* Small **3**, 2070-2075 (2007).

[10] F. Hernandez-Ramirez, A. Tarancon, O. Casals, E. Pellicer, J. Rodríguez, A. Romano-Rodriguez, J.R. Morante, S. Barth, S. Mathur, *"Electrical properties of individual tin oxide nanowires contacted to platinum electrodes"* Phys. Rev. B. **76**, 085429 (2007).

[11] F. Hernandez-Ramirez, J.D. Prades, A. Tarancon, S. Barth, O. Casals, R. Jimenez-Diaz, E. Pellicer, J. Rodriguez, M.A. Juli, A. Romano-Rodriguez, J.R. Morante, S. Mathur, A. Helwig, J. Spannhake, G. Mueller, *"Portable microsensors based on individual SnO₂ nanowires"* Nanotechnol. **18**, 495501 (2007).

[12] See any scientific paper published in the *Journal of Computer-Aided Materials Design* (Springer).

[13] D. Neamen, *"Semiconductor Physics And Devices",* McGraw-Hill: New York (2003).

[14] N. Levine, *"Quantum Chemistry"*, Prentice Hall, Upper Saddle River NJ (1999).

[15] M. Law, J. Goldberger, P. Yang, *"Semiconductor nanowires and nanotubes"* Annu. Rev. Mater. Res. **34**, 83-122 (2004).

[16] H.J. Fan, P. Werner, M. Zacharias, *"Semiconductor Nanowires: From Self-Organization to Patterned Growth"* Small **2**, 700-717 (2006).

[17] F. Hernandez-Ramirez, A. Tarancon, O. Casals, J. Rodríguez, A. Romano-Rodriguez, J.R. Morante, S. Barth, S. Mathur, T.Y. Choi, D. Poulikakos, V. Callegari, P.M. Nellen, *"Fabrication and electrical characterization of circuits based on individual tin oxide nanowires"* Nanotechnol. **17**, 5577-5583 (2006).

[18] Z. Tang, P. Sheng, *"Nanoscale Phenomena: Basic Science to Device Applications"* Springer Series: Lecture Notes in Nanoscale Science and Technology, vol. **2** (2008).

[19] S. Luryi, J, Xu, A, Zaslavsky, *"Future Trends in Microelectronics: The Nano Millennium"*, John Wiley & Sons: New Jersey (2002).

[20] S. Kumar, S. Rajamaran, R.A. Gerhardt, Z.L. Wang, P.J. Hesketh, *"Tin oxide nanosensor fabrication using AC dielectrophoretic manipulation of nanobelts"* Electrochimica Acta, **51**, 943-951 (2005).

[21] G. Eranna, B.C. Joshi, D.P. Runthala, R.P. Gupta, *"Oxide Materials for Development of Integrated Gas Sensors - A Comprehensive Review"* Critic. Rev. Sol. State Mater. Sci. **29**, 111-188 (2004).

[22] F. Hernández-Ramírez, A. Tarancón, O. Casals, J. Arbiol, A. Romano-Rodríguez, J.R. Morante, *"High response and stability in CO and humidity measures using a single SnO₂ nanowire"* Sens. Actuators B: Chem. **121**, 3-17 (2007).

[23] C. Soci, A. Zhang, B. Xiang, S. A. Dayeh, D.P.R. Aplin, J. Park, X.Y. Bao, Y.H. Lo, D. Wang, *"ZnO Nanowire UV Photodetectors with High Internal Gain"* Nano Lett. **7**, 1003-1009 (2007).